Università degli Studi di Roma "La Sapienza"

Scuola di Ingegneria Aerospaziale

Corso di Laurea Speciale in Ingegneria Astronautica

PROGETTO PER L'ASSEMBLAGGIO DI UNA BASE LUNARE MOBILE - MODULARE – ESPANDIBILE

Lunar Expandable-Mobile-Modular Base (LEMMB)

Laureando:
Dott. Ing. Davide Micheli

Relatore:
Prof. Ing. Mario Marchetti

Correlatore:
Prof. Ing. Graziano Cerri

Index

Introduction

This work speaks about the possibility to build a Lunar Base Habitat.
Some of the technologies proposed are not completely yet available they are in developing state.

Many aspects have been covered, from the type of launcher which mainly dictates the masses, dimensions constraints; to the use of inflatable structures which could be adopted to increase the habitat volume while contemporary decreasing the total habitat mass.
Others important aspects analyzed are a new approach to the Micro Meteoroids shielding system and a new method for the Galactic Cosmic Radiation protection system.
This work does not cover problems like Air, Water and Food on the Moon.
LANDER (required to transfer the Moon Base Modules form lunar orbit to lunar surface), are considered and analyzed, only from mass and engine type points of view, the design of LANDER it is not object of this work.

Chapter 1

Describe many Moon Base projects and many of the ideas freely available on the Internet. It also speaks about the problems concerning Sun Light availability, potential Water availability and consequently about the best possible area to build a Lunar Base. At the end of the chapter one the Moon Quakes phenomena are shown too.

Chapter 2

The basic ideas of the Moon Habitat Modules, in this thesis developed, are presented In this chapter. The main constraints which have been adopted in order to design the Moon Habitat Modules are also shwon.
Problems like Mass, Volume, Moon Base Safety during landing of the resting Modules, Module's Inflatable Connection Structures, Solar Array, Mobile Equipment of each Module, Potential Space Vehicle requred to transport these Moon Modules from Earth to the Moon, are analyzed.
The main focus in this chapter is to describe the so called LEMMB (Lunar-Expandable-Mobile-Modular-Base) and, all the main phases required to connect several LEMMBs to each other in order to build a large Moon Habitat.
This chapter reports the main characteristics of LEMMB and tray to explain how the dimensions are compliant to those of Ariane 5 and Soyuz Space Vehicle usable internal firing volume.

Chapter 3

This chapter describes the LEMMB structures and materials, the inflatable structures with relative supports, a new approach to the MM/OD (Micro Meteoroid / Orbital Debris) protections system, and contemporary speaks about a passive shielding system against Galactic Cosmic Rays. This passive shielding could be made by polyethylene which similar to the liquid Hydrogen presents a high ionizing radiation absorption behavior.
The idea of new approach for the MM/OD (Micro Meteoroid / Orbital Debris) protections system is an applications of recent studies made in the Department of Mechanical and Aerospace Engineering, University of California at San Diego, La Jolla, California.
This publication reports the first experimental observation of impulse confinement and the disintegration of shock and solitary waves in one-dimensional strongly nonlinear composite granular materials.

In order understand the phenomena; I have made some assumptions about momentum transfer which are not completely verified in the strongly non linear real system. This assumption simplifies the mathematical model and can help us to understand one of the most processes which contribute to the shock disintegration effect.
The most part of the considerations about LEMMB are discussed here taking into account LEMMB mass constraint which mainly depends on cost of launch and available launcher.
Almost all the pictures have been created by using Autocad 2008.

Chapter 4

This chapter is focused on a possible European Launcher to be used in order to bring up the LEMMB modules from Earth onto Low Lunar Orbit.
Since the total mass of LEMMB plus LANDER should be about 23 tons, the today's version of Ariane 5 can not be used, in fact it can transport maximum a mass of 3.2 tons on a typical lunar orbit.
Recent studies on a new generation of the Ariane launcher called "Ariane Heavy Lift", show the possibility to bring up, on Low Lunar Orbit, a payload mass up to about 40 tons.
Starting from the Ariane 5 usable internal firing volume, it has been defined the dimensions of the LEMMB modules. These dimensions are compliant with Soyuz internal firing volume too.
In order to have an idea of the velocity impulse required to complete a lunar mission, some computations have been performed using Hohmann transfer as a typical transfer method. The results have been compared to those obtained using other typical literature methods like Patched Conic approach. The obtained final values are similar and are also close to the values on literature available.
At the end of chapter some considerations on LANDER engine type and on the LANDER propellant mass have been done.
These considerations starts taking into account Tsiolkovsky equations, storable type of propellant used and, LEMMB plus LANEDR structures and payload total mass.

All off these considerations have the purpose to find the propellant mass of LANDER and consequently the total mass of LEMMB plus LANDER. This total mass of about 23 tons is the mass to be considered as a useful payload in order to choose the best Launcher Space Vehicle.

Chapter 5

This chapter tries to cover the electrical power generation problems. Solar energy could be used by adopting Photovoltaic Solar Arrays.
In order to understand which type of solar array could be used, an extensive analysis of the today's solar array market has been done.
This analysis has taken into account that in the space the most important aspect, are high efficiency, light weight and space environment resistance. Costs of solar cells are not the main driver in space applications.
Thin film amorphous silicon solar cell could be used because they are very tin but their efficiency is lower than single crystalline solar cell. Since the efficiency is a very important aspect in space then, at the end, the final choice is fallen on solar arrays similar to those currently used on ISS (International Space Station). The present *specific power* (P/M, power per unit mass) of *single-crystal silicon solar panels* on the International Space Station (ISS) is < *0.1 kW/kg*.
Note that crystalline-Si cells are ~ 300 μm thick, whereas thin films cells under development for Earth and space applications are ~ 1 μm.
Moreover, ultralight support structures made of inflatable-rigidizable structures are possible for space PV. *Thin-film PV* on "gossamer structures" could raise *P/M* to the *1-10 kW/kg range*.
Inflatable solar array has been considered too, but because of the LEMMB shape, the best solution for a today's solar array application seems a folded and accordion deployable systems like used on ISS where. In place of the *ISS Solar Array Beta Gimbal Assembly (*mechanism used to develop the solar array), the LEMMB connections Inflatable structures has been adopted.

Chapter 6

This chapter covers the most important problems due to space radiations like GCR (Galactic Cosmic Rays) and SPE (Solar Particle Event).
Radiations are very dangerous for astronaut's health. Electronics circuit could be seriously damaged due to this Space Radiations too.
In the first part of chapter, all of the main hazard radiations types are analyzed.
In the second part some shielding method are presented. The methods currently available on literature are mainly *passive* or *static active*.
Passive shield (i.e Conventional method) like Lunar Lava Tube passive shielding system.
Active Shielding as Electrostatic shield – electric field only (time-independent); or Magnetic shield – magnetic field only (time-independent) or *Both Electric and Magnetic fields (time-dependent,) developed in this thesis*.
This last new approach has the advantage of the Electromagnetic wave propagation effect. A propagating Electromagnetic wave can be emitted by an antenna which is a very well proven technology.
By means of the Circular Polarized EM wave it seems possible to deflect a charged particle coming as an example from the Sun. The idea is well explained in this chapter.
In order to find the deflection particle trajectory both, Lorentz equations and Electromagnetic Wave Propagation equations have been combined together. Since their integration is not very easy then, two integration method have been developed; one in a closed form and another one in numerical form.
Result from both method are close to each other.
In numerical Integration method also the Errors problems have been analyzed.

Chapter 7

In order to prove the *active time dependent charged particles deflection method* studied and proposed in chapter 6, an experiment has been done.

The experiment consists in deflecting the electrons beam produced within a CRT (Cathode Ray Tube), by using an Electromagnetic wave circular polarized.
For this experiment all the instrumentations used have been kindly made available by TILAB (Telecom Italia LAB).
The source of charged particles (electrons) is an Oscilloscope CRT.
The experiment results show some effects which could have been produced by the deflection mechanism explained before. The deflection amplitude seems also close to what expected form theory point of view.
Nevertheless, some doubts remain because of the potential errors due to Electromagnetic Compatibility problems.
This aspect is worthy of more studies.

Appendix

The thesis appendix reports the *Matlab* and *C code,* used in order to find the charged particle deflection trajectory, by computing the integration of the second order equations.

1 Chapter 1
Lunar Base on the WEB

1.1 About Space Colonies

Space colonies are hypothetical permanent living and working environments away from Earth. They may be orbital colonies that orbit Earth or other planets or Moons. Colonies are intended to be settlements, cities in space where families live, work, and play.

1.1.1 Why space colonies ?

One reason for space colonies is that they will enable us to explore other planets in our solar system — and eventually explore beyond our solar system. Colonies would be one way to ensure the survival of humans should Earth become uninhabitable because of environmental change, climate change, or because of threats from near-Earth objects such as asteroids. Space colonies offer business opportunities as well; there may be resources we can acquire on other planets, such as mining metals on the Moon, that are not as available on Earth. Research could be enhanced. Microgravity offers many opportunities for creating near-perfect crystals for pharmaceutical and computer applications. Experiments that might involve risks to the environment or population could be undertaken. Being away from the light pollution and atmosphere of Earth allows advanced astronomical observations from telescopes. The reduced gravity of space colonies could also offer wonderful opportunities for people with physical handicaps, as the need for walkers and wheelchairs might be nearly eliminated.

What do people need in order to colonize space or another planet?
If humans are to live in space or on the Moon or Mars, even for brief periods, they are going to need a wide range of support systems. They'll need a place to work, rest, and live that protects them from the cold and dangerous radiation of the space environment. They will need power, light, air, food, water, and heat. They'll need robust transportation and equipment able to operate in low temperatures and the hostile environment of space. They will need to be able to communicate with Earth, other colonies, and shuttles.

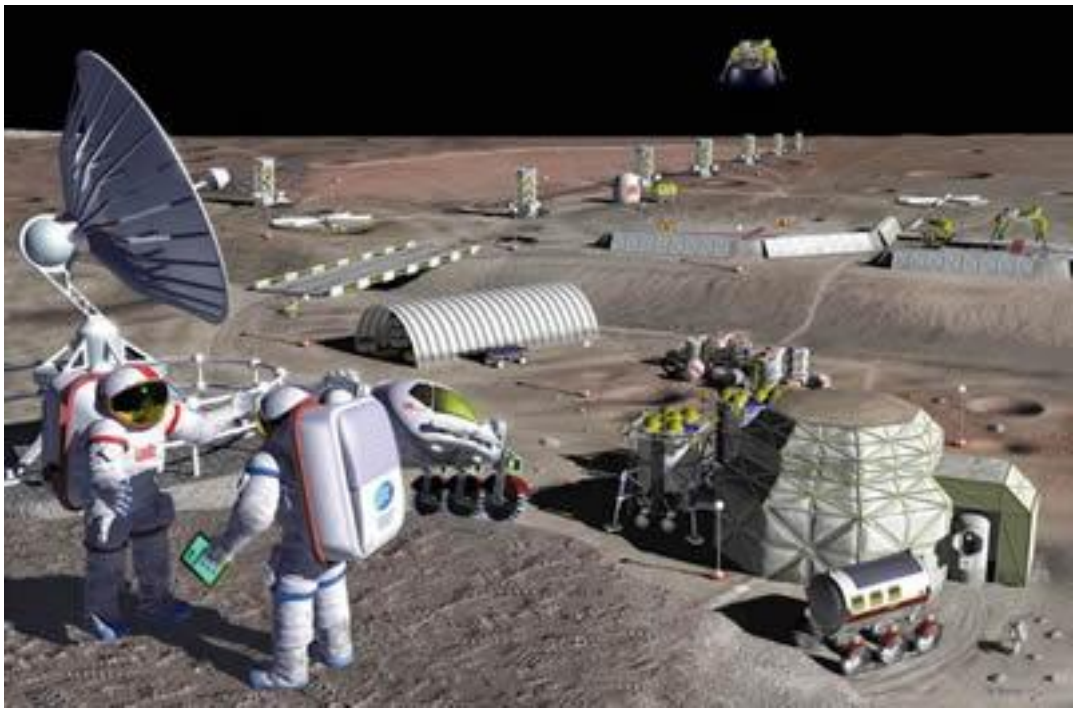

Figure1: Lunar Base of the Future Image by Pat Rawlings

They will also need to deal with health issues. Reduced gravity is a challenge to people living on smaller planets, like Mars with one-third Earth's gravity, like our Moon with one-sixth Earth's gravity. Under reduced gravity conditions, there is less "load" on bones and muscles, so living organisms lose bone mass, muscle tissue, and fluids. Even the heart — a muscle — loses mass because it does not have to work as hard. Humans in space must exercise to maintain their bone and tissue mass so that they can return to Earth's gravity and function well. More research is needed to understand the effects of reduced gravity on the human body — and how to counter these effects. These effects will be especially pronounced on humans living in orbiting colonies. Such colonies will have to rotate to produce a gravity field.

1.1.2 Where might the colonies be located ?

The International Space Station could be viewed as the first step to a colony. It is designed to be a long-term living and working environment for astronauts. NASA will learn many valuable lessons from the space station about what is necessary for even longer-term colonization and its effects on humans.

The Moon is one of the first targets for colonization, mainly because it is close and scientists know more about it than other planetary bodies because of the Apollo missions to the Moon. Its closeness means that people and materials can be transported faster and at lower costs than for a planet farther away; a one-way trip to the Moon takes about 4 days. The Moon may have water ice trapped in the craters around its poles, which could serve as a water supply to the colonies. The Moon has no atmosphere and extreme temperatures: 130°C (265°F) during the day and –110°C (–170°F) at night. Any habitat would have to provide shelter from the extreme temperatures and from incoming radiation. Moon bases may include subsurface buildings to increase protection from radiation and micrometeorites. A lunar outpost could provide valuable information on the long-term physiological and psychological effects on humans living in space. This information could prove invaluable in the eventual planning for a manned Mars mission that would require years of travel. Also, the Moon could serve as a source for the large quantities of oxygen needed to fuel a spacecraft to Mars and back.

1.1.3 Water on The Moon ?

On the Moon, frozen soil and ice at the poles may contain as much as 1–10 billion tons of water locked into deeply shaded craters, according to data from the Lunar Prospector spacecraft. That is an amount equal to what is consumed by U.S. cities in 10 days. It would be enough to supply the population of a lunar base for a long time. In addition to sustaining life in a colony, water can be used for rocket fuel and for air by breaking it into its separate chemicals of hydrogen and oxygen.

1.1.4 Air on the Moon ?

Humans breathe in oxygen and expel carbon dioxide. Just like in Earth's system, carbon dioxide and oxygen probably will be recycled in the colony. If the colony has a greenhouse, the plants can help with the recycling. Plants take in carbon dioxide

and, with sunlight, produce oxygen and food. Oxygen can also be released from the breakdown of some types of rocks or by removing it from water.

1.1.5 Power on the Moon ?

Sunlight is available for near planets and Moons — like Mars and Earth's Moon. Sunlight, captured by solar panels, is converted into energy that can be stored. The International Space Station gets its power from solar panels. The challenge to storing sufficient solar energy on the Moon is in its long night — equivalent to two Earth weeks. On Mars, the prolonged dust storms may inhibit solar energy collection. For planets and Moons far from the Sun, and for transportation between these planets, other energy sources will be necessary. Nuclear power is probably the most efficient power source for transportation to distant planets.

1.1.6 Food on the Moon ?

Settlers can grow plants such as wheat, soybeans, and other vegetables in extensive greenhouses. Plants can be grown hydroponically — using nutrient-rich water rather than soil. Colonists may be able to breed fish and other seafood in enclosed tanks.

1.2 Lunar Base strategy under Moon Surface

1.2.1 Strategy for lunar architectural environment

In our complex planning first we made a strategy study.

The first architectural lunar base constructions of habitability module and structural materials are to be transported to the site. Structural materials are stress holding frames and insulating foliating materials.

For the habitability module the cylindrical geometry, size and arrangement of the International Space Station US and other units are the best first approach. The space station habitability module units are economic preliminary lunar station candidates in our system.

From frame units a spatial skeletal structure is built on the site which holds the stresses and load of the weight of both the cylindrical modules and the other insulating layers.

For insulating material there is a free access for local regolith material. This should be used in two kinds of layers.

- The first layer is surrounding the ISS-like habitability modules by quilted-coat like insulating wall units. Holding material transported to the site and from the lunar soil. The modular units are attached to the outer wall of the ISS cylinder.
- The second layer is a free large masses of regolith used to surround the ISS cylinders so that they became embedded and buried into the local regolith material. This outer insulating layer, which forms a thick regolith mass surrounding the living space bubble architecture has not only role of insulating, but radiation and impact bombardment shielding, too.

The whole living building architectural unit is emplaced into a smaller valley of one of the lunar rilles or rimas.

1.2.2 Thermal equilibrium studies

On of the main physical constraint of the lunar base architecture is the thermal balance. Surface temperature range, lunar heat flow, solar insulation, lunar soil insulating data together with the heat dissipation inside the lunar base architecture all were used in calculating the thermal balance of the base in our regolith-buried architectural arrangement. Thermal properties of the lunar regolith made it excellent insulator for the wall system. This is the first layer of insulation, attached to the wall system.

The outer insulating layer is a thick regolith mass surrounding the living space bubble architecture. The depth of the regolith thickness was calculated from the thermal conductivity of the regolith measured at Apollo 15 and 17 missions, and from the lunar heat flow data. With two insulating layer wall system the estimated burial depth was 6-8 meters from the top and 4-6 meters from the bottom of the groove found for the emplacement of the lunar base on geological basis.

1.2.3 Structure of the building architecture

Functional studies prefer two main energy sources for a lunar base. However the allocation of the nuclear source needs larger distances between the power station and For the living units therefore the direct solar energy conduction was planned. Indirect heat sources may serve as long range containers of this source by phase changes in the salts used for this purpose. The salt layers serve also as units of the insulating system, too. So they are added as a third insulating layer to the two earlier proposed layers.

1.2.4 Technology

Using the insulating and strength data of the lunar soil the following main technology phases of construction of the lunar base architecture was pro-posed. After transport of the primary container ISS type unit blocks from Earth to the lunar surface:

1) grading and basis forming in the bedrock for the frame,

2) assembly of the architectural constructions of the frame,

3) fixing the thermal balancing salt units on the cover of the ISS type habitability modules,

4) parallel filling the insulating quilted-coat like units with lunar fine soil,

5) fixing the quilted-coat like second insulating units to the surface of ISS type unit blocks,

6) final emplacement of the container blocks on the frame,

7) burial of the living bubble units by the lunar regolith from the plains surrounding the valley of lunar base locality. For this a lunar rover type buldoser is used (Fig. below.).

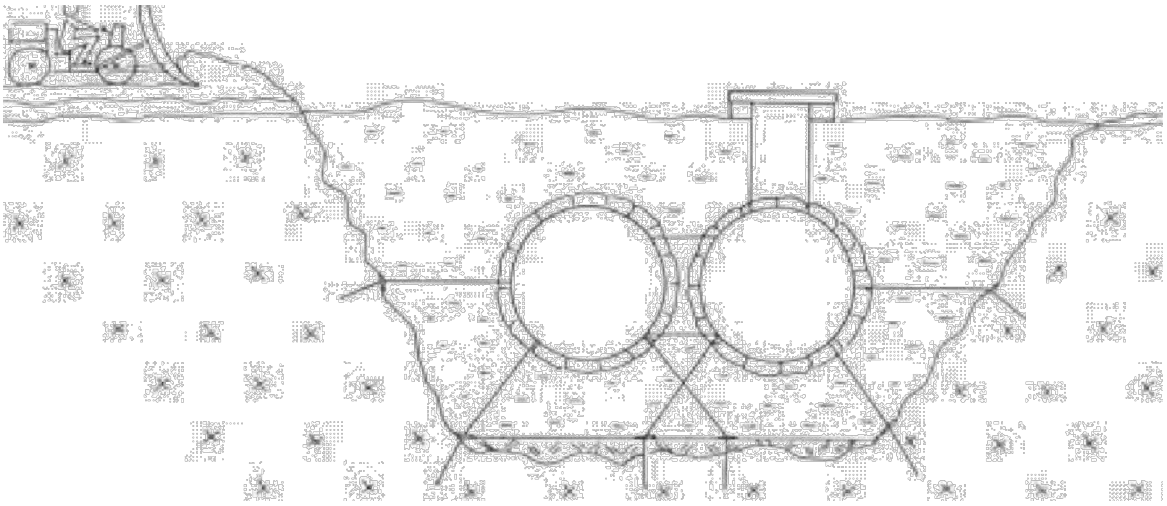

Figure 2: Arrangement of the habitability modules and their embedding into the lunar regolith in a small valley on the Moon.

1.2.5 Geological environment and allocation of the Base

It is economic to place the first long term used buildings below the surface. This way large mass of lunar soil can be used as insulator. Lunar soil can be moved by a lunar rover buldoser to cover the deposited container with regolith. The best geological site is at the mouth of a smaller valley which have about 10 meters width. It has been proposed the locality of the Aristarchus crater, where several rilles can be found (Fig. below Lunar Orbiter 4, 151H, detail). Enlargement of Fig. is shown on Fig. next with at least 10 larger rilles, where many larger valleys contain smaller central valleys on their floor.

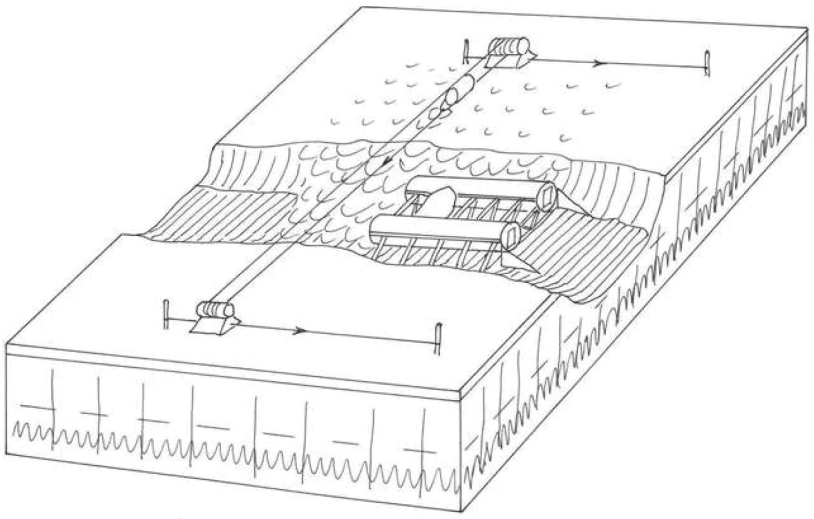

Figure 3: A proposed technology for the burial of the permanent lunar base into the lunar rille.

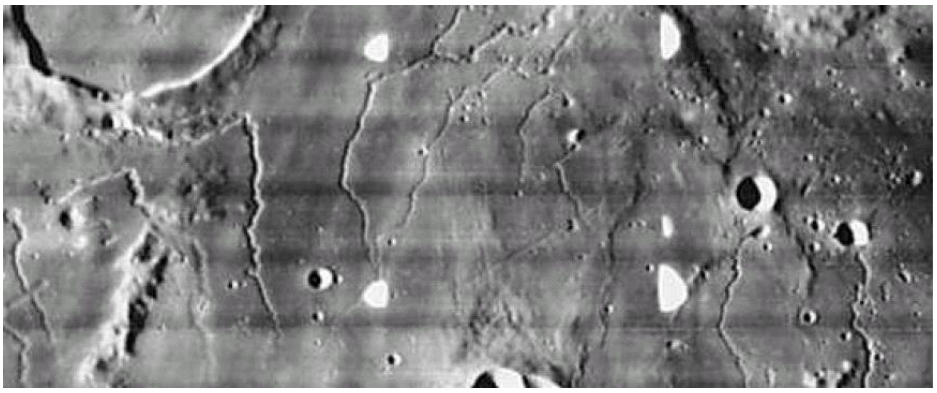

Figure 4: Aristarchus rilles of enlarged details of LO-4, 151H image. South is up.

1.3 Alenia Space – Supporting life on the Moon

1.3.1 Surface Habitat Concepts – "Rigid Cylindrical Module"

- The utilization of a rigid cylindrical module is probably the most traditional and proven approach to realize an habitable structure on the Moon surface.

- Positive aspects of this option are the minimum EVA activities required to the crew for the habitat activation and the typical modularity that allow easy reconfiguration and evolution of the Base

- The launcher and the landing system dictate basic habitat constraints like the maximum mass, the "folded" length and volume available

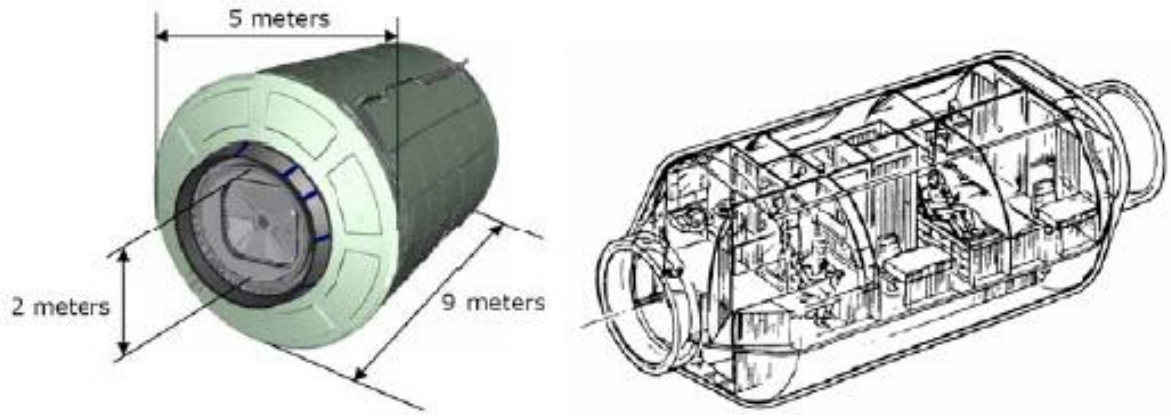

Figure 5: Alcatel Alenia concept of Lunar Base Module

1.3.2 Surface Habitat Concepts – "Inflatable Module"

- The use of inflatable structures is considered for their capability to provide substantially augmented pressurized volume with minimum mass and folded volume requirements.

- The operation requirements to install such an advanced habitat on a planetary surface would require extensive EVA and tele-robotic operations for a proper site preparation including terrain excavation and grading; these operation are not easy to realize.

- Radiation protection shielding shall be provided by covering the structure with a layer of regolith equivalent to about 20 g/cm^3

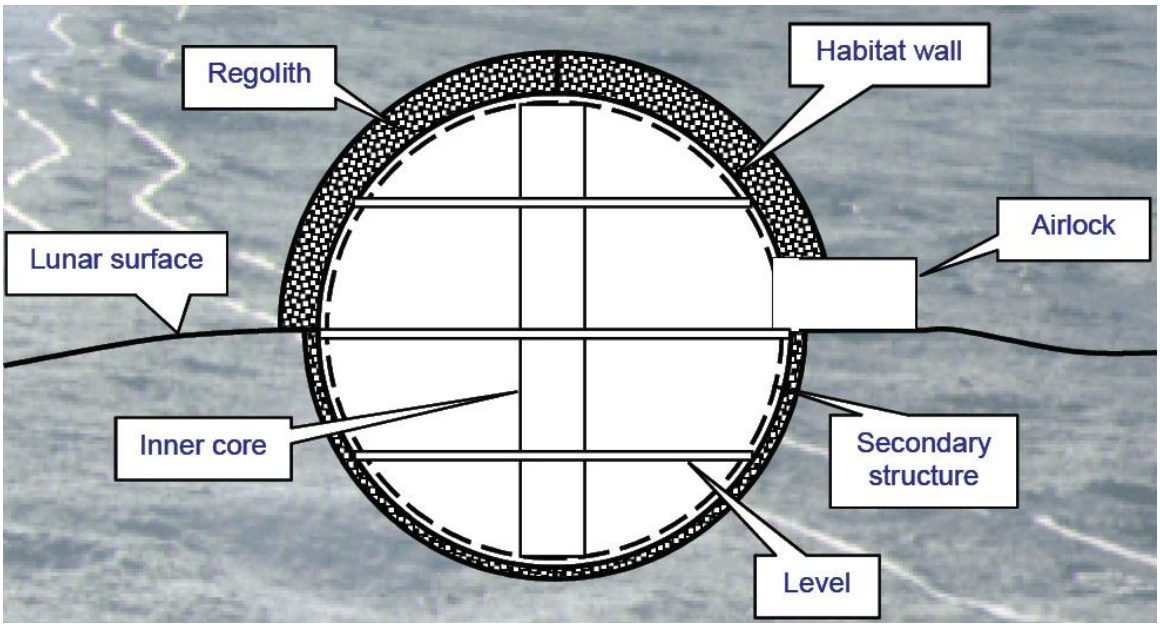

Figure 6: surface Habitat Concepts – Inflatable Module

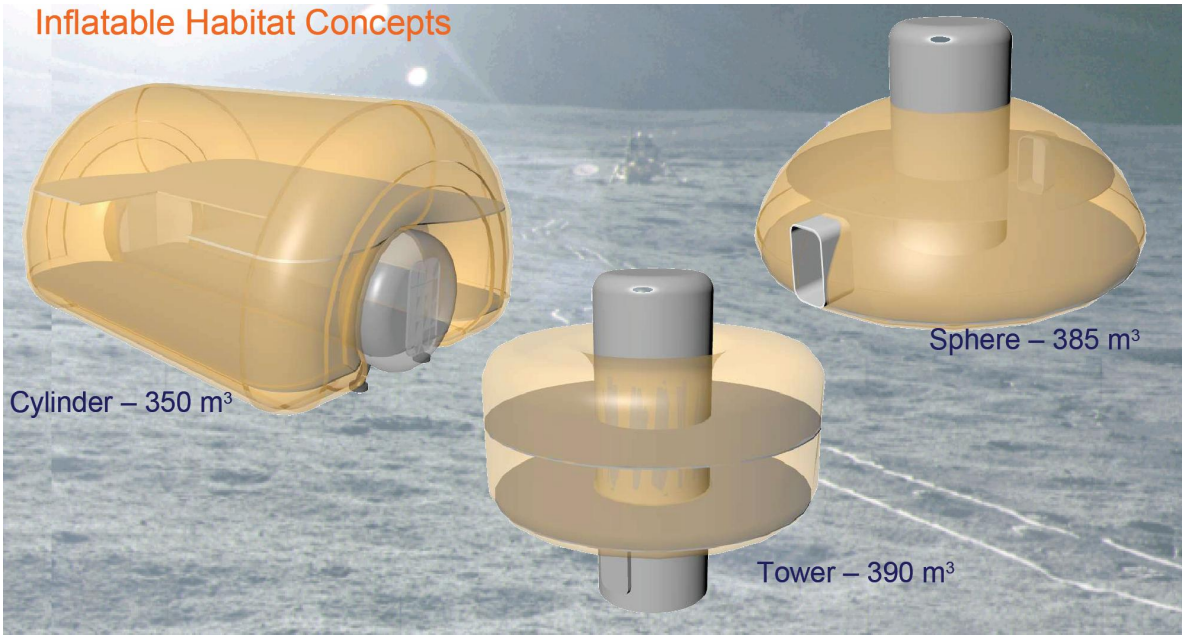

Figure 7: inflatable habitat concept

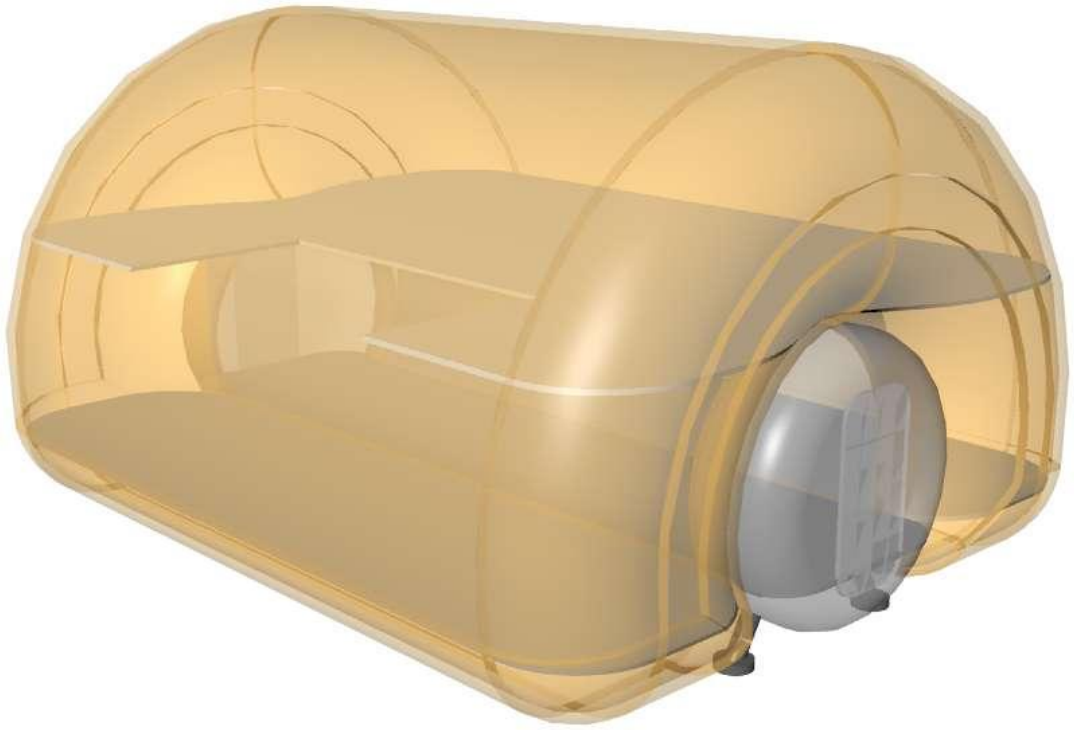

Figure 8: inflatable habitat module

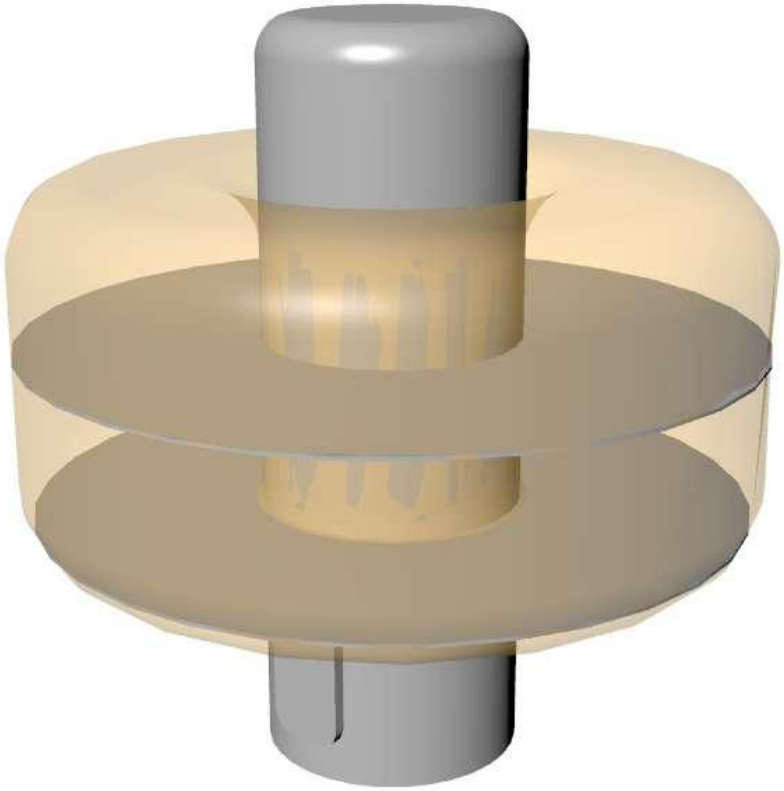

Figure 9: inflatable habitat module

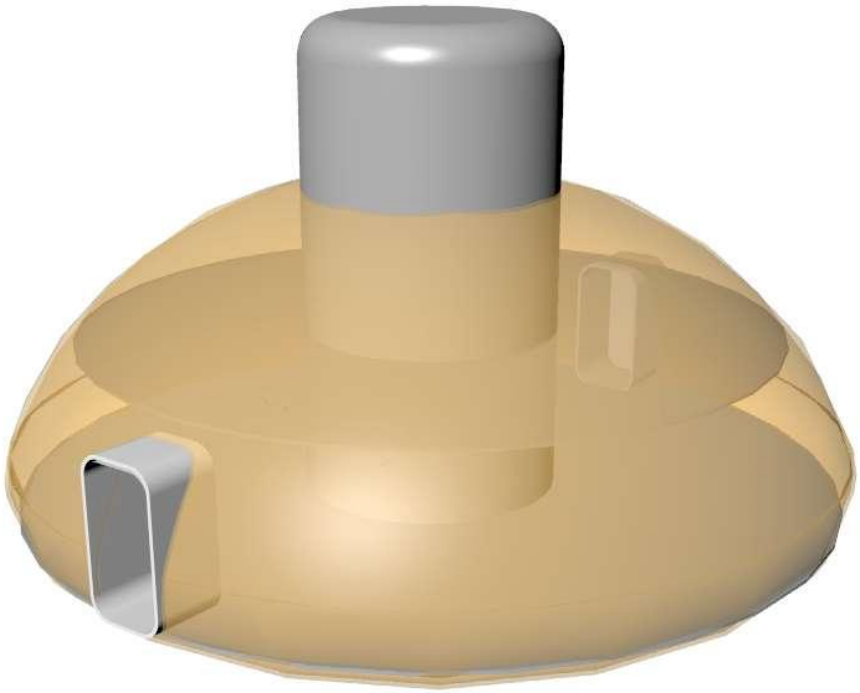

Figure 10: inflatable habitat module

1.3.3 Surface Habitat Concepts – "T-core Inflatable Module"

- T-shaped primary structure composed by the main floor, the hatches flanges and a couple of hollow beams, under the floor and from the top of one flange to the top of the other one for the pipelines passage

- In the packed configuration, the floors are closed by the central core of the module

- High commonality between the different mission scenarios for which these habitation inflatable modules can be adopted (ISS attached, free flyer, planetary transfer, surface outpost and habitat)

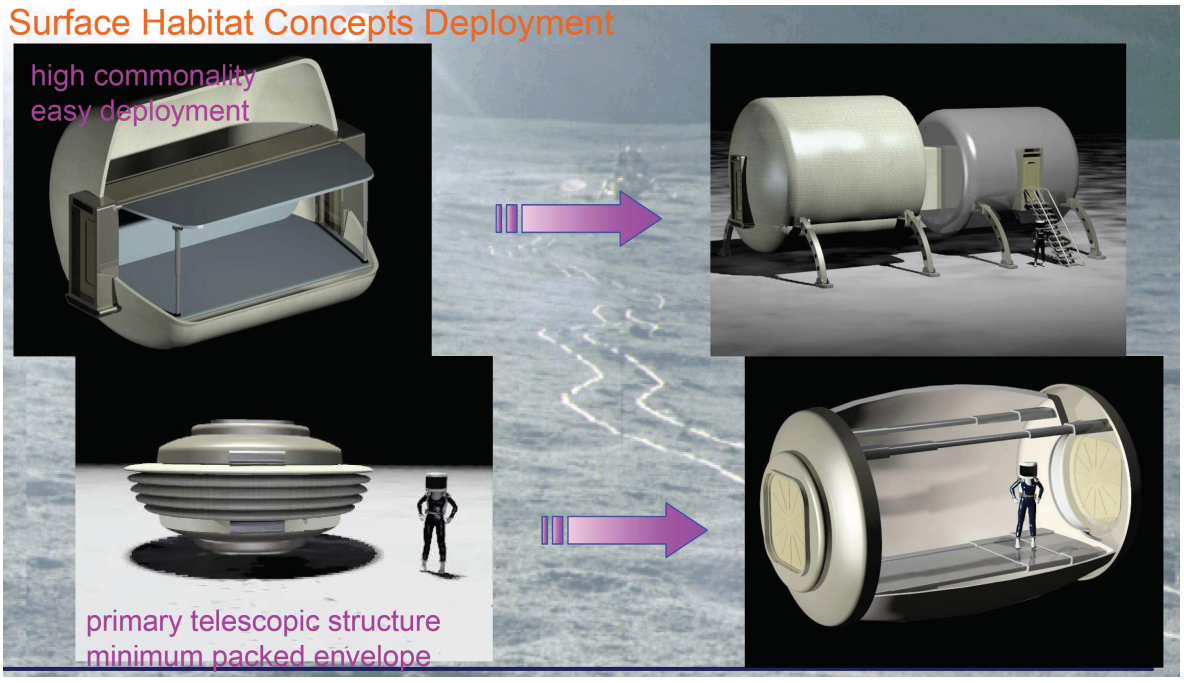

Figure 11 Top: T-core inflatable module; Down: Longitudinal inflatable module

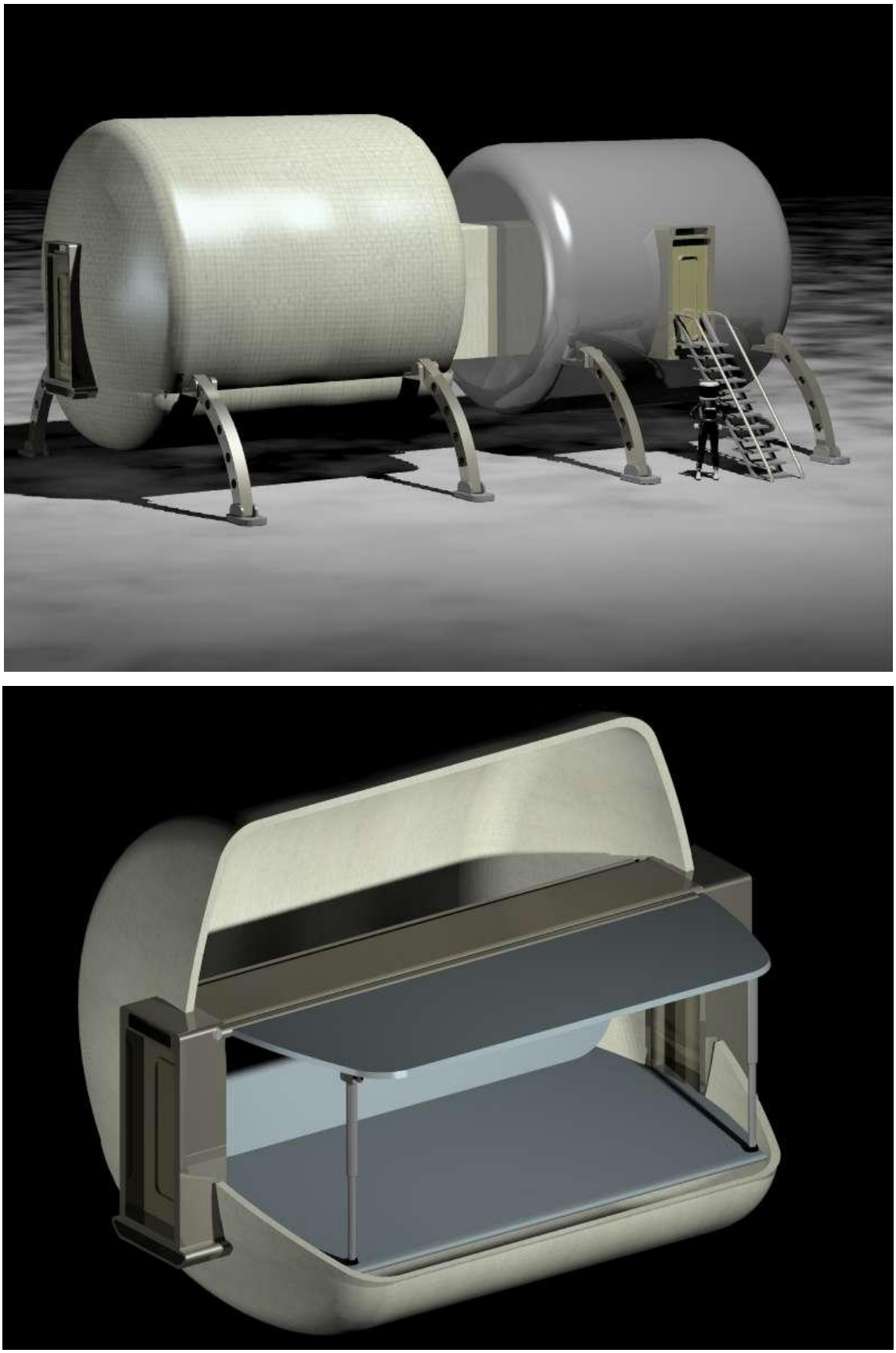

Figure 12: Top: T-core inflatable module

1.3.4 Habitat Concepts– "Longitudinal Inflatable Module"

- This concept is characterized by the presence of a primary telescopic structure directly linked to the end bulk heads that deploys during the module inflation

- The long inflation solution is the one that gives the greatest number of problems regarding the internal outfitting. Nevertheless, this architecture is the one with the minimum envelope in the packed configuration and allows the launch of more than one module per time (up to three) inside the Ariane 5 long fairing.

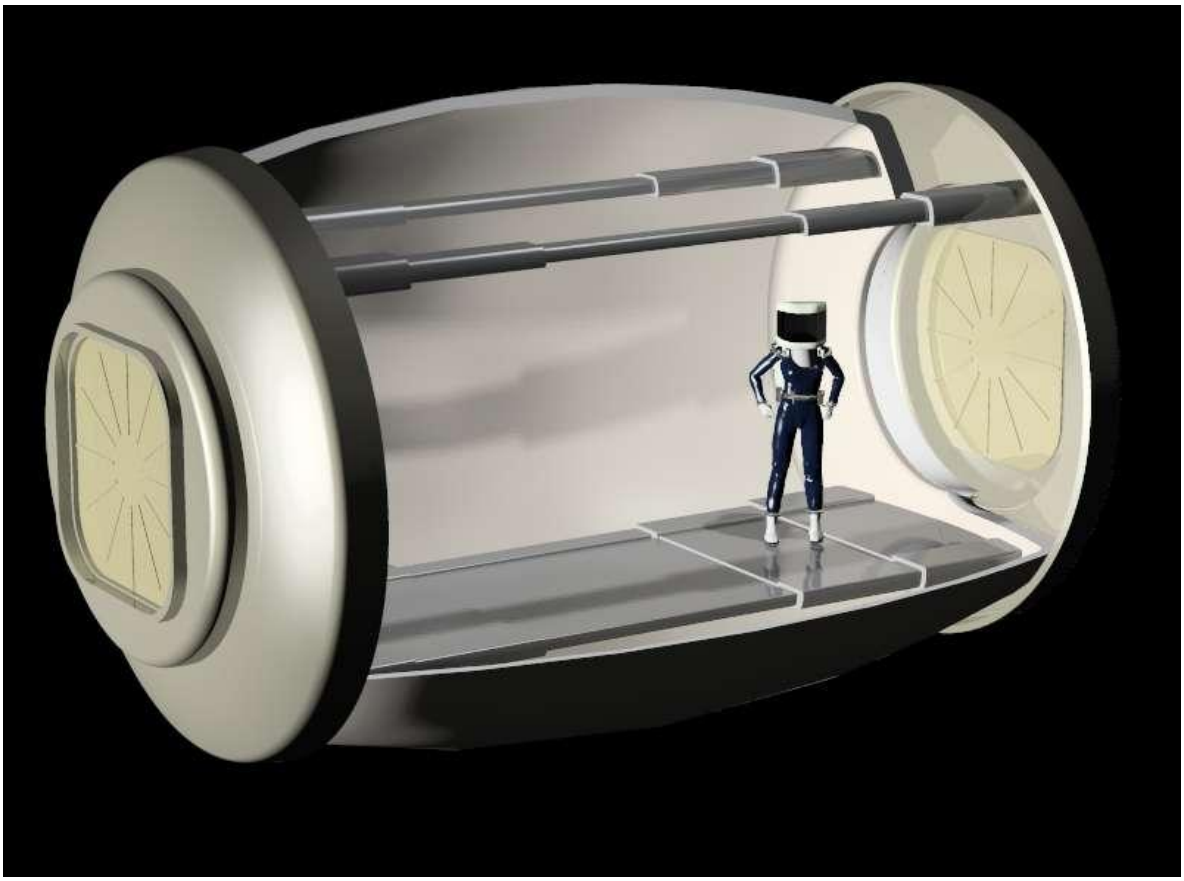

Figure 13: longitudinal inflatable module

Figure 14: longitudinal inflatable module

1.3.5 Surface Habitat Concepts – "Semi-rigid Module"

- Lenght= 8m
- Height (launch)= 3.1 m
- Width (launch)= 3 m
- Total internal volume= 195 m^3
- Int. volume rigid core= 50 m^3
- Infl. membrane thickness = 5 cm

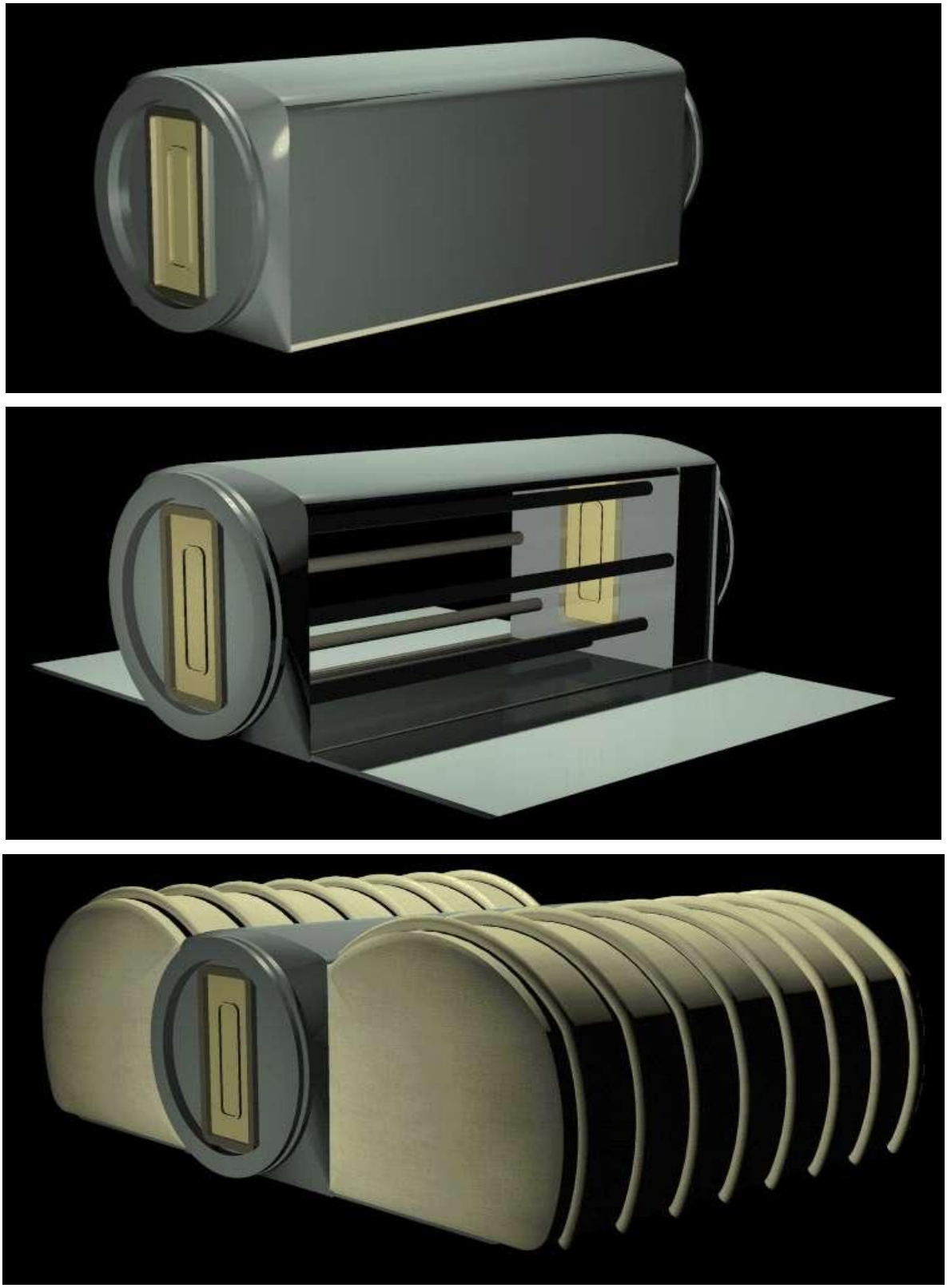

Figure 15: semi-rigid module

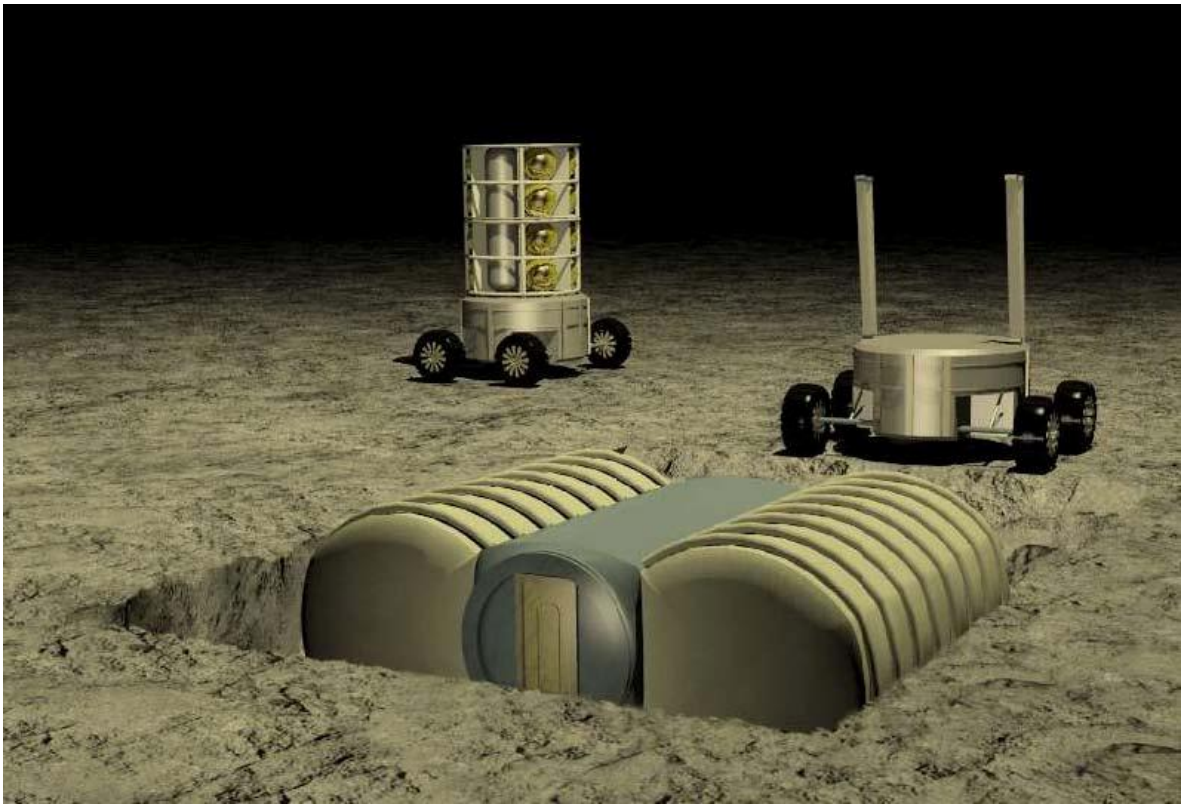

Figure 16: semi-rigid module assembly

1.3.6 Surface Habitat Concepts – "Concrete Structure"

- The utilization of concrete made of cement and aggregate obtained from lunar soil represents another option among the lunar habitat concepts.

- Different concepts can be elaborated based on modular pre-stressed elements built almost exclusively with lunar concrete.

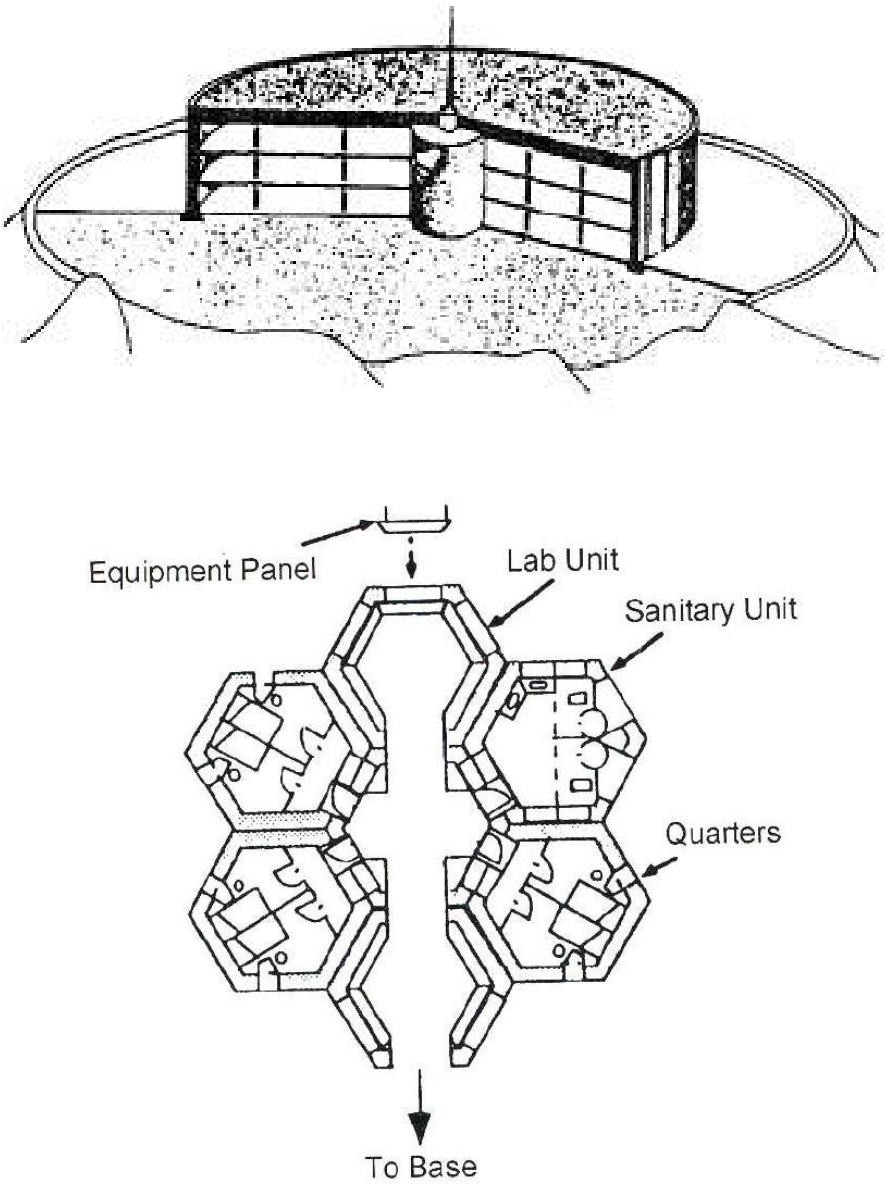

Figure 17: concrete structure

1.3.7 Surface Habitat Concepts – "Lava Tubes"

The naturally sheltered environment would allow using extremely lightweight construction materials because none of the components would have to support any shielding mass.

This natural caverns on the Moon formed by meteoroid impact could be regarded as receptacle for self-enclosed habitats.

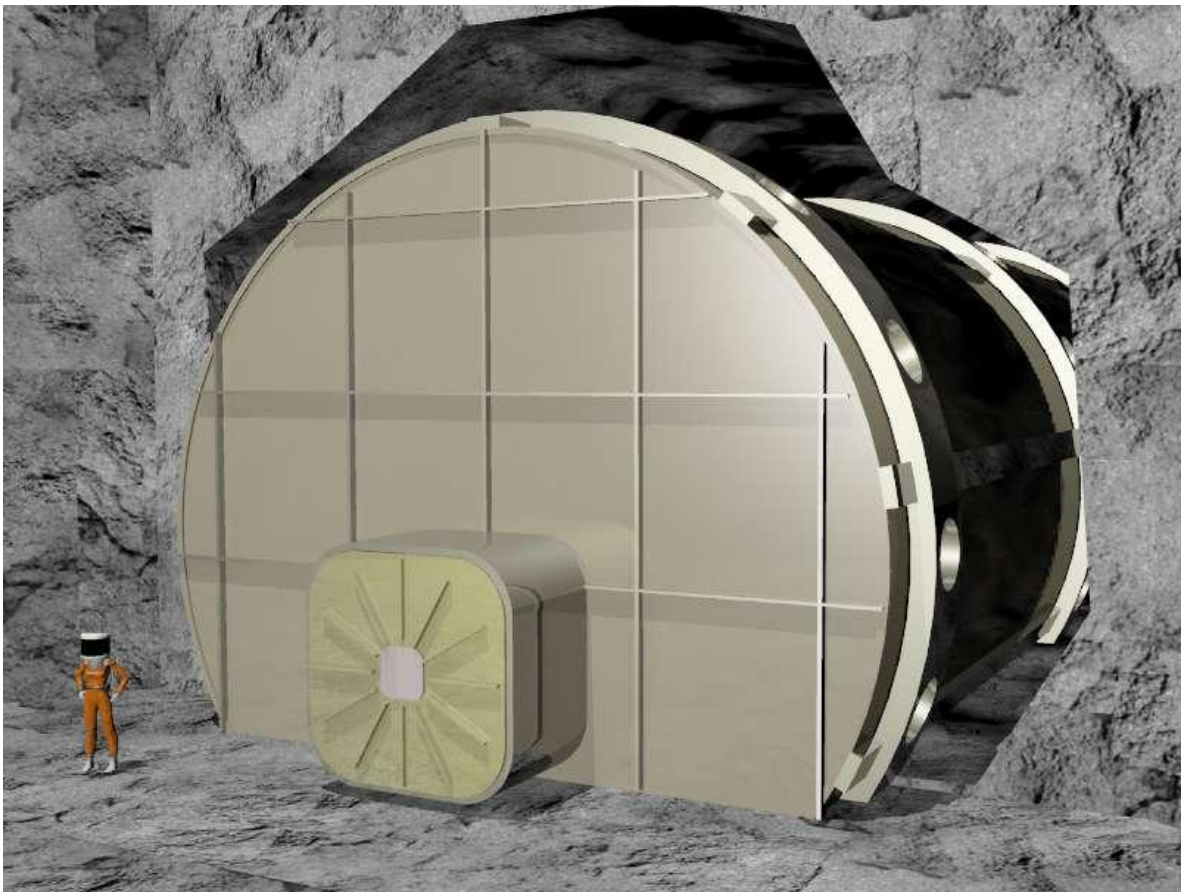

Figure 18: Lunar Lava tube example

Humans on the Moon would be protected from solar and cosmic radiation by building habitats inside lunar lava tubes. Radiation shielding will need to be at least three meters thick to protect residents from cosmic radiation and solar flares. That is why an intact lunar lava tube is an ideal place to build the first lunar base. They are naturally occurring self-supporting radiation shields that have roofs which are tens of

meters thick. Lunar lava tubes are much larger than those on Earth and are large enough to accommodate a large base. They are hundreds of meters wide. They can be thousands of meters long. A base in a lava tube could be easily expanded. An intact lunar lava tube will provide ideal protection from meteors, radiation, extreme temperature fluctuations and the abrasive lunar dust. It is also possible that the lava tubes will contain life support volatiles since they are a stable -20 degrees Celsius (Mendel) any water vapor which entered the tube would freeze and still be there. Intact lava tubes could be found near riles on the border between mare and highland. Partially collapsed lava tubes can be seen in photos of the Moon. They have been considered for use as a location for a lunar base by Coombs and Hawke. These lava tubes have questionable structural integrity because they are partially collapsed. It would be much better to find an intact lava tube. They will be larger since they are whole. They are probably deeper. Also in the future an entire tube could be sealed air tight so there could be earth-like sub-selene cities.

figure 19: Earth example of lavatube

The only problem with using an intact lava tube is finding them. Two possible ways of finding lava tubes are radar or active seismic sounding. There are problems with both. Radar may not work. Seismic sounding only covers a small area at a time. Radar on Earth only penetrates about 10 meters because the Earth is very wet. The Moon is extremely dry but other things, such as metals which, may not allow radar to penetrate the 1 kilometer needed for a complete survey for lava tubes. Even if radar does penetrate, large satellites may be required.
Seismic sounding will only cover a few square kilometers at a time. This would mean we would have to have a good idea where to look. Areas with partially collapsed lava tubes and areas with similar geology are a way to narrow the search. The area could also be narrowed by doing a very accurate gravity survey of the Moon. Areas which have too little mass could be areas with lava tubes. One complication with doing an active seismic survey of the Moon is that the dry lunar rock and regolith do not attenuate seismic waves. The Moon rings like a bell when it is impacted. There is no water to absorb the sound vibrations. When the Apollo 12 Lunar Module was crashed into the Moon, the Moon reverberated for over two hours. This means we can not simply use terrestrial analysis techniques on lunar seismic data. Some one will have to develop new techniques.

Both radar and active seismic survey were done as part of the Apollo program. These experiments only obtained small amounts of data. Also the equipments used were primitive by today's standards. All of the Apollo experiments were designed with limited understanding of the lunar environment. The radar experiments where hindered by the limited data storage technology. This should not be a problem with modern computer equipment. The seismic experiment data had larger error bars then the magnitude of the data. More data and better designed experiments should solve this problem. The experience of Apollo and the technology developed since then along with experiments in the future will give us everything we need to find intact lunar lava tubes.
Once lunar lava tubes are found to use them all we would need to do is to drill an elevator shaft. Then floor of the lava tube will need to be cleared of debris and leveled. A dust-lock could be used to allow a cleaning area for equipment and space suits before entering the base. The ends of the base area could be sealed by stretching

the same material used for the inflatable habitats over the opening sealing the section of the tube air tight, it would be a buffer between the lunar vacuum and the high internal pressure of the base. This would reduce the rate of air leakage from the habitat. Once prepared, the tube will be ready to receive inflatable structures.

1.4 NASA Inflation-deployed expandable structures

One team of experts from NASA's Langley Research Center, NASA's Johnson Space Center and NASA contractor ILC Dover LP is looking at inflation-deployed expandable structures as one possible building block for a lunar base.

"Inflatables can be used as connectors or tunnels between crew quarters and can provide radiation shelter if covered with lunar regolith (soil),"

As a starting point, ILC Dover has delivered a 12-foot (3.65 meter) diameter inflatable structure made of multilayer fabric to Langley for ground-based evaluation of emerging technologies such as flexible structural health monitoring systems, self-healing materials and radiation protective materials. Attached to the structure is a smaller inflatable structure that serves as a demonstration airlock. Both are essentially pressurized cylinders, connected by an airtight door.

The "planetary surface habitat and airlock unit" can also be used to evaluate materials, lightweight structure technologies, astronaut interfaces, dust mitigation techniques, and function with robotics and other lunar surface equipment.

Figure 20: The "planetary surface habitat and airlock unit" has been delivered to NASA Langley for ground-based evaluation of emerging technologies such as health monitoring of flexible structures.

Figure 21: The test structure will help researchers determine the best designs and materials for inflatable lunar habitats, to include connecting tunnels between crew quarters on the lunar surface.

Figure 22: Inflatable Structures Project Leader Karen Whitley stands in the center of the 12-foot (3.65 meter) diameter inflatable lunar habitat at NASA Langley Research Center, Hampton, Virginia.

"Inflatable structures are very robust and adaptable. This demonstrator will show the capabilities of inflatable structures in future demonstrations at Langley and Johnson," said Dave Cadogan, research and development manager at ILC Dover.

In the next phase, the team will perform an architecture study comparing inflatable and rigid structures for crew habitats.

In a related development, the government-industry team -- spurred by a NASA Johnson proposal led by Larry Toups, space architect at Johnson -- will work with the National Science Foundation to build an inflatable structure for demonstration in the Antarctic. While not the lunar surface (or the top of an imaginary mountain), the harsh environment of the Antarctic will provide valuable lessons.

Once inflated, the unit will likely serve as a dry storage facility and be monitored for its behavior. The work is expected to start shortly. ILC Dover is contributing to the manufacturing of the unit, while Langley and Johnson will contribute a modest amount of manpower. The goal is to transport the unit to the Antarctic in 2008 -- in time to learn more about inflatable structures before decisions must be made between competing technologies for NASA's first habitable lunar base.

Whether lunar habitats are ultimately inflatable or constructed in some other way, designing for extreme living and working conditions will likely result in yet-unseen applications for everyday life right here on Earth.

1.5 NASA Mobile Lunar Base Concept

(Ames Research Center)

Landing mobile bases on the Moon is an idea whose time has come, according to a NASA researcher.

Lunar bases that can travel on wheels, or even legs, will increase landing zone safety, provide equipment redundancy and improve the odds of making key discoveries by enabling crews to visit many lunar sites, according to Marc Cohen, a researcher at NASA's Ames Research Center, in California's Silicon Valley. Cohen recently presented his concept in a research paper at the 2004 American Institute of Physics Forum in Albuquerque, N.M.

"If you set up a base at a fixed location on the Moon, you are very limited in the sites of scientific interest that you can reach," Cohen said. "What it comes down to is if you're landing a habitat on legs and wheels, it doesn't take a lot more investment to make it highly mobile, provided you have enough energy resources that would enable it to travel great distance across the Moon with or without the crew onboard.

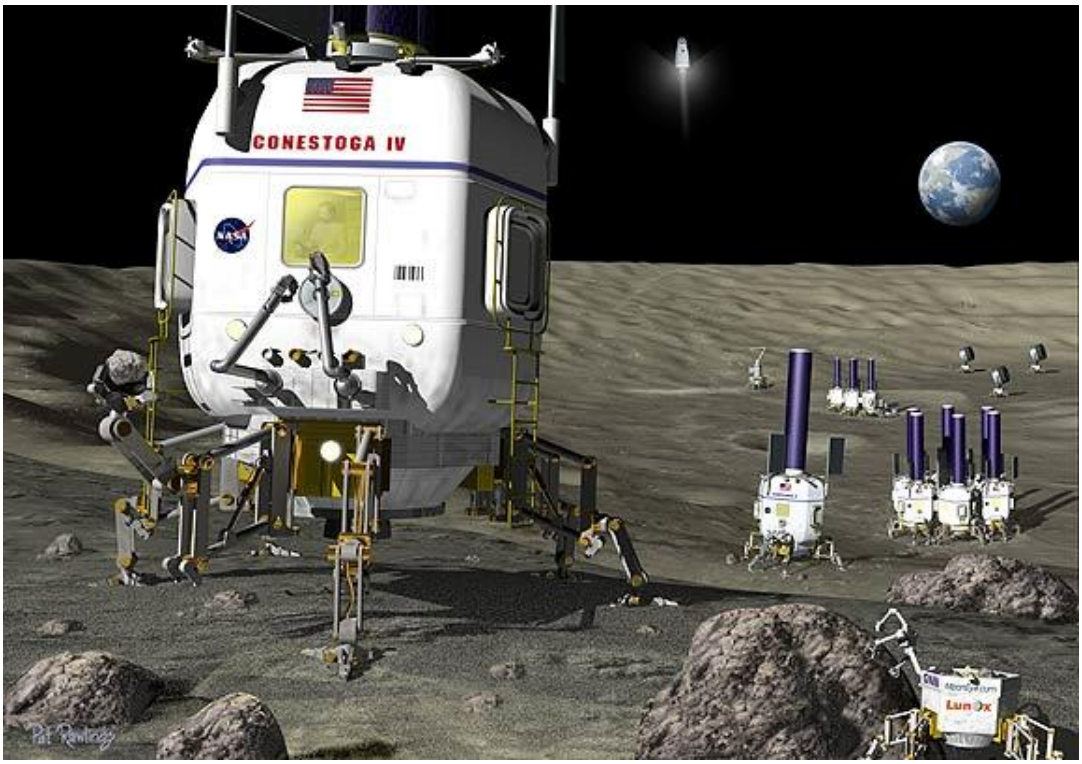

Figure 23

Walking or rolling habitats could dock to one another, or circle close together, when they reach a rest or research site, according to designs suggested by engineers over that last three decades, Cohen noted.

In contrast, a common scenario for exploration of the Moon is that one or more astronauts would travel to a remote site in a pressurized or unpressurized 'rover.' An unpressurized rover trip would only last hours because the astronauts would be in spacesuits for the entire trek. A pressurized rover could sustain astronauts for a much longer trip, lasting days or weeks.

"If you are trying to conduct research with pressurized lunar vehicles, you run into many safety issues," Cohen said. To avoid life-threatening or other compromising situations that might occur with only one rover traveling to a remote place, a second rover might travel with the first.

"But what if the second rover runs into a problem, too - the same or a different problem? Well, that means a third rover," Cohen said. "So, why not make the entire base mobile, so that all the resources, reliability and redundancy of the lunar mission move with the excursion crew?" Cohen reasoned.

"In addition, there's risk if you land lots of immobile modules in one spot -- there is a danger you'll have a very long commute to a place of scientific interest, or can't get there. Then you've wasted billions of dollars. Mobile habitats greatly reduce the risk of finding yourself on the wrong place on the Moon," Cohen added.

Another advantage of mobile Moon habitats is that they will be able to move out of the lunar landing zone, which could be hazardous. "The landing zone poses the problem that once a habitat lands on the Moon, it is not prudent to land another vehicle within several kilometers because of safety concerns from ejecta in a normal landing, and in case of an explosive failure on impact," Cohen said.

Cohen suggests that mobile habitats must have robust radiation shielding for them to be practical. "Radiation protection remains a challenge and a potential showstopper, as it does for all lunar base and rover concepts," Cohen said. However, there are potential shielding concepts that may well be reasonable, according to Cohen.

Others figures below report similar idea

The Office of Exploration Systems, NASA Headquarters, Washington, funds this research. Publication size images are available on the World Wide Web at:

	Photo No. **mobitat01a** Mobitat top view *Photo Credit: Plug-in Creations Architecture, LLC, Eugene, Oregon* Preview Size| Publication Size
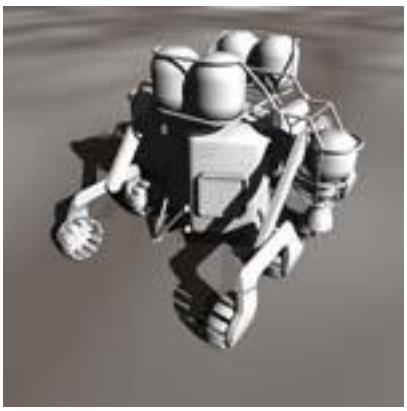	Photo No. **mobitat01b** Mobitat in deployed surface mode *Photo Credit: Plug-in Creations Architecture, LLC, Eugene, Oregon* Preview Size| Publication Size
	Photo No. **mobitat01d** Mobitat in lander configuration *Photo Credit: Plug-in Creations Architecture, LLC, Eugene, Oregon* Preview Size| Publication Size
	Photo No. **mobitat01e-module** Mobitat in surface deployed configuration *Photo Credit: Plug-in Creations Architecture, LLC, Eugene, Oregon* Preview Size| Publication Size

Photo No. **mobitat01e-platform**

Also a derivative of **mobitat01e-module**, the mobility platform with pressure vessel module detatched

Photo Credit: Plug-in Creations Architecture, LLC, Eugene, Oregon

Preview Size| Publication Size

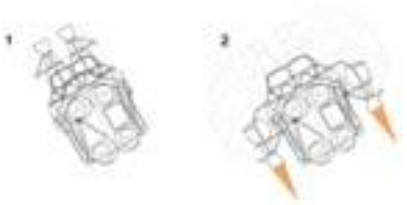

Photo No. **landing1**

Landing sequence 1 and 2

Photo Credit: Plug-in Creations Architecture, LLC, Eugene, Oregon

Preview Size| Publication Size

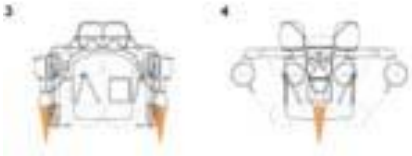

Photo No. **landing2**

Landing sequence 3 and 4

Photo Credit: Plug-in Creations Architecture, LLC, Eugene, Oregon

Preview Size| Publication Size

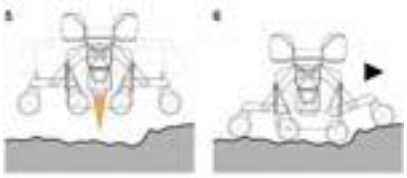

Photo No. **landing3**

Landing sequence 5 and 6

Photo Credit: Plug-in Creations Architecture, LLC, Eugene, Oregon

Preview Size| Publication Size

Photo No. **slope front**

Mobility system on transverse slope

Photo Credit: Plug-in Creations Architecture, LLC, Eugene, Oregon

Preview Size| Publication Size

Photo No. **step over**

Mobitat stepping over obstacles

Photo Credit: Plug-in Creations Architecture, LLC, Eugene, Oregon

Preview Size| Publication Size

1.5.1 Danger from Space Radiation

NASA plans to return to the Moon and eventually build a base there. This base would be the first settlement in the beginning of an interplanetary migration that will eventually take explorers and settlers throughout the Solar System.
Space radiation can have devastating effects on materials and the human body. When astronauts live and work in space, away from Earth's safekeeping, they are *exposed to ultraviolet rays and space radiation*. Current spacecraft materials cannot block all of the radiation, so astronauts are exposed to far more radiation than the average person on Earth. NASA is already working on how to make spacecraft safer by using different materials to provide protection.

The Moon has basically *no atmosphere*. With no atmosphere, there can be no weather (as weather is defined on Earth) and no ozone to protect humans from the sun's ultraviolet rays. *Earth's atmosphere protected the English settlers from ultraviolet rays and its magnetosphere guarded against solar particles and other forms of what is known as "space weather." The same will not hold true on the lunar surface.*

Future settlers on the Moon will have to take additional precautions. *Energetic particles constantly bombard the Moon; they can harm anyone who is not adequately shielded. Exposure dangers include significant long-term risks for cancer.*

1.5.2 NASA Studies about Lunar Base Concept

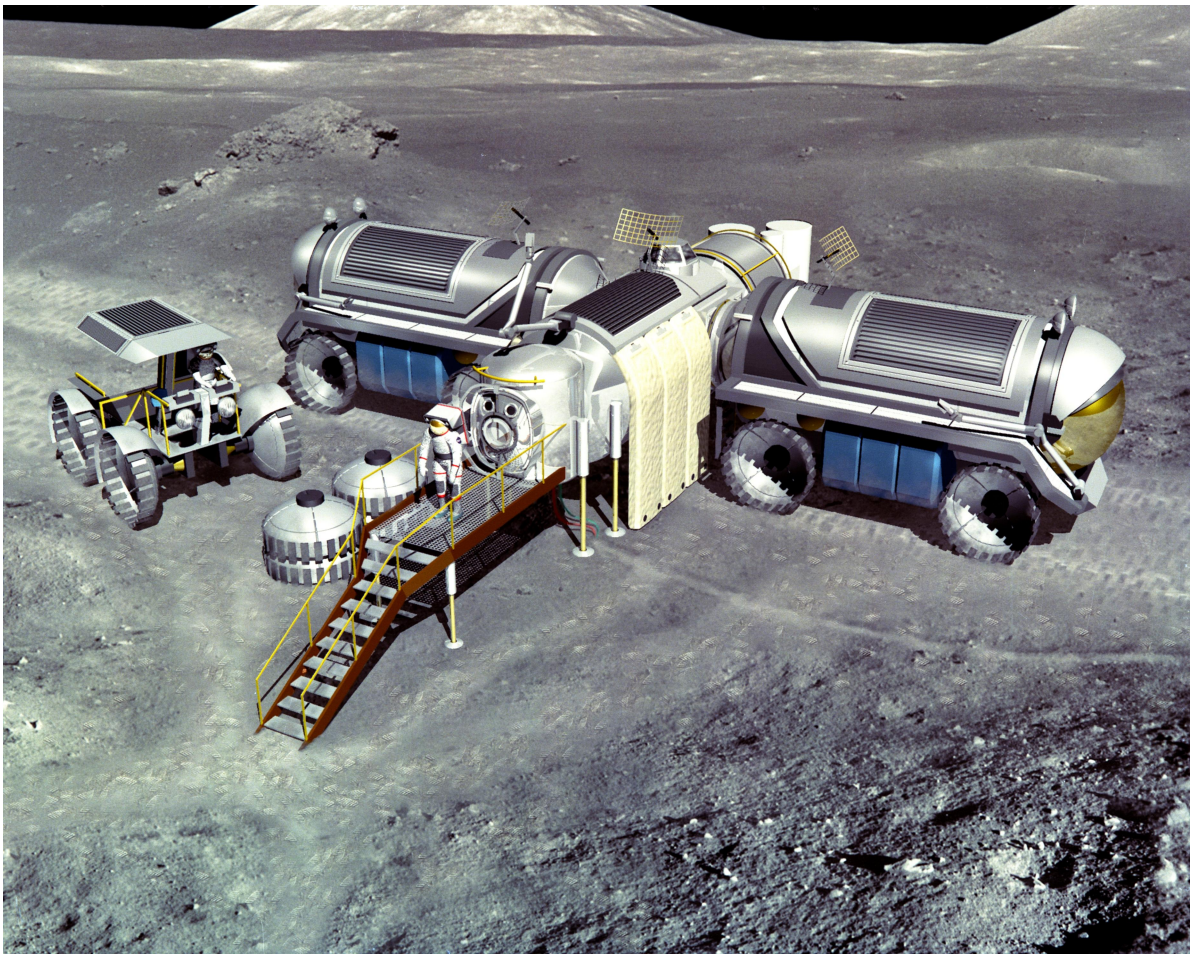

Figure 24

(1993) --- (Artist's concept of possible exploration programs.) A lunar habitat has been assembled out of components delivered by automated cargo flights. Pressurized rovers, logistics modules, and a space suit maintenance and storage module combine to provide the living and working quarters for the crew. This image was produced for NASA by John Frassanito and Associates. Technical concepts from NASA's Planetary Projects Office (PPO), Johnson Space Center (JSC).

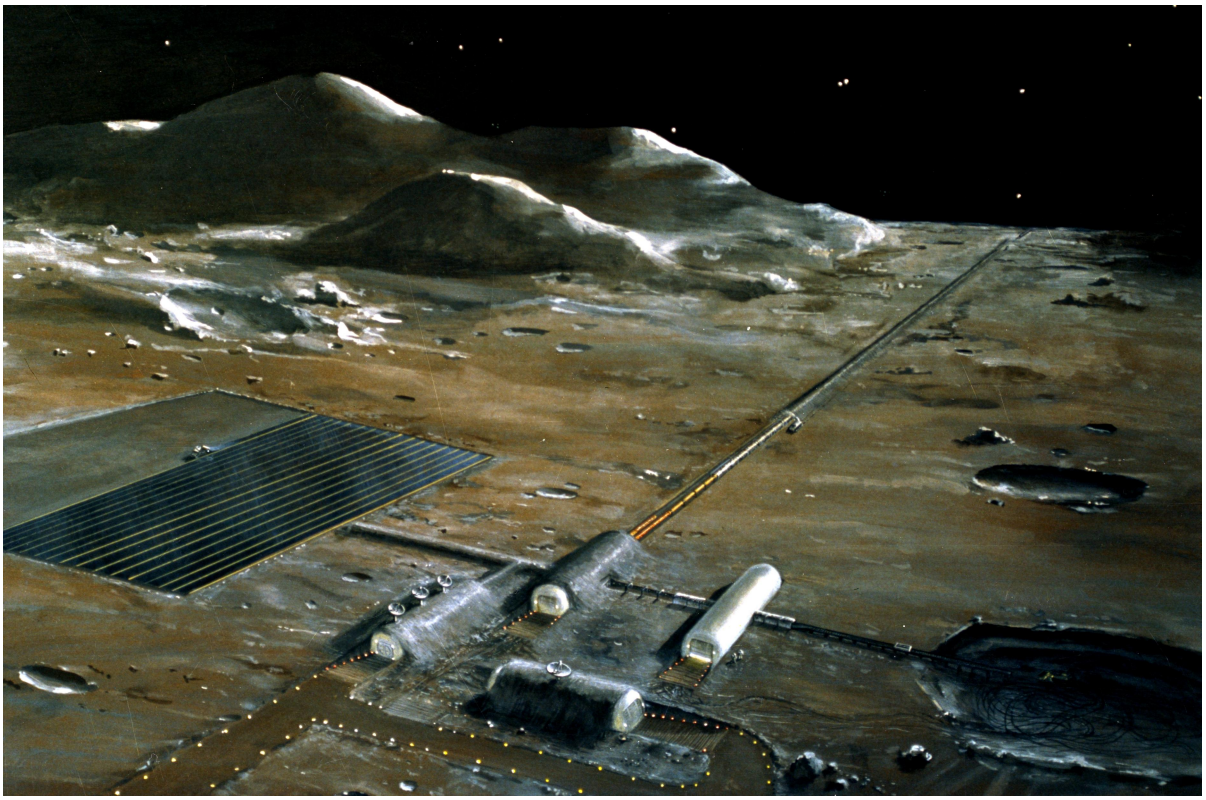

Figure 25

A painting of a lunar supply base which was displayed during the NASA-sponsored Ninth Lunar and Planetary Science Conference in March 1978 in Houston. A study entitled Lunar Resources Utilization for Space Construction is being conducted at the Johnson Space Center (JSC). The study is funded by the NASA Office of Aeronautics and Astronautics. One possible approach to developing industry in space is to use Moon soil as a source of raw materials. Lunar soil contains many major elements which provide the basis for industry and life on earth. A base being constructed to supply lunar materials to chemical plants in space is depicted here. These four large horizontal cylinders contain the base habitat, maintenance facility, soil-packaging plant and loading facility for the lunar mass driver, which is in effect an electromagnetic cannon designed in this particular schemes to eject four-kilogram packages of lunar soil from the Moon to a point in deep space where the packages will be collected and then transferred to a chemical plant nearer the Earth. Solar cell array (left) being deployed will be used to power the base and mass driver. Some 25 persons would work four months to emplace the large base. An operating crew of 10 persons would stay on the lunar surface to provide necessary maintenance.

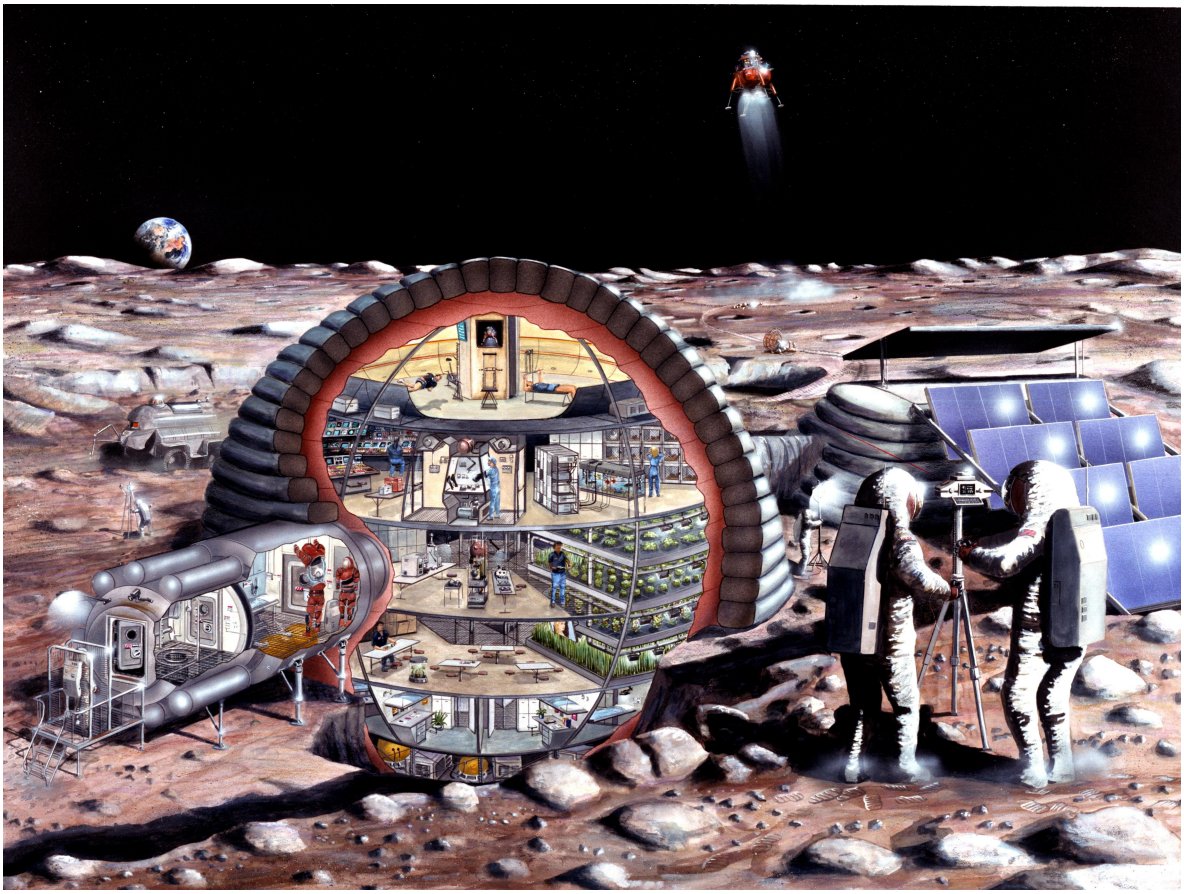

Figure 26

(July 1989)--- With a number of studies ongoing for possible lunar expeditions, many concepts for living and working on Earth's natural satellite have been examined. This art concept reflects the evaluation and study at JSC by the Man Systems Division and Johnson Engineering personnel. A sixteen-meter diameter inflatable habitat such as the one depicted here could accommodate the needs of a dozen astronauts living and working on the surface of the Moon. Depicted are astronauts exercising, a base operations center, a pressurized lunar rover, a small clean room, a fully equipped life sciences lab, a lunar lander, selenological work, hydroponic gardens, a wardroom, private crew quarters, dust-removing devices for lunar surface work and an airlock

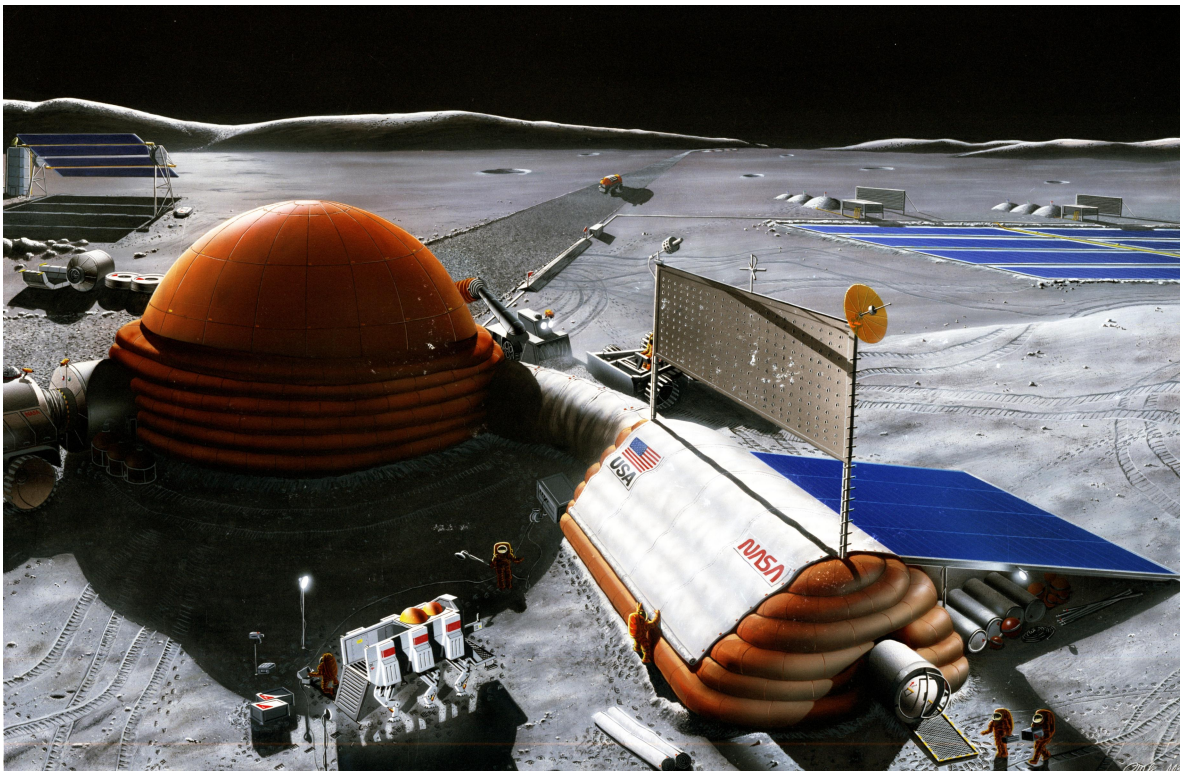

Figure 27

(March 1989) --- An inflatable habitat similar to this could represent part of an outpost, forerunner to a permanent inhabited lunar base. Since 1986, a number of concepts for going to the Moon, living on its surface and adapting to its unique environment have been developed at JSC by designers who drew on experience reaching many years into the past. The habitation system depicted here may be different than represented. Actual scenarios and elements will be based on long-term strategies of the civilian space program, technological advances and public and Congressional input. The artist has depicted here, along with the inflatable habitat a construction shack and related solar shield, connecting tunnel regolith bags for radiation protection, thermal radiation experimental six-legged walker, solar power system for the lunar oxygen pilot plant and other elements. This concept was developed during the Lunar Base Systems Study undertaken by the Advanced Programs Office in the Engineering Office at JSC during the period 1986 to 1988. The study was performed by the Advanced Programs personnel with contractor support from Eagle Engineering, Inc. and Lockheed Engineering and Sciences Co.

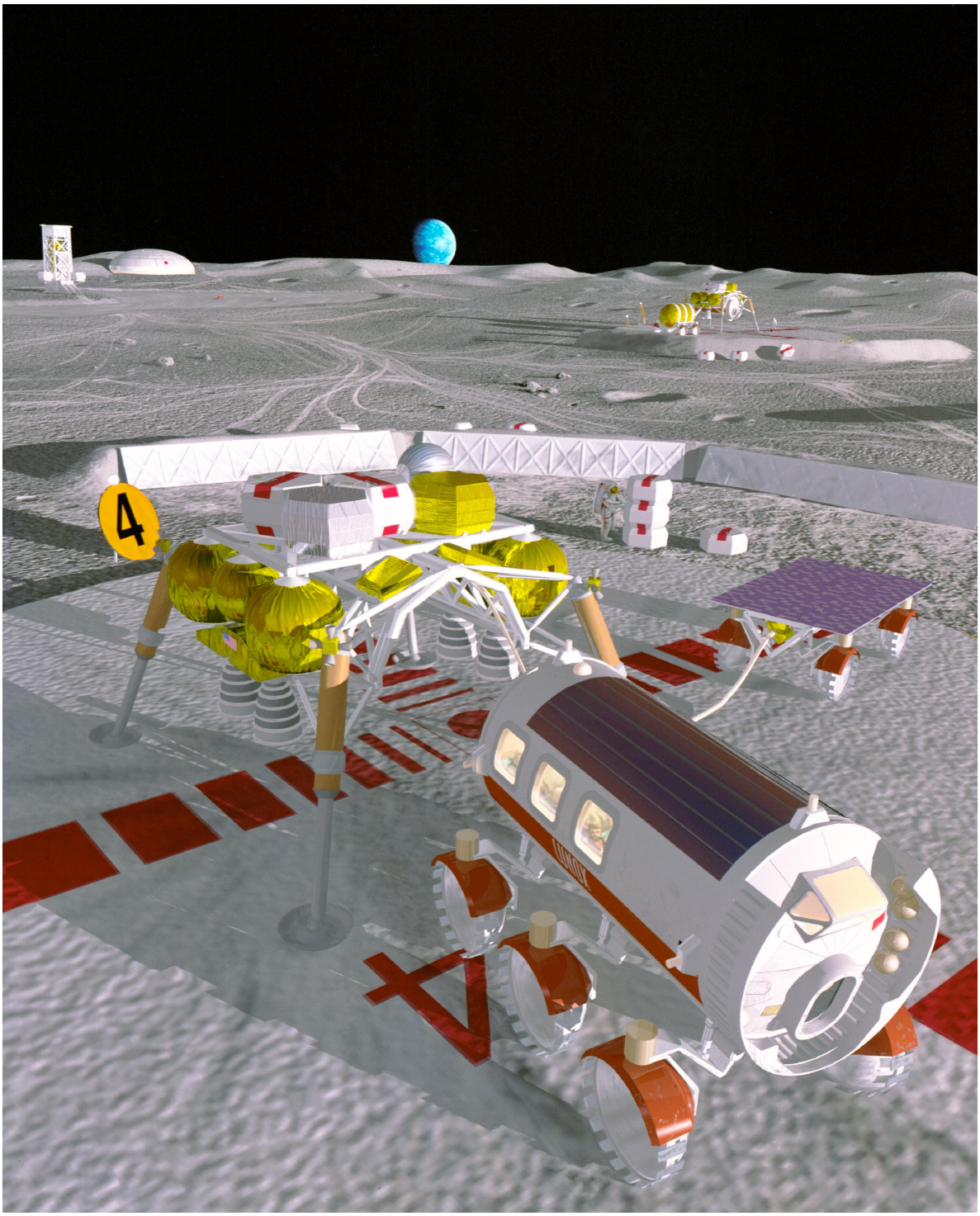

Figure 28

Lunar resources, such as lunar oxygen from regolith or possibly from south pole ice deposits, would increase our motivation to return to the Moon and could significantly enhance the economics of future lunar colonization.

1.6 Lunar surface

1.6.1 Non-Soil, But Useful

More than 80 percent of the Moon is ancient, heavily cratered highland. The rest of the surface is younger basalt-covered, plains-like areas called maria. There are many impact craters, some with bright rays, crater chains and the long, narrow valleys known as rilles.

A mixture of fine dust and rocks called regolith covers the Moon. Some scientists call this "lunar soil," but it contains none of the rich, organic material found in Earth's soils. Lunar regolith is made up mostly of fragments of lunar rocks found in the area. Mixed in with these local rocks are interplanetary and deep space rock fragments, tossed in by the bombardment of meteoroids pounding into the lunar surface.

Above a base of fractured bedrock, the regolith becomes thicker as impacts continue to rework it. With no weathering and erosion on the Moon, the powdery surface does not wash away.

The lunar surface is charcoal gray and sandy, with a sizable supply of fine sediment. Meteorite impacts over billions of years have ground up the formerly fresh surfaces into powder. Because the Moon has virtually no atmosphere, even the tiniest meteorite strikes a defenseless surface at full speed, at least 12 miles (19.3 kilometers) per second.

Some rocks lie thrown about the surface, resembling boulders sticking up through fresh snow on ski slopes. Even these boulders will not last long, maybe a few hundred million years, before they are ground up into powder by the steady rain of high-speed projectiles. Of course, an occasional larger meteoroid, about the size of a car, arrives and carves fresh rock from beneath the blanket of powdery soil. Falling meteoroids continue to grind the fresh boulders down, slowly but inevitably.

The layers of regolith vary, from about 6.5 feet (2 meters) in depth on the youngest maria to perhaps 65 feet (nearly 20 meters) on the oldest surfaces in the highlands. Lunar regolith has mixed local material so that a shovelful contains most of the rock

types that occur in an area. The regolith contains rock and mineral fragments from the original bedrock. It also contains glassy particles formed by the impacts.
In many lunar regoliths, half of the particles are composed of mineral fragments that are bound together by impact glass. The chemical composition of the regolith is similar to the composition of the bedrock. Regolith in the highlands is rich in aluminum, as are the highland rocks. Regolith in the maria is rich in iron and magnesium, elements also found in basalt.
But regolith may prove useful when people establish permanent settlements on the Moon. Life support systems require the life-giving elements hydrogen and oxygen (for water), carbon and nitrogen. Plenty of oxygen is contained within the silicate minerals of lunar rocks, with the solar wind providing the remaining elements.

1.6.2 NASA In-Situ Resource Utilization (ISRU)

Superficial layer or blanket of loose particulate rock material found on planet earth or any other hard celestial object" (R. W. Fairbridge, in Encyclopedia of Astronomy and Astrophysics).
Therefore virtually every surface in the solar system consists of regolith.

- Oxygen is the most abundant element on the Moon
- Solar wind deposited volatile elements are available at low concentrations
- Metals and silicon are abundant

Lunar resources are understood at a global level (>30 km pixel with Apollo point references) except for permanently shadowed craters and possibility of water/ice

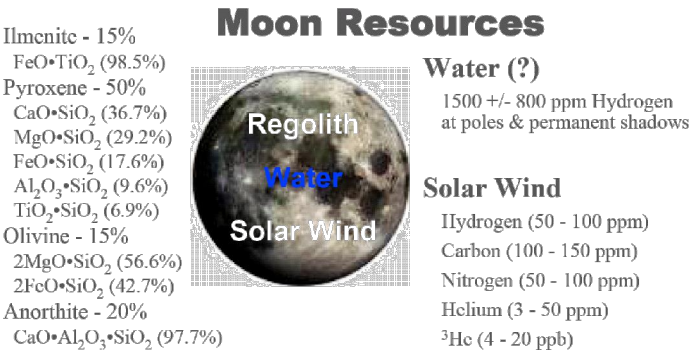

Figure 29: Moon resources

1.6.2.1 Components of the lunar regolith

The main component of the Lunar regolith are:

- Rocks and grains
  - Size limit ~1 cm
- Crystalline and reprocessed components
  - Crystalline components are fragments without further modification
  - Reprocessed rocks are called breccia
  - Reprocessed soils are agglutinates or glasses

1.6.2.2 Basic Process in a Lunar soil formation

Creation of regolith (no atmosphere!): fresh regolith is created by large impacts

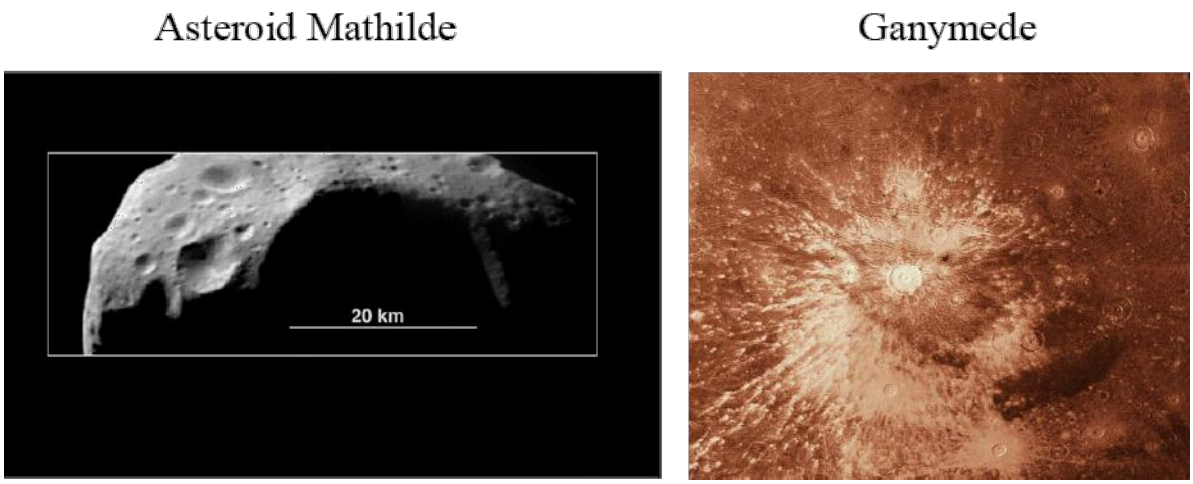

Figure 30: asteroids impact

• A large crater penetrates the existing regolith layer and creates fresh regolith

• A minimum crater size corresponds to a minimum impactor size.

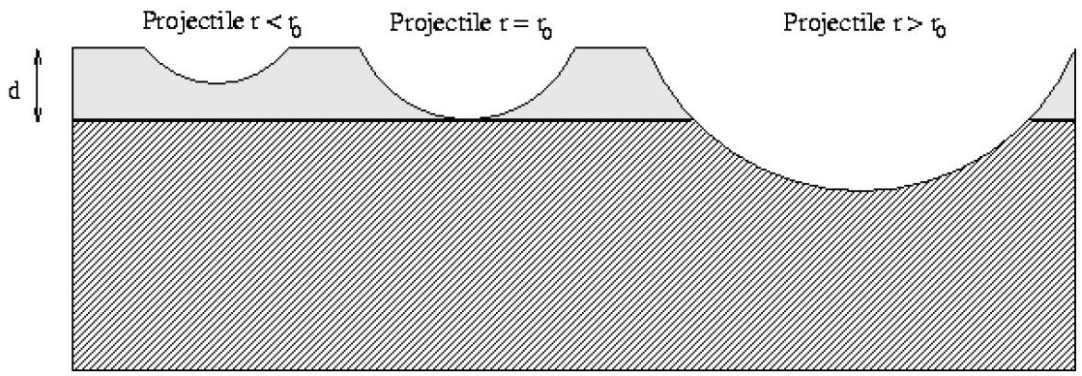

Figure 31: size asteroids impact and fresh lunar regolith creation

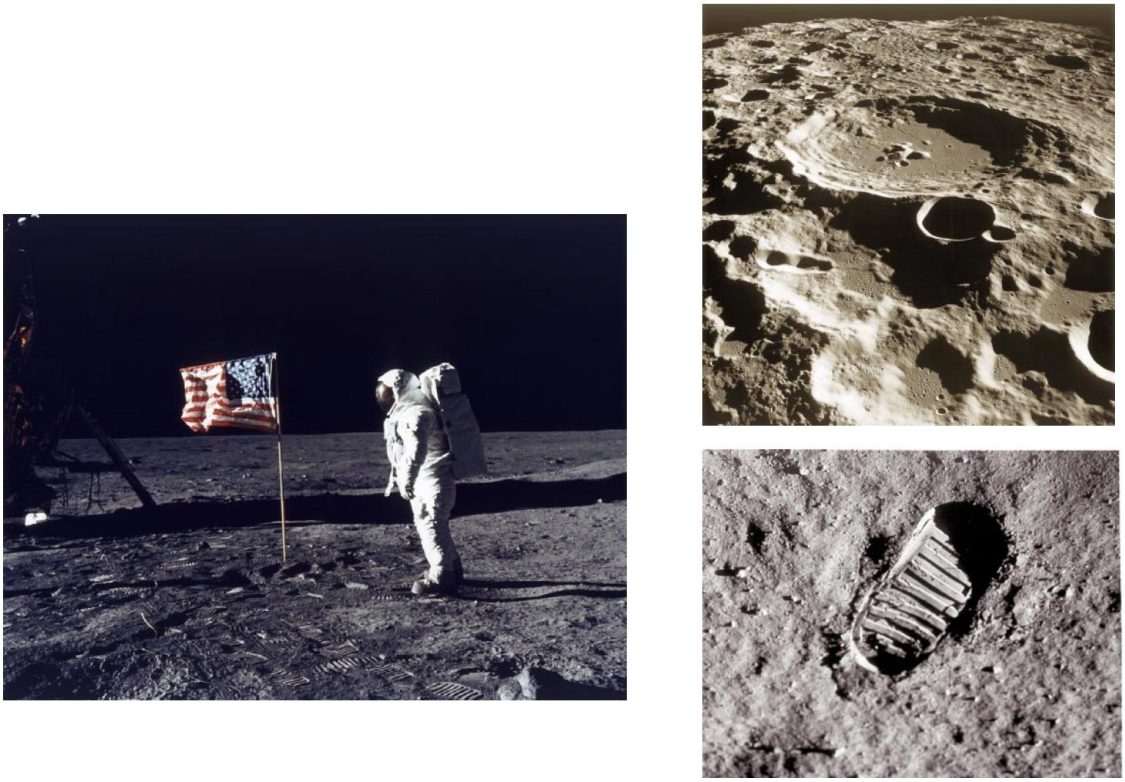

Figure 32: Regolith is created by meteoritic impact

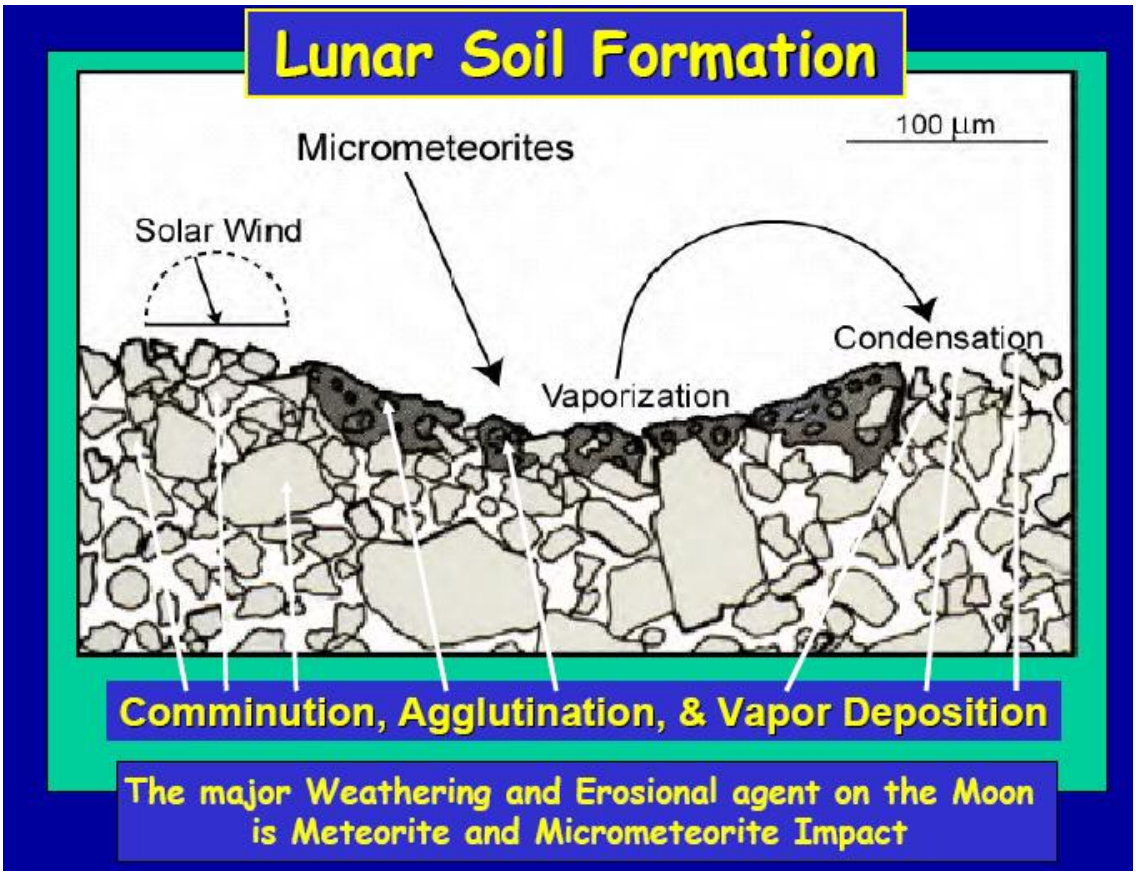

Figure 33: lunar soil formation

Where:

- COMMINUTION: breaking of rocks, minerals, and glasses into smaller particles;
- AGGLUTINATION: welding of rock, mineral, and glass fragments together by micrometeorite-produced, impact-generated melt (quenched to glass);
- IMPACT-MELT VAPORIZATION AND DEPOSITION: Vaporization of volatile components in the micro-meteorite-produced, impact-generated melt.
- SOLAR-WIND SPALLATIONAND PARTICLE IMPLANTATI ON: Erosion and vaporization caused by sputtering from impacting high-energy particles

1.6.2.3 Lunar soil characteristics

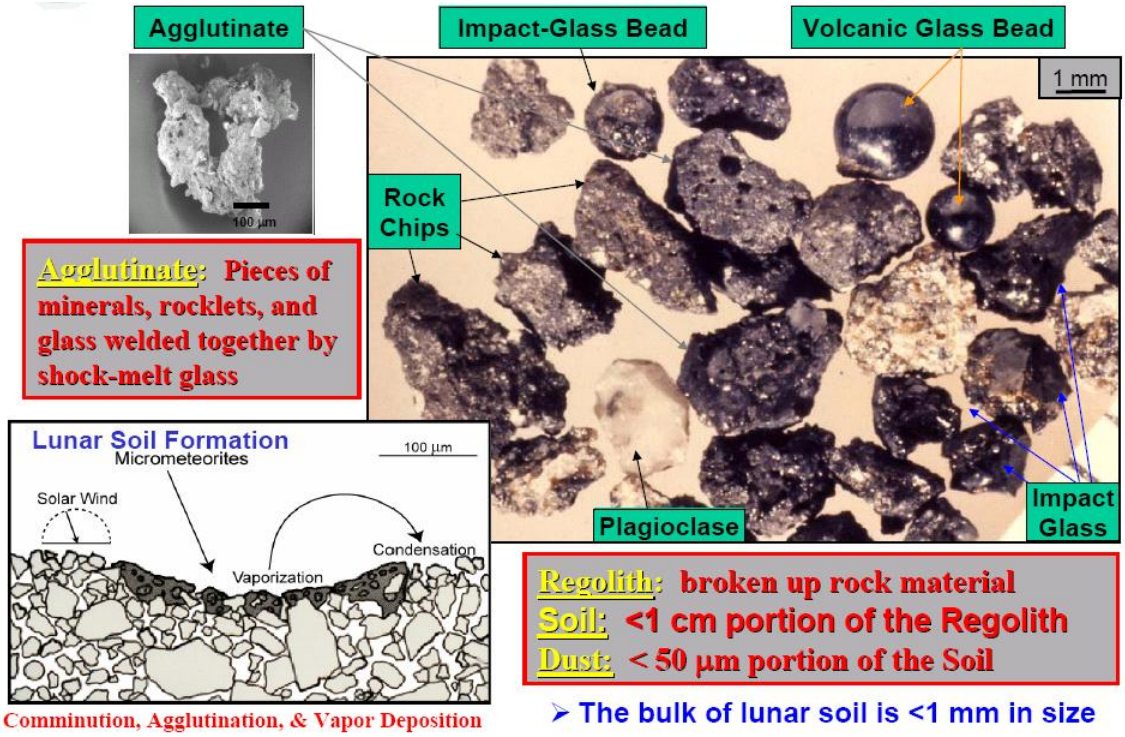

Figure 34: Lunar Soil Characteristics

The bulk of lunar soil is <1 mm in size

Particle Size Distribution

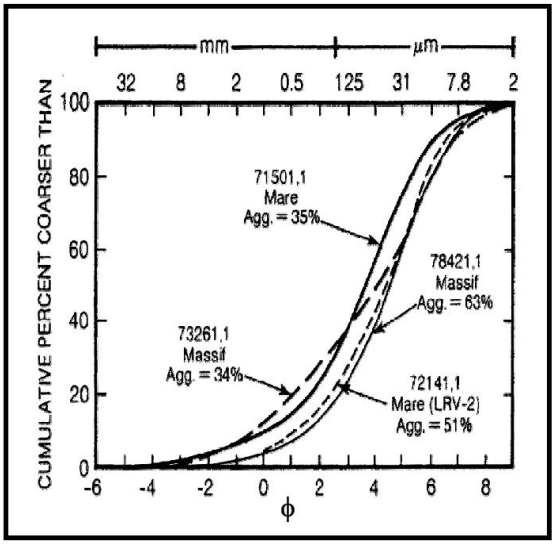

Distribution of particle sizes in separate splits of Apollo 17 soil 78221,8,

Particle Weight Distribution

Soil	Size Fraction (weights in grams)					Mean Size, M_z	
	>1 cm	4-10 mm	2-4 mm	1-2 mm	<1 mm	<1cm (mm)	<1mm (mm)
14163	0.0	196.5	197.1	288.7	4444.0	76	56
15220	0.0	7.0	5.8	2.4	290.0	-	43
68500	1.3	17.3	25.1	37.8	521.1	106	68
72140	1.3	2.7	1.9	5.3	225.9	57	50
72500	3.1	8.0	12.9	24.1	687.2	67	57
73240	1.6	22.3	14.4	14.9	192.7	127	51
74220**	0.0	0.98	0.17	0.68	7.77	-	41
78220	0.0	1.5	2.7	5.2	227.1	50	45

Weight distribution in size fractions of scooped surface soils.

Figure 35: the bulk of lunar soil

1.6.2.4 Lunar Soil Properties

Specific Gravity: Range from 2.3 to >3.2; recommend 3.1 for Engineering use.

Bulk Density:

- top 15 cm = 1.45-1.55 g/cm^3; avg = 1.50 ±0.05 g/cm^3
- 0-30 cm = 1.53-1.63 g/cm^3; avg = 1.58 ±0.05 g/cm^3
- 30-60 cm = 1.69-1.79 g/cm^3; avg = 1.74 ±0.05 g/cm^3
- 0-60 cm = 1.61-1.71 ±0.05 g/cm^3; avg = 1.66 ±0.05 g/cm^3
- values up to 1.9 g/cm3 estimated at depth of cores to 2.98 m

in table below the soil porosity is shown

Soil Porosity		
Depth Range (cm)	**Average Porosity n %**	**Average Void Ratio,**
0-15	**52 ± 2**	**1.07 ± 0.07**
0-30	**49 ± 2**	**0.96 ± 0.07**
30-60	**44 ± 2**	**0.78 ± 0.07**
0-60	**46 ± 2**	**0.87 ± 0.07**

Table 1: Soil Porosity

Lunar soil, in-situ, is very dense, more than that which could be produced with mechanical compaction equipment– the lunar soil has experienced slow shaking over eons of time.

1.7 Malapert Mountain as a strategic site for the next stage of lunar exploration

A prominent mountain ("Malapert Mountain") in the south polar region of the Moon has features that are very attractive for the next stage of lunar exploration and lunar base development. From the results of reinterpreted radar-based topographical data it is concluded that the mountain has high strategic value as a site from which to begin and to coordinate the exploration of the south polar region of the Moon.

Malapert Mountain is located at 0° Longitude, 86° South Latitude in the south polar region of the Moon (Figures below). It was previously reported that the summit of the mountain has an altitude of 8000 meters. Although the distance from portions of the base of the mountain to the summit are approximately 8000 meters, interpretations of Earth-based radar imaging data indicate that the summit of the mountain projects approximately 5000 meters above the reference surface ellipsoid of the Moon. The difference in these elevations is explained by the fact that imaged portions of the base of the mountain are below the reference surface ellipsoid of the Moon. The location of the mountain and elevation of the summit are attractive for the next stage of lunar exploration for four reasons:

1) Abundance of sunlight,
2) Earth visibility,
3) Access to scientific points of interest, and
4) Logistical and operational advantages for lunar science and engineering projects.

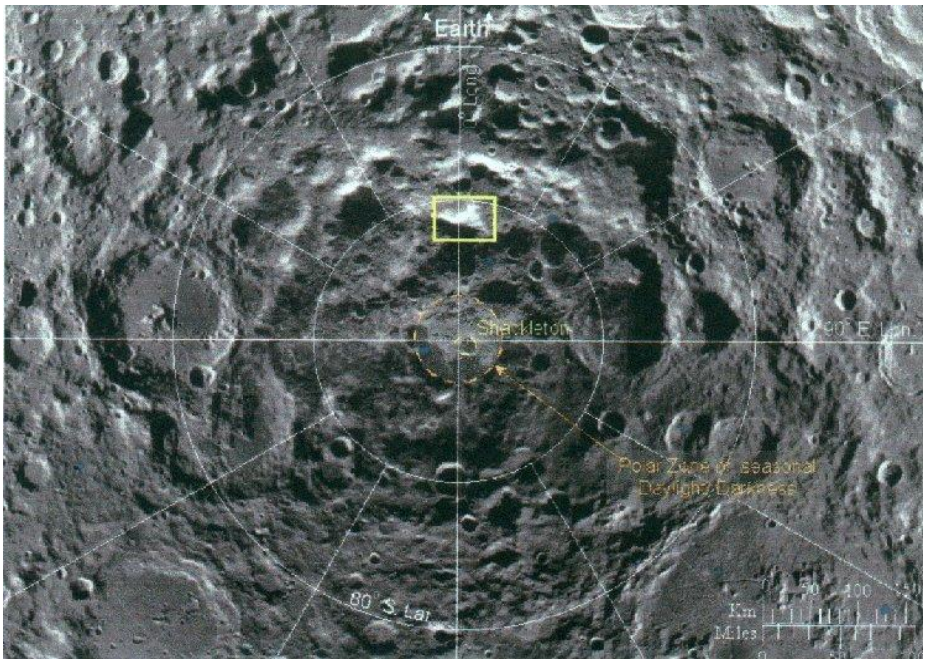

Figure 36: Combined Clementine mosaic and Earth-based radar image of the south polar region of the Moon. The subject mountain is located at 0° Longitude and 86° South Latitude is highlighted (NASA).

Figure 37 Blow-up image of the subject mountain in Figure 1 (NASA).

1.7.1 Abundant Sunlight

Access to sunlight is critical for lunar activities because sunlight is needed for the generation of electric power (with solar panels). By virtue of its location near the South Pole and its 5000-meter elevation, the summit of the mountain receives less than full sunlight for only 11% of the time, which is far greater than non-polar regions that receive less than full sunlight 50 % of the time. The long duration of sunlight at Malapert Mountain thus makes it a very attractive site for lunar base activities. Table below lists the projected sunset / sunrise events over the course of the lunar year at the summit of Malapert Mountain.

CY 2005	Touches	Half	Fully	Breaks	Half	Fully	Total Hrs.	Total Hrs.
Sun	Horizon	Set	Set	Horizon	Risen	Risen	Fully Set	Less than
Position			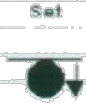					100%
First Sunset	6-May 0400	6-May 1800	7-May 1600	10-May 0200	10-May 2300	11-May 1400	58	130
Second Sunset	3-Jun 1300	3-Jun 2300	4-Jun 1100	10-Jun 0300	10-Jun 1500	11-Jun 0200	136	181
Third Sunset	2-Jul 1300	2-Jul 2200	3-Jul 900	10-Jul 0000	10-Jul 1000	10-Jul 2000	159	199
Fourth Sunset	1-Aug 0300	1-Aug 1400	2-Aug 0100	8-Aug 0300	8-Aug 1400	9-Aug 0000	146	189
Fifth Sunset	31-Aug 1100	1-Sep 0000	1-Sep 1600	5-Sep 0800	6-Sep 0000	6-Sep 1300	88	146
Sixth Sunset	2-Oct 0400					3-Oct 2100	0	41
	Total Hrs of Zero Sunlight in 2005 (7% of the time)						587	
	Total Hrs of Less than 100% sun in 2005 (11% of the time)							986
	Full Sun persists between 4 Oct 2005 and 28 Mar 2006.							
	NOTE: Periodicity of "Sunset Season" is about 348 earth days, not 1 earth year.							

Table 2 Schedule of sunset / sunrise events at Malapert Mountain The table projects the number of hours that the sun passes below the horizon during the year 2005 at lunar 00 Longitude, 860 South Latitude, and 5000 meter elevation. Every year is different, but most years have about 6 sunsets of similar duration, followed by 5-6 months of full sun. For 2005, the summit of Malapert Mountain is projected to receive full or partial sunlight for 93% of the time.

1.7.2 Earth Visibility

The second advantage is that the summit of Malapert Mountain is always in direct line of sight with the Earth for uninterrupted real-time control of robotic devices (a virtual presence for Earth-based operators) on the lunar surface. Figure below illustrates the locus of Earth's libration motions as seen from the summit, over a one-year period the entire disk of the Earth is always above the horizon, allowing for direct Earth-Moon communications 24 hours per day every day.

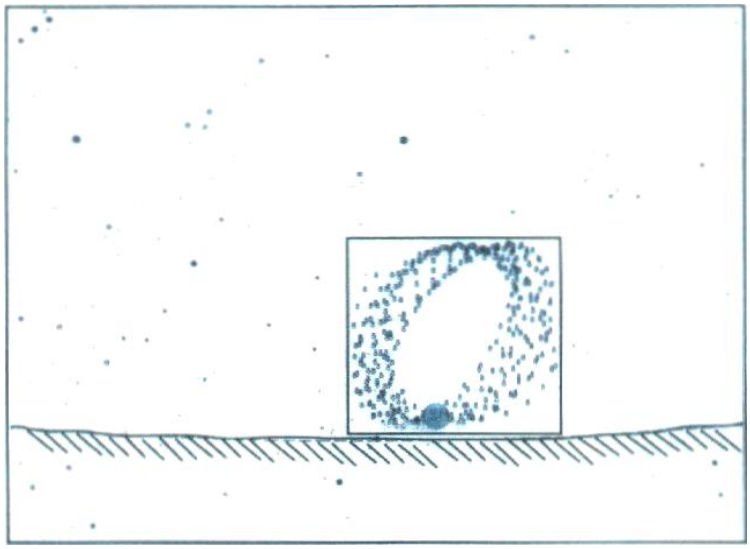

Figure 38: Locus of Earth's libration motion for the year 2005.

For any given location on the Moon, the Earth's libration pattern with respect to the Moon is fixed. From a location at the mountain's summit, the bottom of the libration box is approx. ½ degree above lunar horizon. The field of view for this figure is about 60° by 40° and for the libration box is about 12° by 14°. The always-visible Earth above the lunar horizon means that continuous real-time communications between the Earth and the Moon are possible.

Other high elevations in the south polar region also have the Earth in view continuously and receive long periods of sunlight, and they may be considered as sites for lunar bases. For example, two potential base sites at 84.50 South Latitude, 390 East Longitude and 83.50 South Latitude, 380 West Longitude have the Earth in

view continuously and receive less than full sunlight for 15% and 24% of the year, respectively. However, the combination of Earth visibility and long duration of sunlight strongly favors Malapert Mountain over other candidate locations as the first site for the next stage of lunar exploration.

1.7.3 Science Opportunities

Malapert Mountain may be considered as a prime candidate for the establishment of the first scientific base on the Moon. Long periods of sunlight and a continuous communication link with the Earth, as exist at Malapert Mountain, are highly advantageous for conducting scientific and exploratory missions. (A mission to Malapert Mountain would also provide information about the precise altitude of the mountain and the profile of the horizon as seen from the summit). Interpretations of data indicate that the rim of Shackleton Crater, which is located at the geographic South Pole, is visible from the summit at a distance of 122-Km (76-Mi.). Thus, the mountain could become the center of communications and power generation (and power beaming / energy management) for exploratory missions to the South Pole and surrounding regions.

Malapert Mountain is located near areas that may contain water ice, as suggested by the Clementine and Lunar Prospector Satellite Missions. If the presence of water ice is confirmed, lunar base development will be greatly facilitated because water and its hydrogen and oxygen components will be needed for a host of lunar industrial / scientific processes and for biological systems. The areas at the base of the mountain are well suited for the operation of telescopes, particularly radio telescopes that can be shielded from the radio noise of the Earth and infrared telescopes that are placed on the low-temperature floors of permanently shadowed craters. The difference between the sunlit and shadowed areas of the mountain will permit experiments with circumferential utilities (just below the summit), and long periods of sunlight can be applied to in-situ resource utilization experiments.

1.7.4 Logistics Advantages

The fourth advantage is that the topography of the mountain renders it suitable for initial and follow-on missions. Existing navigation technology will enable automated supply missions to target, maneuver, and land at the mountain's summit, where, by inspection, there appears to be roughly ten square kilometers of area that is suitable for logistical operations. Also, the slope of the mountain to the northwest is less than 100, which would allow wheeled vehicles to egress the mountain on treks to other areas in the south polar region, and return (see Figure below). The summit is also the logical point (the high ground) from which to coordinate and support the growth of bases throughout the south polar region.

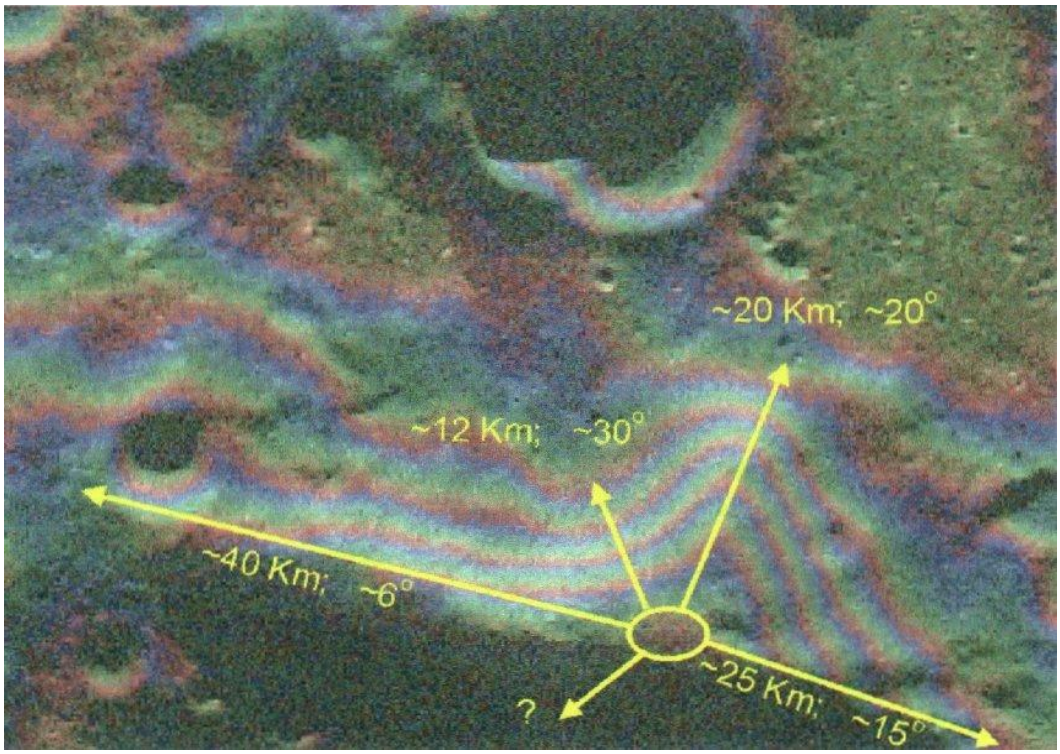

Figure 39 Downslopes away from the summit. The slope to the West-North-West from the summit is less than 100, which can be easily traversed with existing robotic systems.

1.8 Moonquakes

With the development of the new Crew Exploration Vehicle, (CEV), NASA astronauts will again be able to explore the surface of the Moon before the end of the next decade. But, unlike in the earlier, short Apollo visits, these astronauts are planning to build a permanent base that could sustain crews for long periods of time, preparing for further exploration of the solar system.
But according to Clive Neal, Associate Professor of Civil Engineering and Geological Sciences at the University of Notre Dame, these same astronauts may be in for a shocking, and rocking, surprise.
"The Moon is seismically active," he told a gathering of scientists at NASA's Lunar Exploration Analysis Group (LEAG).

Between 1969 and 1972, Apollo astronauts placed seismometers at their landing sites around the Moon. The Apollo 12, 14, 15, and 16 instruments faithfully radioed data back to Earth until they were switched off in 1977.

What Did These Seismometers Reveal?
Surprising evidence suggests that there are at least four different kinds of Moonquakes:
(1) deep Moonquakes about 700 kilometers below the surface, probably caused by tides;
(2) vibrations from the impact of meteorites;
(3) thermal quakes caused by the expansion of the frigid crust when first illuminated by the morning sun after two weeks of deep-freeze lunar night; and
(4) shallow Moonquakes only 20 or 30 kilometers below the surface.

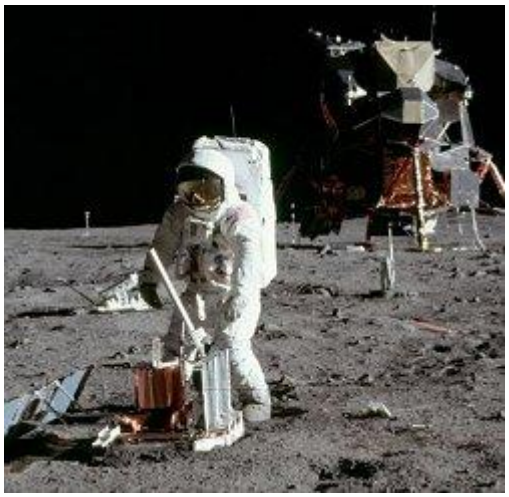

Figure 40: Buzz Aldrin deploys a seismometer in the Sea of Tranquility.

The first three were generally mild and harmless. However, the Apollo seismic network recorded 28 powerful shallow Moonquakes between 1972 and 1977-- some of them registering up to 5.5 on the Richter scale. A magnitude 5 quake on Earth is energetic enough to move heavy furniture and crack plaster.

Furthermore, according to Neal, shallow Moonquakes tended to last five times longer than on Earth. Recorded shallow Moonquakes lasted more than 10 minutes, whereas on Earth, even the biggest, most devastating earthquakes stop shaking after about two minutes.

The reason, according to Neal, has to do with chemical weathering. On Earth, vibrations from quakes usually die away in only half a minute. Water weakens stone, expanding the structure of different minerals. When energy propagates across such a compressible structure, it acts like a foam sponge? it deadens the vibrations.

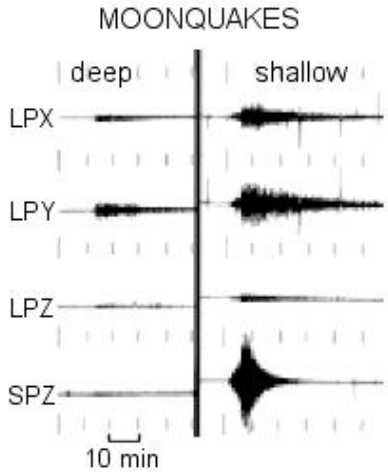

Figure 41: Representative lunar seismograms from the Apollo 16 station.

The Moon, however, is dry, cool and mostly rigid, like a chunk of stone or iron. Therefore, Moonquakes cause it to vibrate, much like a tuning fork. And with this, even a mild Moonquake could cause persistent vibrations that could prove more significant than the Moonquake's magnitude.

1.8.1 What Causes Moonquakes?

There has not been significant evidence to pinpoint the exact cause of shallow Moonquakes or where they are most likely to occur. Neal explains that because the Apollo seismometers were all in one relatively small area on the front side of the Moon, the exact locations of the quakes could not be measured.

Neal contends that any permanent lunar base would have to be built of materials that are flexible, not unlike skyscrapers in earthquake prone cities on Earth. They would also need to know the fatigue threshold of building materials-- that is, how much repeated bending and shaking they could withstand.

1.9 Reference Table

1. Lunar and Planetary Science XXXVII (2006)
2. http://www.lpi.usra.edu/resources/lunar_orbiter/
3. http://www.Moonsociety.org/blog/index.php?m=200612
4. http://www.spaceref.com/news/viewpr.html?pid=14485
5. http://amesnews.arc.nasa.gov/releases/2004/lunarbase/lunarbase.html
6. http://amesnews.arc.nasa.gov/releases/2004/mobitat/mobitat.html
7. http://www.spacearchitect.org
8. http://aoss.engin.umich.edu/class/eng450/archives/06_eng450/index.html
9. http://www.nyjtimes.com/Stories/2007/NASATacklesChallengeOfBuildingMoonBase.htm
10. http://spaceflight.nasa.gov/gallery/images/mars/lunarbases/html/s78_23252.html
11. http://spaceflight.nasa.gov/gallery/images/mars/lunarbases/ndxpage1.html
12. http://www.nasa.gov/centers/ames/news/releases/2004/04_64AR.html
13. http://www.nasa.gov/centers/ames/news/releases/2004/mobitat/mobitat.html
14. http://amesnews.arc.nasa.gov/releases/2004/lunarbase/lunarbase.html http://ic.arc.nasa.gov/
15. http://www.angelfire.com/space/usis/malapertmtn.htm
16. MALAPERT MOUNTAIN REVISITED David G. Schrunk
17. Moon Base : a Challenge for Humanity – Washington DC, Oct 11-12, 2005 [M.A. Perino Alcatel Alenia Space – Italia]
18. Moonquakes: Understanding our Seismically-Active Neighbor [Clive Neal, Associate Professor of Civil Engineering and Geological Sciences at the University of Notre Dame]
19. NASA In-Situ Resource Utilization (ISRU) Research & Development
20. Regolith [M. Küppers]

SAPIENZA
UNIVERSITÀ DI ROMA

2 Chapter 2
The basic idea of Lunar Expandable-Mobile-Modular Base (LEMMB)

2.1 Abstract

The future space mission exploration aim to reduce the costs associated with design, fabrication and launch for ISS (International Space Station), Moon and Mars Modules, while simultaneously increasing the useful volume.
Flexible, expandable and inflatable structures, offer many advantages over conventional structures for space applications.
Principal among the advantages is the ability to package these structures into small volumes for launch.

The purpose of this thesis is to describe a rapid Lunar Base Station development by mobile - expandable - modular structures called LEMMB (Lunar Expandable - Mobile - Modular Base).
Positive aspects of this idea are the minimum EVA activities required to the crew for the habitat activation and the typical modularity that allow easy reconfiguration and evolution of the Base.

The launcher and the landing system dictate basic habitat constraints like the maximum mass, the "folded" length and volume available.

A great advantage of mobile lunar habitats LEMMB is the ability to move out with respect of the lunar landing zone, which could be an hazardous place. The landing zone poses the problem that once the habitat is landed on the Moon, it is not safe to land another vehicle on the same area because of ejection in a normal landing and, in case of an explosive failure on impact.
Plus the mobile base concept could be useful in terms of Moon exploration; the entire Moon base can be moved from one place to another one if required.
Thanks to mobility, each module can also be used as a rover decreasing the astronauts EVA and increasing the exploration capability in long time duration exploration.

The main problem in building a Lunar Base concern the ability to have at the same time at least the following characteristics:

- Be enough volume capable in order to grant a permanent and acceptable human presence inside the Lunar Base Module;
- Be self sufficient from energy point of view;
- Be Earth to Moon transported as much easily and at the lowest cost as possible.

The main problems from safety point of view are:

- Solar Cosmic Rays and Galactic Cosmic Rays radiation protection;
- Micro meteorites protection;
- Moonquakes resistant.

The main problems concerning crew surviving are:

- Air
- Water
- Food

Air, Water and Food are not object of this book.

As far as building problem is concerned, a possible approach based on flexible and expandable modular structures is presented in this thesis.

As far as safety problem is concerned a radiation protection system from Solar Cosmic Rays in chapter six is presented.
For micro meteorites protection the standard systems already adopted on ISS could be used, anyway a new system in chapter three is proposed.

Speaking about Moon quakes, the Moon is seismically active, between 1969 and 1972, Apollo astronauts placed seismometers at their landing sites around the Moon. The Apollo 12, 14, 15, and 16 instruments faithfully radioed data back to Earth until they were switched off in 1977.

The Apollo seismic network recorded 28 powerful Moonquakes between 1972 and 1977-- some of them registering up to 5.5 on the Richter scale. A magnitude 5 quake on Earth is energetic enough to move heavy furniture and crack plaster. Furthermore some Moonquakes tended to last five times longer than on Earth. Some Moonquakes lasted more than 10 minutes, whereas on Earth, even the biggest, most devastating earthquakes stop shaking after about two minutes.
The reason has to do with chemical weathering. On Earth, vibrations from quakes usually die away in only half a minute. Water weakens stone, expanding the structure of different minerals. When energy propagates across such a compressible structure, it acts like a foam sponge? it deadens the vibrations.
The Moon, however, is dry, cool and mostly rigid, like a chunk of stone or iron. Therefore, Moonquakes cause it to vibrate, much like a tuning fork. And with this, even a mild Moonquake could cause persistent vibrations that could prove more significant than the Moonquake's magnitude.
The Moon rings like a bell when it is impacted. There is no water to absorb the sound vibrations. When the Apollo 12 Lunar Module was crashed into the Moon, the Moon reverberated for over two hours.
Moon quakes have been taken into account, the LEMMB structures are not implanted on the lunar surface, LEMMB structure is like of a car.

In this chapter the basic ideas about the Lunar Base building method are presented.
Since we spoke about a modular system, let us start saying that each module should be transported from Earth To Moon by preferably conventional vehicle system (conventional and as a consequence low cost compared in building a new launcher for this specific mission) and, once located on the Moon surface, it should be volume expandable capable.

Step by step several modules of the same type could be located and connected to each other by using the expandable (inflatable) structures (i.e. connection structures), obtaining a complete LBS (Lunar Base Station).

As far as energy is concerned, each module are covered with PV (Photo Voltaic) solar array, in addition since the LEMMB connection structure are covered with PV solar array also, then once expanded, each of them will be like a big PV solar array. By some computations, the average electrical power available for each LEMMB should be about 5-6 kW, in this manner each module should be energy self sufficient. Each module once located will permanently remain on the Moon surface, unless provided by independent propulsion system and transformed into space vehicle.
A single LEMMB module in figure below is shown.

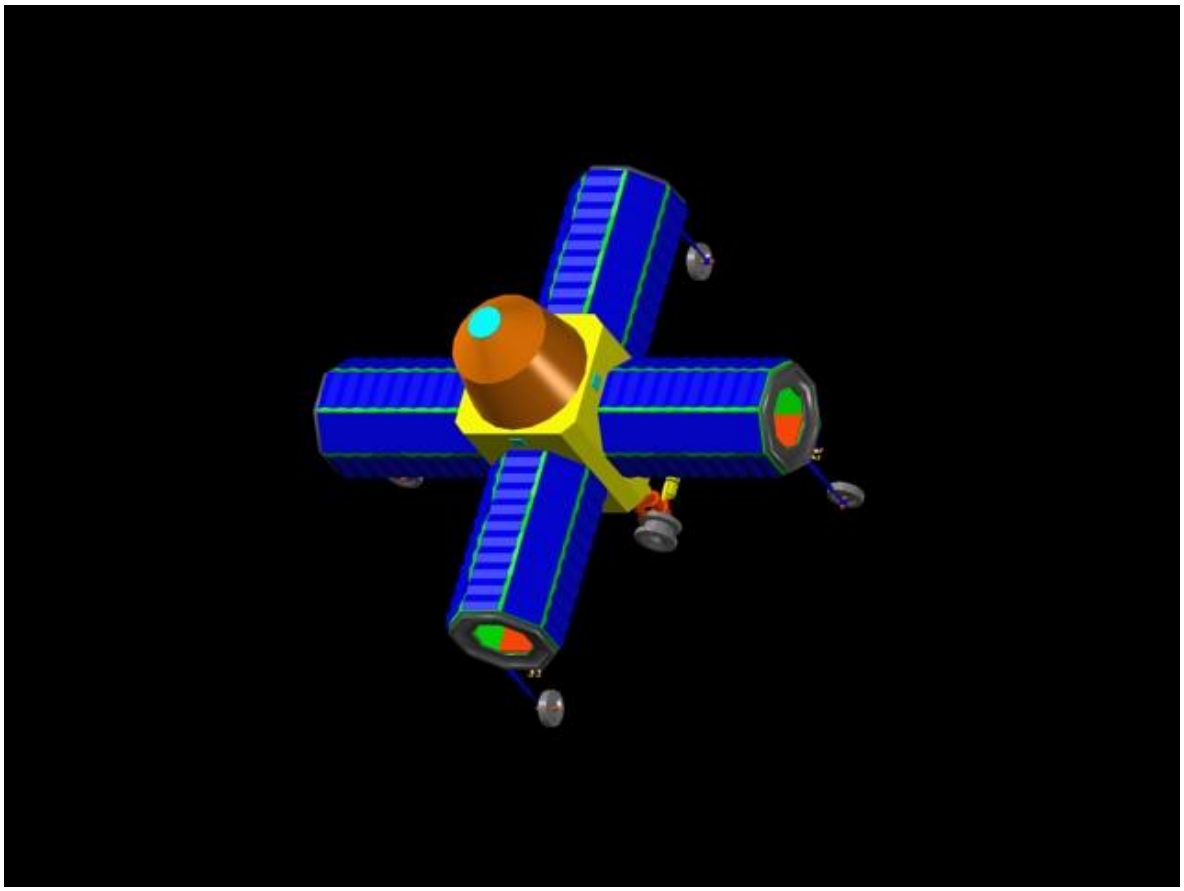

Figure 42: single LEMMB (Lunar Expandable Mobile Modular Base)

A Moon base obtained connecting several single LEMMB modules in figure below are shown.

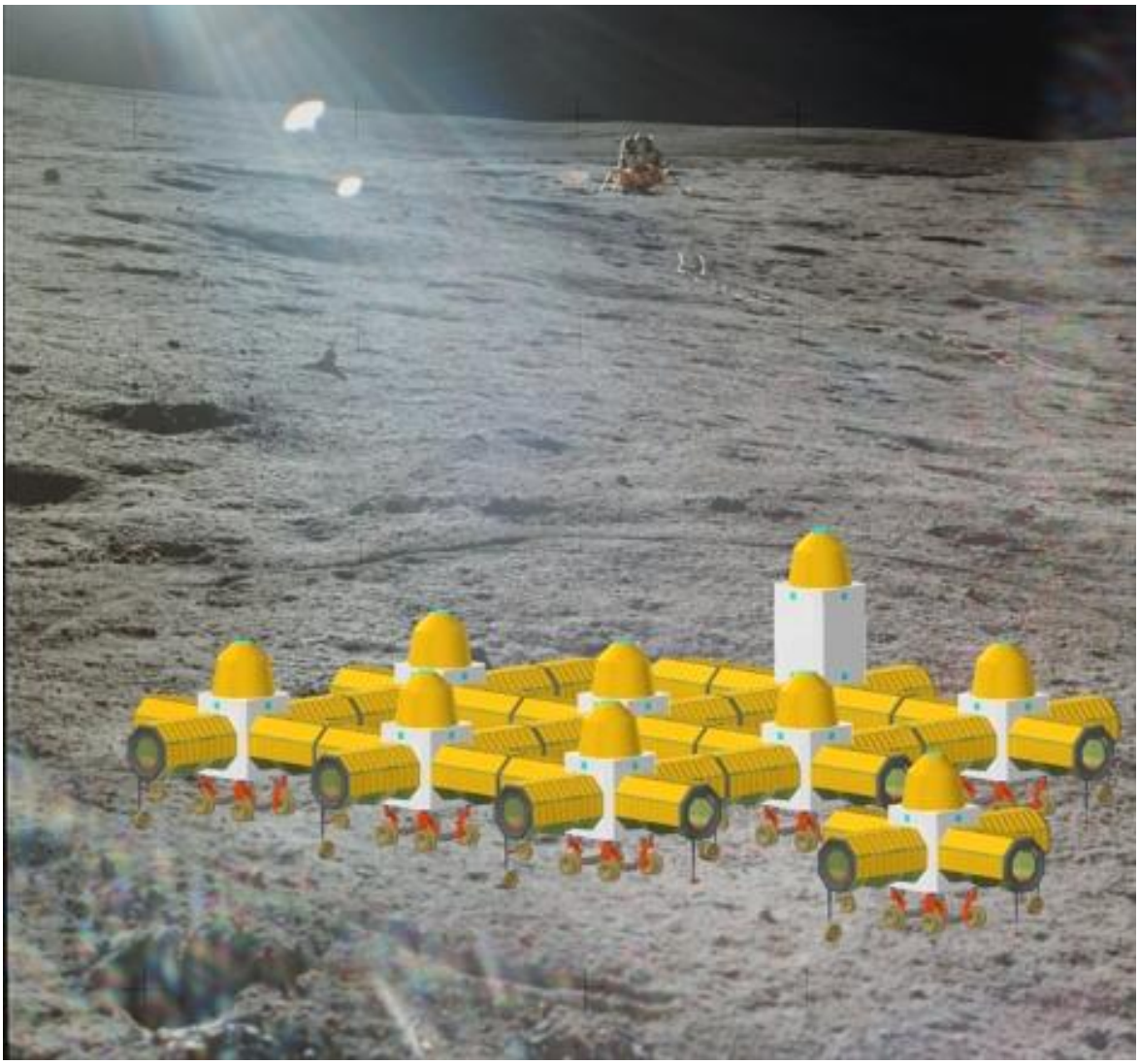

Figure 43: Lunar Base Station made connecting more LEMMB module on lunar surface

2.2 Space Transport Vehicle System

The basic idea is to use, if possible, a European Space Lunch Vehicle like, as an example the Ariane vehicle. In this book a modified version of the Ariane 5 has been taken into account for this mission. Here after some Ariane 5 characteristic are shown, more details in chapter four are presented.

The LEMMB dimensions are compliant with the Ariane 5 and Soyuz volume dimension capability constraint.

2.2.1 Ariane 5 launch vehicle general data

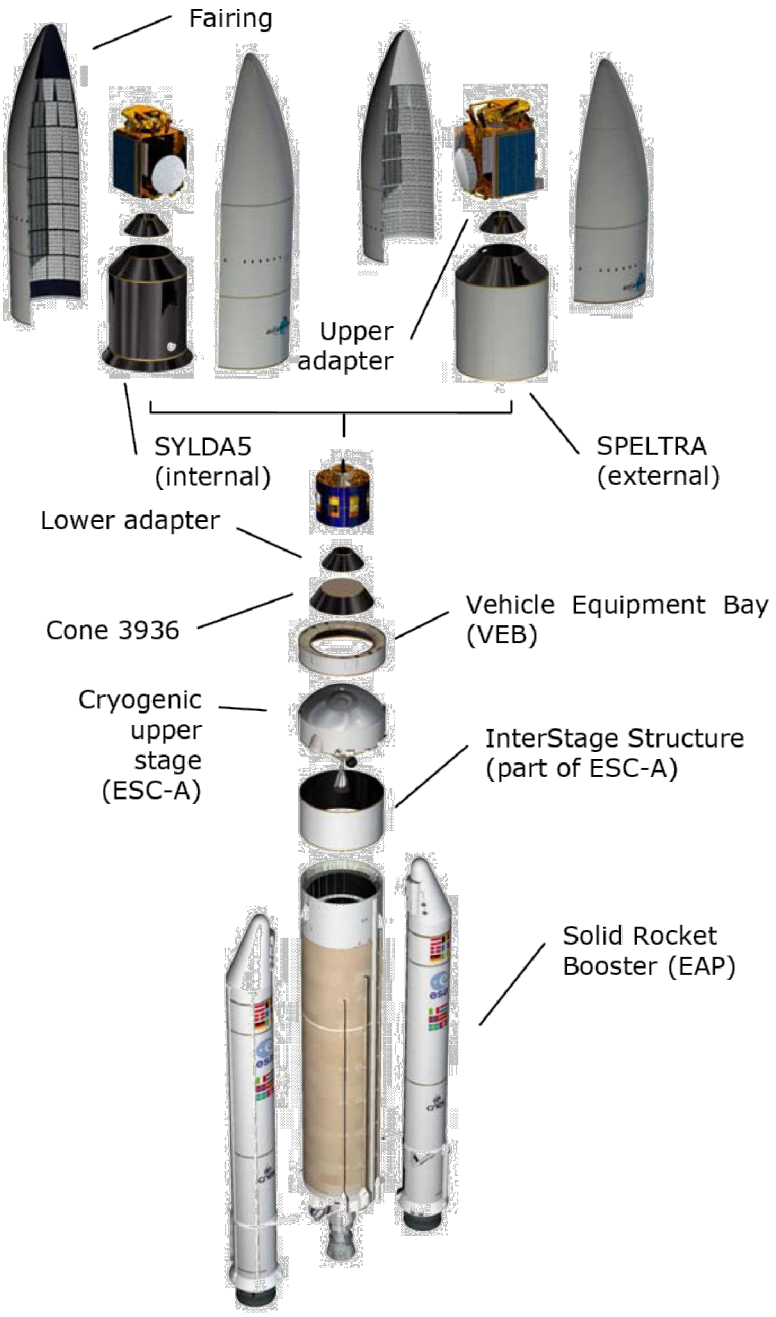

Figure 44: Ariane configuration Sylda5 and Speltra

Two solid rocket boosters provide 90 percent of Ariane 5's thrust at lift-off, a cryogenic core stage ignited and checked on ground provides for the first part of the Launch.

PAYLOAD FAIRING	Short	Medium	Long
Diameter	5,4 m	5,4 m	5.4 m
Height	12,728 m	13,813 m	17 m
Mass	1970 kg	2060 kg	2675 kg
Structure	Two halves - Sandwich CFRP sheets and aluminium honeycomb core		
Acoustic protection	Foam sheets		
Separation	Horizontal and vertical separations by leak-proof pyrotechnical expanding tubes		

SPELTRA	SPELTRA 4160	SPELTRA 5660
Diameter	5,4 m	5,4 m
Total height	5,5 m	7 m
Cylinder height	4,16 m	5,66 m
Mass	715 kg	830 kg
Structure	Sandwich CFRP sheets and aluminium honeycomb core	
Separation	Leak-proof pyrotechnical expanding tube at the base	

SYLDA5	
Diameter	4,56 m
Height	Total height of standard version: 4,903 m Adjustable cylinder height : +0.3/+0.6/+0.9/+1.2/+1.5 m w.r.t. standard
Mass	From 407 to 512 kg, depending on height
Structure	Sandwich CFRP sheets and aluminium honeycomb core
Separation	Leak-proof pyrotechnical expanding tube at the base of the cylinder

ADAPTERS	off-the-shell devices
Clampband	∅937 ∅1194 ∅1666 ∅2624
4 pyronuts	∅1663

CONE 3936	
Height	783 mm
Mass	200 kg
Structure	Monolithic CFRP cone and glass fiber membrane

VEB	
Structure	Sandwich CFRP sheets and aluminium noneycomb core
Avionics	Flight control, flight termination, power distribution and telemetry subsystems

Table 3: Ariane Vehicle Data

2.2.2 Ariane 5 Performance definition

The performance figures below given in this chapter are expressed in term of payload mass.

- The mission performance includes the mass of:
  - the spacecraft(s)
  - the dual launch system (if used), which mass is mission dependant and approximately of:
    - Standard SYLDA 5 425 kg
    - SYLDA 5 + 900 mm 475 kg
    - SYLDA 5 + 1500 mm 505 kg
    - SPELTRA 4160 715 kg
    - SPELTRA 5660 830 kg
  - the adapters or dispensers
  - the raising Ø 5400 cylindrical structure (if used):
    - H = 500 mm m = 180 kg
    - H = 1000 mm m = 220 kg
    - H = 1500 mm m = 265 kg
    - H = 2000 mm m = 305 kg
- Performance computations are based on the following main assumptions:
  - Cryogenic main core and upper stage carrying sufficient propellant to reach the targeted orbit with the specified probability of 99 % except otherwise specified
  - Aerothermal flux at fairing jettison and second aerothermal flux less or equal to 1135 W/m^2
  - Altitude values given with respect to a spherical earth radius of 6378 km
  - Launch from the CSG (French Guiana), taking into account the relevant safety requirements
  - Medium fairing

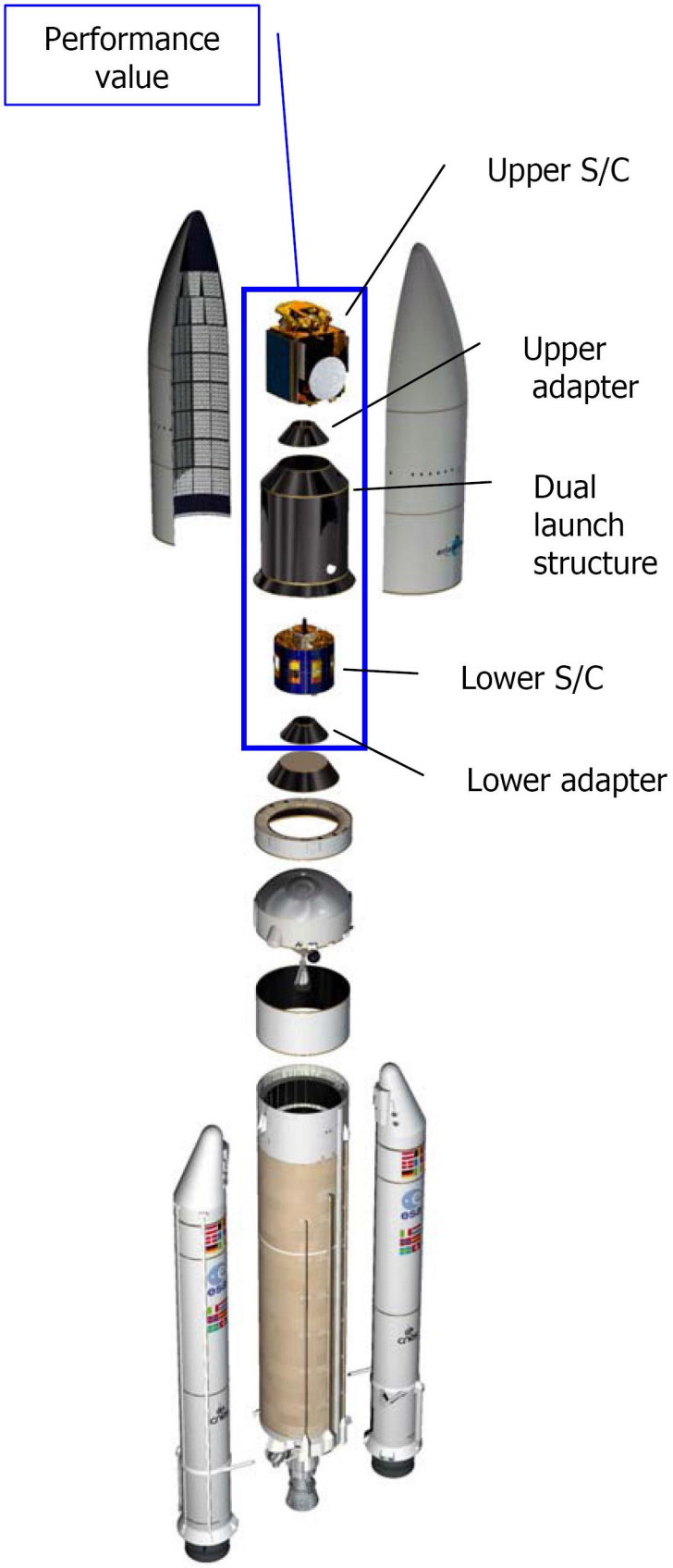

Figure 45: Ariane5 performance definition

2.2.3 Ariane 5 Spacecraft interfaces

The Ariane 5 launch vehicle provides standard interfaces that fit all spacecraft buses and allow an easy switch between the launch vehicles of the European Transportation Fleet.

This paragraph covers the definition of the spacecraft interfaces with the payload adaptor, the fairing, the SYLDA 5, and the SPELTRA.

The spacecraft is mated to the L/V through a dedicated structure called an adaptor that provides mechanical interface, electrical harnesses routing and systems to ensure the spacecraft separation. Off-the-shelf adaptors, with separation interface diameter of 937 mm, 1194 mm, 1663 mm, 1666 mm and 2624 mm are available.

For a spacecraft in single launch, one of the available fairing designs protects the spacecraft mounted on top of an adaptor which can be a standard Ariane or Customer's design.

For dual launch, two configurations are available, with the two carrying structures SPELTRA and SYLDA 5:

- the fairing protects the upper spacecraft mounted on top of an adaptor (standard Ariane or Customer's design) fixed on to the SPELTRA or the SYLDA 5 upper interface flange,
- the SPELTRA or the SYLDA 5 protects the lower spacecraft mounted on top of an adaptor (standard Ariane or Customer's design) fixed on the launcher interface flange,
- the difference between SPELTRA and SYLDA 5 lies in the fact that SYLDA 5 is totally protected by the fairing while the SPELTRA is an external carrying structure.

Note: ∅ 5400 mm extension structures (ACY 5400) allow to adapt the existing fairing, SPELTRA or SYLDA 5 to the Customer need.

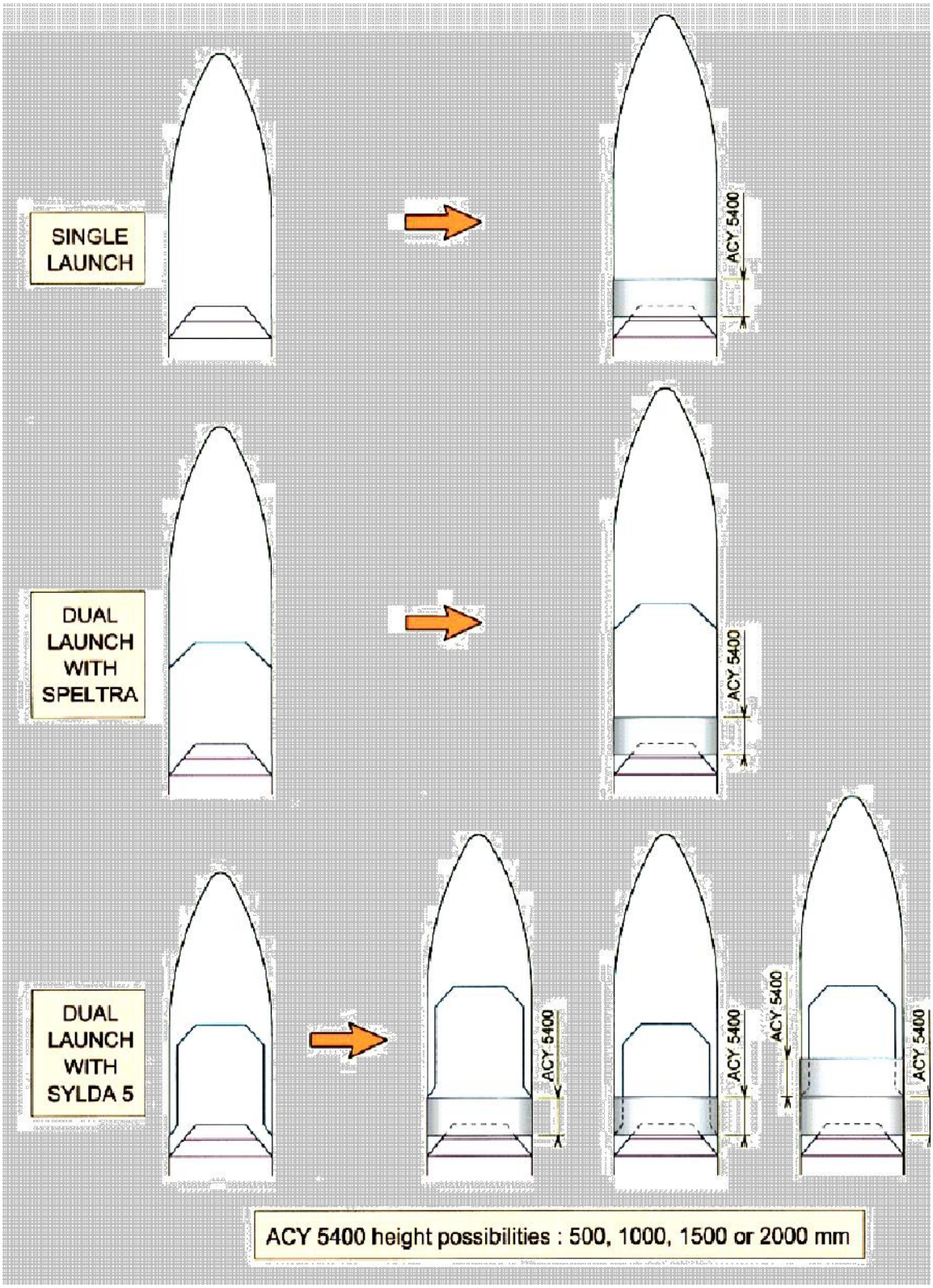

Figure 46: Ariane 5 Fairing and adaptors system

2.2.4 Usable volume under fairing, SYLDA5 and SPELTRA

The free volume available to the payload, known as the "static volume", is shown in the following figures. This volume constitutes the limit that the static dimensions of the spacecraft, including manufacturing tolerance, thermal protection installation, appendices…etc, may not exceed.

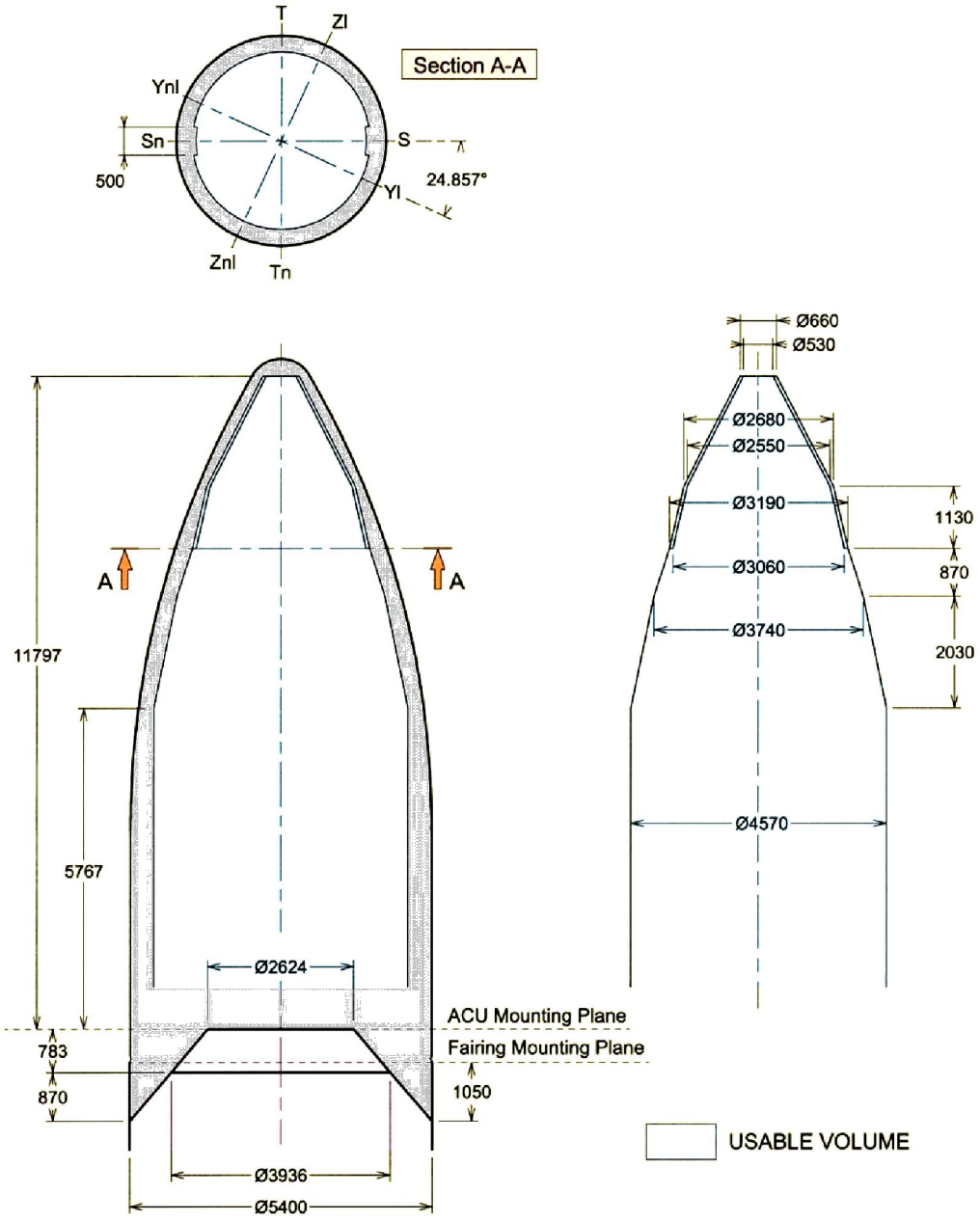

Figure 47: Ariane5 Usable volume beneath payload short fairing

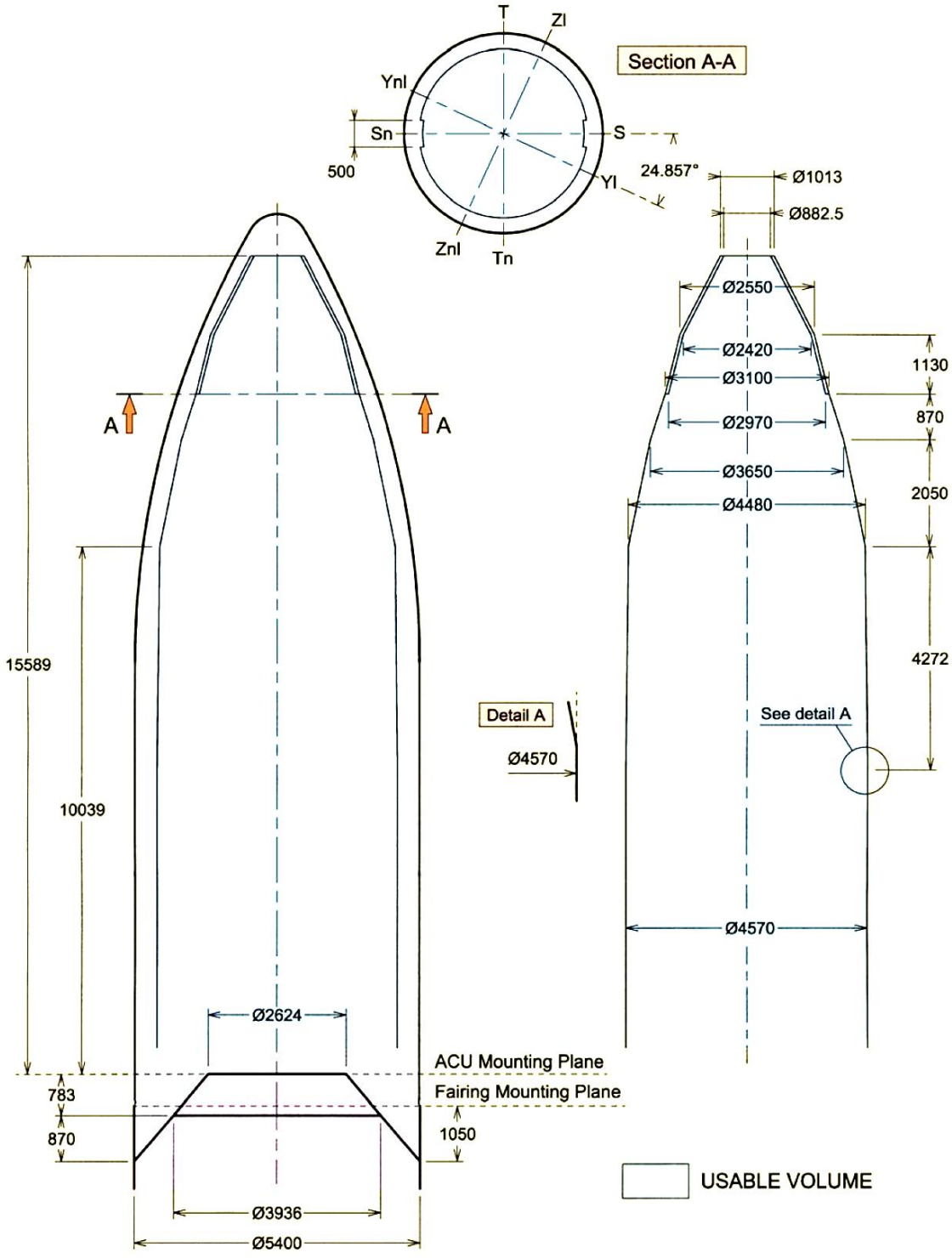

Figure 48: Ariane5 Usable volume beneath payload long fairing

2.3 Lunar Expandable-Mobile-Modular Base idea

The LEMMB (Lunar Expandable-Mobile-Modular Base) is dimension compliant with the Ariane Spacecraft-Stack Allocated Volume and Soyuz Fairing allocated volume. In the next Figure the comparison between the Ariane5 Spacecraft-Stack Allocated Volume within the ST-Fairing and the contained LEMMB is reported.

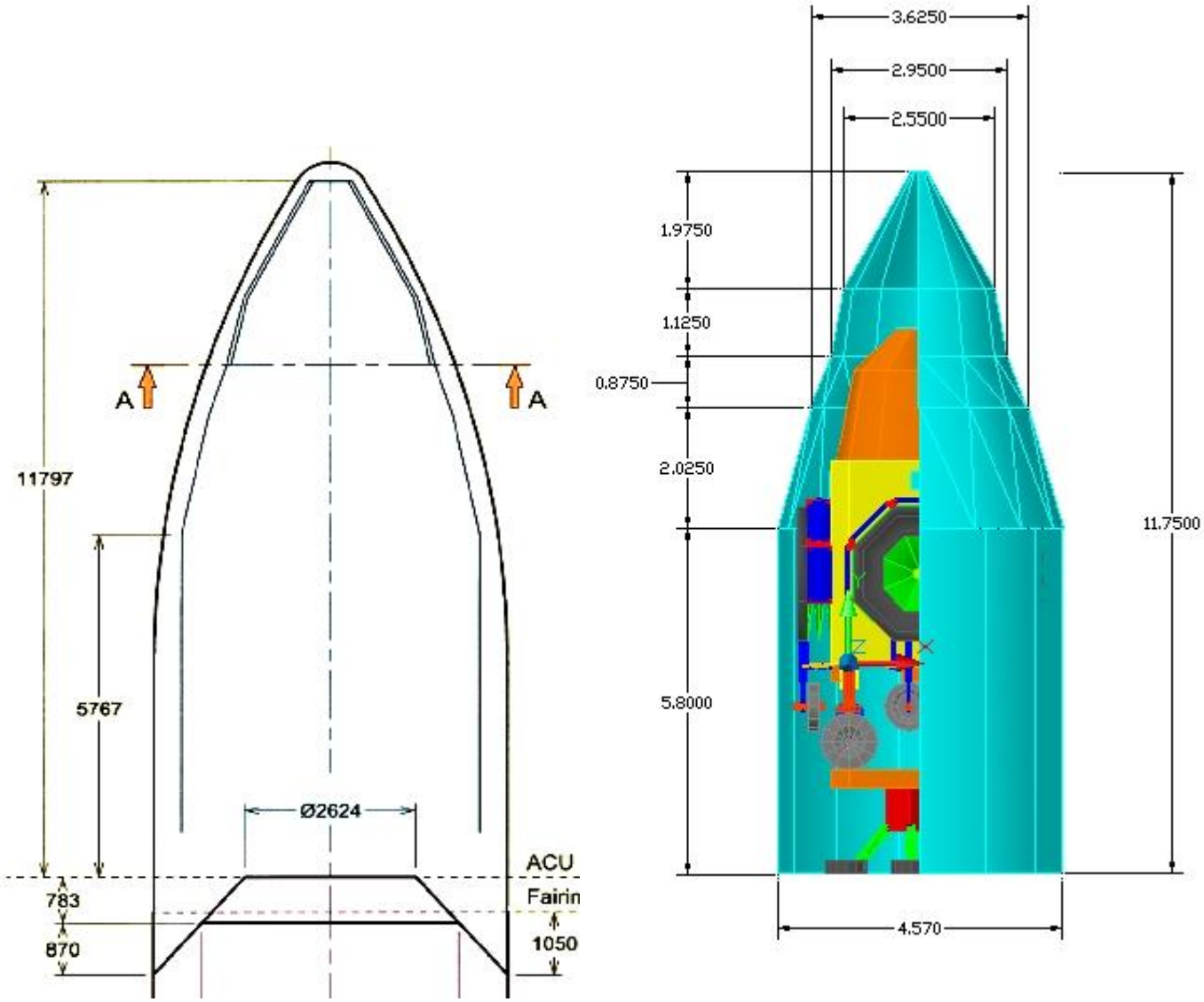

Figure 49: Ariane Fairing Volume and LEMMB

In the next Figure the comparison between the Soyuz Spacecraft-Stack Allocated Volume within the ST-Fairing and the contained LEMMB is reported.

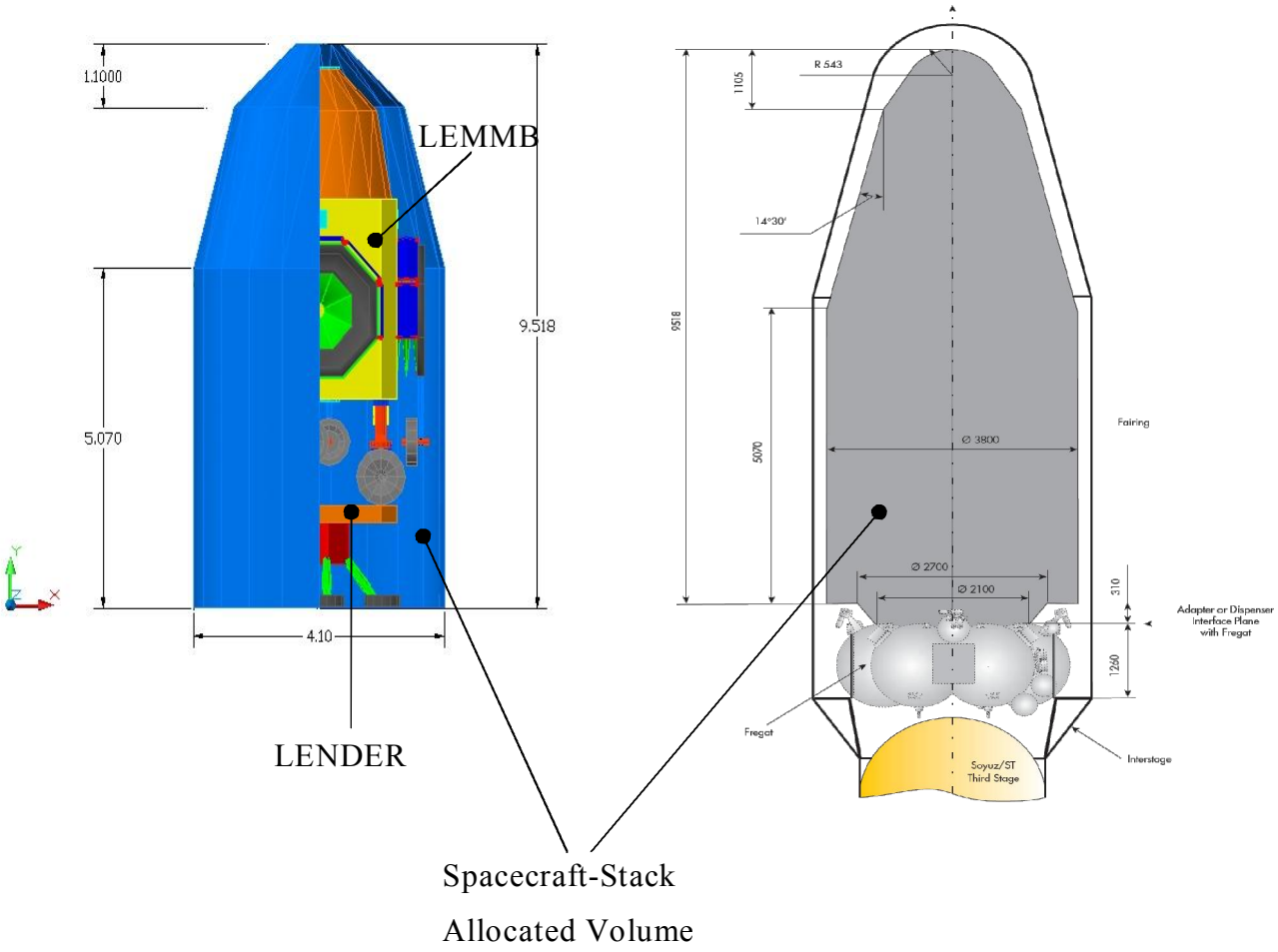

Figure 50: comparison between Soyuz Fairing volume and LEMMB Volume

In order to transport the LEMMB from Moon Parking Orbit, through the final destination on a lunar surface, the LEMMB is provided by a LANDER able to locate the LEMMB close to the desired location.

To increase the safety, the mission is initially unmanned. Once approached the Moon surface, the final location for each LEMMB can be obtained driving LEMMB by the LEMMB remote control system. The mobility of each LEMMB module is given by four independents wheel commanded by four independent electrical motor.

At the end, once the module is located to the final destination, the four ASI (Arm Structures Inflatable) is commanded to open, stretching itself completely.

The connection of several modules to each other by ASI will make, step by step, a Lunar Base Station for a permanent presence of the human life.

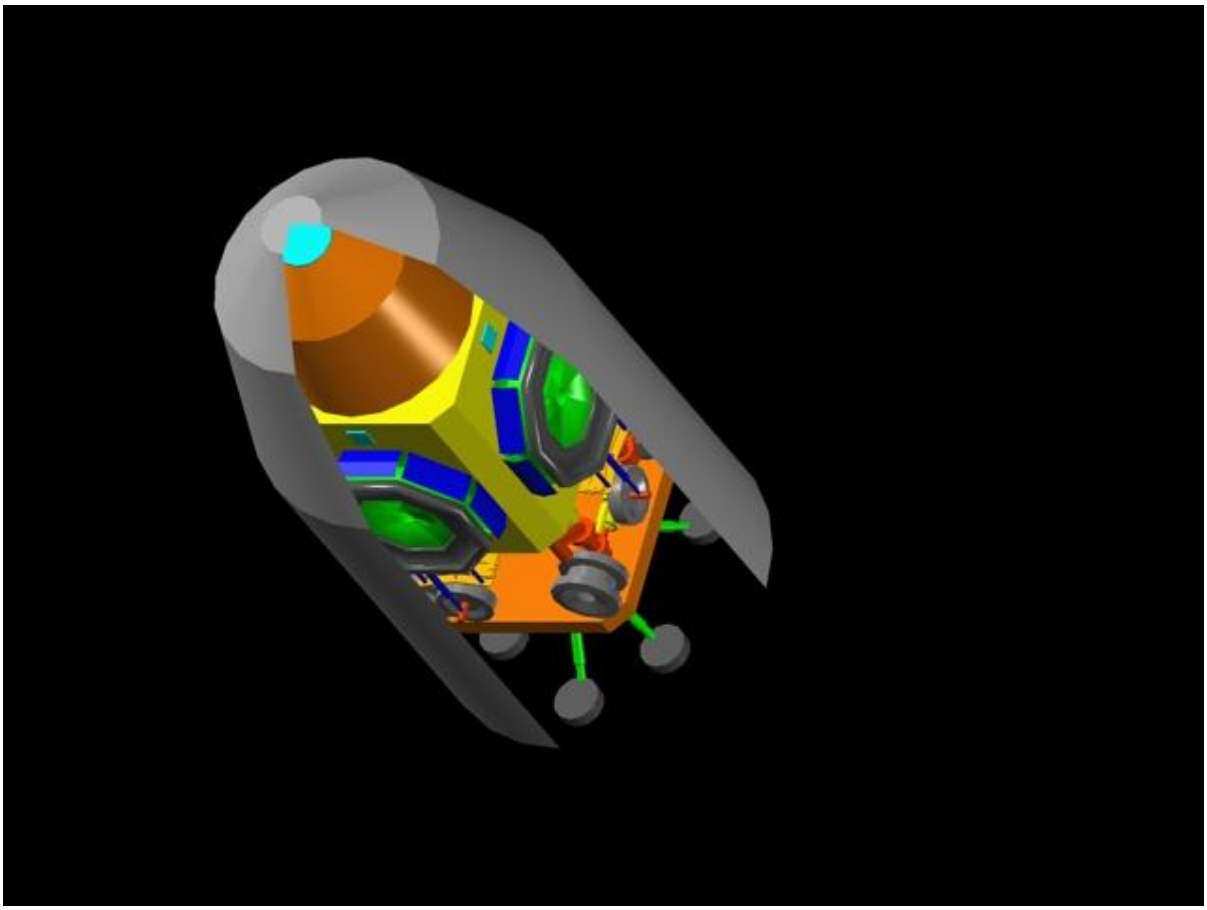

Figure 51: LEMMB and LANDER under the Soyuz or Ariane 5 Fairing

The next sections describe the required five plus one phases to develop the Moon base.
Each LEMMB module is assumed to be already landed on the lunar surface.

LANDER vehicle is not object of this book anyway some approach with respect to structure mass, engine dimension, propellant mass, propellant type, are computed in chapter four.

2.3.1 Lunar Base Building phases

Figures below show the five primary phases to locate the LEMMB and develop the Lunar Base.

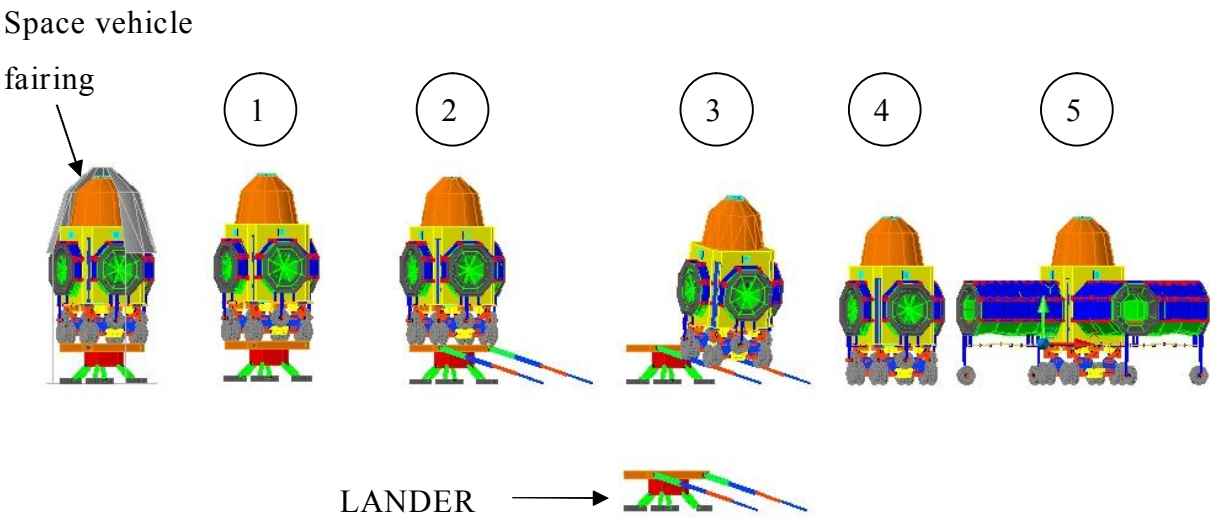

Figure 52: phases representation

- Phase 1) LANDER approach the Moon surface;
- Phase 2) Ramp of LANDER is deployed;
- Phase 3) LEMMB is driven down through the Ramp;
- Phase 4) LEMMB is driven by remote control to the precise final location on the lunar surface;
- Phase 5) The AIS (Arms Inflatable Structures) are deployed;
- Phase 6) Several LEMMBs are connected to each other to make a Lunar Base;

Here after is described each single phase.

2.3.1.1 Phase 1) LANDER approach the lunar surface

In the first phase when the LANDER approaches the lunar surface, the LEMMB is located on and fixed to the LANDER platform.

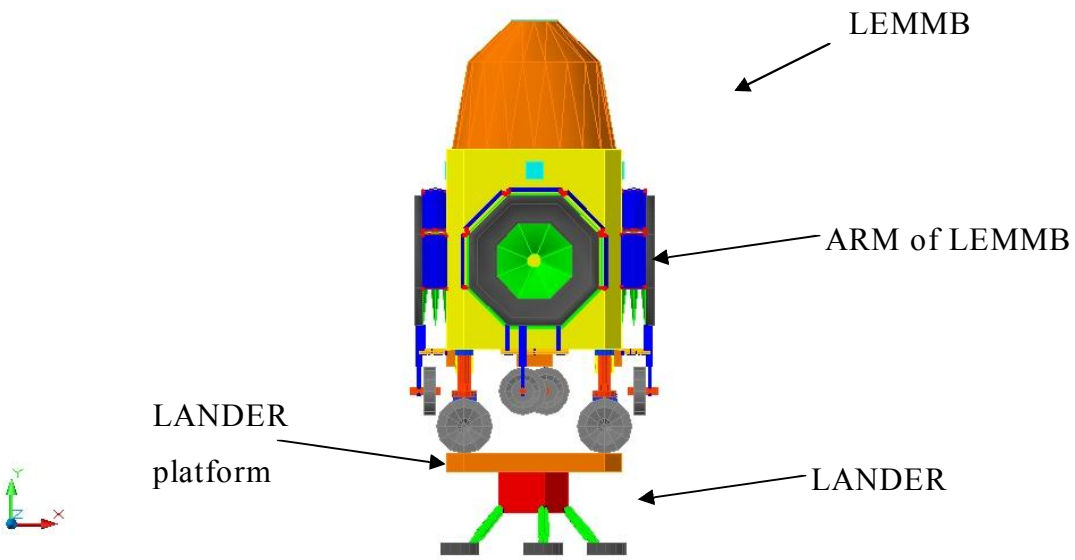

Figure 53: phase 1 " LEMMB on LANDER platform"

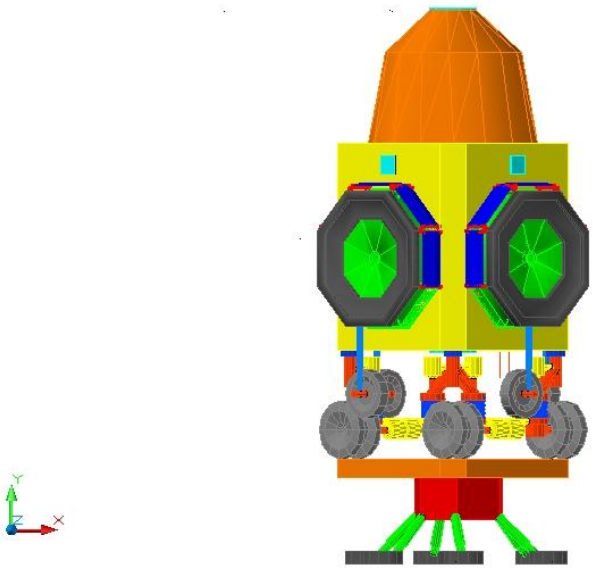

Figure 54: phase 1 " LEMMB on LANDER platform"

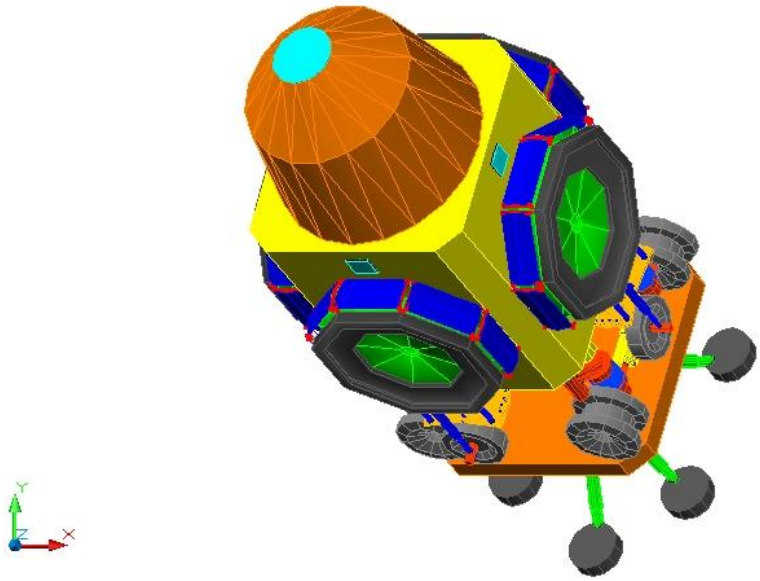

Figure 55: phase 1 " LEMMB on LANDER platform"

Figure 56: rendering phase 1 "LEMMB on LANDER platform"

2.3.1.2 Phase 2) Ramp of LANDER is deployed

After the landing, a deployable ramp contained within the LANDER platform start to be stretched out forming two binaries on which the LEMMB is driven down.
The binaries are conceived as a telescope system deployed in rotation. This system is known as ballscrews system.
A system like this is already patented and used to get off some satellite from the space vehicle. For further information about ballscrews system see: http://www.umbragroup.it/EN/Industrial/Products/index_html?id_fam=Fam1 web site.

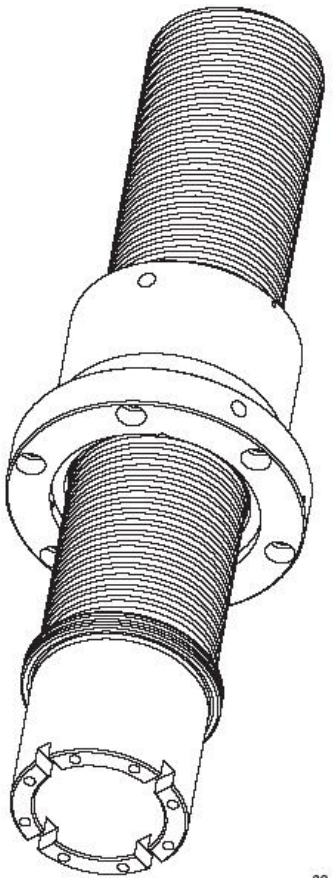

Figure 57: ballscrews external views

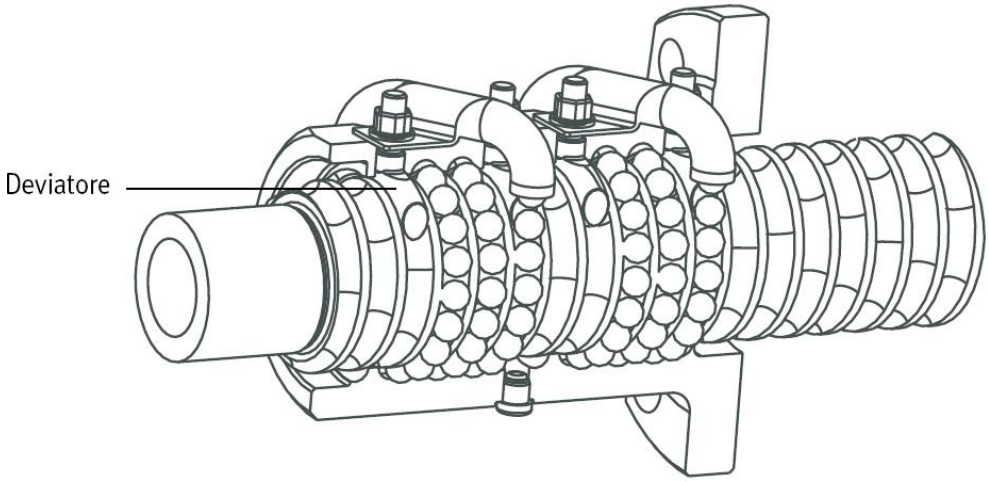

Figure 58: ballscrews section

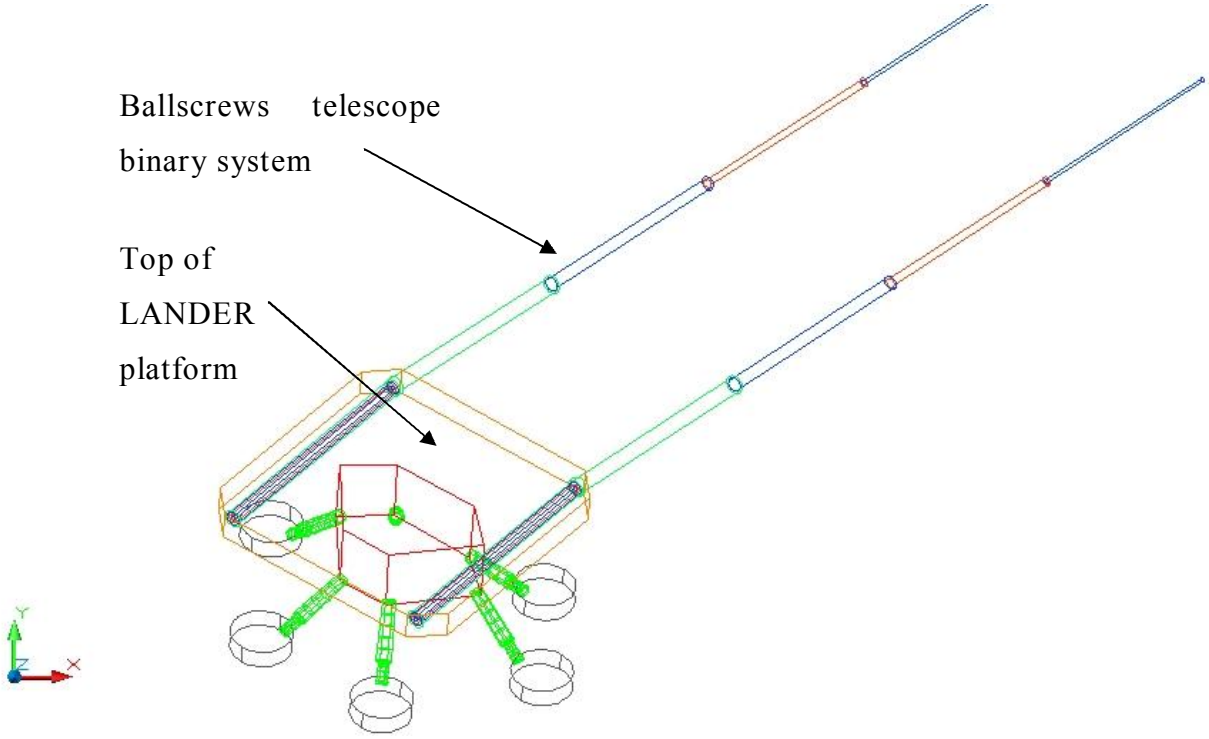

Figure 59: LANDER platform and ballscrews system

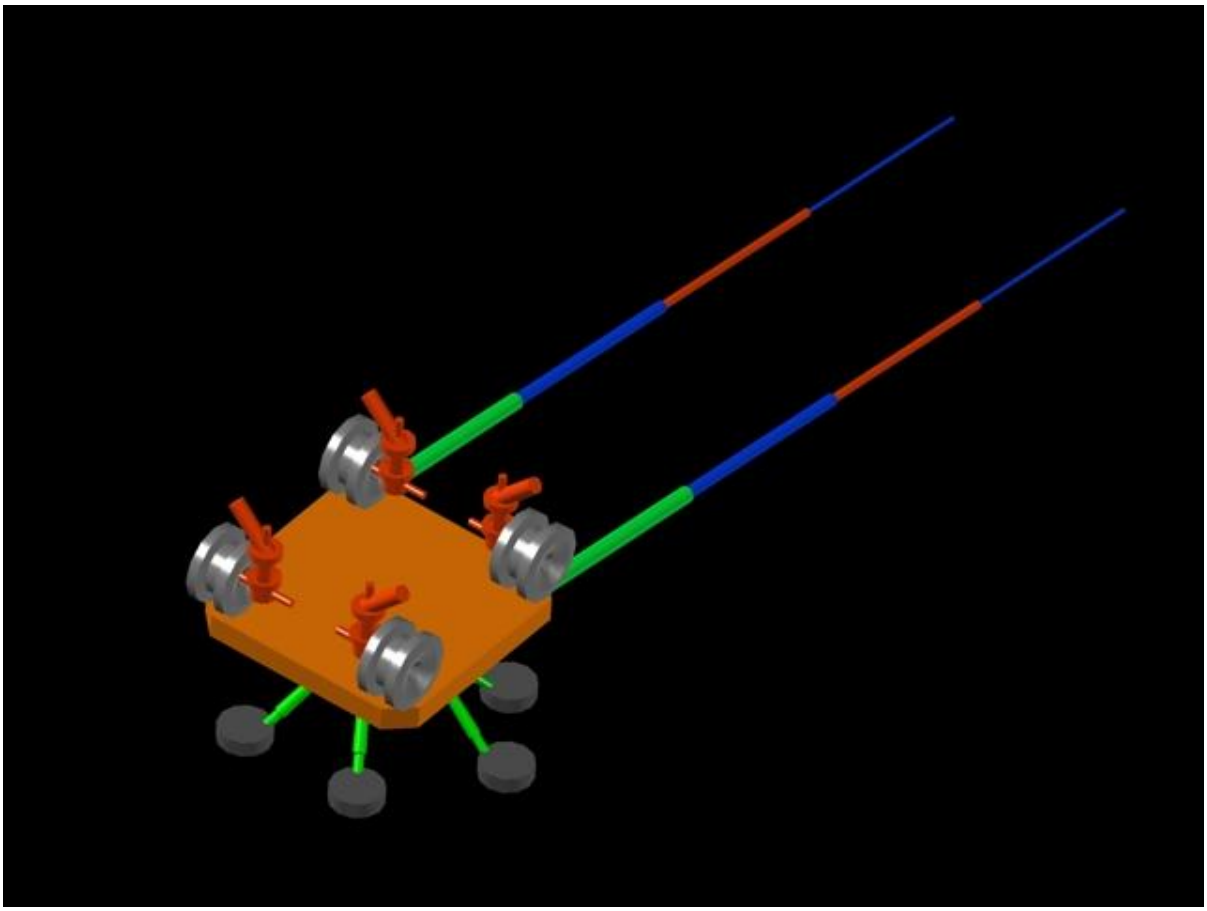

Figure 60: rendering LANDER platform " extended binary and wheel of LEMMB"

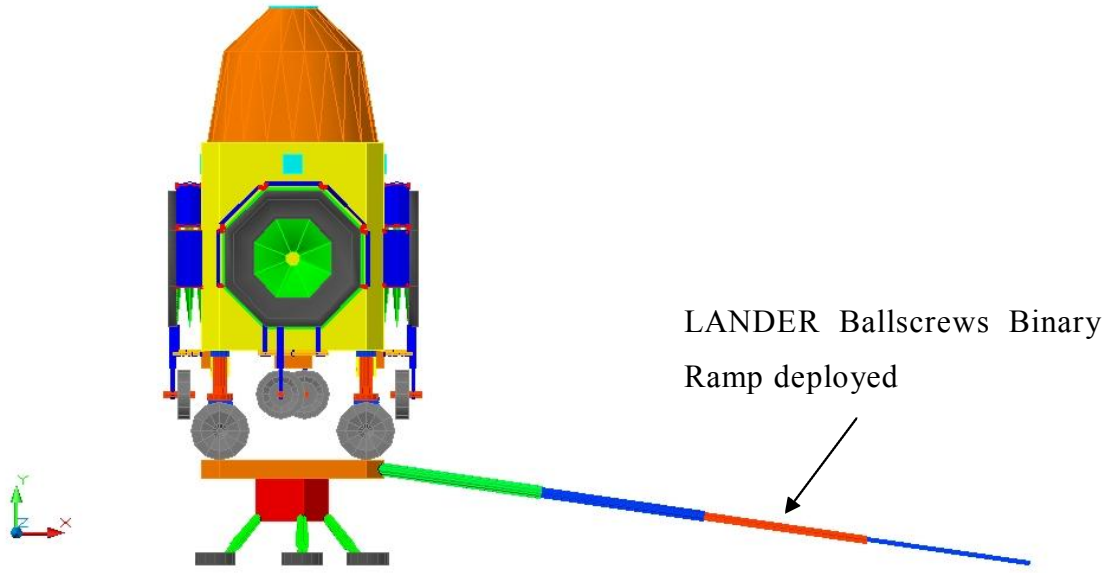

Figure 61: phase 2 "LANDER ramp is deployed"

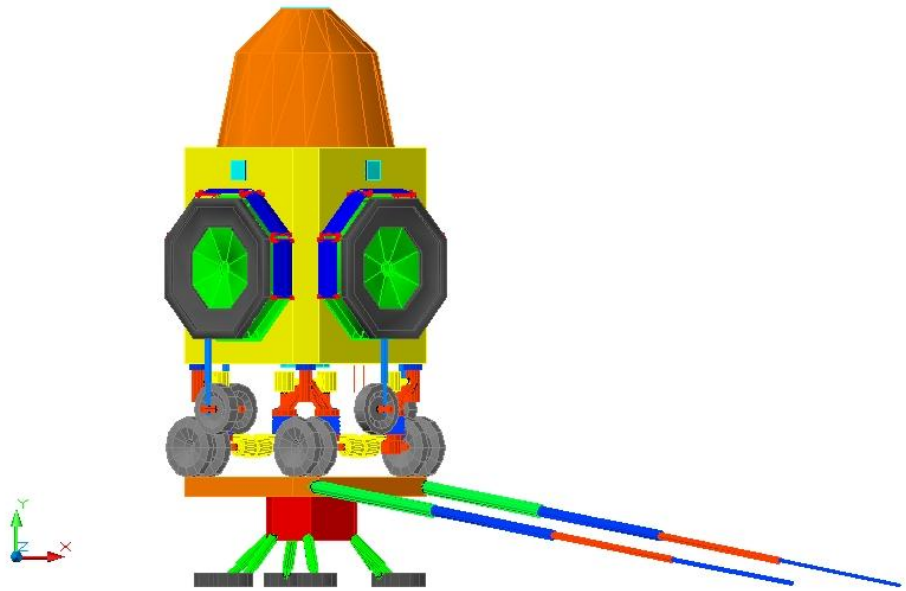

Figure 62: phase 2 “LANDER ramp is deployed”

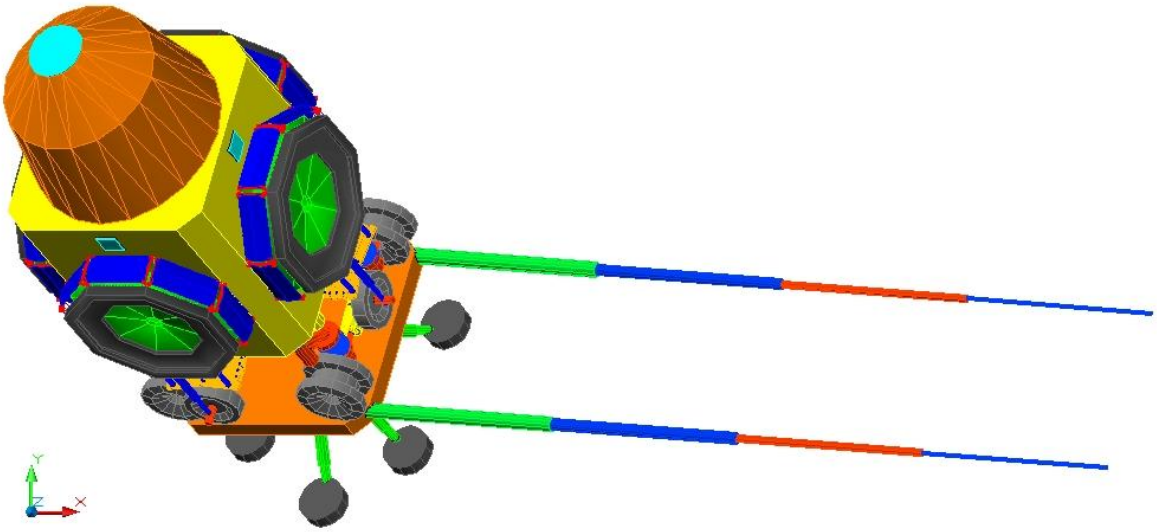

Figure 63: phase 2 “LANDER ramp is deployed”

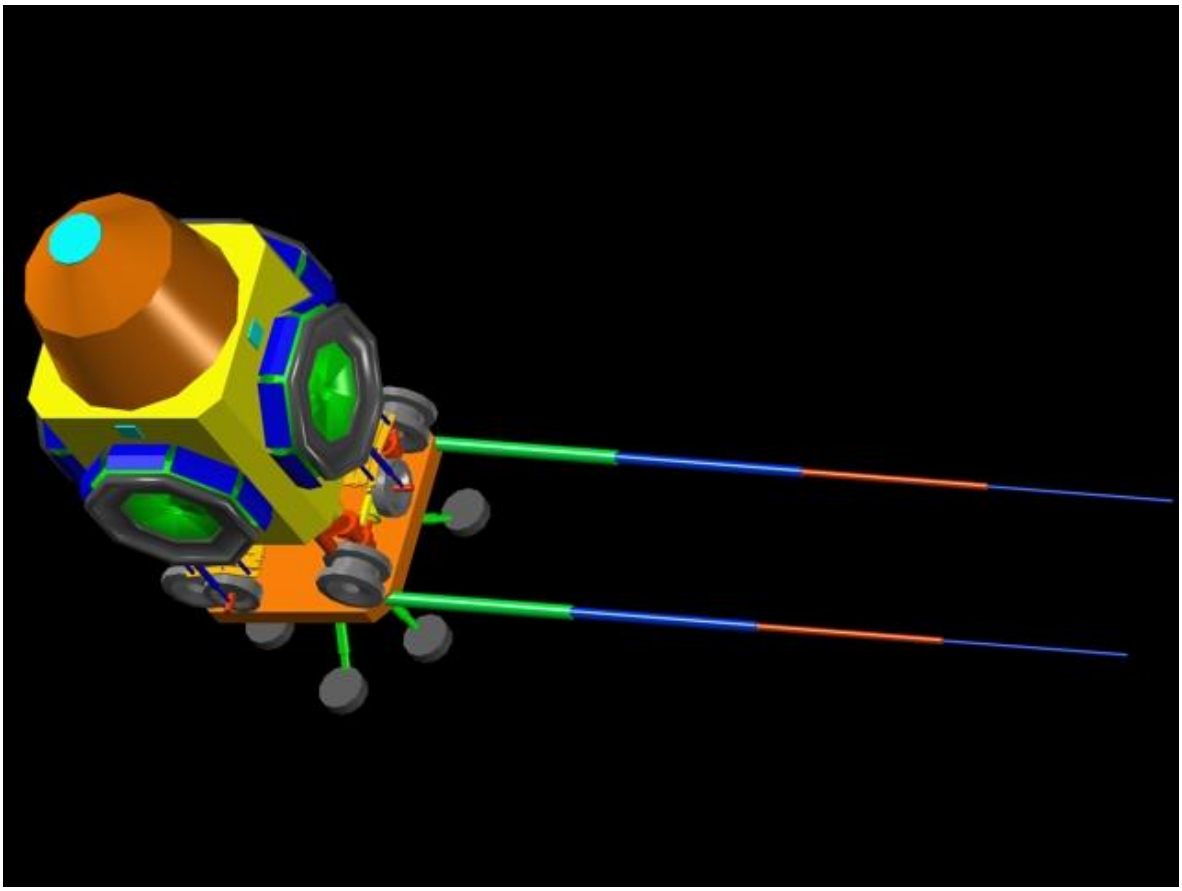

Figure 64: rendering phase 2 "LANDER ramp is deployed"

2.3.1.3 Phase 3) LEMMB is driven down through the Ramp

Once the Ramp is deployed, then the phase 3 can start; the LEMMB is taken down from LANDER.

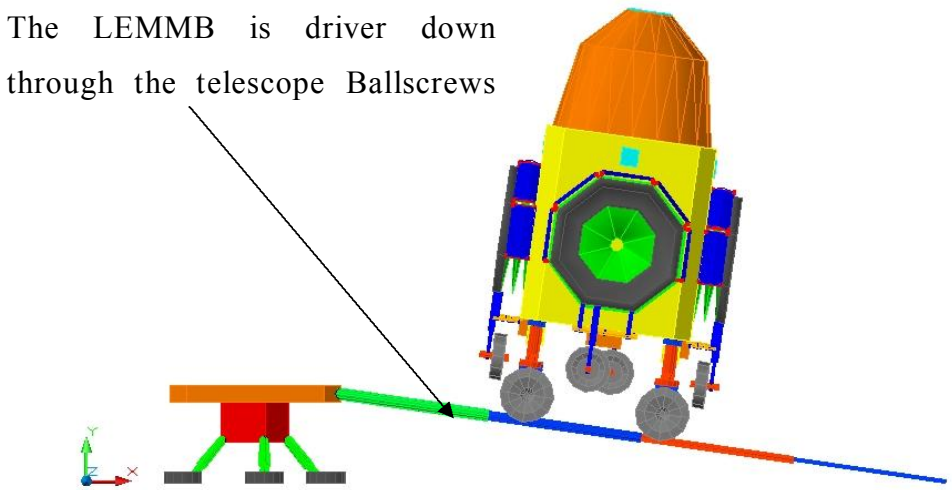

Figure 65: phase 3 "LEMMB is driven down from LANDER platform"

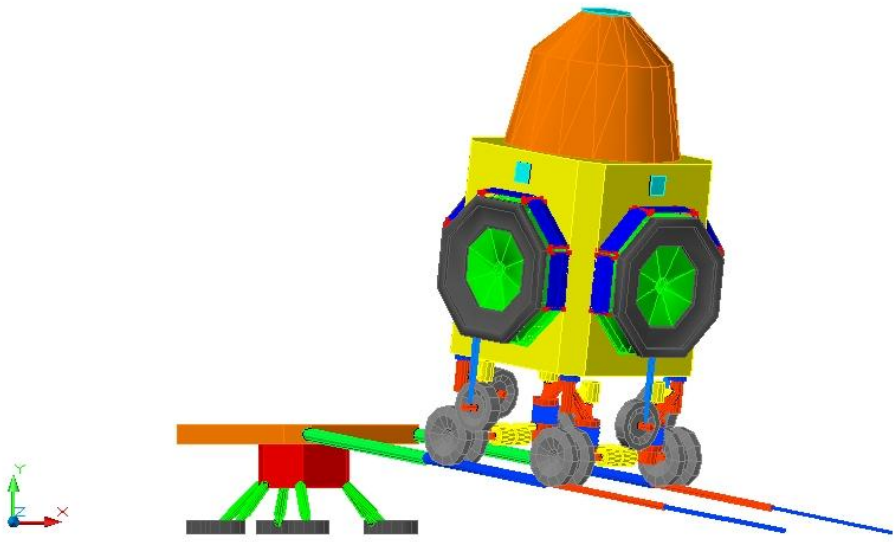

Figure 66: : phase 3 "LEMMB is driven down from LANDER platform"

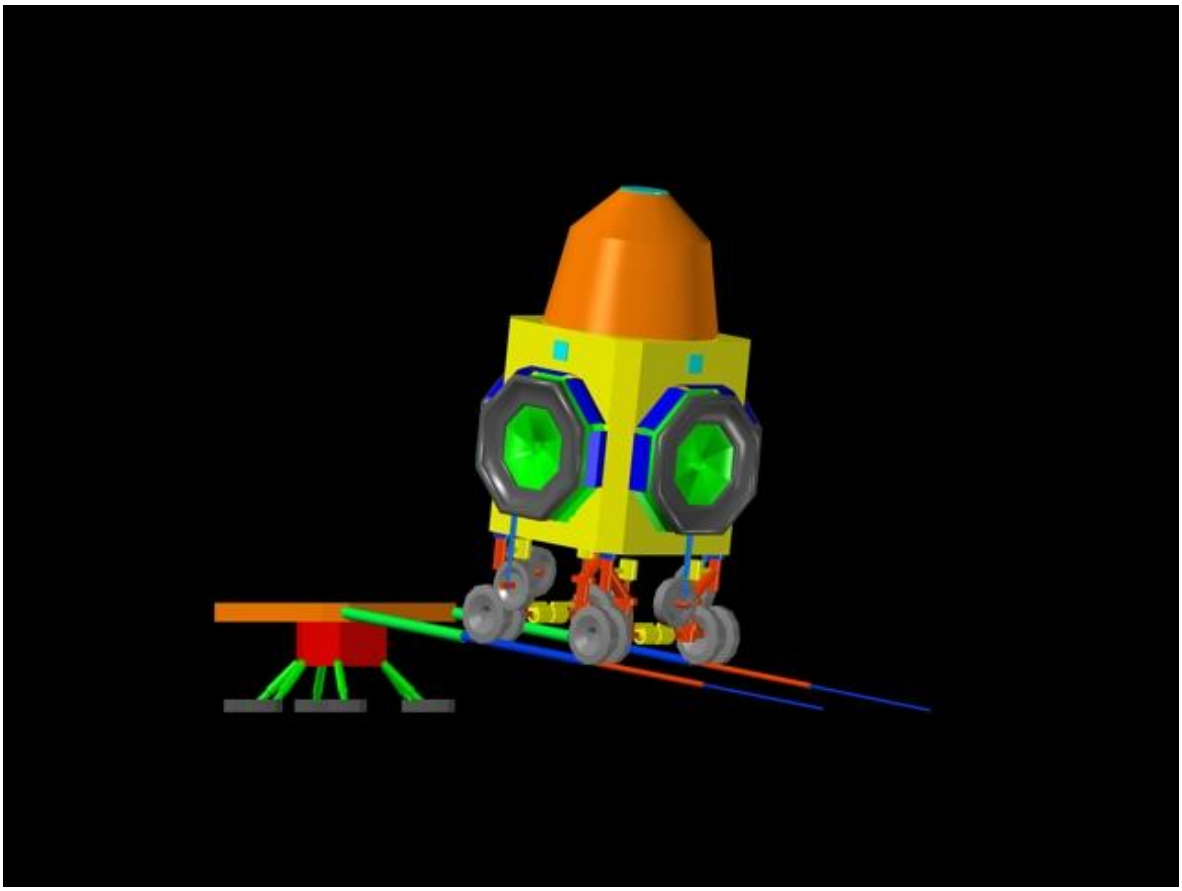

Figure 67: rendering phase 3 "LEMMB is driven down from LANDER platform"

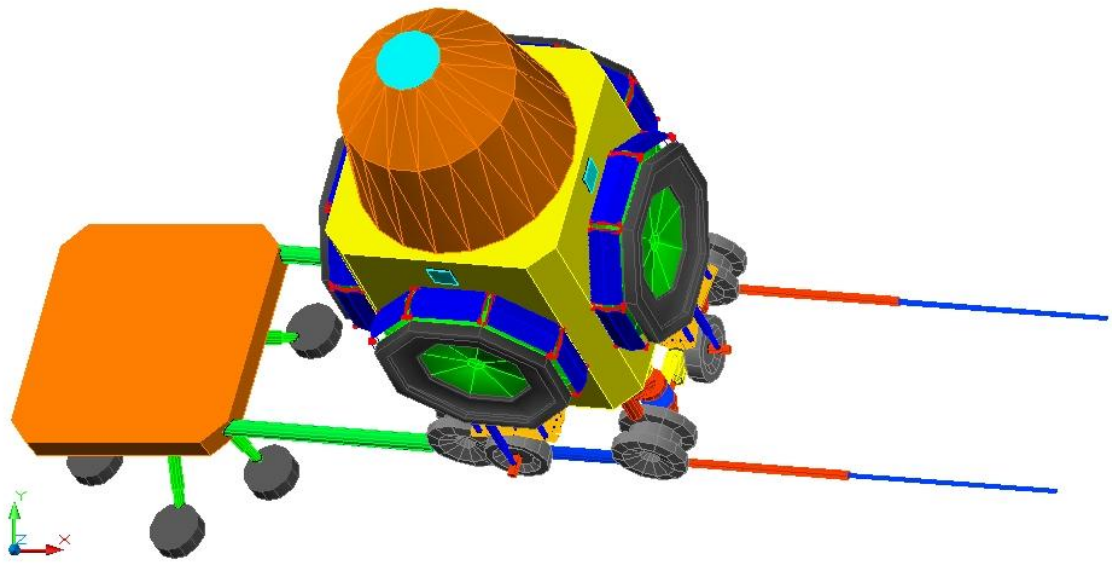

Figure 68: phase 3 "LEMMB is driven down from LANDER platform"

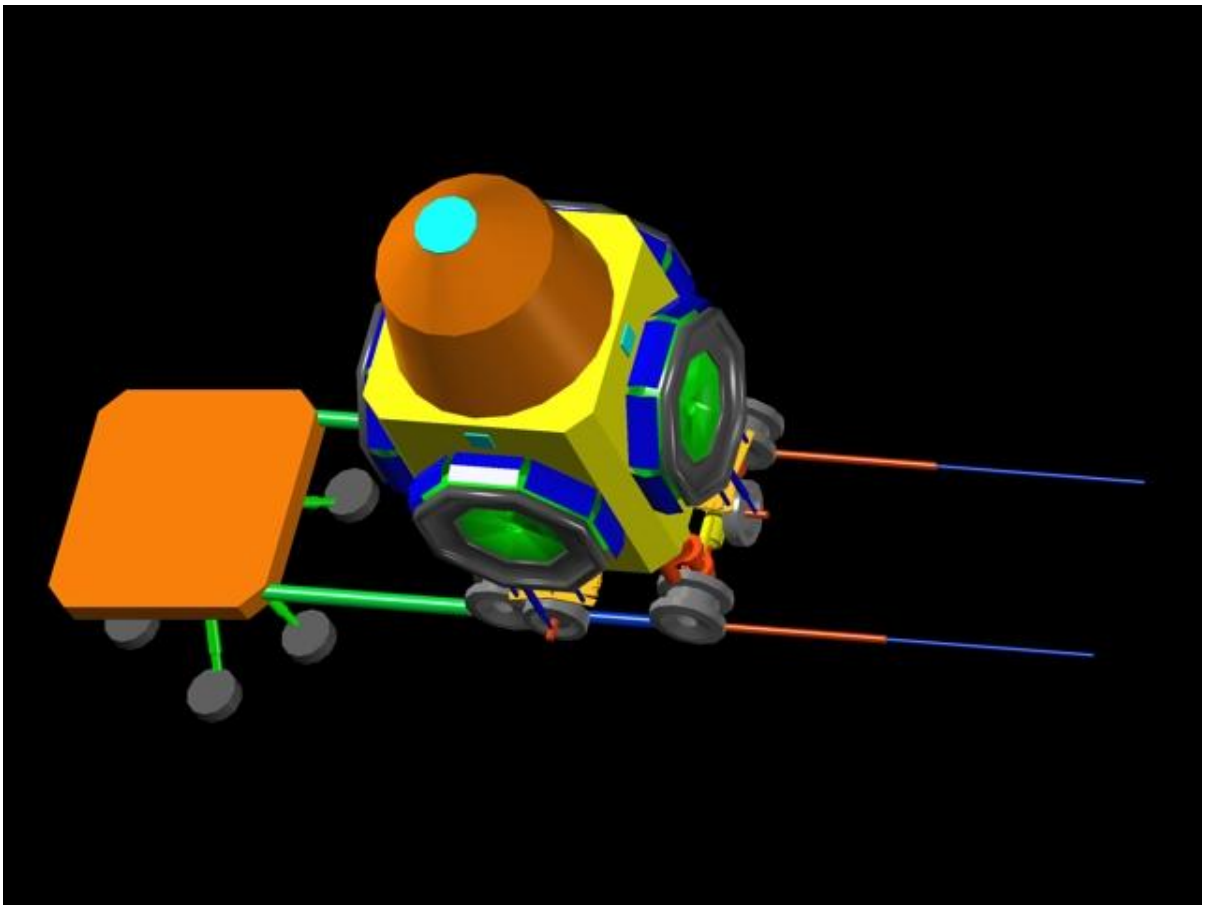

Figure 69: rendering phase 3 "LEMMB is driven down from LANDER platform"

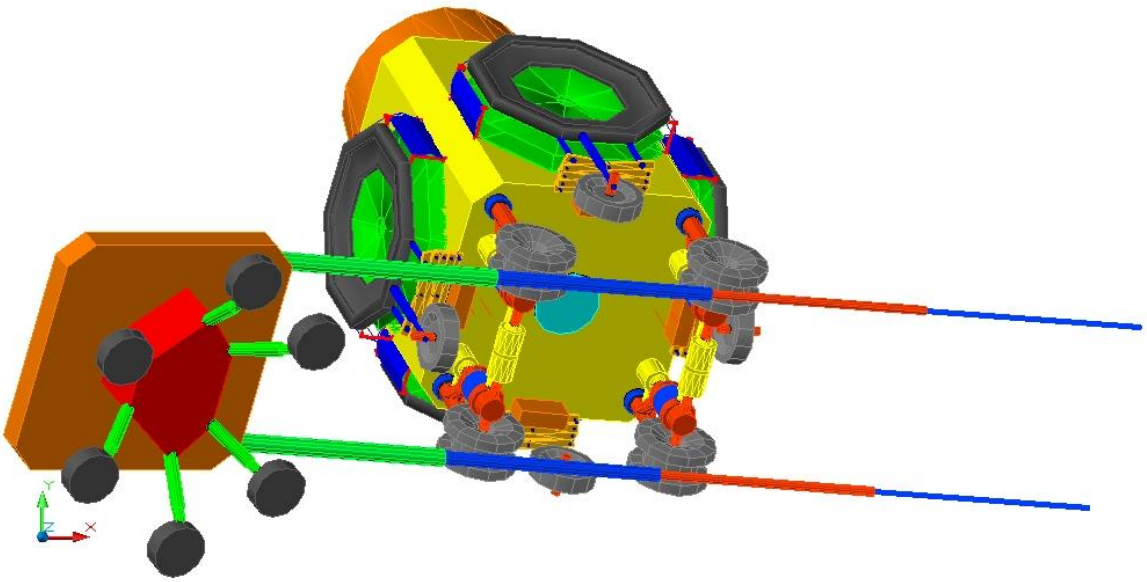

Figure 70: phase 3 "LEMMB is driven down from LANDER platform"

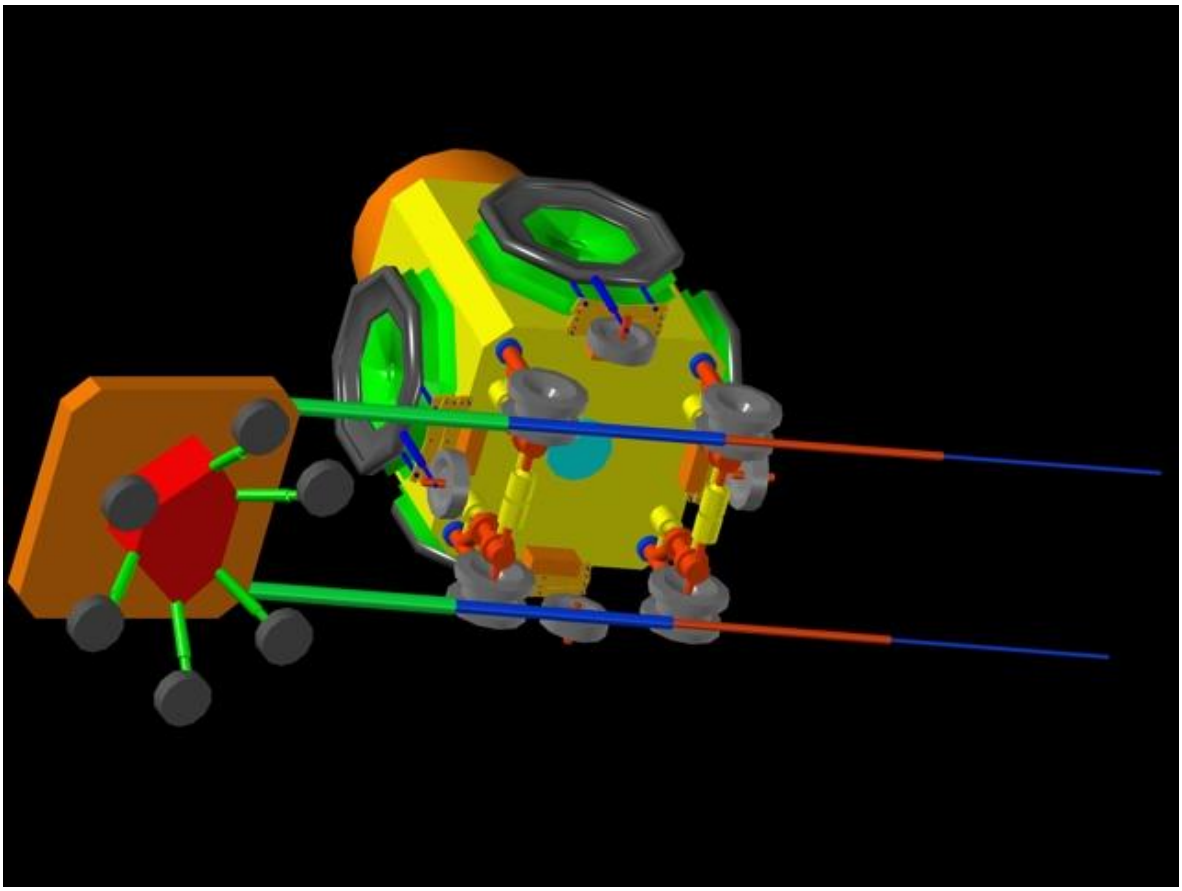

Figure 71: rendering phase 3 "LEMMB is driven down from LANDER platform"

2.3.1.4 Phase 4) LEMMB is driven by remote control to the precise final location on the lunar surface

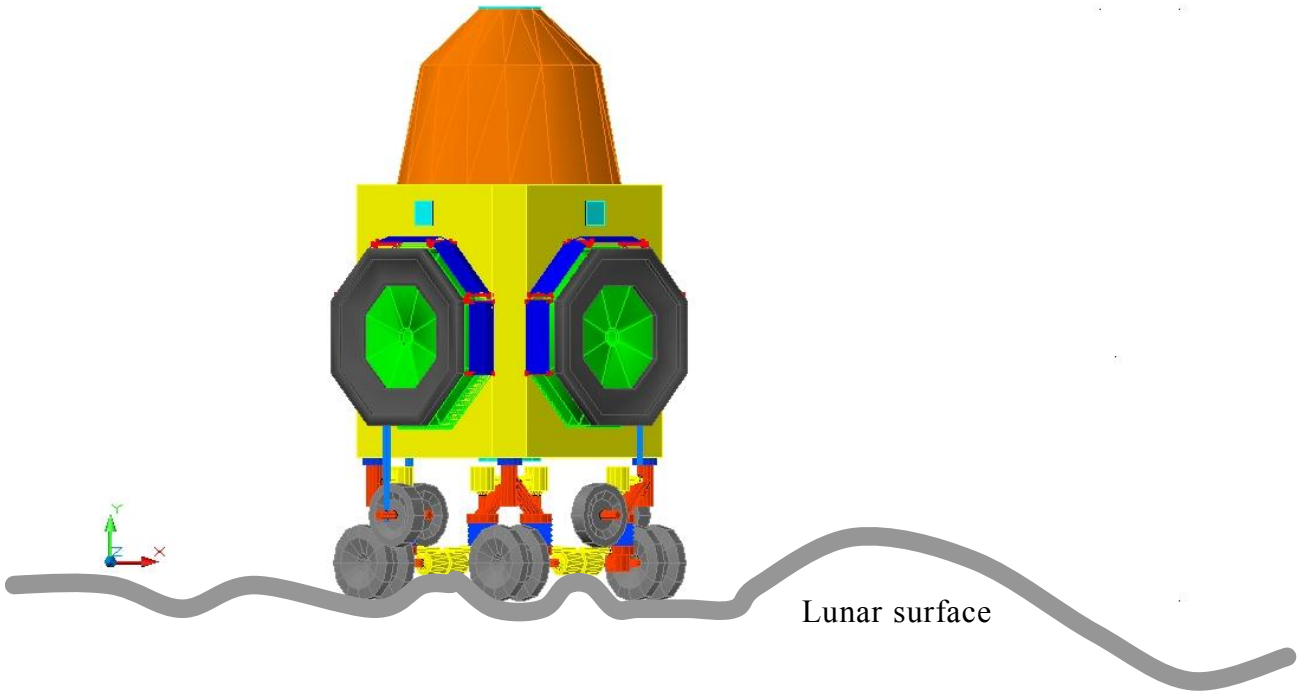

Figure 72: phase 4 "LEMMB is driven by remote control to the precise final location"

In order to increase the mission safety, the landing point should be not so close to the Lunar Base, so once landed, thanks to the motorized wheel, the LEMMB is capable of being driven out, while placed close to the rest of the LEMMBs modules.

2.3.1.5 Phase 5) The AIS (Arms Inflatable Structures) are deployed

There are two main type of AISs structures, the first is similar to that used on ISS (International Space Station) which is developed, together with ARMs, like an accordion.
This structures type is, called ASICSP (Arm Structures Inflatable Covered by Solar Array).

The second type is provided by the arms itself on the surface of which is applied a Solar Array film. This last type of arms will be called ASIISA (Arm Structures Inflatable Intrinsic Solar Array).

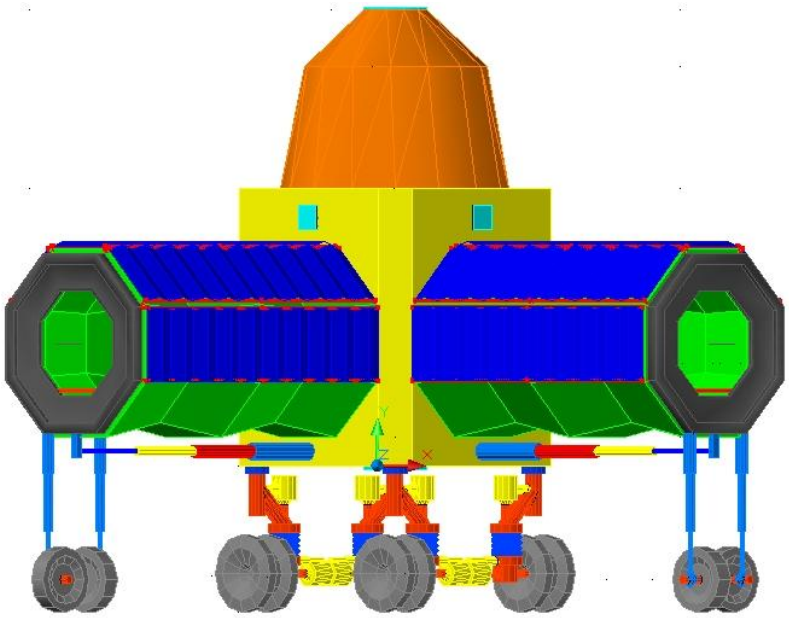

Figure 73: phase 5 "the ASICSA (Arm Structures Inflatable Covered by Solar Array) are deployed"

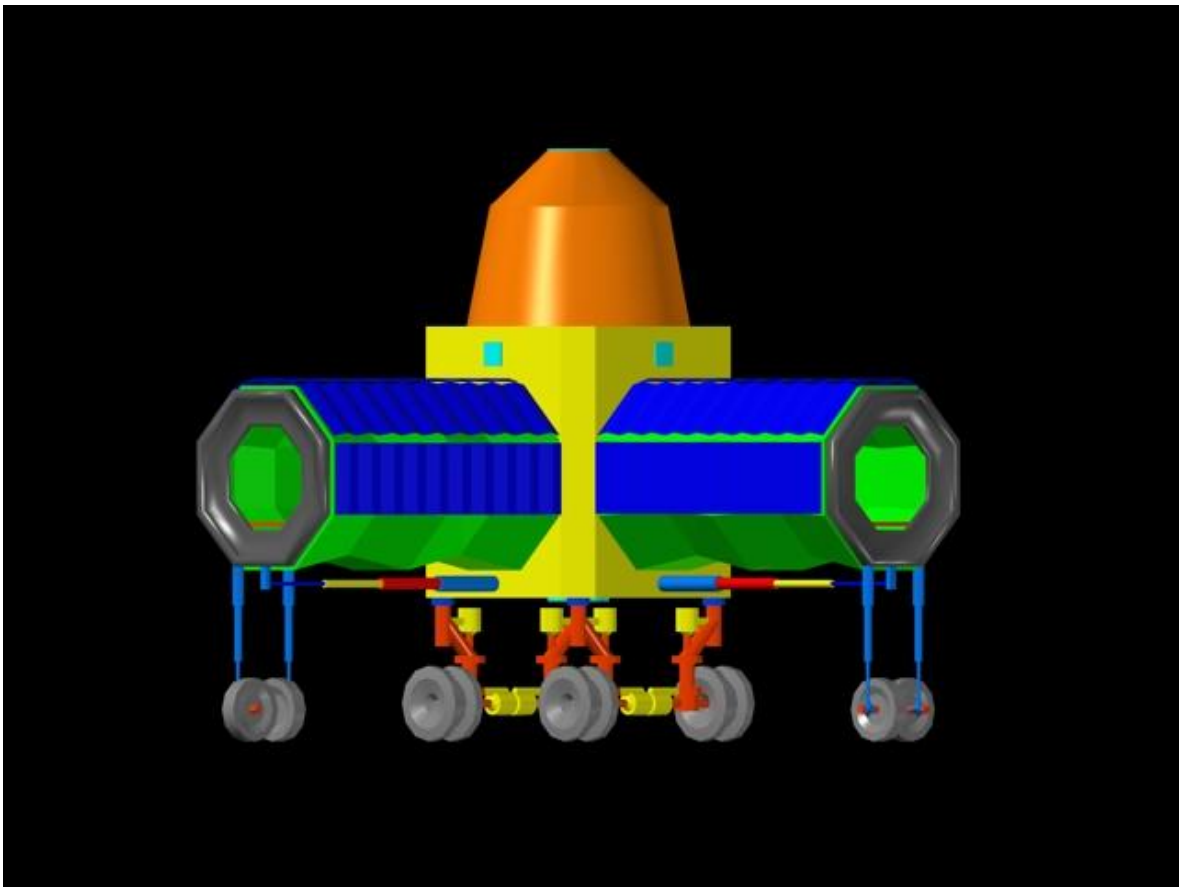

Figure 74: phase 5 "the ASICSA (Arm Structures Inflatable Covered by Solar Array) are deployed"

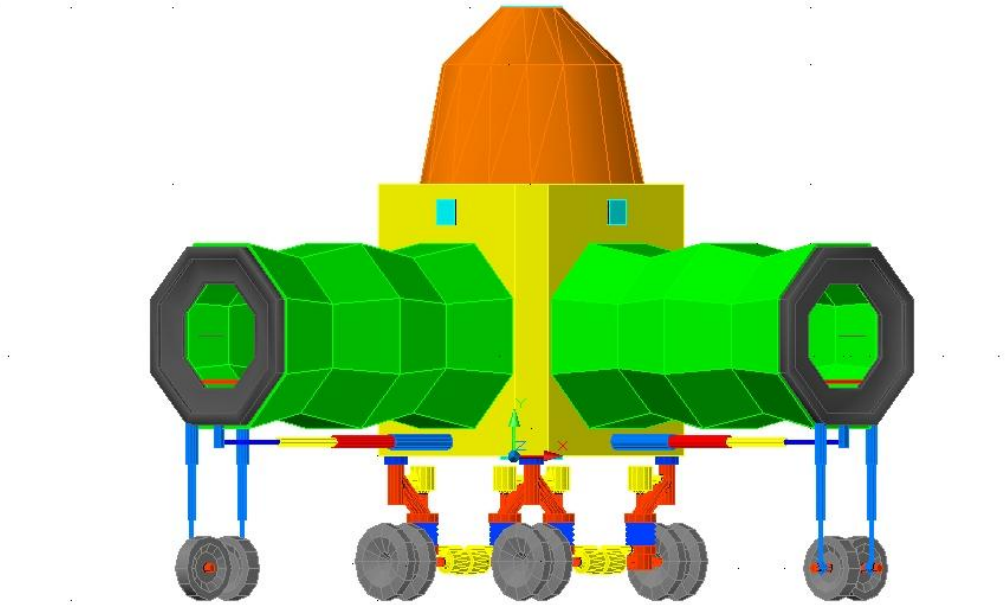

Figure 75: phase 5 "the ASIISA (Arm Structures Inflatable Intrinsic Solar Array) are deployed"

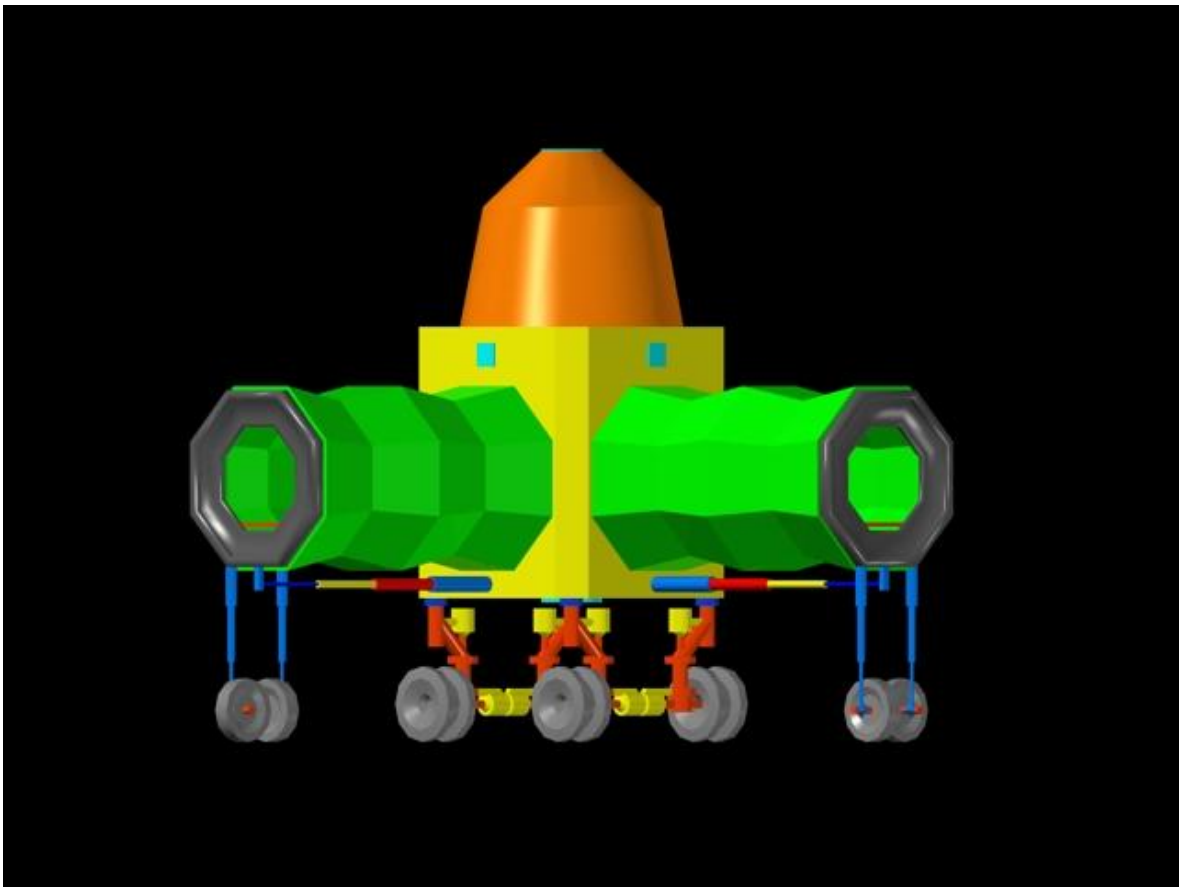

Figure 76: phase 5 "the ASIISA (Arm Structures Inflatable Intrinsic Solar Array) are deployed"

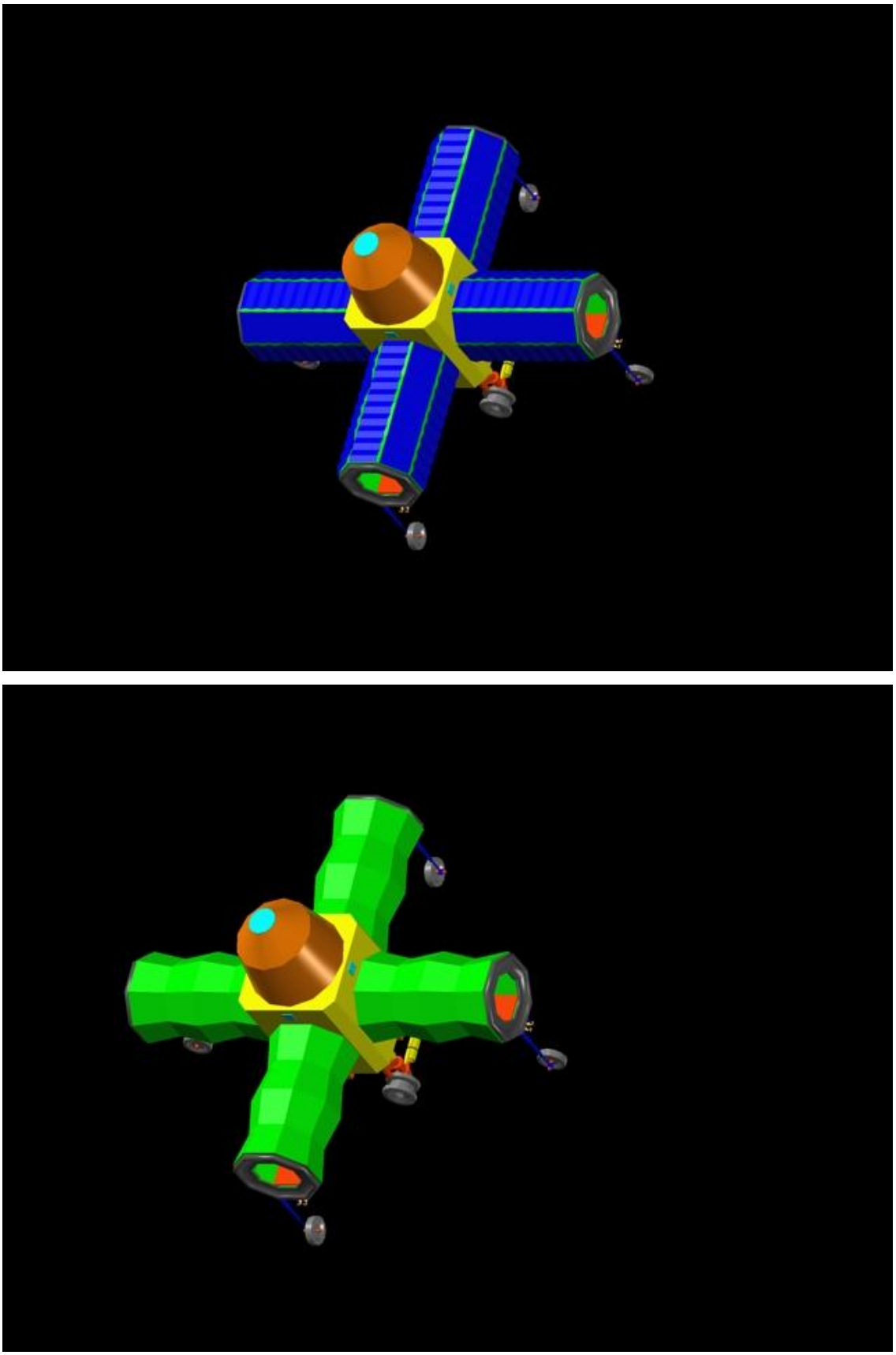

Figure 77: phase 5 " deploying of ASIISA and ASICSA"

2.3.1.6 Phase 6) Several LEMMBs are connected to each other to make a Lunar Base

In pictures below a rendering example of several LEMMBs connected to each other, by means of the inflatable arms, are represented.
The structure is conceived completely modular. Therefore several blocks can be assembled together, even one over another too to form several floors.

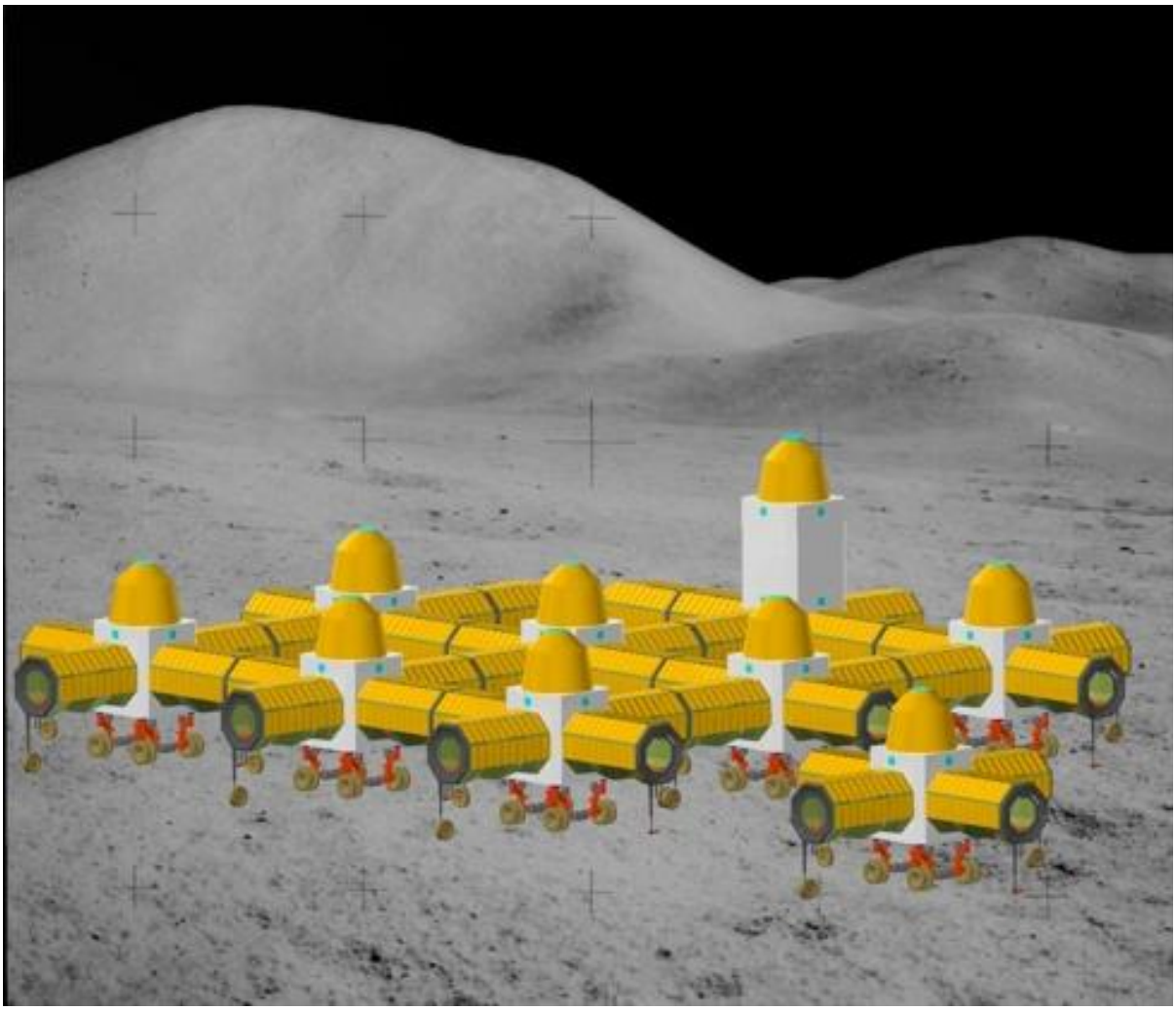

Figure 78: phase 6 "several LEMMBs connected to each other to make a Lunar Base Station"

Each LEMMB has an access point located on the LEMMB bottom but the ARMS connection structures can also be used as a pressurized astronauts access from the lunar external environment.

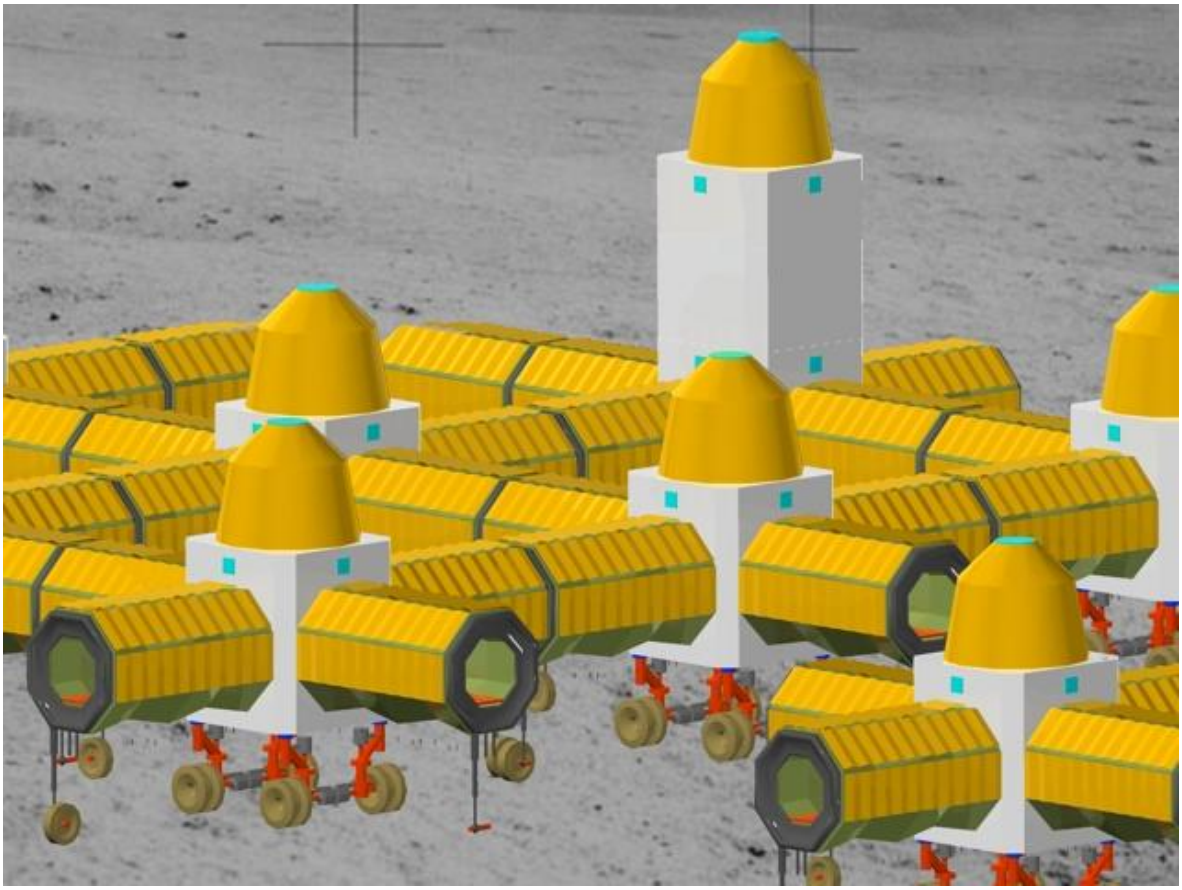

Figure 79: phase 6 " connection of several LEMMBs"

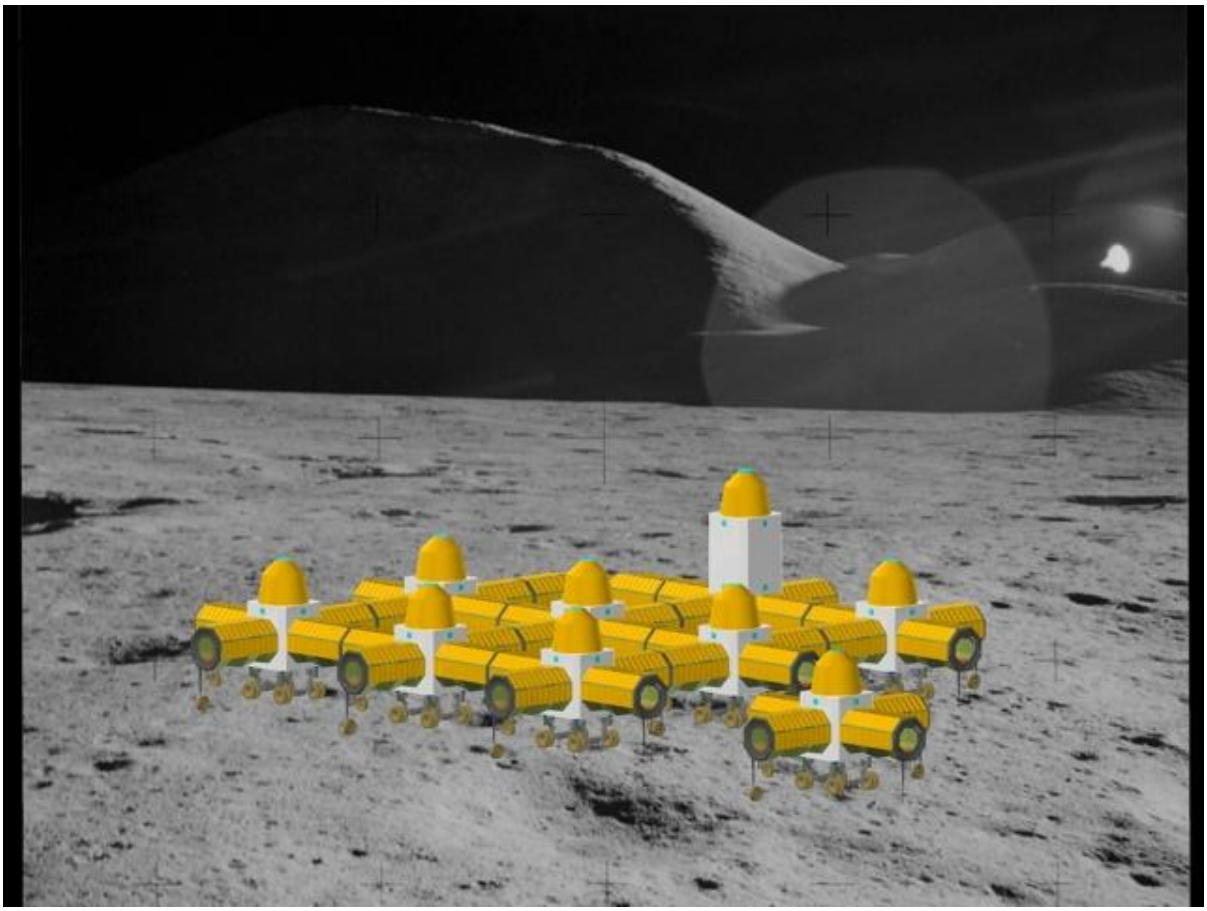

Figure 80: Lunar Base Station

2.4 LEMMB Particulars

Some details of LEMMB are shown on figures below.
Basically, the ASI (Arms Structures Inflatable) are inflatable structures but some mechanism can be used to help the deployment/retirement of the Arms.

A first simple mechanism could be like scissors extension system.
Some figures of this system are reported below.

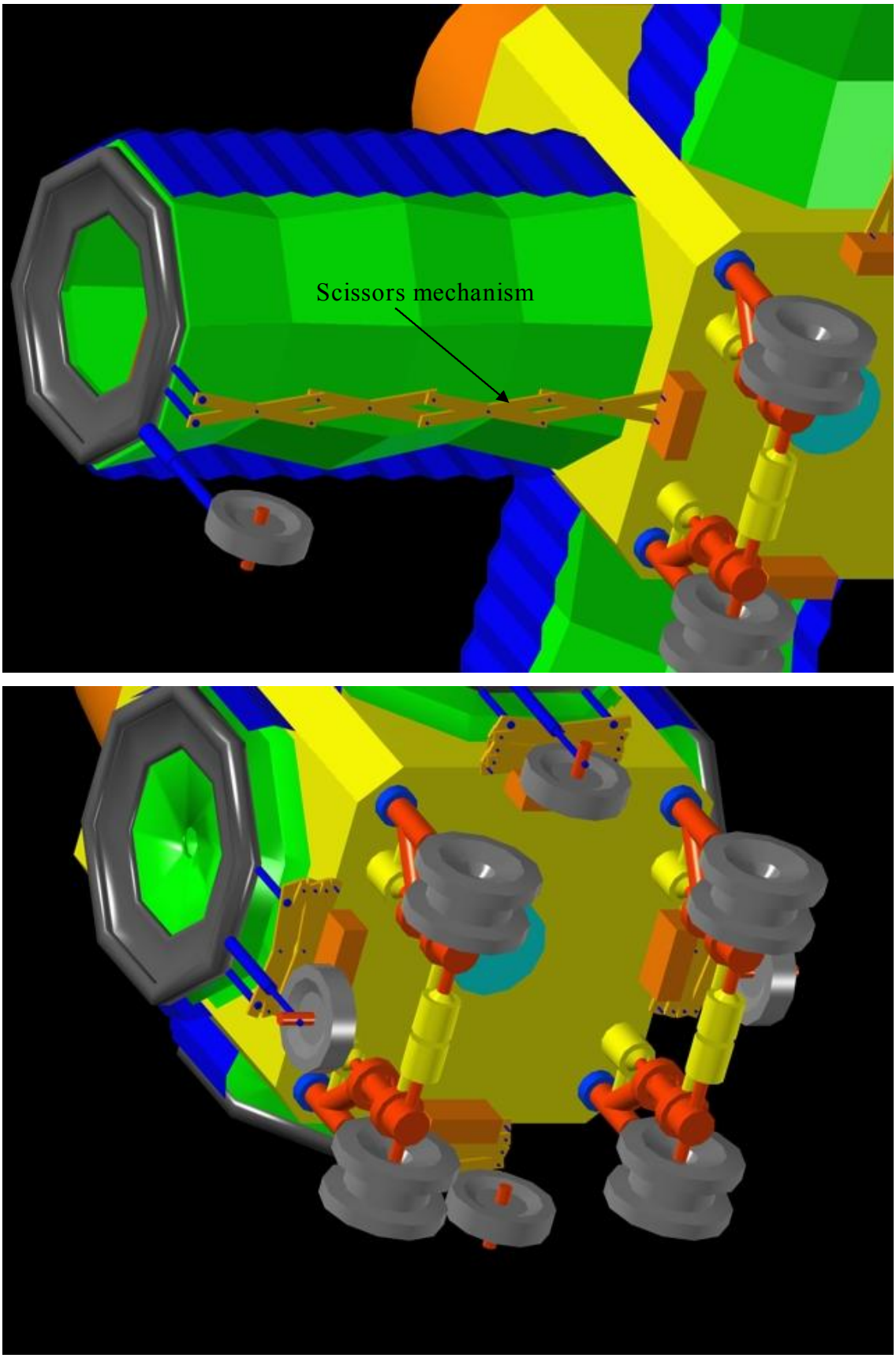

Figure 81: scissors mechanism: Top, opened, Down closed

Another system that can be used is like that used for the Ramp LANDER deployment, i.e. BALLSCREWS. This for sure is a more precise deployment mechanism. The system is illustrated on figure below.

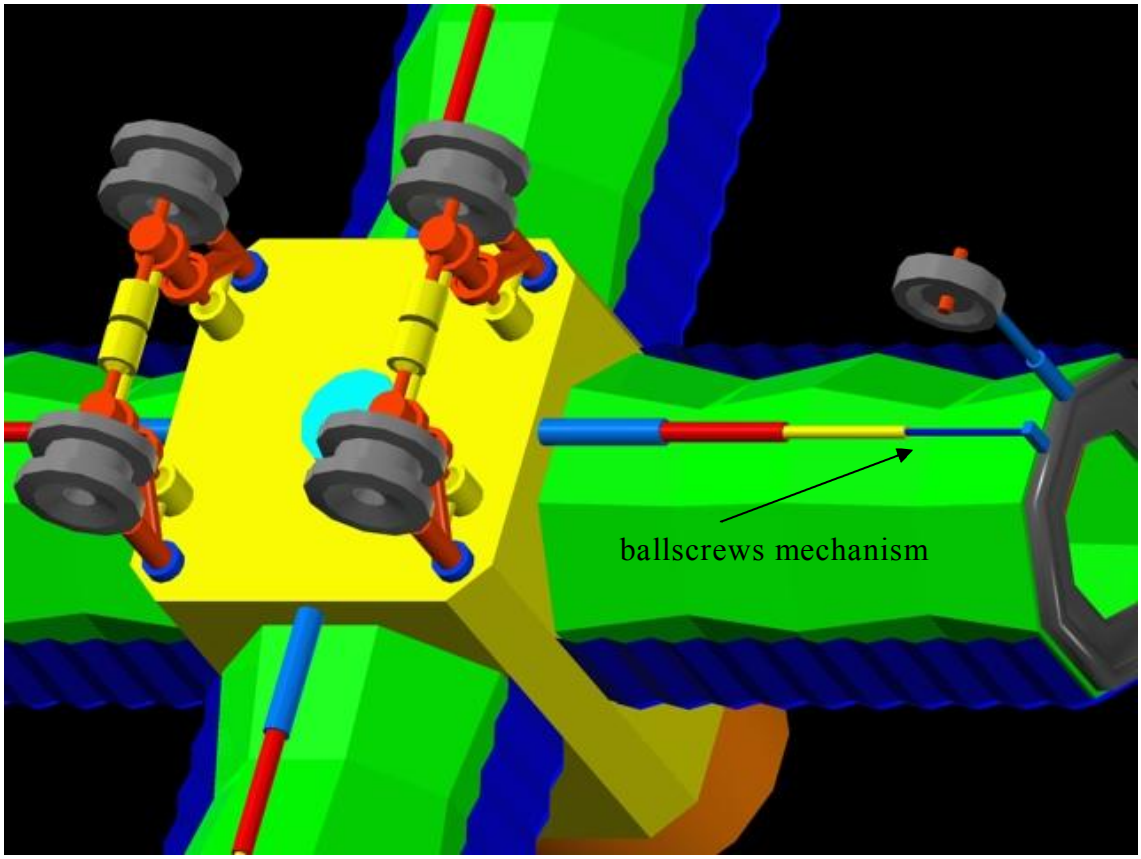

Figure 82: ballscrews deployment system

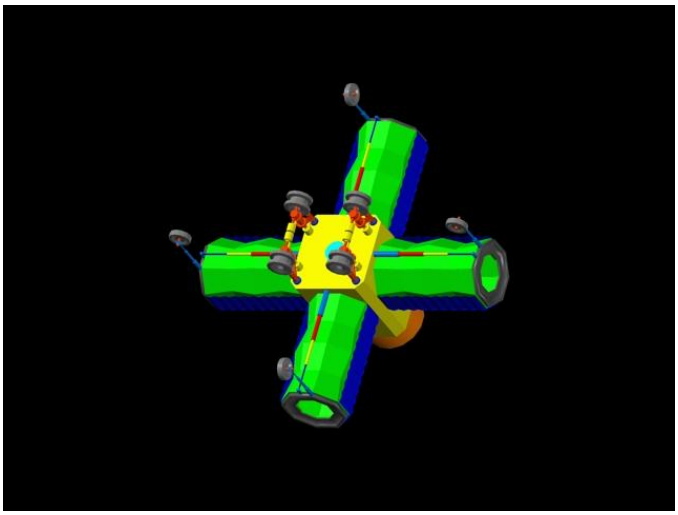

Figure 83: bottom view and ballscrews deployment system.

The system is conceived completely modular where each module is equal to the others. As a consequence, two or several modules could be assembled one over another too.

This is a very useful system to easily increase the volume of the habitat, the entire system not only can be developed in horizontal way by connecting several LEMMB but, could also be developed vertically in several floor.

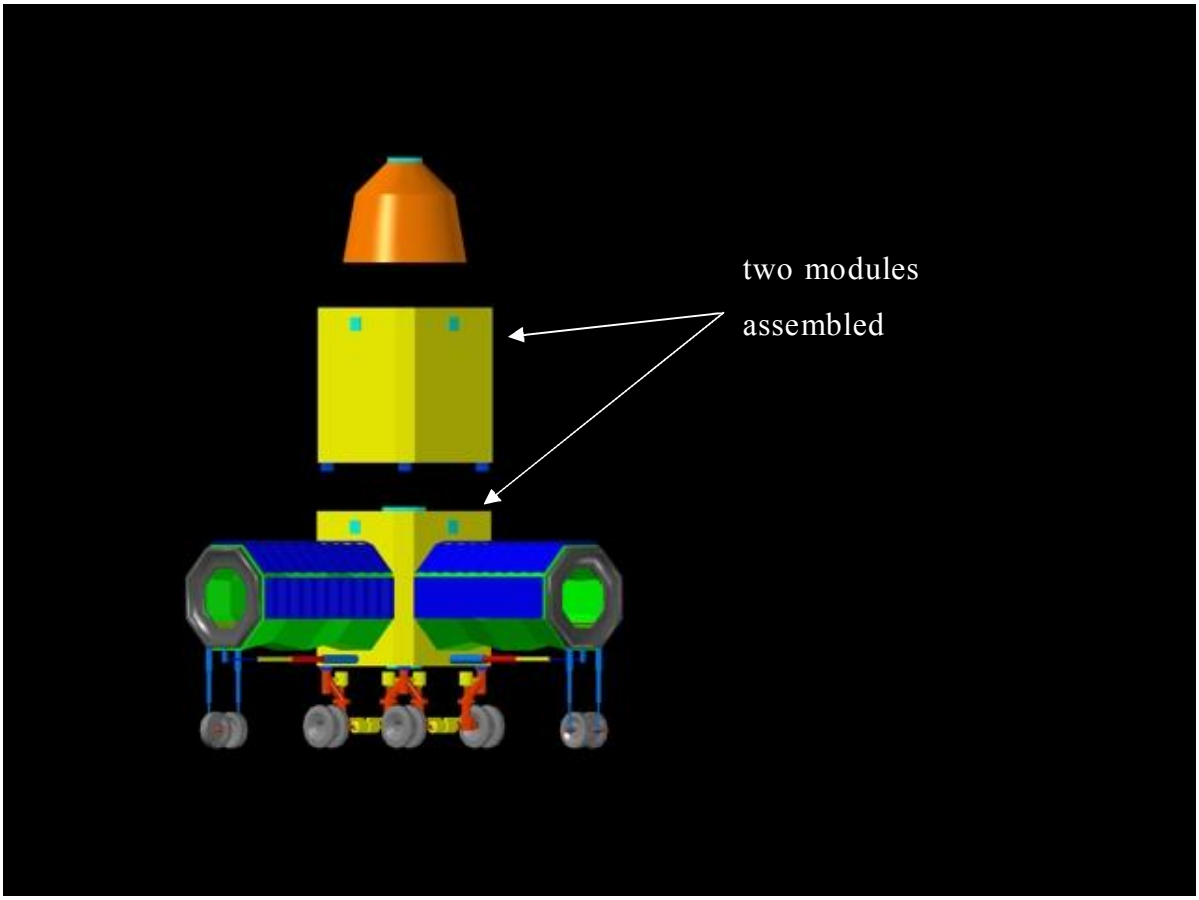

Figure 84: modular structures and LEMMB assembly

Here after, some LEMMB section particulars are reported.

- Inside each ASI (Arm Structures Inflatable) is possible to observe the bridge used as the astronauts passages from one LEMMB to another one.
- Each module is provided by an internal and an external access point for astronauts. In any case the ASI structures can be used for this purpose, since it could have a pressurized / un-pressurized volume within them.

- The four completely independent motorized wheels systems are used to provide the final location of LEMMB. The four independent systems provide a greater reliability than a unique motor system.
- Each wheel is assembled, on a telescope system which provide the LEMMB final attitude once located definitely on lunar surface point.

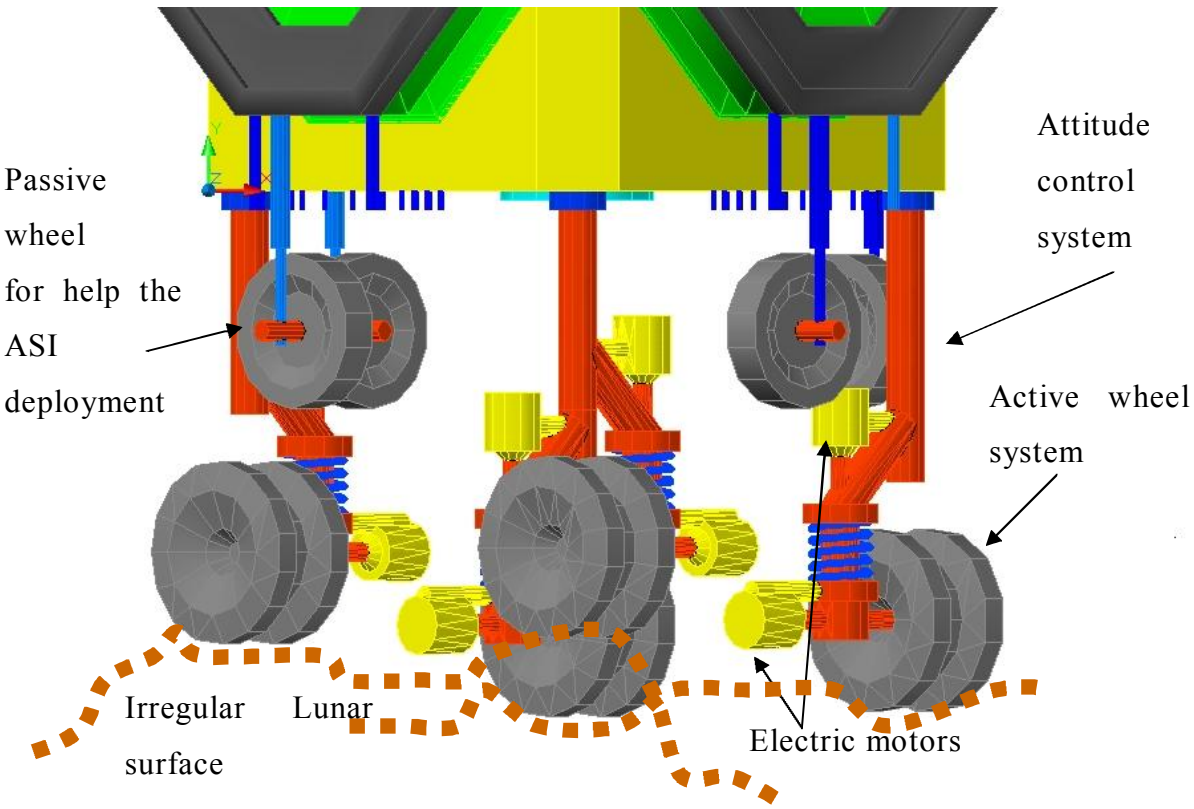

Figure 85: LEMMB attitude control system

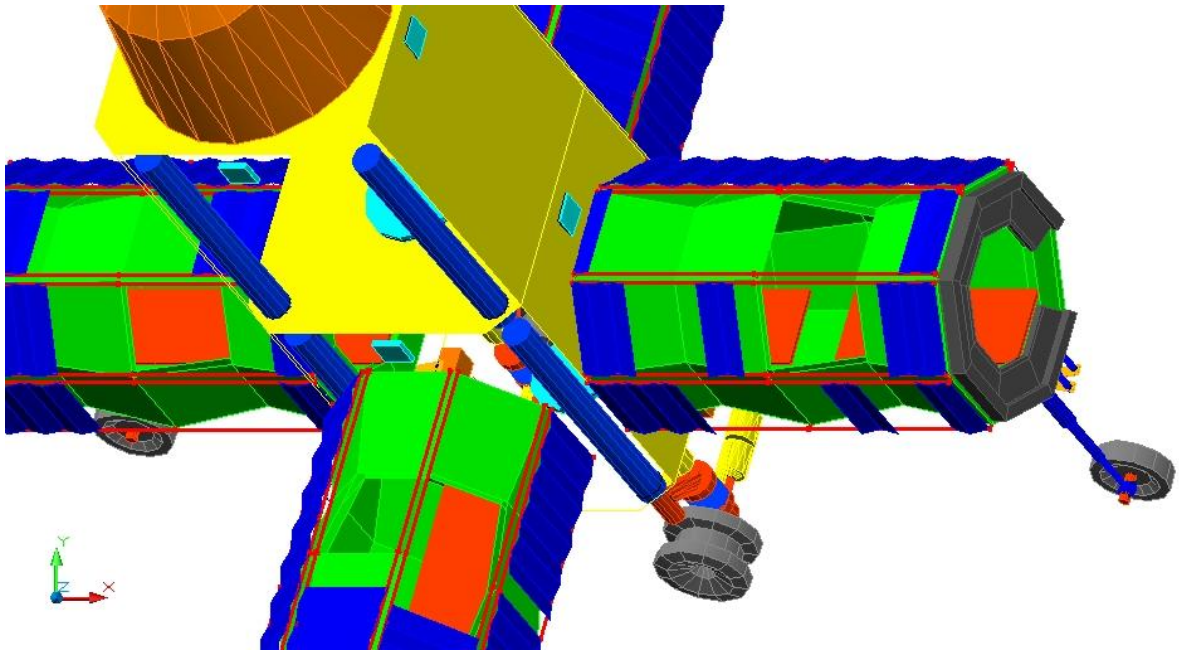

Figure 86: section of LEMMB

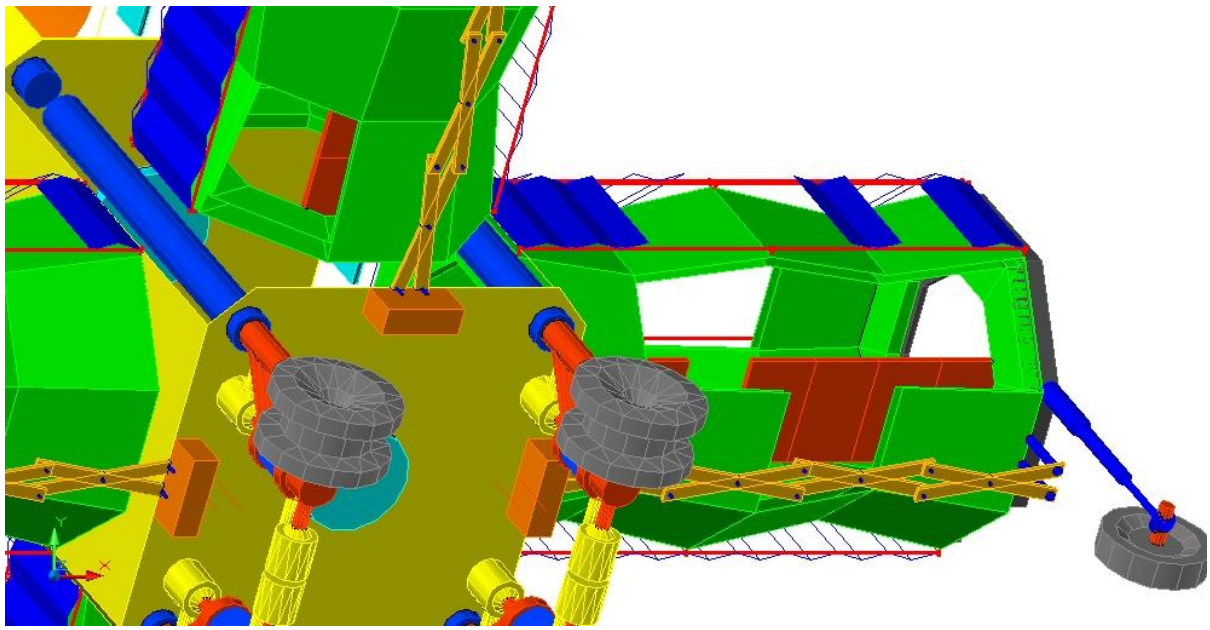

Figure 87: section of LEMMB

2.5 LEMMB Dimensions

2.5.1 Starting idea

The LEMMB is designed to be transported by using space vehicle like, for example, the Ariane 5.

As a consequence the LEMMB dimensions have been chosen Ariane 5 Fairing complaint.

The main problem encountered is on the max diagonal dimension of the Core Module.

Obviously, the more the number of expandable structures and their relative dimensions, the greater the volume available for human inhabitant and the greater will be the solar energy collected by solar photovoltaic array spread out on the entire LEMMB surface exposed to the Sun.

At the beginning of this work, the structure examined was hexagonal as shown below but this structure was too large to be transported by standard Ariane 5 or Soyuz vehicle system.

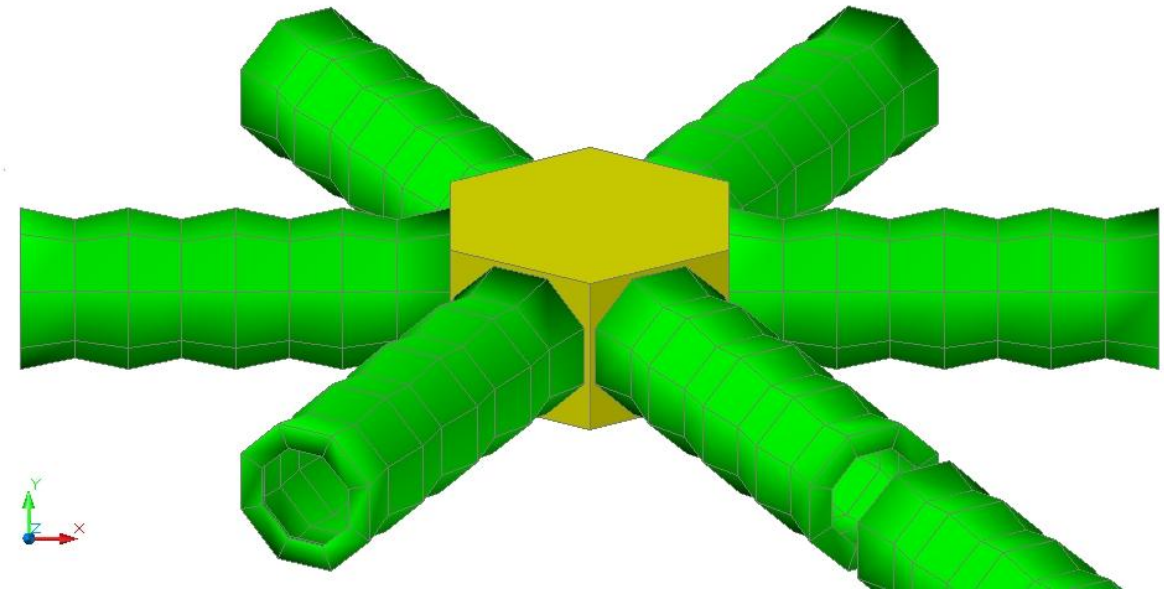

Figure 88: first starting idea about shape of LEMMB

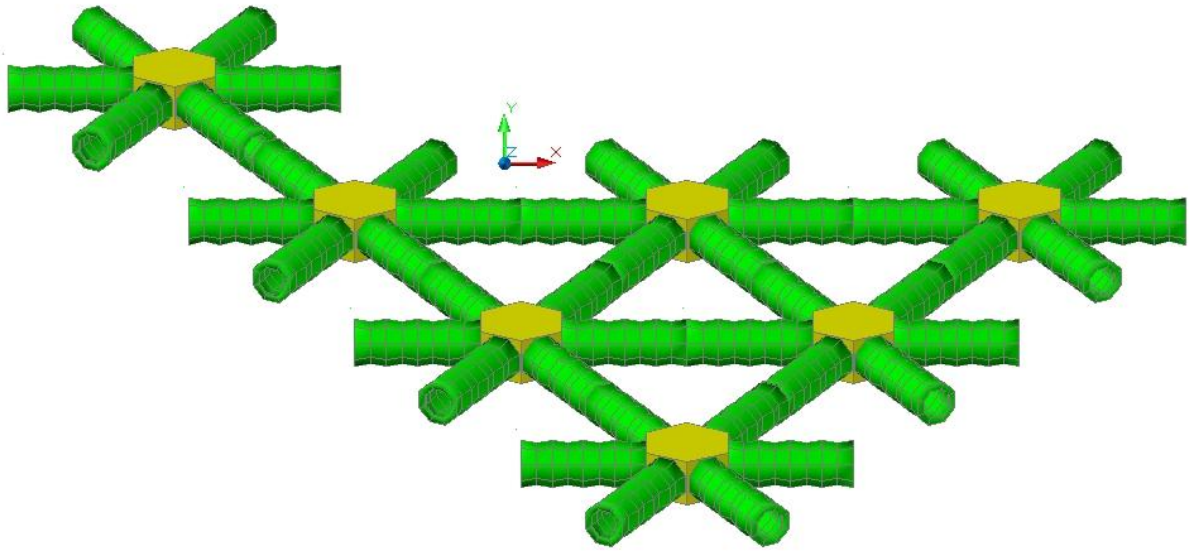

Figure 89: connection of several LEMMB module.

2.5.2 Actual Dimensions

As a matter of fact, the last LEMMB structure dimensions in [m] are as shown below.

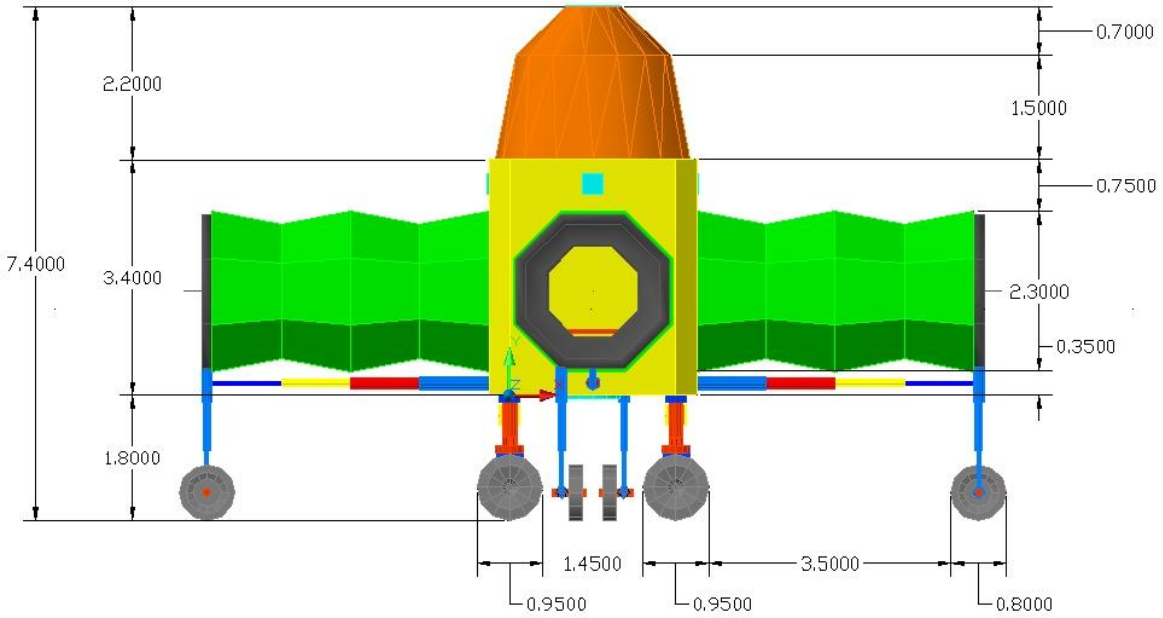

Figure 90: structure dimension for a Ariane 5 or Soyuz Vehicle system. ASIISA (Arm Structures Inflatable Intrinsic Solar Array)

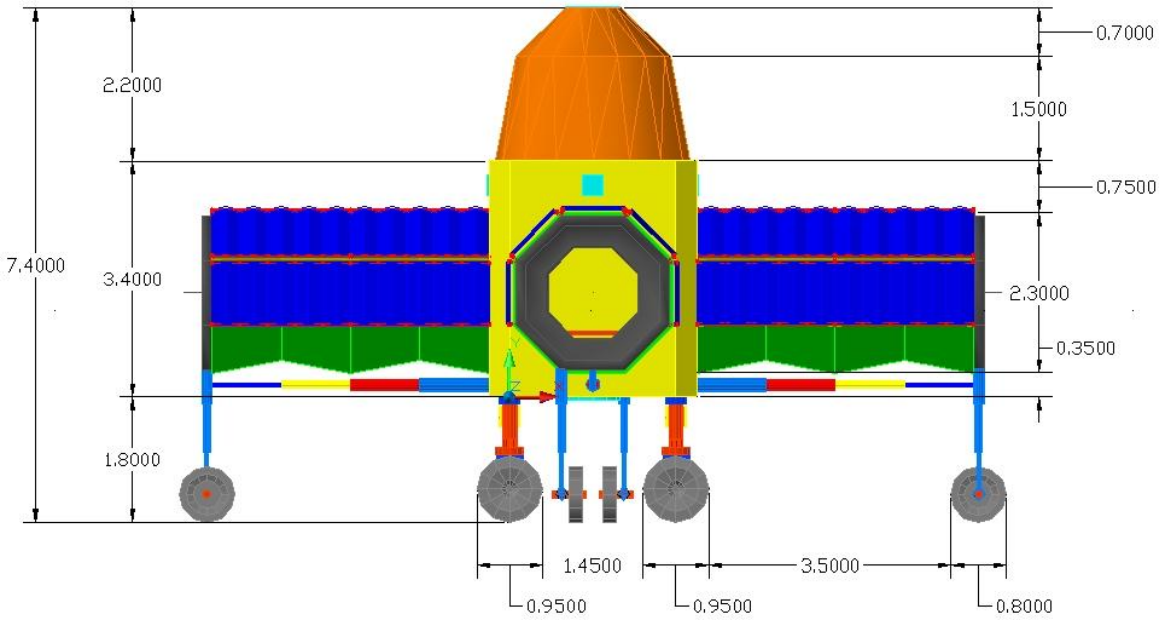

Figure 91: structure dimension for a Ariane 5 or Soyuz Vehicle system. ASICSP (Arm Structures Inflatable Covered by Solar Array)

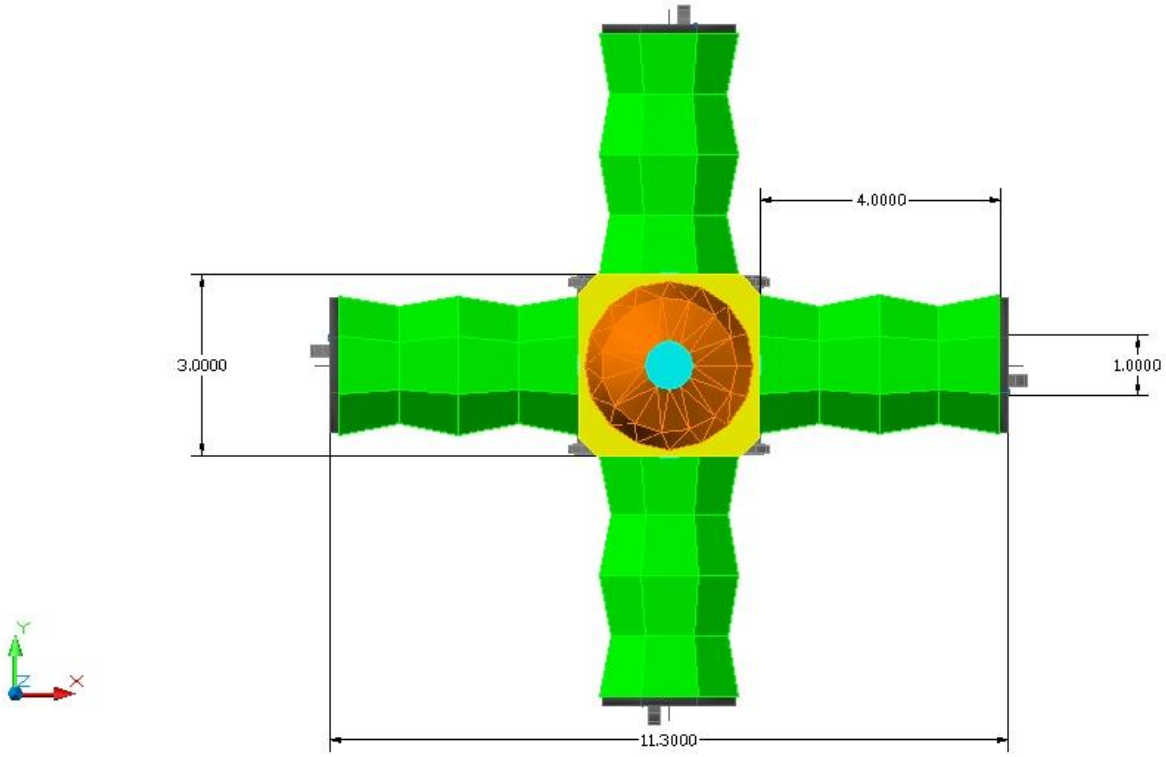

Figure 92: structure dimension for a Ariane 5 or Soyuz Vehicle system.
ASIISA (Arm Structures Inflatable Intrinsic Solar Array)

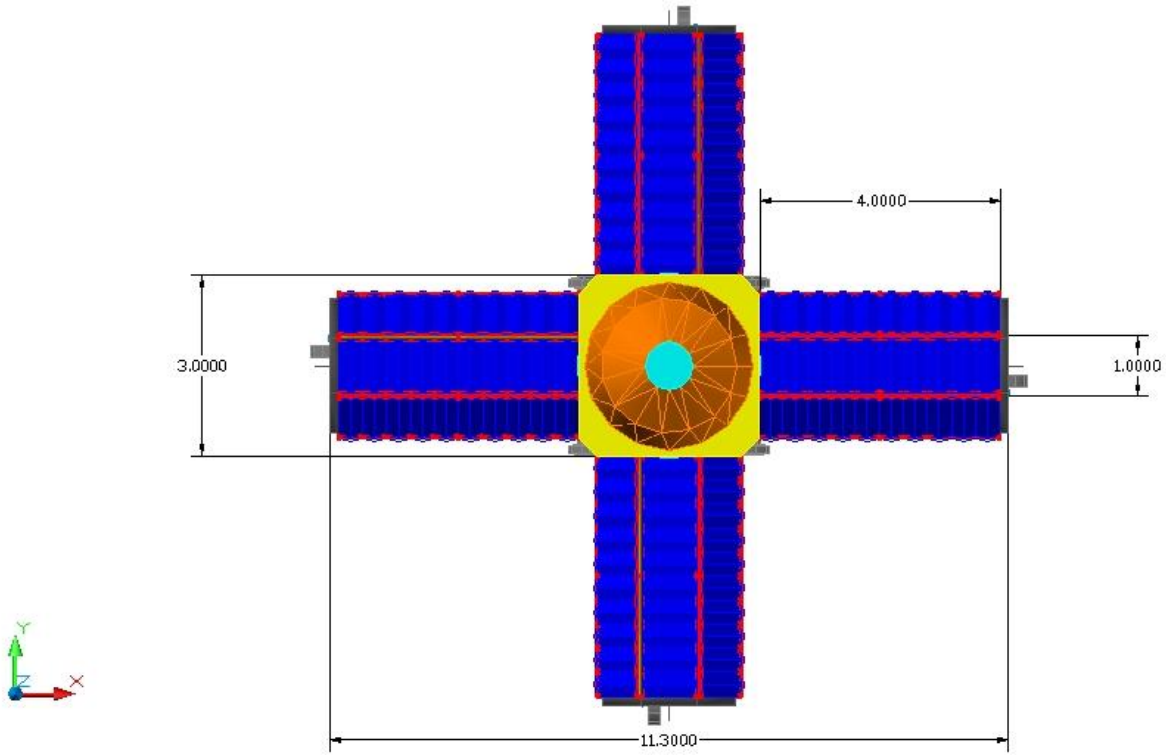

Figure 93: structure dimension for a Ariane 5 or Soyuz Vehicle system.
ASICSP (Arm Structures Inflatable Covered by Solar Array)

Below the external fairing volume dimension for the standard Soyuz system are reported.

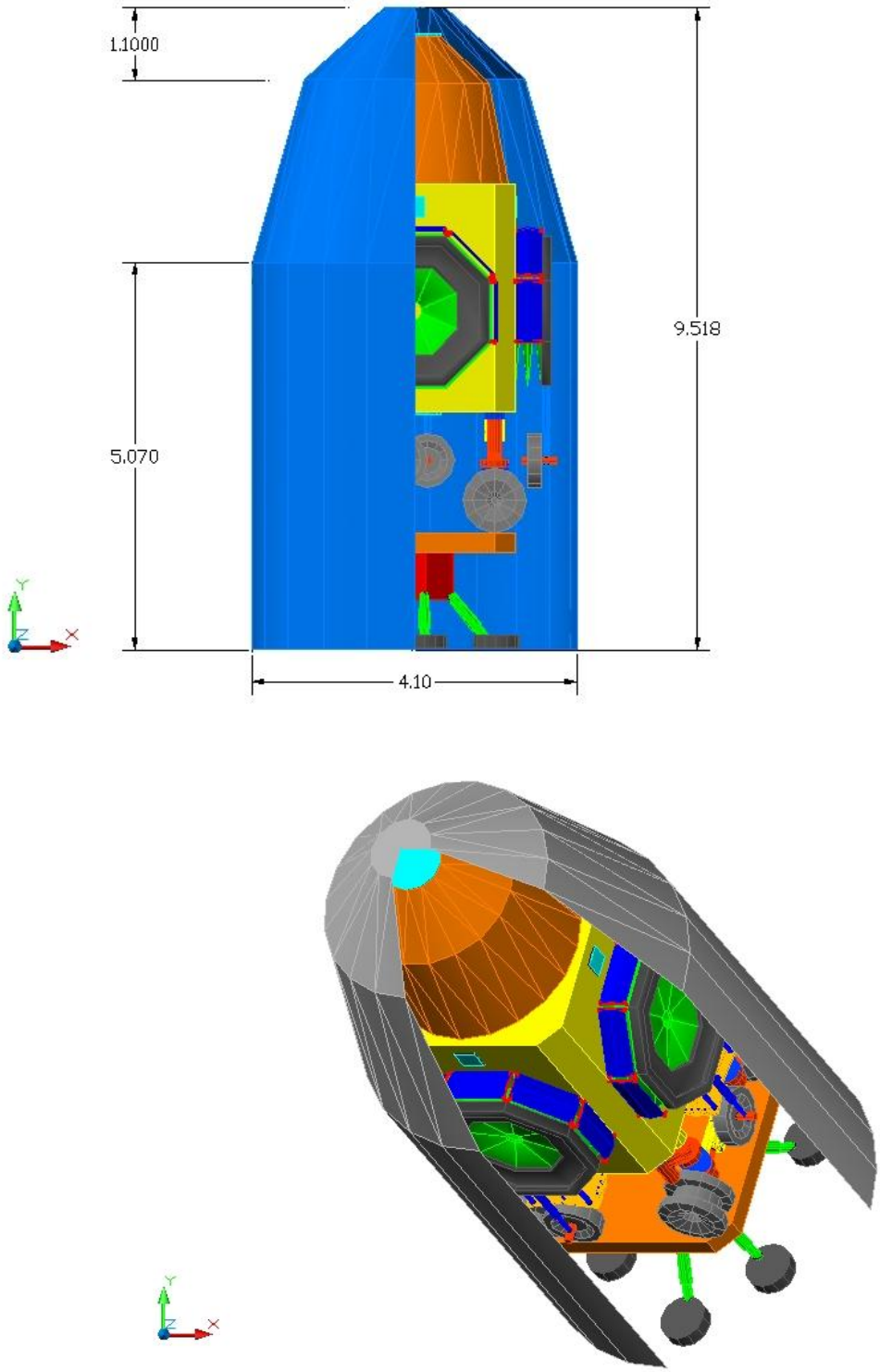

Figure 94: external fairing volume for Soyuz system

Below the internal fairing volume dimension for the standard Ariane 5 system are reported.

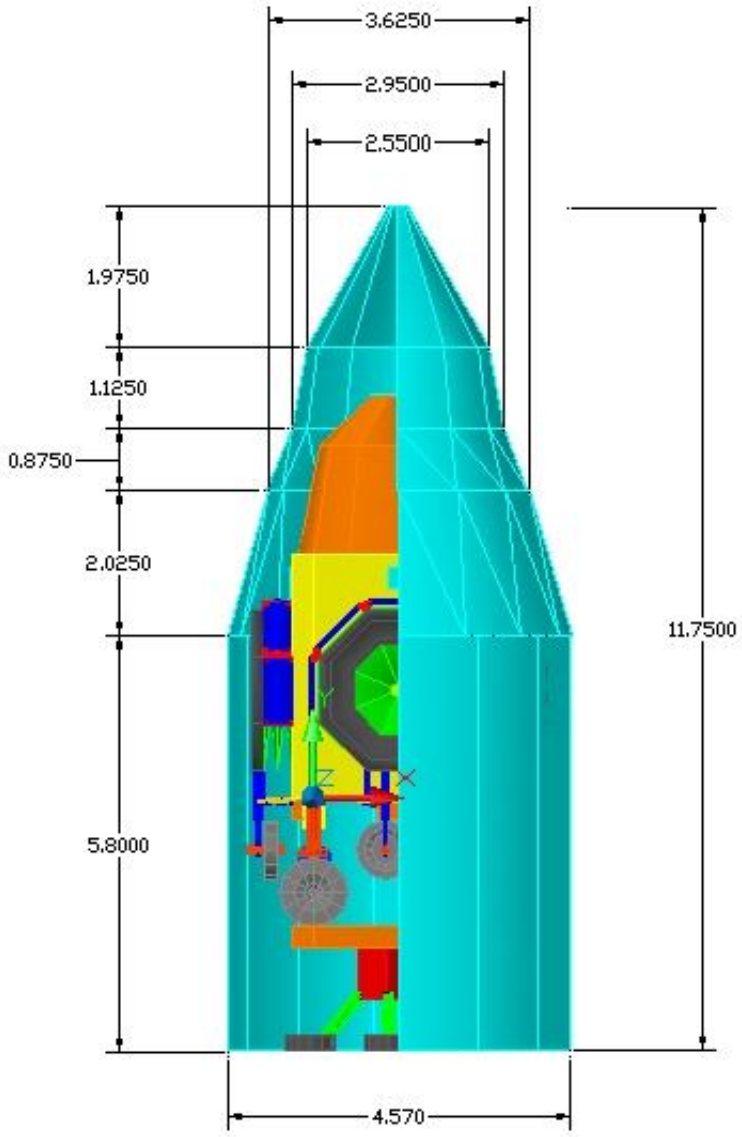

Figure 95: dimension for Standard Ariane 5 fairing system

The dimension of LEMMB has been made Soyuz and Ariane 5 compliant in order to grant a sort of standard for lunar module dimension point of view.

2.6 Reference Table

1. Ariane5_users_manual_Issue4

http://www.arianespace.com/site/documents/Ariane5_users_manual_Issue4.pdf

http://www.arianespace.com/site/documents/ariane5_man_index.html

2. soyuz_users_manual_190401

http://www.arianespace.com/site/images/soyuz_users_manual_190401.pdf

http://www.arianespace.com/site/documents/soyuz_man_baikonur_index.html

4. Soyuz_Users_Manual_CSG_June06

http://www.arianespace.com/site/documents/Soyuz_Users_Manual_Part1.pdf

http://www.arianespace.com/site/documents/Soyuz_Users_Manual_Part2.pdf

SAPIENZA
UNIVERSITÀ DI ROMA

3 Chapter 3
Expandable and Core LEMMB's Structures

3.1 Abstract

This chapter shows the structures of the two main part of LEMMB:

- The four inflatable ARMS
- The Core.

3.2 Moon Environment

Recalling briefly the Moon environment

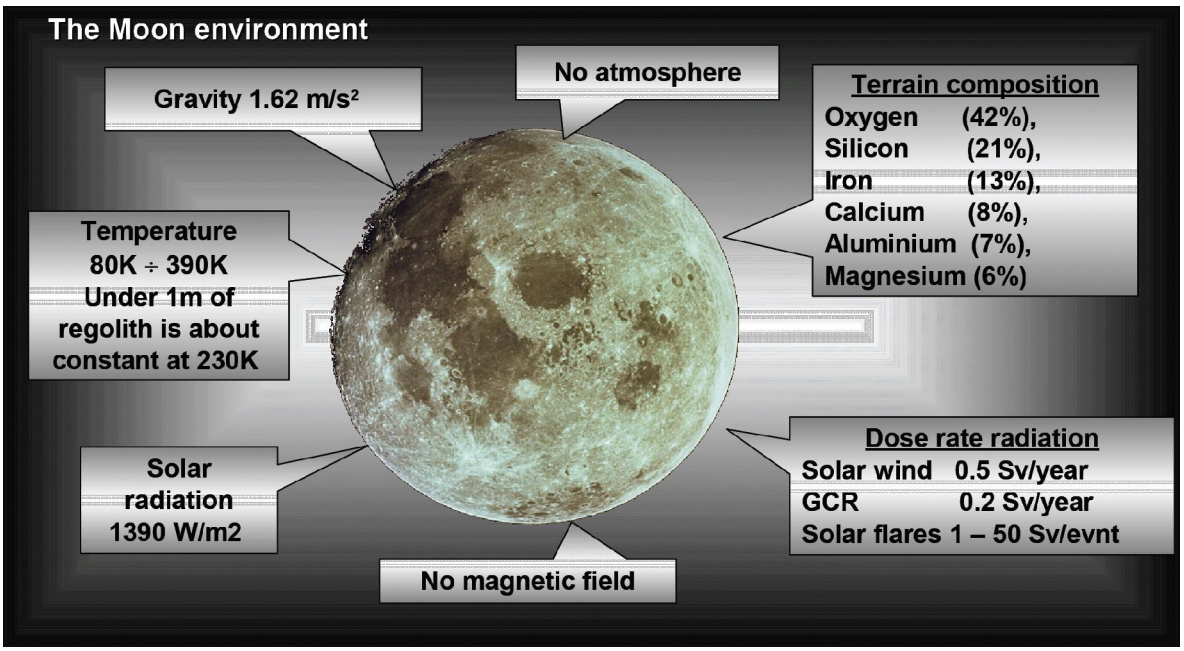

Figure 96: Moon environment

3.2.1 Moon Temperature

- Surface temperature depends on solar incidence
  - Noontime surfaces ~ 100°C
  - Coldest night temperatures ~ -150°C
- Temperature variations minimal below surface >30 cm (-23°±5°C)
- Polar areas are always either dark or at grazing solar incidence

- Lit polar areas have sunlight ~ 1°incidence
    - Average temperatures ~ -50°±10°C
- Dark areas are very cold
    - Uncertainty in lunar heat flow values suggest cold traps between 50 and 70 K

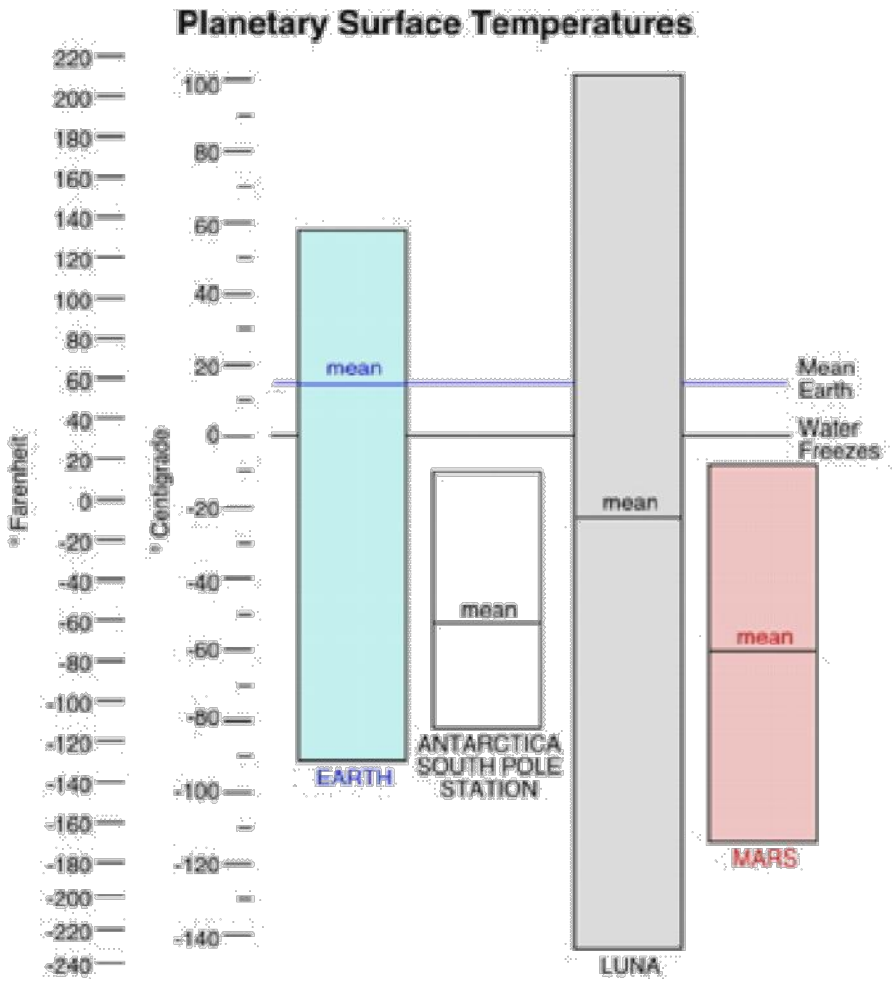

Figure 97: Moon temperature range

Under these conditions has been developed the LEMMB's structures.

3.3 The Inflatable ARM's Structures

The inflatable Arms structures main purpose is allowing the astronauts passages from one LEMMB to another. They also have the function to increase the habitable volume. Finally they have the purpose to extend the solar array needed to collect and transforms the solar energy in electrical power.

The main advantages of the inflatable structures are the lower mass than the equivalent metal structures.
Another advantages of the inflatable structures is the possibility to be packaged into a smaller volume then a traditional metal rigid structure, as consequence within the same Space Vehicle we can transport more useful volume.

Along the space traveling toward the Moon, the structures remain packed and compressed all the time.
Once arrived to the Moon the main problem is the expansion of the structures which for a long time has been remained compressed for the package purposes. The structures during the package process is folded and compressed and most probably stressed in some point.
The same structures during the expansion process is inflated, and most probably subjected to some stress. The consequence of these two phases could be formation of some weak points where the structures become subjected to a potential breakdown.

In order to prevent this stressfully work we can use some method to force the structures to folding and unfolding in a certain way.
As an example we can think to an umbrella; when we closing it the canvas is folded every time in the same way. This is due to the umbrella's skull structure which helps the folding and unfolding phase, every time, in the same way.
We can apply the same concept in our LEMMB inflatable ARMs.
In figure below are shown some details about the ARM's structures. In particular we can distinguish two main shape for the Inflatable structures, the first one has an octagonal base while the second one cylindrical.

3.3.1 Octagonal inflatable structure

This shape provide a good system to force the desired folding and unfolding shape.
In fact along the folding line, the structures are forced to be packaged and unpackaged in the same manner, plus along these folding lines we can estimate the stress a priori.
In order to have the best package and unpackaged process we can provide the inflatable structures with an inner skull system. The skull rings are based on light Carbon composite material. The simplest skull we could thinking consists of three rings as in figure below.

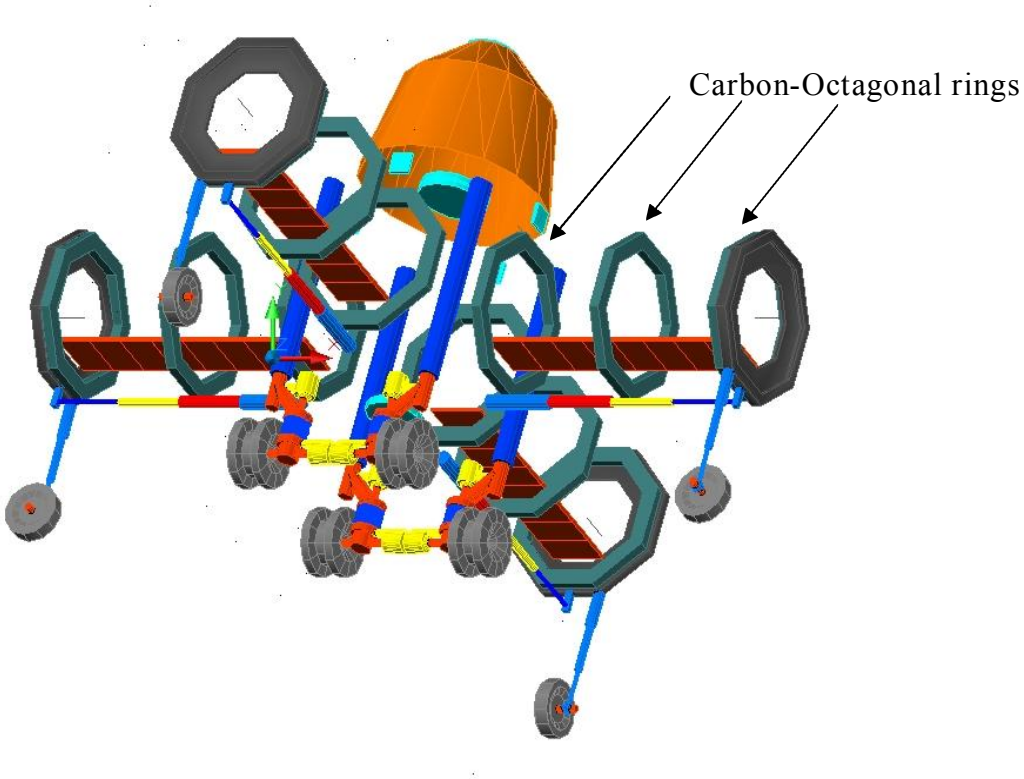

Figure 98: three octagonal skull rings within each LEMMB Arms inflatable structure

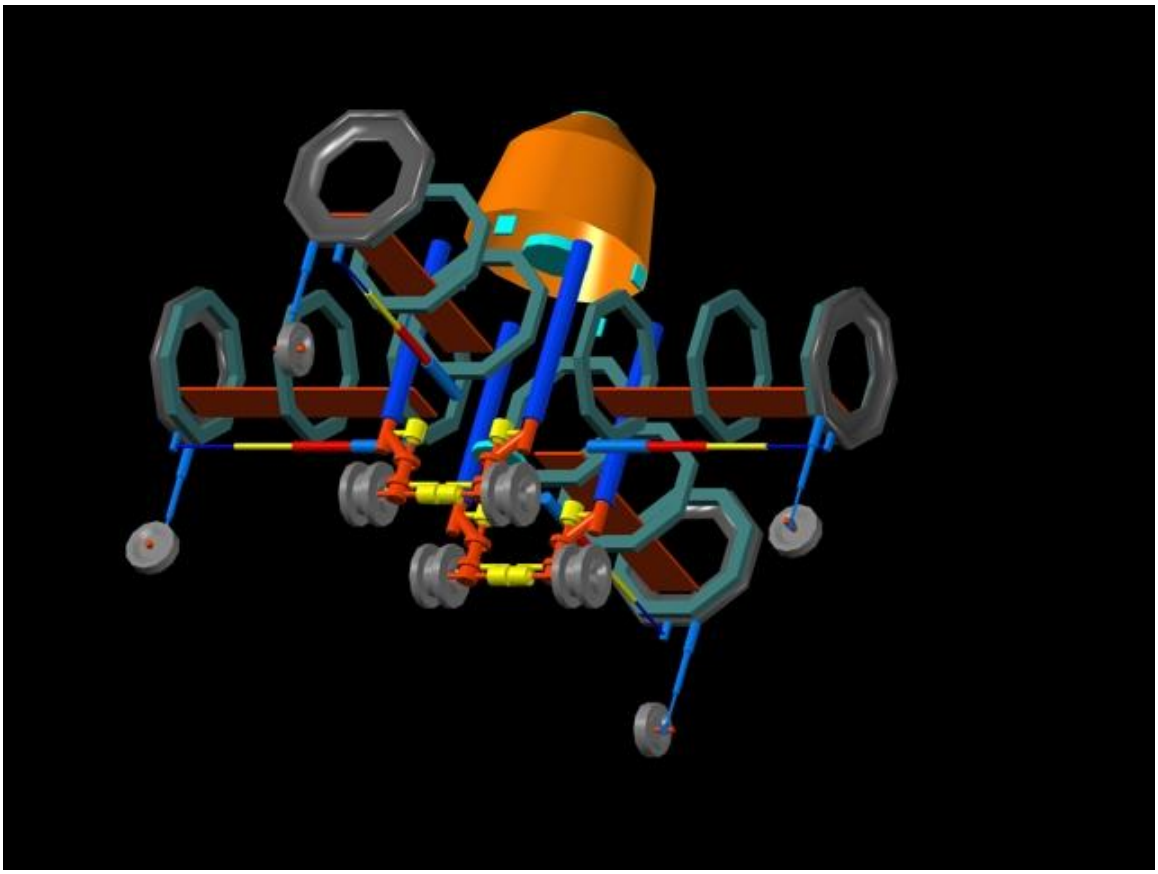

Figure 99: rendering of three octagonal skull rings within each LEMMB Arms inflatable structure

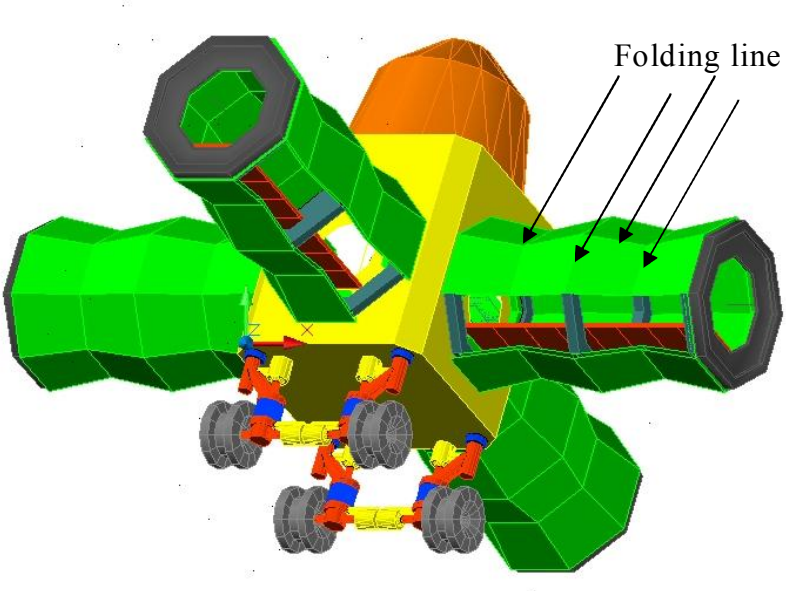

Figure 100: folding line for LEMMB's ARM

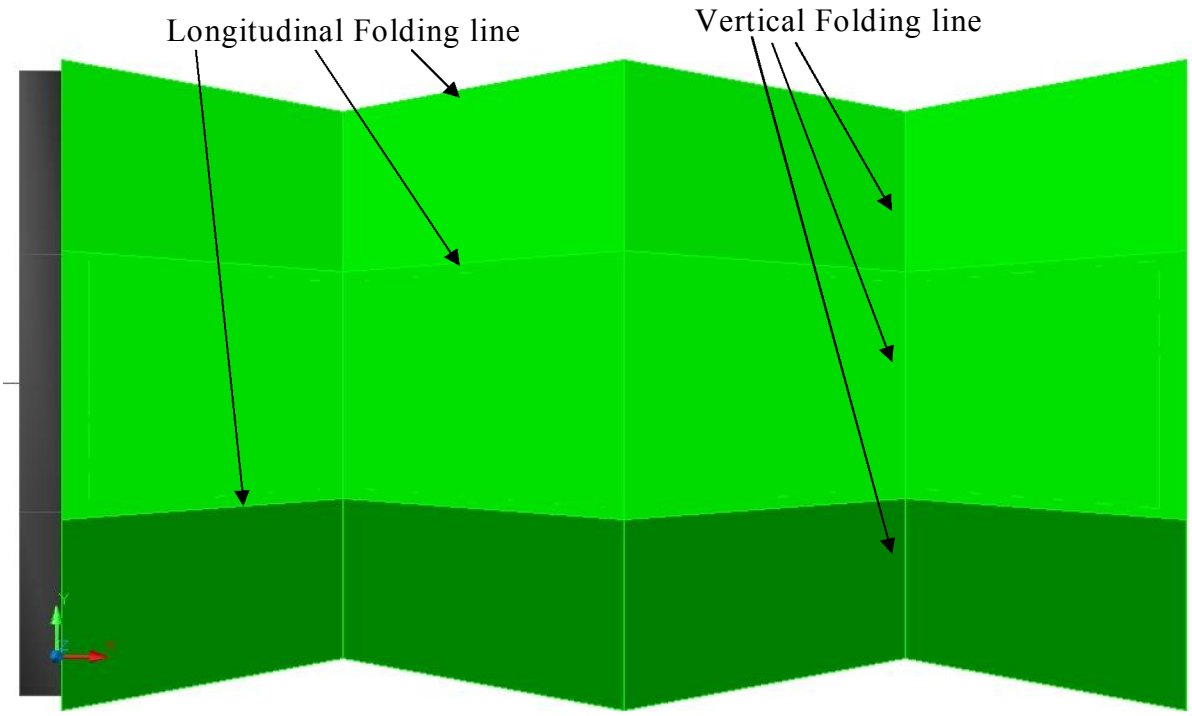

Figure 101: single octagonal inflatable Arm

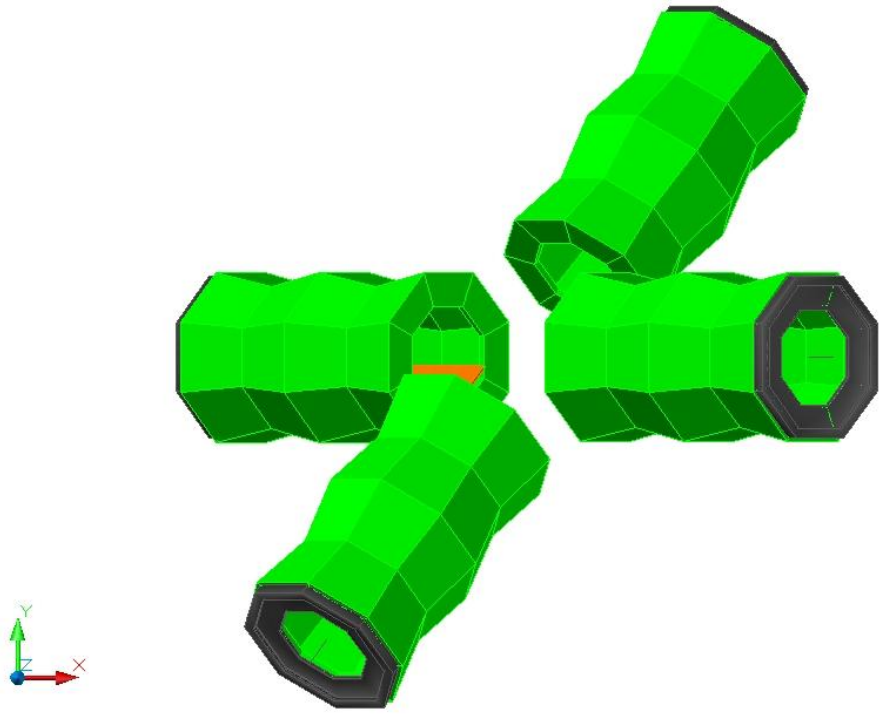

Figure 102: four octagonal Inflatable Arms

3.3.1.1 Carbon fiber composite

Carbon fibers exhibit generally superior performance in tensile, compressive and flexural properties as well as fatigue resistance. Also excellent interlaminar and, in plane shear strengths. Best tensile strength, flexural modulus, heat distortion temperature and linear expansion compared with other epoxy laminates.
The typical characteristics are:

Property	Value
Density (g/cm^3).	1.5
Surface Hardness	RM113
Tensile Strength (MPa)	600
Flexural Modulus (GPa)	80
Notched Izod (kJ/m)	0.5
Linear Expansion (/°C x 10^{-5})	0.05
Elongation at Break (%)	1.3
Strain at Yield (%)	N/A
Max. Operating Temp. (°C)	130
Water Absorption (%)	0.2
Oxygen Index (%)	28
Flammability UL94	V0
Volume Resistivity (log ohm.cm)	2
Dielectric Strength (MV/m)	NA
Dissipation Factor1kHz	NA
Dielectric Constant 1kHz	NA
HDT @ 0.45 MPa (°C)	260+
HDT @ 1.80 MPa (°C)	230
Material Drying hrs @ °C	NA
Melting Temp. Range (°C)	NA
Mould Shrinkage (%)	NA
Mould Temp. Range (°C)	NA

Table 4: carbon fiber characteristics

3.3.2 Cylindrical structure

The second inflatable structures has a cylindrical shape.

This second shape type its easier to build then the first octagonal one but it could exhibit potential folding problems since there is no one prefixed folding line.

The vertical folding line could be forced using similar rings structures within the inflatable structure.

Figure 103: cylindrical inflatable Arm structure

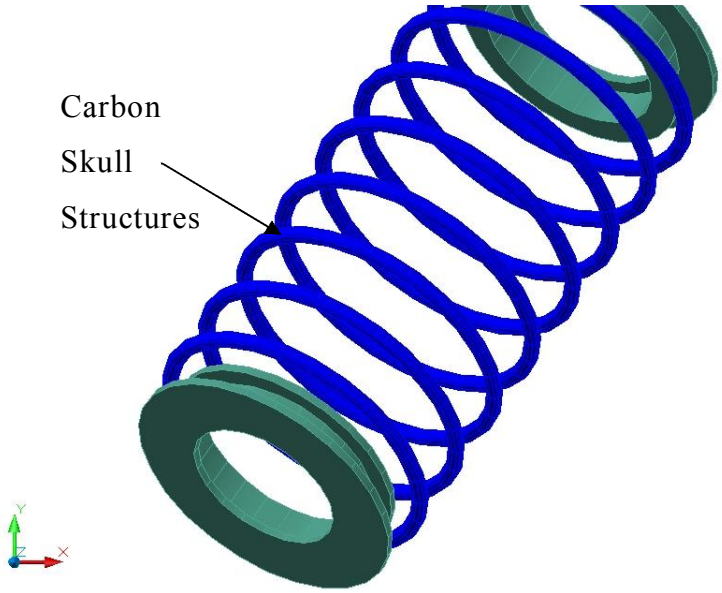

Figure 104: Cylindrical inflatable Carbon Skull structures

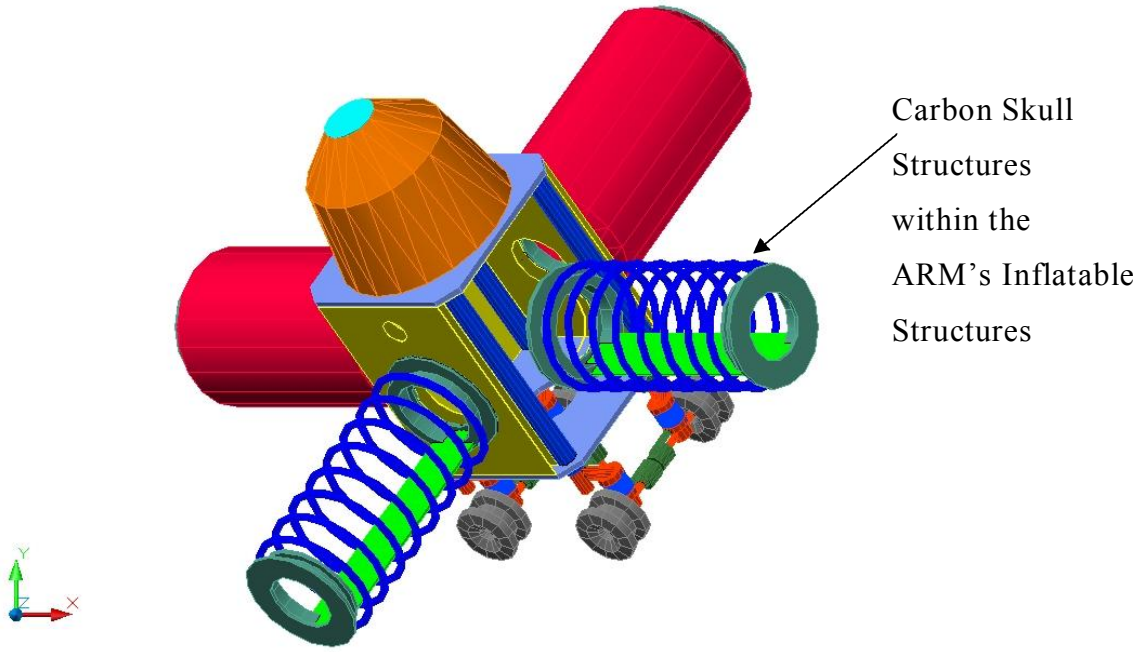

Figure 105

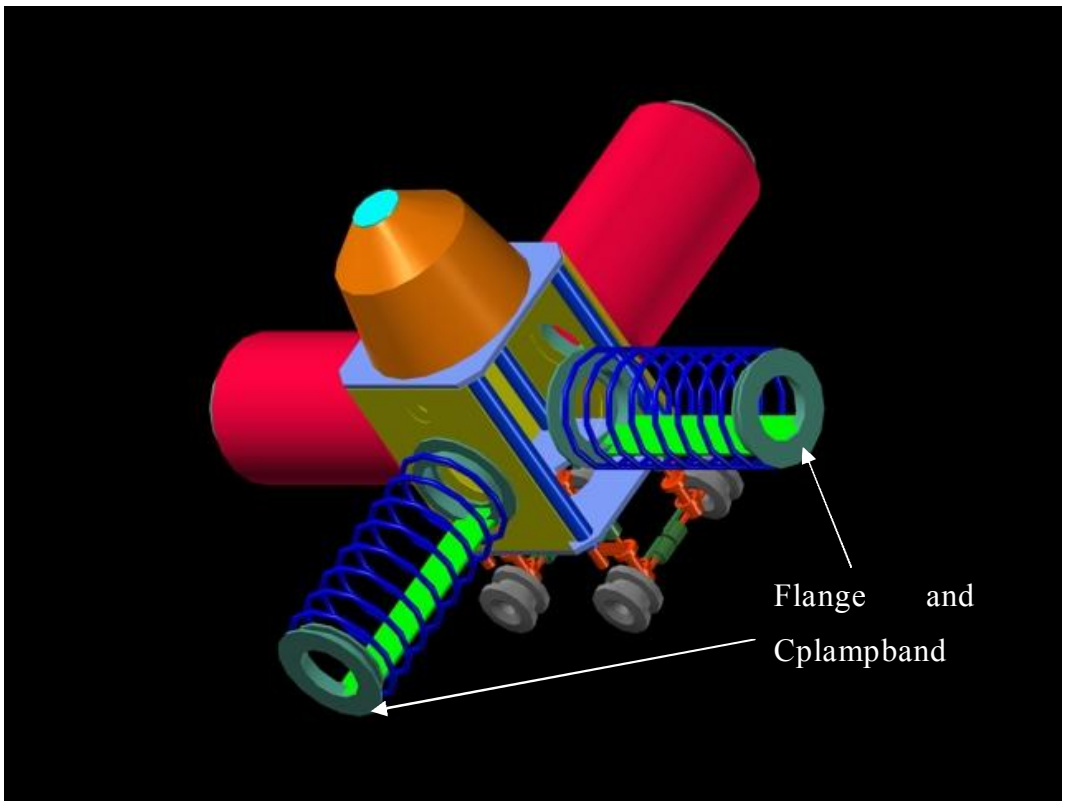

Figure 106: rendering

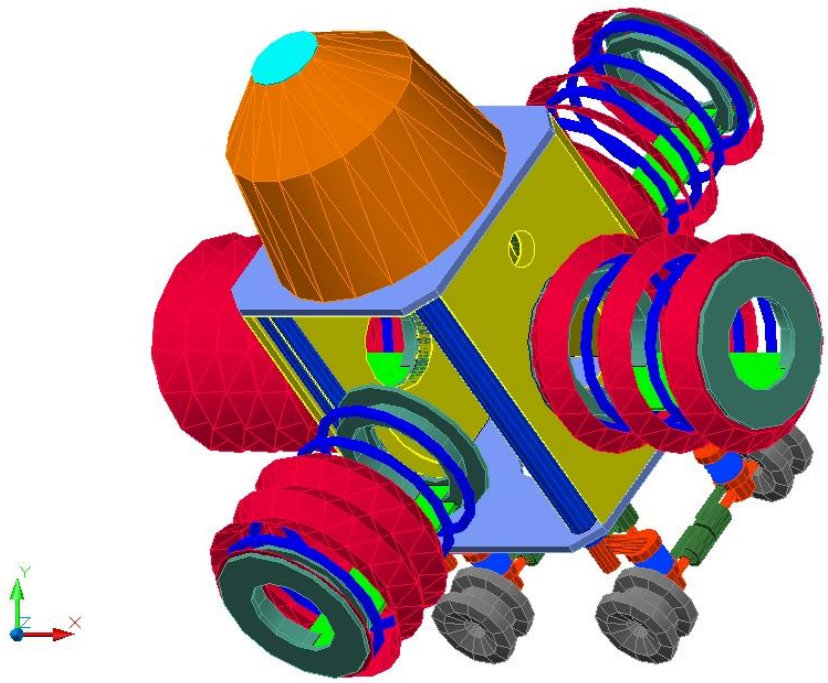

Figure 107: ARMs in expansion phase

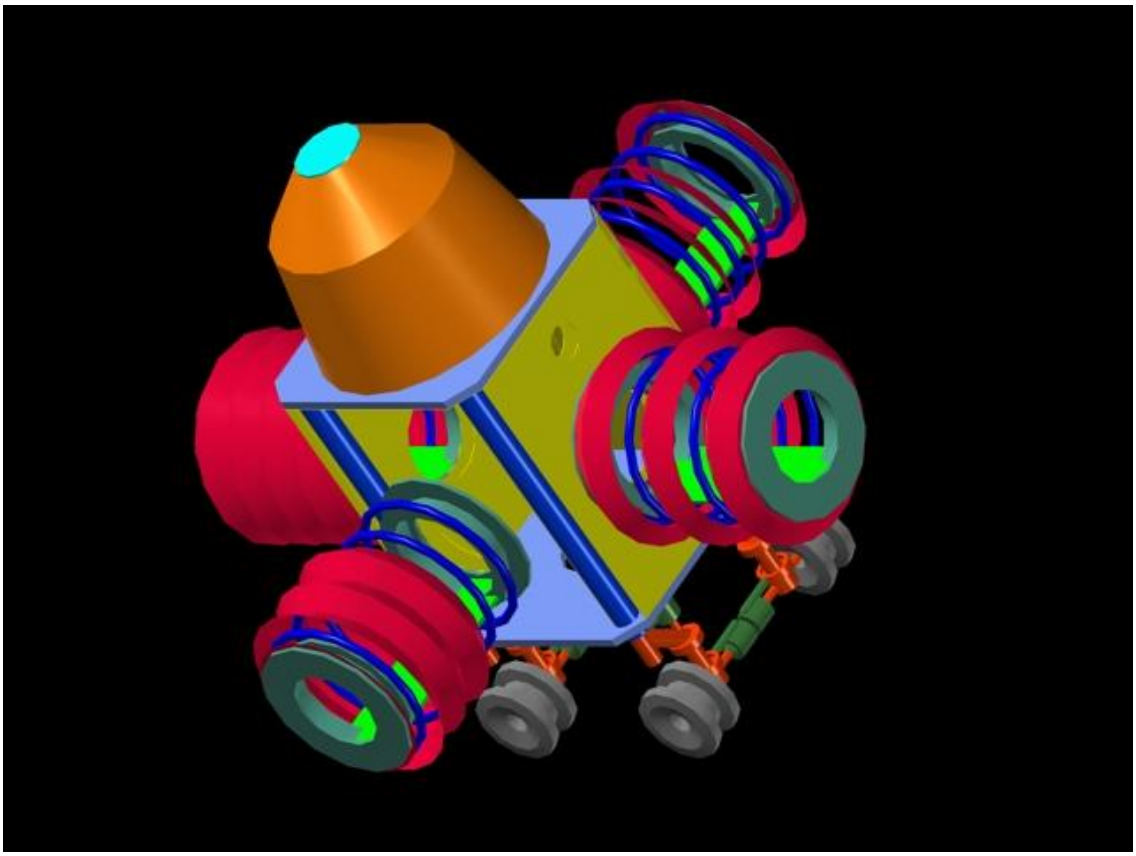

Figure 108

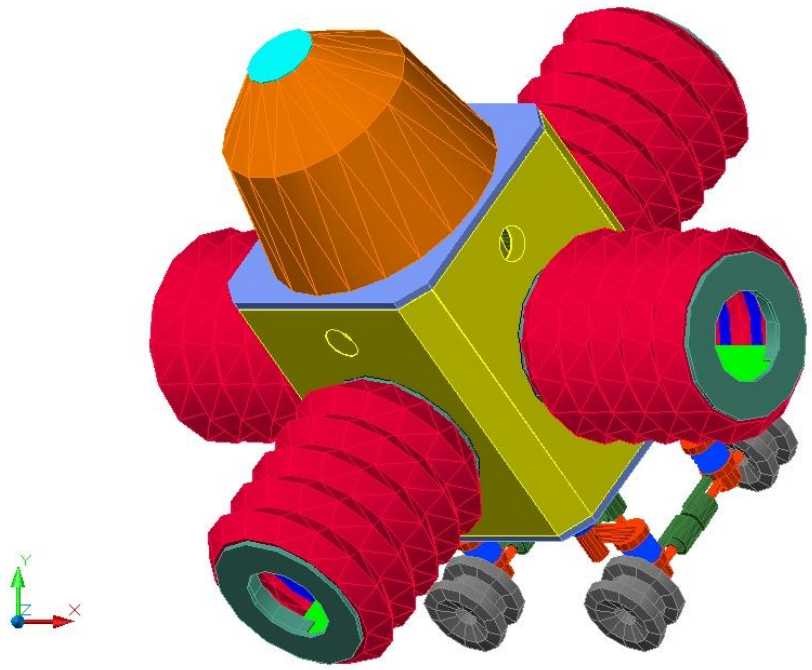

Figure 109

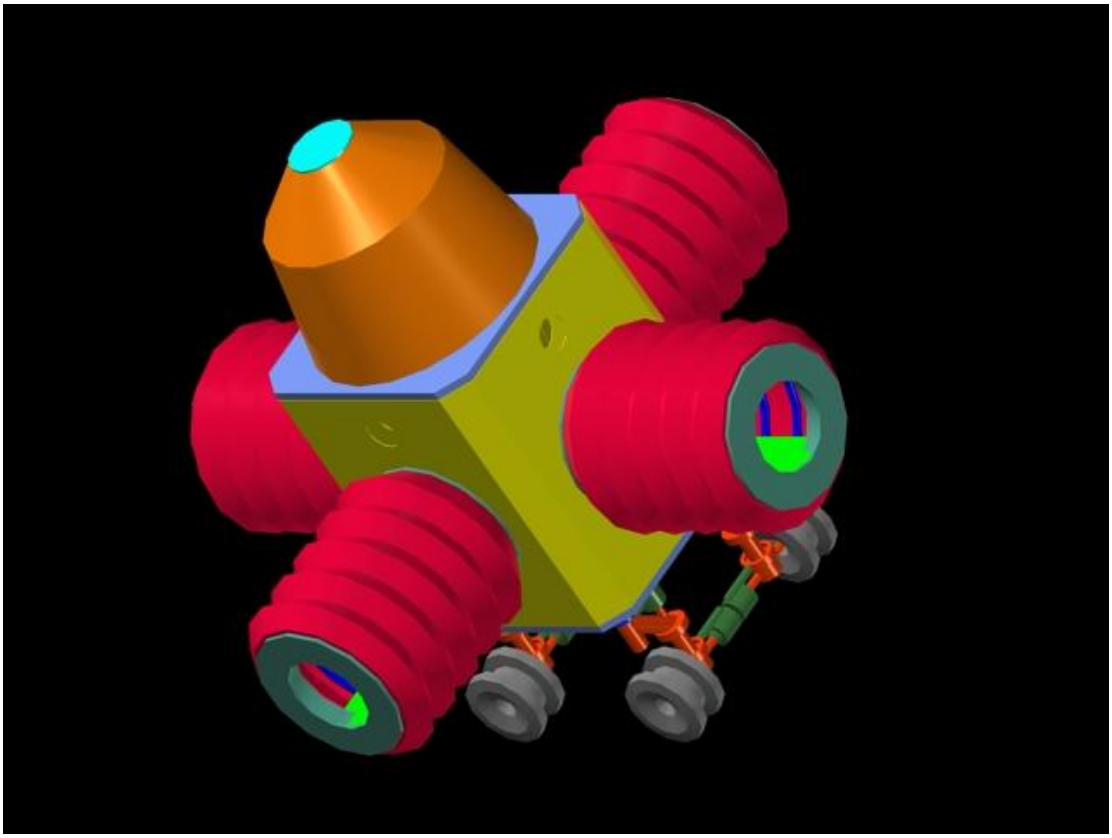

Figure 110

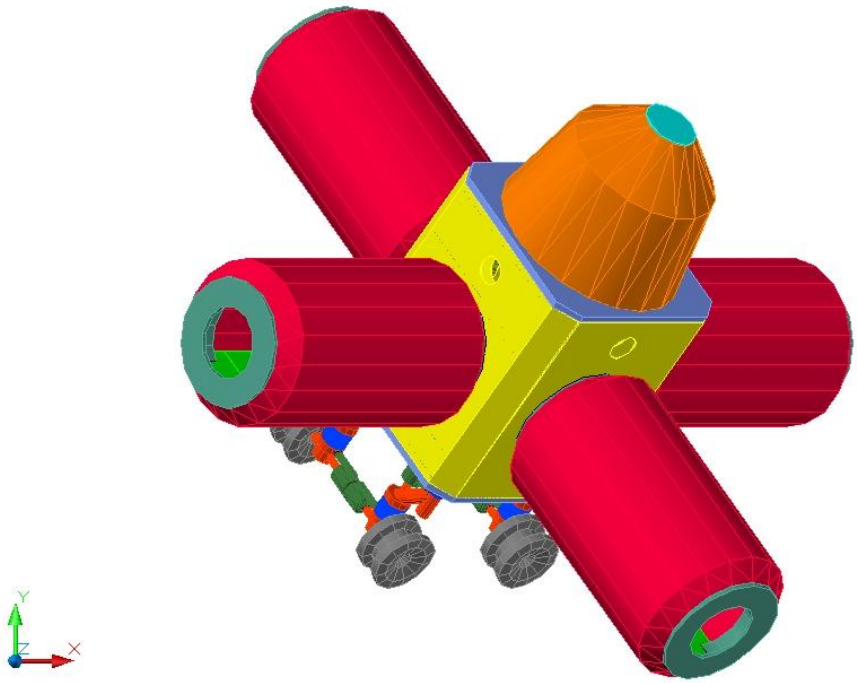

Figure 111: LEMMB with cylindrical inflatable Arms fully expanded

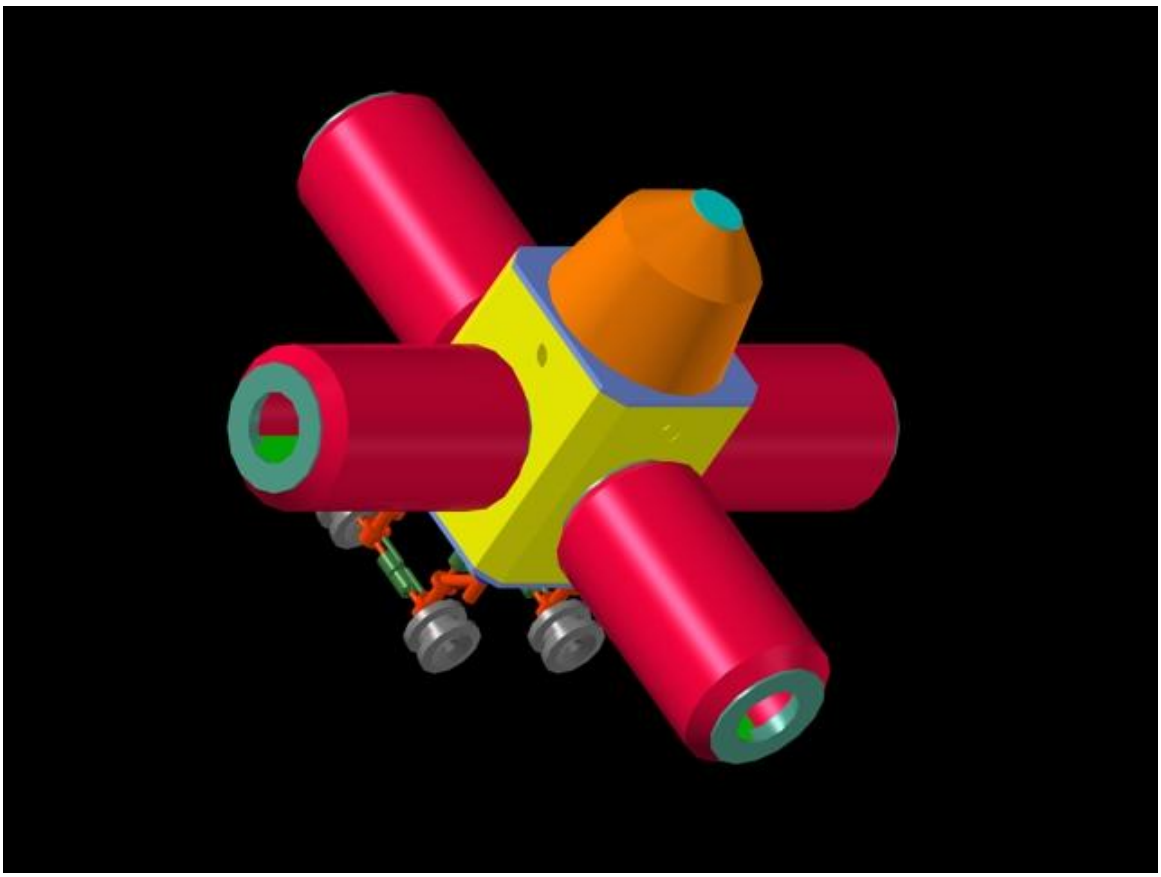

Figure 112: rendering of LEMMB with cylindrical inflatable Arms

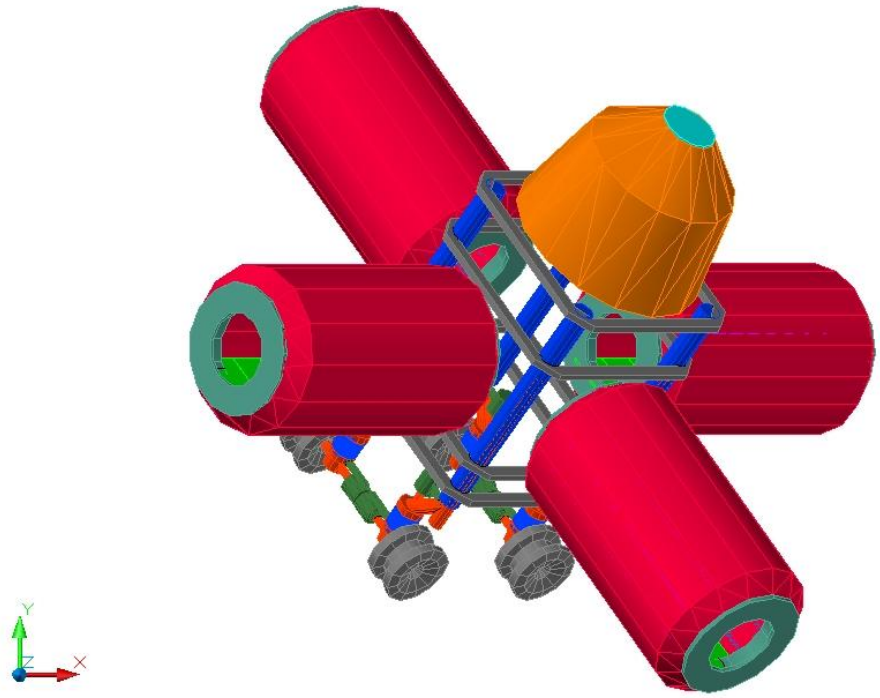

Figure 113

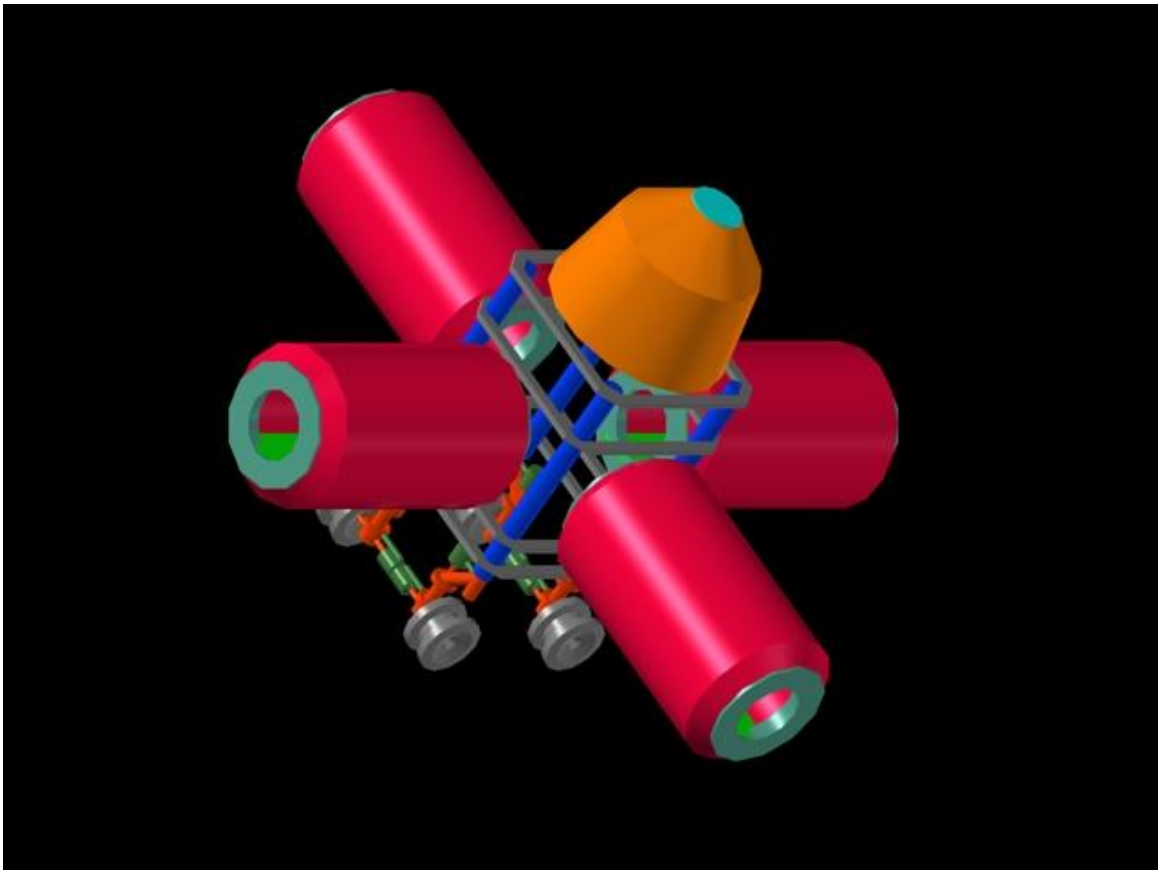

Figure 114

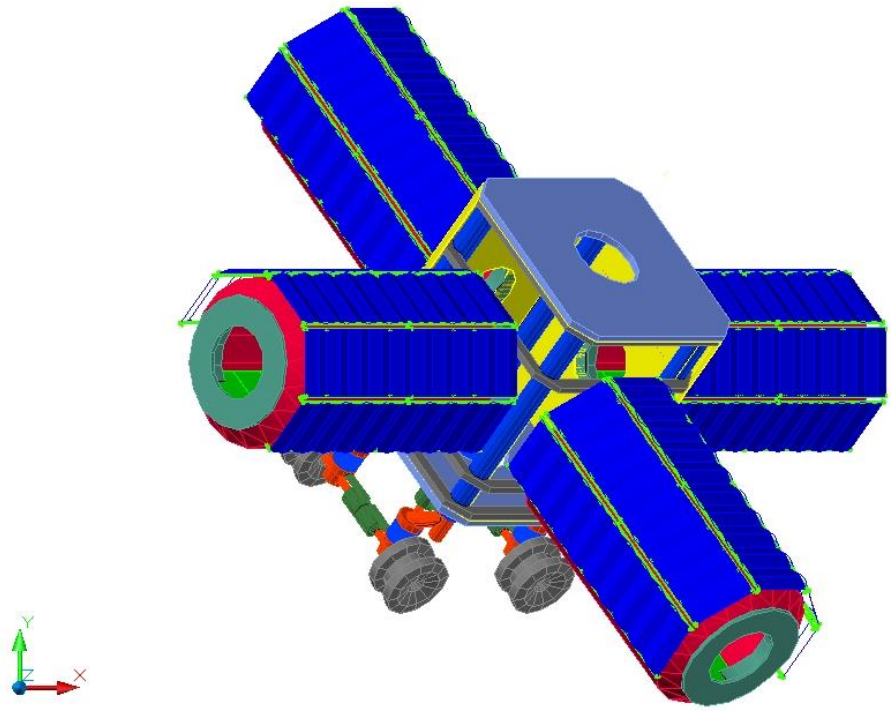

Figure 115: solar panels of LEMMB

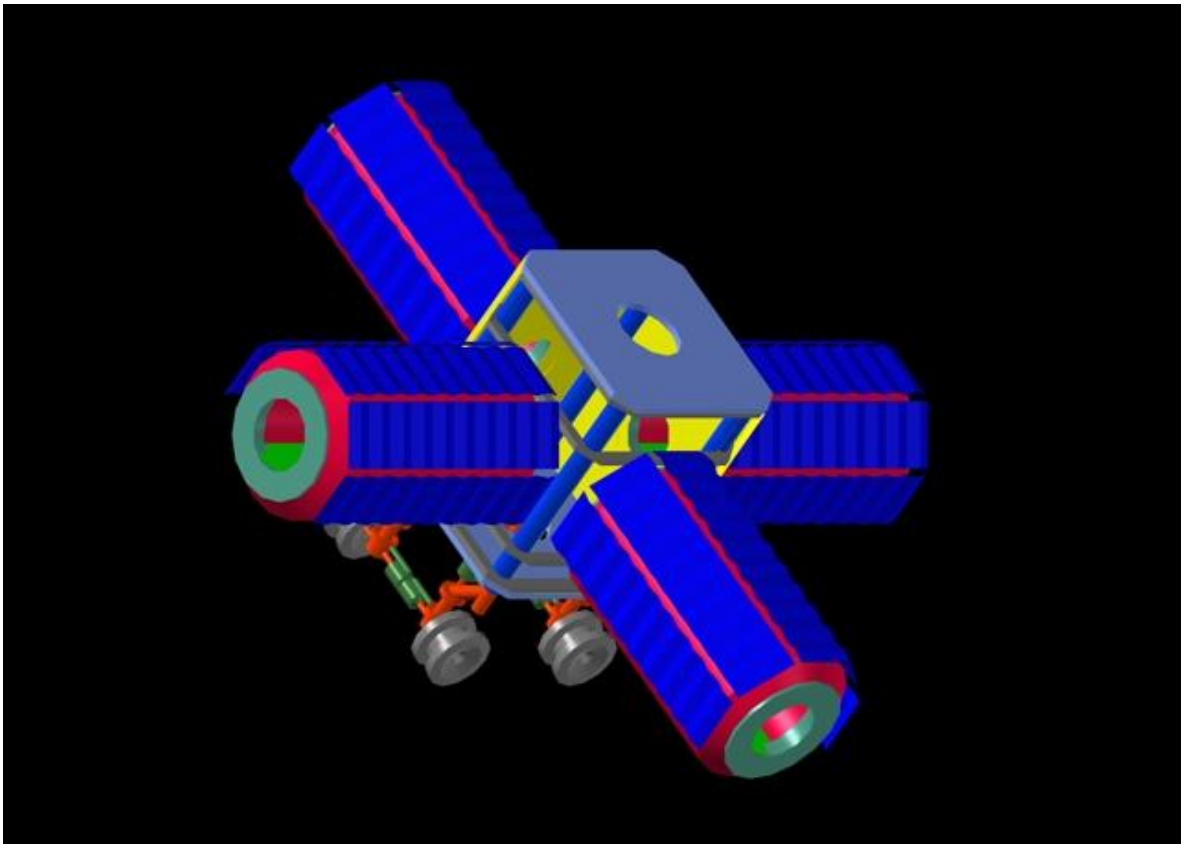

Figure 116: rendering solar panel of LEMMB

3.4 Multi Layer Strategy Inflatable Structure

In figures below the multilayer structures of each inflatable Arm is shown. The same method is applied in octagonal Arms structures.

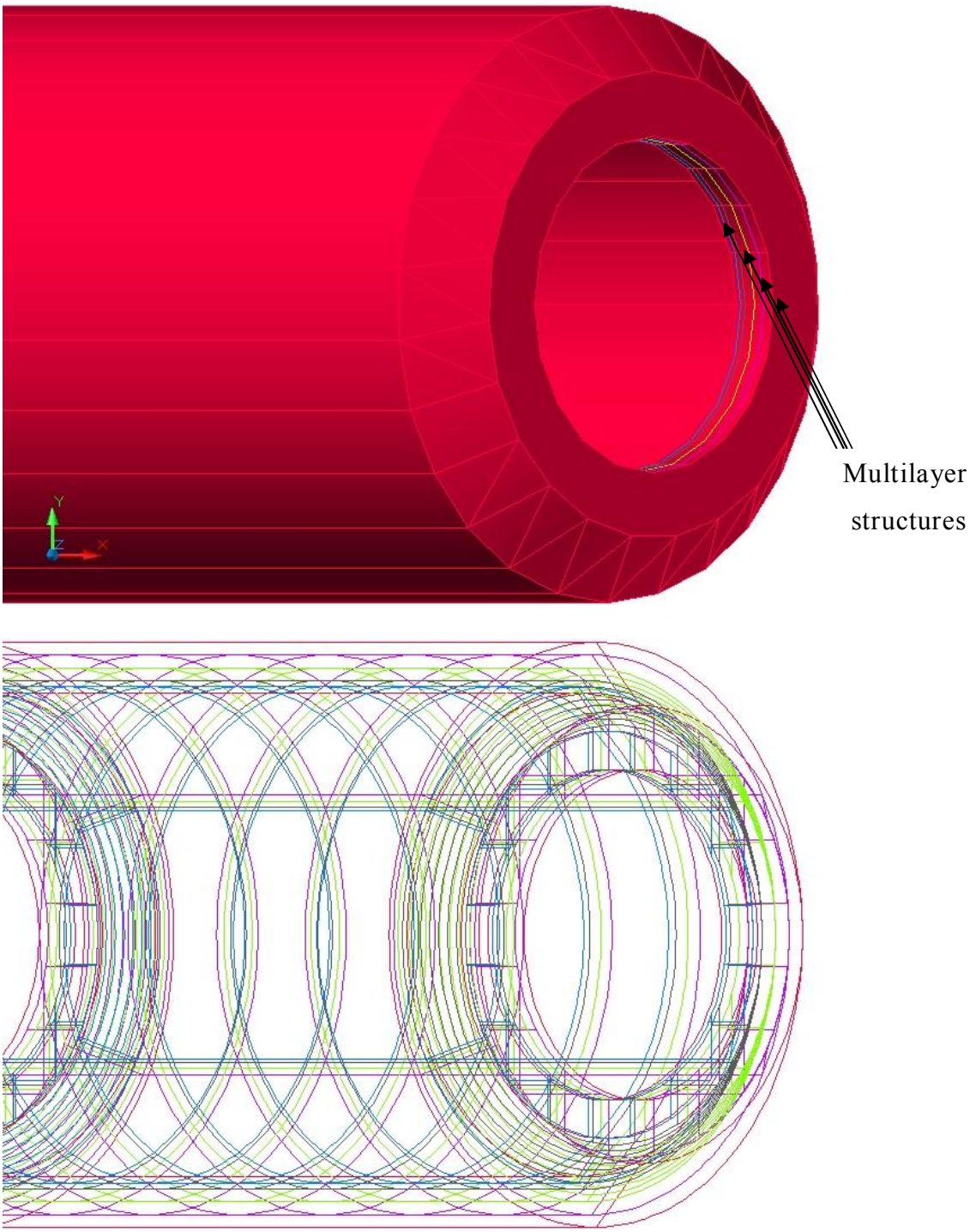

Figure 117: multilayer structures of the inflatable Arms

An inflatable shell is a compilation of structural materials that are flexible and are combined together as to provide comparable structures as their rigid metallic counterparts.
The inflatable structures here shown is conceived like the FLECS (Flexible and Economic Space Structures) structures.
The FLECS structures is available on web at www.sciencedirect.com, it is designed as Expandable Module concept for future space mission.
The FLECS is basically composed of three different functional sub-layers.

- The inner layer defined as "bladder" is the air retention sub-layer whose properties are to be non toxic, fire retardant and have good puncture resistance and low leakage.

- The intermediate layer are the backbone material that aid in supporting the structural load due to inlfaction/pressurization and also increase the puncture resistance. Advanced flexible high strength fibers such as Kevlar, Vectran, Zylon, have been selected as candidates for the fabrication of these resistant layer and their very low mass structures are deployable from a density packet state.

- The ultimate outer layer belong to the Micrometeorid/Orbital Debris (MMOD) Impact Protection Shield. The MMOD impact protection is being accomplished by a series of woven Nextel and Kevlar layers separated by from spacers to create a multi-hull structures.

Similar to FLECS structures, in LEMMB Inflatable Arms there are totally four main layers, the first 3 layer are the same as in FLECS while, the target of the added layer is to increase the reduction of the energetic particle flux. From recent studies, new and alternative engineering design with respect to the traditional hard shell Habitat, offers a similar radioprotection behavior from GCR with respect to traditional aluminum structures.
In the Simplified Inflatable Module **water and polyethylene** have an equivalent shielding behavior.

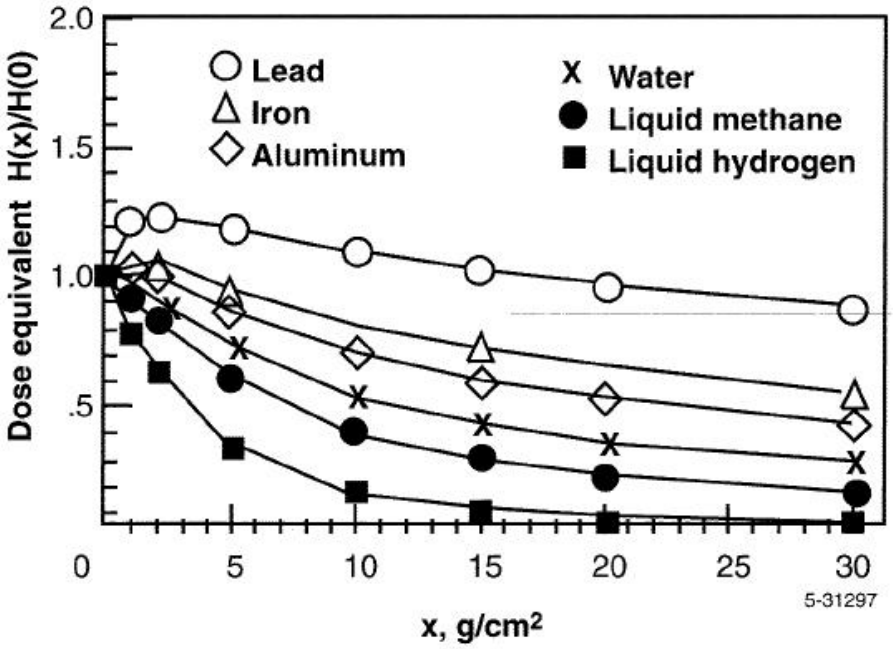

Figure 118: shielding property of several materials and liquid

In the LEMMB flexible structures:

1. The external layer has the main purpose to stop the micrometeorites and it should be high variable temperature resistant. Typically, between night and day, the temperature excursion on the Moon surface is of the order of 200 C°, some material useful could be blanket of Solimide, which are resistant to U.V. radiation and outgassing.
2. The immediately adjacent internal layer has the purpose to stop some Energetic particles like the some Galactic Cosmic Rays. From some recent researches seems that, material with high percentage of hydrogen show a better radiation protection than material with low content of hydrogen. As an example some granular material based on Polyethylene could be used.

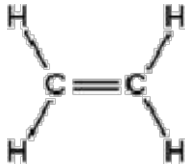

Figure 119: polyethylene

3. The immediately adjacent internal layer has the purpose to make the structures flexible but resistant to the mechanical solicitations. Like the sail of boat, Kevlar, Vectran based material could be used for such layer, it is light and more resistant than aluminum.
4. The immediately adjacent internal layer is based on anti fire and no toxic layer since it is at direct contact with astronaut's environment.

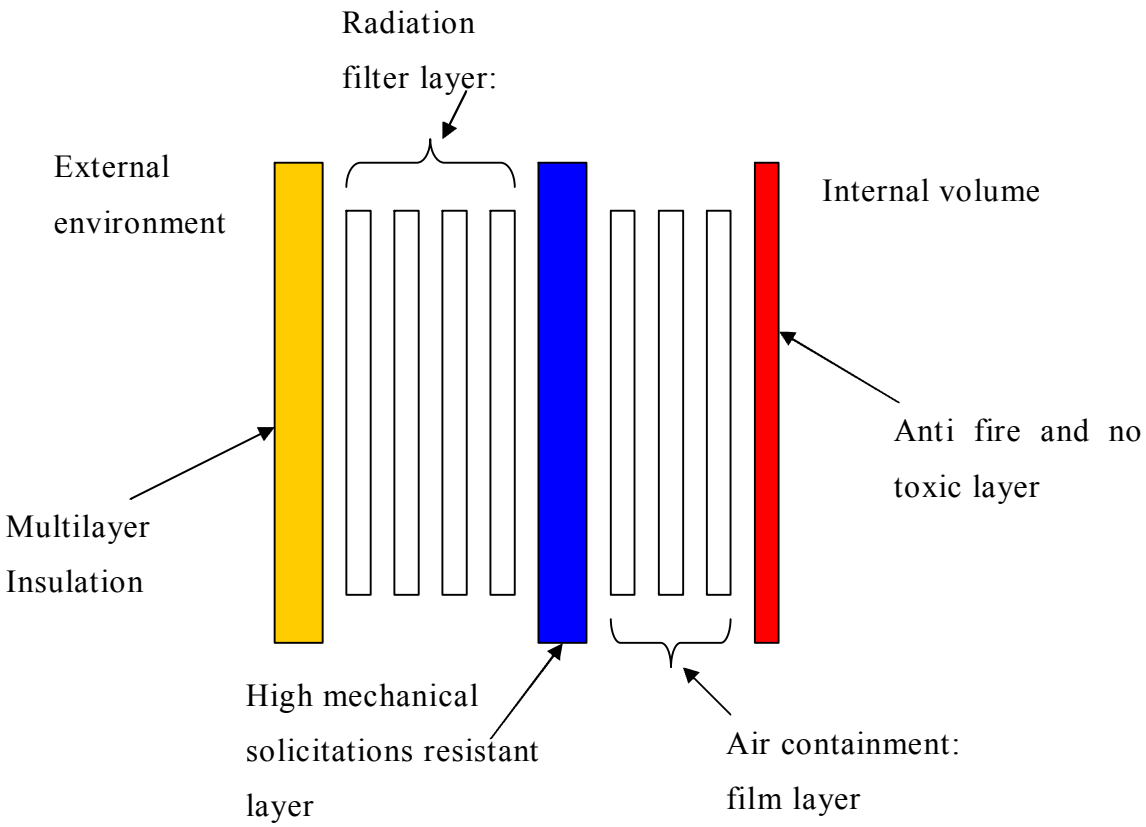

Figure 120: Multilayer structures of Inflatable Arms

3.4.1 Kevlar Technical Data

The main data are summarized in table below:

CHARACTERISTICS	
Continuous Temp	750°F (399°C)
Melt Temp	1,000°F (538°C)

PROPERTIES
• Low thermal conductivity • Will not burn or smolder • Will not stretch or shrink • High strength-to-weight ratio • Resistant to sparks & welding spatter • Superior resistance to abrasion • Resistant to most chemicals • Excellent flexibility up to 750°F

Table 5: Kevlar main data

3.4.2 Solimide main characteristics

Minimizing fire hazards on the Space Shuttle has inspired production of a polyimide foam that is finding secondary commercial benefit as a lightweight thermal and acoustic insulating material.

Early in NASA's history, Johnson Space Center engineers called for a decrease in the flammability, smoke and toxicity of materials used in spacecraft. That need was adopted in the construction of the Space Shuttle fleet. Initial Space Shuttle uses of the foam were for thermal insulation, as well as packaging and protecting fragile equipment.

Manufactured for use by NASA, Inspec Foams Inc. (formerly named ImiTech) supplied the lightweight, fire-resistant Solimide polyimide foam. Two big pluses offered by the product are its exceptionally low density and low flammability.

There is no question, the harshness of space is tough on any material. Yet Solimide foam remains flexible and resilient, despite the wild temperature swings of the space environment. It has become the ideal choice for lightweight insulation in space applications. One such use is cryogenic insulation for fuel tanks on major rocket propulsion systems. Another is thermal insulation on the louvers of communications satellites where intermittent exposure to sun and darkness requires the responsiveness of the foam. Still another characteristic is its minimal outgassing. Therefore, contamination of delicate equipment and space sensors is one less worry. Solimide polyimide foam has been qualified for placement on Marshall Space Flight Center's materials specification selection list.

A variety of densities and structural configurations can be produced, with the foam remaining resilient under exposure to temperatures ranging from minus 300 to plus 500 degrees Fahrenheit. Virtually no smoke or toxic byproduct is generated upon decomposition. Furthermore, the product's flame retardant qualities have prompted their application in ships and surface transportation systems, such as cars, trains, buses and automobiles. Solimide foams allow aircraft manufacturers to improve the designs of their insulation systems at an overall reduction in installed and life-cycle costs. That also means fuel cost efficiency. Aircraft applications include cockpit and cabin insulation, ducting, bulkhead insulation and under floor insulation.

3.4.3 Vectran main characteristics

Vectran™ is a high-performance multifilament yarn spun from liquid crystal polymer (LCP). Vectran™ is the only commercially available melt spun LCP fiber in the world.
Vectran™ fiber exhibits exceptional strength and rigidity.
Pound for pound Vectran™ fiber is five times stronger than steel and ten times stronger than aluminum. These unique properties characterize Vectran™:

- High strength and modulus
- Excellent creep resistance
- High abrasion resistance
- Excellent flex/fold characteristics
- Minimal moisture absorption
- Excellent chemical resistance
- Low coefficient of thermal expansion (CTE)
- High dielectric strength
- Outstanding cut resistance
- Excellent property retention at high/low temperatures
- Outstanding vibration damping characteristics
- High impact resistance

Vectran™ fiber's performance at low temperature was evaluated by ILC Dover during the design of the airbag system for the 1997 Mars Pathfinder mission. ILC reported that Vectran™ actually increased in strength in tests at -62°C, leading to its selection for the airbag fabric and external assembly tendons. This distinguishing characteristic of Vectran™ is shown in Figure below.

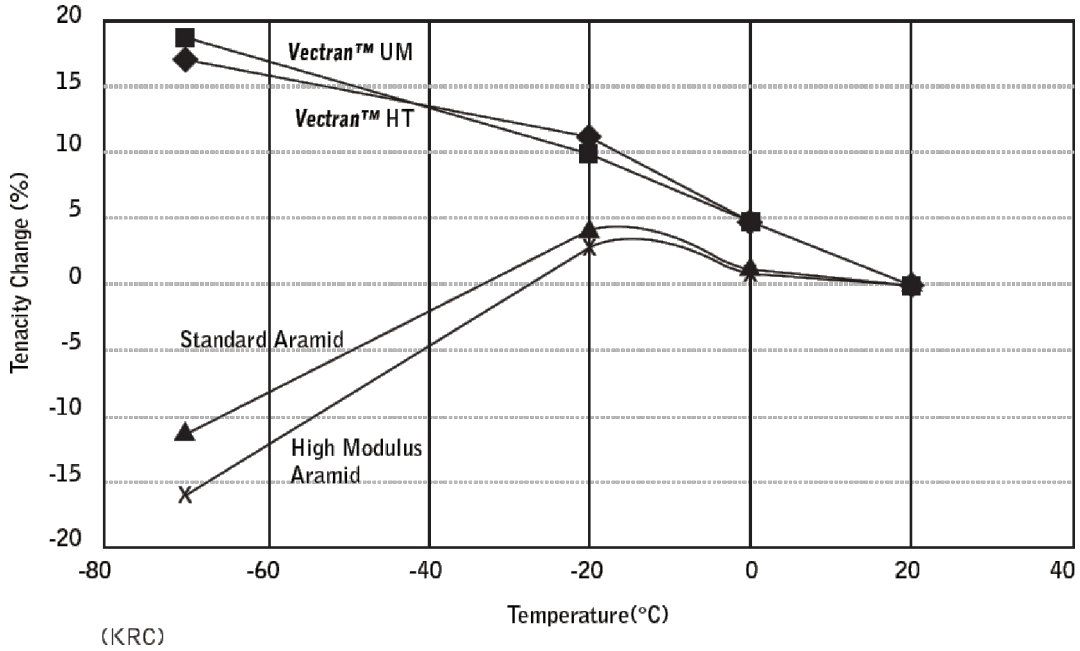

Figure 121: Low Temperature Properties of Vectran™ Fiber

3.4.3.1 Vectran Offgassing/Outgassing

In aerospace applications, material candidates are often screened for outgassing and offgassing properties. Outgassing is the release of chemicals from non-metallic substances under vacuum conditions. Test method ASTM E595 is routinely used to assess material outgassing characteristics. In this test, a material is held at 125°C for 24 hours in vacuum, and condensing volatiles are collected on a cooled plate. Test results include the sample's percent total mass loss (TML%), the percent collected volatile condensable materials (CVCM%), and percent water vapor regained (WVR%).

Offgassing refers to the release of chemicals from materials at ambient or higher pressure. Test method NHB 8060.1C is commonly used to measure offgassing characteristics. In this test, the candidate material is held at 125°C and ambient pressure for 72 hours. Gas sample analysis yields offgassed product identities and their concentration. For each species, the ratio of the sample concentration to its SMAC (spacecraft maximum allowable concentration) is calculated.

The sum of these ratios is the T value of the material, or the Toxic Hazard Index.

Vectran™ fiber with either T97 or T150 finish provides excellent offgassing and outgassing characteristics in a wide variety of aerospace applications.

3.4.3.2 Vectran UV Resistance

The UV resistance of products made from high performance fibers is highly dependent upon a number of variables, including final product form (for example, rope or fabric, filament and yarn size, finishes/coatings, twist/pick levels, etc).The impact of UV on braided cords made from high performance fibers is illustrated in Figure below.

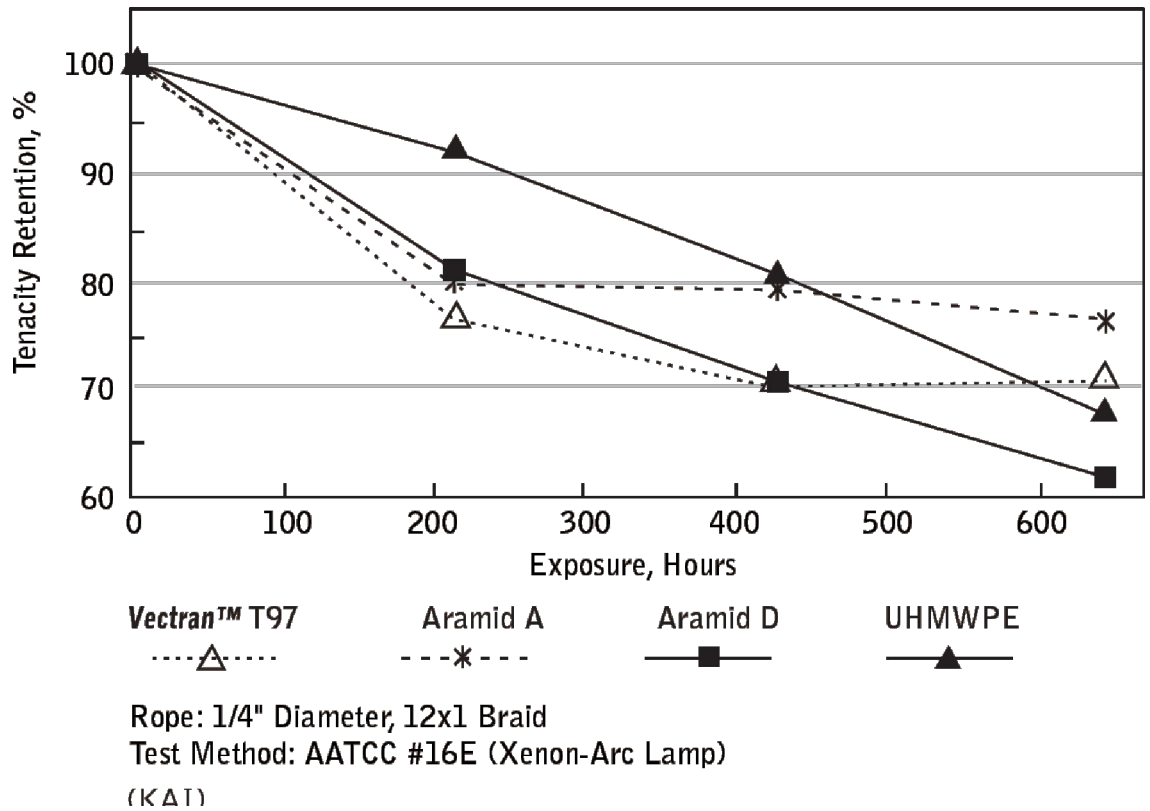

Figure 122: Tenacity Retention

3.5 Core Structures

The main purpose of the Core structures is to be the LEMMB safety place.
Mainly it must protect them from micrometeorites and radiation point of view. Within this core structures there are computers, mechanism, scientific instrumentation, support life, and electrical power storage system. This part is where the people pass the most part of their time.

3.5.1 Habitable volume

Since their modular structures, two or more LEMMB core structures could be assembled together, one over another. The lower part of Core structures contain the equipment and payload while the upper part should be like a living room.
An example of structure is:

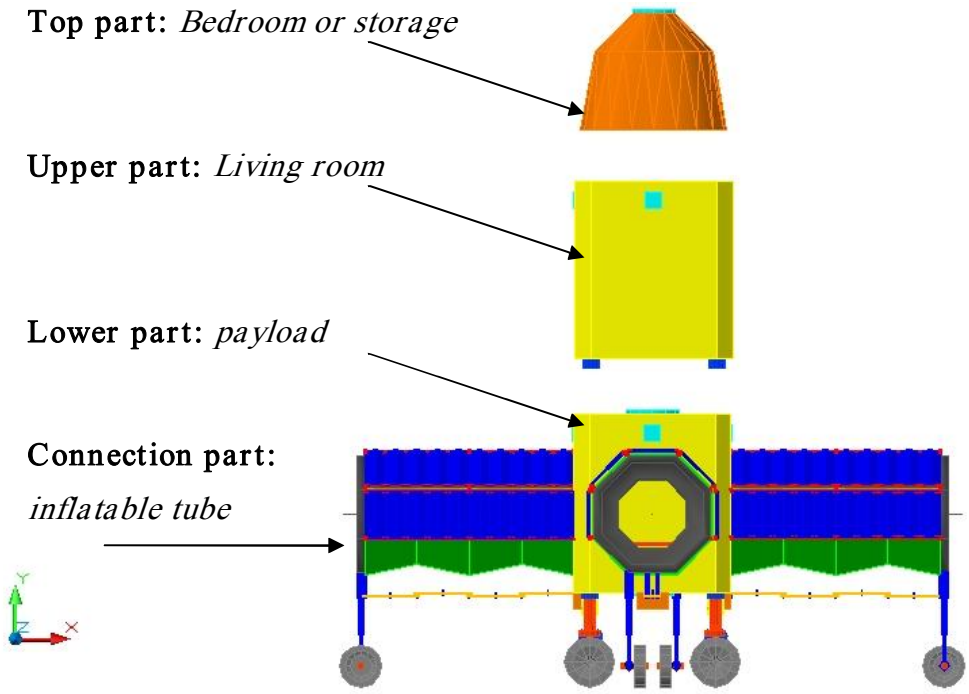

Figure 123: Core Structures functions

NASA define the Habitable volume as a function of the mission duration.

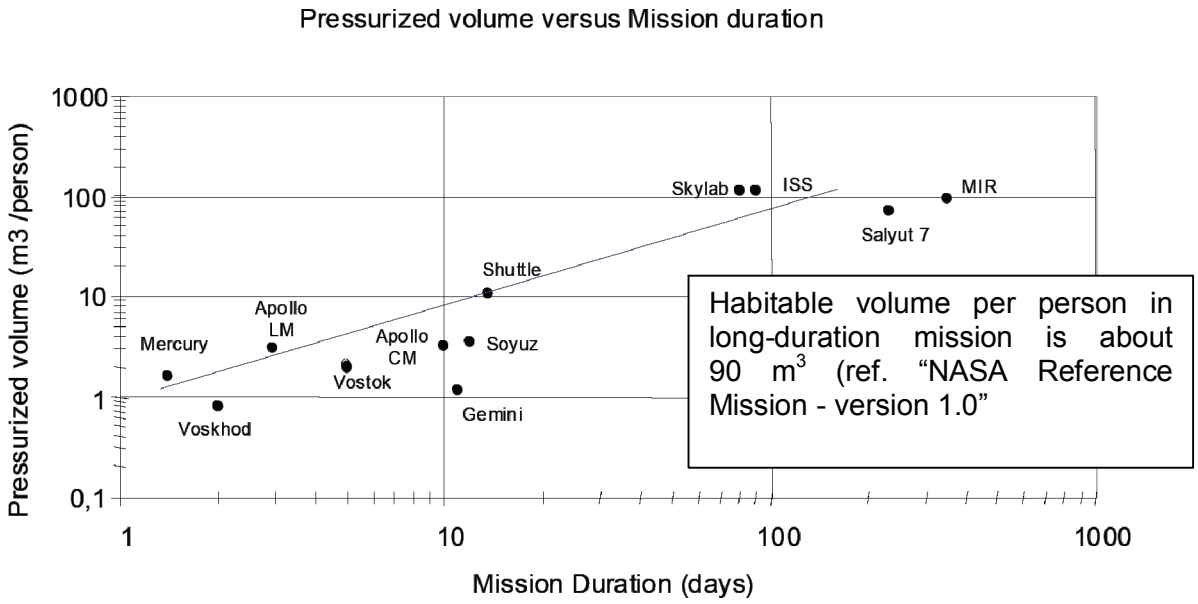

Figure 124: pressurized volume versus Mission duration

In LEMMB case, the total Core internal living surface is like those of today's city little apartment !

Top part	Radius=1.5, h=1.7	Surface ≅ 7 m^2
Upper part	2.8×2.8	Surface ≅ 7.8 m^2
Lower part	2.8×2.8	Surface ≅ 7.8 m^2
Inflatable Arms	4×(4×1.5)	Surface ≅ 24 m^2
tot		Total Surface ≅46 m^2

Table 6: total living surface of two assembled LEMMB.

And the total Core internal living is:

Top part	Radius=1.5, h≅1.7	Volume ≅ 7×1.7≅ 12 m^3
Upper part	2.8×2.8×h h≅3.4	Volume ≅ 7.8×3.4≅ 26.5 m^3
Lower part	2.8×2.8×h h≅3.4	Volume ≅ 7.8×3.4≅ 26.5 m^3
Inflatable Arms	4×(4×1.5) ×h h≅1.7	Volume ≅ 24×1.7≅ 41 m^3
tot		Total Volume ≥100 m^3

Table 7: total living volume of two assembled LEMMB.

3.5.2 LEMMB Micro Meteoroid Orbital Debris (MM/OD) protection system approach

Core Structures protect the crew from the harsh environment of space. Structures transfer loads and provide support for the various systems. Loads are the mechanical, pressure, vibration, inertial, and thermal forces applied to structural elements.

The Core structures of LEMMB like on ISS modules, are made of aluminum alloys, which are the preferred metal for aerospace applications. They are lightweight, corrosion resistant, and have favorable electrical conductivity which aids in grounding electrical systems.

The double layer of Core has a function of radiation and micro meteorites protection.

- The Micro-Meteoroid shields protect the crew modules, and other critical components from Micro-Meteoroid.

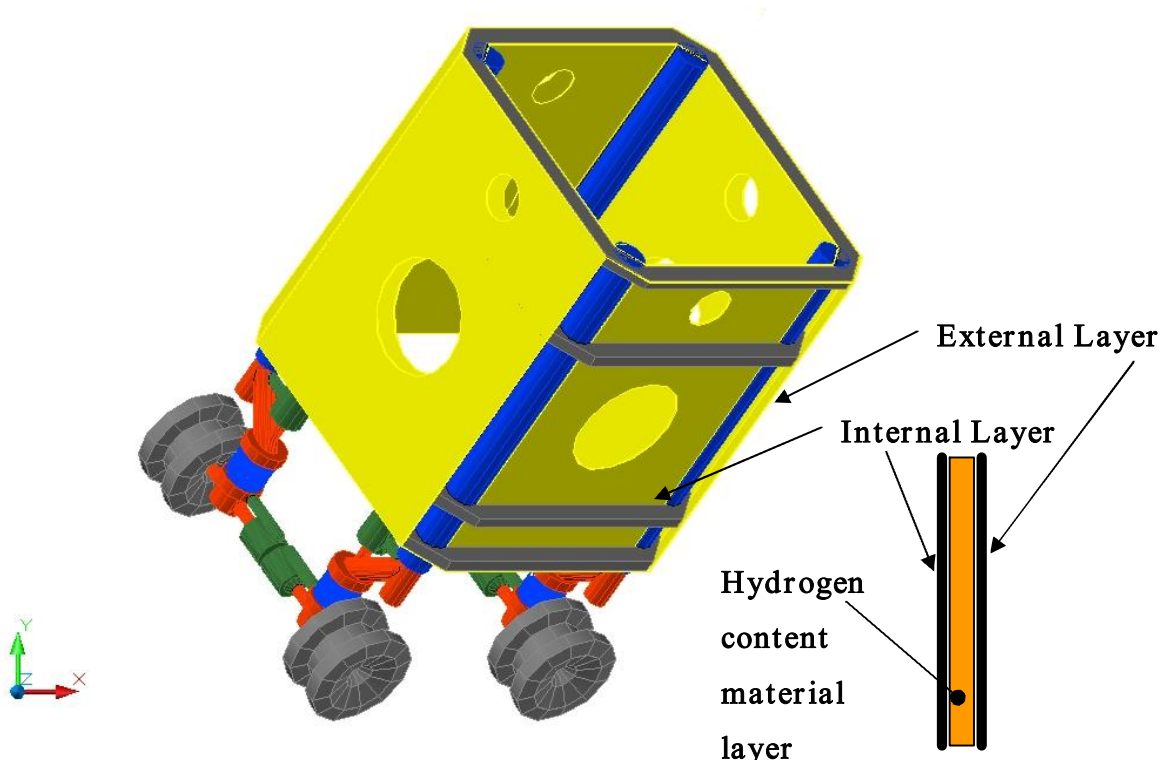

Figure 125: basic Core

The aluminum internal and external shielding layers are separated by about 19 cm in space. In order to increase: the Energetic Particles Radiation shielding capabilities and the resistance to Micro Meteoroids impact capability, a 19 cm thickness layer based on high hydrogen content material like polyethylene, could be put between these two aluminum stratum.

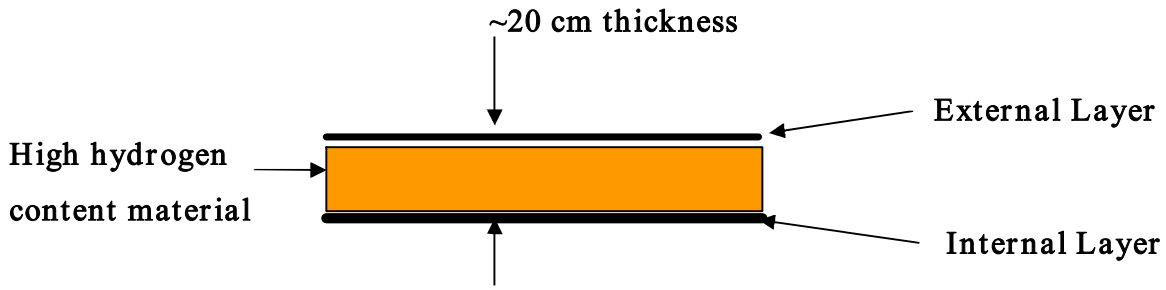

Figure 126: Energetic particle radiation protection system for LEMMB Cores Structures

The internal aluminum layer thickness is around 5 mm while the external is about 1.2 mm. The double aluminum layer works like the system used on ISS U.S. system (see next chapter).

The **high hydrogen** content material between the two metal layers instead, has two main function:

1. *Increase the protection against mechanical impact pulse;*
2. *Increase the protection against radiation like CGR*;

3.5.2.1 New Protection approach against mechanical impact pulse

A new approach in Shock Protection systems could be developed by the use of granular medium.

In 2006 a publication named "*Energy Trapping and Shock Disintegration in a Composite Granular Medium*" [10], reported the first experimental observation of impulse confinement and the disintegration of *shock* and *solitary waves* in one-dimensional *strongly nonlinear* composite granular materials.

The chains consist of alternating ensembles of beads with high and low elastic moduli (more than 2 orders of magnitude difference) of different masses. The trapped energy is contained within the ''*softer*" sections of the composite chain and is slowly released in the form of weak, separated pulses over an extended period of time.

Granular matter has many known applications, but it is difficult to understand its intrinsic dynamic properties due to the strong nonlinearity of forces between particles and their complex distributions. In the past, the design of shock protectors focused mainly on the wave transformation provided by layered systems or porous media. Yet an entirely different way of protecting materials is through the confinement of an impulse in a particular region of the shielding medium called a ''*granular container*'' using a series of sections with particles interacting according to different contact forces and masses as predicted by theoretical analysis, but not experimentally demonstrated.

The idea of the impulse confinement in this case is based on the anomalous features of an incident wave interacting with an interface between two different chains of *stainless* steel and *polytetrafluoroethylene (PTFE) beads*. It was shown that a solitary wave passing from the stainless steel side transmits all of its energy through the interface into the PTFE section. Furthermore, the transmitted signal disintegrates into a sequence of solitary waves [see Figure below]. On the other hand, when a solitary wave approaches the same interface from the PTFE side, numerical calculations and experiments have shown that a significant part of the incident pulse's energy is reflected back into the PTFE side. The amplitude of the reflected solitary wave is

≅75% of the incident wave's amplitude and the pulse transmitted to the stainless steel chain decomposes into a train of three solitary waves.

A *shock wave* is a qualitatively different type of pulse in comparison with a *solitary wave*. It is usually characterized by a longer duration which may affect the reflection and transmission at the interfaces.

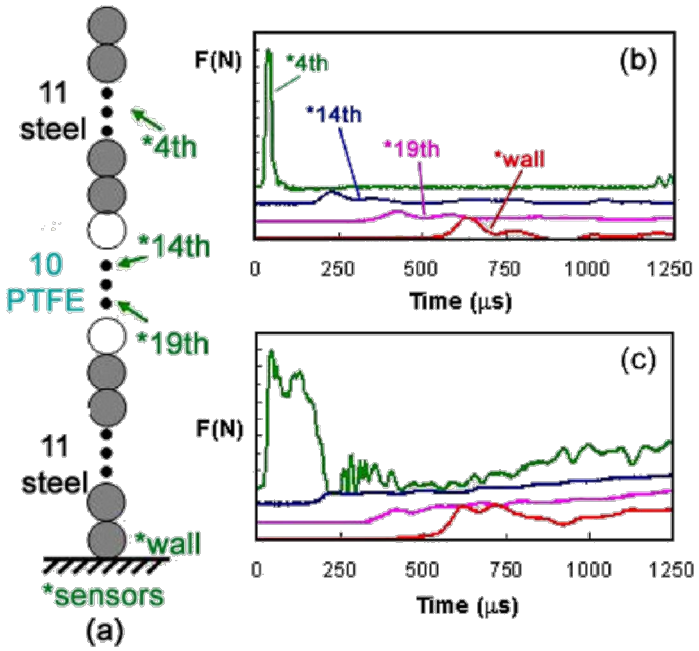

Figure 127: Trapping of pulses in the granular protector with a single PTFE section.
(a) Schematic diagram of the experimental setup with indicated sensors.
(b) Experimental data for the incident solitary pulse. The striker was an Al2O3 cylinder of 0.47 g with an impact velocity of 0:44 m=s.
(c) Experimental data for the incident shock like pulse excited by an Al2O3 striker (63 g).
The y-axes scale is 1 N per division for (b) and (c).

In the case of the granular protector with a single PTFE central section, the trapping of the incident solitary pulse in the softer region is clearly evident in experiments [Figure (b)] and qualitatively matched the numerical calculations.

The experimental data clearly demonstrate that the incident solitary pulse (~40 μs long and 8 N in amplitude) is quickly transformed by the PTFE portion of the chain to a much longer signal and it is decomposed into a train of pulses arriving at the wall.

Specifically, it has been observed

(i) a complete transmission of the energy of the incident solitary wave into the PTFE section without any wave reflection to the steel section.

(ii) a significant reflected pulse propagating back into the PTFE section when the incident pulse arrives from the PTFE side of the interface, and

(iii) the disintegration of the transmitted impulse into a train of solitary waves.

The solitary wave speed in the steel section of the chain is 357 m=s. The experimental data [Figure (b)] show that the signal speed decreases to 137:4 m=s when the pulse passes through the first interface. This decrease can be attributed to the drastically lower elastic modulus of PTFE (1.46 GPa) compared to steel (193 GPa), which enables the pulses to remain mostly trapped in the softer section of the chain for a relatively long time ''bouncing'' back and forth between the two interfaces releasing the energy of the impact in both directions very slowly.

To investigate the influence of the particle arrangement in the system on the protection efficiency, it has been reorganized the PTFE beads as shown in Figure below (a), increasing the number of interfaces. This geometry resulted in a much better protection of the wall in comparison to the first case studied [compare Figure (b)] by more efficiently trapping most of the incoming pulse and releasing its energy more slowly.

3.5.2.2 Shock disintegrating principle application on LEMMB

The shock disintegrating principle could be utilized for practical three-dimensional composite structures used for protection against impact pulses like those caused from Micro Meteoroids / Debris. Qualitative pictures in 2D are shown below:

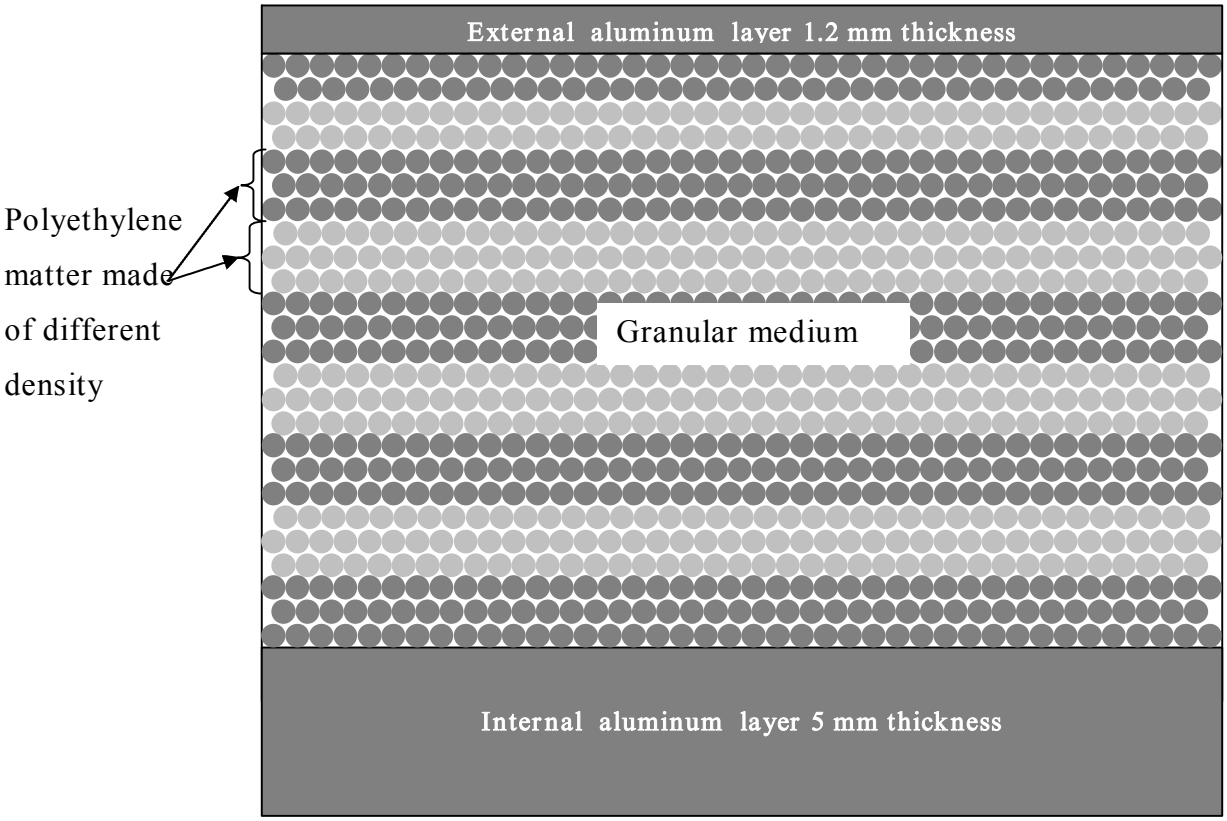

Figure 128: granular medium between internal and external layer, plot is not in scale

The different granular matter composition has the function of confining the back wave propagation within the granular medium.

This phenomenon has been observed in some experiment where using two different matter for the spherical particle, result in an energy trapping by the softer section of the composite. This trapped energy is slowly released in the form of weak, separated pulses over an extend period of time.

3.5.2.3 Haw does the granular medium works against mechanical shock impact ?

Let us suppose the following example.
Hypothesis:

- Every particle is of the same type i.e. density, material, dimension, elasticity;
- Every particle do the transferring, to the other particles surrounding it, of all of the incident "momentum"; this is not completely true in a real system but this assumption can help us to simplify the mathematical model and consequently help us to better understand, one of the several phenomena which contribute to reduce the impact shock wave.
- The system is isolated and non subjected to other forces, like gravity or losses;
- The particle are supposed perfectly spherical in shape;
- Every spherical particle has unitary mass $m=1$ and unitary ray $r=1$;
- The impulse incident on the first particle has an impulsive force called F_1;
- In order to simplify the computation we take into consideration only the main forces, i.e. the forces involved in the triangular shape, see here after figure;

Suppose the following figure shown below on which there are four sphere stratum. Now, suppose a force applied like in figure i.e. in one sphere of the first stratum.

Observing the figure, we have two subsequent forces applied along the lines forming an equilateral triangular.
Each one of these forces are exactly of the half module in length with respect to the initial original force applied, these forces are applied from the sphere located in the first stratum to the two subsequent adjacent sphere located in the second stratum and so on for the rest of the stratum.

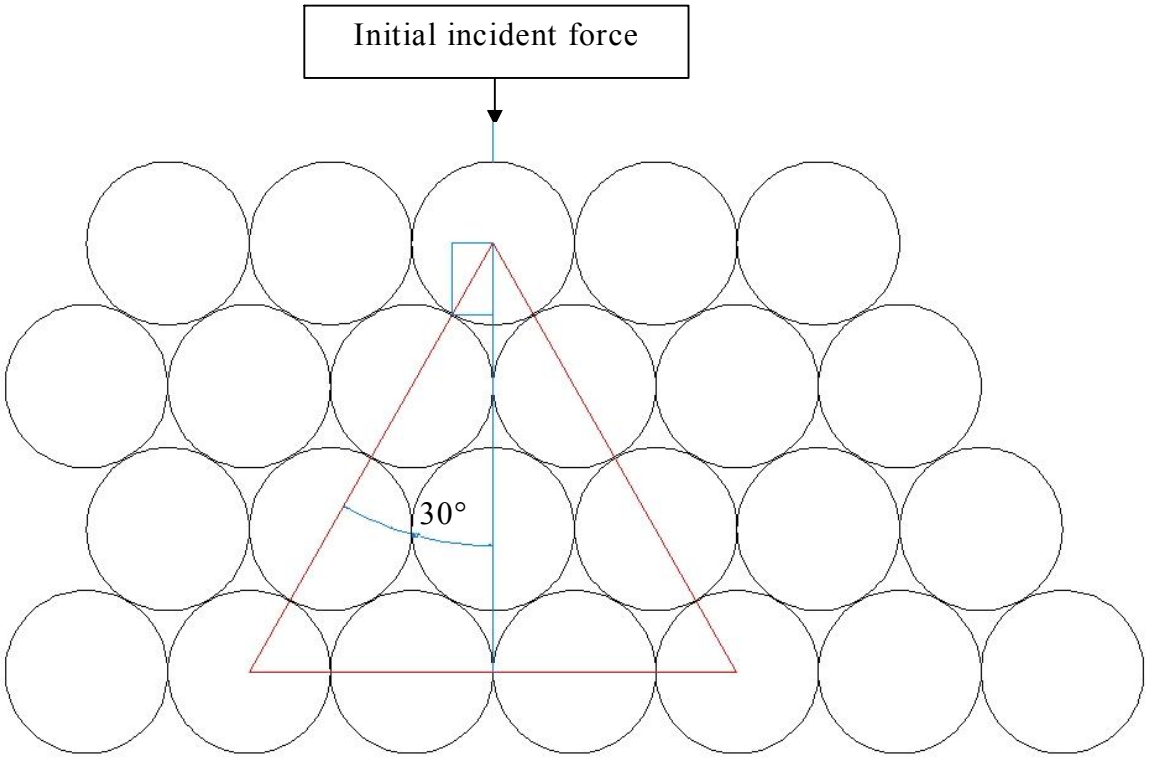

Figure 129: example of four sphere stratum

Each of the subsequent forces can be seen as composed by two vector component; one is horizontal, directed toward the adjacent sphere of the same stratum and the other one is vertical, directed to the subsequent stratum of spheres.

By the geometry of the system (30° of angle), we can observe that, approximately, the vertical component (triangular height), is about 6/7 of the triangular side while the horizontal component is about 1/2 of the diagonal length.

In fact suppose the length L=1 then:

$$L = 1 \cong \sqrt{\left(\frac{6}{7}\right)^2 + \left(\frac{1}{2}\right)^2} \cong 0.99 \qquad \textbf{eq 1}$$

By the assumption above it is possible to compute a simple simulation of the system composed by 3 stratums made of spherical particles.

On figure below the 2D spherical particles are defined by means of matrix coordinate *xy* where *x* is the vertical position and *y* is the horizontal position on 2D matrix.

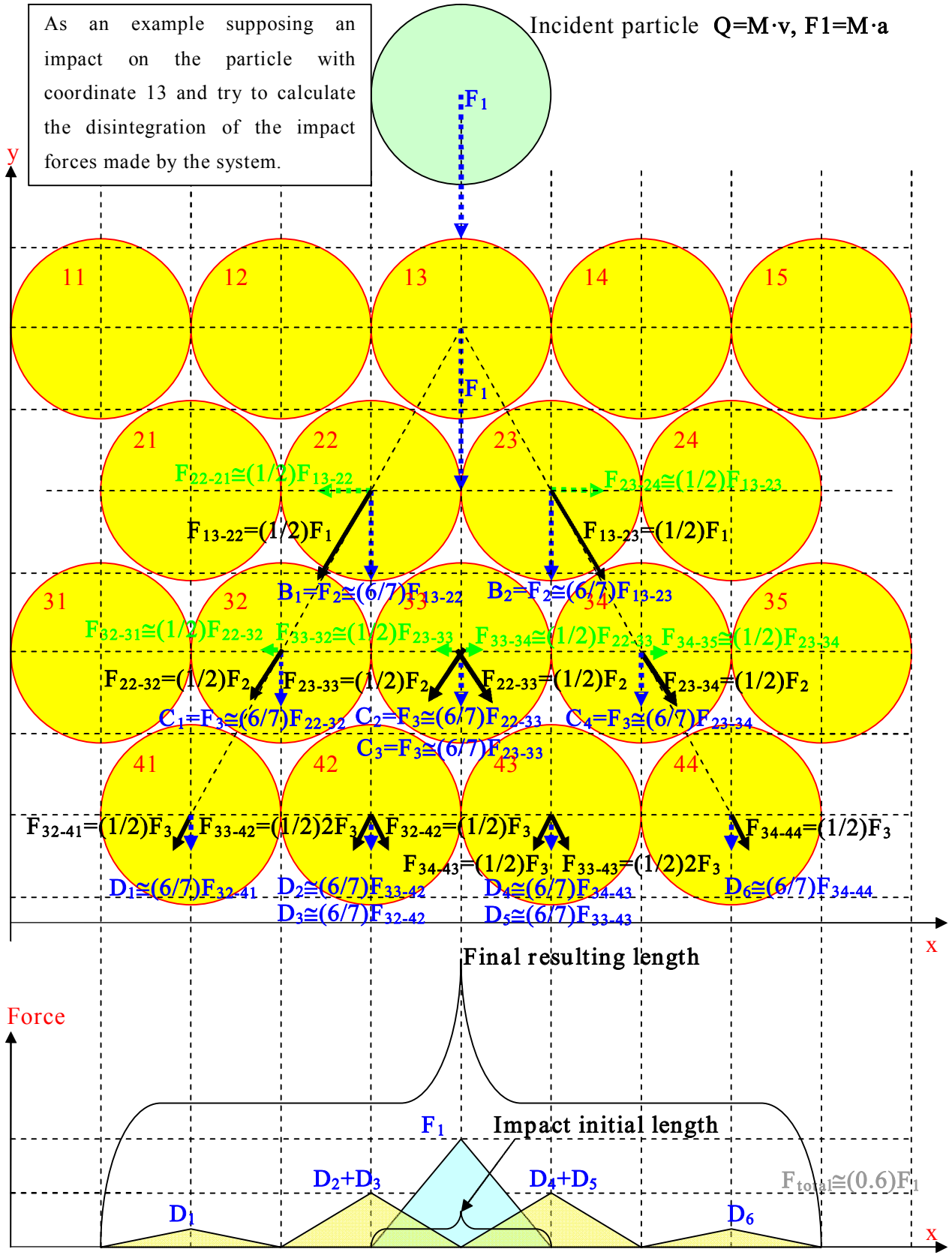

Figure 130: three layer of spherical particles and applied forces along the axes *y* as a function of length *x*

Third Stratum analysis

After 3 stratum of spherical particles we have the following forces applied vertically and horizontally respectably:

Vertical forces

- $A=F_{13\text{-}22}=F_{13\text{-}23}=(1/2)F_1$
- $B=F_2\cong(6/7)F_{13\text{-}22}\cong (6/7)F_{13\text{-}23}\cong (6/7)A$
- $F_{22\text{-}32}\cong (1/2)F_2$
- $F_{22\text{-}33}\cong (1/2)F_2$
- $F_{23\text{-}33}\cong (1/2)F_2$
- $F_{23\text{-}34}\cong (1/2)F_2$
- $C=F3\cong (6/7)F_{22\text{-}32}\cong (6/7)(1/2)F_2\cong (6/7)(1/2)B=(6/7)(1/2)\ (6/7)A=(9/49)F_1$
- $C=F3\cong (2/3)F_{22\text{-}33}\cong (2/3)(1/2)F_2\cong (2/3)(1/2)B=(6/7)(1/2)\ (6/7)A=(9/49)F_1$
- $C=F3\cong (2/3)F_{23\text{-}33}\cong (2/3)(1/2)F_2\cong (2/3)(1/2)B=(6/7)(1/2)\ (6/7)A=(9/49)F_1$
- $C=F3\cong (2/3)F_{23\text{-}34}\cong (2/3)(1/2)F_2\cong (2/3)(1/2)B=(6/7)(1/2)\ (6/7)A=(9/49)F_1$

The vertical force are doubled on particle 33;

The total forces F1 initially applied on the particle 13 have became spread on a greater length by means of particle 32, 33, 34. the resulting force is:

$F_{tot}=4C\cong 4(9/49)F_1=(36/49)\ F_1\ \cong 0.7\ F_1$

We can see haw the system perform an attenuation of the impact force applied in the particle 13. This is due to the horizontal forces component, created by the particles system, they act horizontal and not vertical, and consequently they determine a decreasing of the initial impact vertical force components.

Since the total force, is at the end, applied on a greater length then the initial impact lenght, the resulting pressure is lower if compared to the pressure applied on top of particle impact 13.

$P_{total}\cong F_{total}/3$

Horizontal forces

- $D = -F_{32-31} \cong -(1/2)F_{22-32} = -(1/2)(1/2)F_2 = -(1/2)(1/2)(6/7)(1/2)F_1 = (3/28)F_1$
- $E = -F_{33-32} \cong -(1/2)F_{22-33} = -(1/2)(1/2)F_2 = -(1/2)(1/2)(6/7)(1/2)F_1 = (3/28)F_1$
- $F = +F_{33-34} \cong +(1/2)F_{22-33} = +(1/2)(1/2)F_2 = -(1/2)(1/2)(6/7)(1/2)F_1 = (3/28)F_1$
- $G = +F_{34-35} \cong +(1/2)F_{23-34} = +(1/2)(1/2)F_2 = -(1/2)(1/2)(6/7)(1/2)F_1 = (3/28)F_1$

The horizontal forces have a result equal to zero on particle 33;

Fourth Stratum analysis

Supposing we continuing our analysis on the following fourth spheres stratum, then we have:

- $D_1 \cong (6/7)(1/2)\,F_3 = (6/7)(1/2)(9/49)F_1$
- $D_2 \cong (6/7)\,F_3 = (6/7)(9/49)F_1$
- $D_3 \cong (6/7)(1/2)\,F_3 = (6/7)(1/2)(9/49)F_1$
- $D_4 \cong (6/7)(1/2)\,F_3 = (6/7)(1/2)(9/49)F_1$
- $D_5 \cong (6/7)\,F_3 = (6/7)F_1$
- $D_6 \cong (6/7)(1/2)\,F_3 = (6/7)(1/2)(9/49)F_1$

The forces distributions are:

- D_1 on the equivalent 41 diameter sphere length
- $D_2 + D_3$ on the equivalent 42 diameter sphere length
- $D_4 + D_5$ on the equivalent 43 diameter sphere length
- D_6 on the equivalent 44 diameter sphere length

The total vertical force component on the fourth sphere stratum length is:

$F_{tot} = D_1 + D_2 + D_3 + D_4 + D_5 + D_6$

$$Ftot = \frac{6}{7}\frac{9}{49}\left(\frac{1}{2}+1+\frac{1}{2}+\frac{1}{2}+1+\frac{1}{2}\right)F_1 = 4\frac{6}{7}\frac{9}{49} = \frac{216}{343}F_1 \cong 0.62F_1$$

As a consequence we can find the correlation law between the total resulting force and the number of sphere layer considered:

- <u>in case of two plane</u>

$$F_{tot}^{2\_stratum} = B_1 + B_2 = 2\left(\frac{6}{7}\frac{1}{2}\right)F_1$$

eq 2

and the total force is applied on a length two time greater than the impact length.

- <u>in case of three plane we have:</u>

$$F_{tot}^{3\_stratum} = C_1 + C_2 + C_3 + C_4 = 4\left(\frac{6}{7}\frac{1}{2}\frac{6}{7}\frac{1}{2}\right)F_1 = 2^2\left(\frac{6}{7}\frac{1}{2}\right)^2 F_1$$

eq 3

and the total force is applied on a length three time greater than the impact length.

- <u>in case of four plane we have:</u>

$$F_{tot}^{4\_stratum} = D_1 + D_2 + D_3 + D_4 + D_5 + D_6 = 2^2\left(\frac{6}{7}\frac{1}{2}\right)\left(\frac{6}{7}\frac{1}{2}\frac{6}{7}\frac{1}{2}\right)F_1 + 2\left(\frac{6}{7}\frac{1}{2}\right)2\left(\frac{6}{7}\frac{1}{2}\frac{6}{7}\frac{1}{2}\right)F_1 =$$

$$= 2^2\left(\frac{6}{7}\frac{1}{2}\right)^3 F_1 + 2^2\left(\frac{6}{7}\frac{1}{2}\right)^3 F_1 = 2^3\left(\frac{6}{7}\frac{1}{2}\right)^3 F_1$$

eq 4

and the total force is applied on a length four time greater than the impact length.

- We can generalize the expression as a function of the sphere layers number ***n***:

$$F_{tot}^{n\_stratum} = 2^{n-1}\left(\frac{6}{7}\frac{1}{2}\right)^{n-1} F_1 = \frac{2^{n-1}}{2^{n-1}}\left(\frac{6}{7}\right)^{n-1} F_1 = \left(\frac{6}{7}\right)^{n-1} F_1$$

eq 5

The total force is applied on the total length given by:

$$Length_{total} = Lenght_{impact} \cdot [n]$$
where the stratum number is
$$n = 1,2,3,4.....$$

eq 6

as a consequence the total 2D pressure (force/length) applied on a certain level is:

$$\text{Pressure}_{tot} = \frac{F_{tot}^{n\_stratum}}{Length_{total}} = \frac{2^{n-1}\left(\frac{6}{7}\frac{1}{2}\right)^{n-1} F_1}{Length_{impact} \cdot (n)} = \frac{\left(\frac{6}{7}\right)^{n-1} F_1}{Length_{impact} \cdot (n)}$$

eq 7

The method applied so far doesn't take into account the mass of the sphere and the material type used to build them.

This method is a pure geometrical explanation which is useful to understand the *wall sphere system behavior* in disintegrating a certain force applied on one spheres at the first plane stratum.

On a real system we need to consider the behavior at the contact surface between adjacent spheres too, it is not a linear function; we could discover the wave-forward and wave-back propagation phenomenon as a function of the material used to build the sphere stratum.

In the previous example we used a 2D wall system, we can try to find what happen for a 3D wall system like in figure below:

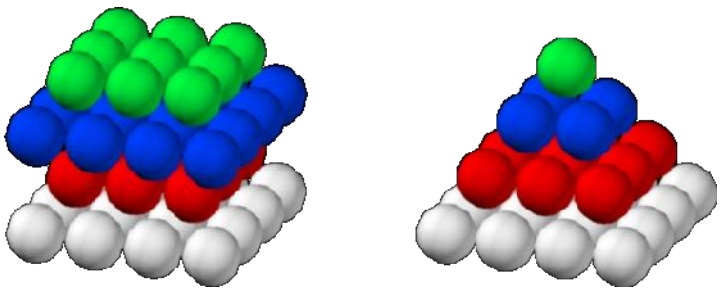

Figure 131: on the left a 3D wall structure, on the right the sphere useful in order to applying the method.

As an example supposes a force F_1 applied as in figure below:

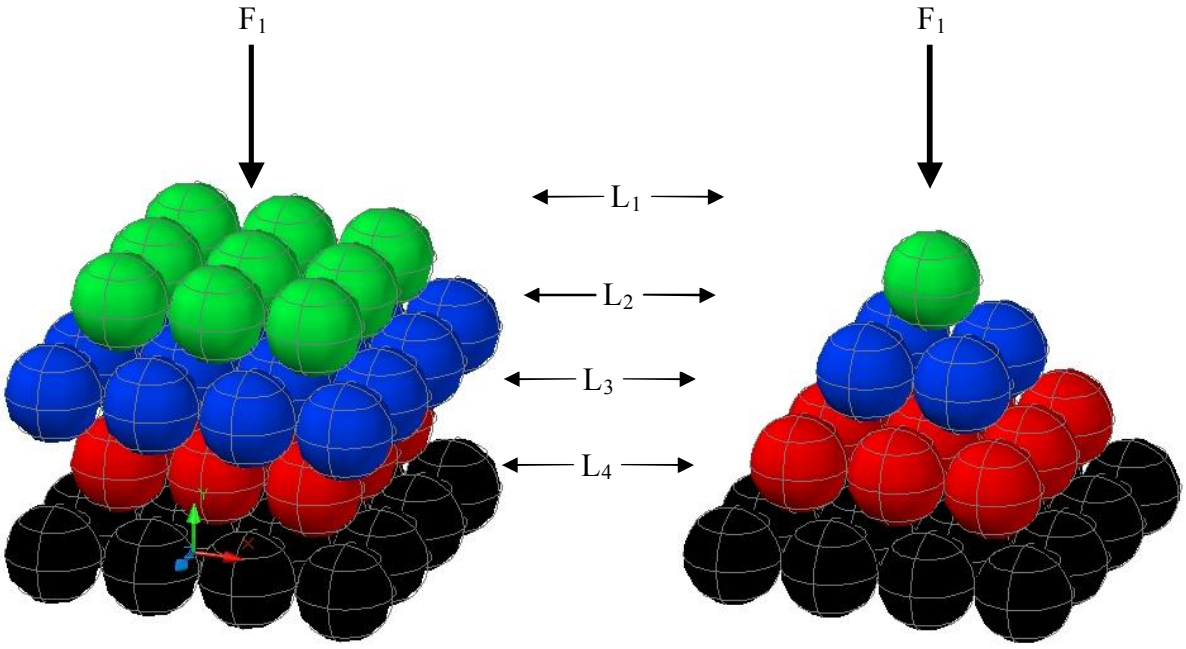

Figure 132: on the left the 3D-sphere wall, on the right the main spheres involved in disintegrating the F1 force applied on L1 layer.

Respect to the preceding 2D example, in this 3D example each sphere of e certain layer L_i, is adjacent to four spheres of the subsequent layer L_{i+1}.
As a consequence the force applied on one sphere is, each time, equally divided into four components and not into two as in 2D model.
For each of these vectors we can apply the same decomposition in horizontal and vertical components respectably close to 1/2 and 6/7 of the main vector.
As a consequence we have:

Vertical forces

- $A= (1/4)F_1$
- $B=F_2\cong (6/7)A$
- $F_{2\text{-}3}\cong (1/4)F_2$
- $C=F3\cong (6/7)F_{2\text{-}3}\cong (6/7)(1/4)F_2\cong (6/7)(1/4)B=(6/7)(1/4)(6/7)A=(9/49)F_1$

The vertical force found in 3D configuration is the same as before in 2D configuration!

As a consequence we can find the correlation law between the total resulting applied force and the number of the stratum considered:

- in case of two plane

$$F_{tot}^{2\_stratum} = B_1 + B_2 + B_3 + B_4 = 4\left(\frac{6}{7}\frac{1}{4}\right)F_1$$

eq 8

and the total force is applied on a surface four time greater than the impact surface.

- in case of three plane we have:

$$\begin{aligned} F_{tot}^{3\_stratum} &= C_1 + C_2 + C_3 + C_4 + \\ &+ C_5 + C_6 + C_7 + C_8 + \\ &+ C_9 + C_{10} + C_{11} + C_{12} + \\ &+ C_{13} + C_{14} + C_{15} + C_{16} = \\ &= 16\left(\frac{6}{7}\frac{1}{4}\frac{6}{7}\frac{1}{4}\right)F_1 = \\ &= 4^2\left(\frac{6}{7}\frac{1}{4}\right)^2 F_1 \end{aligned}$$

eq 9

and the total force is applied on a surface 16 time greater than the impact surface

- We can generalize the expression as a function of the stratum number ***n***:

$$F_{tot}^{n\_stratum} = 4^{n-1}\left(\frac{6}{7}\frac{1}{4}\right)^{n-1} F_1 = \frac{4^{n-1}}{4^{n-1}}\left(\frac{6}{7}\right)^{n-1} F_1 = \left(\frac{6}{7}\right)^{n-1} F_1$$

eq 10

The total force applied on a total surface is given by:

$$Surface_{total} = Surface_{impact} \cdot (n)^2$$
where the stratum number is
$n = 1,2,3,4.....$

eq 11

As a consequence the total pressure applied on a certain stratum level is:

$$\text{Pressure}_{tot} = \frac{F_{tot}^{n\_stratum}}{Surface_{total}} == \frac{\left(\frac{6}{7}\right)^{n-1} F_1}{Surface_{impact} \cdot (n)^2}$$

eq 12

We can plot this function assuming as an example a certain force F_1 and an impact surface of about 1, we are supposing approximately the same dimension for the sphere equatorial plane surface section. In this example the linear dimension could be expressed in *cm*, or *mm*, or *m*.

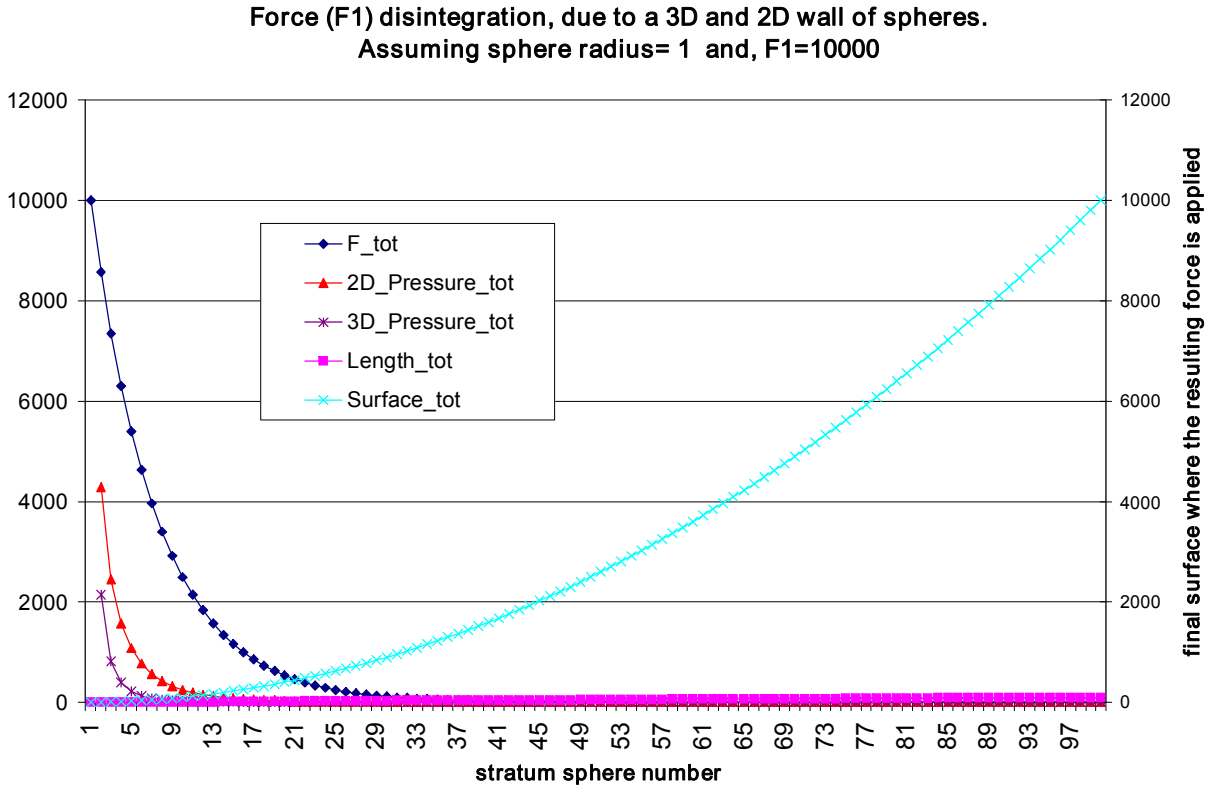

Figure 133: 2D and 3D force system disintegration

n°_stratum	Length_impact	F1	F_tot	Length_tot	2D_Pressure_tot	Surface_tot	3D_Pressure_tot
1	*1*	*10000*	10000.0	1.0		1.0	
2			8571.4	2.0	4285.7	4.0	2142.9
3			7346.9	3.0	2449.0	9.0	816.3
4			6297.4	4.0	1574.3	16.0	393.6
5			5397.8	5.0	1079.6	25.0	215.9
6			4626.6	6.0	771.1	36.0	128.5
7			3965.7	7.0	566.5	49.0	80.9
8			3399.2	8.0	424.9	64.0	53.1
9			2913.6	9.0	323.7	81.0	36.0
10			2497.3	10.0	249.7	100.0	25.0

Table 8: first ten row of data plotted above

3.5.2.4 Increase the protection against radiation like CGR;

As we already have seen **hydrogen** has a very high shielding behavior against radiation like GCR.

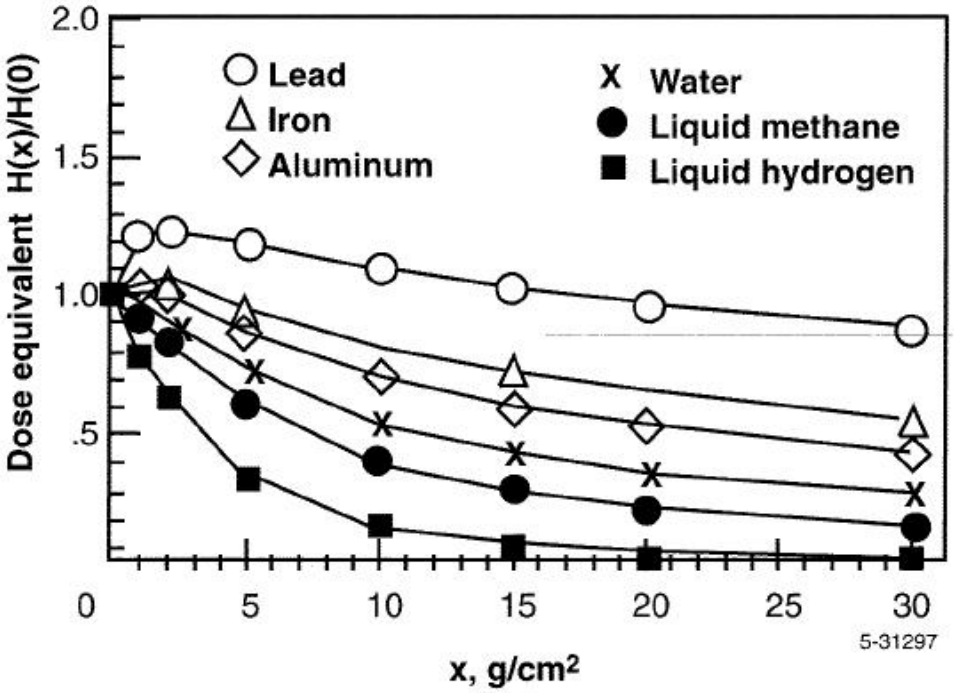

Figure 134: shielding property of several materials and liquid

This property suggests the use of polyethylene as a shielding medium against cosmic radiations.

3.5.2.5 International Space Station (ISS) Micro Meteoroid Orbital Debris (MM/OD) protection system

The Micro-Meteoroid Orbital Debris (MM/OD) shielding on the U.S.-developed segments consists of a 1.27 mm (.05 in.) thick sheet of aluminum separated from the pressure shell by a 101.6-mm (4-in.) gap. The debris shielding shocks the orbital debris and breaks it into small fragments creating a debris cloud.

The debris cloud spreads the energy of the impact over a much larger area causing much less damage. MM/OD shielding is provided for windows by the use of window shutters.

The design philosophy behind the Russian micro-meteoroid debris shield is significantly different from the U.S. system. The two systems are compared in Figure below.

MM/OD shielding is an important component to Station structures and crew safety while in orbit.

There are 20,000 objects greater than 50 mm (1.97 in.) in low Earth orbit. Because of the MM/OD design, the chance one of these objects penetrating a U.S. pressurized element is 7.5 percent, and 5 percent for a Russian pressurized element.

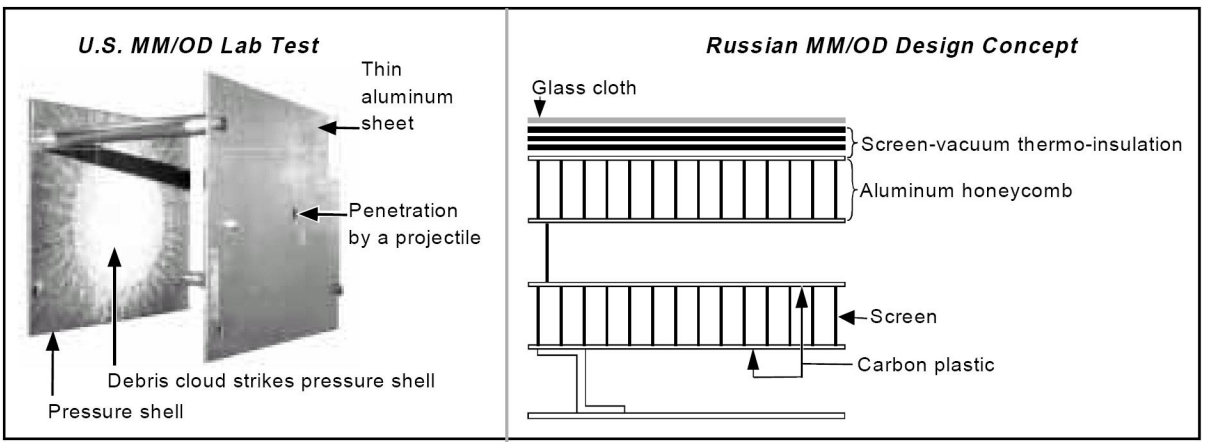

Figure 135: Micro-Meteoroid Orbital Debris (MM/OD) shields Comparison of U.S. and Russian MM/OD systems

In order to better understand the Core structures we could think to the mechanical structures of Columbus laboratory on ISS (International Space Station) shown in figure below.

These data will helps us to have an idea of the mass that LEMMB could have.

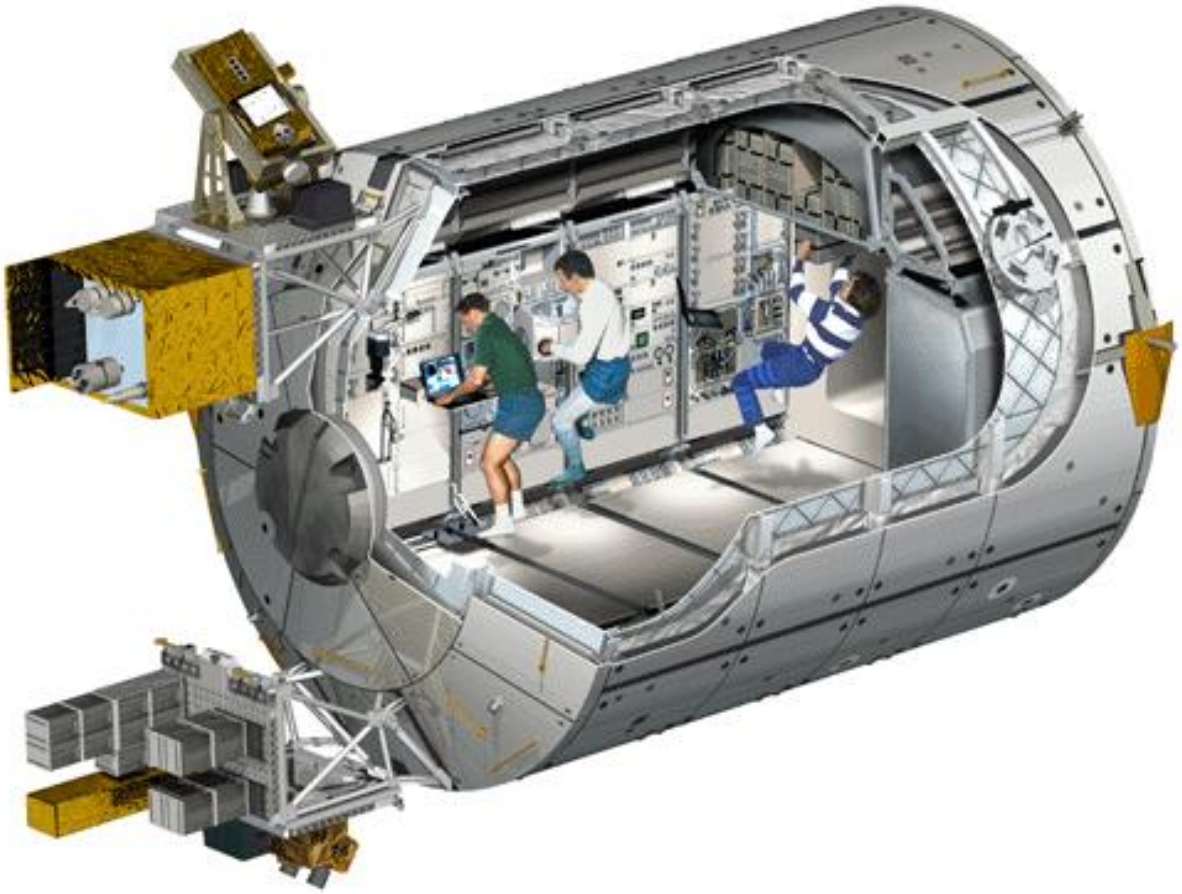

Figure 136: Columbus Laboratory on ISS

The Columbus Characteristics are summarize on table below:

Mass budget	
Mass without payload	10 275 kg
Launch mass	12 775 kg (2500 kg payload)
Maximum payload mass	9 000 kg (maximum)
Maximum on orbit mass	21 000 kg

Dimensions	
Total module length	6 871 mm
Largest diameter	4 477 mm
Total internal volume	75 m^3
Total volume of payload racks	25 m^{3}</SUP< font>

Table 9

3.5.3 Internal Core reinforcement longerons and structures

In order to reinforce the mechanical LEMMB Core structures then, like the ISS module structures, the Core structure are provided by a reinforcement system based on longitudinal and transverse longerons like on figure below.
The longitudinal longerons provide the telescopic mechanism based on ballscrews system needed to find the LEMMB horizontal equilibrium as function of the Lunar surface irregularity.

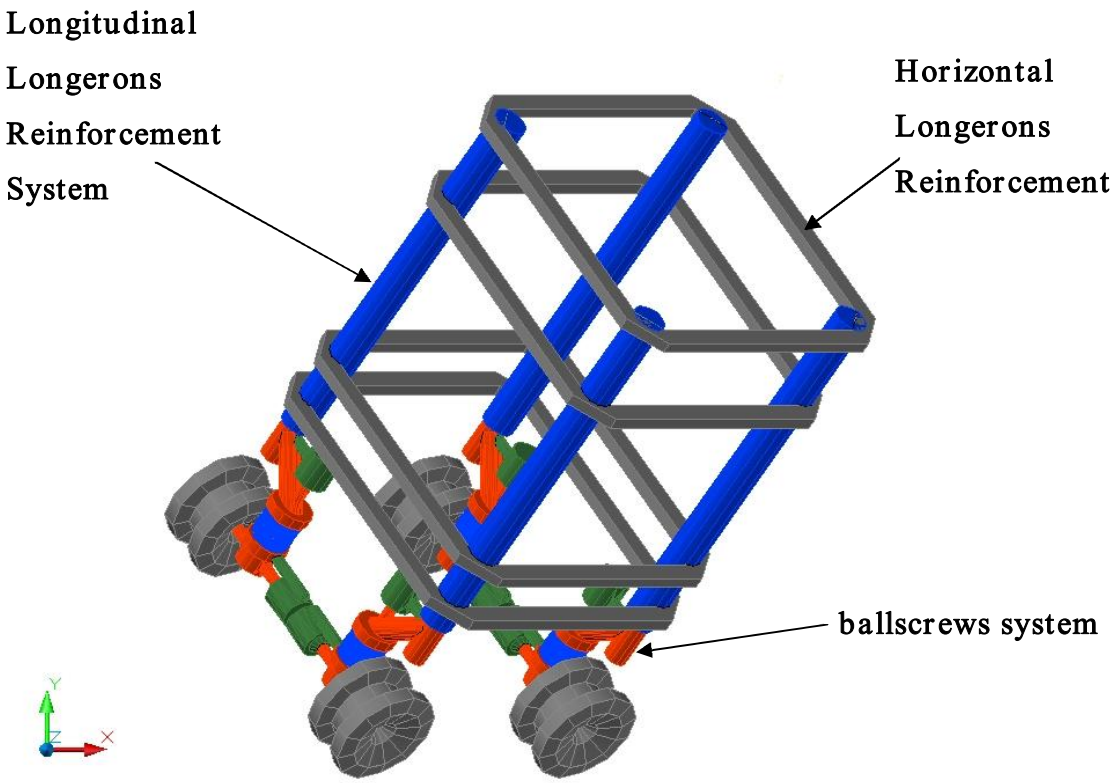

Figure 137: skull of basic Core

In figure below, the principle about the telescopic longerons used to adjust the position and attitude of LEMMB once located on the lunar surface, are shown.

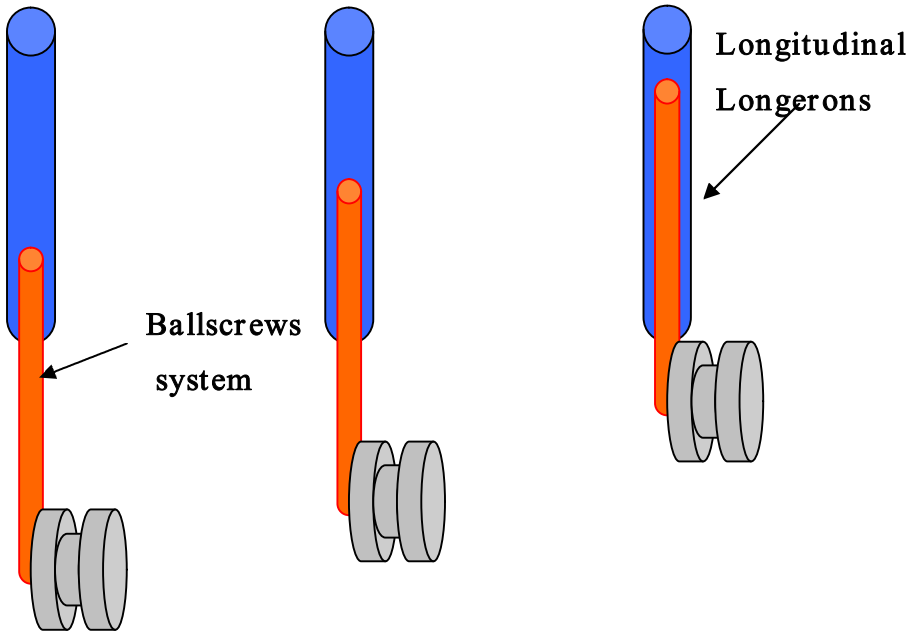

Figure 138: several stretching of the ballscrews system used in the longitudinal longerons

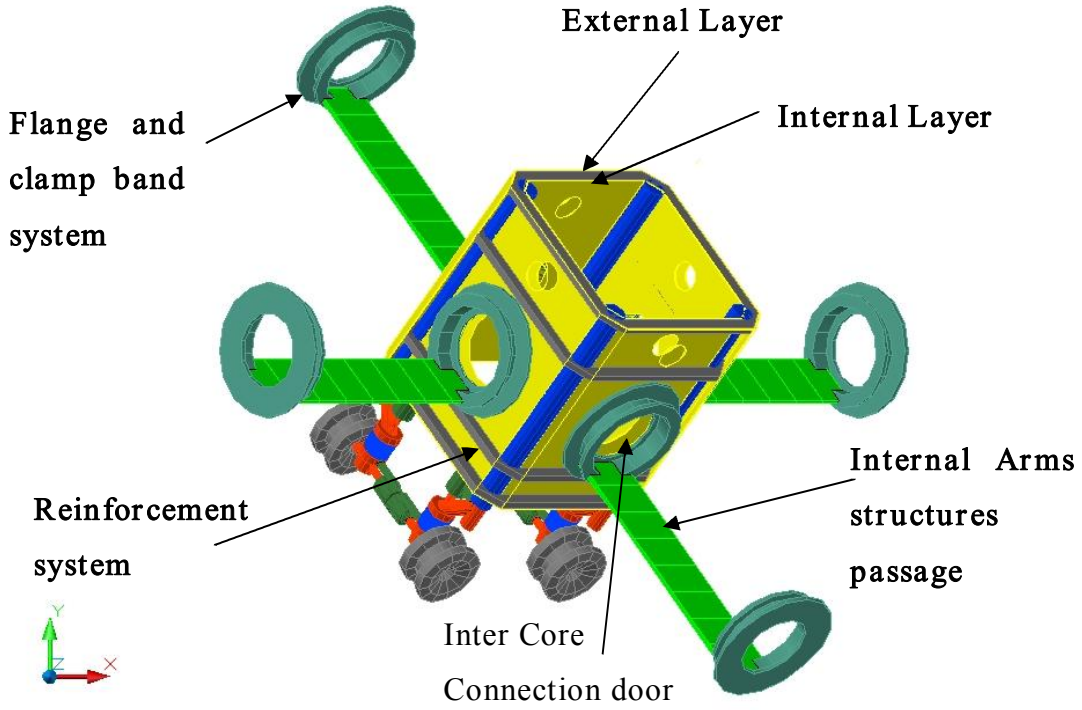

Figure 139: Core particulars

Assembling two identical modules we have:

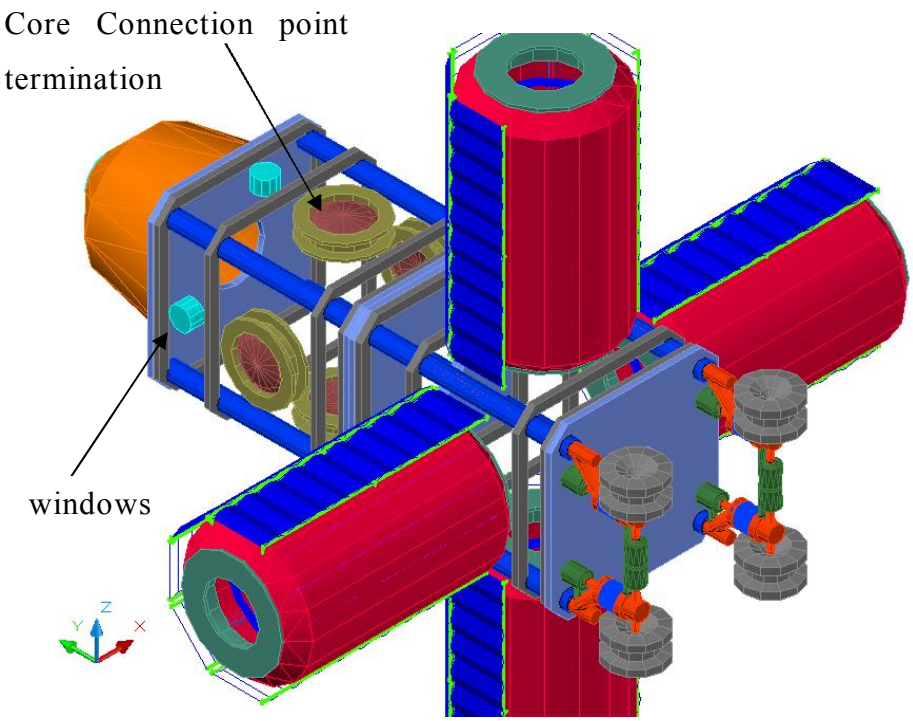

Figure 140: two core LEMMB assembled together

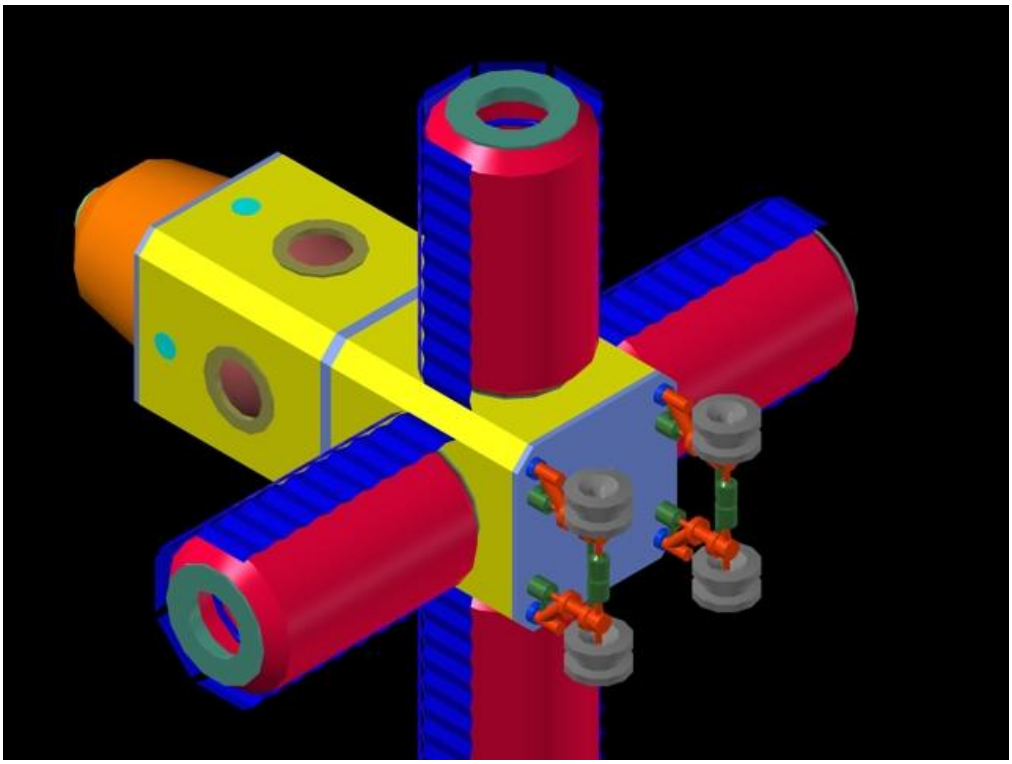

Figure 141: rendering of two LEMMBs assembled together and cylindrical ARMs

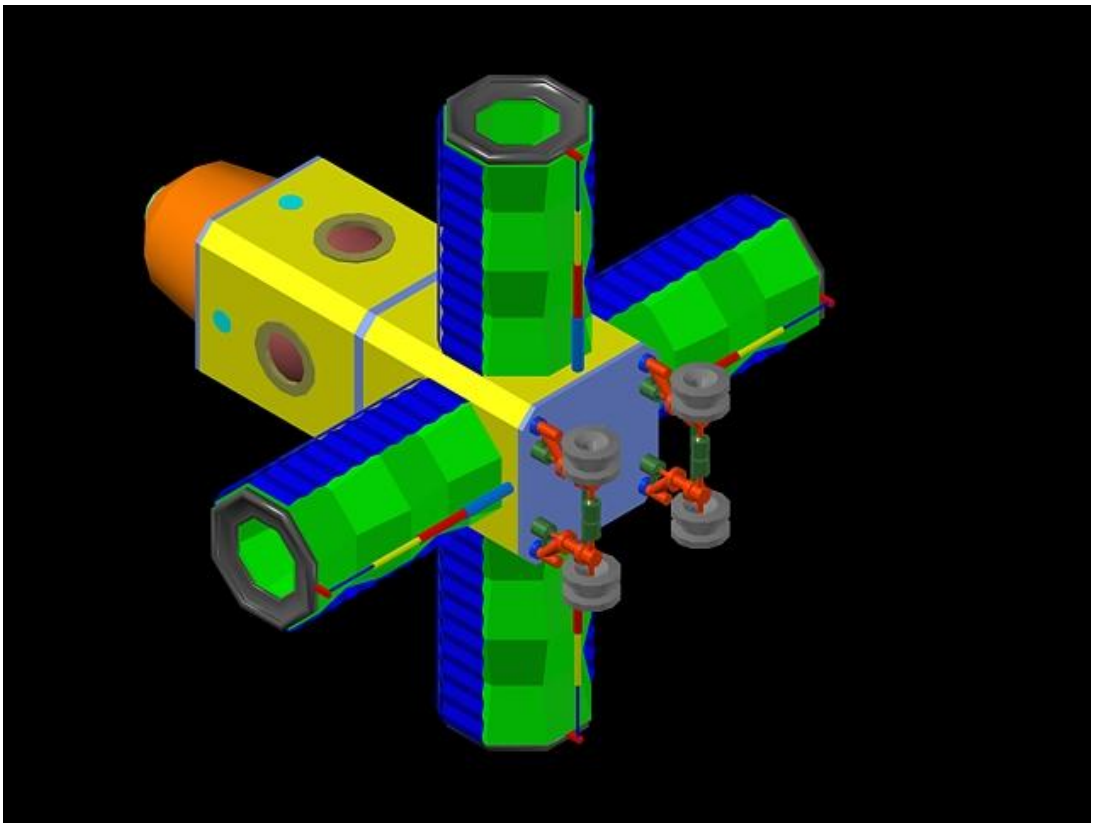

Figure 142: rendering of two LEMMBs assembled together and hexagonal ARMs

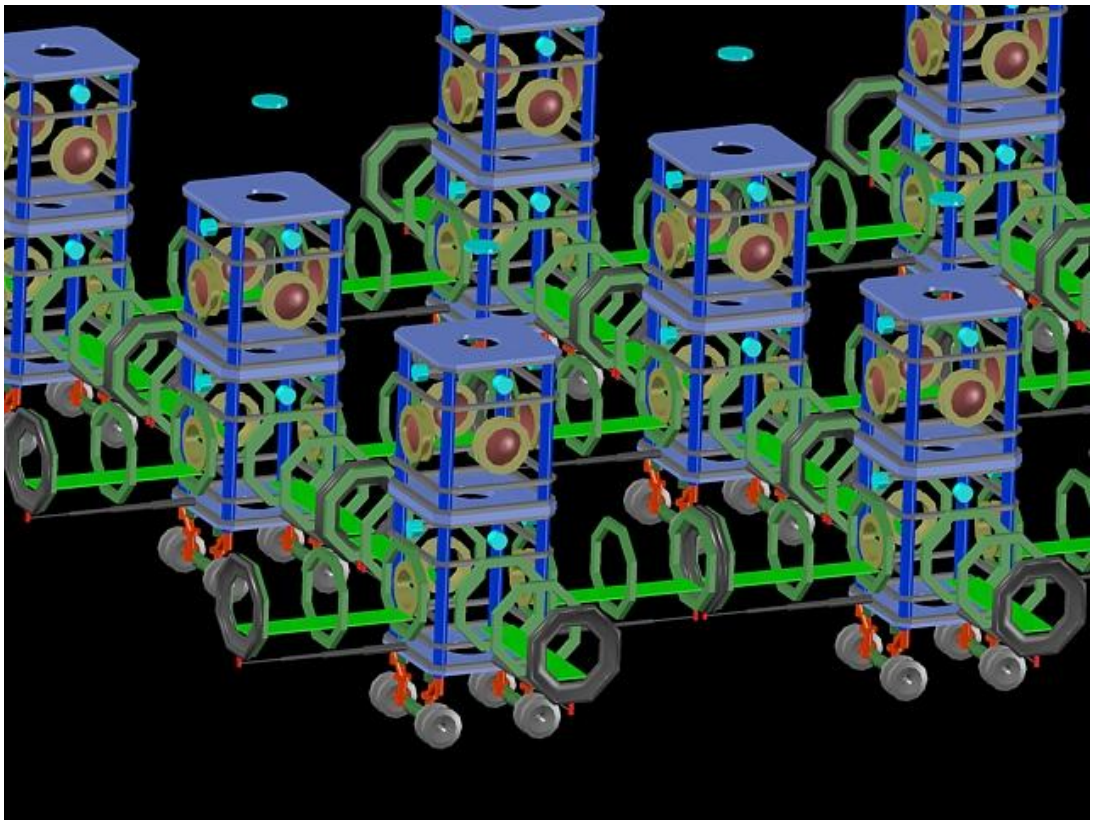

Figure 143: several modules connected to each other

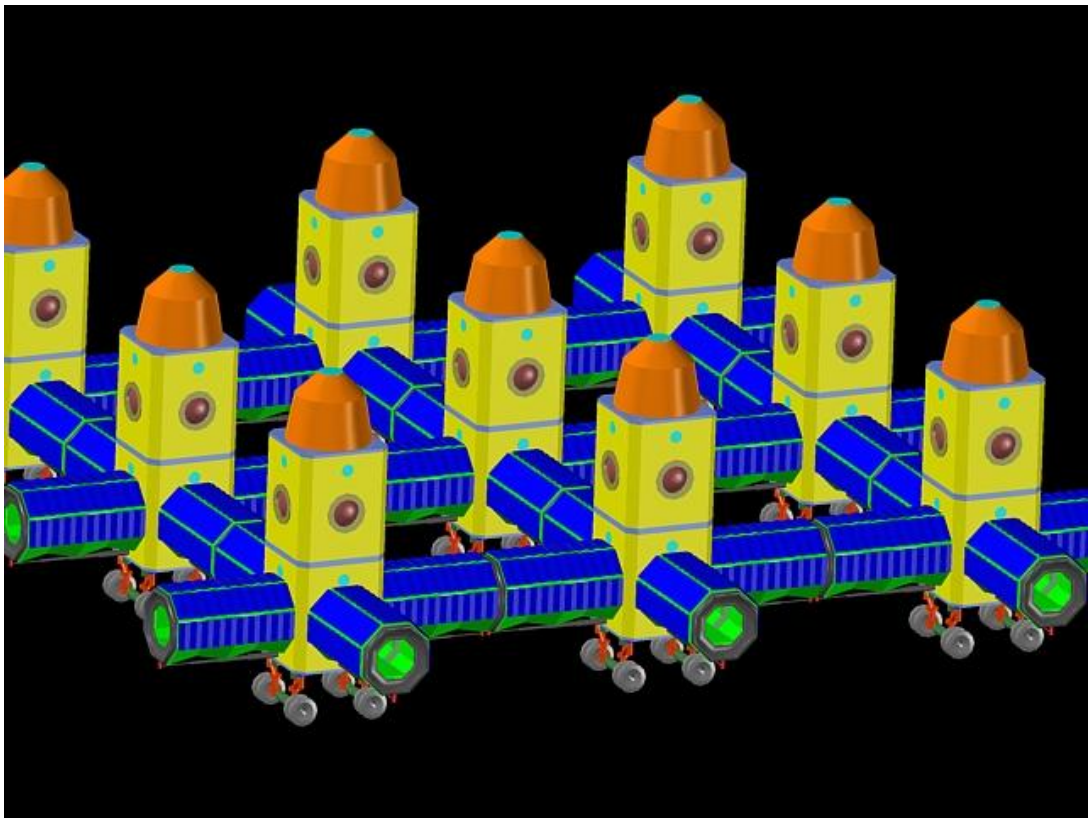

Figure 144: several modules connected to each other

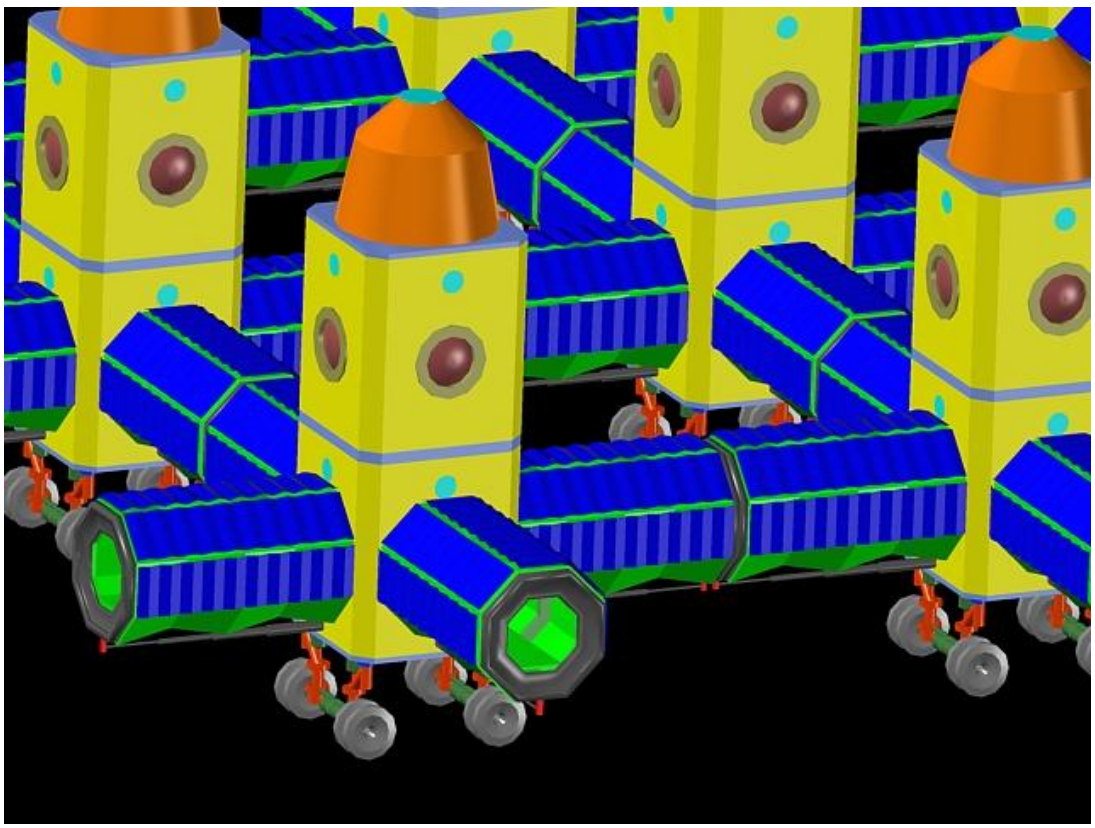

Figure 145: several modules connected to each other

3.5.4 ALENIA Radiation Protection system made of water tank

Spacecraft shielding concept drivers include mass minimization and human related factors, such as pressurized volume architecture and crew location. The proposed concept to shield the crew cabins includes:

- An operational shielding around the habitable volume for the permanent radiation (GCR)
- A storm shelter protection for a reduced volume to protect the crew against large sporadic event (large SPE)

Fig below shows the complete experimental set-up of the study adopted in the Geant4 simulations. The multilayer consists of a fixed component, corresponding to the basic vehicle structure, and of optional components representing the shielding. The thickness and material of the shielding layer can be selected; the modeled example cases included shielding consisting of **water** and **polyethylene**, with **5** and **10 cm** thickness.

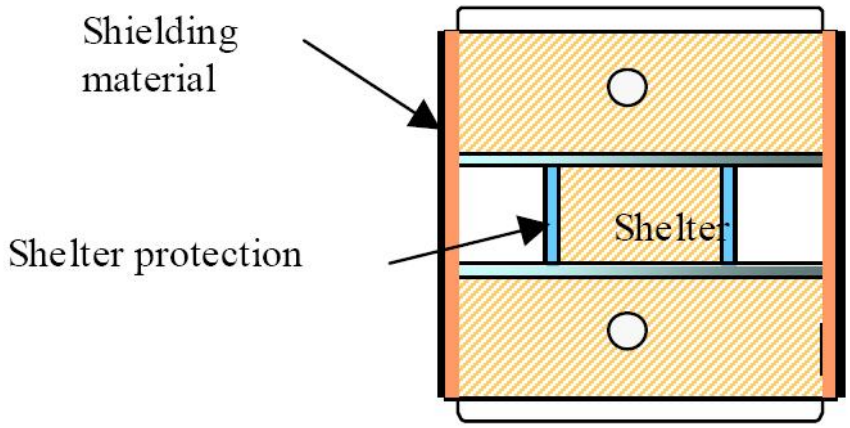

Figure 146: SIH (Simplified Inflatable Habitat) + Shielding + Shelter + Partitions Configuration

The astronaut concept is the geometrical component where the energy deposit given by primary and secondary particles is collected; it is a **water box**. The result of the simulation is the energy deposit given by GCR and SPE radiation components with respect to the depth.

The simplified simulation model is not adequate for absolute dose calculations, but some comparisons may be performed. Hence, from this first iteration of the study, it is possible to infer that the SIM (Simplified Inflatable Module), new and alternative engineering design with respect to the traditional hard shell Habitat, offers a similar radioprotection behavior from GCR with respect to traditional aluminum structures. **In the Simplified Inflatable Module water and polyethylene have an equivalent shielding behavior**. The Geant4 REMSIM simulation shows that a water SPE shelter is a possible solution to limit the exposure of the astronauts to the harmful effects of SPE.

A planet surface habitat built out of local material looks like a possible solution to protect the crew from the GCR and SPE effects.

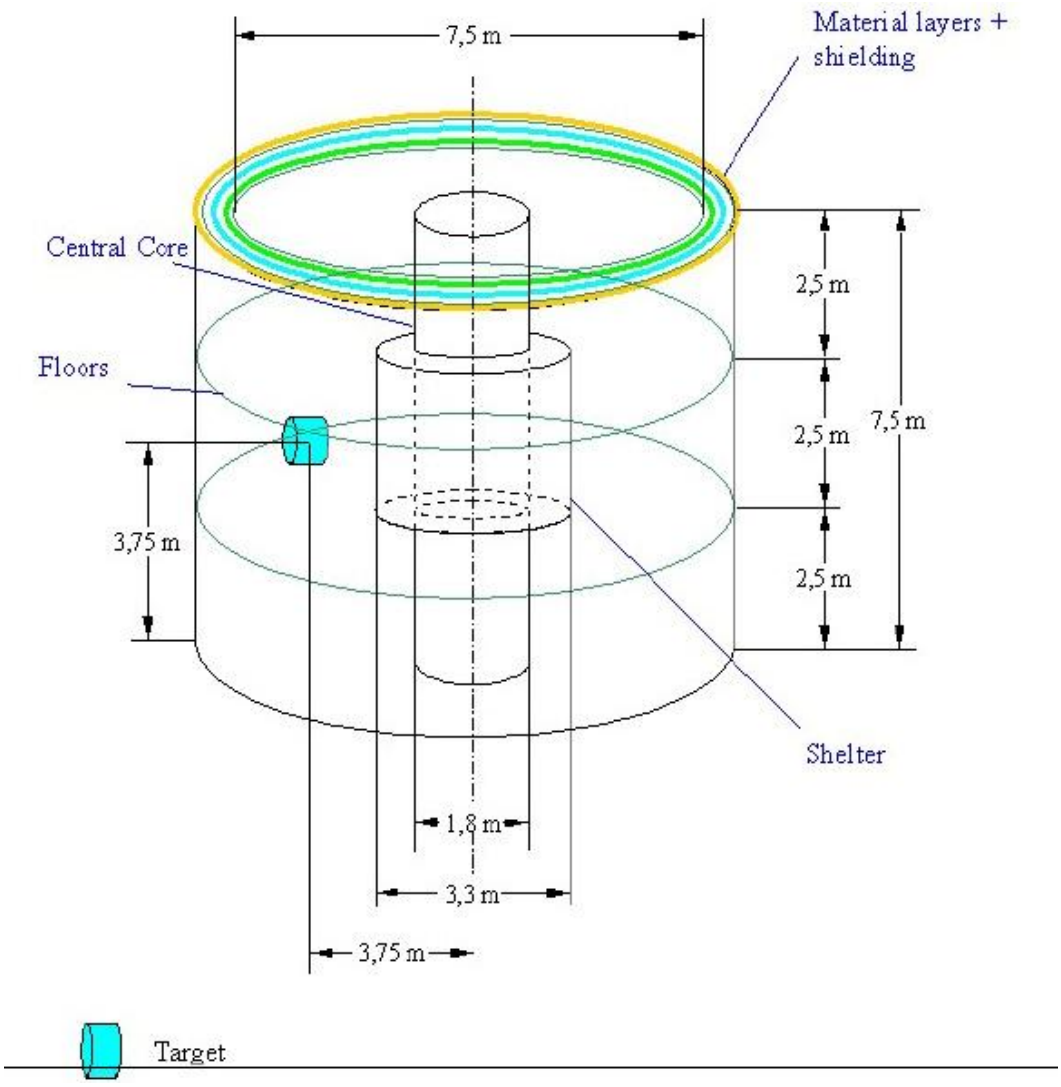

Figure 147: SIH (Simplified Inflatable Habitat) + Shielding + Shelter + Partitions Configuration

3.5.4.1 Effects Dose Threshold Definition (ALENIA Spazio)

In parallel to the environment definition, and from known effects of radiation on humans, "acceptable" thresholds for the doses absorbed by an astronaut during an interplanetary mission have been defined.

	1 minute	1 hour	1 day	1 month	1 year	mission
Warning	3 µSv	0.8 mSv	10 mSv	0.20 Sv	0.40 Sv	0.80 Sv
Alarm	3 Warning	1.0 mSv	12 mSv	0.25 Sv	Sv 0.50	1.00 Sv

Table 10: Proposed dose equivalent limits for a mission to Mars

These limits are much higher than the existing ones for radiation exposed workers on Earth. *Mission limits, valid for elder crew (male above 35 and female above 45 yrs old), are based on a 3% stochastic increase of cancer risk, which can be considered acceptable for manned deep space operations compared with other mission risks.*

- Annual and monthly limits aim to control the radiation exposure during the mission, in order to avoid deterministic effects.
- Daily and hourly limits aim to monitor astronaut activities during the mission.
- The one minute limit is intended as a tool for the early detection of SPE.
- To avoid false alarms, only for three consecutive warnings (i.e. for a cumulative dose higher than 9 µSv in three minutes) the alarm is activated.

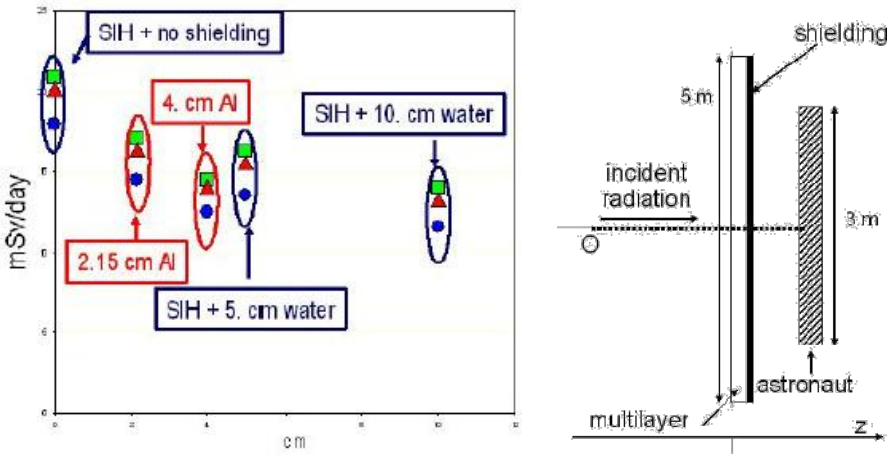

Table 11: left: Total equivalent dose in the astronaut concept resulting from GCR beams, incident on the SIH configuration; right: SIH configuration.

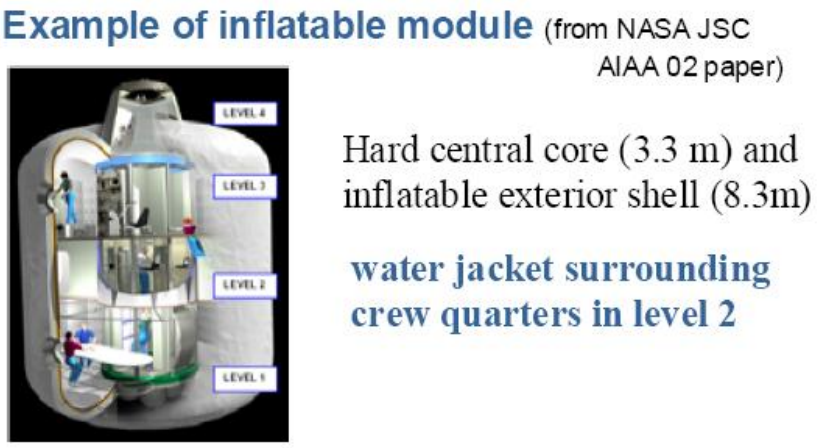

Figure 148: TRANSHAB solution

Figure 149: Internal view of TRANSHAB Inflatable Space Module

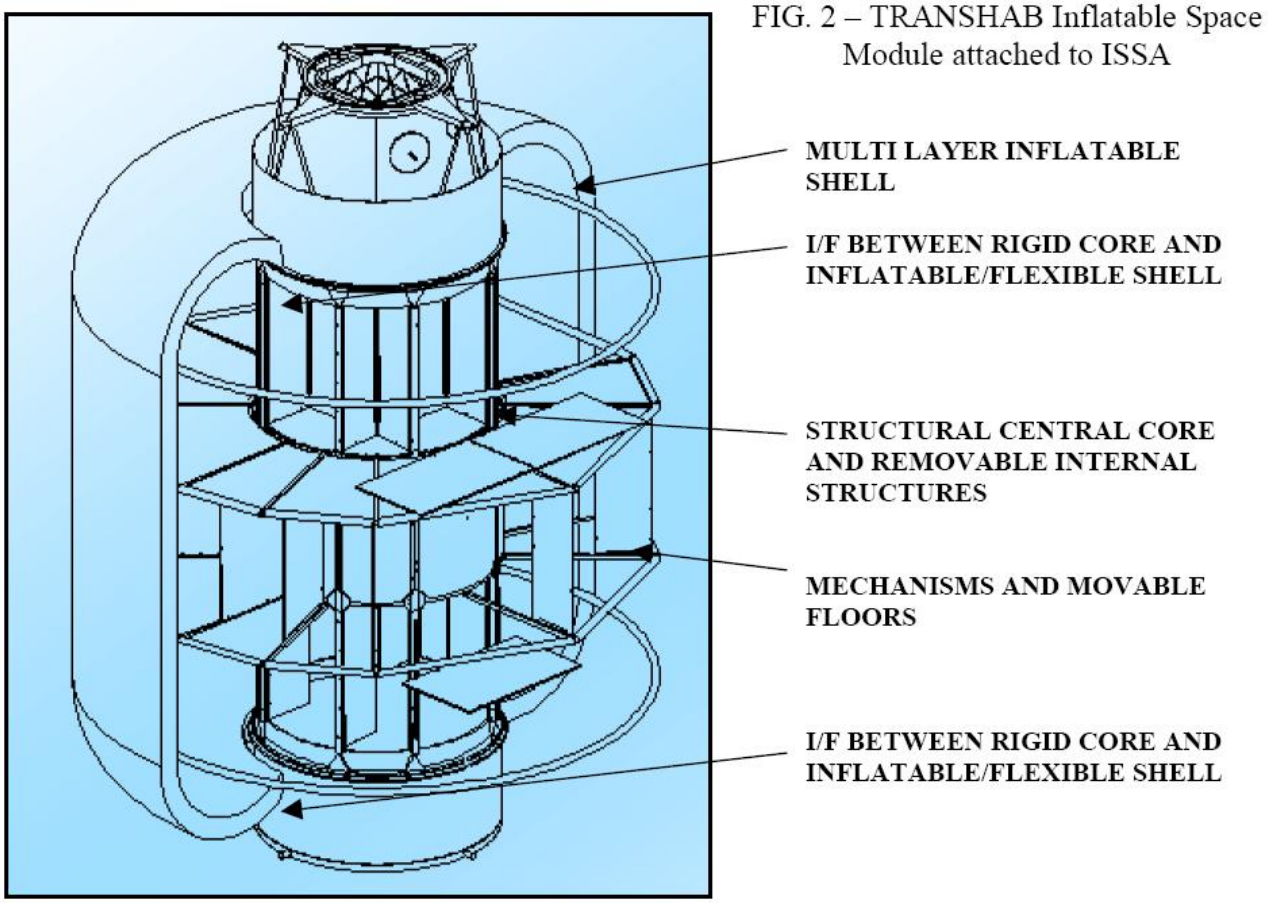

Figure 150: TRANSHAB structural solution

Transhab was a concept pursued by NASA to develop the technology for expandable habitats inflated by air in space. Specifically, Transhab was intended as a replacement for the already existing rigid International Space Station crew habitation module. When deflated, inflatable modules provide an 'easier to launch' compact form. When fully inflated, Transhab would expand to 8.2 meters in diameter (compare to the 4.4 meter diameter of the Columbus ISS Module).

The name of the project is a contraction of Transit Habitat reflecting the original intention to design an interplanetary vehicle to transfer humans to Mars.

Considerable controversy arose during the Transhab development effort due to delays and increased costs of the ISS program. In fact, the National Space Society issued a policy statement recommending that NASA cease development of Transhab. Finally in 2000, despite objections from The White House, House Resolution 1654 was signed into law banning NASA from conducting further research and development of

Transhab. Since that time, the private company Bigelow Aerospace has purchased the rights to the patents developed by NASA and is pursuing a similar scheme for a private space station design.

3.5.5 FLECS structures

The FLECS expandable module concept for future space mission is sponsored by ASI (Italian Space Agency) with the innovative solution of inflatable technology.
FLECS is a project managed by "La Sapienza" University; Aerospace Engineering Department (Proff. Mario Marchetti). It has been designed using advances textiles and films in order to guarantee the structural reliability necessary for the deployment and packaging configuration.
The multi-layer pneumatic retention bladder and the intermediate restraint layer are composed of polymers sheets, ortho-fabrics and elastomers like polyurethanes.
The external protection shield is configured using several layers of impact absorption materials and also several layers of space environment (UV, IR, atomic oxygen) protection material such as Kapton, Mylar and Nextel.
The validation of the fabrics, the films and the final prototype assembly are tested in Space Environment Simulator (SAS), located in the SASLab laboratory of the Aerospace Engineering Department of the "La Sapienza" University of Rome.

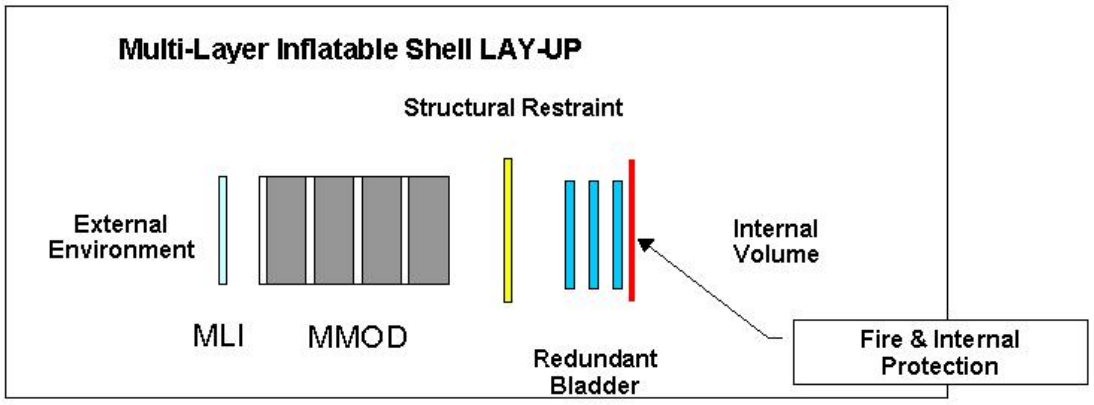

Figure 151: FLECS multilayer configuration

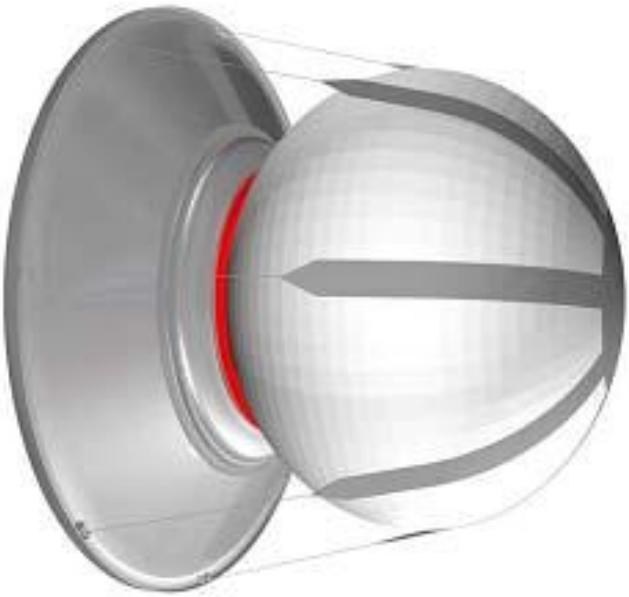

Figure 152: FLECS attached on ISS module

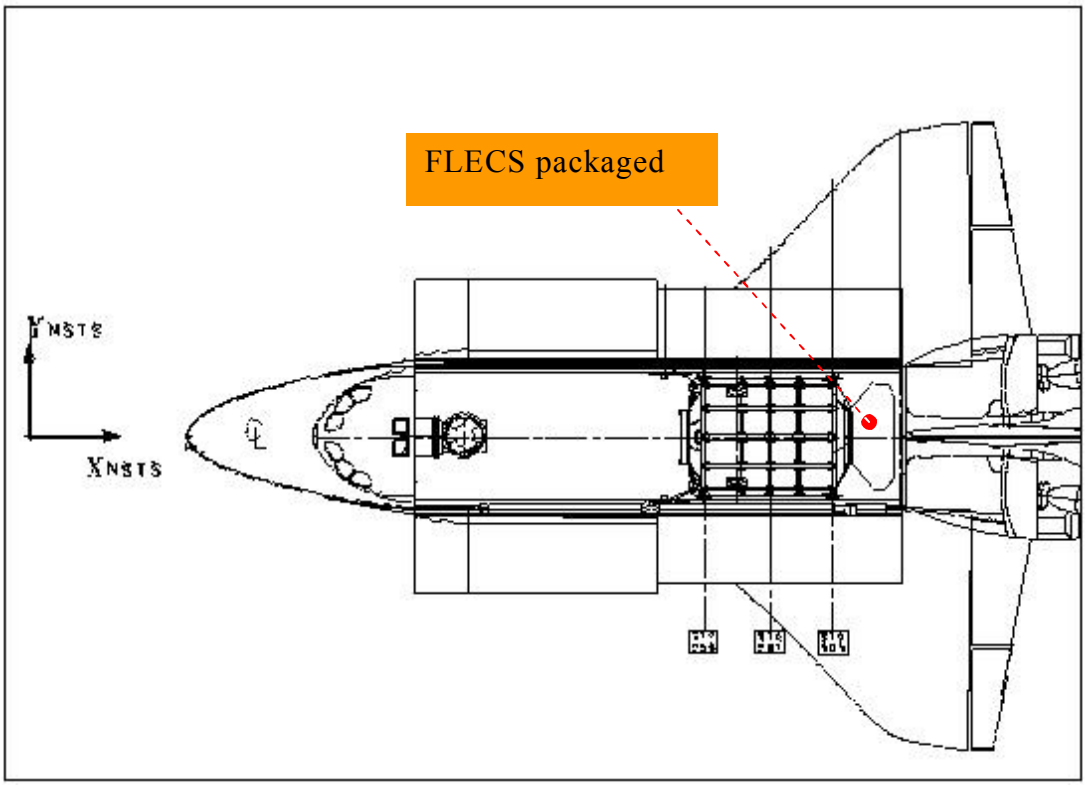

Figure 153: Packed FLECS to be transported on Space Shuttle

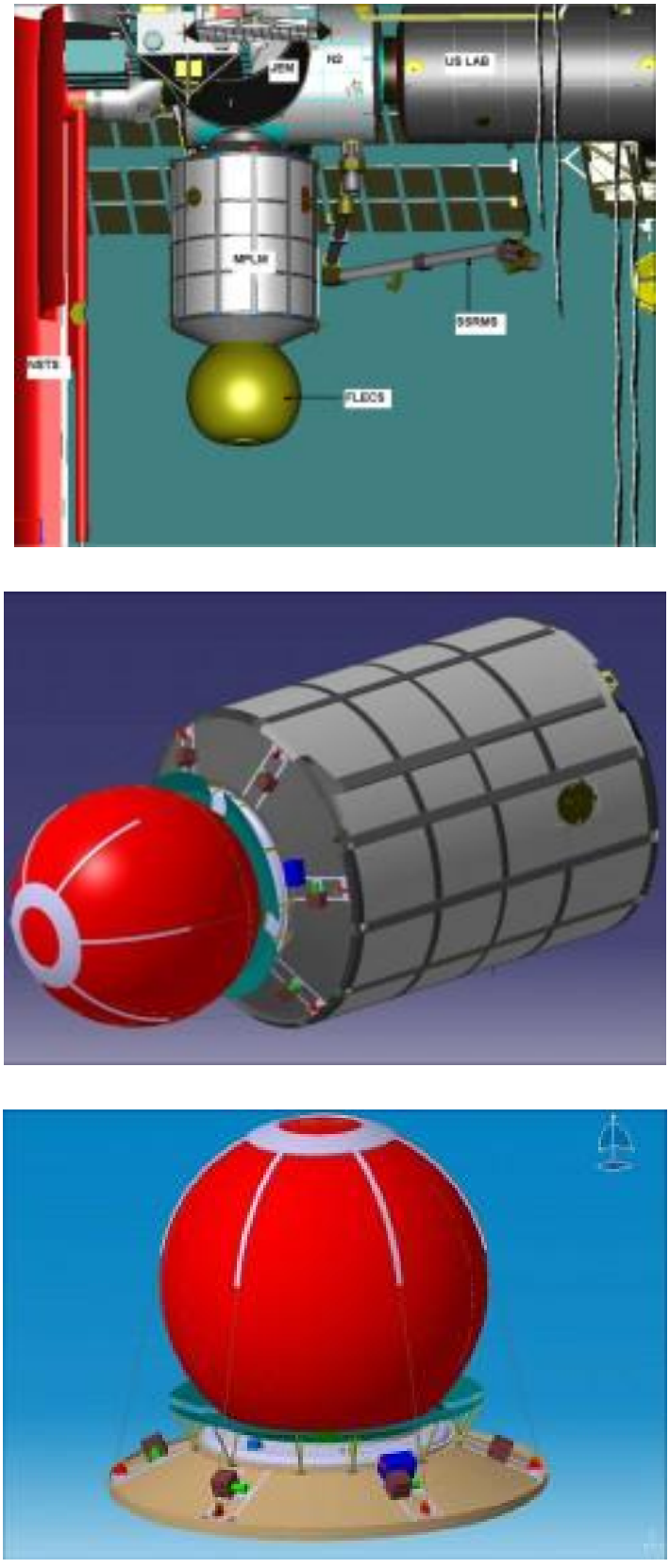

Figure 154: FLECS configuration

3.6 LEMMB Mass

In order to compute the mass of LEMMB we can start dividing the mass basically between:

- LEMMB Empty Core structure
- LEMMB Inflatable Arms structures
- LEMMB payload
- LEMMB Solar array
- LEMMB Mobility equipment

3.6.1 LEMMB Empty Core structure

3.6.1.1 Mass as a function of High-Energy Cosmic Rays shielding – The effect of leakage through the radiation shield.

Any type of radiation shielding has an upper limit to the energy of particles against which it can shield. Above this energy, there will be leakage through the shield.

However, the effects of this leakage differ greatly between magnetic shielding and passive absorption shielding. Spacecraft structures have traditionally been made of aluminum, and many studies and measurements have been done to show cosmic ray shielding by different thicknesses of aluminum. Results are shown in figure below.

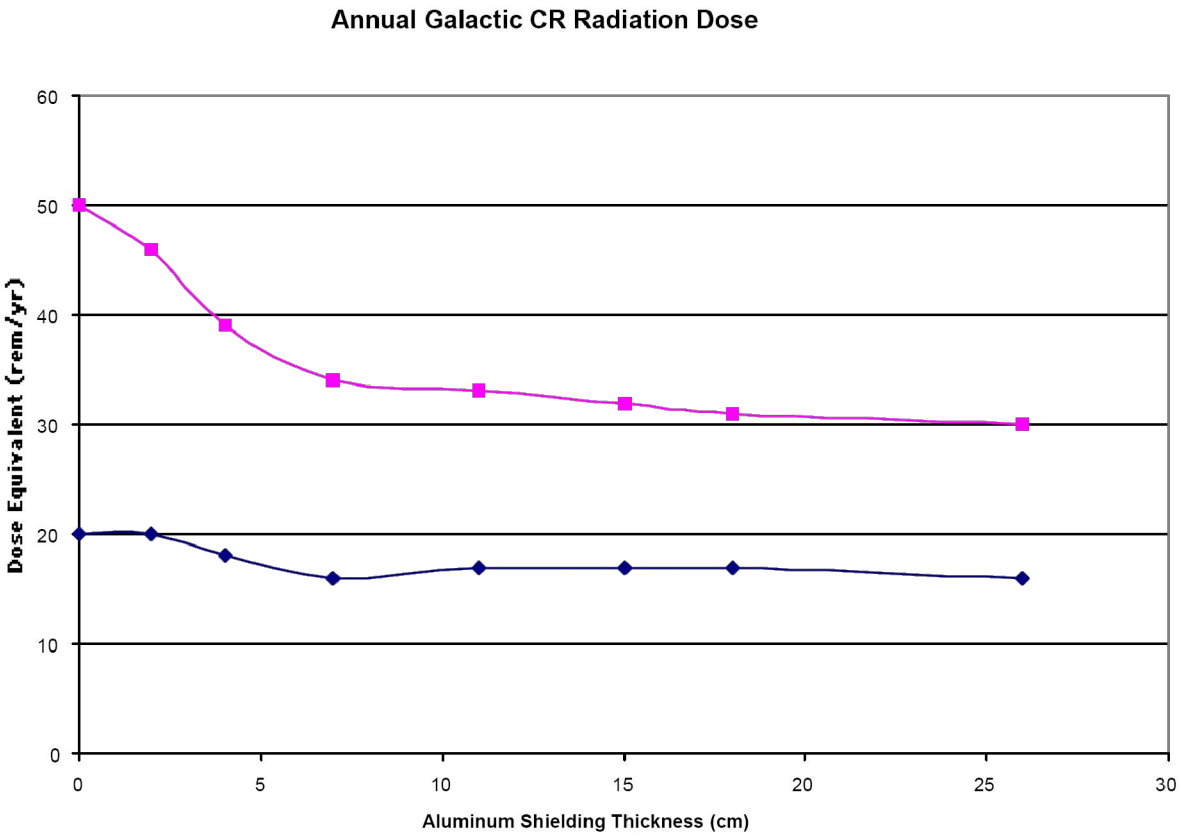

figure 155: Radiation doses received from galactic cosmic radiation with difference thicknesses of passive aluminium shielding. (Top curve: solar minimum; Bottom curve: solar maximum)

Passive shielding can be quite effective for particles with **energies < 1 GeV/nucleon.** However, for higher energy particles, nuclear interactions with the shielding material produce secondary particles which can actually be more numerous and detrimental to Astronaut health than the incident radiation. Figure above shows that the first ~10 cm. of aluminum partially reduces the radiation, but doubling the thickness produces almost no more net reduction. If the thickness is increased sufficiently, of course, all radiation can be absorbed, but the resulting mass will be impractically large.
Passive shielding only makes the problem worse for high-energy cosmic rays, which interact in the shielding to create secondary particles with a higher "quality factor" (i.e.more physiologically damaging) than the primary radiation. Using hydrogen as a passive shield reduces but does not eliminate secondary shower generation.

In two pictures below there are the relationship between the equivalent radiation dose and the shielding thickness.

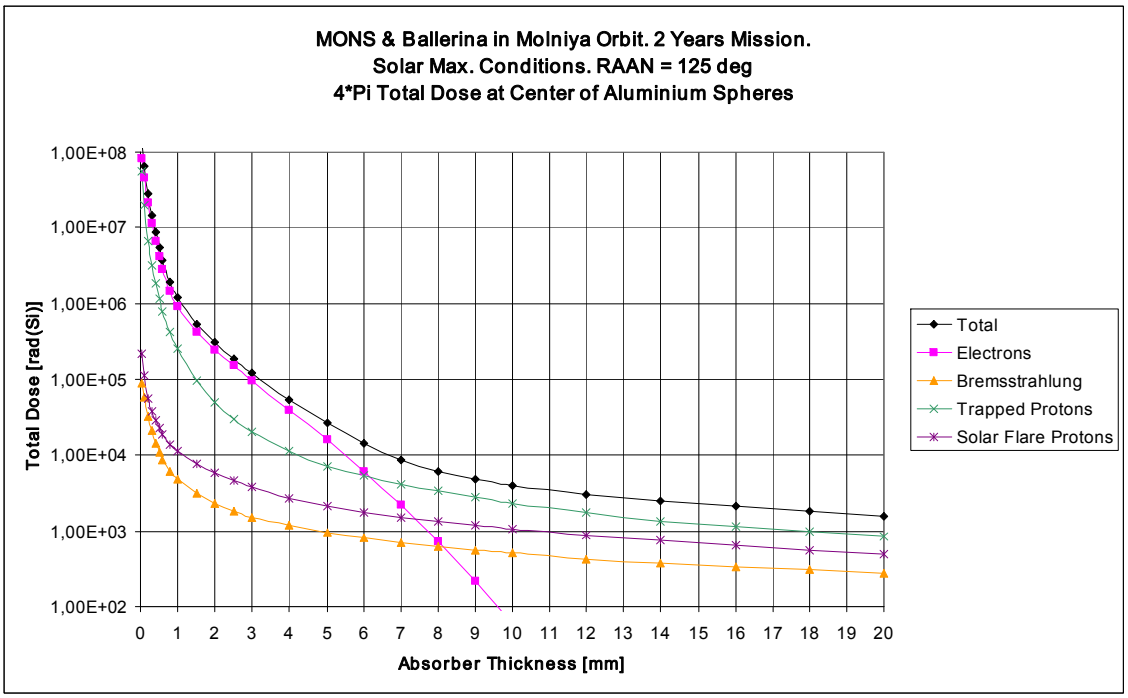

Figure 156: The Earth radiation belts; Radiation Environment in Molniya Orbit - Total Dose

3.6.1.2 LEMMB Core shielding mass

In order to find out the Core mass, we need to consider the shielding material used for LEMMB Core structures.

From the last pictures and from literature a thickness around 5 mm could be used.

So we have two layers for a total thickness around 6.2 mm (5 mm internal layer + 1.2 external layer).

Considering now the aluminium density of about **2.7 g/cm^3** then, in order to compute the mass of LEMMB Core structures we need to compute the total area of the Core.

$$LEMB\_Core\_area\_(cm^2) = 10000 \times \{[(3 \times 3.4) \times 4] + [(3 \times 3) \times 2]\} = 5.88 \times 10^5$$

$$LEMB\_Core\_mass\_(tons) = 0.62 \times 2.7 \times 5.88 \times 10^5 \cong 0.985 \qquad \textbf{eq 13}$$

LEMB core internal structure ≅ 1

3.6.2 LEMMB Inflatable Arms structures

The mass of each Arm is approximately around 500 kg so the total mass is about 2 Tons

3.6.3 LEMMB payload

The payload mass is variable and depend on the type of payload. Taking into account that he main function of LEMMB is for habitat then we can estimate the mass around 2 Tons. i.e. about 1/3 of the ISS Columbus laboratory payload.

3.6.4 LEMMB Mobility equipment

As a final step, the mass of LEMMB Mobility equipment could be 1 tons.

3.6.5 LEMMB Solar Array

Like ISS solar array the mass of LEMMB solar array should be approximately around **100 W/kg.** Below are reported some data about ISS solar array

Figure 157: each ISS solar array produces about 30 kW

The mass of each ISS solar panel should be approximately:

$$Mass\_ISS\_Solar\_array = \frac{30\,(kW)}{100\,(W/kg)} = 300 \quad (kg) \qquad \text{eq 14}$$

3.6.5.1 LEMMB Solar Array Mass

Because the power generated on LEMMB by solar array should be approximately about 10 kW/LEMMB, with η=19 %, then the Solar Array mass should be around:

$$Mass\_LEMB\_Solar\_array = \frac{10\,(kW)}{100\,(W/kg)} = 100 \quad (kg) \qquad \text{eq 15}$$

3.6.6 Total LEMMB mass

Summing the preceding mass, the total LEMMB mass could be around 6÷7 tons. As a consequence in order to transport the LEMMB+LENDER on the lunar surface we can use the Ariane configuration called Heavy Lifter.

LEMMB component	quantities	Single component mass (tons)	Total mass (tons)
LEMMB Empty Core structure	1	2	≅ 2
LEMMB Inflatable Arms structures	4	0.5	≅ 2
LEMMB Solar array	1		≅ 0. 1
LEMMB Payload	1	2	≅ 2÷4
LEMMB Mobility equipment	1	1	≅ 1
LEMMB Total mass			**≅ 7÷9**

Table 12: LEMMB mass

3.7 Reference Table

1. Radiation Exposure and Mission Strategies for Interplanetary Manned Missions (REMSIM)" [Alenia]
2. [RD01] REMSIM Final Report, doc.ALS-RMS-VRP-0001 dated 22/DEC/04
3. [RD02] REMSIM Geant4 Simulation User Requirement Document (URD)
4. http://www.ge.infn.it/geant4/space/remsim/requirements/URD_remsim.html
5. Investigation of Structural Analysis Themes related to Inflatable Space Structures, by the use of the Non-Linear, Multibody Finite Element Code SAMCEF Mecano February 2 - 3, 2005 Salon de l'Aveyron PARIS, Bercy FRANCE
6. INTERNATIONAL COOPERATION FOR SUSTAINABLE SPACE EXPLORATION Session 4
7. Enabling Exploration Capabilities / Technologies International Cooperation for Sustainable Space Exploration ISS as Spaceport for Human Moon Mission 3-6 May 2005 - Abbazia di Spineto, Sarteano,-Italy
8. Stutture Gonfiabili per Applicazioni Spaziali Moduli Abitati e Infrastrutture Orbitali
9. Supporting Life on the Moon [M.A. Perino Alcatel Alenia Space – Italia]
10. Energy Trapping and Shock Disintegration in a Composite Granular Medium [C.Daraio, V.F. Nesterenco, E.B. Herbord, S.Jin—University of California at Sand Diego]
11. http://www.sti.nasa.gov/tto/spinoff1998/t3.htm
12. http://www.vectranfiber.com/

SAPIENZA
UNIVERSITÀ DI ROMA

4 Chapter 4
Earth to Moon LEMMB Transfer

4.1 Abstract

This thesis wants to show a feasible plan to build up a Lunar Base. One phase is the transportation of the modules from the Earth to the Moon. LEMMB's transportation analysis has been made by using Space Vehicle (SV), like Soyuz and Ariane 5. This is made because the dimensions of LEMMB have been chosen compliant to both SV.

Before analyzing the main characteristics of the two SVs (Soyuz or Ariane 5), some theory will be presented. This will help us to understand which could be the more appropriate SV for such kind of mission.

4.2 Moon Fact Sheet

Some Moon useful data are shown on figure below.
http://nssdc.gsfc.nasa.gov/planetary/factsheet/Moonfact.html

Figure 158: Moon picture

4.2.1 Moon/Earth Comparison

4.2.1.1 Bulk parameters

	Moon	*Earth*	*Ratio (Moon/Earth)*
Mass (10^{24} kg)	0.07349	5.9736	0.0123
Volume (10^{10} km3)	2.1958	108.321	0.0203
Equatorial radius (km)	1738.1	6378.1	0.2725
Polar radius (km)	1736.0	6356.8	0.2731
Volumetric mean radius (km)	1737.1	6371.0	0.2727
Ellipticity (Flattening)	0.0012	0.00335	0.36
Mean density (kg/m^3)	3350	5515	0.607
Surface gravity (m/s^2)	1.62	9.80	0.165
Surface acceleration (m/s^2)	1.62	9.78	0.166
Escape velocity (km/s)	2.38	11.2	0.213
μ=GM (x 10^6 km^3/s^2)	0.0049	0.3986	0.0123
Bond albedo	0.11	0.306	0.360
Visual geometric albedo	0.12	0.367	0.330
Visual magnitude V(1,0)	+0.21	-3.86	-
Solar irradiance (W/m)	1367.6	1367.6	1.000
Black-body temperature (K)	274.5	254.3	1.079
Topographic range (km)	16	20	0.800
Moment of inertia (I/MR2)	0.394	0.3308	1.191
J_2 (x 10^{-6})	202.7	1082.63	0.187

4.2.1.2 Orbital parameters (for orbit around the Earth)

	Moon
Semimajor axis (10^6 km)	0.3844
Perigee (10^6 km)*	0.3633
Apogee (10^6 km)*	0.4055
Revolution period (days)	27.3217
Synodic period (days)	29.53

Mean orbital velocity (km/s)	1.023
Max. orbital velocity (km/s)	1.076
Min. orbital velocity (km/s)	0.964
Inclination to ecliptic (deg)	5.145
Inclination to equator (deg)	18.28 - 28.58
Orbit eccentricity	0.0549
Sidereal rotation period (hrs)	655.728
Obliquity to orbit (deg)	6.68
Recession rate from Earth (cm/yr)	3.8
Mean values at opposition from Earth	
• Distance from Earth (equator, km)	378,000
• Apparent diameter (seconds of arc)	1896
• Apparent visual magnitude	-12.74

* These represent mean apogee and perigee for the lunar orbit.
The orbit changes over the course of the year so the distance from the Moon to Earth roughly ranges from 357,000 km to 407,000 km.

4.2.1.3 Orbital Mechanics of the Earth-Moon System

Orbital mechanics in cislunar space are made quite complex by the different and varying orientations of the ecliptic plane, the Earth's equatorial plane, the Moon's orbital plane, and the Moon's equatorial plane. Figure below attempts to illustrate these different planes. Inclinations of the Earth's equatorial plane (the "obliquity of the ecliptic"), is approximately 23.45°, but varies due to tidal forces exerted by the Sun and Moon. The angle i_m between the Moon's equatorial plane and a plane through the Moon's center that is parallel to the ecliptic plane is constant, about 1.58°. The inclination of the Moon's orbit relative to the ecliptic plane is also constant, about λ_m =5.15°. The line of nodes of the Moon's orbit regresses slowly, revolving once every 18.6 years. As a result, the inclination of the Moon's orbit relative to the Earth's equator varies between 18.3÷28.6 degrees. The Moon's orbit also has a slight eccentricity, approximately e_m = 0.0549.

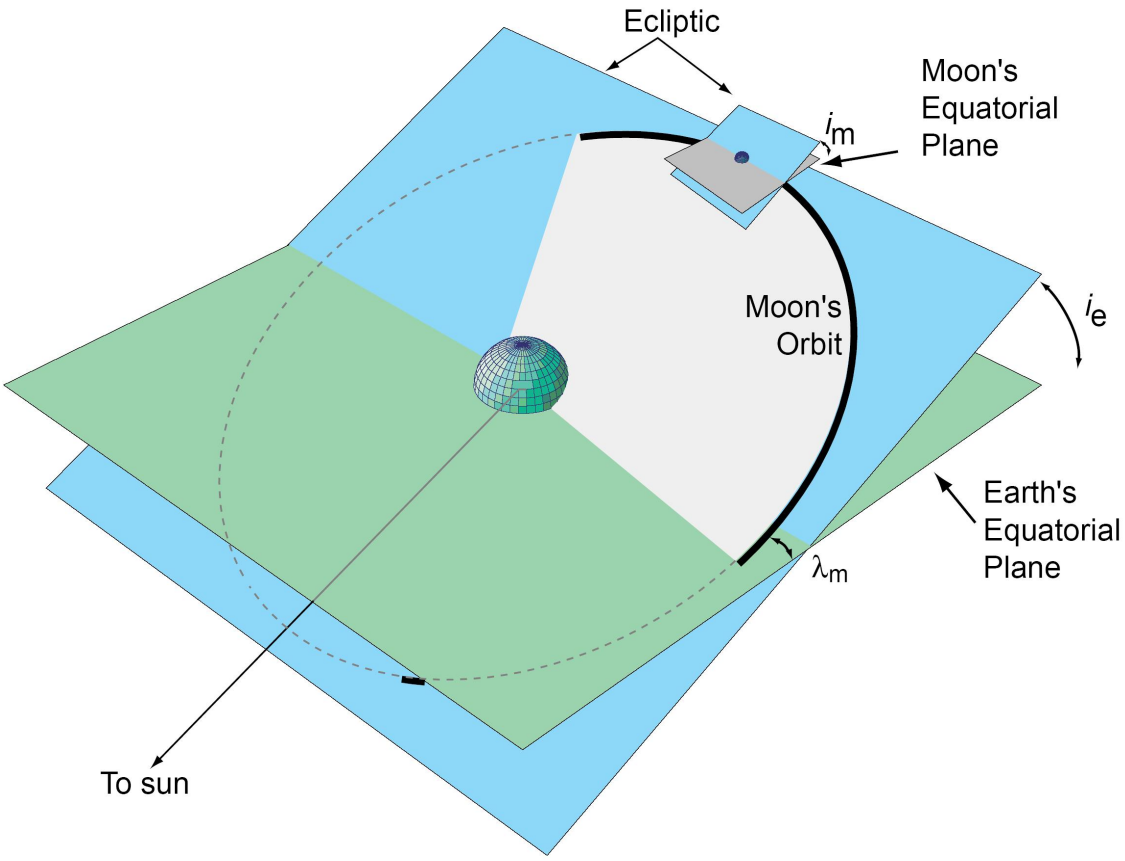

Figure 159: Schematic illustrating the geometry of the Earth-Moon system

4.2.1.4 Lunar Atmosphere

Diurnal temperature range: >100 K to <400 K (roughly -250 F to +250 F)

Total mass of atmosphere: ~25,000 kg

Surface pressure (night): 3 x 10^{-15} bar (2 x 10^{-12} torr)

Abundance at surface: 2 x 10^5 particles/cm^3

Estimated Composition (particles per cubic cm):

Helium 4 (^4He) - 40,000 ; Neon 20 (^{20}Ne) - 40,000 ; Hydrogen (H_2) - 35,000

Argon 40 (^{40}Ar) - 30,000 ; Neon 22 (^{22}Ne) - 5,000 ; Argon 36 (^{36}Ar) - 2,000

Methane - 1000 ; Ammonia - 1000 ; Carbon Dioxide (CO_2) - 1000

Trace Oxygen (O^+), Aluminum (Al^+), Silicon (Si^+)

Possible Phosphorus (P^+), Sodium (Na^+), Magnesium (Mg^+)

Composition of the tenuous lunar atmosphere is poorly known and variable, these are estimates of the upper limits of the nighttime ambient atmosphere composition. Daytime levels were difficult to measure due to heating and outgassing of Apollo surface experiments.

4.3 Orbital energy equation

The following considerations are useful in order to roughly find out the velocity impulse required to perform the lunar mission. It start with SV (space Vehicle) Liftoff form the Earth surface and end with the SV lending on the Moon surface.
In order to compute the velocity impulse ΔV, required to complete the mission, we can use the Orbital Energy equation:

$$E = \frac{1}{2} v^2 - \frac{\mu}{r}$$

where :

eq 16

E = Constant Orbital Energy per mass unit m

$\frac{1}{2} v^2$ = Kinetic energy per mass unit m

$-\frac{\mu}{r}$ = Potential energy per unit mass m $\left[\text{different from potential } \frac{\mu}{r}\right]$

- That Energy is constant only under the assumption that there are not any dissipative external forces acting on the body along the orbital trajectory.
- Plus what remaining constant is the potential and kinetic energy sum and not each single term alone. Since along the orbit both, r and v varies; then only for a circular orbit each single term will remain constant.

Because the energy is constant then it can be calculated in a particular point of the orbit, as an example at the perigee. This is can be done by means of the following equations:

$$\begin{cases} r_p = a(1-e) = \left[\dfrac{p}{(1-e^2)}\right](1-e) = \dfrac{p}{(1+e)} = \dfrac{\dfrac{h^2}{\mu}}{(1+e)} = \dfrac{h^2}{\mu(1+e)} \\ v_p = \dfrac{\mu}{h}\left(e\hat{p}+\hat{\theta}\right)\Big|_{\hat{\theta}_{perigeo}=\hat{p}} = \dfrac{\mu}{h}\left(e\hat{\theta}_p+\hat{\theta}_p\right) = \dfrac{\mu}{h}(e+1)\hat{\theta}_p \quad \Rightarrow \quad |v_p| = \dfrac{\mu}{h}(e+1) \end{cases}$$

where :

- $r_p = a(1-e)$ is perigee radius
- $v_p = \dfrac{\mu}{h}\left(e\hat{p}+\hat{\theta}\right)\Big|_{\hat{\theta}_{perigeo}=\hat{p}}$ is perigee orbital velocity
- $p = \dfrac{h^2}{\mu}$ is the square semi side and $a = \dfrac{p}{(1-e^2)}$ is the elliptic semi axses
- e is the orbital eccentricity $0 \le e \le 1$

by substituting in the energy equation we have :

$$E = \frac{1}{2}v_p^2 - \frac{\mu}{r_p} = \frac{1}{2}\left[\frac{\mu}{h}(e+1)\right]^2 - \frac{\mu}{\dfrac{h^2}{\mu(1+e)}} = \frac{1}{2}\frac{\mu^2}{h^2}(1+e)^2 - \frac{\mu^2}{h^2}(1+e) =$$

$$E = \frac{1}{2}\frac{\mu^2}{h^2}(1+e)^2 - \frac{2}{2}\frac{\mu^2}{h^2}(1+e) = \frac{1}{2}\frac{\mu^2}{h^2}(1+e)[(1+e)-2] = \qquad \textbf{eq 17}$$

$$E = \frac{1}{2}\frac{\mu^2}{h^2}(1+e)[e-1] = -\frac{1}{2}\frac{\mu^2}{h^2}(1+e)(1-e) =$$

$$E = -\frac{1}{2}\frac{\mu^2}{h^2}(1-e^2) = -\frac{1}{2}\mu\frac{(1-e^2)}{\dfrac{h^2}{\mu}} = -\frac{1}{2}\mu\frac{(1-e^2)}{p} = -\frac{1}{2}\mu\frac{1}{\dfrac{p}{(1-e^2)}} = -\frac{1}{2}\frac{\mu}{a}$$

This result mean that the satellite total mechanical energy per unit of mass along the orbit, is a function of the semi major axes ***a*** of the orbit only and, it is constant under the assumption that there aren't any dissipative external force acting along the trajectory.

$$E = \frac{1}{2}v^2 - \frac{\mu}{r} = -\frac{\mu}{2a} \qquad \textbf{eq 18}$$

Where:

- v= SV (Space Vehicle) velocity on the orbital trajectory generic point;
- r = orbital trajectory generic point distance from the pole attraction;
- a = semi axes of the orbit;

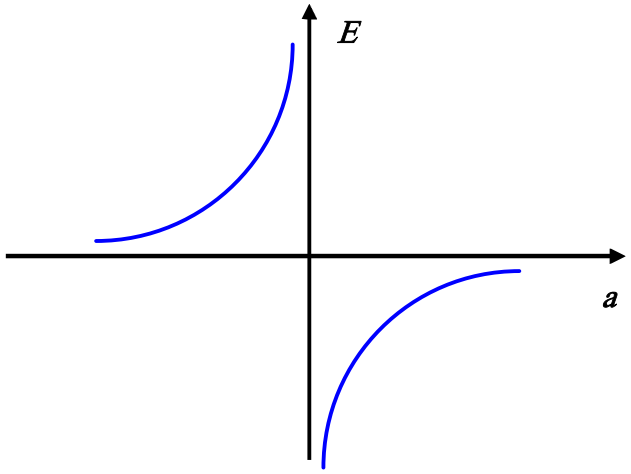

Figure 160: Orbital Energy as a function of the semi major axess

In particular referring to a circular orbit where $r = a =$ constant we have:

$$E = \frac{1}{2}v^2 - \frac{\mu}{r} = -\frac{\mu}{2r} = \text{cost} \quad \Rightarrow \quad \frac{1}{2}v^2 = \frac{\mu}{2r} \quad \Rightarrow \quad v = \sqrt{\frac{\mu}{r}}$$

eq 19

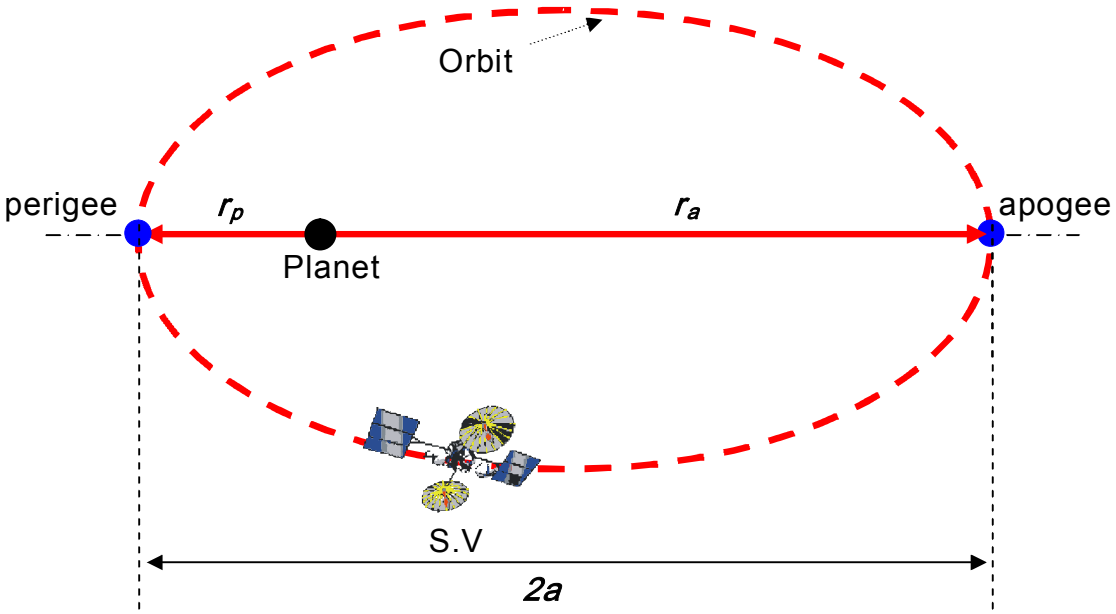

Figure 161: main geometric orbital parameters

If r_a end r_p are the elliptic Earth orbit apogee and perigee radius. Knowing the semi major axes a and eccentricity e, it can be find out the corresponding perigee and apogee SV velocities v_p and v_a:

$$\begin{cases} E = \frac{1}{2} v_a^2 - \frac{\mu}{r_a} = -\frac{\mu}{2a} \\ v_a^2 = 2\frac{\mu}{r_a} - \frac{\mu}{a} \\ v_a = \sqrt{2\frac{\mu}{r_a} - \frac{\mu}{a}} \end{cases} \qquad \begin{cases} E = \frac{1}{2} v_p^2 - \frac{\mu}{r_p} = -\frac{\mu}{2a} \\ v_p^2 = 2\frac{\mu}{r_p} - \frac{\mu}{a} \\ v_p = \sqrt{2\frac{\mu}{r_p} - \frac{\mu}{a}} \end{cases}$$

where $a = \frac{r_p + r_a}{2}$ end $e = \frac{r_a - r_p}{r_a + r_p} \Rightarrow \begin{cases} r_p = a(1-e) \\ r_a = a(1+e) \end{cases}$ **eq 20**

substituting in v_a end v_p we obtain :

$$v_a = \sqrt{2\frac{\mu}{r_a} - \frac{\mu}{a}} = \sqrt{\frac{\mu}{a}\frac{(1-e)}{(1+e)}} \qquad v_p = \sqrt{2\frac{\mu}{r_p} - \frac{\mu}{a}} = \sqrt{\frac{\mu}{a}\frac{(1+e)}{(1-e)}}$$ **eq 21**

As we have seen, the mechanical orbital energy depends exclusively from the semi major axes a of the orbit.

As a consequence, as a function of the orbit type, the velocity become:

Ecc.	*S Axess*	*Energy*	*Orbit type*	*Velocity equation*
$e = 0$	$a > 0$	$\Rightarrow E < 0$	circular orbit	$\Rightarrow \left\{ v = \sqrt{\frac{\mu}{a}} = \sqrt{\frac{\mu}{raggio}} \right\}$
$e < 1$	$a > 0$	$\Rightarrow E < 0$	elliptic orbit	$\Rightarrow \left\{ v_p = \sqrt{\frac{\mu}{a}}\sqrt{\frac{1+e}{1-e}} \right\} \quad \left\{ v_a = \sqrt{\frac{\mu}{a}}\sqrt{\frac{1-e}{1+e}} \right\}$
$e = 1$	$a \to \infty$	$\Rightarrow E = 0$	parabolic orbit	$\Rightarrow \left\{ \begin{array}{l} v_p = \sqrt{\frac{\mu}{r_p}}\sqrt{1+e} = \sqrt{\frac{\mu}{r_p}}\sqrt{1+1} = \sqrt{2}\sqrt{\frac{\mu}{r_p}} \\ v_\infty = 0 \\ v_p = v_{\text{perigee parabolic isertion}} \end{array} \right\}$
$e > 1$	$a < 0$	$\Rightarrow E > 0$	hyperbolic orbit	$\Rightarrow v_\infty > 0$

eq 22

- trajectory are elliptic when the kinetic energy is lower than the potential energy;
- trajectory is parabolic when the kinetic energy is equal to potential energy;
- trajectory is hyperbolic when the kinetic energy is greater than the potential energy and the satellite can overcame the gravitational sphere influence of the planet with a residual velocity greater than zero.

In figure below are shown some examples of the orbital trajectories:

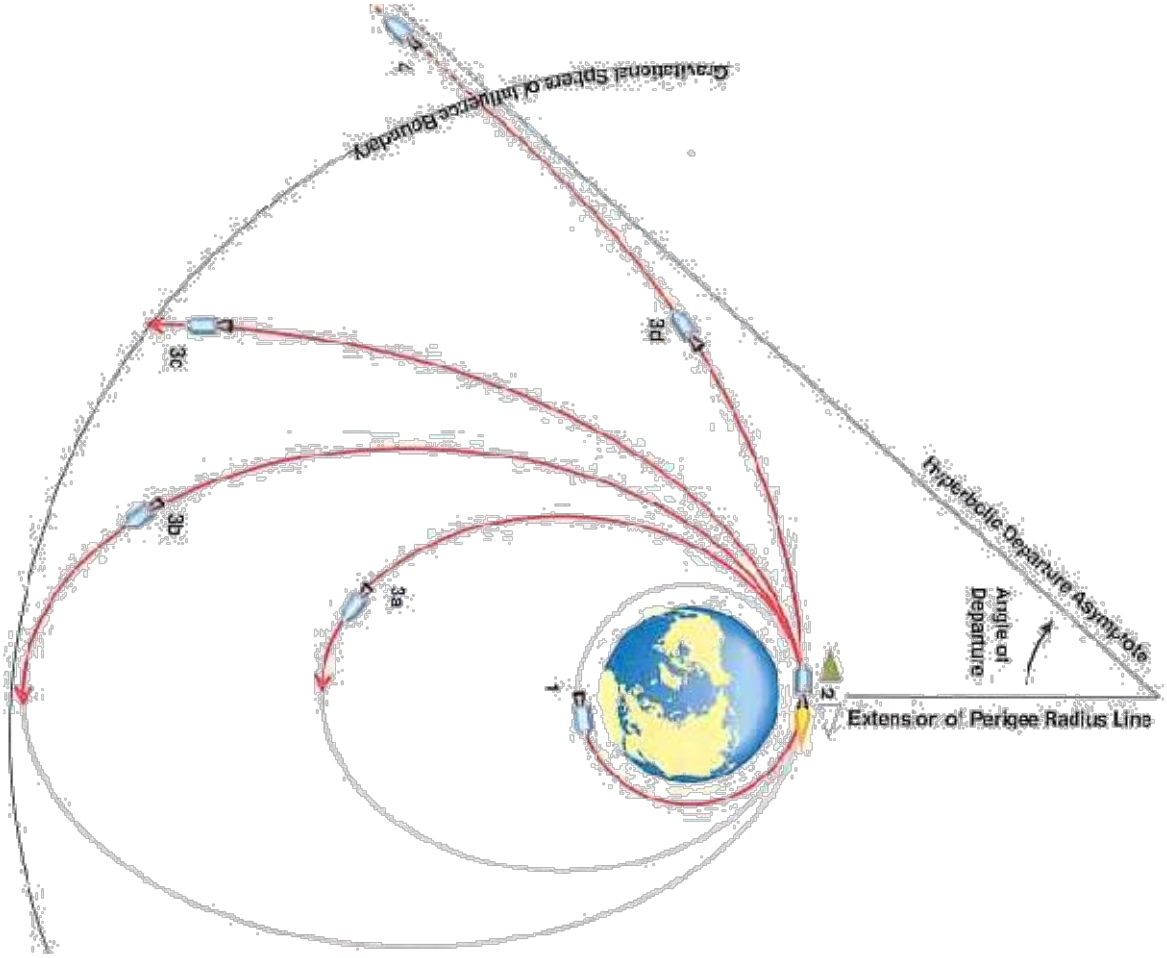

Figure 162: orbit type

4.3.1 Orbital transferring between orbits located on the same plane

Supposing a as an example a SV (space Vehicle) orbital transfer from a LEPO (Low Earth Parking Orbit) towards a GEO (Geostationary Earth Orbit) located approximately at 36000 km from the Earth surface.

Hohmann suggested to doing the ORBIT ACQUISITION by using an elliptical orbital transferring.

The periapsis (perigee) of Hohmann method is located at quote r_1 of the initial orbit LEPO, while the apoapsis (apogee) is located at r_2 quote of the final target orbit GEO.

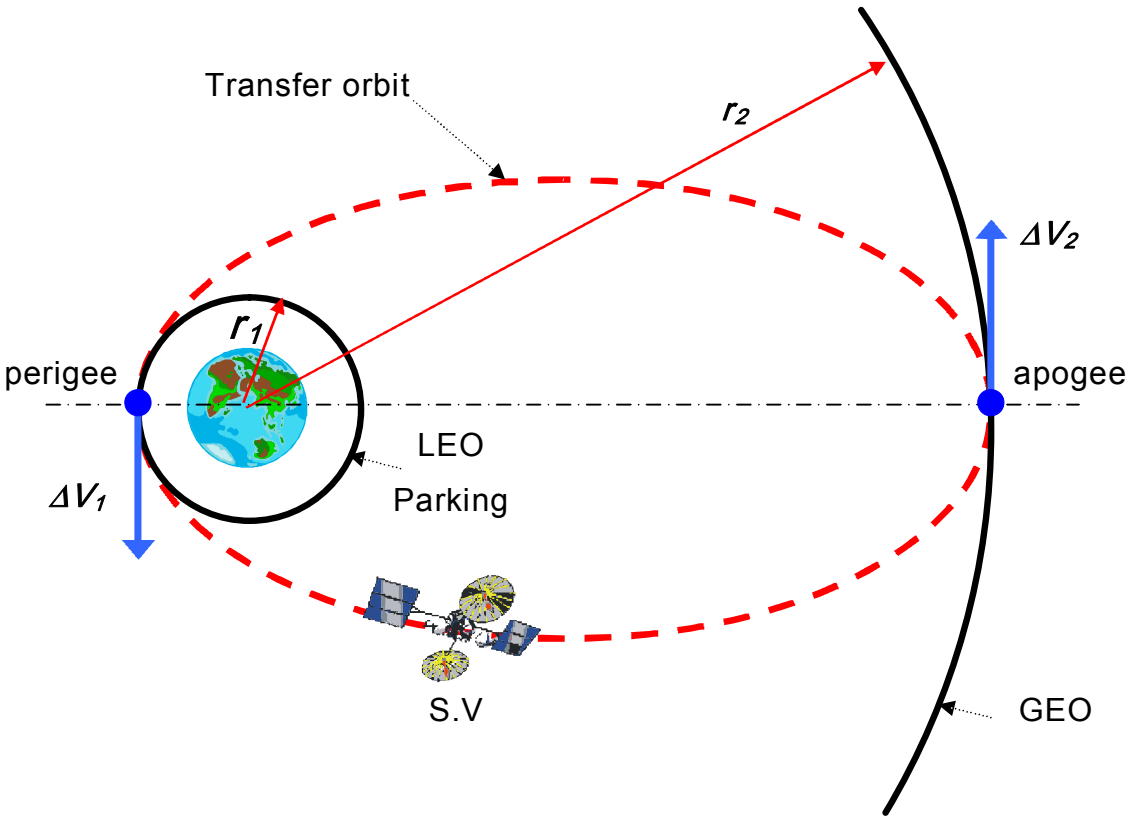

Figure 163: classic Hohmann orbital transferring method

The SV velocity in the two circular orbits periapsis and apoapsis (***LEPO*** and ***GEO***) are:

$$V_{LEO} = \sqrt{\frac{\mu}{r_1}} \qquad V_{GEO} = \sqrt{\frac{\mu}{r_2}} \qquad \text{eq 23}$$

The semi major axis and the eccentricity of the transfer orbit are

$$a = \frac{r_1 + r_2}{2} \qquad e = \frac{r_a - r_p}{r_a + r_p} = \frac{r_2 - r_1}{r_2 + r_1} \qquad \text{eq 24}$$

On figure below are shown the Velocity Impulse **ΔV1** and **ΔV2**. The first is required in order to place the SV on to elliptical transferring orbit, the second is required in order to circularize the final orbit of the SV.

The first impulse is fired at the Perigee of the transfer orbit; it is located at the same altitude of the LEPO (Low Earth Parking Orbit).

The second impulse is fired at the apogee of the elliptic transfer orbit; apogee point is located at the same altitude of the GEO.

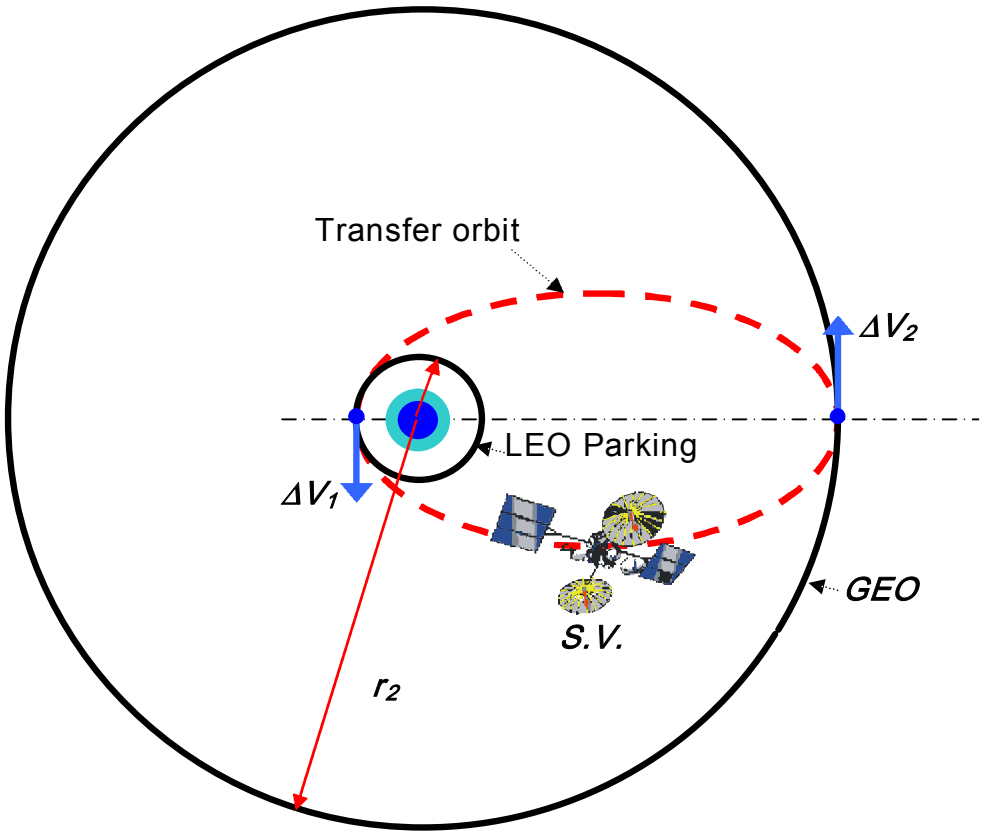

Figure 164: Hohamann transfer and velocity impulse at perigee and apogee

The orbital transferring happens in two phases:

- The first ΔV_1 velocity impulse is applied at the periapsis of the elliptical transfer orbit, this is required in order to move the satellite from LEO parking orbit to elliptical transfer orbit.
- The second impulse ΔV_2 is given at the apoapsis of the elliptical transfer orbit in order to circularize the final orbit which becomes a GEO.

$$\Delta V_1 = V_{Perigeo} - V_{LEO} = \sqrt{\frac{\mu}{a}\frac{(1+e)}{(1-e)}} - \sqrt{\frac{\mu}{r_1}} = \sqrt{\frac{\mu}{r_1}(1+e)} - \sqrt{\frac{\mu}{r_1}} = \sqrt{\frac{\mu}{r_1}}\left[\sqrt{(1+e)} - 1\right] = V_{LEO}\left[\sqrt{(1+e)} - 1\right]$$

$$\Delta V_2 = V_{GEO} - V_{Apogeo} = \sqrt{\frac{\mu}{r_2}} - \sqrt{\frac{\mu}{a}\frac{(1-e)}{(1+e)}} = \sqrt{\frac{\mu}{r_2}} - \sqrt{\frac{\mu}{r_2}(1-e)} = \sqrt{\frac{\mu}{r_2}}\left[1 - \sqrt{(1-e)}\right] = V_{GEO}\left[1 - \sqrt{(1-e)}\right]$$

eq 25: velocity impulses at perigee and apogee of the transferring orbit

As a consequence the final total transferring velocity impulse is:

$$\Delta V_{tot} = \Delta V_1 + \Delta V_2 = V_{LEO}\left[\sqrt{(1+e)} - 1\right] + V_{GEO}\left[1 - \sqrt{(1-e)}\right]$$

eq 26: total velocity impulse

4.3.2 Orbital transferring between orbits located on different planes

In order to change the orbital plane we can observe that the initial and final orbit share the same nodal points. As a consequence the orbital maneuvers have to be executed at this points.

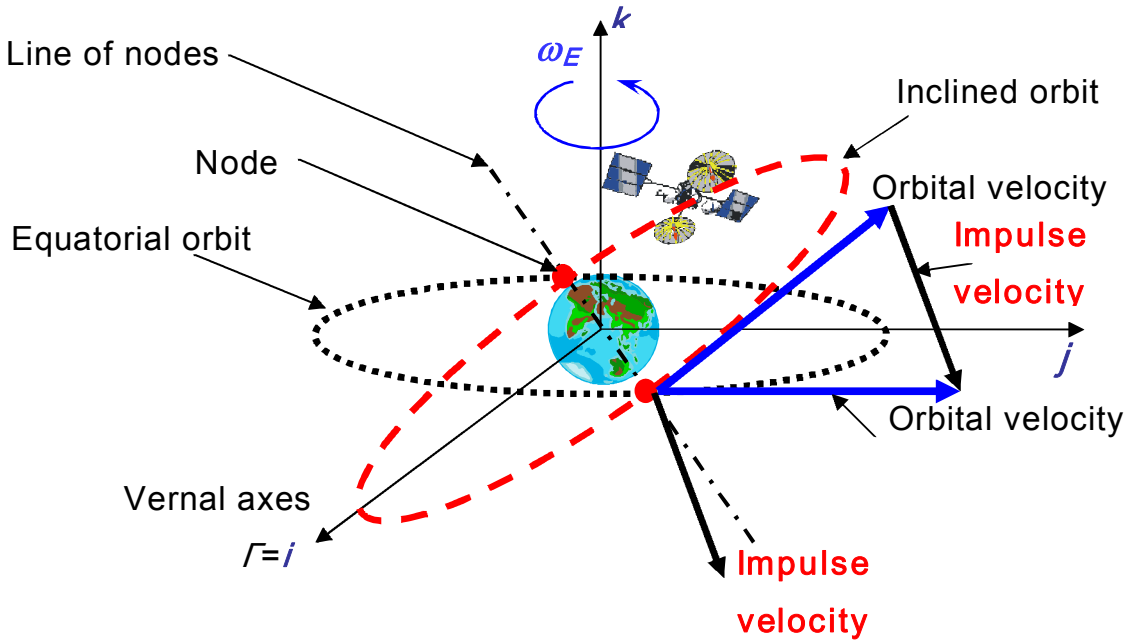

Figure 165: orbital transferring between orbit located on different plane

The equation required to compute the absolute value of ΔV must take into account that the absolute value of the satellite velocity should remain the same in the new orbit (in fact we are interested only in changing the inclination of orbit).

As a consequence we can consider an isosceles triangle the sides of which, are the required satellite orbital velocity and the base of which, is the ΔV velocity impulse needed at the nodal point to complete the orbital transfer:

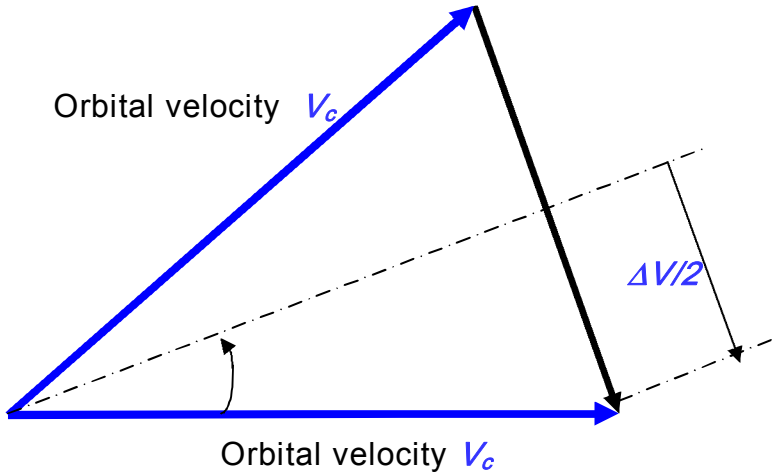

Figure 166

$$\Delta V = 2 V_c \sin\left(\frac{i}{2}\right)$$

In order to minimize the total ΔV velocity impulse, it can be observed that this impulse is nearly the minimum when the orbital velocity V_c is close to the minimum too.

Since the minimum of orbital velocity happens at the apoapsis, then it convenient to do this operation in this point.

As an example considering a circular orbit located about 200 Km from the Earth surface, then the corresponding $V_c \approx 7780\ m/s$. If the inclination $i = 28.5°$ (typical Cape Canaveral launch polygon reachable inclination orbit), then the ΔV required to obtain an equatorial orbit is *3382 m/s* which is a considerable part of the initial V_c.

As a consequence such type of the inclination orbit changing maneuvers is extremely expansive, so follows the importance to have and equatorial launch base.

4.3.3 Orbital velocity on the ground

The minimum value that the radius r can assume corresponds to the Earth radii, R_E. The corresponding orbital velocity and orbital period are:

$$v = \sqrt{G\frac{M_E}{r}} = \sqrt{\frac{\mu_E}{R_E}} = \sqrt{\frac{\mu_E}{R_E}} \approx 7800 \quad \text{m/s}$$
$$T = 2\pi\sqrt{\frac{r^3}{\mu}} = 2\pi\sqrt{\frac{R_E^{\,3}}{\mu_E}} \approx 5300 \quad \text{s} \cong 90 \quad \text{min} \qquad \text{eq 27}$$

This obviously is an hypothetical orbit, useful as a reference velocity value, a more realistic example for a Low Earth Orbit is with $h=200$ km (r =R_E+h=6578 km), then the orbital velocity became around *7800 m/s*.

4.3.4 Earth Escape Mission

An escape mission is such that the useful payload can overcome the Earth gravitational field of influence boundary with a certain residual velocity.
To do this a ΔV velocity impulse capable to push the spacecraft toward an infinite distance with respect to the Earth, is required.

Since the total mechanical energy remains constant then, by equalling the energy equation in two point, the first one located close to the Earth and the second one far from the Earth, can permit us to find out the ΔV impulse velocity required for an escape Earth mission.

$$E = \frac{v^2}{2} - \frac{\mu_E}{R_E} = \frac{v_\infty^2}{2} - \frac{\mu_E}{r_\infty} \qquad \text{eq 28}$$

At an infinite distance, the term $\frac{\mu_E}{r_\infty}$ tends to zero, while $\frac{v_\infty^2}{2}$ is greater or equal to zero.

As a consequence:

$$E = \frac{v^2}{2} - \frac{\mu_E}{R_E} = \frac{v_\infty^2}{2} \quad \Rightarrow \quad \begin{cases} v_\infty = \sqrt{v^2 - 2\frac{\mu_E}{R_E}} \\ v = \sqrt{v_\infty^2 + 2\frac{\mu_E}{R_E}} \end{cases}$$

eq 29

Let us suppose now that at the infinite distance from the Earth, the excess of the Spacecraft velocity (the square of this velocity is called C_3^2) must be zeroed, then, in order to escape from the Earth gravitational field, the minimum impulse velocity ΔV to be imparted to the SV is:

$$0 = \sqrt{v^2 - 2\frac{\mu_E}{R_E}} \quad \Rightarrow \quad v = v_{escape} = v_e = \sqrt{2\frac{\mu_E}{R_E}} = \sqrt{2}\, V_c \approx \sqrt{2} \cdot 7800 = 11180 \text{ m/s}$$

eq 30

In the previous equation has been assumed that the propulsive Spacecraft phase and the corresponding running distance is negligible with respect to the Earth radii, so

$$r \cong R_E$$

In the opposite case, if the launch velocity v is greater then the escape velocity v_e, then the Spacecraft will reach the Earth Gravitational Influence Sphere Boundary, with a residual velocity greater the zero:

$$v_\infty = \sqrt{v^2 - 2\frac{\mu_E}{R_E}} = \sqrt{v^2 - v_e^2} \quad \Rightarrow \quad v = \sqrt{v_\infty^2 + v_e^2}$$

eq 31

Here, v_i is the launch velocity that the SV must have in order to obtain an excess of velocity v_∞ at the end of the Gravitational Earth Sphere of influence.
For an escape mission, the trajectory, in general, is hyperbolic.

If the launch velocity v_i is equal to the escape velocity v_e, then the trajectory is parabolic.

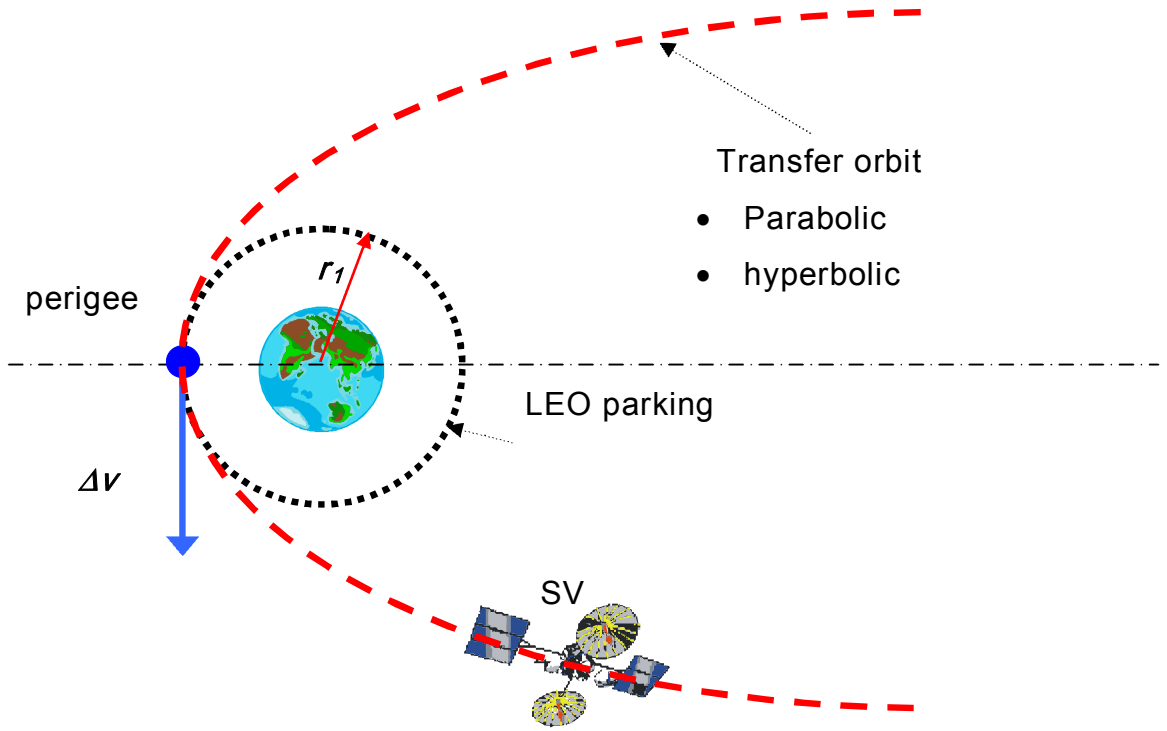

Figure 167: Escape Mission trajectory example

The impulse velocity Δv is the difference between the launch velocity needed to obtain a desired residual velocity at the infinite distance from the Earth and, the parking orbital velocity of the Spacecraft around the Earth.

4.4 Earth to Moon Transfer Paths

4.4.1 Introduction

Ever since the beginning of space exploration, the Moon has been the target of countless missions, and everything leads to believe that this will continue to be so. This certainty is focused on the recent discoveries of signs that point to the possible existence of ice at the lunar poles made by the American probes Clementine in 1994 and Lunar Prospector in 1998. The estimates indicate that there may be some 10 billion tons of ice at the lunar poles. Therefore, if the existence of this ice were confirmed, future lunar bases would have a water source capable of sustaining life. This ice could also serve as a source for rocket fuel, by separating the water into hydrogen and oxygen, thus making the Moon into a trampoline for future manned interplanetary missions.

The classical method for design of lunar transfer trajectories is the Hohmann transfer orbit. A spacecraft is injected into an orbit around the Earth at perigee that intersects the Moon's orbit near apogee. An orbit transfer maneuver is performed at lunar periapsis that places the spacecraft in a closed orbit about the Moon. This type of trajectory was used by the Apollo mission and other missions to the Moon and includes many variations including free return trajectories.

4.4.2 Earth to Moon minimal energy transfer path

The calculation of a transfer path between the Earth and the Moon can only be made through numerical integration of the equations of motion. These equations must take into account the Earth's, Moon's, and Sun's gravitational fields, and the mutual interactions between these bodies. In addition, given the complexity of the Moon's movement, a lunar mission must be planned and executed on an hour-by-hour and day-by-day basis. However, we can consider some approximations, based on the two-

body and restricted three-body problem, to reach an initial estimation of the impulse needed to transfer a probe from the proximity of the Earth to the proximity of the Moon.

We are supposing the Moon orbiting around the Earth and the orbit is circular.

An analytic solution for the optimum transfer trajectory between two circular orbits, ‚was obtained by Walter Hohmann' in 1925 for the restricted two body problem.

This solution is called the Hohmann transfer orbit which is an ellipse with the periapsis at the point of tangency with a circular Earth orbit and the apoapsis at the Moons orbit. In order to transfer a spacecraft from Earth orbit to Moon orbit, large thrusting propulsive maneuvers are performed both at perigee and apogee.

When the masses of the Earth, Moon and Sun are included, a minimum propellant consumption solution that is close to the Hohmann transfer orbit may be obtained numerically.

Travel between the Earth to the Moon involves the solution of a two point boundary value problem. In its simplest form, we have a launch site on Earth and a landing site on the Moon and we are interested in finding the path that connects these two points with minimum fuel expenditure. The problem of travel to the Moon may be conveniently separated into three separate phases; these being:

- *launch into Earth parking orbit,*
- *transfer to lunar orbit, and*
- *descent from lunar orbit to the surface of the Moon*

Here after each phase will be described.

4.4.2.1 Launch into Earth orbit

The first phase is the space vehicle lift off and its ascent to circular parking orbit located as an example at an altitude of 200 km with respect to the Erath surface.

An example of SV ascent profile, SV equatorial parking orbit and Moon orbit about the Earth are shown on figure below:

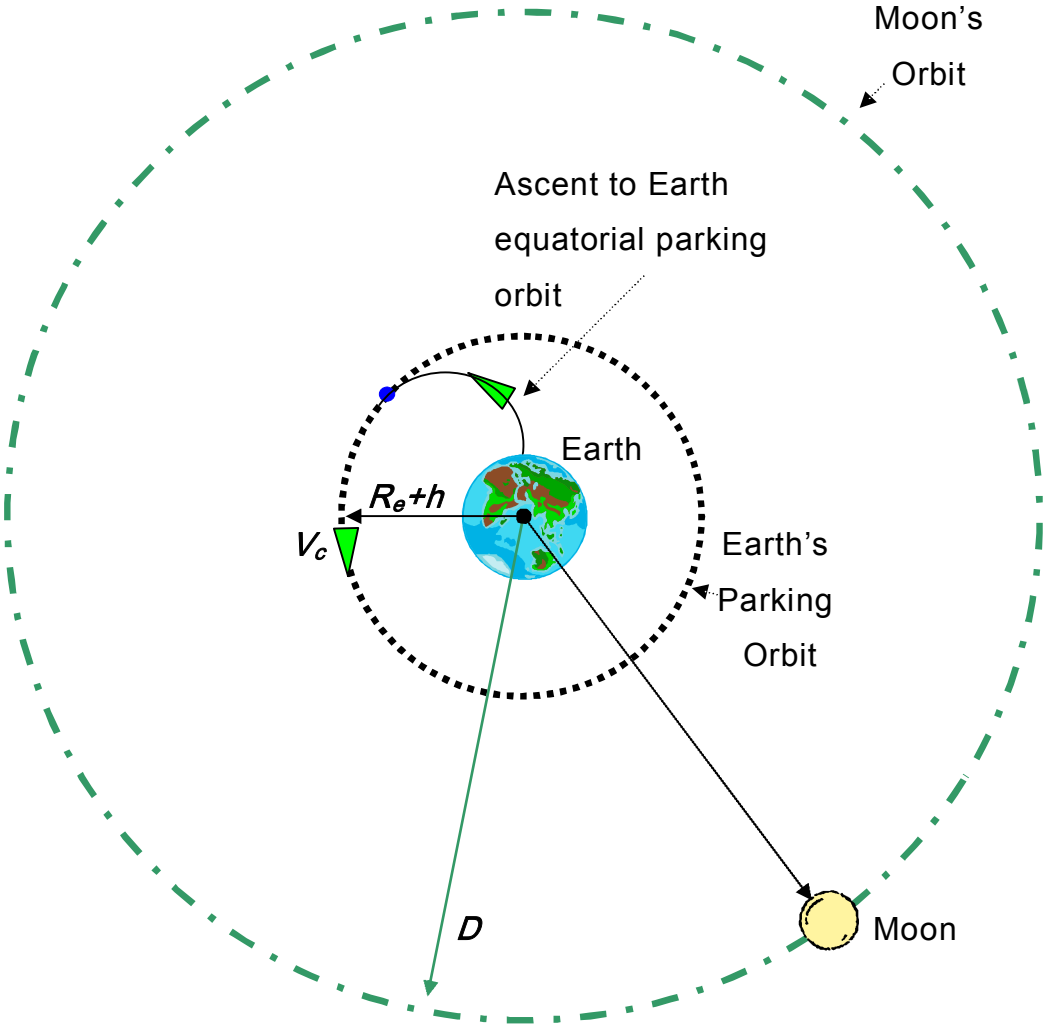

Figure 168: insertion to Earth Parking Orbit

Let us consider the altitude of the Earth parking orbit then, the corresponding orbital velocity is:

$$v_c = \sqrt{\frac{\mu_E}{R_E + h}} \cong \sqrt{\frac{398604}{6378 + 200}} \cong 7{,}800 \text{ km/s} = 7800 \text{ m/s} \qquad \text{eq 32}$$

Let us consider now a certain launch polygon P, where Φ is the polygon latitude and Az is the direction of the launch velocity **V** with respect to the Nord.

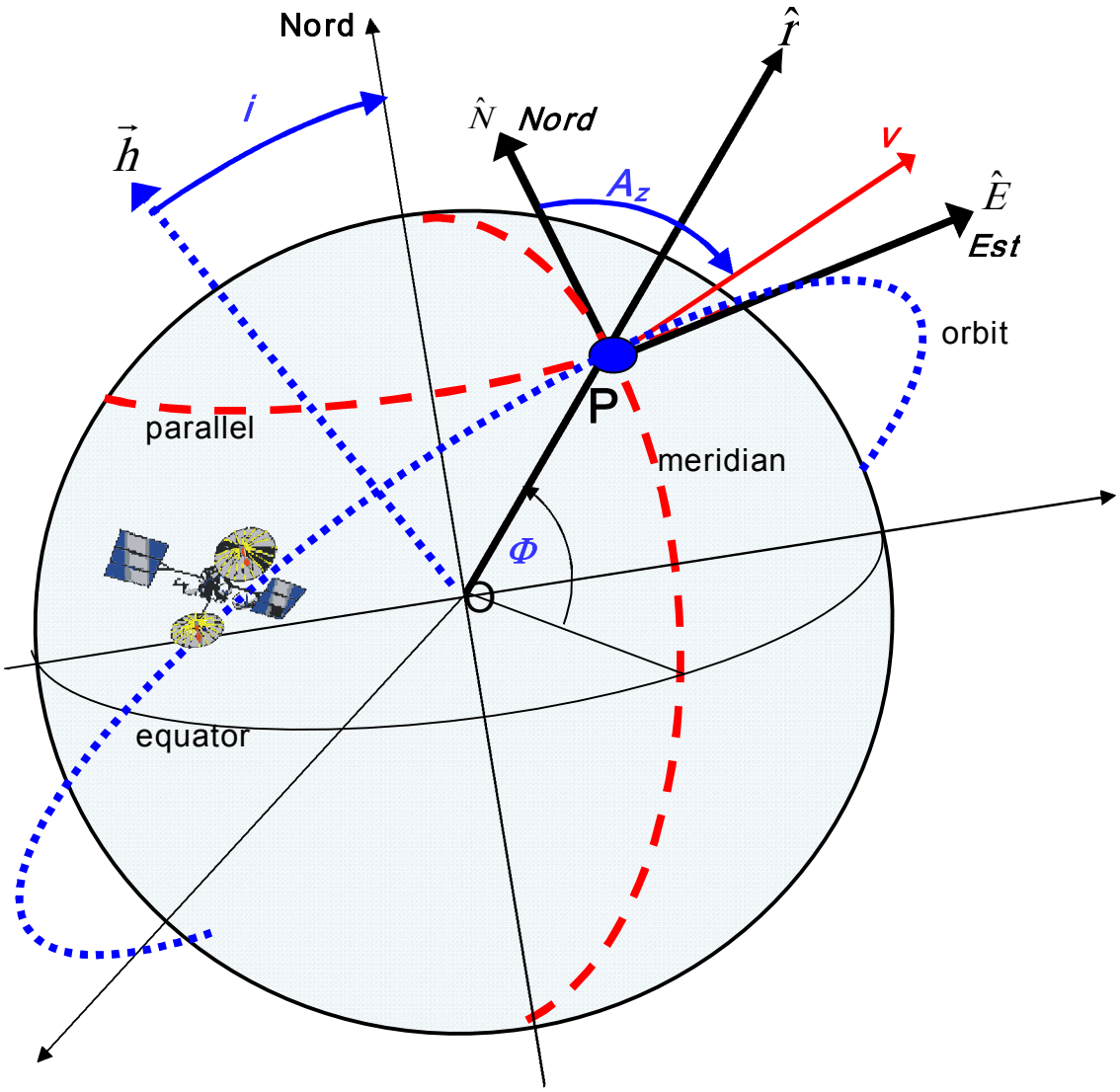

Figure 169: launch polygon and Earth rotation contribution to the impulse velocity

The Earth velocity contribution is:

$$\vec{V}_{\max} = \vec{V}_{rot,eq}\cos\phi\sin Az = \vec{\omega}_E \times \vec{R}_E \cos\phi \sin Az \qquad \text{eq 33}$$

Where the Earth velocity contribution at the equator is:

$$\vec{V}_{rot,eq} = \vec{\omega}_E \times \vec{R}_E = \frac{2\pi}{T_s} 6378 \cdot 10^3 = \frac{2\pi}{86164} 6378 \cdot 10^3 \cong 460 \ \ m/s \qquad \text{eq 34}$$

Where:

- **Ts** is the day's sideral time;
- R_E is the Earth equatorial radius;
- ω_E is the Earth rotation angular velocity;
- **Az** is the Azimuth of the Launch velocity direction;
- $\phi°$ is the latitude of the Launch base;

As we already have seen, the inclination of the Moon's orbit relative to the ecliptic plane is also constant, about λ_m =5.15°. The line of nodes of the Moon's orbit regresses slowly, revolving once every 18.6 years.
As a result, the inclination of the Moon's orbit with respect to the Earth's equator varies between 18.3÷28.6 degrees.

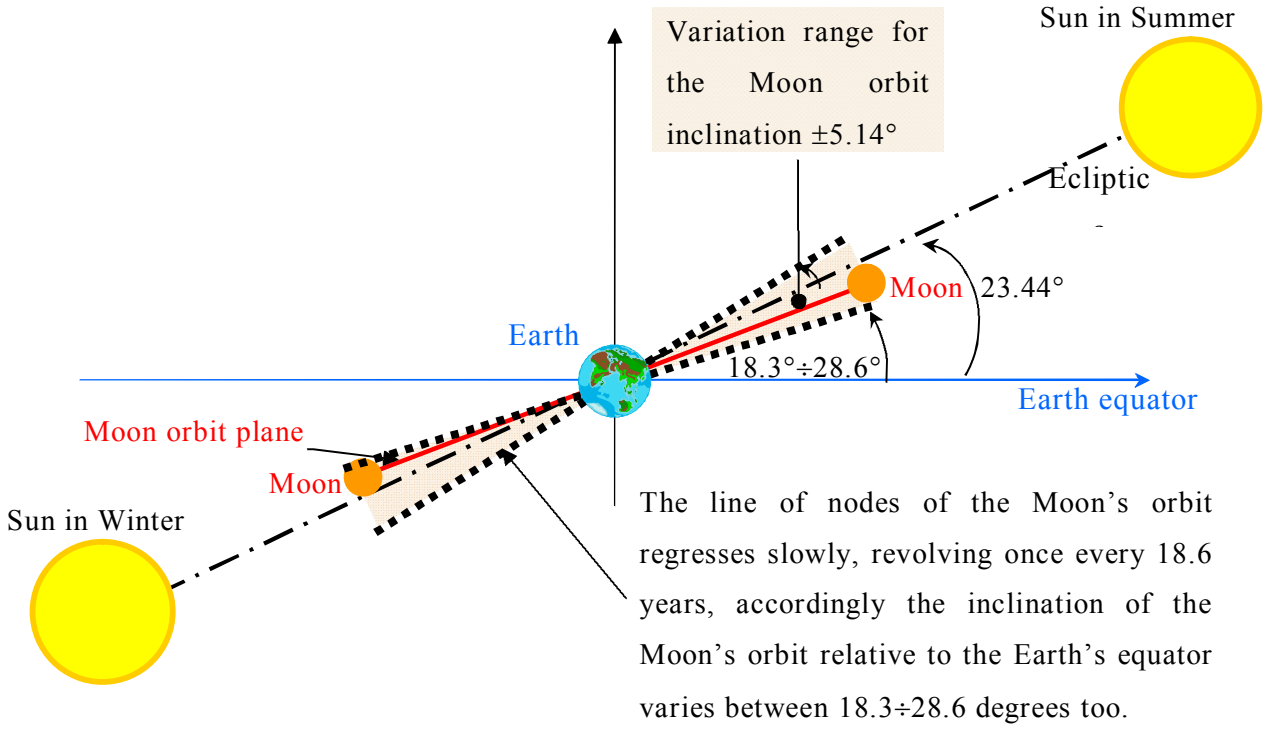

Figure 170: inclination of the Moon's orbit with respect to the Earth's equator

In case of equatorial orbit, equatorial launch base polygon and a launch velocity East directed also, we have:

- **Az**=90° is the Azimuth of the Launch velocity direction;
- **ϕ°**=0° is the latitude of the Launch base;

Then the velocity impulse contribution to the total velocity impulse is:

$$\vec{V}_{\max} = \vec{V}_{rot,eq}\cos\phi\sin Az = \vec{\omega}_E \vec{R}_E \cong 460 \quad m/s \qquad \text{eq 35}$$

Suppose now that the SV (Space Vehicle) transfer orbit trajectory lie on the lunar orbit plane, as a consequence the Earth parking orbit inclination must be chosen within 18°19' and 28°35' as a function of the launch time.

As a consequence the Earth velocity contribution to be subtracted from the total impulse velocity computation is within **408,5 m/s** (for i = 28°35') and **441,5 m/s** (for i = 18°19'), the difference is about 33 m/s so the launch time affect the propulsive ΔV requirements not so much.

$$\vec{V}_{\max} = \vec{V}_{rot,eq}\cos\phi = 460\cos\phi \qquad \textbf{eq 36}$$

The Moon's orbit inclination variation with respect to the Earth's equator, in figure below is shown.

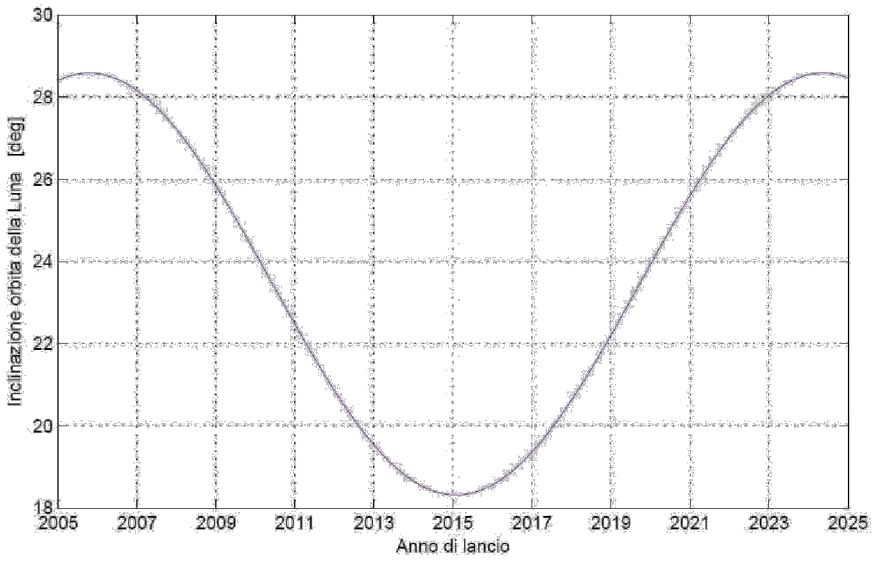

Figure 171: Moon's orbit relative to the Earth's equator inclination variation

4.4.2.2 Tsiolkovsky equation without any losses forces considered

Tsiolkovsky's rocket equation or ideal rocket equation is named after Konstantin Tsiolkovsky who independently derived it and published in his 1903 work, considers the principle of a rocket: a device that can apply acceleration to itself (a thrust), by expelling part of its mass with high speed in the opposite direction, due to the conservation of momentum.

The equation relates the Δv (delta-v) with the effective exhaust velocity **c** and the initial mass M_0 and the end mass M_f of a rocket.

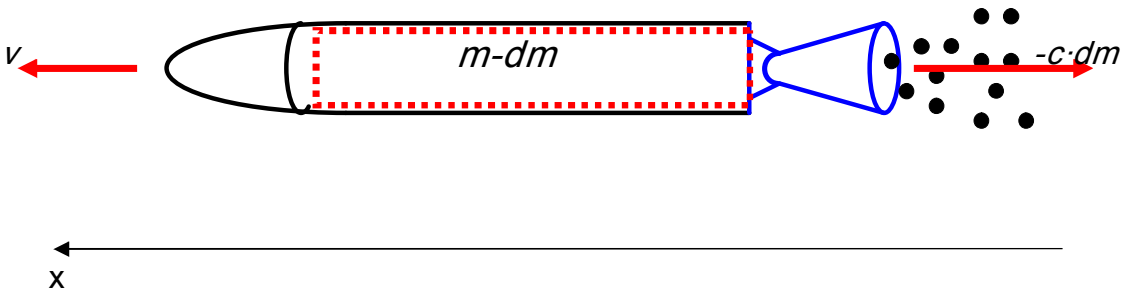

Figure 172: rocket system

We are interested to compute the useful payload velocity increment produced by a mono-stadium propulsive system which is characterized by the effective exhaust velocity **c.**

The hypotheses are:

- Thrust is the only forces which affect the rocket (we are neglecting all losses forces like Gravitational Losses, Atmospheric Drag Losses and so on);

Now suppose the following data:

- m, is the rocket mass at the generic instant t;
- v, is the absolute rocket velocity at the generic instant t;
- After little time dt, we suppose that a certain mass $-dm$ is ejected by the rocket with an effective exhaust velocity **c**. Then we aspect that for the conservation of momentum, the rocket velocity increases from v to $v+dv$;

- in fact, the momentum of the system made by the rocket and by the expelled gas in the time ***dt*** remain constant because we supposed that no external forces are affecting the rocket (Thrust, is an internal force).
- The effective exhaust velocity **c** are given by:

  $c = I_{sp} \cdot g_0$

  where:

  I_{sp} = specific impulse of a certain engine

  g_0 = gravity acceleration at the surface of the planet

  For liquid propellant like Hydrogen and Oxygen ***c ≅ 4000 m/s***

  For storable propellant engine ***c ≅ 3000÷ 3100 m/s***

Then in the time **dt** we can write the following equation:

$$(m - dm) \cdot dv = -c \cdot dm \qquad \textbf{eq 37}$$

$$m \cdot dv - dm \cdot dv = -c \cdot dm \qquad \textbf{eq 38}$$

$$m \cdot dv \cong -c \cdot dm \qquad \textbf{eq 39}$$

$$dv \cong -c \cdot \frac{dm}{m} \qquad \textbf{eq 40}$$

$$\int_{v_0}^{v_f} dv \cong -c \cdot \int_{M_0}^{M_f} \frac{dm}{m} \qquad \textbf{eq 41}$$

$$v_f - v_0 \cong -c \cdot \ln \frac{M_f}{M_0} \qquad \textbf{eq 42}$$

Finally the Tsiolkovsky equations are;

$$\Delta v = -c \ln \frac{M_f}{M_0} \quad \Rightarrow \quad \frac{M_f}{M_0} = e^{-\frac{\Delta v}{c}}$$

eq 43: Tsiolkovsky equation

Because of the exponential function, the useful payload mass are extremely affected by ***Δv/c***:

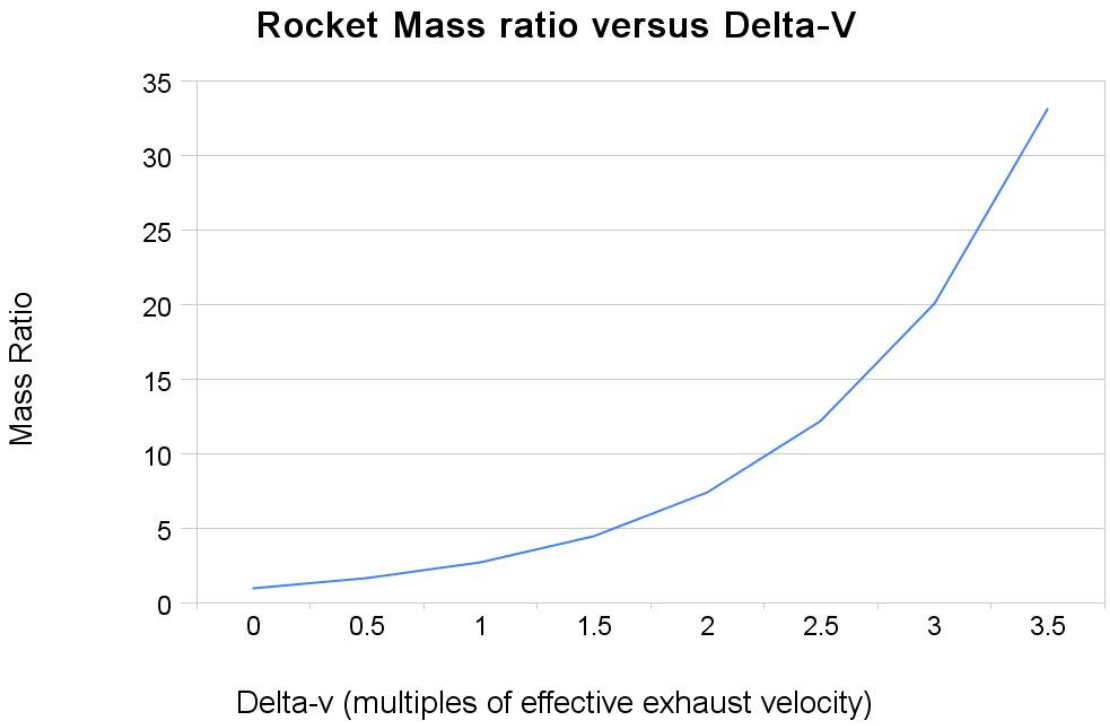

Figure 173: rocket mass ratio versus multiple of effective exhaust velocity c

4.4.2.3 Tsiolkovsky equation with some losses forces considered

In the presence of losses forces, the Tsiolkovsky equation can still be used by taking into account the velocity losses contributions in the total required Δv equation:

$$\Delta v = v_f - v_0 + \Delta v_{Losses}$$ **eq 44: total velocity requirement**

Where, the Losses are mainly due to:

- gravitational Losses ≅ 830 m/s (for Ariane)
- atmosphere drag Losses ≅ 120 m/s (for Ariane)
- not alignment Losses ≅ 800 m/s (for Ariane)

The Losses need to be considered in order to find the total velocity requirements.

Taking into account several losses the total impulse velocity required to insert a SV into **Low Earth Parking Orbit** is:

$$\Delta v = v_c - v_{Earth} + \Delta v_{Losses} = \sqrt{\frac{\mu_E}{R_E + h}} - \omega_E R_E + \Delta v_{Losses}$$
$$= 7800 - 425 + (120 + 830 + 800) \cong 9.1 \text{ km/s} = 9100 \text{ m/s}$$

eq 45

From the Tsiolkovsky equation above, we can see that once the **Δv** is fixed, then knowing the effective exhaust velocity **c** of the SV propulsive system, we can compute the amount of the entire mass system $\mathbf{M_0}$.

- $\mathbf{M_0}$=(mass_strucutres+mass_propellant+mass_usefull_payload)=***Ms+Mp+Mu***

Where:

- ***Ms***= mass of the Structures
- ***Mp***=mass of the Propellant
- ***Mu***=mass of the useful Payload

The more is **c**, the greater the useful payload mass that can be located by the SV on a certain orbit.

The Tsiolkovsky equation is plotted in the following Figure, here the parameter is the exhaust escape velocity ***c***

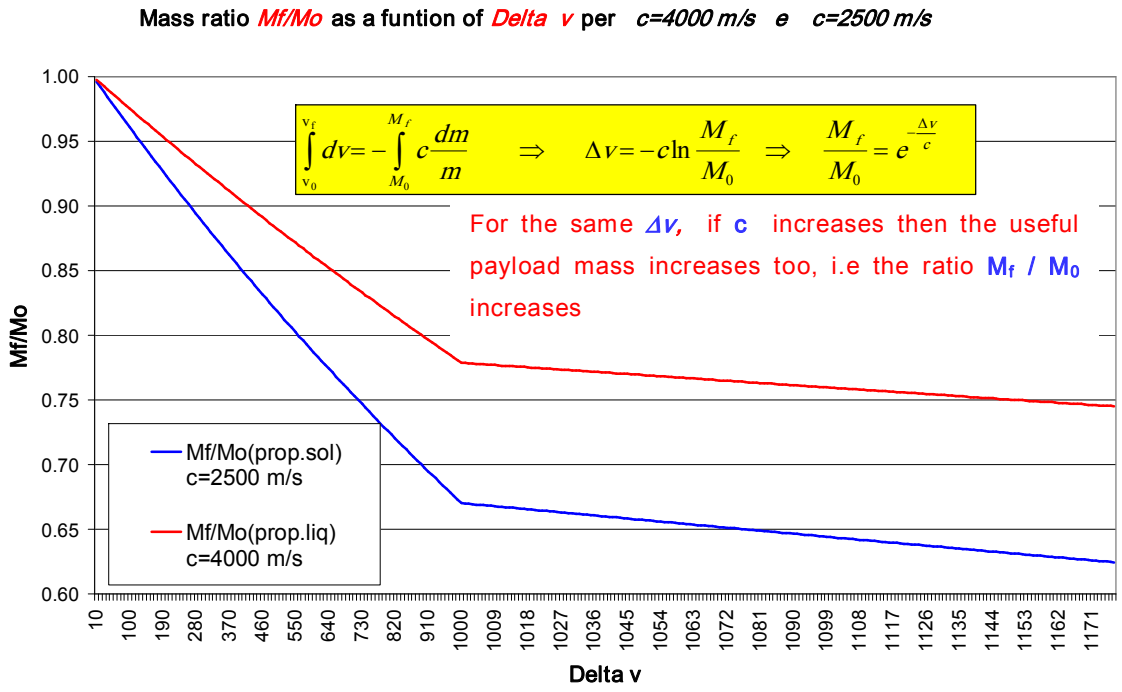

Figure 174

4.4.2.4 Transfer into lunar orbit

In order to simplify the analysis, supposing now the same orbital plane for Earth and Moon.

It is possible to establish a sort of minimal energy path required for SV transferring from the Earth to the Moon. This approach is based on the two-body (Earth-probe and Moon-probe) problems.

This maneuver is divided into two parts. In the first part, the Moon's gravitational field is neglected, and in the second part, the Earth's gravitational field is neglected. In this way, we can establish a simple procedure to estimate the impulses required for the maneuver based on Hohman's transfer.

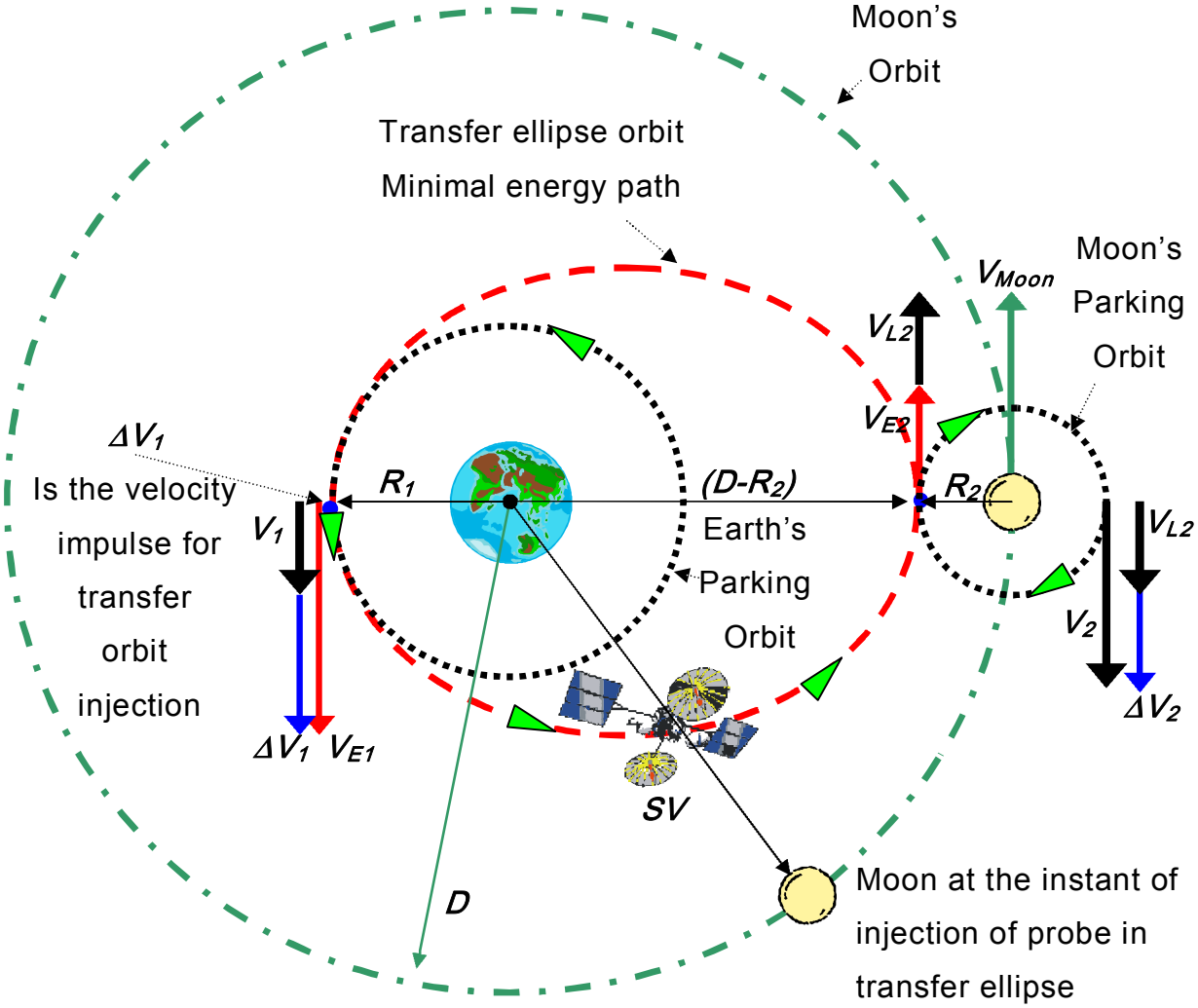

Figure 175: Hohmann minimal energy path

Figure above shows the minimal energy path, an ellipse, which is tangent to Earth's and Moon's parking orbits. The first part starts with the application of a Δ_{V1} when the vehicle attains the perigee's transfer ellipse. From Figure above, we obtain the semimajor axis of transfer ellipse, a_{min}, by

$$a_{\min} = \frac{R_1 + D - R_2}{2} = \frac{(6378+200)+384000-(1738+100)}{2} = \frac{388740}{2} = 194370 \ km$$

eq 46

where

- R_1 is the perigee's radius of the transfer ellipse and also of the Earth's parking orbit radius in the point of tangency with the transfer ellipse, suppose $R_1=R_E+200=6378+200=6578$ *km;*
- D = 384400 km is the Earth-Moon average distance considered constant, that is, we are considering the Moon to be in a circular orbit around the Earth;
- R_2 is the Moon's parking orbit radius in the point of tangency between it and the transfer ellipse, suppose $R_2=R_M+100=1738+100=1838$ *km.*

The energy per unit of mass is a function of the semi major axes. In such a way we can figure out the perigee's and apogee's speed for the transfer ellipse, V_{E1}, V_{E2}:

$$E=\frac{v^2}{2}-\frac{\mu_{Earth}}{r}=-\frac{\mu_{Earth}}{2a_{\min}}$$

$$\Downarrow$$

$$E=\left\{\begin{array}{l}\dfrac{v_{E1}^2}{2}-\dfrac{\mu_{Earth}}{R_1}\\ \dfrac{v_{E2}^2}{2}-\dfrac{\mu_{Earth}}{D-R_2}\end{array}\right\}=-\frac{GM_{Earth}}{2a_{\min}}=-\frac{\mu_{Earth}}{2a_{\min}} \qquad \text{eq 47}$$

where

- G = 6.67×10^{-11} $m^3/(s^2\ kg)$ is the universal gravitational constant and
- M_{Earth}=5.9742×10^{24} kg is the mass of the Earth.
- $\mu_{Earth}=G\cdot M_{Earth}\cong398604\ km^3/s^2$

Supposing $R_1=200$ km and $R_2=100$ km, then the velocity at the perigee and apogee are:

$$V_{E1} = \sqrt{2\left[-\frac{\mu_{Earth}}{2a_{\min}} + \frac{\mu_{Earth}}{R_1}\right]} = \sqrt{-\frac{\mu_{Earth}}{a_{\min}} + 2\frac{\mu_{Earth}}{R_1}} = \sqrt{\mu_{Earth}\left(-\frac{1}{a_{\min}} + 2\frac{1}{R_1}\right)} = \sqrt{\frac{\mu_{Earth}}{a_{\min}}\frac{(1+e)}{(1-e)}} =$$

$$= \sqrt{398604\left(-\frac{1}{194370} + 2\frac{1}{6578}\right)} \cong 10.92 \text{ km/s} = 1092 \text{ m/s}$$

$$V_{E2} = \sqrt{2\left[-\frac{\mu_{Earth}}{2a_{\min}} + \frac{\mu_{Earth}}{D - R_2}\right]} = \sqrt{-\frac{\mu_{Earth}}{a_{\min}} + 2\frac{\mu_{Earth}}{D - R_2}} = \sqrt{\mu_{Earth}\left(-\frac{1}{a_{\min}} + 2\frac{1}{D - R_2}\right)} = \sqrt{\frac{\mu_{Earth}}{a_{\min}}\frac{(1-e)}{(1+e)}} =$$

$$= \sqrt{398604\left(-\frac{1}{194370} + 2\frac{1}{380000 - 1838}\right)} \cong 0.24 \text{ km/s} = 240 \text{ m/s}$$

eq 48

4.4.2.5 Insertion into elliptical Transfer Orbit

If we consider that the Earth's and Moon's parking orbits are circular with radius R_1 and R_2, respectively, the first impulse required to insert the vehicle in the transfer ellipse, ΔV_1, is given by:

$$\Delta V_1 = V_{E1} - \sqrt{\frac{\mu_{Earth}}{R_1}} = \sqrt{-\frac{\mu_{Earth}}{a_{\min}} + \frac{\mu_{Earth}}{R_1}} - \sqrt{\frac{\mu_{Earth}}{R_1}} = \sqrt{\frac{\mu_{Earth}}{a_{\min}}\frac{(1+e)}{(1-e)}} - \sqrt{\frac{\mu_{Earth}}{a_{\min}(1-e)}} =$$

$$= \sqrt{\frac{\mu_{Earth}}{a_{\min}}\frac{1}{(1-e)}}\left[\sqrt{(1+e)} - 1\right] = \sqrt{\frac{\mu_{Earth}}{R_1}}\left[\sqrt{(1+e)} - 1\right] = V_{LEO\_Parking}\left[\sqrt{(1+e)} - 1\right]$$

$$\Delta V_1 = V_{E1} - \sqrt{\frac{\mu_{Earth}}{R_1}} = 10.92 - \sqrt{\frac{398604}{6578}} \cong 3.1 \text{ km/s} = 3100 \text{ m/s}$$

eq 49

As we can see, the first part of the maneuver is equal to classical Hohmann's transfer.

4.4.2.6 Insertion in Lunar Orbit - first method

The second part of the maneuver corresponds to the application of a second impulse to insert the vehicle in lunar orbit and not to put it in a circular orbit with radius ($D - R_2$).

Therefore, the second part is different from Hohmann's transfer procedure, because the ΔV_2 required for this maneuver should be applied in the opposite direction of the vehicle's motion.

In order to compute the magnitude of ΔV_2, we should consider the apogee's vehicle speed, V_{E2}, relative to the Moon. This speed we denoted by V_{L2}, and its magnitude is given by:

$$V_{L2} = \left| V_{E2} - V_{Moon} \right| = \left| 0.24 - 1.023 \right| = \left| -0.783 \right| = 0.783 \text{ km/s} = 783 \text{ m/s}$$

where $V_{Moon} = 1.023$ km/s is the Moon's orbital speed around the Earth (assuming circular orbit).

Since V_{Moon} is greater then V_{E2} the Moon will reach the SV.

The magnitude of ΔV_2 is immediately calculated by

$$\Delta V_2 = V_{Moon\_parking} - V_{L2} = \sqrt{\frac{GM_{Moon}}{R_2}} - V_{L2} = \sqrt{\frac{\mu_{Moon}}{R_2}} - V_{L2} = \sqrt{\frac{4903}{1838}} - 783 = 0.85 \text{ km/s} = 850 \text{ m/s}$$

eq 50

where

- $M_{Moon} = 7.3483 \times 10^{22}$ kg is the Moon's mass, and
- $\mu_{Moon} = G \cdot M_{Moon} = 4903 \text{ km}^3/\text{s}^2 = 4.903 \cdot 10^{12} \text{ m}^3/\text{s}^2$

This is an overestimation for the required impulse velocity in fact at a certain distance from the Moon, the SV will enter into gravitational Moon sphere of influence (Moon sphere influence radius Rs≅66000 km) and the SV orbit will be affected of some modifications.

The computed impulse for the insertion in Hohamann transfer orbit end finally in Lunar orbit is;

- *ΔV_1=insertion in Hohmann elliptical Transfer orbit≅ 3100 m/s*
- *ΔV_2=insertion in circular Lunar orbit at about 100 km form the Lunar surface=850 m/s*

4.4.2.7 Insertion in Lunar Orbit - second method

Another method to calculate ΔV_2 is by using the equation energy and the conservation energy principle supposing an hyperbolic orbit approaching the Moon gravitational sphere of influence.

In this method the transferring orbit, lead the probe (SV), from the outside of the Moon gravitational sphere of influence toward the Moon, the trajectory is of hyperbolic type.

Supposing now that the hyperbolic trajectory lead the probe to a certain periapsis distance with respect to the Moon.

Let us call this distance $r_{p,m}$

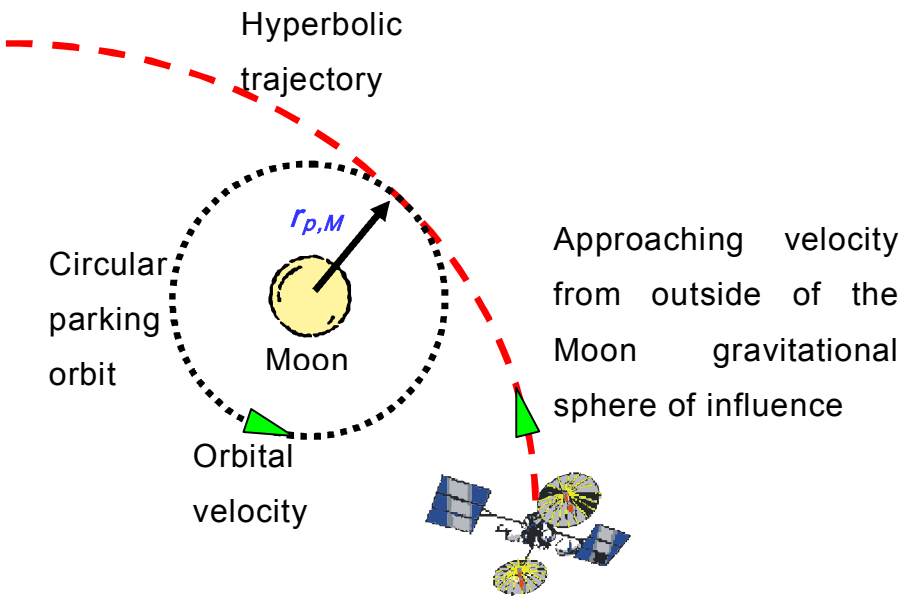

Figure 176: hyperbolic orbit close to the Moon

Then from the energy conservation equation, the velocity is:

$$E = \frac{V_{p,M}^2}{2} - \frac{\mu_M}{r_{p,m}} = \frac{V_{\infty,M}^2}{2} \quad \Rightarrow \quad \begin{cases} V_{\infty,M} = \sqrt{V_{p,M}^2 - 2\dfrac{\mu_M}{r_{p,m}}} \\ V_{p,M} = \sqrt{V_{\infty,M}^2 + 2\dfrac{\mu_M}{r_{p,m}}} \end{cases}$$

eq 51

Here, $V\infty$ is the probe (SV) velocity on the hyperbolic transfer orbit with respect to the Moon.

$V_{p,M}$, is the probe (SV) velocity at the periapsis of the Moon hyperbolic orbit:

$$v_{p,M} = \sqrt{v_{\infty,M}^2 + v_{e,M}^2} = \sqrt{v_{\infty,M}^2 + 2\frac{\mu_M}{r_{p,M}}} = \sqrt{(0.783)^2 + 2\frac{4903}{1738+100}} \cong 2.44 \text{ km/s} = 2440 \text{ m/s}$$

where :

- $v_{\infty,M} = V_{L2} = |V_{E2} - V_{Moon}| = |0.24 - 1.023| = |-0.783| = 0.783 \text{ km/s} = 783 \text{ m/s}$
- $r_{p,M} = \text{distance of the periapsis from the center of the Moon} = 1738 + 100 \quad \text{km}$
- $v_{e,M} = \sqrt{2\frac{\mu_M}{r_{p,M}}} = \sqrt{2\frac{4903}{1738+100}} \cong 2.30 \text{ km/s} = 2300 \text{ m/s}$ Moon escape velocity

eq 52

Since at 100 km of the Moon surface altitude, the Moon orbital velocity $v_{c,M}$ is

$$v_{c,M} = \sqrt{\frac{\mu_M}{r_{p,M}}} = \sqrt{\frac{4903}{1738+100}} \cong 1.633 \text{ km/s} = 1633 \text{ m/s}$$

eq 53

Then the excess of the velocity required to be zeroed is about

$$\boxed{\Delta V_2 = \Delta V_M = v_{p,M} - v_{c,M} \cong 2.44 - 1.633 \cong 0.80 \text{ km/s} = 800 \text{ m/s}}$$

eq 54

This velocity decreasing is required because the probe (SV) can be captured by the Moon gravity field and can finally orbit around the Moon at 100 km of altitude, on a circular orbit.

4.4.2.8 Flight time into elliptical transfer orbit

The flight time for this maneuver is simply half of the transferring ellipse orbital period, that is,

$$T_{Flight} = \frac{1}{2}\left(2\pi\sqrt{\frac{a_{\min}^3}{GM_{Earth}}}\right) = \pi\sqrt{\frac{a_{\min}^3}{\mu_{Earth}}} \cong 3.14\sqrt{\frac{194370^3}{398603}} \cong 426189\ s \cong 118\ \mathrm{h} \cong 5\ d$$

eq 55

The procedure described in this section is the simplest method to estimate the magnitude ΔV_{Total} for a direct transferring maneuver from the Earth to the Moon.
It makes use of two-body dynamics, for this reason, the ΔV_{Total} given above is not sufficient to put the vehicle to the desired final lunar orbit, requiring additional ΔV's to complete the mission.
We can take into account about these errors by an additional $\Delta V_{correction}$ ranging form 50 to 200 m/s.
Here it is assumed about 100 m/s.

4.4.2.9 Descent from lunar orbit to the Moon surface

In the final phase we are interested in landing on the lunar surface. So we have to figure out the velocity which the probe (SV) could have on lunar surface.
Because of the Moon rotation we should have to be take into account this effect too but, since it correspond to and additional $\Delta V \cong 10$ m/s we will neglect this effect.

4.4.2.10 Moon surface descent directly from hyperbolic orbit

Using the equation already seen above end substituting the equatorial radius of the Moon we have

$$v_{surface,M} = \sqrt{v_{\infty,M}^2 + v_{e,M}^2} = \sqrt{v_{\infty,M}^2 + 2\frac{\mu_M}{R_M}} = \sqrt{(0.783)^2 + 2\frac{4903}{1738}} \cong 2.501 \text{ km/s} = 2501 \text{ m/s}$$

where :

- $v_{\infty,M} = V_{L2} = |V_{E2} - V_{Moon}| = |0.24 - 1.023| = |-0.783| = 0.783 \text{ km/s} = 783 \text{ m/s}$
- $R_M = \text{Moon radius} \cong 1738 \text{ km}$
- $v_{e,M} = \sqrt{2\frac{\mu_M}{R_M}} = \sqrt{2\frac{4903}{1738}} \cong 2.37 \text{ km/s} = 2370 \text{ m/s}$ Moon escape velocity on the surface

eq 56: landing on the Moon surface required velocity impulse, starting form hyperbolic orbit

Since on the Moon surface the probe velocity should be zeroed then the excess of the velocity required to be zeroed is opposite i.e. -2501 m/s.
Considering the Losses of about 300 m/s (gravitational Losses for the most part), then the total impulse velocity required is about **2800 m/s**.

4.4.2.11 Moon surface descent from Moon parking orbit

The most probability landing phase will happen starting from Moon parking orbit around 100 km of altitude and not directly from hyperbolic orbit.

In these conditions, in order to landing on lunar surface, the velocity required to be zeroed is between **1600÷1700 m/s**.
This is evident by the equation below.

$$V_{c,M} = \sqrt{\frac{\mu_M}{r_{p,M}}} = \sqrt{\frac{4903}{1738}} \cong 1.679 \ \text{km/s} \cong 1700 \ \text{m/s}$$

Considering also the Losses required for a soft landing procedure close to the Moon normally about of $\Delta V_{Losses,Moon}$*=300 m/s,* (this data is also compatible with landing acceleration of 2.3 m/s^2 normally found in literature). Considering the velocity correction during the orbital transfer and orbital injection phases: ΔV_{Corc}*=100 m/s* then, in order to launch a probe (SV) from the Earth and have it safely landed on the Moon surface, the total impulse velocity required for all of the phases become:

$$\begin{aligned}\Delta V_{Total} &= V_{Eart\_orbit} - V_{Earth\_rotation} + \Delta V_{Losses,Earth} + \Delta V1_{Hohamn\_Transef} + \Delta V_{Corr} + \\ &+ \Delta V2_{Moon\_orbit\_insertion} + \Delta V_{Corr} + \Delta V_{landing} + \Delta V_{Losses,Moon} = \\ &\cong 7800 - 425 + 1750 + 3100 + 100 + 800 + 50 + 1700 + 300 \cong 15180 \ \text{m/s}\end{aligned}$$

eq 57

In the elliptical minimal energy path transfer approach, the **Δv** requirements to complete the mission are shown in Table below.

Phase	ΔV need (m/s)	ΔV Losses (m/s)	Correction (m/s)	Total impulse (m/s)
Launch into Earth orbit (from equatorial polygon)	*7800-425= =7375*	*~1750*		*~9100*
Insertion into Elliptical transfer orbit	*~3100*		*~100*	*~3200*
Total standard launcher				***12300***
Injection in Lunar Orbit 100 km altitude	*~800*		*~50*	*~850*
Lending on lunar surface	*~1700*	*~300*		*~2000*
Total LANDER				***~2850***
Total impulse	*~12940*	*~2050*	*~150*	***~15150***

Table 13: minimal energy path required ΔV for Lunar mission

The first two phases could be made by the Ariane 5 Evolution while the lunar orbit insertion and lunar surface landing phases could be made by an appropriate Lander

The previous analysis has been computed in order to have a roughly idea of the main ties and of the ΔVs required for this type of mission.
The data of the total velocity impulse is about 15.150 m/s. This velocity is an input for the Tsiolkovsky equation used to find the mass of propellant.

4.4.3 Patched-conic approach

Similar to the transfer via minimal energy ellipse, the patched-conic approach is also divided into two parts.

The basic idea is to consider the probe (Space Vehicle) as being under the influence of Earth's gravitational field starting from the moment of launch in transfer path, called geocentric conic, until the instant it reaches the Moon's sphere of influence (first part).

At this time, the probe is considered to be under the influence of the Moon's gravitational field only (second part).

The transition from geocentric motion to selenocentric motion occurs naturally along a finite arch of the probe's path when it is in the region where the geocentric conic touches or intercepts the Moon's sphere of influence; whose radius is R_S = 66300 km.

Figure below illustrates the basic geometry of patched-conic transfer.

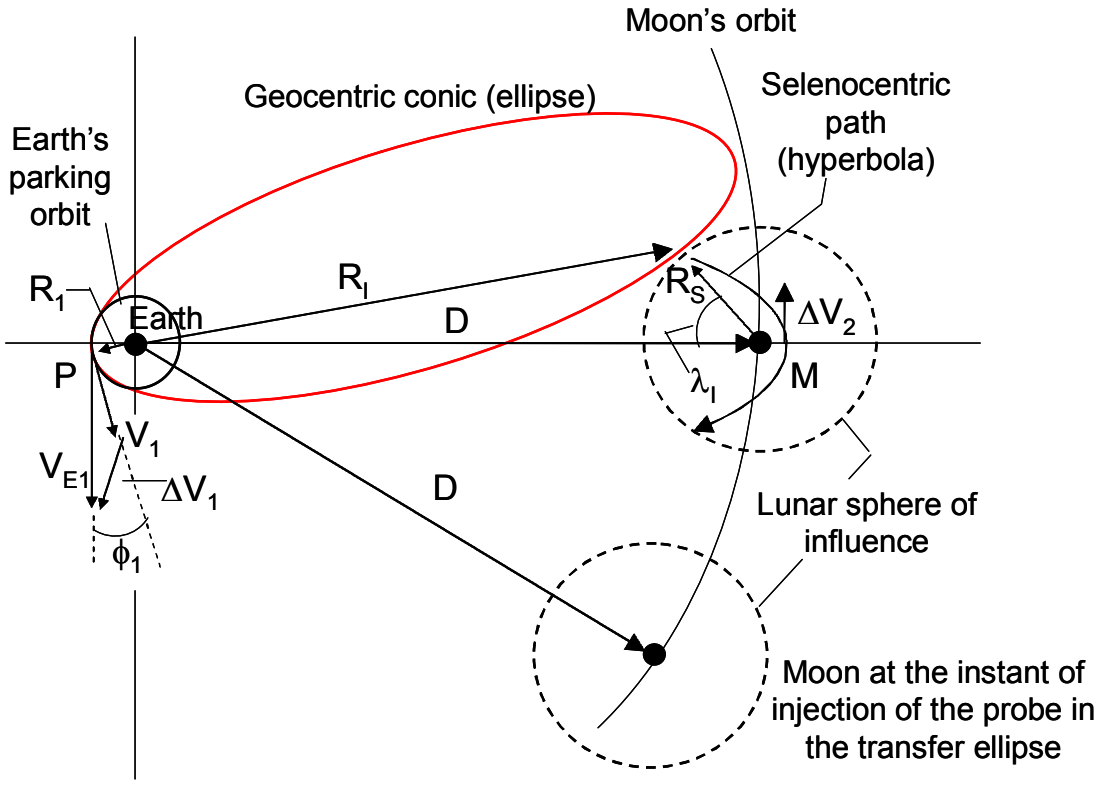

Figure 177: Geocentric conic of transfer (ellipse) and the transfer geometry seen in the geocentric coordinates system (not to scale).

In this figure, we can see the first part of the maneuver that is, leaving the Earth's parking orbit and, the geocentric-conic tangency of the Moon's sphere of influence. Theoretically, the geocentric conic could be an ellipse, a parabola, or a hyperbola, but generally, ellipses require the smallest ΔV's for the maneuver.
Figure above also shows the second part of the maneuver in which the probe gets inside the lunar sphere of influence.

The transfer starts when a ΔV_1 is applied injecting the probe into geocentric conic, this occurs at point P (Figure above). At the point at which the probe reaches the Moon's sphere of influence, point I (Figure above), it begins to move under the influence of the Moon.
When the probe reaches the periselenium of the selenocentric path, point M (Figure above), a ΔV_2 must be applied to conclude the maneuver.
In order to calculate the elements of the geocentric and selenocentric paths and the ΔV's required to transfer, we need to know at least four independent initial quantities, or three independent initial quantities and one intermediary (on the lunar sphere of influence), or final quantities. The search for these quantities is an iterative procedure. Particularly, a convenient set for these quantities is $\mathbf{R}_1$, $\mathbf{V}_{E1}$, φ_1, and λ_I (see Figure above), where:

- $\mathbf{R}_1$ is the radial distance at the point P;
- $\mathbf{V}_{E1}$ is the injection speed into geocentric conic;
- φ_1 is the flight-path angle, and
- λ_I specifies the point at which the geocentric trajectory crosses the lunar sphere of influence.

Thus, if the values attributed to $\mathbf{R}_1$, $\mathbf{V}_{E1}$, φ_1, and λ_I lead the probe to periselenium equal to the radius of the final lunar orbit planed, the procedure is complete, otherwise, a new search for other values for $\mathbf{R}_1$, $\mathbf{V}_{E1}$, φ_1, and λ_I must be started until the selenocentric path reaches periselenium equal to the radius of the final lunar orbit desired.
The procedure described above is a good approximation for preliminary mission analysis, but, in practice, errors occur in the encounter with the Moon's sphere of influence due to the disturbance of the Sun's gravitational field, and also due to the

Moon's gravitational field in the first part of the maneuver and the Earth's in the second part of the maneuver. The calculations needed to reach the values of the ΔV's are extensive and for this reason, we will not demonstrate them here. For further information's, please consult [1] and [10].
Typical ΔVs are shown on the following examples.

Considering propulsive losses caused around the Earth of about 1800 m/s and trajectory corrections of about 100 m/s then for an insertion in lunar orbit mission at an altitude around 100 km from the lunar surface we can estimate:

$$\Delta V_{orbit} \cong V_0 - V_0^{Earth} + \Delta V_{Losses\_Earth} + \Delta V_{mid\_course\_correction} + \Delta V_{circ\_lunar\_orbit} + \Delta V_{Losses\_Moon} \cong$$
$$\cong 10825 - 425 + 1800 + 100 + 700 + 50 \cong 13100 \quad \text{m/s}$$

eq 58

Where propulsive losses equal to **50 m/s** has been considered close to the Moon.

For a typical lunar surface soft landing mission we have:

$$\Delta V_{soft\_land} \cong V_0 - V_0^{Earth} + \Delta V_{Losses\_Earth} + \Delta V_{mid\_course\_correction} + \Delta V_{break} + \Delta V_{Losses\_Moont} =$$
$$\cong 10825 - 425 + 1800 + 100 + 2400 + 300 \cong 15000 \quad \text{m/s}$$

eq 59

Where, for this more demeaning mission, a propulsive losses equal to **300 m/s** has been considered close to the Moon

For a typical go-back lunar surface soft landing mission we have:

$$\Delta V_{soft\_land\_go\_back} \cong V_0 - V_0^{Earth} + \Delta V_{Losses\_Earth} + 2\Delta V_{mid\_course\_correction} + 2\Delta V_{break} + 2\Delta V_{Losses\_Moont} =$$
$$\cong 10825 - 425 + 1800 + 200 + 2400 + 2400 + 600 \cong 17800 \quad \text{m/s}$$

eq 60

Where, in order to take into account the double go/back phases, we doubled the losses and the break velocity impulses.

4.4.4 Earth-Moon transfer by gravitational capture.

Methods of Earth-Moon transfer by gravitational capture. The phenomenon of gravitational capture can be understood as the mechanism by which an object, subject only to gravitational forces, approaches a celestial body at a low speed, relative to this body, in such a way the object can be captured, and then temporarily orbits around that body. For the capture to be permanent, a dissipative force must act upon the object, such as atmospheric drag, for example. This phenomenon has been considered by various researchers to explain the origin of planetary satellites, see d Brunini [8].

Gravitational capture is possible for the general three-body problem. Usually, the initial distance between the three bodies is infinite, and after the approach, the distance between two of them remains limited. For the restricted three-body problem, the dynamical system considered in the great majority of the studies found in the literature, the third body (particle) approaches one of the primary bodies from an infinite or finite distance. After the approach, the distance between the particle and one of the primary bodies varies between well-determined values, and the primary-particle orbital energy remains negative as long as the capture lasts, as this is a temporary phenomenon.

Transfer methods based on the phenomenon of gravitational capture cannot be called conventional, especially due to the wealth of information that they offer from the semi-analytic point of view. But the mechanism can be conveniently exploited to place spacecraft in orbit around celestial bodies as a technique to reduce fuel consumption.

Some of the first studies of this theme were conducted by Belbruno and Miller.

4.5 LANDER

The purpose of LANDER is to perform the LEMMB descent from the circular orbit around the Moon to the lunar surface.

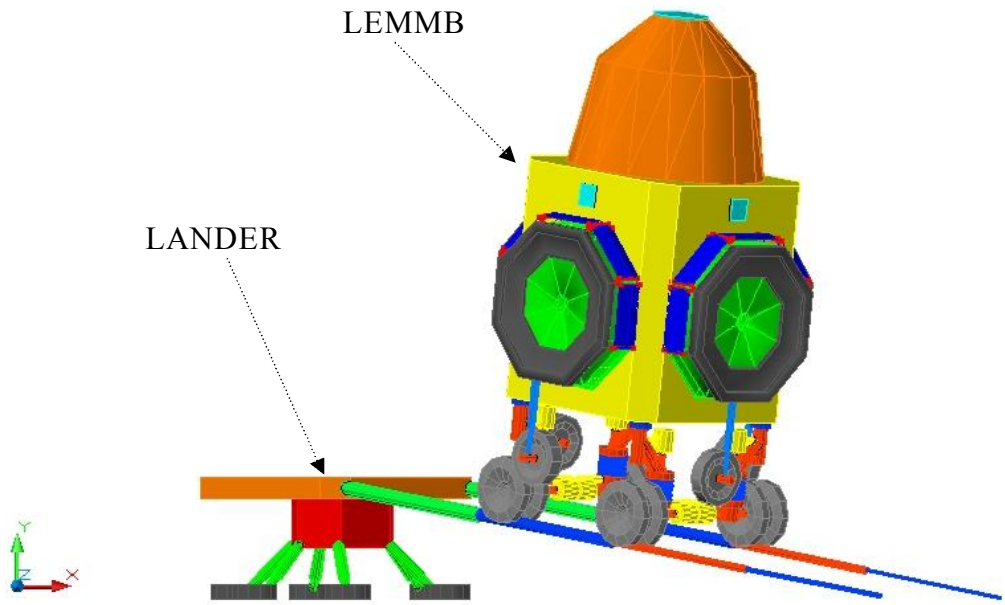

Figure 178: LEMMB living the LANDER

LANDER design is not object of this book, anyway in order to take into account the total LANDER mass we can use the Tsiolkovsky equation.

As we have seen the total useful final mass of LEMMB+LANDER should be approximately around 9÷11 tons.

- 6÷7 tons for LEMMB
- 3.5 tons for LANDER structures

Since the total Δv required to lunar orbit LEMMB insertion and to Lunar surface LEMMB landing is about 2850 m/s, then the LANDER propellant mass should approximately be:

$$M_{\text{Lander\_Propellant}} = M_0 - M_f = e^{+\frac{\Delta V}{c}} M_f - M_f = M_f\left(e^{+\frac{\Delta V}{c}} - 1\right) = 10.5 \cdot 10^3\left(e^{+\frac{2850}{3000}} - 1\right) \approx 16.6\ tons$$

eq 61

Where:

- **c** ≅ 3000 is the effective exhaust escape velocity for a storable propellant engine.
- **Δv** ≅ 2850 m/s is the required impulse velocity for LEMMB+LANDER lunar orbit injection and lunar surface landing.
- $\mathbf{M_f}$ ≅ 10.5 tons is the Useful payload+structure mass of LEMMB (7 tons)+LANDER(3.5 tons).
- 16.6 tons ≅ LANDER propellant mass.

In addition we need to consider several efficiency losses. As an example is difficult to use all the LANDER propellant in the tank, probably a little portion of the propellant could remain unburned;
In order to take into account for this effect, a usual approach is to do an overestimation around 3÷4 % for the required propellant mass. Consequently the LANDER propellant mass should be around 17.3 tons. As a matter of fact the total mass of LANDER and LEMMB should be as in table below:

LANDER mass	Mass (tons)
LANDER Structure	3.5
LANDER Propellant	17.3
Total LANDER	~21

Table 14: LANDER mass

LEMMB + LANDER mass	Mass (tons)
LANDER Structure + propellant	21
LEMMB structures + payload	7
Total	28

Table 15: LANDER + LEMMB mass

The Engine used on LANDER should have the capability of a variable thrust, in fact in order to safely land on lunar surface we need of an adaptive thrust.
Another requirement in this book is to design a launcher architecture using technologies developed or to be developed in Europe (ESA Countries).
Actually there are not European adjustable thrust engine available on the market, anyway the main engine thrust characteristics could be like that of AESTUS engine.

Aestus- Bipropellant rocket engine

Characteristics	
Propellants	MMH / N2O4
Thrust vac	30 kN
Power	43,70 kW
Specific impulse vac	324 sec
Propellant mass flow rate	8.8 kg/s
Chamber pressure	11 bar
Nozzle area ratio	84
Overall length	2.2 m
Nozzle Diameter	1.32 m
Mass	111 kg

Table 16: Aestus engine characteristics

Now for the landing phase, let us consider an average acceleration of about $a_0 \cong 2.3\ m/s^2$ then the total thrust we need is:

$$Total\_Thtust = mass_{(LEMMB+LANDER)} \cdot a_0 = 28 \cdot 10^3 \cdot 2.3 \cong 64000 \quad N \qquad \text{eq 62}$$

Using 2 Aestus engine we have approximately a thrust of 60000 N

C:\tesi_aerospaziale\lanciatori\engines.xls

Click to xls file to open a table containing the main exixting engines

4.6 Choosing between Soyouz and Ariane

Both, Soyuz and Ariane 5 are able to transport a certain payload and insert it on lunar orbit.
The main difference between Soyuz and Ariane 5 performances is the useful payload mass in an Earth escape mission, this is the fundamental information required to evaluate the best launcher for the lunar mission.

4.6.1 Soyuz Performance in Earth Escape Mission

Earth escape missions can be performed using a suborbital ascent profile with two Fregat burns. However, if Fregat fuel is used to circularize to the parking orbit after separation from the third stage, the propellant capacity of the Fregat becomes a constraint when trying to attain hyperbolic excess velocities in excess of 5.0 km/sec.

High hyperbolic excess velocity requirements must then be traded off with the amount of fuel used in the first circularization burn of Fregat. Using the third stage to achieve higher cut-off velocities will leave more fuel in the Fregat upper stage, which will allow for the attainment of escape velocities up to 6.6 km/sec by using the direct ascent profile.

Taking this all into account, two approaches are taken for presenting launch vehicle performance data for earth escape missions in Figure below as a function of the parameter C3 (square of velocity at infinity). A suborbital ascent profile is used for lower hyperbolic excess velocities (<5.0 km/s), and a direct ascent profile is used for higher ones (>5.0 km/s).

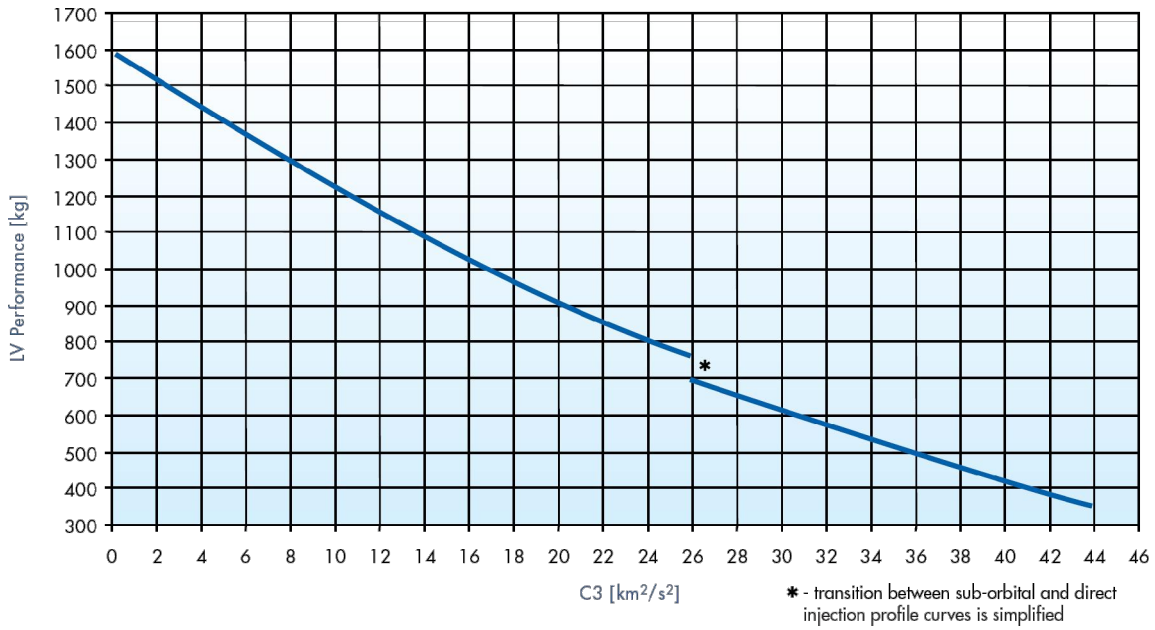

Figure 179: Soyuz LV performance for escape mission ($C3=V_\infty^2$)

We know that the Earth gravitational sphere of influence has a radius of about 1000000 km. This boundary distance should be the place where the Earth gravitational field became negligible.

Since the Moon is located about at 380.000 km from the Earth then even C3=0 could permit us to carry and insert the payload on lunar orbit.

The Soyuz performance decreases with C3, so an appropriate value of C3 could be C3=0.

This parameter can be used to evaluate the performance in the case of Lunar mission.

From the plot above the maximum performances at C3=0 is a mass of about 1600 kg. The LEMMB plus Lunar LANDER mass is around 28 tons so the Soyuz Vehicle is not able to perform the mission.

4.6.2 Ariane 5 Performance in Earth Escape Mission

The Ariane 5 family includes the Ariane 5G currently operated. The Ariane 5E is based on an evolution of the Vulcain engine that powers the cryogenic core stage. This evolution, called Vulcain 2, provides an increased thrust through an overall mixture ratio and liquid oxygen mass flow increase. The upper stage can be either cryogenic (A5ECA) or storable (A5ES). After an overlap period with the A5ECA, the A5G will be phased out.

Using a storable propellant upper stage, through a delayed ignition of this upper stage, Ariane 5, in the A5G version, has demonstrated its ability to carry a satellite weighing 3065 kg, leading to a total required performance of 3190 kg, towards the following earth escape orbit:

- infinite velocity $V\infty = 3545$ m/s
- declination $\delta = -2°$

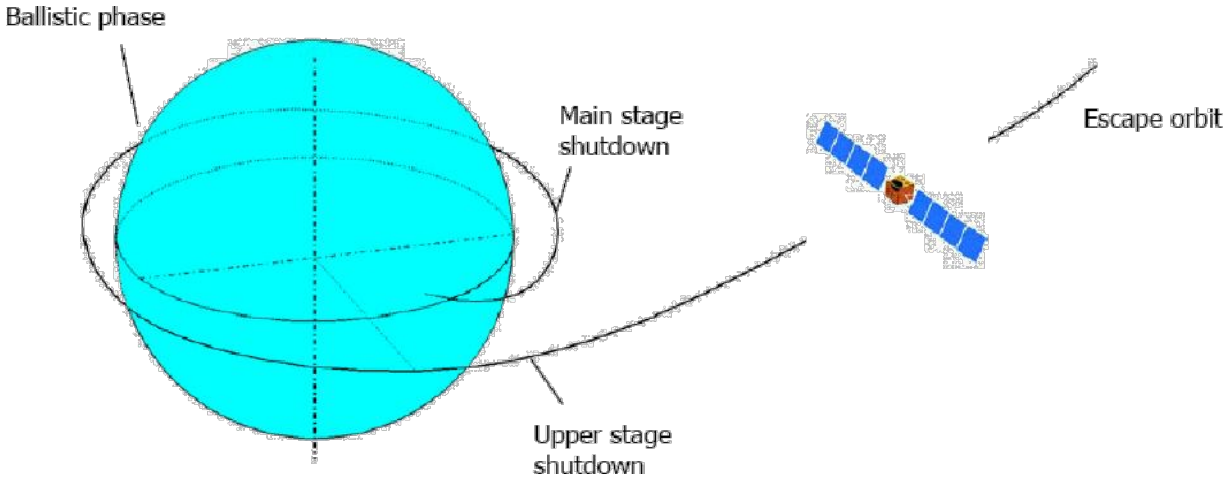

Figure 180: typical Ariane 5ECA performance

Approximately the actual Ariane 5 configuration can bring up about 3200 kg in an escape mission but, because of the mass constraint it doesn't seems the more feasible

SV (Space Vehicle) to bring up the LEMMB+LANDER (28 tons) and inserting them into lunar orbit.

Figure 181: Ariane 5G currently equipped

As a function of the stage equipment we can have several configurations which are different mass payload capable.

4.6.3 Currently Ariane 5G Typical mission profile

The engine of the cryogenic main core stage, Vulcain 2, is ignited at H_0. During 7.05 seconds, the on-board computer checks the good behavior of the engine and authorizes the lift-off by the ignition of the two solid rocket boosters.

The boosters' separation is triggered by acceleration threshold detection and the fairing is released approximately one minute later when the aerothermal flux becomes lower than the required flux (1135 W/m^2 is the standard GTO value).

The main stage shutdown occurs when the intermediate target orbit is aimed and the separation happens 6 seconds after.

After its separation, the main stage is put in a flat spin mode by opening a lateral venting hole in the hydrogen tank. This control procedure provides a re-entry and a splashdown in the Atlantic Ocean for standard A5ECA GTO missions.

The upper stage ignition occurs a few seconds after main stage separation. The upper stage cut-off command occurs when the guidance algorithm detects the final target orbit.

The separation sequence of the payloads begins 2 seconds later.

After satellites separation, the passivation sequence of the upper stage is realized by:

- the orientation of the stage towards a safe direction with respect to the satellite orbits;
- the spinning of the stage up to 45 deg/s for stabilization purpose;
- the outgassing of the tanks through valves.

A typical sequence of events for the GTO mission is presented in the figure below together with the ground track and typical evolution of altitude and relative velocity as a function of time.

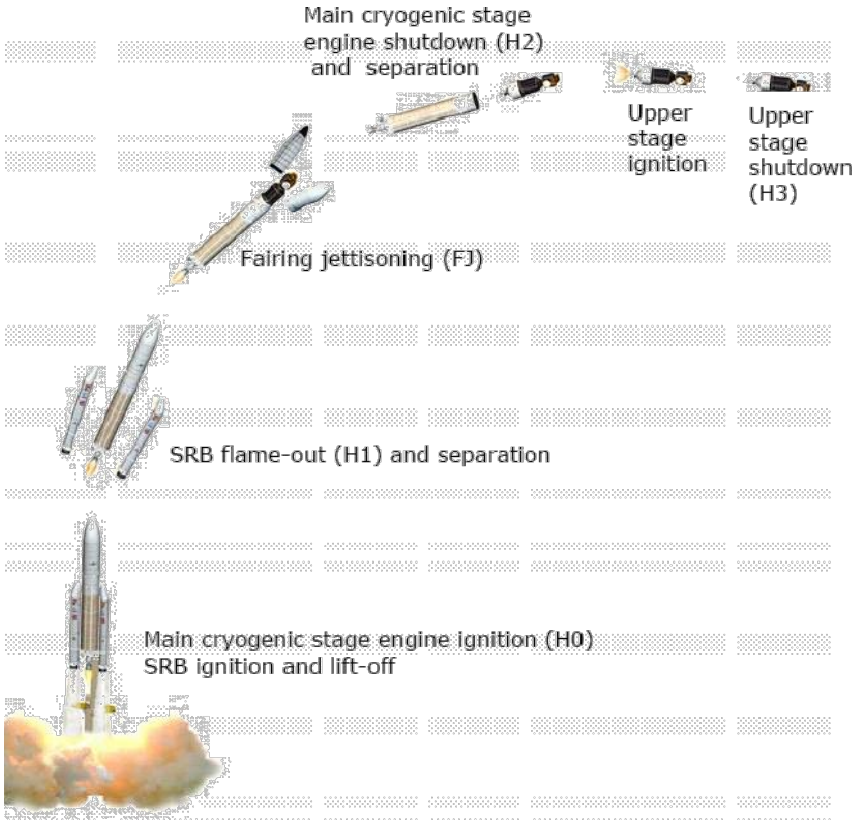

Figure 182: Ariane 5 typical sequence of events

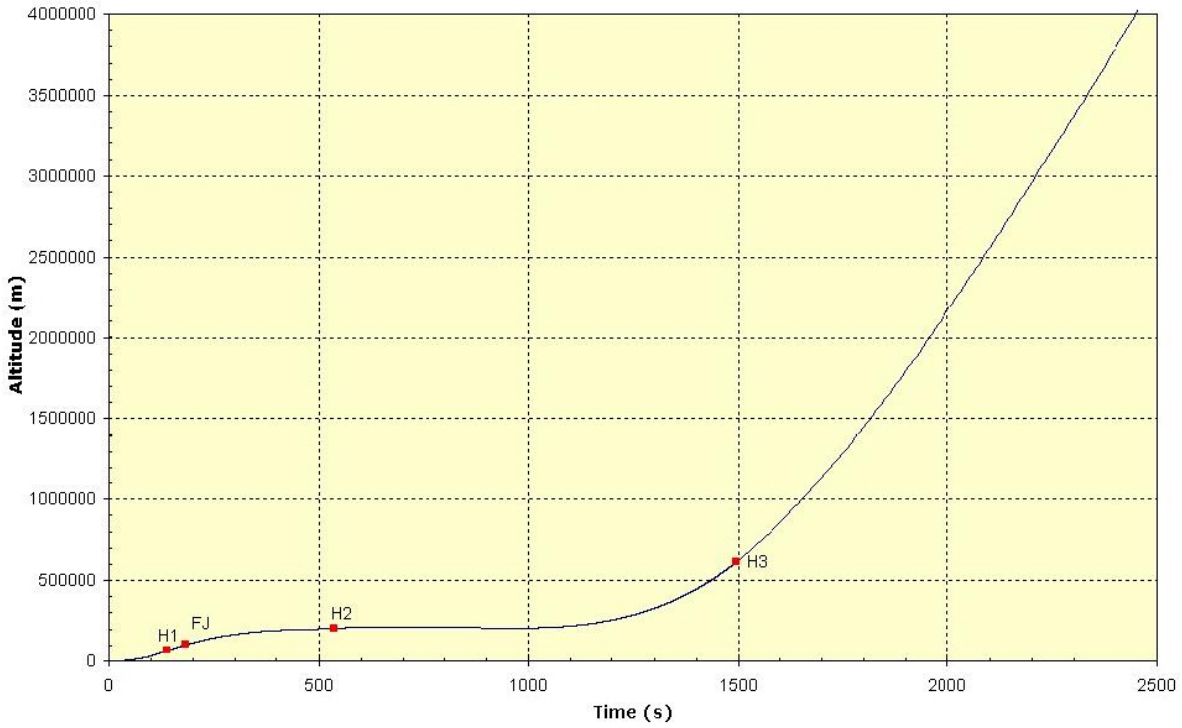

Figure: Ariane 5 typical GTO – Altitude 183

4.7 Ariane 5E–Launcher for Space Exploration

Below some performance of the Ariane 5 used like European Launcher Options for Exploration are shown. These information's are freely available on the EADS SPACE Transportation web site:

1. www.astron.nl/p/news/LO/**Iranzo**_Ariane5_LOFARworkshop.**ppt**
   Ariane 5 – A European Launcher for Space Exploration workshop [David Iranzo-Greus Head of Advanced Studies Launchers, Propulsion and Defence EADS SPACE Transporation Bremen, March 23rd, 2005]
2. *IAC-06-D2.7./A3.7.07*
   THE EUROPEAN LAUNCHER OPTION FOR EXPLORATION
   D. IRANZO-GREUS, C. CHAVAGNAC
   ASTRIUM SPACE Transportation, Les Mureaux, France

The following of the presentation is basically divided in three parts:

- in the first part the Ariane 5 launcher is analyzed;
- in the second part the standard Ariane 5 is used for a typical lunar mission where the max payload mass to bring up is around 3.2 tons;
- in the third part, a new version of the Ariane 5 called "**heavy lift**" is used in order to bring up a payload mass up to 40 tons on lunar surface.

These data are reported in this book in order to have an official lunar mission example (proposed by space launcher manufacture), we can use as a reference data sheet.
In the following paragraph we will observe how the previous computation about velocity impulses required for our lunar mission are very close to those reported in EADS SPACE example of lunar mission.

In order to evaluate the European Launcher Options for Exploration is necessary to fix some reference mission design before.

4.7.1 Design reference missions

The design reference mission are:

- Design Reference Mission #1 (Moon) : Injecting a payload directly into a Lunar Transfer Orbit (LTO): apogee altitude at 379 862 km, inclination at 5.24° and 18°, corresponding to the best and worst case scenarios.
- Design Reference Mission #2 (Mars) : Injecting a payload directly into an Earth-escape hyperbolic orbit towards Mars (typical orbital parameters): infinite velocity of 3.5 km/s (C3 = 12.25 km^2/s^2).
- Design Reference Mission #3 (LEO) : Injecting a payload into a Low Earth Orbit (LEO) capable of reaching the ISS: 400-km circular orbit, inclined at 51.6°

Below the launcher architectures are evaluated.

4.7.2 Launcher architectures to be evaluated

The launcher classes to be evaluated are the following:

- "**Standard**" - Class versions, currently operated or under evaluation since years, namely:
  - A521S version (A5ES),
  - A521A version (A5ECA),
  - A521B version (A5ECB).

- "**Enhanced**" - Class versions of ARIANE 5, combining the ARIANE 5 System's Stages as they are, at least for Propulsion Systems:
  - Clusters of 2 or 4 or 6 EAP Solid boosters & 1 EPC :
    - A521C
    - A541C
    - A561C versions,
  - Common Core Architecture with 3 EPC Core boosters (Delta-IV Heavy-like) :
    - A5X3C version with TBD EAP.

- "**Super-Heavy**" - Class version of ARIANE 5 (A5SH), designed with building blocks derived from the ARIANE 5 System, namely the VULCAIN II and VINCI engines as well:
  - Cluster of 5 VULCAIN II engines for the main stage,
  - A number of EAP solid boosters,
  - A target performance of 100 metric tons in LEO.

Therefore the possible combinations are:

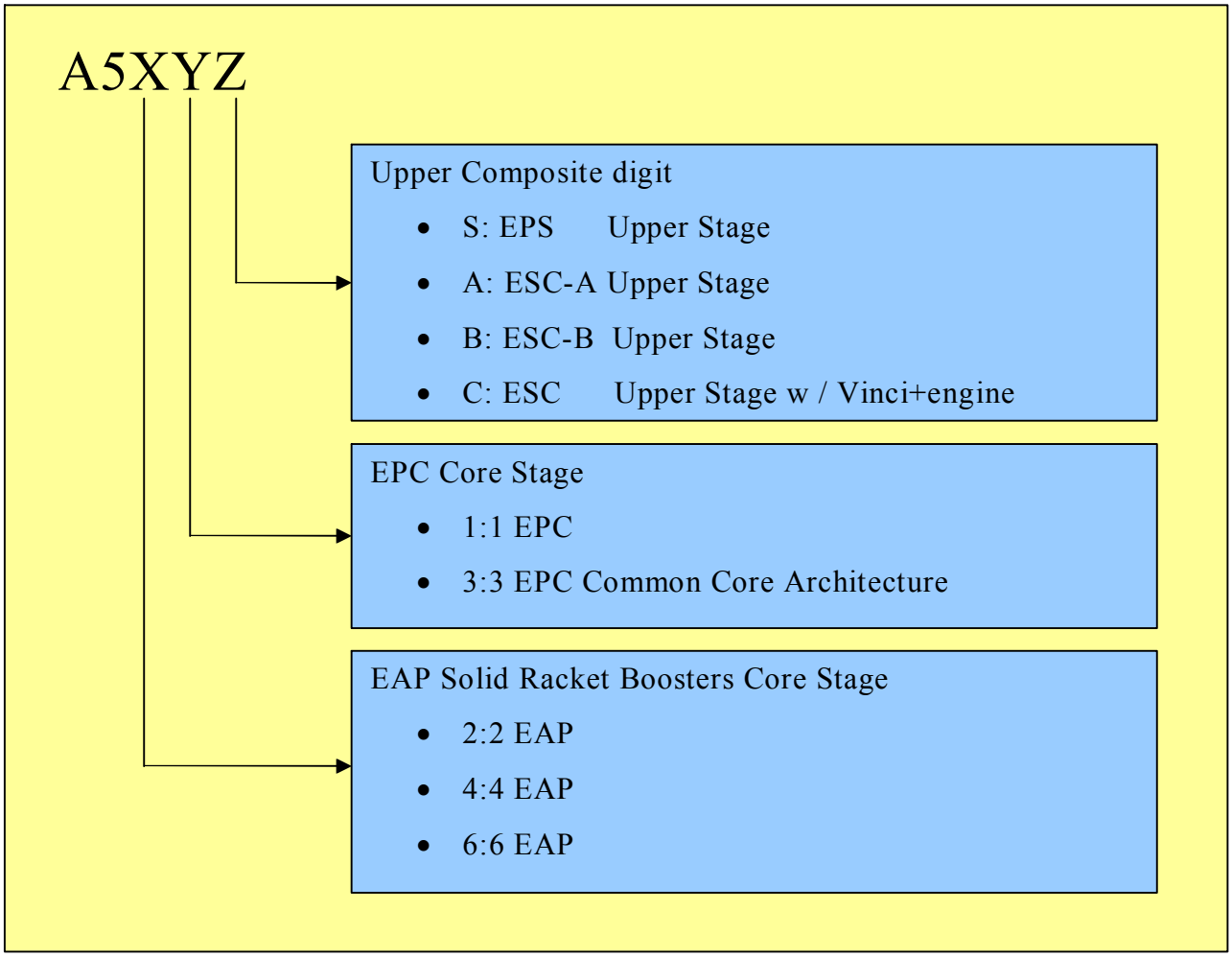

Figure 184: Ariane 5 combinations

The major assumptions used in the design of the launchers are the following:

- EAP solid boosters with as few changes as possible with respect to the current version.
- The modifications to the Cryogenic Core stage may vary depending on the version investigated: for "**enhanced**" versions, at least the interfaces with other stages either to Solid boosters, Core stages or Upper stages have to be redesigned; while for the A5SH version the Cryogenic Core Stage has to be designed from scratch with the assumption of a Propulsion System featuring 5 VULCAIN engines.

- Beyond the A5ES (A521S) version, it is assumed that the Upper stage is cryogenic and the engine depends on the version considered:
    - the HM7-B for the A5ECA version (A521A),
    - the VINCI engine for the A5ECB version (A521B),
    - an enhanced (or double) version of the VINCI for the A521C and "enhanced" versions,
    - the VULCAIN engine with an adapted nozzle for the A5SH version.

- For "**enhanced**" versions and the **A5SH** version, the nose fairing size will be adapted depending on the P/L (Payload) mass and volume.

The Ariane 5 currently used version has the main characteristics shown in table below.

CRYOGENIC UPPER STAGE (ESC-A)	
Size	∅ 5,4 m x 4,711 m between I/F rings
Dry mass	4540 kg
Structure	Aluminium alloy tanks
Propulsion	HM7B engine - 1 chamber
Propellants loaded	14,9 t of LOX + LH_2
Thrust	64,8 kN
Isp	446 s
Feed system	1 turbopomp driven by a gas generator
Pressurization	GHe for LOX tank and GH_2 for LH_2 tank
Combustion time	945 s
Attitude control powered phase	Pitch and yaw: gimballed nozzle Roll: 4 GH_2 thrusters
Attitude control ballistic phase	Roll, pitch and yaw : 4 clusters of 3 GH_2 thrusters Longitudinal boost : 2 GO_2 thrusters
Avionics	Guidance from VEB
Inter Stage Structure (ISS)	
Structure	Sandwich CFRP sheets and aluminium honeycomb core
Separation	Pyrotechnical expanding tube at the top of the ISS and 4 ullage rockets

CRYOGENIC MAIN CORE STAGE (EPC)	
Size	∅ 5,4 m x 23,8 m (without engine)
Dry mass	14700 kg
Structure	Aluminium alloy tanks
Propulsion	Vulcain 2 - 1 chamber
Propellants	170 t of LOX + LH_2
Thrust	960 kN (SL) 1350 kN (Vaccum)
Isp	~310 s (SL) 432 (Vacuum)
Feed system	2 turbopomps driven by a gas generator
Pressurization	GHe for LOX tank and GH_2 for LH_2 tank
Combustion time	540 s
Attitude control	Pitch and yaw: gimballed nozzle Roll: 4 GH_2 thrusters
Avionics	Flight control, flight termination, power distribution and telemetry subsystems, connected to VEB via data bus

SOLID ROCKET BOOSTER (EAP)	
Size	∅ 3,05 m x 31,6 m
Structure	Stainless steel case
Propulsion	Solid propellant motor (MPS)
Propellants	240 t of solid propellant per SRB
Mean thrust	5000 kN (SL)
Isp	274,5 s
Combustion time	130 s
Attitude control	Steerable nozzle
Avionics	Flight control, flight termination and telemetry subsystems, connected to VEB via data bus + autonomous telemetry

Table 17: Ariane 5 currently version; main characteristics

4.7.3 Ariane 5 with EPS

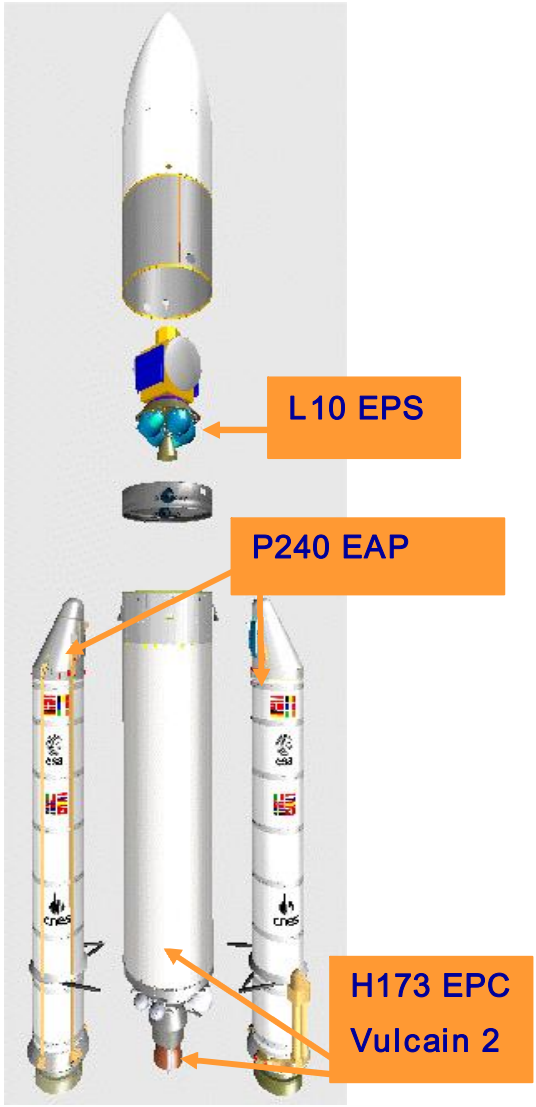

Figure 185: Ariane 5 EPS

Where:

- EAP Solid Rocket Booster
- EPC Cryogenic main core stage
- EPS Storable Propellant Stage

4.7.4 Ariane 5 with ESC-A

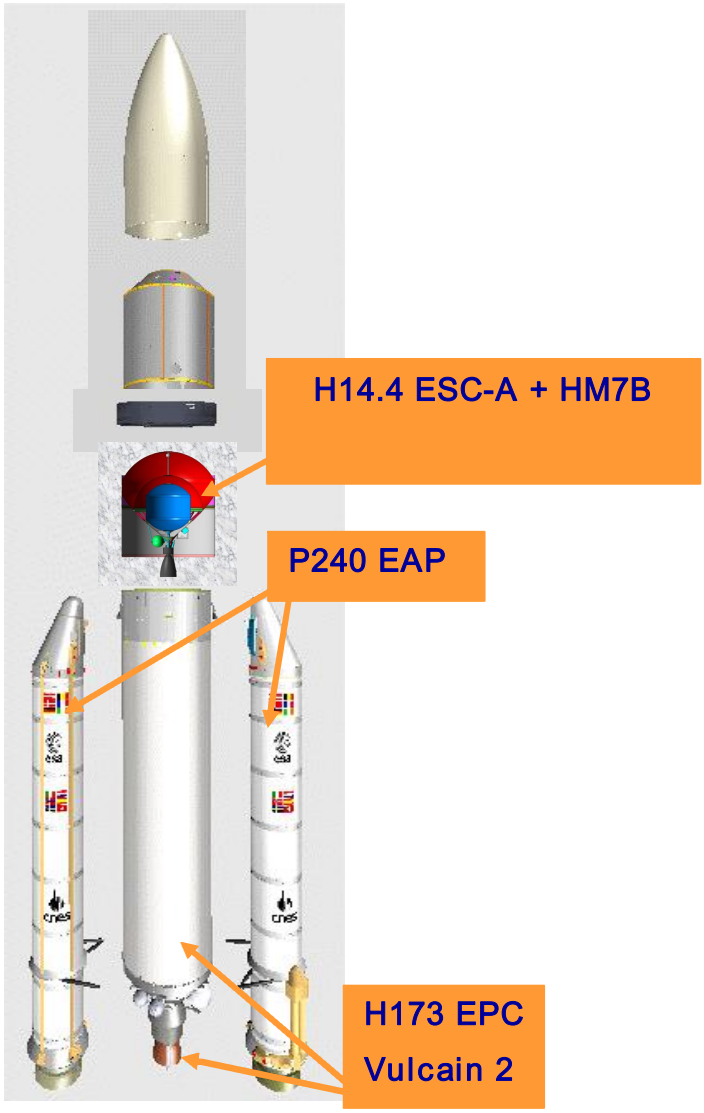

Figure 186: Ariane 5 ESC-A

Where:

- EAP Solid Rocket Booster
- EPC Cryogenic main core stage
- ESC Cryogenic upper stage

4.7.5 Ariane 5 with ESC-B

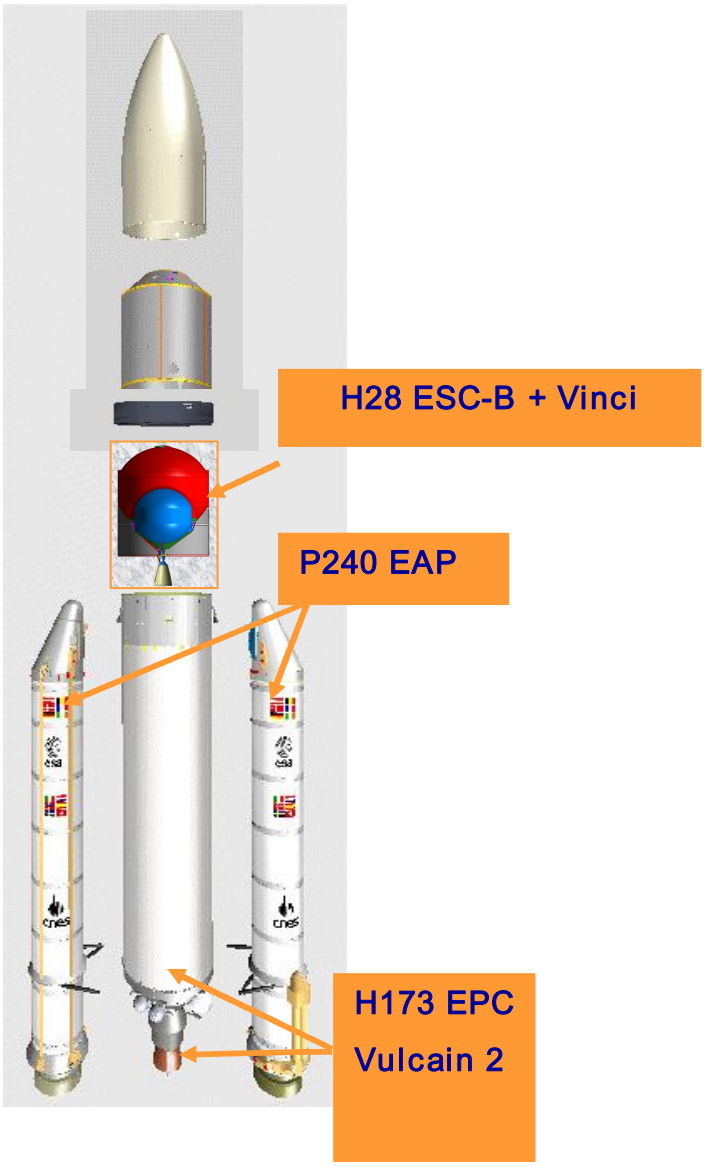

Figure 187: Ariane 5 ESC-B

Where:

- EAP Solid Rocket Booster
- EPC Cryogenic main core stage
- ESC Cryogenic upper stage

4.7.6 Evaluation of the Standard Versions

The performance of the three "**Standard**" ARIANE 5 versions has been calculated and is presented in this section.

The EAP definition corresponds to the versions with welded structure and overloaded S1 segment. The EPC stage is a H170 using a VULCAIN II. The 3 upper stage characteristics are summarized in the following table:

	A521S (EPS)	A521A (ESC-A)	A521B (ESC-B)
Engine	Aestus	HM7	VINCI
Propellant	N2O4/MMH	LH2/LO2	LH2/LO2

Table 18: standard Ariane 5 upper stage

The following table summarizes the performances of ARIANE 5 with the various upper stages.

	TARGET ORBIT	PAYLOAD (tons)
A521S	LTO (i free = 5.24°)	5,0
	LTO (i = 18°)	4,6
	Mars (Vinf = 3.5 km/s)	3,2
	LEO (400 km, 51.6°)	19,7
A521A	LTO (i free = 5.24°)	7,8
	LTO (i = 18°)	6,8
	Mars (Vinf = 3.5 km/s)	5,1
	LEO (400 km, 51.6°)	18,3
A521B	LTO (i free = 5.24°)	10,2
	LTO (i = 18°)	9,7
	Mars (Vinf = 3.5 km/s)	8,0
	LEO (400 km, 51.6°)	23,2

Table 19: standard Ariane 5 performance

4.7.7 Evaluation of Enhanced Version

The performance of the three "**Enhanced**" ARIANE 5 versions has been calculated and is presented in this section.

4.7.7.1 Upper Composite Propulsion: VINCI 200-kN

During earlier VINCI program steps, reference thrust has been modified from 155 kN to 200 kN.
The engine mechanical layout will be close to the current engine definition

4.7.7.2 Upper Composite Propulsion: VINCI 360-kN

This engine is composed of:
• two thrust chambers (combustion chamber + CMC nozzle extension)
• one hydrogen turbo-pump and one oxygen turbo-pump,

Figure 188: 360-kN CAD views

Thrust	360 kN
Mixture ratio	5.8
Isp	464 s
Design life	6 starts, 1 300 s
Total Mass	1 207 kg

Table 20: VINCI 360 kN - Performances summary

For the performance evaluations and launcher architecture related tasks, the VINCI 360-kN engine has been assumed.

4.7.7.3 Performance side

Five "Enhanced" versions were analyzed: A521C, A541C, A561C, A543C and A563C. These configurations vary the number of EAP and EPC stages and include a cryogenic upper stage with a loading to be optimized.

The EAP definition corresponds to the versions with welded structure and overloaded S1 segment.

The EPC stage is a H170 using a VULCAIN II. The upper stage is based on a bi-chamber VINCI engine described above. The following table summarizes the performances of the "Enhanced" launcher versions for DRM 1 and 2.

	ORBIT	PAYLOAD (tons)
A521C	LTO (i free = 5.24°)	10,2
	Mars (Vinf = 3.5 km/s)	7,9
	LEO (400 km, 51.6°)	24,8
A541C	LTO (i free = 5.24°)	17,1
	Mars (Vinf = 3.5 km/s)	13,6
	LEO (400 km, 51.6°)	37,9
A561C	LTO (i free = 5.24°)	21,9
	Mars (Vinf = 3.5 km/s)	17,7
	LEO (400 km, 51.6°)	48,0
A543C	LTO (i free = 5.24°)	26,7
	Mars (Vinf = 3.5 km/s)	21,6
	LEO (400 km, 51.6°)	57,1
A563C	LTO (i free = 5.24°)	35,8
	Mars (Vinf = 3.5 km/s)	29,2
	LEO (400 km, 51.6°)	76,4

Table 21: performance of "Enhanced" version

4.7.7.4 Architecture

Two versions were analyzed from an architecture standpoint:

- one A5X1C featuring 1 EPC and TBD EAP (2 or 4 or 6) and
- another A5X3C featuring 3 EPC and TBD EAP (4 or 6).

For the A5X1C versions, the version featuring 4 EAP was evaluated.
The increase of dynamic pressure, maximum static acceleration and the number of boosters of the enhanced version compared to those of A5ECB will involve an increase of lower central core structure masses of A5ECB. The impacted lower composite structures are:

- JAVE-C (Jupe AVant Equipée-C): Front skirt ;
- RIE (Réservoir Isolé Equipé): Tank;
- BME (Bâti-Moteur Equipé): Engine thrust frame;
- Nose Fairing;

The overall mass increase of the EPC core stage for a A541C version (wrt A5ECB) is estimated at 1,4 tons.

4.7.7.5 Launcher Design

For the EAP distribution, there are two options.

- Option 1: EAP equally distributed (90°): This solution requires some modifications on the EPC especially the line layout and the engine thrust frame (BME) and JAVE front skirt. Moreover the impacts one the EAP are minor (except the DAAR rear connections).

- Option 2 : EAP clustered together in pairs (Energia-type configuration): This solution requires a dedicated connection between the EAP two by two and the separation phase could be an issue. This solution allows keeping the line layout as it is and hence limits impacts to the EPC Vulcain feeding S/S. Some modifications to the EPC engine thrust frame and to the JAVE have to be implemented.

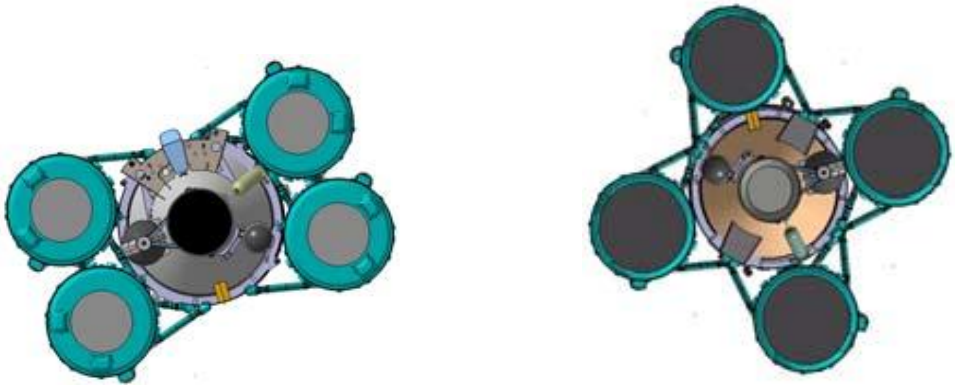

Figure 189: A541C configurations (option 1 on the left and option 2 on the right)

Summarized the advantages and disadvantages, the option 1 is considered as the most suitable alternative limiting the set of modifications and complexity mainly on the EAP.

Thus the 90° EAP distribution is selected.

The following EPC design impacts are identified through this preliminary assessment:

- EPC feedings line layout
- EPC Front skirt-LAVE (need to strengthen radial load behavior using a central beam fro instance);
- EPC engine thrust frame –(need to strengthen the box structure to withstand EAP loads);
- Ground-to-launcher I/F shifting from the current radial location to a lateral disconnection system;

4.7.7.6 H48 Upper stage design

When taking into account the loads derived from trajectory computations, different upper stage computation may be traded.

Basically two options rise:

- ARIANE 4 H10-like (both tanks have a diameter equal to the diameter of the upper stage) and
- ESC-A & B like (one of the tanks has a smaller diameter).

An ARIANE 4 H10-like architecture is preferred for optimizing the stage overall mass budget and maximizing the commonalities with the EPC lower stage (bulkheads and commonalities with the EPC lower stage (bulkheads and tanks cylindrical sections).

The Engine Thrust Frame design has to fit with the bi-chamber engine so the most suitable configuration from an equipment integration standpoint is a cylinder cross design.

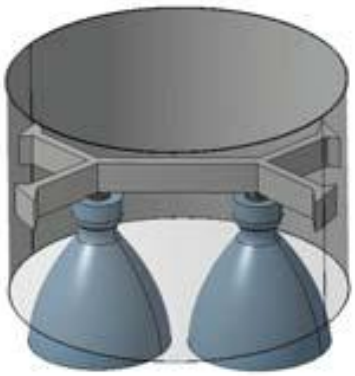

Figure 190: H48 upper stage Engine Thrust Frame

Allowing for a volume between the upper and lower composites, there is the need for a stretched interstage structure.

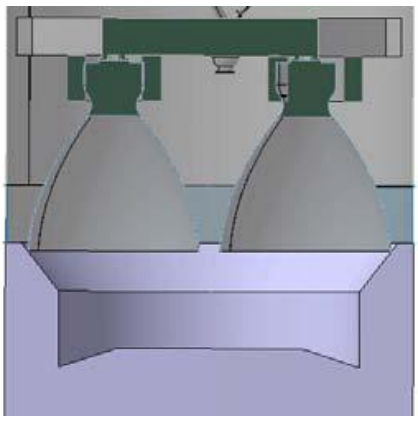

Figure 191: Section of the H48 Engine Thrust Frame and the EPC JAVE Front Skirt

The design of this inter-stage structure will have to be carefully addressed: the mass budget of the side remaining on the upper composite is a direct penalty to the P/L

mass. So an alternative option is to get a two-side structure with additional separation plane in the vertical direction.

The layout of the lines, LAO and LAH for VINCI Engine and LPO and LPH for pressurization is sketched hereafter. The part above the upper stage is derived from ARIANE 5, with a VEB and a long version of the fairing.

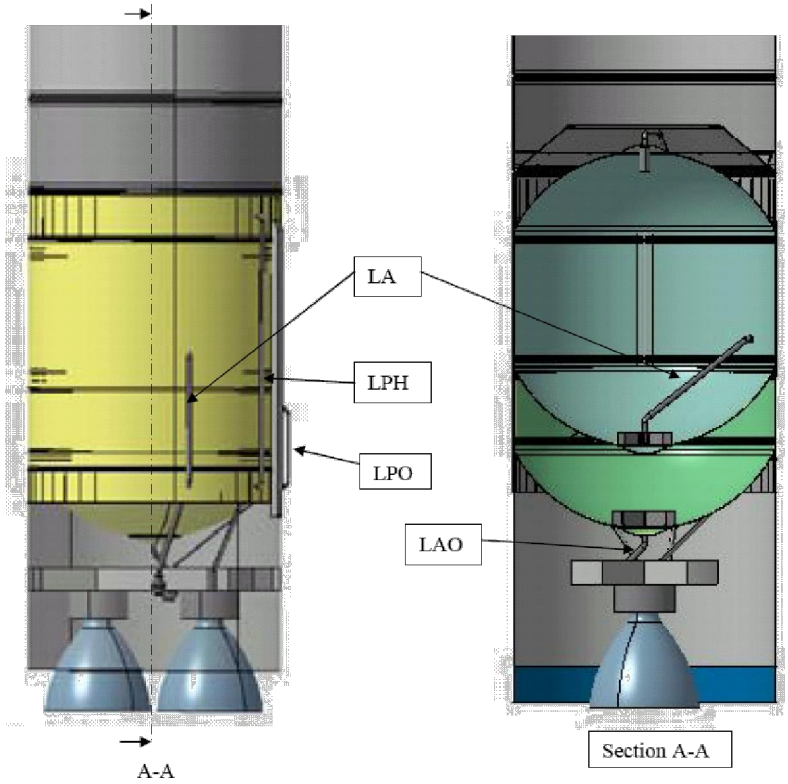

Figure 192: upper stag H48 main lines

The upper stage mass budget is estimated extrapolating the current ESC-A mass budget and results from other advanced projects (especially ESCB studies), leading to an overall mass of 6,7 tons.
The main dimensions of the A541C enhanced version of Ariane 5 featuring an H48 upper stage are sketched below. The overall length is 60.7 meters and the GLOW is around 1400 metric tons.

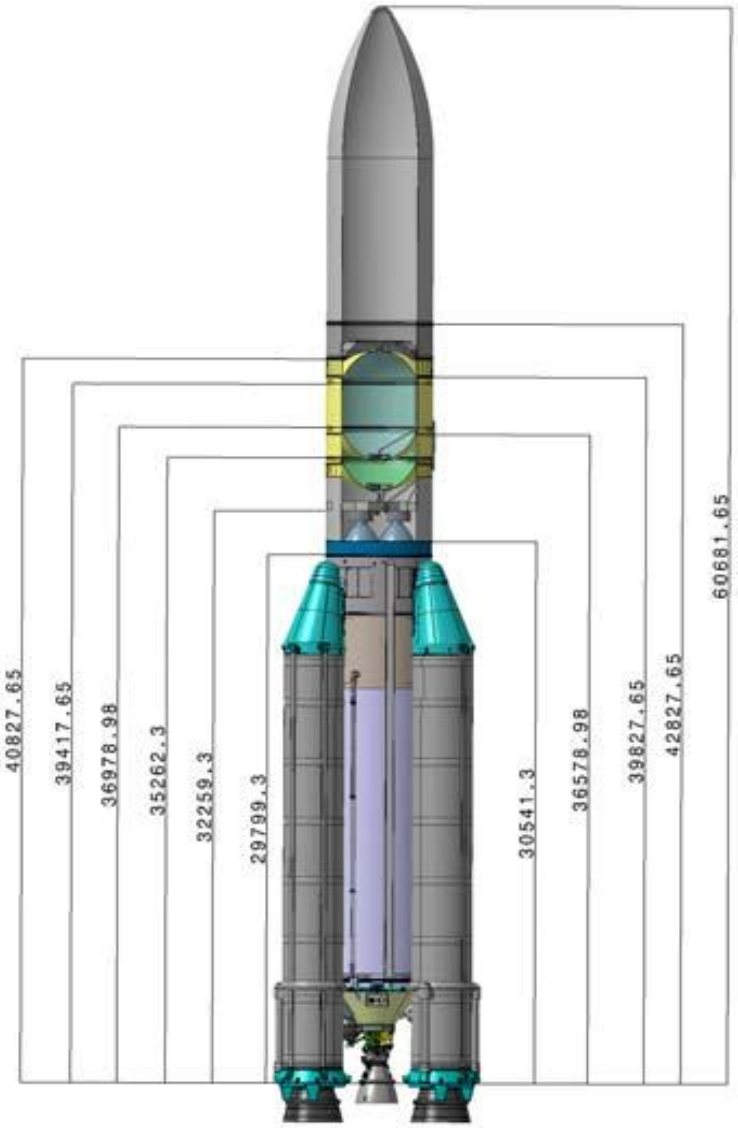

Figure 193: A541C version general view

4.7.8 Evaluation of the Super-Heavy Version

The assumed architecture is the following:

6 EAPs are required to reach the target performance with 5 VULCAIN II engines on the first stage (A5SH-1) and 1 VULCAIN II engine on the upper stage (A5SH-2). The high mass of the upper composite does not allow using a VINCI engine on the upper stage.

A5SH-1 architecture: to simplify the architecture separate bulkheads are chosen. Even if the feasibility of large-diameter separate bulkheads is not demonstrated, it is clear that it will represent a smaller challenge than using a common bulkhead.

A5SH-2 architecture: the optimum staging leads to a propellant loading of 540 tons. Given the length of the EAPs, these can be attached in the inter-tank structure or above the tanks. The architecture analysis below shows the final configuration chosen and its justification.

The final staging obtained is the following:

EAP	P1427
A5SH-1	H540
A5SH-2	H115
LEO P/L (Payload)=100000	
GLOW=2470	

Table 22: A5SH staging

The EAP definition (6EAPs per launcher) corresponds to the version with welded structure and overload S1 segment.

The A5SH1 stage is an H540 using 5 VULCAIN II engines. The A5SH2 upper stage is an H115 using 1 VULCAIN II engine.
The VULCAIN II performance has been assumed to be the same as the current performance.

4.7.8.1 A5SH Performance result

The following table summarize the performances of the Super Heavy Launcher version on the reference mission:

ORBIT	PAYLOAD (tons)
LEO (400 km, 51.6°)	100,4
LTO (i free=5.24°)	44,7
LTO (I =18°)	44.3
Mars (V∞=3.5 km/s)	35.8

Table 23: performance of A5SH super heavy version

4.7.8.2 Propulsion of the lower composite

A preliminary architecture study has been performed in order to initiate propulsion system trade off. Three main assumptions have been made:
five Vulcain II engines, LOX tank in upper position with common bulkhead and engine gimballing angle: ±10° ,

One of the main topics is the LOX feeding system architecture. Three main alternatives are to be considered:

- Ariane 5 EPC like external LOX line with an upper elbow;
- For each engine, one internal LOX line passing through the LH2 tank within insulating tunnels. This solution has been used for Saturn IV first stage;
- One common internal LOX line ended by a manifold (proposed solution);

The first solution is easier to manufacture than the others. But an upper elbow brings more pressure losses. LOX pumps cavitations is more likely. The second one is the best on regarding hydraulic pressure losses, but is heavier than the third one.

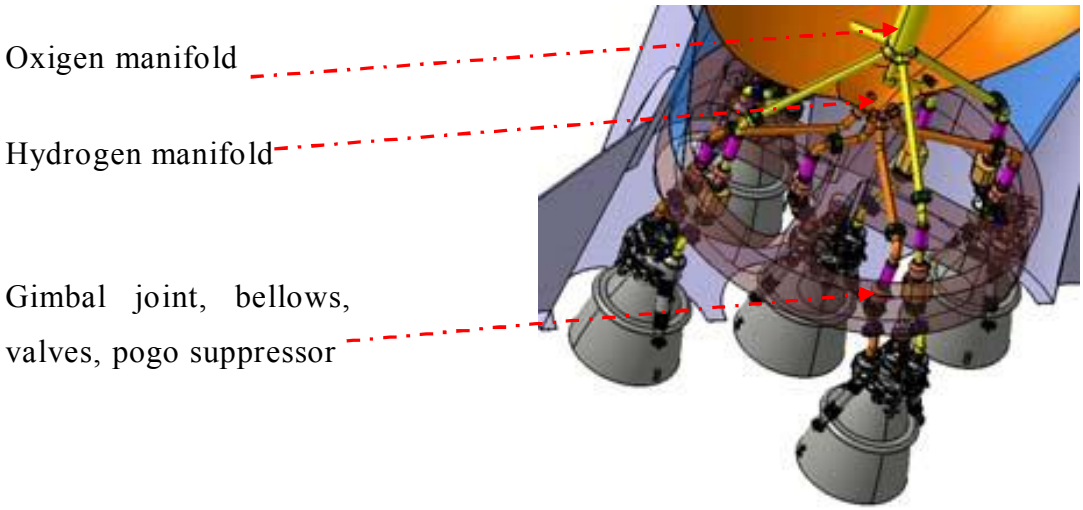

Figure 194: A5SH propulsion bay feeding system

4.7.8.3 Architecture: A5SH-1 (H540) core stage

When taking into account the required diameter for the lower stage to accommodate 5 Vulcain II engines, the common-bulkhead solution does not seem feasible. Thus, a separate tanks configuration is chosen.

The minimum stage diameter required to fit 5 VULCAIN engines, with 8 degrees steering angle, is ∅ 9.8 m. Larger diameters haven been traded trying to get the EAPs interfaces to the core stage at feasible locations.
The following figure shows the various configurations. The red lines represent the functional length of EAP (i.e. that the EAP interfaces are located at the extremity of the red lines). The ∅ 9.8 m has been selected as the most feasible one. The DAAR rear interfaces are located to the Engine Thrust Frame, and the DAAV front interfaces are located to the inter tank structure.

The EAP are equally distributed around the A5SH-1 core stage.

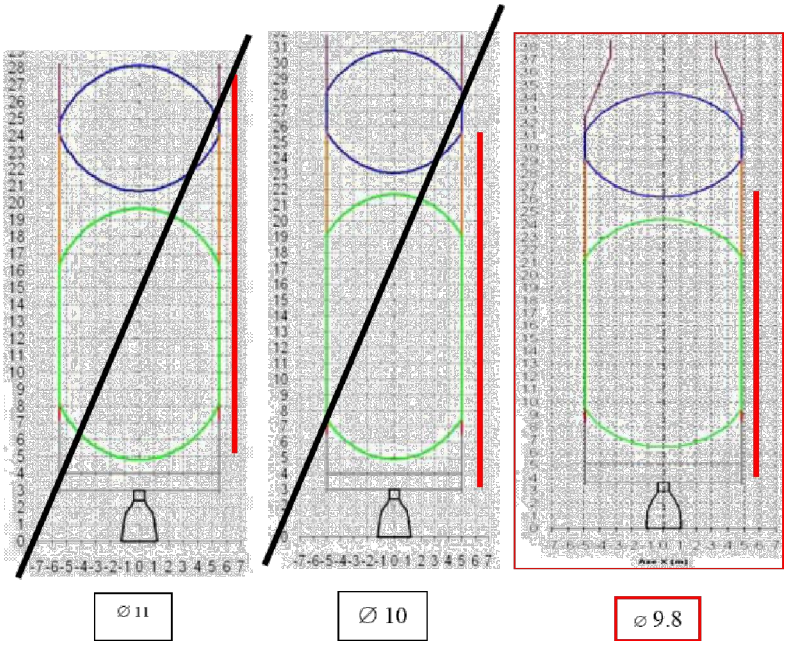

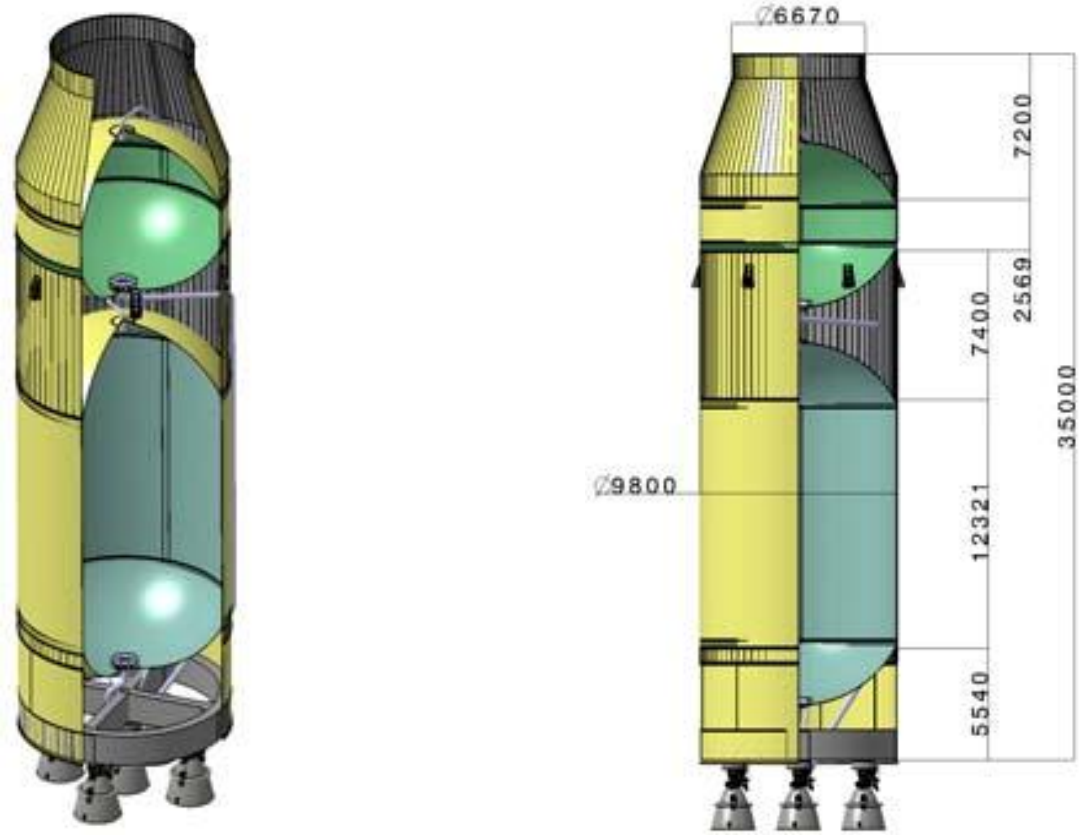

Figure 195: A5SH-1 Core stage

4.7.8.4 Architecture: A5SH-2 (H115) upper stage

The most adapted architecture for the upper stage is selected according to the propellant loading and the upper-to-lower composite diameter ratio.

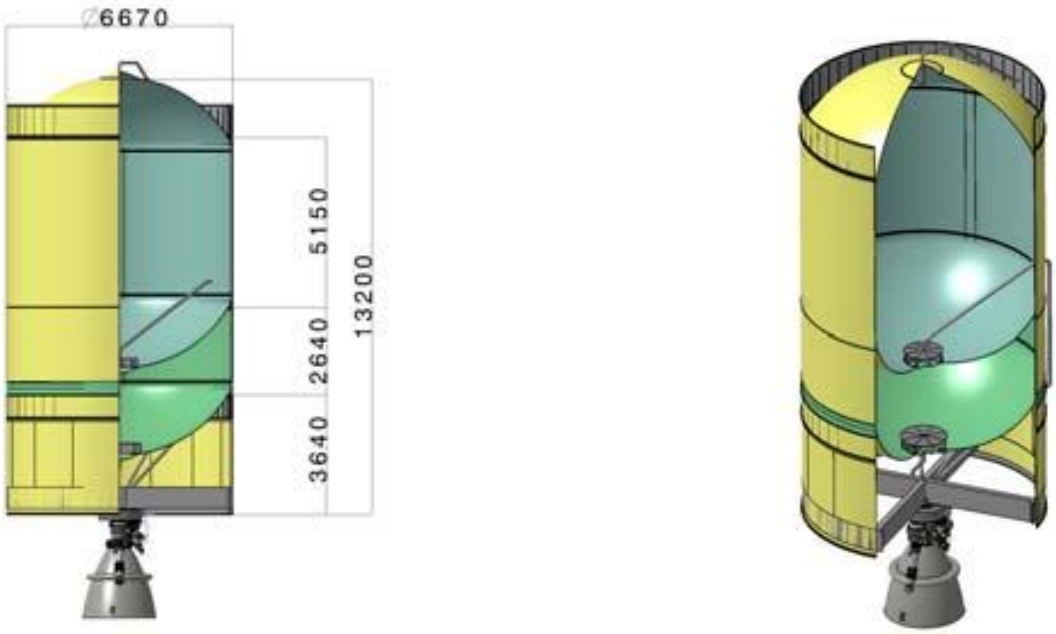

Figure 196: A5SH-2 upper stage

So the upper stage diameter is minimized in order to lengthen the LH2 and LOX tanks and gain a correct shape of tank. So the Ø 6.6 m diameter is the minimum value to have an acceptable ratio of 1.5 between the lower and upper stage diameters (Ø 9.8 m of the lower stage).

The fairing useful volume is 959 m^3, derived from the payload mass: a cylinder with a 7500 mm diameter and 17400 length.

The general design take into account aerodynamic performance:

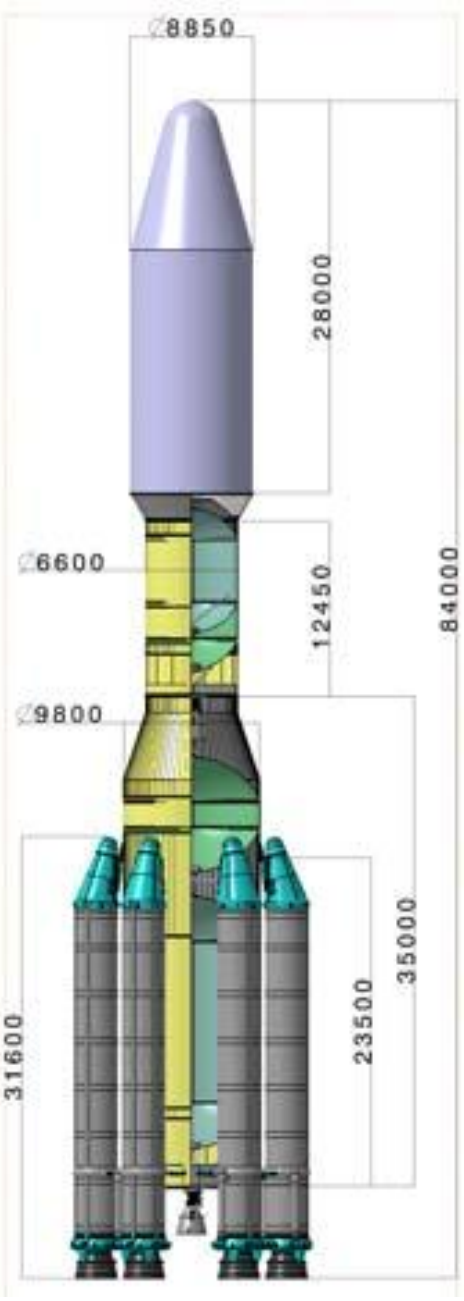

Figure 197: A5SH general view

4.7.9 Synthesis and recommendations

The major outcomes of the study are recorded in the table and figure below

			STANDARD A5ES-A5ECA-A5ECB	ENHANCED A541C-A543C	SUPER HEAVY A5SH
Launch System Architecture	Launcher	Lower Composite	1 EPC 2 EAP	A541C:1 EPC & 4 EAP A543C:3 EPC & 4 EAP	Core stage featuring 5 VULCAIN II 6 EAP
		Upper Composite	EPS or ESC-A or ESC-B	ESC featuring a "double VINCI" engine	ESC featuring a VULCAIN II engine
Gross Lift-Off Weight (tons)				A541C: 1400 A543C: 2350	2500
Performance (tons)	Moon		5 - 10	17 - 27	45
	Mars		3.3 - 8	13 - 22	36
	LEO		18 - 23	25 - 57	100

Table 24: major features for European Launcher for Exploration

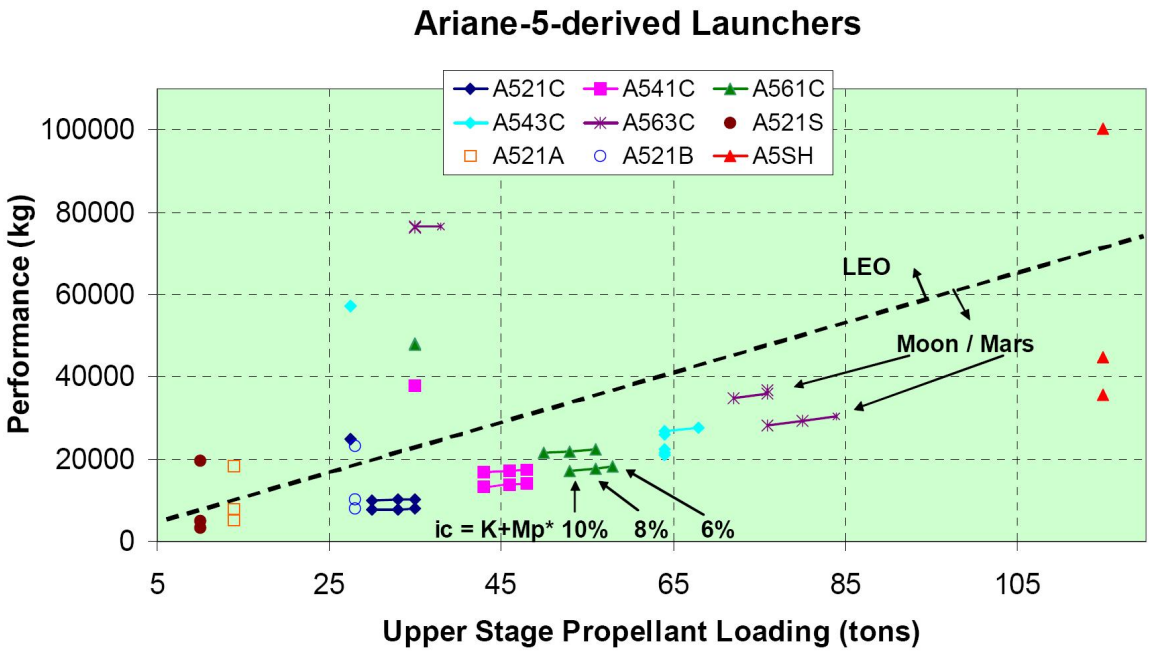

Figure 198: performance synthesis

4.7.10 Lunar Mission Example

Form EADS SPACE Transportation documents it is available an example of Lunar mission. The value of the ΔV required are close to that figure out in the previous analysis, we made to evaluate the best transport vehicle system

4.7.10.1 EADS SPACE Lunar Mission profile example

Below a lunar mission profile is shown.

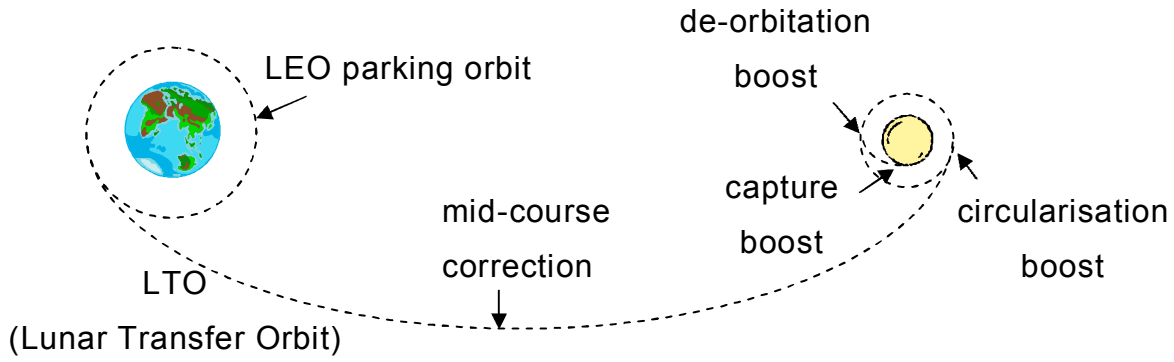

Figure 199: lunar mission profile

4.7.10.2 Hypotheses

- LTO performance assumed equal to the performance into a parabolic escape trajectory (C3=0 / sizing hypothesis)
- Storable propellant stage for LTO injection
- (13% structural coefficient used: idem EPS)
- Storable propellant stage for mid-course correction, circularization, descent and lunar landing (18% structural coefficient used)
- I_{sp} *: 324 s (idem EPS)* i.e. $c=I_{sp}\cdot g_0=324\cdot 9.8 \cong 3100$ *m/s*

4.7.10.3 Required Δv velocity impulse

Table below shows some Δv value. We can see that the value are lower but close to those find out before in the theoretical analysis, confirming our previous computations.

Phase	ΔV	Notes
LTO injection	3131 m/s	Duration ~140 hours
Mid-course correction	30 m/s	
LOI (Lunar Orbit Injection)	780 m/s	Altitude = 100 km
Descent	1780 m/s	
Moon landing	200 m/s	Preliminary estimate

Table 25: impulse velocity needed for a lunar mission

4.7.11 Conclusions

- Ariane 5 performance is interesting mainly for robotic exploration missions (21 to 23 tons in LEO)
- Maximum performance increase to 27 tons in LEO while keeping the general Ariane 5 architecture
- Ariane 5 heavy-lift derivatives could be considered but high development costs have to be expected even with proven technologies

As a matter of fact, after this analysis we can conclude that the LEMMB+LANDER could bring up close to the Moon by the Ariane 5 heavy-lift Space Vehicle.

4.8 Appendix

4.8.1 Launch Vehicle Propulsion

http://cs.space.eads.net/sp/LauncherPropulsion/LaunchVehiclePropulsion.html#300Ncryo

4.8.1.1 Cryogenic and bipropellant rocket engines for launch vehicles and upper stages

Since 1957, rocket propulsion technology has been one of our most important and successful core businesses. During that time, Ottobrunn has become a European centre of space propulsion excellence, having set a number of World and European achievements.

Rocket engine technologies developed at Ottobrunn have contributed to the success of such programmes as the Ariane launch vehicle family and the US space shuttle.

As in the past, today, we are at the forefront of propulsion technology and product excellence based on proven analytical tools, thermodynamic and structure mechanics engineering, the latest manufacturing and production facilities, materials technology, surface technologies, welding technologies, quality management, readily available test facilities - and a wealth of experience.

The Ottobrunn Space Propulsion Centre is the European leader in high efficiency, rocket engine combustion chambers - the heart of every rocket engine. These are not only used in our own engines, but are also supplied to customers, such as SNECMA, for use in their own rocket engines.

The Ottobrunn team designs and manufactures rocket engines and thrust chambers for both pressure-fed and turbopump systems. Rocket engines and thrust chambers using bipropellants and cryogenic propellants include the following:

Aestus- Bipropellant rocket engine

Characteristics	
Propellants	MMH / N2O4
Thrust vac	30 kN
Power	43,70 kW 59,400 hp
Specific impulse vac	324 sec
Propellant mass flow rate	8.8 kg/s
Chamber pressure	11 bar
Nozzle area ratio	84
Overall length	2.2 m
Nozzle Diameter	1.32 m
Mass	111 kg

h

Aestus rocket engine powers the Ariane 5 bipropellant upper stage for the insertion of payloads into LEO, SSO and GTO.

Astrium Space Transportation is responsible for the complete Ariane 5 upper stage, under contract to the French Space Agency CIEs.

The Aestus rocket engine was developed at the Ottobrunn Space Propulsion Centre during the period 1988 - 1995. The first operational flight of Aestus was on 30 October 1997 on Ariane 5 flight 502.

The Ottobrunn team are currently working on a modification to Aestus so that it can be re-ignited up to five times during its 30 minute flight. This modification will enable Ariane 5 to inject several satellites into different orbital positions.

More detailed information about Aestus can be found here.

Vulcain - cryogenic propellant rocket engine

enlarge

Characteristics	
Propellants	LOX / LH2
Thrust vac	1075 kN
Specific impulse vac	431 sec
Propellant mass flow rate	234 kg/s
Chamber pressure	100 bar
Nozzle area ratio	45
Overall length	3.1 m
Nozzle Diameter	1.85 m
Mass	625 kg

The Vulcain rocket engine powers the cryogenic core stage of Ariane 5.
The Ottobrunn facility is responsible for the development and manufacture of the Vulcain thrust chamber comprising:

- Regeneratively cooled combustion chamber.
- Coaxial propellant mixing injectors.
- Dump cooled nozzle extension.
- Gimbal joint.

The LOX and LH2 propellant valves are also manufactured and produced at the Ottobrunn Production Centre.
The thrust chamber design is based on the regenerative cooling concept that was developed at Ottobrunn and has since been continually refined. Before its combustion, LH2 is pumped into a distribution manifold and then flows through closely arranged small tubular cooling channels within the combustion chamber wall. The LH2 then enters an injector head where it is uniformly distributed to 516 coaxial injector elements.
The coaxial injector elements cause the LOX and LH2 propellants to be mixed together. LOX is injected at the centre of the injector, around which the LH2 is injected. These propellants are mainly atomised and mixed by shear forces generated by the velocity differences between LOX and LH2. Although the injector design is

complex, it does assure consistent and reliable combustion efficiencies greater than 99 %, which are reached in the remaining process in the combustion chamber.
At the combustion chamber, the mixed propellants are burned and accelerated up to sonic conditions. The combustion temperatures in the chamber almost reach 3250 degrees Celcius at pressures greater than 100 bar.
Combustion temperature control is achieved by the flow of LH2 in the cooling channels within the combustion chamber wall. This thin copper alloy wall, just 1.5 mm thick separates the combustion temperatures from the - 239 to - 120 degree Celcius LH2 cooling flow.
The final acceleration of hot gases, up to supersonic velocities, is achieved by gas expansion in the nozzle extension, thereby increasing the thrust.
The Vulcain thrust chamber operation is available on movie. (German language mpg file).
The Vulcain, together with other engines on test at Lampoldshausen, can be seen on the test movie (mpg).

Vulcain 2 - cryogenic propellant rocket engine

Characteristics	
Propellants	LOX / LH2
Thrust vac	1350 kN
Power	2,900,000 kW
	4,000,000 hp
Specific impulse vac	434sec
Propellant mass flow rate	309 kg/s
Chamber pressure	115 bar
Nozzle area ratio	
Overall length	3.6 m
Nozzle Diameter	2.1 m
Mass	2100 kg

Vulcain 2 is the new gas generator cycle rocket engine for the Ariane 5 core stage. As with Vulcain 1, the Ottobrunn facility is responsible for the development and manufacture of the Vulcain 2 thrust chamber comprising:

- Regeneratively cooled combustion chamber.
- Coaxial propellant mixing injectors.
- Dump cooled nozzle extension.
- Gimbal joint.

Development and production of the Vulcain 2 thrust chamber is available on movie (mpg file)

The LOX and LH2 propellant valves are also manufactured and produced at the Ottobrunn Production Centre.

By making design enhancements to the Vulcain 1 engine and introducing innovative production technologies, the thrust of Vulcain 2 will increase up to 135 tonnes - an increase of more than 30% compared to its predecessor.

Vulcain 2 will increase the payload capacity of Ariane 5 to 6.8 tonnes.

More detailed information about Vulcain 2 can be found in a PDF file.

HM-7B - cryogenic propellant rocket engine

enlarge

Characteristics	
Propellants	LOX / LH2
Thrust vac	70 kN
Power	152,000 kW
	210,000 hp
Specific impulse vac	447 sec
Propellant mass flow rate	14.4 kg/s
Chamber pressure	35 bar
Nozzle area ratio	83.1
Overall length	1.8 m
Nozzle Diameter	1.0 m
Mass	69 kg

The HM-7 rocket engine feature Ottobrunn's unique regenerative cooling technology whereby hydrogen propellant is efficiently used to cool the combustion chamber before being injected for combustion.

In 1973, the Ottobrunn team started development of the HM-7 thrust chamber for Ariane's upper stage rocket engine. Six years later, the HM-7 engine was successfully qualified with the first launch of Ariane 1 in December 1979.

With the introduction of Ariane 2 and Ariane 3, it became necessary to increase the performance of the HM-7 engine.

This was achieved by raising the combustion chamber pressure from 30 to 35 bar and extending the nozzle, thereby raising the specific impulse. The burn time was also increased from 570 to 735 seconds. The upgraded engine was thus designated HM-7B and was qualified in 1983.

The HM-7 engine versions have reliably powered the third stages of Ariane's 1 through 4 from 1979 to 2003.

The HM-7B engine, will be integrated from the third stage of Ariane 4 into the new Ariane 5 cryogenic upper stage - A tribute to the performance and flight proven reliability of an engine first developed 30 years ago. The resulting upper stage will be designated ESC-A (Etage Superieur Cryotechnique A) and will increase the performance of Ariane 5 to 10 tons.

Use of HM-7B on Ariane 5 is a first step toward increasing the launcher's payload performance. A second step will be the introduction of the new Vinci expander cycle engine to the new cryogenic upper stage, increasing the payload performance to 12 tons.

The Ottobrunn facility is responsible for the development and manufacture of the HM-7B thrust chamber comprising:

- Regeneratively cooled combustion chamber.
- Coaxial propellant mixing injectors.
- Dump cooled nozzle extension.
- Gimbal joint.

The LOX and LH2 propellant valves are also manufactured and produced at the Ottobrunn Production Centre.

Important principles used in the HM-7 combustion chamber were adopted by NASA under licence and it is this technology that formed the basis of today's US space shuttle main engines - the first reusable rocket engine in the world.

Vinci - Advanced cryogenic propellant rocket engine

Characteristics

Propellants	LOX / LH2
Thrust vac	180 kN
Power	985,000 kW
	1,300,000 hp
Specific impulse vac	465 sec
Propellant mass flow rate	39.4 kg/s
Chamber pressure	61 bar
Nozzle area ratio	-
Overall length:	
- nozzle retracted	2.3 m
- nozzle deployed	4.2 m
Nozzle Diameter	2.15 m
Mass	280 kg

Vinci is an advanced expander cycle cryogenic propellant rocket engine currently under development. It will be the first European re-ignitable cryogenic upper-stage engine. The Vinci rocket engine is planned to enter service in 2006 on the new Ariane 5 cryogenic upper stage, designated ESC-B (Etage Superieur Cryotechnique B).

Unlike traditional turbopump cryogenic engines, the Vinci expander cycle engine does not need a gas generator to drive the LOX and LH2 turbo-pumps.

On 20 May 2005, the Vinci engine performed its first flawless ignition and hot-fire test at Lampoldshausen's P4.1 test stand. The test marked a further milestone in the development of a more efficient cryogenic engine for the future evolution of Ariane5.

Ariane 5's new cryogenic upper stage is planned to enter service in 2003. As a first step, the stage will be powered by the well proven and reliable HM-7B rocket engine. The stage configuration with the HM-7B version is designated ESC-A (Etage Superieur Cryotechnique A).

Vinci will increase the payload performance of Ariane 5 to 12 tonnes and it will be possible to re-ignite the engine a total of five times.

Vinci is the first European Expander Cycle Engine. The Ottobrunn Space Propulsion Centre is responsible for the development of the Vinci Thrust Chamber under contract to SNECMA.

The Ottobrunn facility is responsible for:

- Regeneratively cooled combustion chamber.
- Coaxial propellant mixing injectors.
- Dump cooled nozzle extension.
- Gimbal joint.

The LOX and LH2 propellant shut-off valves are also manufactured and produced at the Ottobrunn Production Centre.

On 20 May 2005, the Vinci engine performed its first flawless ignition and hot-fire test at Lampoldshausen's P4.1 test stand. The test marked a further milestone in the development of a more efficient cryogenic engine for the future evolution of Ariane5.

More detailed information about Vinci can be found in a PDF file.

4.9 Reference documentation

1. R. R. Bate, D. D. Mueller, and J. E. White, Fundamentals of Astrodynamics, Dover, New York,1971.
2. Ariane5_users_manual_Issue4 http://www.arianespace.com/site/documents/Ariane5_users_manual_Issue4.pdf
3. Ariane 5 – A European Launcher for Space Exploration workshop [David Iranzo-Greus Head of Advanced Studies Launchers, Propulsion and Defence EADS SPACE Transporation Bremen, March 23rd, 2005] www.astron.nl/p/news/LO/Iranzo_Ariane5_LOFARworkshop.ppt
4. IAC-06-D2.7./A3.7.07
   THE EUROPEAN LAUNCHER OPTION FOR EXPLORATION
   D. IRANZO-GREUS, C. CHAVAGNAC
   ASTRIUM SPACE Transportation, Les Mureaux, France
5. http://cs.space.eads.net/sp/LauncherPropulsion/LaunchVehiclePropulsion.html#300Ncryo
6. soyuz_users_manual_190401 http://www.arianespace.com/site/images/soyuz_users_manual_190401.pdf
7. Soyuz_Users_Manual_CSG_June06 http://www.arianespace.com/site/documents/Soyuz_Users_Manual_Part1.pdf http://www.arianespace.com/site/documents/Soyuz_Users_Manual_Part2.pdf
8. Brunini, On the satellite capture problem, capture and stability regions for planetary satellites, Celestial Mechanics & Dynamical Astronomy. 64 (1996), no. 1-2, 79–92.
9. Analisi di Missione [Proff Diego Lentini Università la Sapienza Roma]
10. Astrodinamica [Proff Graziani Università la Sapienza Roma]
11. Alternative Path to Earth.Moon Transfer [Cristiano Fiorilo De Melo and Othon Cabowinter 23 August 2005]
12. AIAA 99-2690 Cislunar TETHER Transportation System
13. Introduction to Space Systems Engineering [Dr Roger Moses Department of

Aerospace Engineering University of Bristol]

SAPIENZA
UNIVERSITÀ DI ROMA

5 Chapter 5
Solar Array for electrical power generation on (LEMMB)

5.1 Abstract

Electrical power generation could be made by solar array. Solar array is the method used on ISS (International Space Station) and in the most part of the today's satellites.

Here after some types of solar array and LEMMB solar array are presented:

- Traditional solar array like on ISS;
- New inflatable solar array;
- LEMMB's solar array approach;

Before the analysis some data concerning solar array are shown This literature data are useful in order to do the best choice for the solar array type to be used on LEMMB .

5.2 The origins of solar cells

- **1767** Swiss scientist Horace de Saussure was credited with building the world's first solar collector, later used by Sir John Herschel to cook food during his South Africa expedition in the 1830s. http://solarcooking.org/saussure.htm

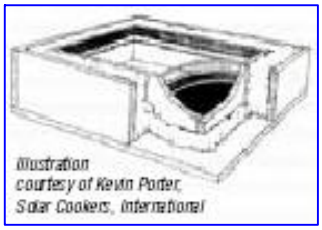

Figure 200

- **1839** Edmund Becquerel, a French physicist observed the photovoltaic effect. (E. Becquerel,"Mčmoire sur les effets électriques produits sous l'influence des rayons solaires", C. R. Acad. Sci. Paris, 1839, 9, 561-567)

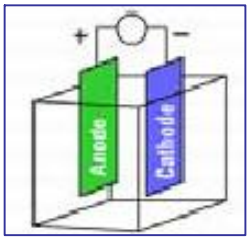

Figure 201

- The effect was first observed (Willoughby Smith, **1873**) in a solid material (metal selenium); and at **1876**, William Grylls Adams and Richard Evans Day discover that selenium produces electricity when exposed to light, solid material could change light into electricity without heat or moving parts.
- **1880** Samuel P. Langley, invents the **bolometer**, which is used to measure light from the faintest stars and the sun's heat rays.
- **1883** Charles Fritts, an American inventor, described the first **solar cells** made **from selenium wafers**.
- **1887** Heinrich Hertz discovered that **ultraviolet light** altered the lowest voltage capable of causing a spark to **jump between two metal electrodes**.
- **1891** Baltimore inventor Clarence Kemp patented the **first commercial solar water heater**. For more information on the water heater, see the http://www.californiasolarcenter.org/history_solarthermal.html
- **1905** Albert Einstein published his paper on the photoelectric effect (along with his theory of relativity). 1921 – Nobel Prize for theory explaining the photovoltaic effect.
- **1914** The existence of a barrier layer in photovoltaic devices was noted.
- **1916** Robert Millikan provided experimental proof of the photoelectric effect.
- **1918** Jan Czochralski developed a way to grow single-crystal silicon. In the early **1950's** the **Czochralski** meter was developed for producing highly pure crystalline silicon.
- In the early **1950's** the **Czochralski** meter was developed for producing highly pure crystalline silicon.
- **1954** Daryl **Chapin**, Calvin **Fuller**, and Gerald **Pearson** develop the silicon photovoltaic (PV) cell at Bell Labs. Bell Telephone Laboratories produced a silicon solar cell with **4%** efficiency and **later achieved 11%** efficiency. See the http://www.californiasolarcenter.org/history_pv.html for more

information. (D.M. Chapin, C.S. Fuller and G.L. Pearson, "A New Silicon p-n JunctionPhotocell for Converting Solar Radiation into Electrical Power ", *J. Appl. Phys.*, 1954, 25, 676-677)

- **1958** T. Mandelkorn, U.S. Signal Corps Laboratories, fabricates **n on p silicon photovoltaic cells** (critically important for **space** cells; more resistant to radiation.
- **1958, 1959, 1960** Hoffman Electronics achieves **9, 10, 14%** efficient photovoltaic cells.
- **1962** Bell Telephone Laboratories launches the first **telecommunications satellite**, the **Telstar** (initial power 14 watts).
- **1963** Sharp Corporation succeeds in producing practical **silicon photovoltaic modules**.
- **1963** Japan installs a 242-watt, **photovoltaic array on a lighthouse**, the world's largest array at that time.
- **1968** NASA launches the first Orbiting Astronomical Observatory, powered by a 1-kilowatt photovoltaic array, to provide astronomical data in the ultraviolet and X-ray wavelengths filtered out by the earth's atmosphere.
- **1970s** Dr. Elliot Berman, with help from Exon Corporation, designs a **significantly less costly solar cell**, bringing price down from $100 a watt to $20 a watt.
- **1972** The French install a cadmium sulfide (**CdS) photovoltaic system to operate an educational television** at a village school in Niger.
- **1972** The Institute of Energy Conversion is established at the University of Delaware to perform research and development on **thin-film photovoltaic (PV)** and solar thermal systems, becoming **the world's first laboratory dedicated to PV research and development.**
- **1973** The University of Delaware builds "**Solar One**," one of the world's first photovoltaic (PV) powered residences. The system is a **PV/thermal hybrid**. The roof-integrated arrays fed surplus power through a special meter to the utility during the day and purchased power from the utility at night. In addition to electricity, the arrays acted as flat-plate thermal collectors, with fans blowing the warm air from over the array to phase-change heat-storage bins.

- **1976** David Carlson and Christopher Wronski, RCA Laboratories, fabricate **first amorphous silicon photovoltaic cells**.

There a now a **variety of methods** for the practical production of silicon solar cells:

- amorphous, single crystal, polycrystalline,
- other materials for solar cells (copper indium, diselenide, cadmium telluride, etc).

Today's commercially available silicon solar cells have efficiencies of about **18-19%.**

In figure below**, progress in solar cell efficiencies** (1976 to 2005) for various research or laboratory devices are presented.

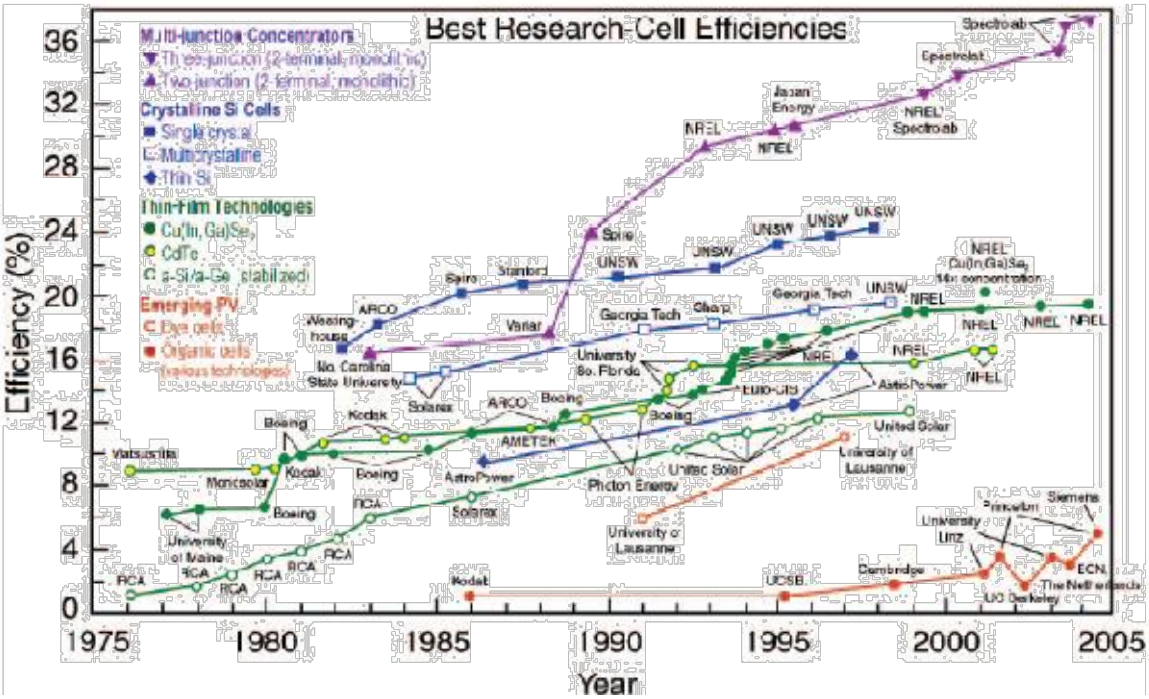

Figure 202

5.3 Photovoltaic effect

Photons can sometimes strike an electron in some material, and free it from the bonds which hold it to the atom. Under certain conditions, such a **free electron** can be made to flow in an external circuit, and produce electricity.

The energy associated with a photon is

$$E = hf$$

where h = *Planck's constant* ($6.63 \cdot 10^{-34}$ *Js*)

Example:
Calculate the energy (in eV) associated with photons of wavelength 550nm (mean value of visible sunlight).

Note: $1\ eV = 1.602 \cdot 10^{-19}\ J$

$E = h \cdot f = h \cdot c/\lambda$ since $f = c/\lambda$, where c is vel. of light.

$= 6.63 \cdot 10^{-34}\ \text{Js} \cdot 3 \cdot 10^{8}\ \text{ms}^{-1} / (550 \cdot 10^{-9})\ \text{m}$

$= 3.62 \cdot 10^{-19}\ \text{J}$

so $E = 3.62 \cdot 10^{-19}\ \text{J} / 1.602 \cdot 10^{-19}\ \text{J} \cdot \text{eV}^{-1}$

$= 2.26\ \text{eV}$

- A photon hitting a silicon atom can give to electron within the atom enough energy to leave it and move off through the structure.
- The negatively charged electron leaves a positively charged hole (a position once occupied by an electron) in its place; so the photon has created an electron/hole pair.
- An electron orbiting a surrounding atom near to a hole can move into the hole

leaving a new hole in it's place; in this way the positively charged holes can also move through the structure.

- In the presence of an electric field the electrons move in one direction and the holes in the other, because they have opposite electric charges with holes behaving in nearly all respects as positive particles.
- In semiconductor materials, electric current is the flow of oppositely charged electrons and holes.

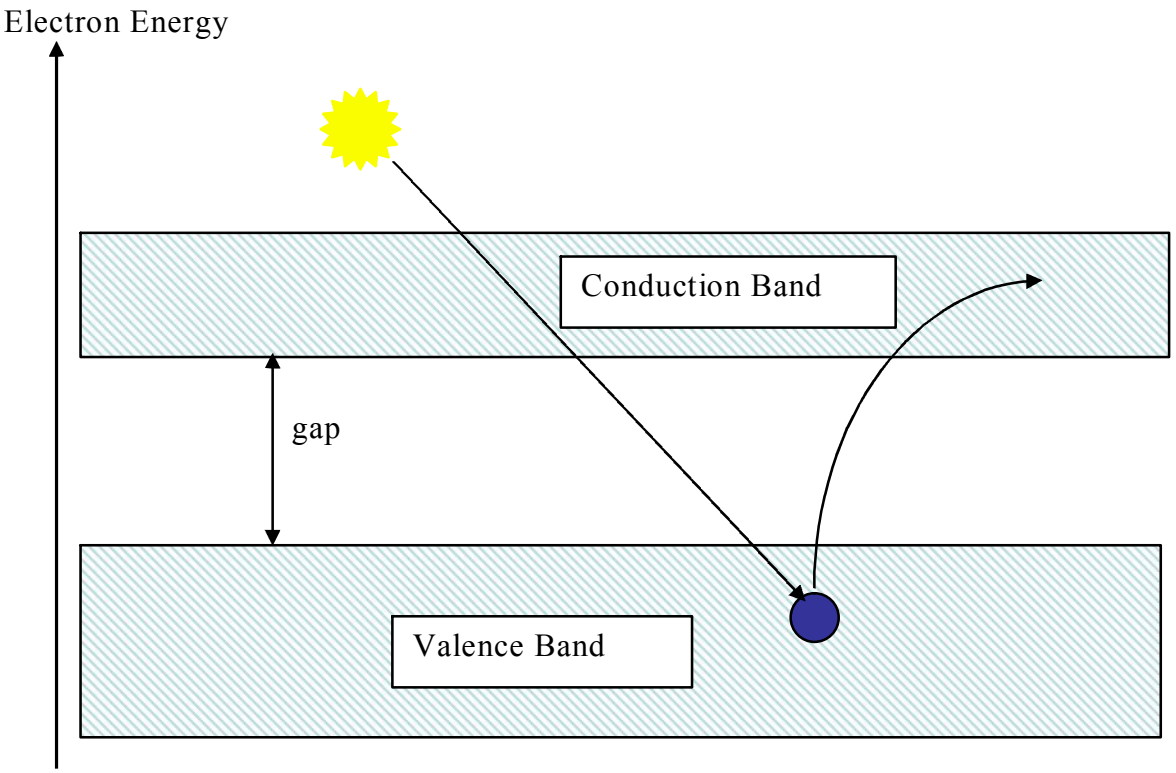

Figure 203

- Without an electric field to separate the electrons and holes created by the light they would soon recombine and there would be no net current. To avoid this, a photovoltaic cell (PV cell) is a wafer or thin film of semiconductor material which is arranged to have an internal electric field, pointing from the top surface of the wafer or film to the bottom surface (or vice versa).
- An electrical contact, usually aluminum, covers the bottom surface. The top surface also has an electrical contact, but this one is transparent so as to let in the light.
- When the silicon (or other semiconductor material) in the PV cell absorbs

light, electron/hole pairs are generated.

- Because of the internal electric field the electrons move to one contact and holes to the other thus building up a voltage.
- The cell acts as a voltage source. If you connect the two contacts with a wire an electric current will flow in the wire; this is known as the "*short-circuit current*" of the PV cell; you can measure it with an ammeter.
- If you don't connect the contacts the electrons and holes build up on opposite surfaces of the cell, producing a voltage between the contacts that you can measure with a voltmeter; this is called the "*open-circuit voltage*" of the PV cell.

In the case of ***pure silicon***, the *band gap energy* is ***1.11 eV***. This corresponds to some minimum frequency (max. wavelength) that solar radiation must have to lift electrons from the *valence band* to the *conduction band*.

This λ value can be calculated as follows:

$E_g = h \cdot f_{min}$ and $\lambda_{max} = c/f_{min}$

$\lambda_{max} = c \cdot h/E_g = 3 \cdot 10^8 \cdot 6.63 \cdot 10^{-34} / (1.11 \cdot (1.602 \cdot 10^{-19}))$

$= 1.12 \cdot 10^{-6}$ m $= 1.12$ μm.

Only about 77% of solar energy is contained in radiation with a wavelength $\lambda < 1.12$ μm.

In reality, efficiency is much less than **77%** as any electron energy in excess of **1.11eV** does not go into producing power, but does heat the crystal. For **Si**, efficiencies of about **25%** are the theoretical maximum.

Theoretical Limits to efficiencies

Incident Sunlight	1.00	1.00-
Spectral Wavelength	0.77	0.77
Heat Loss	*0.44*	23% max
Reflection at surface	*0.43*	
Quantum Efficiency	*0.42*	
Other Losses/Resistance	*0.29*	

Table 26

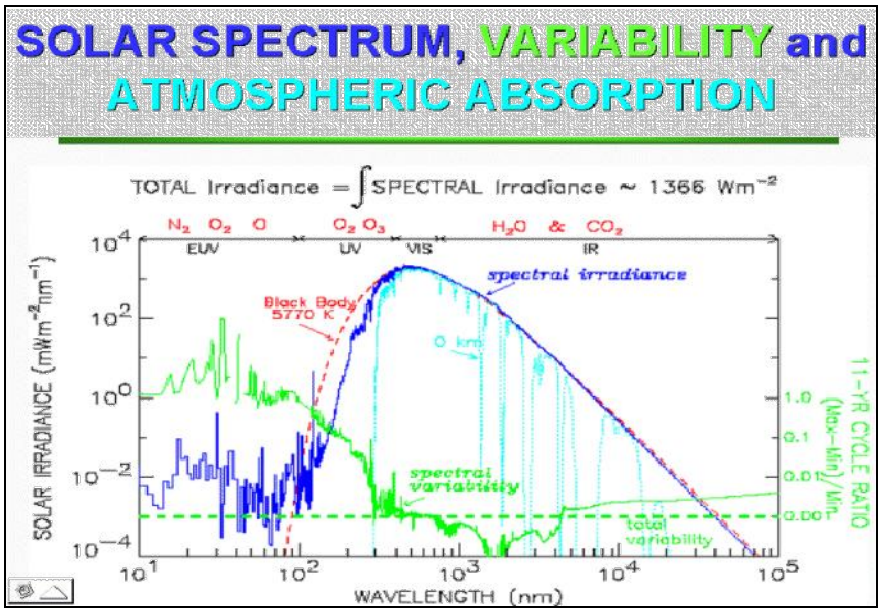

Figure 204: solar spectrum

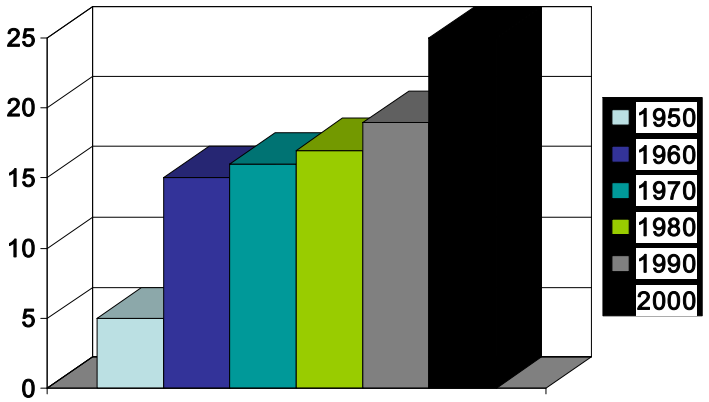

Figure 205: efficiency changing

5.3.1 Solar cells made by semiconductors –materials

Solar cells convert incident solar flux to electric currents. They all have at least one photoactive layer that is itself a sandwiched layer of two semiconductors -materials that are insulators at absolute zero but become electrically conducting under certain conditions.

A semiconductor has a band of fully occupied electron states (a valance band) and a band where electrons can flow (a conduction band). The conduction band is empty at zero kelvins. At room temperature some electrons exist in the conduction band from random thermal motion -- hence the term semiconductor. The energy in photons of light incident on PV cells (photo voltaic cells) is what produces electric currents. The energy difference between valance and conduction bands is the bandgap energy $\varepsilon_0 = h\nu_0$, where h is Planck's constant $\approx 6.63 \times 10^{-3}4$ J-s $\approx 4.14 \times 10^{-1}5$ eV-s and ν_0 the bandgap frequency. Each semiconductor has a characteristic bandgap typically of the order of magnitude of an electron-volt (eV).

Quantum mechanics mandates that incident photons with energy $< \varepsilon_0$ dissipate their energy as heat, and are thus wasted. Only photons with energy $> \varepsilon_0$ can raise electrons to the conduction band. Even photons with $h\nu \geq \varepsilon_0$ only contribute a fraction of their energy, $\varepsilon_0 / h\nu$, to raising electrons to the conduction band.

The excess above ε_0 is also dissipated. Electrons energized to the conduction band leave positively charged "holes" in the semiconductor matrix. This is crucial to PV cell operation.

5.3.1.1 The internal field; p-n junctions

To produce the necessary internal electric field we make use of two types of "doped" semiconductor material; these are called "n-type" and "p-type" material.

n-type silicon

Contains a small percentage of phosphorus atoms. These fit quite well into the structure of the silicon, except that each has one more electron than each silicon atom. These extra electrons escape from the phosphorus and are free to move round

the structure; what they leave behind are positively charged phosphorus ions, (which are fixed in the structure and can't move). The phosphorus is called an **n-type** dopant because of the negative electrons it adds to the silicon; the resulting material is called n-type silicon because of the electrons it contains (though you should remember it contains an equal number of positive fixed charges).

p-type silicon

Contains boron atoms. These fit quite well into the structure of the silicon, except that each has one fewer electrons than each silicon atom. They therefore grab electrons from the silicon, creating holes that are free to move round the structure; what the holes leave behind are negatively charged boron ions, (because of the extra electron they've grabbed); the boron ions are fixed in the structure and can't move. The material is called p-type because of the positive holes it contains; it also contains an equal number of negative fixed charges. Boron is said to be a p-type dopant in silicon.

Now consider a wafer of silicon that has excess boron in the top half (p-type silicon) and excess phosphorus in the bottom half (n-type silicon). In the middle there is what is called a **pn-junction**, where the material changes from **p-type to n-type**.

On the n-type side of the junction there will be electrons and fixed positive charge (phosphorus ions); on the p-type side there will be holes and fixed negative charge (boron ions).

Because there are many electrons in n-type and very few in p-type material the electrons from the n-side will tend to spread into the p-side, leaving some net positive charge on the n-side (because of the positive phosphorus ions); this positive charge will stop the electrons diffusing too far into the p-type material and is further increased by holes spreading from the p-side, (which also leaves negative charge on the p-side, because of the negative boron ions). The result is fixed positive electric charges on the n-type side of the junction and negative fixed charges on the p-type side.

This produces an internal electric field pointing across the junction, which is precisely what is needed for a PV cell.

This accelerates electrons from electron-hole pairs separated by light from the p-type material into the n-type material where there are many electrons and few holes and so

not much chance of recombining. Similarly the junction accelerates holes from electron-hole pairs in the n-type material to the p-type material where they are similarly unlikely to recombine.

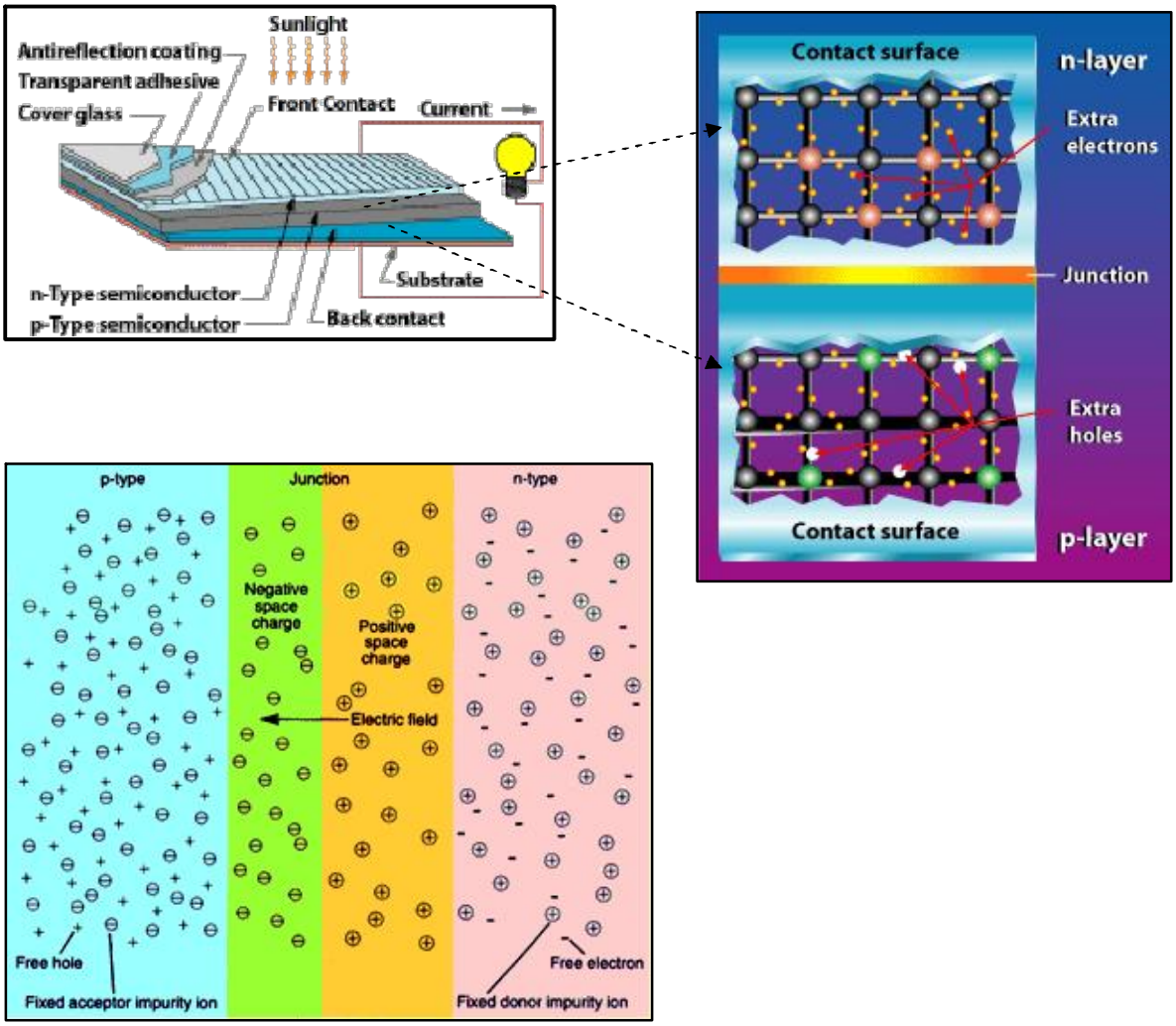

Figure 206

Semiconductor layers are "doped" with impurities during manufacture to produce either an abundance of carrier electrons (n-layers) or an abundance of holes (p-layers), and the dissimilar layers are sandwiched together to produce a permanent electric field $\mathbf{E}_{\text{diffusion gap}}$ near the p-n junction, as shown in the inset for crystalline-Si cells.

At equilibrium some electrons goes through PN junction towards low level of potential energy, in figure motion in left versus, at the same time some Holes moves toward rigth side in order to minimize their potential.

Eg is the **energy gap (band gap)** of semiconductor that is required in order to create an Electron-Hole pair.

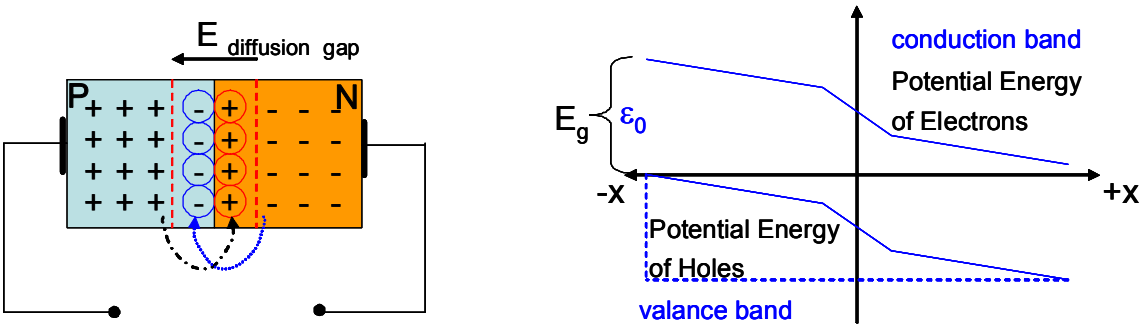

Figure 207

Supposing now that a photon with band-gap energy = $h\nu > \varepsilon_0$ strike the P component of the junction, then a couple electron-hole will be created and the electron will move toward right side crossing the junction in order to obtain a lower potential.

This is the mechanism by which the charges are separated by the junction. In this process the life time of minor carriers must be long enough in order to prevent annichilation and recombination between electron and hole just created before.

The more the life time of minor carriers, the greater the probability of carriers separation made by junction.

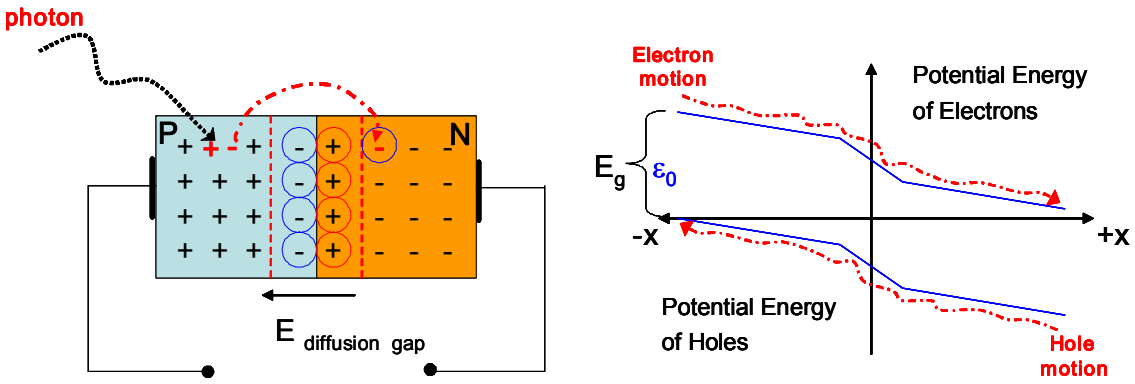

Figure 208

The more the bad gap, the greater is the $\mathbf{V_{oc}}$ (V open circuit) but the more is the band gap , the lower will be the $\mathbf{I_{sc}}$ (I Short Circuit Current).

In fact increasing the energy gap of semiconductor will affect the number of photons which will be able to create a couple Electron-Hole when they will strike the solar cell.

The relations for efficiency and power are:

$$\eta = \frac{power_{out}}{power_{incidence}} = k\frac{V_{oc} I_{sc}}{power_{incidence}} \qquad \text{k(0.25--1)}$$

eq 63

$$power_{out} = k' V_{oc}(E_g) I_{sc}(1/E_g)$$

Electricity is only produced when electrons recombine with holes after traveling through an external circuit. If there's no external load and the sun is shining an open-circuit voltage exists at the contacts.

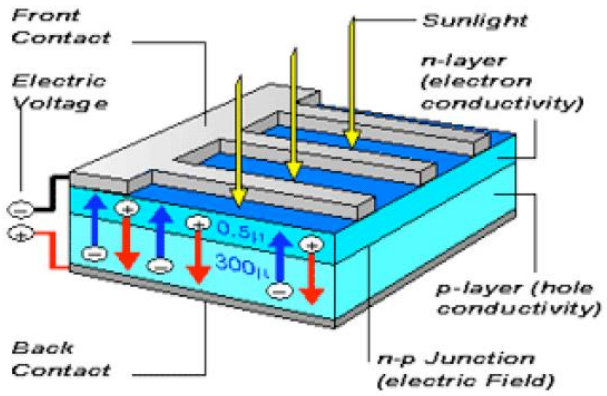

Figure 209

5.3.2 Factors that affect the efficiency of the solar cells

5.3.2.1 Front contact shading

Good design is a matter of striking the best compromise between low series resistance (closely-spaced, highly conductive grid lines with good adhesion and low contact resistance) and high light transmission (fine, widely-spaced grid lines). Typically, the loss from front contact shading is 10% in commercial cells.

5.3.2.2 Reflection

Since the current is generated by photons incidence and consequently Electron-Hole couple created, then is necessary to have a low reflectivity at solar cell surface. Approximately the reflection index ***R*** can be obtained to start by *refration index **n***:

$$R = \frac{(n-1)^2}{(n+1)^2} \Rightarrow \text{between air and semiconductor we have if } n_{semicond} = 4 \text{ and } n_{air} = 1$$

$$R = \frac{(4-1)^2}{(4+1)^2} \cong \frac{3^2}{5^2} = 36\%$$

eq 64

to reduce the reflection effect some method are:

- The application of a single layer antireflective coating of titanium oxide or tantalum pentoxide;
- A **textured front surface** of **minute pyramids**, produced by a special etching process, which widens the region of low reflectivity on both sides of the optimum wavelength; similar effect has also been achieved by **micro-grooving** the surface;
- Multilayer antireflective coatings.

5.3.2.3 Incomplete absorption

Photons with energy less than the energy gap are wasted as they simply generate heat or pass right through the silicon and are absorbed in the back contact.

5.3.2.4 Partial utilization of photon energy

An energy gap of **0.9eV** gives maximum utilization of the terrestrial solar spectrum in the generation of minority carriers.
Crystalline silicon, with an energy gap of **1.1eV**, utilizes about **44%** of the incident energy (not far from the optimum **46%**).

5.3.2.5 Collection losses

Electrons and holes that are separated by the barrier layer and reach the contacts contribute to the output current, the rest, which recombine in the bulk of the silicon and at the front and back surfaces, generate heat and do no useful work.
The ratio of the useful charge carriers to the total generated is called the "**collection efficiency**".
Collection efficiency in the base region of the cell between the junction and the back contact in modern cells is optimized by:

- using good quality material with a high minority carrier lifetime (the average time elapsing between the generation and recombination of electrons in p-type material and holes in n-type);
- choosing processes which minimize degradation of the minority carrier lifetime in manufacture; and
- forming an impurity concentration gradient or "back surface field", which accelerates minority carriers from the back surface towards the junction.
- in thin cells - to use a highly-reflective material at the interface between the silicon and the back contact;

- long-wavelength photons reaching the interface before being absorbed are reflected and given another chance to generate carriers;
- using a grid configuration can reduce recombination of carriers at the back contact, as at the front, but, in doing this, care must be taken not to cancel the gain by increased series resistance;
- the surface layer of the cell, between the junction and the front contact, is very highly doped and therefore has an extremely short minority carrier lifetime;

In most good quality commercial cells, **collection losses are now less than 5%**.

5.3.2.6 Voltage factor

The **open-circuit voltage** is always less than the **energy gap Eg** for the following reasons:

- the barrier height is less than **Eg;**
- a voltage equal to the barrier height can only be obtained at extremely high injection levels, which can never be reached by photon absorption from sunlight;

There is an optimum value of **Eg** for any particular spectral irradiance distribution, at which the product of $\mathbf{I_{sc}}$ and $\mathbf{V_{oc}}$ is a maximum. For terrestrial sunlight, the theoretical optimum is **1.4 eV** (silicon is near the optimum).

5.3.2.7 Series resistance

In the cell causes a flattening of the current-voltage characteristic and a consequent loss of output power, it can be minimized by:

- good contact grid geometry;
- good ohmic contacts and;
- low sheet resistance in the surface layer.

5.3.2.8 Efficiency summary

- Increasing solar cell efficiency while maintaining a low production cost is the primary objective of solar power research;
- the use of low cost materials such as *silicon ribbon* and *multi-crystalline silicon mc-Si,* provides a cheaper means of producing crystalline silicon solar cells;
- in terms of cell efficiency, *mc-Si* suffers from lower charge carrier lifetimes if compared to *single-crystalline Si*;
- in addition, the surface is not easy to texture. In order to increase cell efficiency, texturing is a major factor; it allows for a lower overall reflection that leads to higher short circuit current;
- high efficiency solar cells often include some sort of texturing. Either random pyramid or "inverted" pyramid texturing is used for *single Si crystal*;
- industrially established silicon solar cell technologies either fabricate 200 to 400 µm-thick solar cells from high-quality Si wafers or use *half-a-micron-thin cells* from *amorphous Si*;
- the thick wafer cells exhibit long carrier lifetimes and their cost-efficiency suffers from the high consumption of expensive Si material;
- In contrast, the carrier lifetime is small in thin amorphous Si cells. Their cost-efficiency is reduced by small cell efficiencies.

5.3.3 How has this efficiency increasing been achieved

1. By choosing materials carefully to make optimal use of the available spectrum of light.
2. -->es thin films, absorption

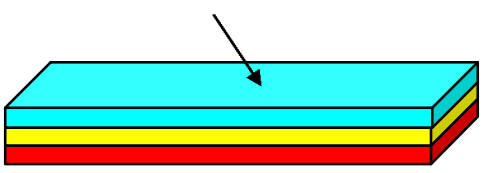

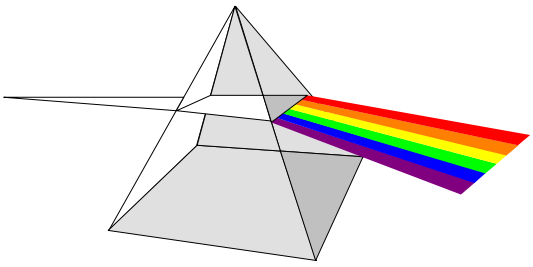

Figure 210

3. By choosing geometry carefully

   -->es. "inverted pyramid" structure, which significantly reduces the light reflection at the cell surface

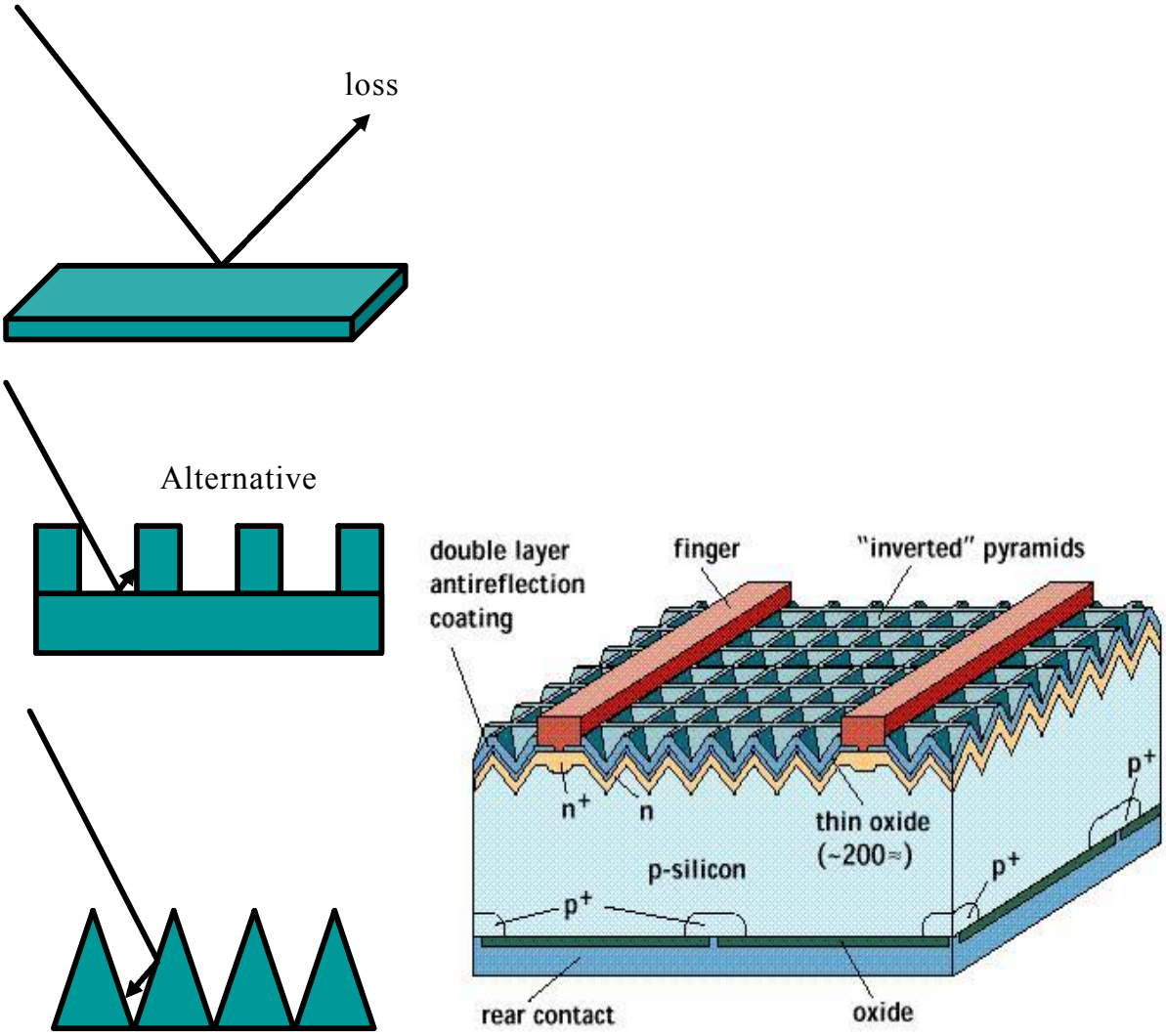

Figure 211

5.3.4 Key technologies and materials for raising the efficiency

5.3.4.1 Key materials

Confirmed module efficiencies calibrated at $I_p = 1$ kW/m^2 intensity are:

- 25.1% for gallium arsenide/gallium antimony (GaAs/GaSb; with a solar concentrator), 22.3% for crystalline silicon (Si),
- 13.9% for copper indium diselinide ($CuInSe_2$),
- 12% for amorphous silicon (a-Si) and
- 10.5% for cadmium telluride (CdTe) (Kazmerski, 1997, table 10).

On table below the efficiency of several materials used to build the solar cells are summarized.

Material	Laboratory Efficiency [%]	Production Efficiency [%]
Single crystal silicon	~ 24	14-17
Polycrystalline silicon	~ 18	13-15
Amorphous silicon	~ 13	5-7

Table 27

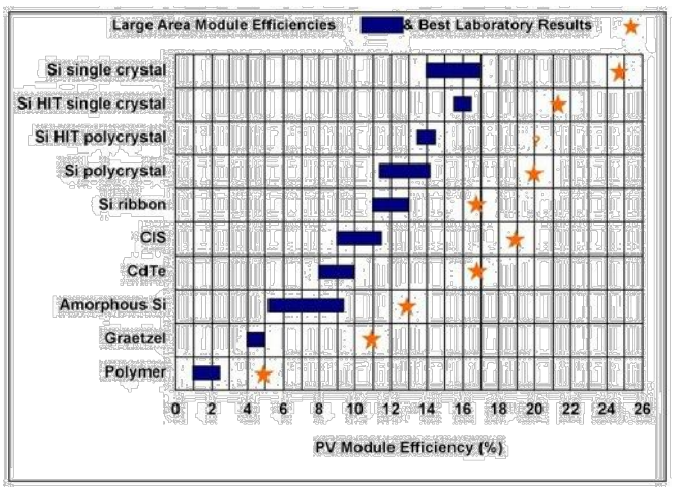

Figure 212: efficiency versus solar cell technology

The PV single band-gap limit efficiency has been already been surpassed with innovative (not cheap) cells. Efficiencies > 40% have been attained, often with concentrators requiring two-axis suntracking and active cooling.

5.3.4.2 Key technologies for raising η are:

- **Hetrojuction cells**, single bi-layer sandwiches (as in crystalline silicon PV cells), but with top and bottom layers made of different semiconductors with different bandgaps, not just different p- or n-doping;
- **Multijunction cells**; multiple stacked semiconductor layers of different bandgap capturing otherwise wasted photons;
- **Quantum dot cells**, incorporating nanocrystals producing as many as three electrons per absorbed photon, instead of the usual one.

The problem to be overcome is the broad solar spectrum; a typical stellar photosphere.

Below a Graph of Semi-conductor band gap vs. Efficiency are shown.
In this graph a band gap of ~1.4eV matches the photon energies where the sun's spectral intensity is strongest;

- **GaAs** is an example of a material with an optimal band gap;
- **Silicon** Band Gap is 1.1 eV, not optimal

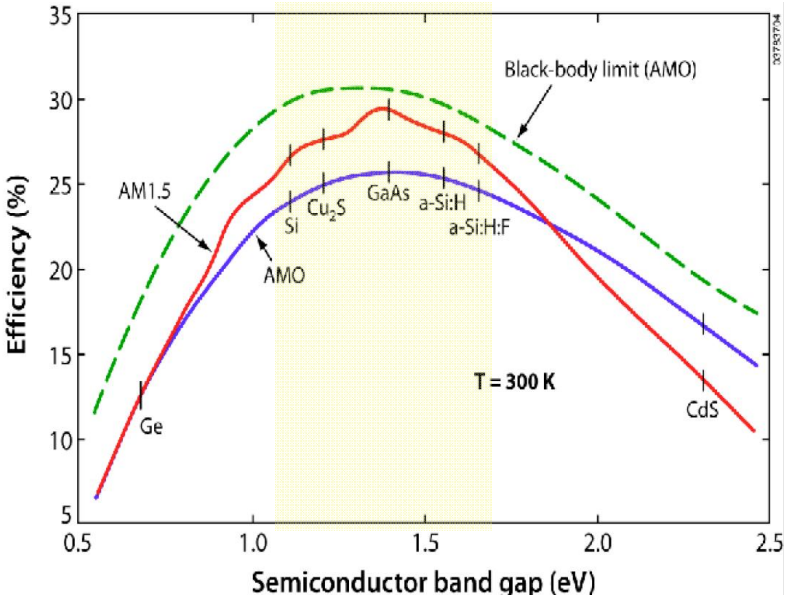

Figure 213

On figure below some typical Silicon Cell Design are reported

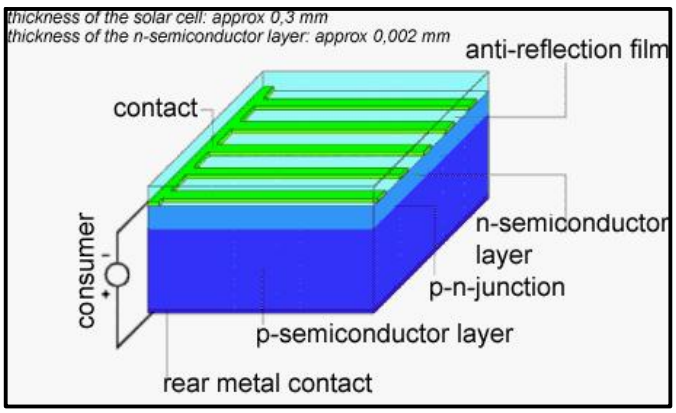

Figure 214: Single crystalline Silicon

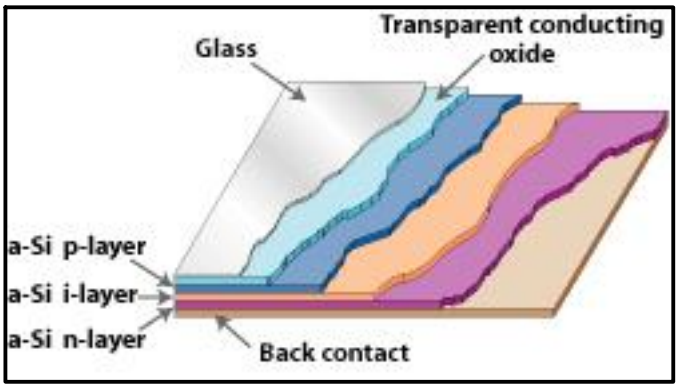

Figure 215: Amorphous Silicon

5.4 Manufacturing costs of solar cells versus efficiency

5.4.1 Crystalline Silicon Solar cells

A solar cell is a PV cell designed to convert sunlight to electricity. The simplest cells consist of a circular silicon wafer with a **pn-junction** sandwiched in the middle, a metallic bottom contact (e.g. aluminium) and a transparent top contact (either a transparent conducting oxide or a grid-like metal structure).

They are expensive to produce because silicon wafers are expensive to produce (mainly because they are high-purity single crystals) but their cost was unimportant in the space race.

crystalline silicon PV cell

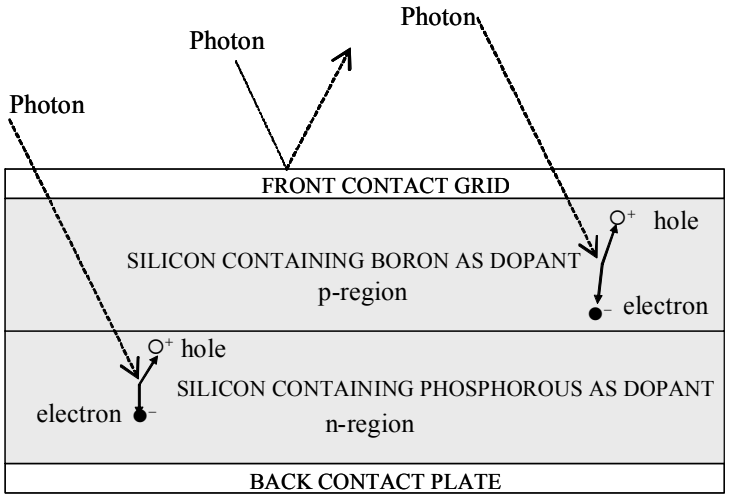

Figure 216

5.4.2 Amorphous Silicon Solar cells

In recent years there has been a continuous search for cheaper forms of PV cell, economical enough to be used in applications here on earth **(terrestrial applications)**.

One possibility has been to replace the single-crystal wafer by polycrystalline squares, (consisting of many small grains of crystalline material).

A more radical approach is to use amorphous silicon, having no crystalline structure at all. This material has the advantage of being much more light-absorbing than crystalline silicon: a thin film on a suitable substrate only a few microns thick (a thousandth of a millimeter) absorbs most of the sunlight falling on it; by contrast crystalline cells have to be about 100 microns and in practice are 0.5mm thick. This means that you need far less amorphous silicon to make the cells, and they can even be made flexible, whereas crystalline cells are very fragile. The electrons and holes don't move so easily in amorphous silicon, but this is partly compensated for by the fact that they don't have to move as far (because the cell is so thin).

Cell efficiencies are perhaps only half those in crystalline silicon, but the amorphous cells potentially cost much less than half for the same surface area, so they seem to be the most economical choice at the moment.

The manufacture of amorphous silicon cells is very different from that of crystalline cells. No wafers are involved. Instead the silicon is deposited as a thin film on a substrate, usually either stainless steel or a glass sheet covered with a layer of tin oxide acting as a transparent contact.

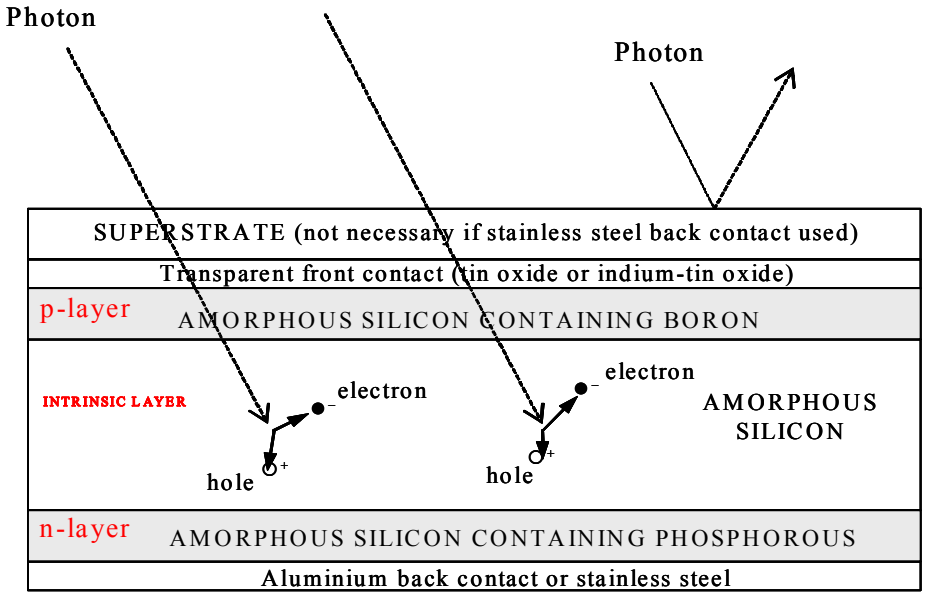

Figure 217

Unfortunately electron-hole recombination of **n- or p-type** amorphous silicon is very high. To get round this problem the cell is made mostly from undoped amorphous silicon (i.e. using just silane): the thin film of undoped amorphous silicon is sandwiched between far thinner layers of n- and p-type amorphous silicon, as shown in Figure above.

The n- and p-layers serve to produce the internal field across the undoped layer, but almost all the light is absorbed in the un-doped layer. (The undoped material is referred to as intrinsic, and the cell is said to have a **p-i-n** structure, as opposed to the p-n structure of crystalline silicon cells).

5.5 Tandem cell or Multi-junction cell

We have dealt with the main principles of amorphous silicon solar cell production. Cell efficiencies can be increased to some extent by including a **second p-i-n** structure under the first, using an alloy of amorphous silicon with germanium. This absorbs a longer wavelength part of the solar spectrum. This is called a tandem cell or multi-junction cell.

Spectrum-splitting cell, constructed of three separate p-i-n type, amorphous semiconductor solar sub-cells, each with a different spectral response characteristic. In this way, the cell can convert the different visible and near infrared wavelengths of sunlight with optimal efficiency

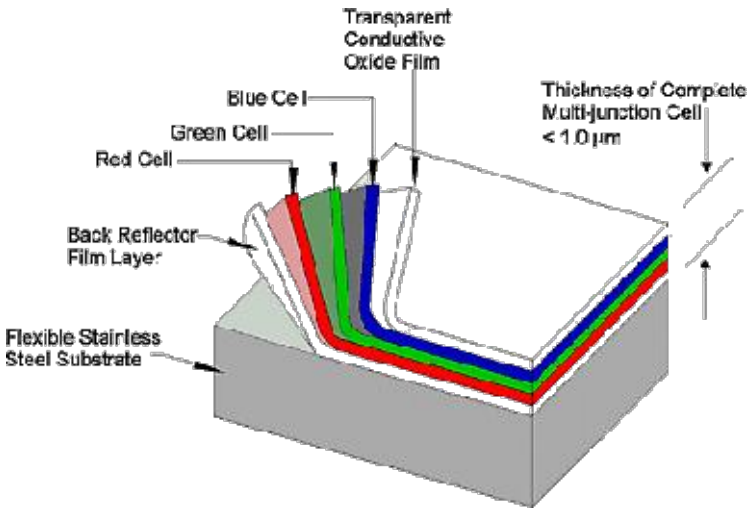

Figure 218: amorphous silicon solar cells and multijunction cells

5.6 Space transportation end PV cell cost reduction

Highly efficient cells are important, but the main factor holding back solar PV is cost.

Polycrystalline (Amorphous) thin films are driven today by the prospect of dramatic cost reductions despite their lower than single crystal silicon efficiency. These films are of order 1 µm thick compared to 300 µm thick for crystalline Si. A recent US Department of Energy workshop on solar research identified a as major priority "harvesting of solar energy with 20 percent power efficiency and 100 times lower cost (http://www.sc.doe.gov/bes/reports/abstracts.html).

A frequent objection is that space transportation is too expensive. But what drives these costs? Can innovative technologies drop them significantly? That launch costs with the Space Shuttle ($20,000/kg).

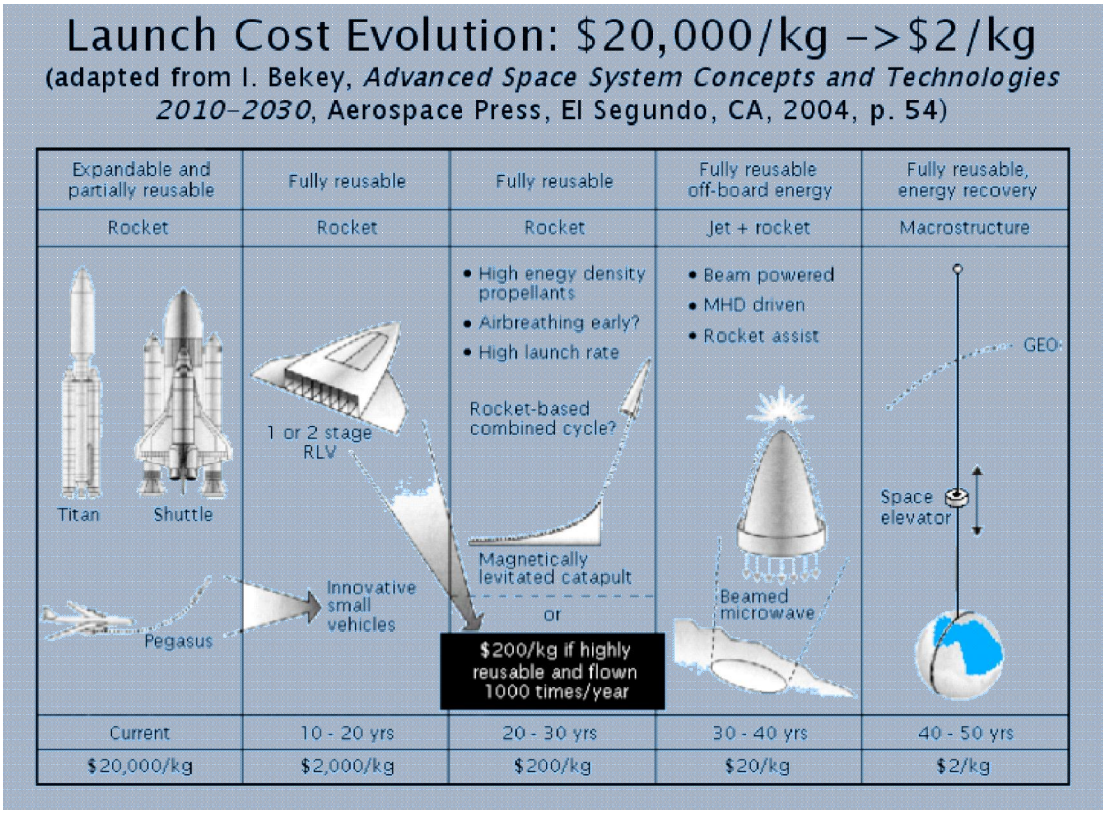

Table 28: Launch Cost Evolution

5.6.1 Efficiency and Cost of Silicon Solar Cells

A nearer-term opportunity to reduce launch costs is reducing the mass of solar collectors

- The present **specific power** (**P/M, power per unit mass**) of single-crystal silicon solar panels on the **International Space Station** (**ISS**) is ***< 0.1 kW/kg*** (breakdown is in the inset, but it doesn't include support structure that roughly halves P/M).
- Note that crystalline-Si cells are ~ 300 µm thick, whereas thin films cells under development for Earth and space applications are ~ 1 µm.
- Moreover, ultralight support structures made of inflatable-rigidizable structures are possible for space PV. **Thin-film PV** on "gossamer structures" could raise **P/M** to the ***1-10 kW/kg range*** (Hyde et al., 2003).
- Deployable light weight solar arrays are near term technologies being tested now. The inset, for example, shows a PV panel deployable in space from an inflatable structure under development by the L'Garde Company of Tustin, CA.

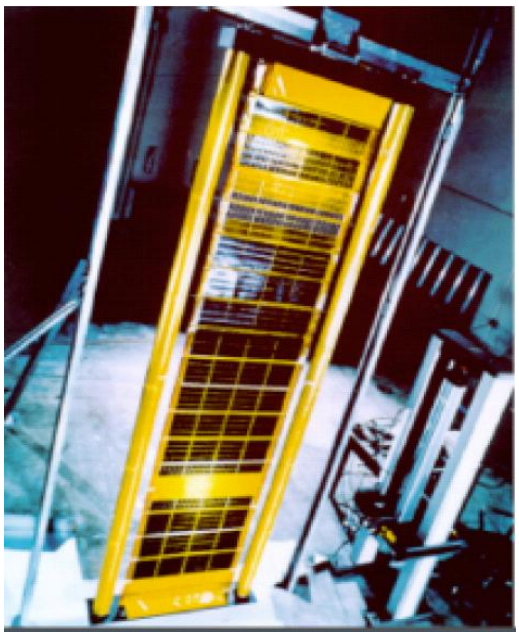

Figure 219: inflatable structures for solar panel

5.6.2 Silicon Solar Cells: Market for Solar PV

- PV market grows at fast rate especially in recent years;
- Cumulatively, about 2GW of solar cells are being used in a variety of applications;

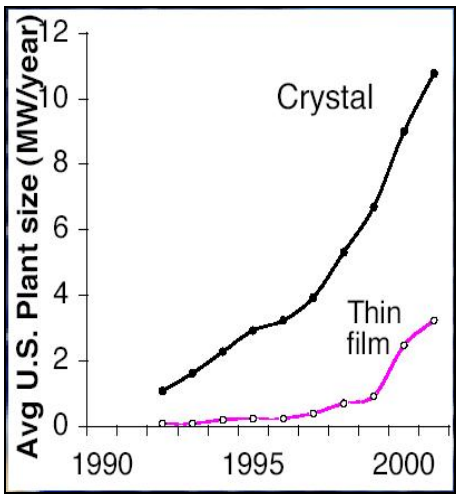

Figure 220: market of PV solar cell

On figure below different technology comparison in efficiency & cost are reported;

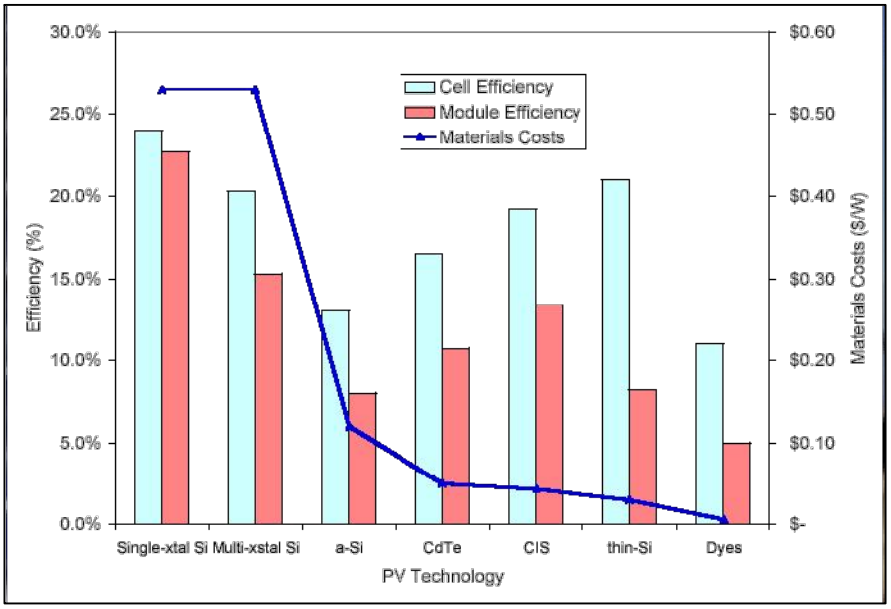

Figure 221

On figure below the comparison between type of application, cost and efficiency are reported. It can be observed that there is a difference between terrestrial and space applications In space application the main driver is the light weight of the solar array and the radiation resistance. The today's technologies in figure below are shown.

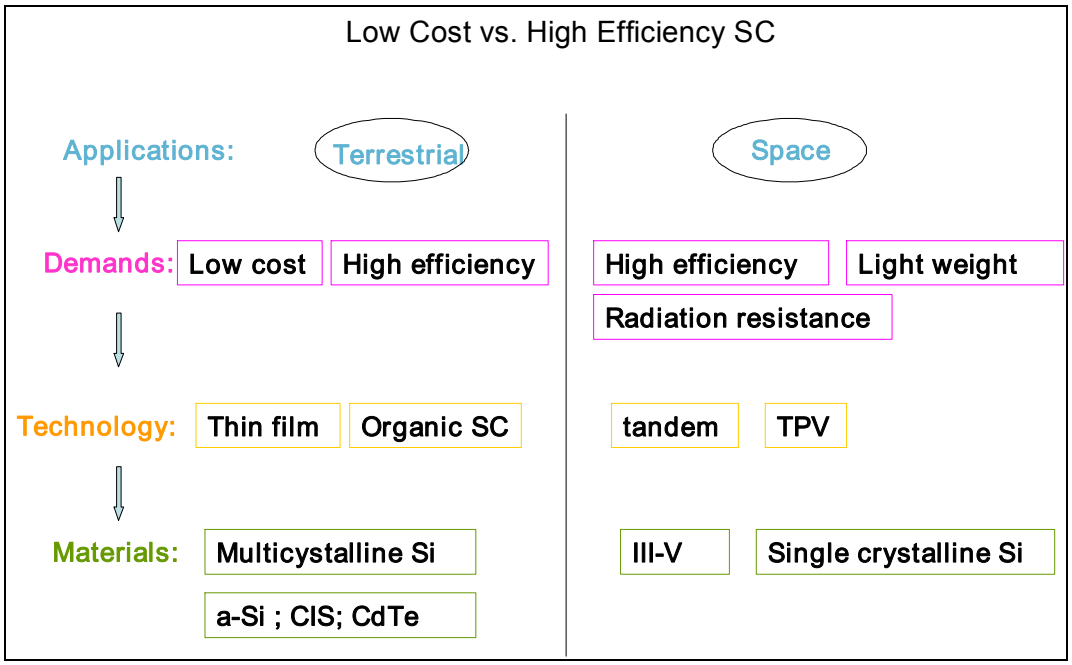

Figure 222: terrestrial and space requirements comparison

5.7 Space solar cell application

Many space applications uses solar cell application. Here after are reported some example of them.

Depends on the mission requirements there are:

- Near Sun missions
  - Venus
  - Mercury
- Outbound
  - Mars

- Asteroids

- Earth orbital
  - International Space Station
  - Mir
  - Skylab
  - Communication satellites
  - Earth observation satellites
  - Weather satellites
  - Global Positioning System
- Surface
  - Mars Pathfinder
  - Mars Exploration Rover

Below are showed some example of that

Figure 223: ISS Solar cell application

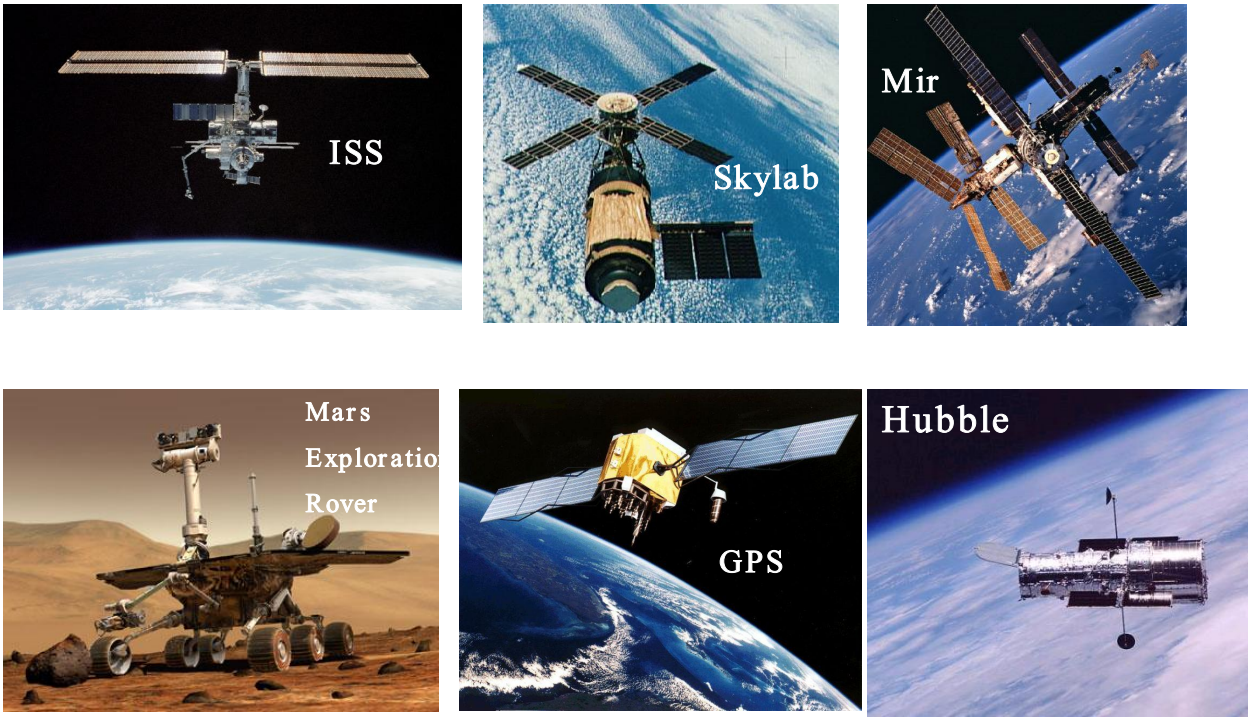

Figure 224: several space application examples

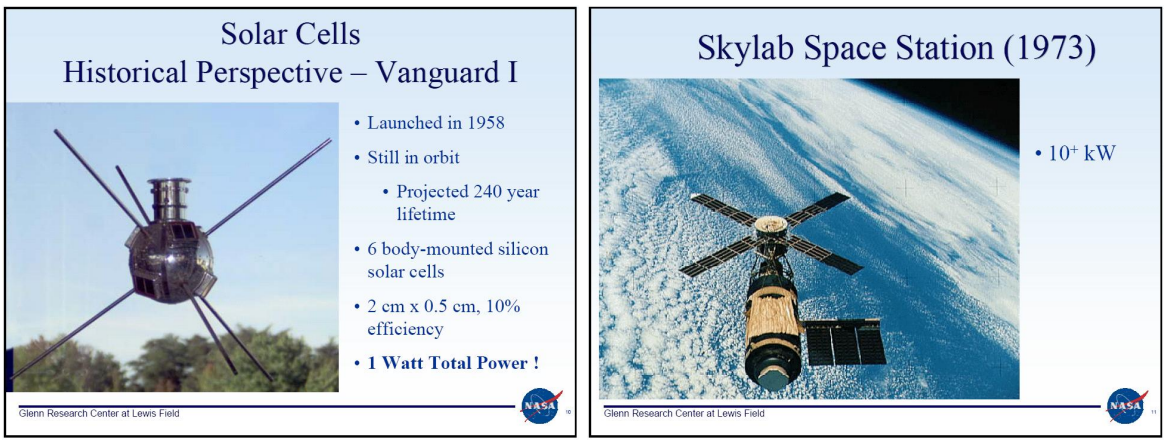

Figure 225: history of solar cell application

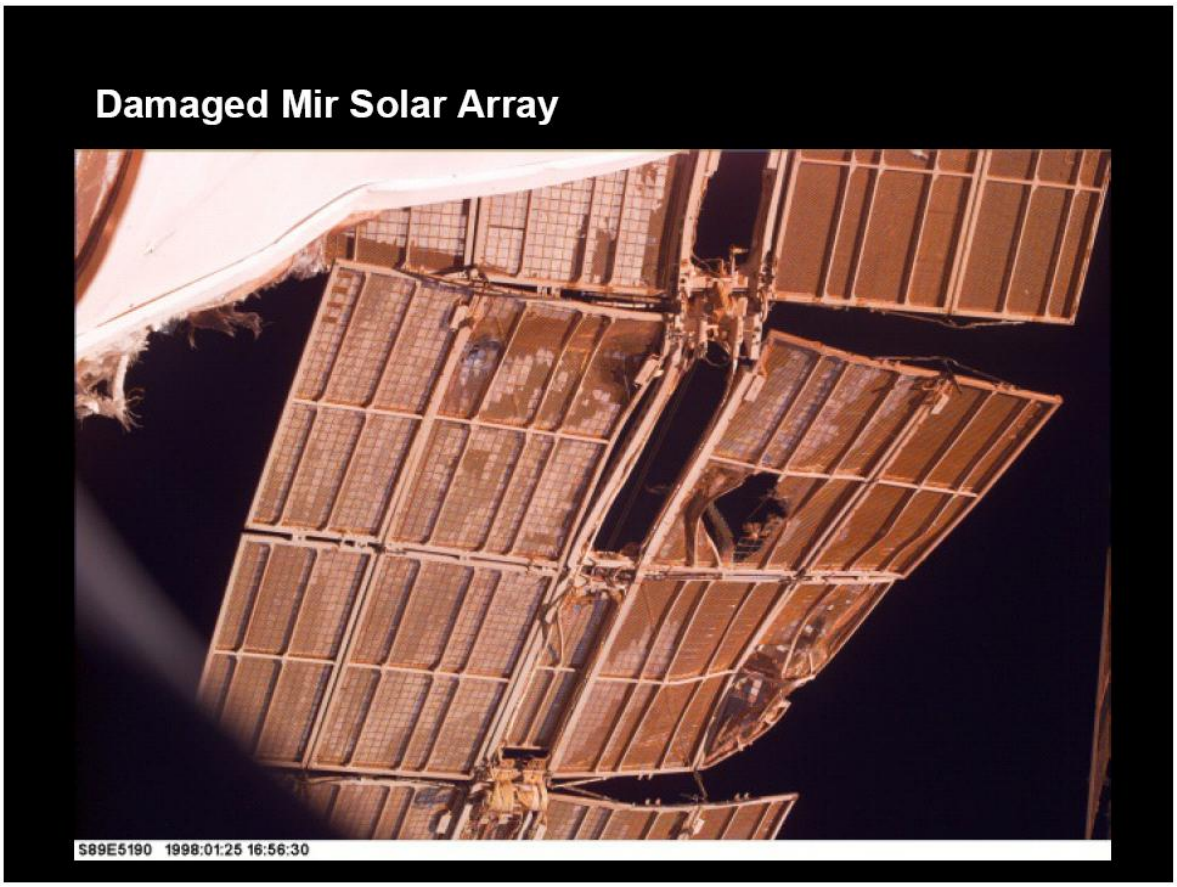

Figure 226: damaged solar array of MIR

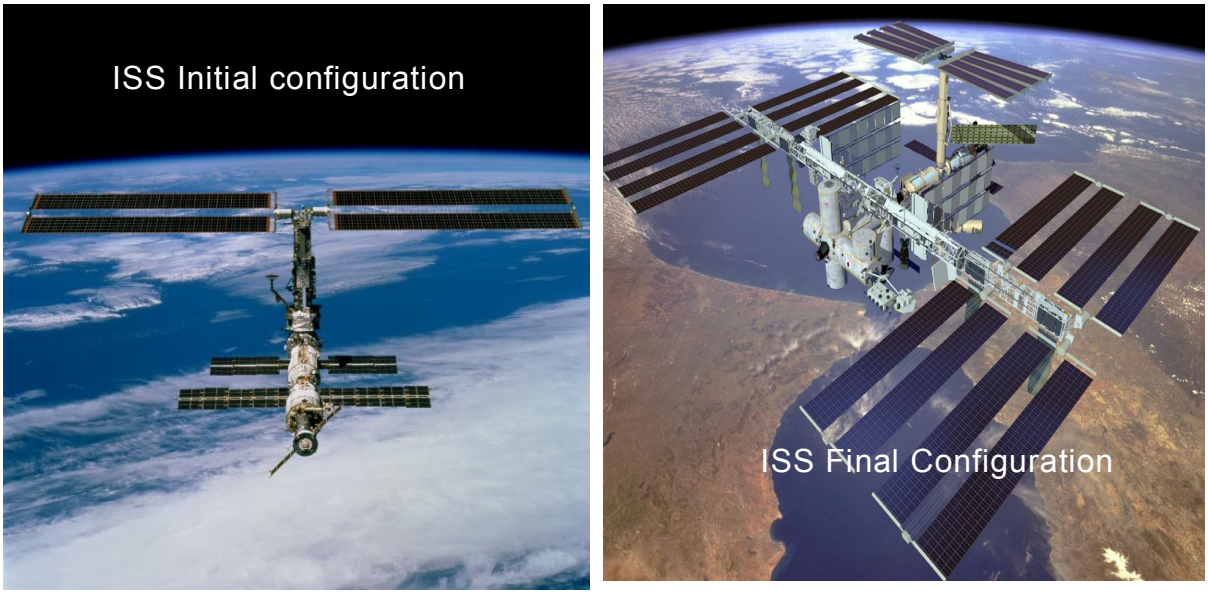

Figure 227: ISS solar array application: initial and final configuration

5.7.1 Solar Power Evaluation

The use of the solar power in space applications, presents some advantages and some drawback.

5.7.1.1 Advantages

- Unlimited energy supply
  - Mission duration not limited to on-board energy consumables
- Modular
  - Solar panel systems can be built independently of specific space system
- Established manufacturing base
- Cost effective
  - Proven technology does not require significant research expenditures
- No energy by-products or waste material

→ Best option for long-duration near-sun missions

5.7.1.2 Disadvantages

- Requires a significant illumination source
  - Sunlight strength diminishes as the distance from the sun increases
- Solar illumination insufficient for most applications beyond Mars
  - Most solar-powered space systems require additional energy storage (battery) systems
- Most free-flight systems are dependant on a vehicle control system to point the space craft and/or solar arrays

→ Unfeasible option for deep space missions

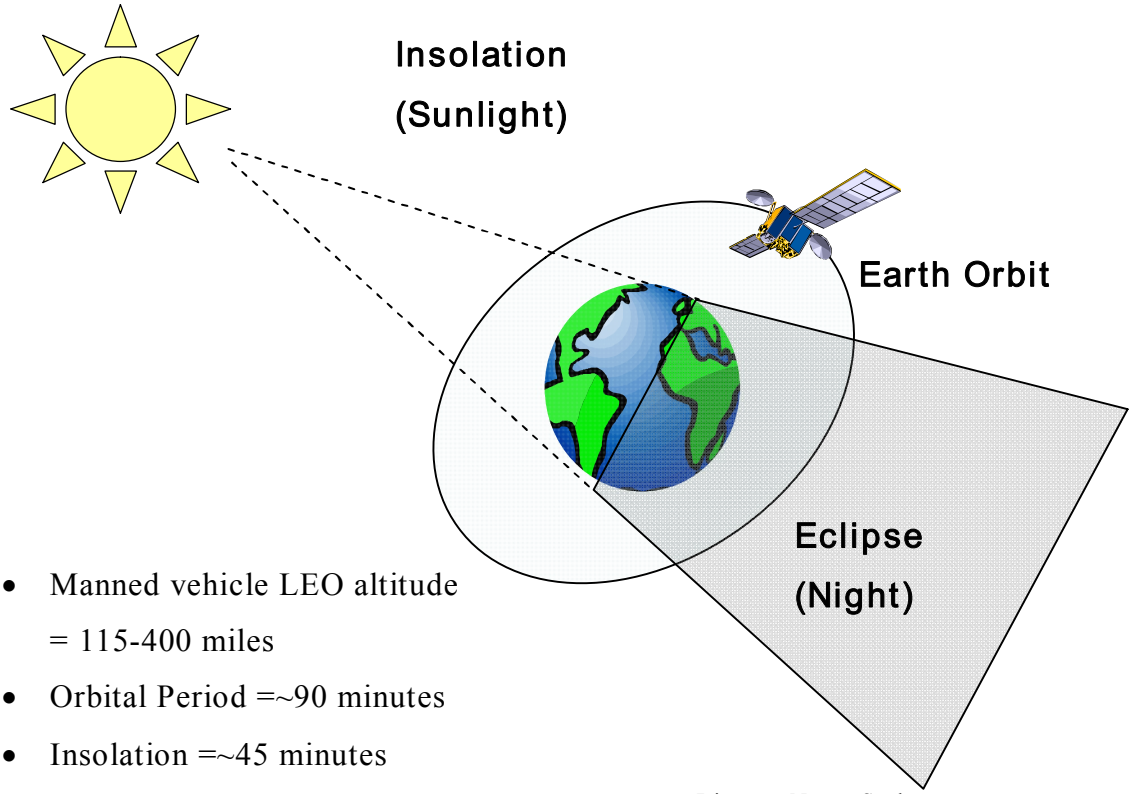

- Manned vehicle LEO altitude = 115-400 miles
- Orbital Period =~90 minutes
- Insolation =~45 minutes
- Eclipse =~45 minutes

Figure 228: problem with solar power application

5.7.2 ISS Solar Array Specifications

As an application example, the main specifications of ISS Solar Array are shown:

- One solar blanket has 16,400 cells
- Bypass diodes are located every 8 cells
- Final configuration 262,400 cells available for producing power
- Total area of 27,000 square feet approximately half an acre
- Each solar blanket has 82 active panels.
- 41 strings
- Each string is wired in parallel to produce the required power output.
- Primary power (150-160V DC)
- Secondary power (124.5 +/- 1.5 V DC)

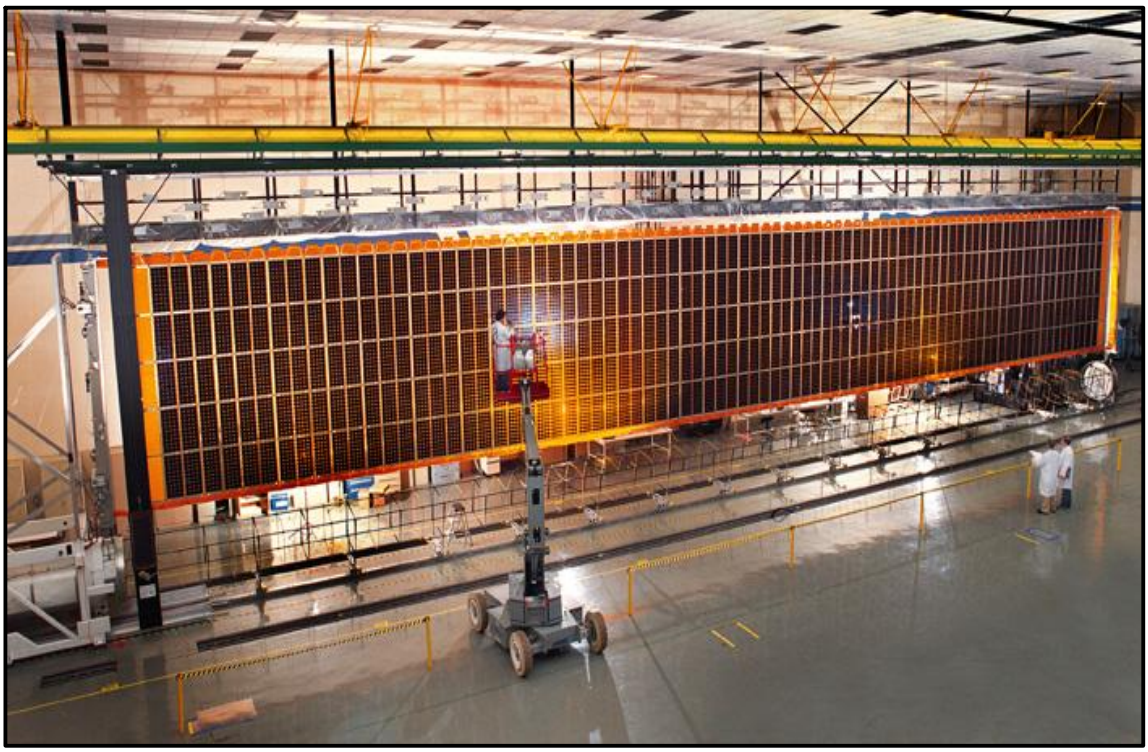

Figure 229: one ISS solar array

Figure 230: ISS solar array

5.7.3 Space Radiation effect on solar cells

- Radiation can wreak havoc on materials, causing either permanent or transient changes in their physical and electrical properties. Radiation comes in electromagnetic and particle forms. Nearly 99% of the solar electromagnetic radiation at one astronomical unit (distance from the earth to the sun) has a wavelength between 0.3 and 11 μm. In fact, visible light accounts for 41% of the total electromagnetic energy emitted from the sun. Together, both the ultraviolet and infrared spectrums account for most of the remaining energy. X-Rays, extreme ultraviolet, and radio wavelengths account for less than 0.1% of the solar energy.
- Solar electromagnetic radiation changes with solar activity and season (the distance between the earth and the sun changes, as the earth's orbital path is slightly elliptical). Reflected radiation (albedo) from both the earth and the Moon contribute to the total irradiance. The albedo is important to low earth orbits and varies with clouds and terrain.
- Ultraviolet radiation (UV) is particularly damaging to some materials. Most UV radiation is absorbed by the Earth's ozone layer. However, in space, high intensity UV radiation can severe organic chemical bonds. In addition, UV can lead to discolorations in polymeric materials and ceramics (e.g. glasses), which change the solar absorptivity of materials.
- Changes to a material's performance, such as the absorptance of white thermal control coatings must be accounted for in the design process, since the rate of heat transfer will change proportionately.
- The sun also emits a continuous stream of energetic charged particles. These electrons and protons (and some heavier ions) are called the "**solar wind**". On average these particles travel at over 400 km/s with a density of 5 particles per cubic centimeter.

5.7.4 Consequences of Atomic Oxygen Undercutting of Protected Polymers in Low Earth Orbit

Some concerns about solar cells demeaning are the effects of atomic oxygen on the Polymers in Low Earth Orbit. By the way the atomic oxygen is not present on the Moon surface so the problems remaining are mainly due to the solar radiation effect.

- *Hydrocarbon based polymers* that are exposed to *atomic oxygen* in low Earth orbit are slowly oxidized which results in recession of their surface.
- *Atomic oxygen protective coatings* have been developed which are both durable to atomic oxygen and effective in protecting underlying polymers.
- However, scratches, pin window defects polymer surface roughness and protective coating layer configuration can result in erosion and potential failure of protected thin polymer films even though the coatings are themselves atomic oxygen durable.
- *Metal atoms or metal oxide molecules* have been used extensively for the protective coating materials. Typically *silicon dioxide, fluoropolymer filled silicon dioxide, aluminum oxide or germanium* has been sputter deposited on polymers to provide atomic oxygen protection. For example, the large solar array blankets on International Space Station have been coated with *1300 Angstroms of SiO_2* for atomic oxygen protection

5.7.4.1 Testing of ISS Photovoltaic Array in space environment

- Prior to deployment, the ISS photovoltaic arrays were folded into a box that allows the array to be compressed in a controlled manner against a cushion of open pore polyimide foam that was covered with a 0.0254 mm thick aluminized Kapton blanket. The Kapton was coated on both surfaces with 1000 Angstroms of vacuum deposited aluminum.
- The array was exposed to the LEO atomic oxygen environment from December 2000 through December 2001.

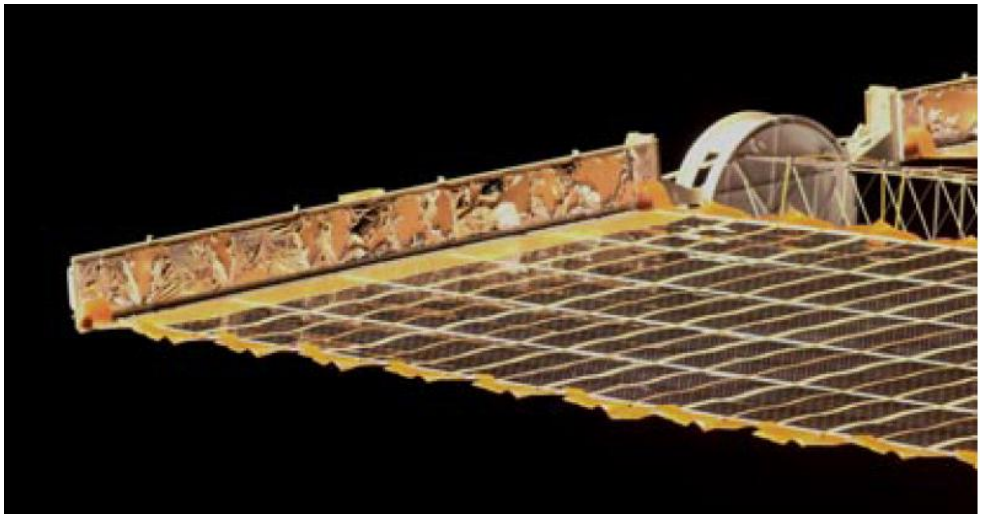

Figure 231

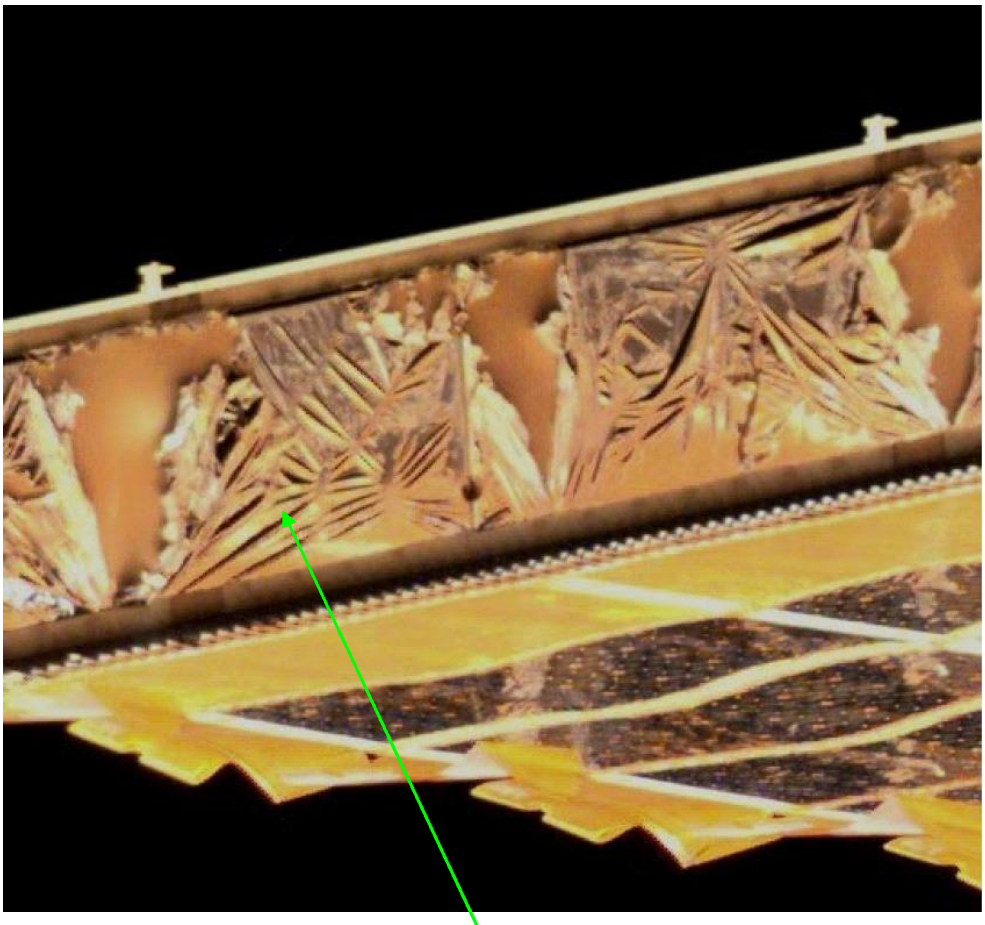

ISS photovoltaic array showing effects of *atomic oxygen erosion of the double aluminized Kapton blanket cover* for the ISS photovoltaic arrays box

Figure 232: consequence of atomic oxygen

5.7.4.2 Conclusions

- Atomic oxygen protective coatings have been developed and used in space. However, rough surface substrates cause defects in the protective coatings that allow atomic oxygen to react and gradually undercut the protective coating.

- *Atomic oxygen undercutting of the double aluminized Kapton blanket covers for the ISS photovoltaic array box cushions has occurred resulting in a torn and partially detached aluminum film.*
- *Based on computational modeling, atomic oxygen atoms that become trapped between the two aluminized films on each side of the Kapton blanket appear to cause accelerated undercutting damage in comparison to the use of a single top-surface coating*

5.8 Inflatable Solar Array

The following paragraphs speaks about new solar array technologies, the basic idea is to reduce the heavy of the solar array structures.

- The advantages of using inflatable systems technology in designing a large solar array are reduced stowage volume and mass, increased specific power (greater than 100 W/kg), and reduced cost over current mechanically deployed solar arrays.
- The inflatable solar array is particularly attractive for missions that demand high power output with launch vehicle size restrictions.

5.8.1 ST4 Inflatable Solar Array

- The JPL ST4 spacecraft requires high power output arrays (2 wings at 6 kW per wing) to accomplish the mission of rendezvous with the Temple 1 comet and landing to perform scientific measurements. The ST4 inflatable solar array is a 3-meter by 15-meter solar array capable of producing 6 kW of power.
- The basic configuration of the ST4 inflatable solar array, next Figure, consists of four major subsystems:

    - Solar Array Blanket
    - Structural Support Components
    - Controlled Deployment System
    - Inflation System

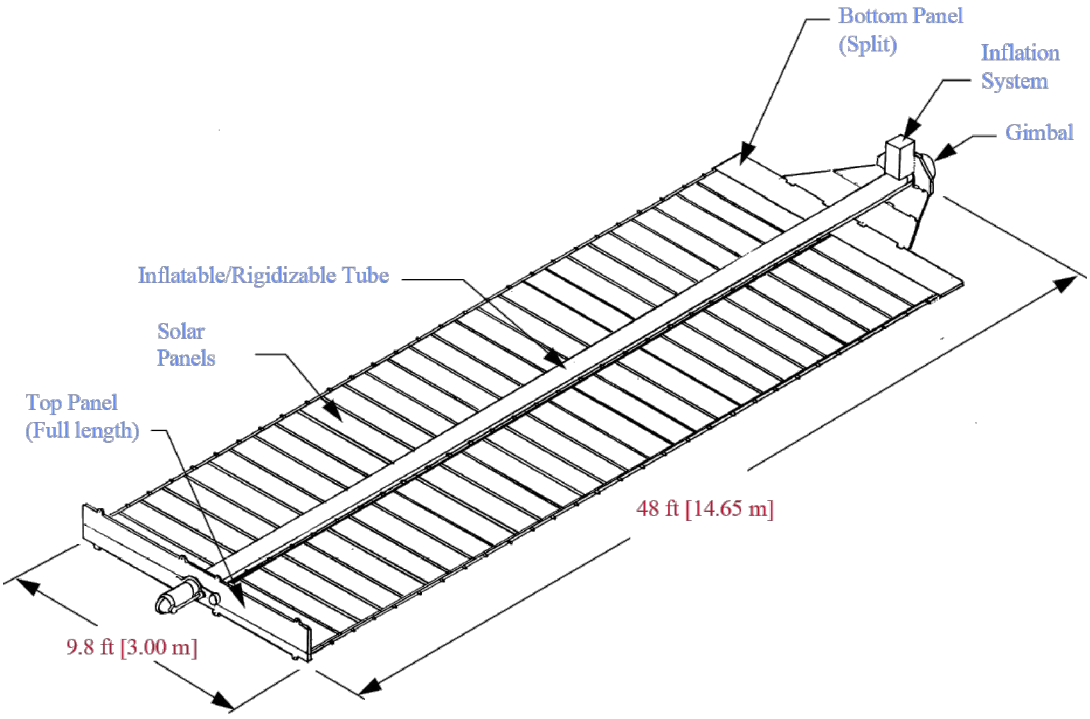

Figure 233: ST4 Inflatable solar array

5.8.1.1 Solar Array Blanket

- The configuration of the ST4 solar array is a modular split blanket style with the deployment tube located on the array centerline. When stowed, the solar array modules are accordion-folded. Currently, Sharp's rigid high-efficiency silicon photovoltaic assemblies are the basic building blocks for the modular blanket solar array. Flexible thin film solar cells using amorphous silicon, *copper indium gallium diselenide* or other materials hold great promise to provide even lower cost and lighter weight photovoltaic modules in similar arrays in the future.

5.8.1.2 Structural Support Components

- This subsystem includes the inflatable beam, stowage panels, plume-offset panels, launch ties, and launch tie release mechanism.

- The purpose of the inflatable beam is to provide a deployment mechanism and support structure for the solar array. It is similar in function to the mechanical deployment truss masts currently utilized on spacecraft. The beam is located on center of the split blanket and is stowed by rolling the tube, see next Figure.

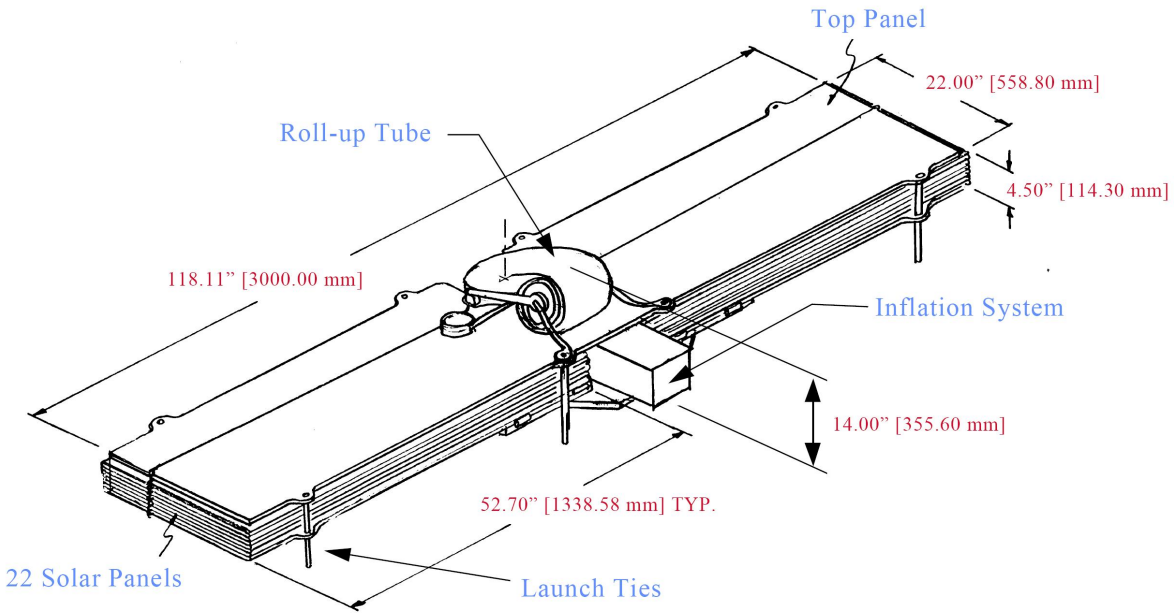

Figure 234: ST4 Inflatable Solar Array Stowed Configuration

5.8.1.3 Controlled Deployment System

- The ILC roll-up device with the embedded torque mechanism is the current baseline design for the ST4 inflatable solar array deployment system. When gas is introduced in the base of the tube, the tube inflates and begins to unfurl. The torque mechanism provides resistance to the unrolling action and builds

pressure in the tube at a uniform and constant level. The pressure in the tube yields a tensile stress in the tube wall, which provides interim beam stiffness during deployment. The torque mechanism is attached to the tip spreader plate on the array, which deploys the array blanket. Guide wires are also attached to both spreader plates and the blanket for control of the blanket during deployment.

5.8.1.4 Inflation System

- Inflation systems for the space inflatable structures have included compressed gas, gas generators, and sublimation of powders and liquids into gases.
- Each of these approaches has its advantages and disadvantages depending on the specific application.
- In recent years, compressed gas systems have become very low mass and highly reliable, making them the most practical option for most space inflatable applications. A compressed gas system is currently baselined for the ST4 inflatable solar array inflation system.

5.8.2 TELEDESIC Inflatable Solar Array

The Teledesic program envisions a constellation of 288 satellites in low earth orbit to provide high data rate communication from anywhere on earth. Original concepts for the satellite included a pair of 6 kW solar array, see Figure below, with a cost target of $100/W in production. Inflatable technology was considered to be a leading candidate in meeting this goal and was therefore investigated by the Teledesic team.

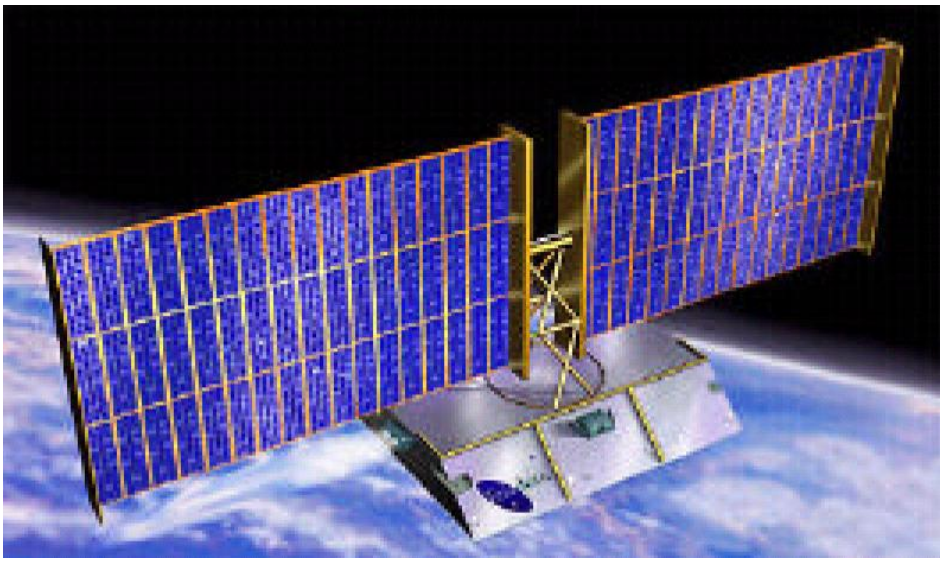

Figure 235: TELEDESIC Inflatable Solar Array

5.8.2.1 Inflatable structure prototype example

- ILC Dover, under contract to Boeing, designed an inflatable structure to support a 3-meter by 10-meter rectangular satellite solar array.
- Due to the limited packing volume of the array, the mast system is designed with a deployment tube, whose only function is to deploy the array, and two composite rigidizable tubes to provide structural support after deployment.
- This design was also constrained by a requirement for limiting frontal area in any orientation to reduce drag during orbital ascent. This requirement forced the use of a three-tube system rather than a single multifunctional tube structure.

Figure 236: Inflatable Solar Array Prototype

5.8.3 Power-Scalable Inflation-Deployed Solar Array

- Power scalable version of the Inflatable Torus Solar Array Technology (ITSAT) Developed by L'Garde funded by a Phase I DARPA SBIR.
- The design studied herein centered around Triple Junction GaAs/Ge cells mounted on a flexible Kapton blanket.
- This cell/blanket choice will provide the best technology that is currently available. By packing a high efficiency solar cell, it is possible to use a smaller structure and benefit from the mass savings since the area required to achieve a design power will be smaller. This design was further exercised to meet the New Millennium Program's, ST-8 requirements.
- The design for the ST-8 study was a 7 kW array with a power density >175 W/kg, a very small stowed volume <0.22 m3, and a deployed natural frequency >0.1 Hz.
- The typical conceptual configuration is shown in next Figure in the deployed configuration.

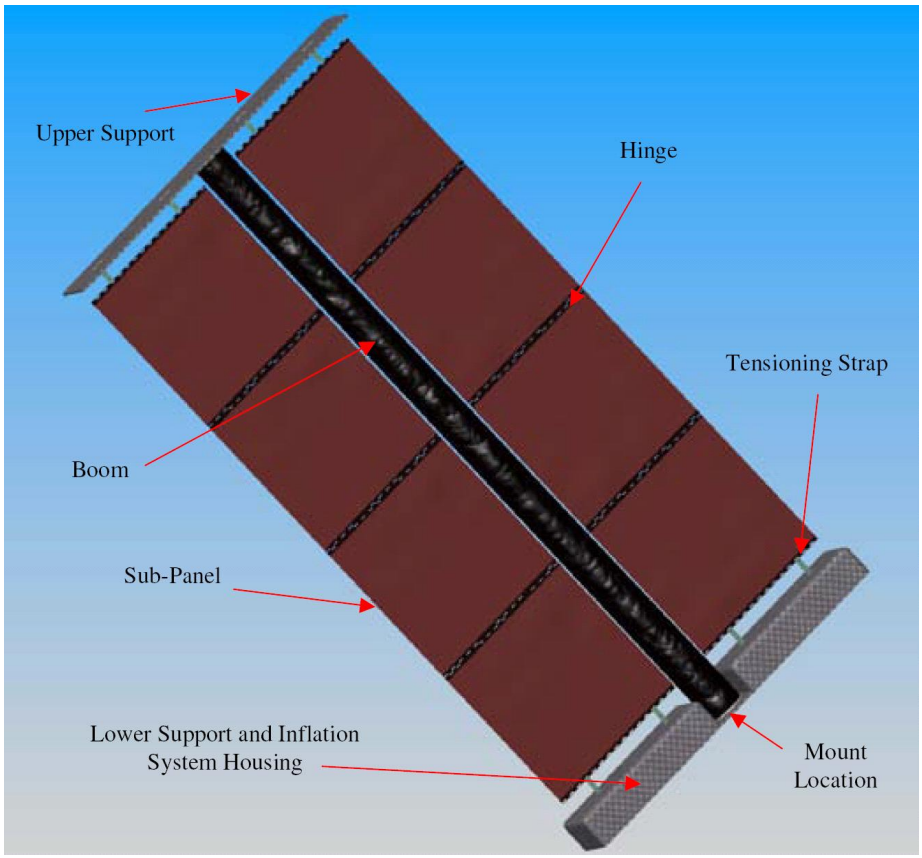

Figure 237: Typical Deployed Configuration

Figure 238: ITSAT Solar Array

5.8.3.1 Sub-Tg rigidizable materials used for Solar Array deployment

- Recent advancements allow the design to be more scalable and include the use of sub-Tg rigidizable materials and conical deployment of the booms.
- These coupled technologies form the basis for the advancements in the ITSAT design.
- Sub-Tg or cold rigidization takes advantage of the phase change of certain materials at specific temperatures to achieve structural strength. Instead of a thin sheet of aluminum as used on ITSAT, the material is made up of a specialized composite weave utilizing strong, lightweight fibers impregnated with a specialized L'Garde developed elastomer.

- Though called cold rigidizables they do not necessarily require cold temperatures.
- Elastomers can be formulated which rigidize at temperatures tailored to specific mission requirements. Cold rigidized structures can be constructed for a variety of missions, from LEO to deep space applications.
- At the heart of the composite is L'Garde's sub-Tg or cold rigidization matrix. The matrix is a thermoplastic elastomer tailored to be space hazard resistant and become rigid below a designed temperature.
- Current matrix Tg's include +50C, +20C, 0C, and –20C to meet the peak temperature requirements that would be seen on a variety of missions.
- The material is completely passive, reversible, and in general requires only moderate heating to soften for deployment if the spacecraft environment is below the composite Tg. This is a low power option to thermosetting plastics.
- After deployment, outside the spacecraft's thermal environment, the boom cools passively and becomes rigid.
- In a space application, prior and during deployment, the MLI-covered rigidizable boom is kept above its Tg and hence flexible. Once deployed by inflation it is allowed to passively cool down to its operating temperature, which is well below its Tg.

- As an example, for a 1000 km orbit altitude- thermal analysis shows that after a few orbits, the temperature will have fallen to about -60°C. The temperature-time history of such an orbiting boom is shown in next Figure.

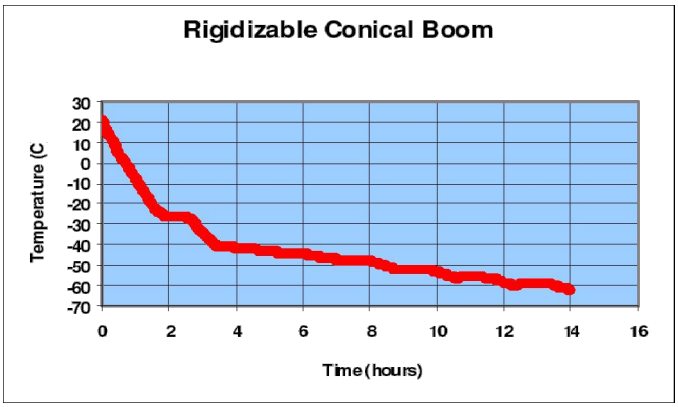

Figure 239: rigidizable conical boom temperature analisys

5.8.3.2 Conical Deployment

- Next Figure shows the conical boom deploying in the laboratory environment (US Patent Pending Serial Number 10/234047, "Deployable Inflatable Boom and Methods for Packaging and Deploying a Deployable Inflatable Boom," filed August 29, 2002).
- It uses a unique concentric packaging arrangement about the boom axis shown in Figure and provides a high degree of deployment control. In this method, a tapered tube is packaged in a manner similar to a telescoping tube.
- Because there is a very low mass associated with the deployment control method, it scales very well both up and down in size and provides excellent packaging efficiency.
- To deploy the conical boom, inflation gas is introduced at the base.
- Pressure is exerted against the walls of the tube, the tip, and base end caps. The inflation pressure squeezes the walls against the outer folds and also unfolds and deploys the leading folds. This provides stability both during and upon completion of deployment.

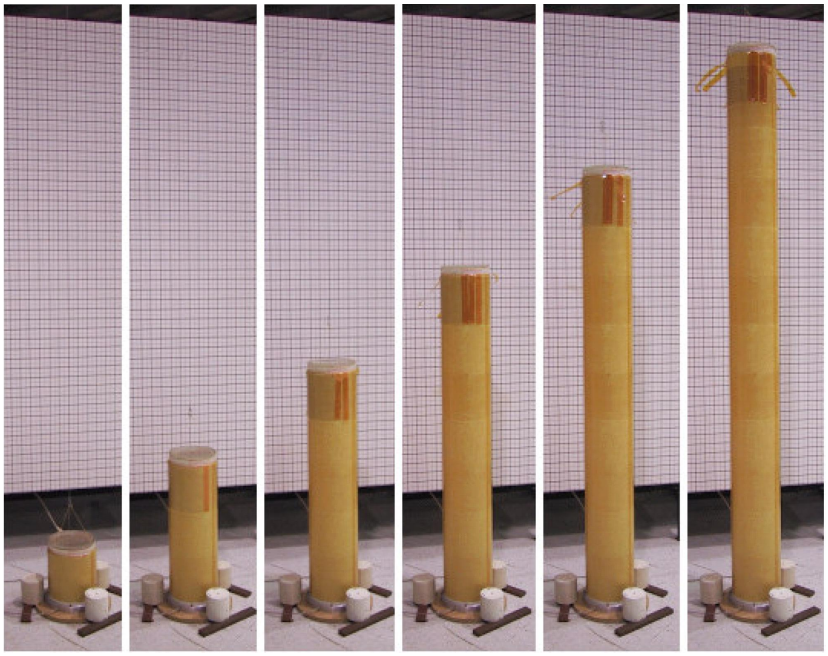

Figure 240: Boom Deployment in Laboratory Environment

5.8.3.3 Current Design Description

- The structural system changes from the ITSAT design are centered on the use of the conical boom.
- The system design is comprised of an inflation deployed boom flanked by two solar array blankets.
- The boom is a telescoping, thin-walled, conical tube that when inflated deploys the solar array system.
- The solar array blanket is a flexible, thin film polyimide curtain populated with solar cells as previously described.

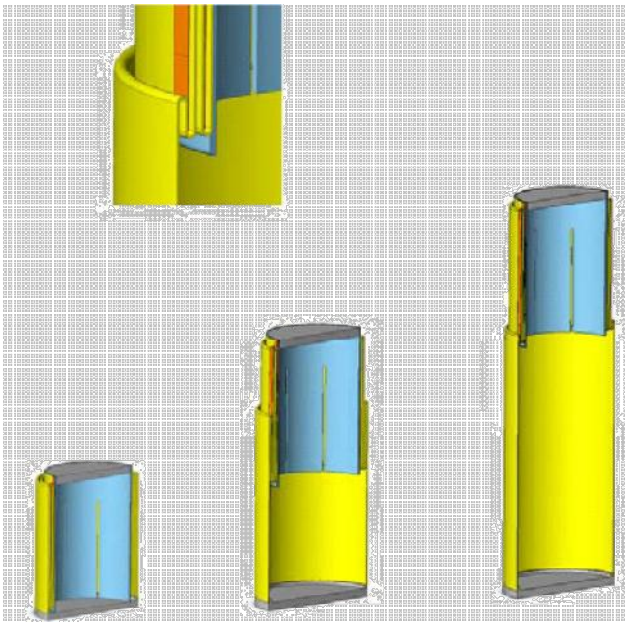

Figure 241: Typical Conical Deployment Unfolding the First Section from Left to Right

5.8.3.4 The Conical Boom

- The material chosen for this boom design can vary but its usual construction is of a Kevlar fabric impregnated with L'Garde's proprietary sub Tg matrix.
- Kevlar is used in the composite to achieve the fabric flexibility required to deploy.
- The sub-Tg conical boom has a robust capability for dealing with buckling phenomena. Using thicker materials mitigates local buckling effects; using larger diameters mitigates long column buckling effects..

5.8.3.5 Deployment Sequence

- The first step of the deployment sequence is to energize a heater to allow the boom material to become pliable. This is required if the spacecraft thermal environment is colder than the Tg of the boom composite.
- During deployment, the boom is always enclosed in multi-layered insulation

(MLI) to reduce the heat needed to make the boom pliable and minimize thermal gradients on orbit during operation.

- The outer layer of MLI is coated to have optical properties that allow the temperature of the boom to fall below the Tg of the matrix.
- During deployment and until the boom is rigidized, the boom remains inflated (pressure-stabilized) and can carry load both in its partially and fully deployed state, see Figure below.
- Finally, once the boom is fully extended the heater is de-energized. The inflation gas remains while the boom passively cools below its Tg to rigidize. Once rigidized, the inflation gas is no longer required for support and is non-propulsively vented.

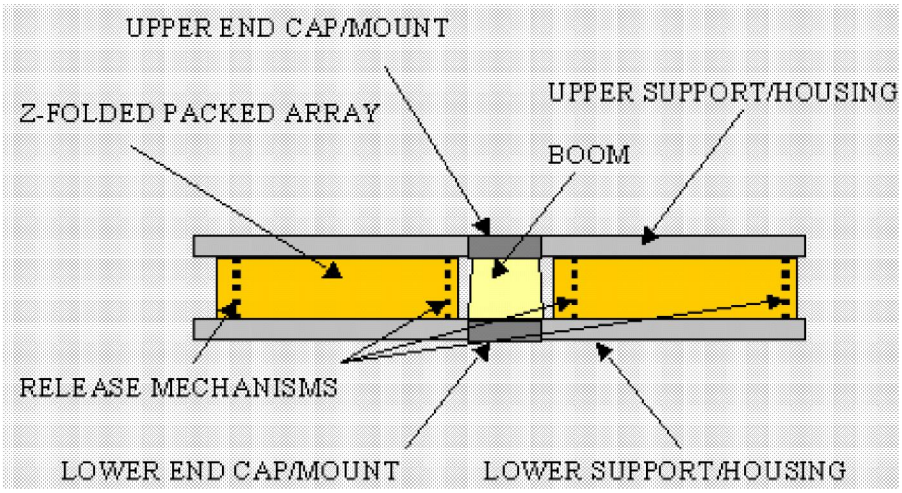

Figure 242: Stowed Configuration

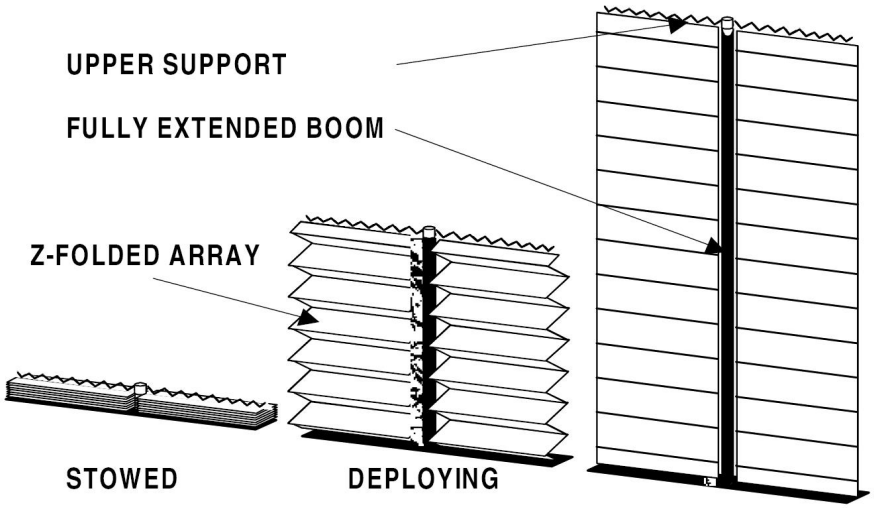

Figure 243: Deployment Configuration

Specification	Goal	Design
System		
EOL Power	1250 W/wing	1244 W/wing
BOL Power	-	1320 W/wing
BOL Power Density	-	115 W/kg
EOL Power Density	-	108 W/kg
Mass	-	11.5 kg
Packaged Volume	-	0.04 m3
Packaged Dimensions	-	1.37 m x 0.24 m x 0.12 m
Deployed Dimensions	-	1.37 m x 0.24 m x 4.05 m
Natural frequency		
System	> 0.5 Hz	0.66 Hz
Array		
Type	-	Triple Junction GaAs/Ge
Cell Thickness	-	140 um
Cell Size	-	3.716 cm x 7.16 cm
Cover Glass Thickness	None	3 mil
Cell Efficiency	-	27.6%
Aspect Ratio of Blanket	-	6.2:1 (each array)
Deployment Characteristics		
Tube Deployment Temp.	-	~ 20 C
Tube Ridgidization Temp.	-	-20 C
Tube Operating Temp.	-	~ -45 C
Deployment Time	-	2~5 min
Rigidization Time	-	~ 6 hours
Orbital Parameters		
Lifetime	-	5 yr
Altitude	-	600-800 km (750 km nominal)
Inclination	-	28.5 degree
Acceleration	> 0.03 g	> 0.03 g

Table 29: Specifications

5.8.4 Passively Deployed Roll-Out Solar Array

5.8.4.1 Introduction

- Future satellite power subsystems will be designed to achieve higher power levels (kW), power densities (kW/kg), launch packaging densities (kW/m^3), and lower unit costs ($/kW) than can be achieved with current solar array technologies.
- The largest currently available commercial solar arrays provide only about 15 kW end-of-life power, with power densities of 50-70 W/kg, packaging efficiencies of 10-15 kW/m^3, and costs of about $1,000/Watt.
- Future large spacecraft may require up to 50 kW of power at power densities greater than 250W/kg, as well as lower costs and improved-packaging density and power density.
- Scale-up of current technologies, such as rigid flat-panel solar arrays, is likely to be very expensive and require larger launch vehicles due to their inherent packaging limitations and low mass efficiency.
- Thin film photovoltaic (TFPV) solar arrays offer the potential for providing very high power levels in a lightweight configuration that can be compactly packaged for launch. However, the lower power-conversion efficiency of TFPV as compared to existing photovoltaic technologies means that larger deployed areas are required to provide a given total power.
- This limitation in TFPV technology means that TFPV systems will only be practical if more efficient deployment technologies and structural designs can be developed.
- Current deployable solar array systems are based on designs that have been in existence for more than 30 years. In general, these heritage designs can be divided into two classes:
    - hinged-panel arrays, which are mechanically simple but mass inefficient, and
    - tensioned-membrane arrays, which are mechanically complex but mass efficient.

- Arguably, no deployable solar array designs exist that are both mechanically simple and mass efficient.
- To address this need, the:
  Roll Out and Passively Deployed Solar Array (RAPDAR) combines an innovative structural concept with TEMBO Elastic Memory Composite (EMC) technology for efficient packaging, deployment control, and post-deployed stiffness and strength.
- RAPDAR is being developed as an enabling technology for future ultra-large, ultra-efficient TFPV solar arrays.

5.8.4.2 TEMBO Elastic Memory Composites

- TEMBO EMC materials exhibit many favorable qualities for deployable space structures and have piqued a broad interest within America's deployable space structures industry.
- TEMBO EMC materials, which combine a fully-cured thermoset TEMBO shape memory polymer matrix with traditional fiber reinforcements, are characterized by an ability to "freeze" and release induced strain energy via a specific thermo-mechanical cycle.
- Furthermore, TEMBO EMC materials can achieve significantly higher induced packaging strains than traditional hard-resin composites without damage to the fibers or the resin, which leads to TEMBO EMC components that can be packaged more compactly than traditional designs.
- TEMBO EMC materials also provide high strength and modulus, and low density, which leads to lightweight component designs.
- Finally, TEMBO EMC materials provide the added advantage of much lower stored strain energy than traditional high-strain, high-stiffness materials, thus significantly reducing parasitic mass associated with launch-containment devices.
- These unique capabilities are currently being exploited in the development of the highly efficient RAPDAR structural system.

5.8.4.3 RAPDAR System overview

- The overall layout of the RAPDAR array system is shown in Figure. The design is scalable to between 1 and 50 kW size, and is applicable to a variety of future large commercial and government solar arrays.
- The RAPDAR system features two TEMBO EMC primary longerons that are flattened and rolled for stowage and regain their original cross-section during deployment.
- The primary longerons are connected by a series of battens, forming a central panel.
- Wing panels attach to the outsides of both primary longerons, and stow by folding across the center panel.
- As the center panel unrolls, the wings open and are held at a slight angle to the center panel by tensioned diagonals running from the tip of one wing to the tip of the other. TFPV blankets span the length and width of the deployed structure.

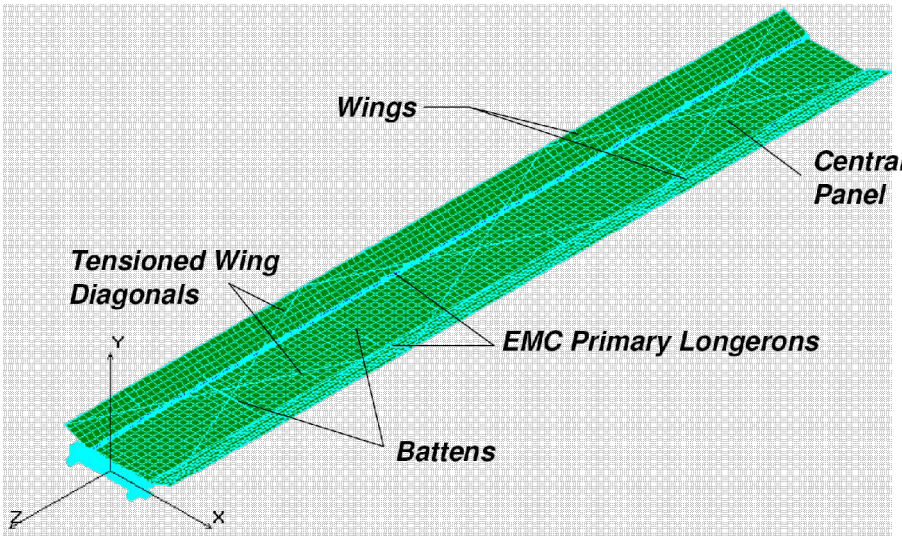

Figure 244: RAPDAR solar array system.

5.8.4.4 Packaging and Deployment Concept

- As shown on next Figure, the TEMBO EMC primary longeron is a slit-tube design. This allows the tube to be flattened and rolled.
- The battens and wing-edge longerons are made of an elastic material and have open cross-sections to allow them to be flattened during packaging.
- The TEMBO EMC primary longeron also functions as the wing hinge during packaging and deployment.
- The wings are folded onto the central panel while flattening the primary longeron, which puts the three-panel assembly into a single plane configuration that can be rolled into a cylindrical package.

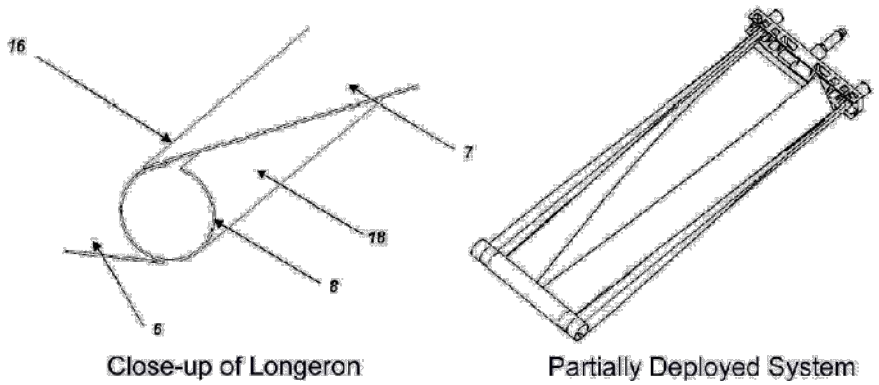

Figure 245: *Packaging and Deployment Concept*

- The deploying force is primarily derived from the strain energy stored in the rolled TEMBO EMC primary longerons. Additional strain energy is stored in the other frame elements, which are flattened and rolled into the stowed configuration.
- Most importantly, the TEMBO EMC primary longerons are designed to "freeze" all of the stored strain energy in their cold state, and release this energy in a controlled fashion when heated passively by the sun. (as will be discussed in the next section).
- While the TEMBO EMC primary longerons are unrolling, the wings are being deployed due to their integral nature (Figure next). The depth established by the deploying wings minimizes the ability for the partially unrolled array to

roll back on itself like a yo-yo. When deployment is complete, the wing-to-wing diagonal cables are tensioned to stabilize and stiffen the structure. Figure next shows four stages of deployment overlaid on one another.

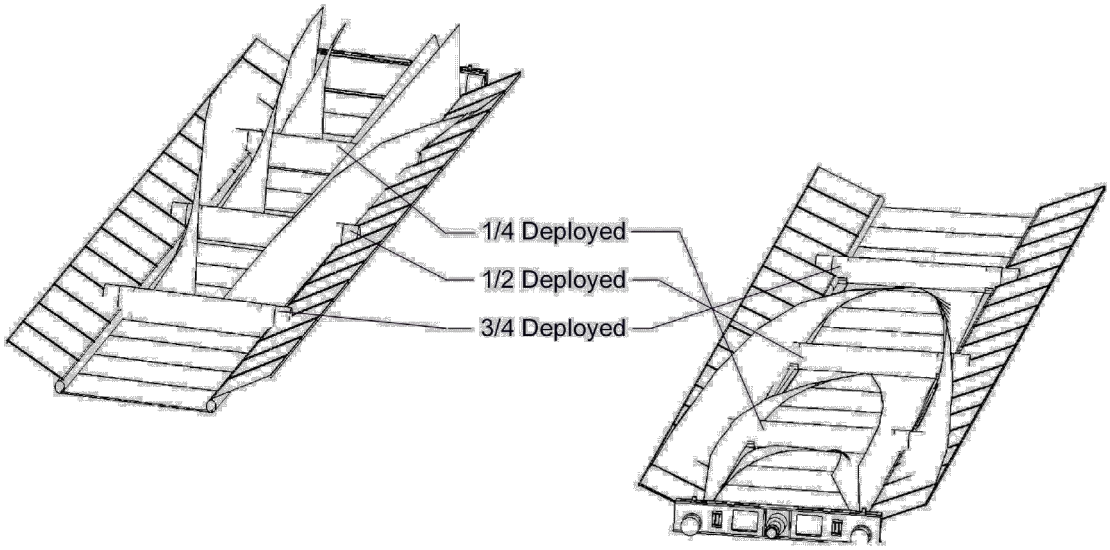

Figure 246: The deploying force system; stages of deployment.

5.8.4.5 System Scalability

As previously stated, the array system is scalable to between 1 and 50kW size. This is a key system feature that differentiates it from other TFPV flight development programs. By incorporating the wings, the RAPDAR system achieves deployed stability and structural depth, which is a feature key to maintaining reasonable deployed frequencies at larger sizes.

Furthermore, the spooled packaging method takes full advantage of the TFPV's flexibility resulting in a highly efficient array system with projected power densities several factors greater than other TFPV solar array concepts.

For example, analyses have shown that a 50kW version of the RAPDAR solar array system would be approximately 6m wide by 60m in length, possess a total mass of approximately 140 kg, and exhibit a fundamental frequency of 0.23 Hz. This frequency is relatively high for the size and mass of the system, a key performance metric that will moderate demands on actuation and control systems. Note, the

projected power density for the system would be over 350 W/kg, which is significantly higher than the 200 W/kg threshold identified as a market requirement.

5.8.4.6 RAPDAR Passive Deployment

- Deploying a TEMBO EMC structure requires the presence of heat, since both packaging and deployment must be accomplished above the polymer's glass transition temperature, Tg.
- Historically, TEMBO EMC components have incorporated surface-bonded heaters for packaging and deployment control.
- A unique aspect of the RAPDAR solar array is the use of solar energy to control deployment.
- Referred to as passive deployment, the concept of exploiting the solar thermal environment to enable deployment significantly reduces the system's complexity and eliminates the need for on-board power during deployment, thus improving the system's overall efficiency.
- The feasibility of passive deployment has been demonstrated through thermal analyses and ground testing, as described in the following slide.

5.8.4.7 Analysis

- These analyses considered only heating from the solar flux (i.e., no heating from the Earth's albedo was considered).
- The analyses assumed optical properties (i.e., absorbtance and emmittance) of bare graphite epoxy on the inside surface of the TEMBO EMC primary longerons, and either bare or white-coated optical properties on the outside surface.
- Next Figure presents steady-state thermal analysis results where the inside of the roll is solar pointing. The temperature contours indicate a temperature variation of over 200°C between the top and bottom of the roll.

- The maximum realized temperature exceeds 100°C and occurs throughout the transition region of the slit tube longeron. This is key since recovering induced strains in the transition region enables longeron deployment.
- It should be noted that the glass transition temperatures and hence, deployment temperatures, of the TEMBO EMC shape memory polymer matrix systems considered for RAPDAR are between 60 and 80°C.
- Therefore, this steady-state analysis indicates the feasibility of using in-orbit solar energy to achieve laminate temperatures that exceed the matrix's glass temperature thus enabling longeron deployment.
- Analysis for rate deployment, assume that a white coating is applied to the longeron's outer surface to aid in cooling the deployed longeron thus stiffening the EMC longerons once they achieve full cross-section (i.e., deployment).
- The transient thermal analysis was based on the single-longeron model shown in Figure and assumed that the longeron rotates relative to the sun to mimic the unrolling motion that occurs during deployment.

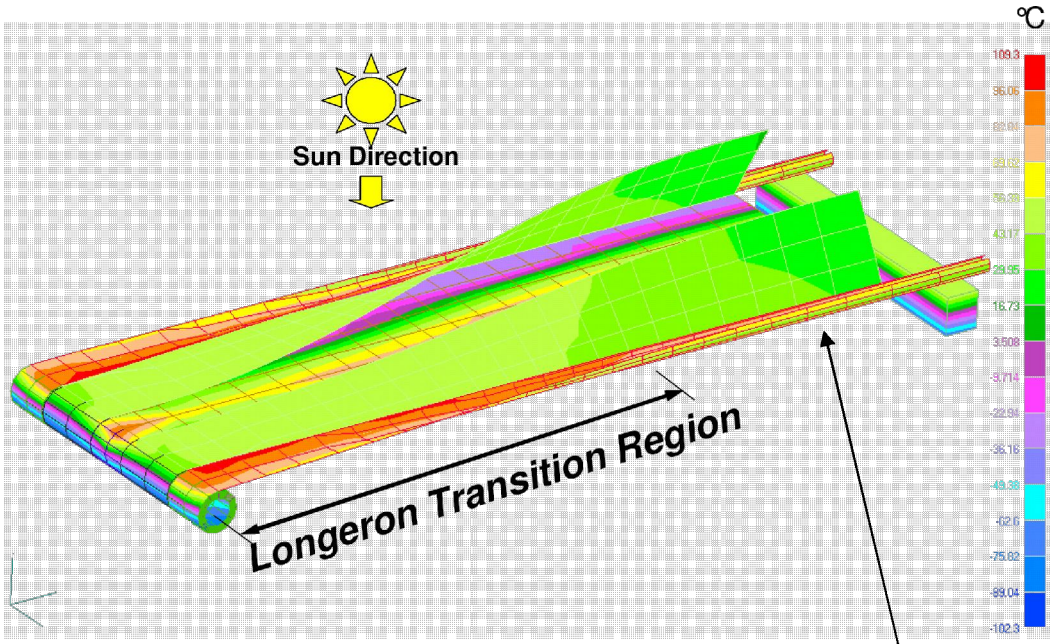

Figure 247: deployment as a function of temperature

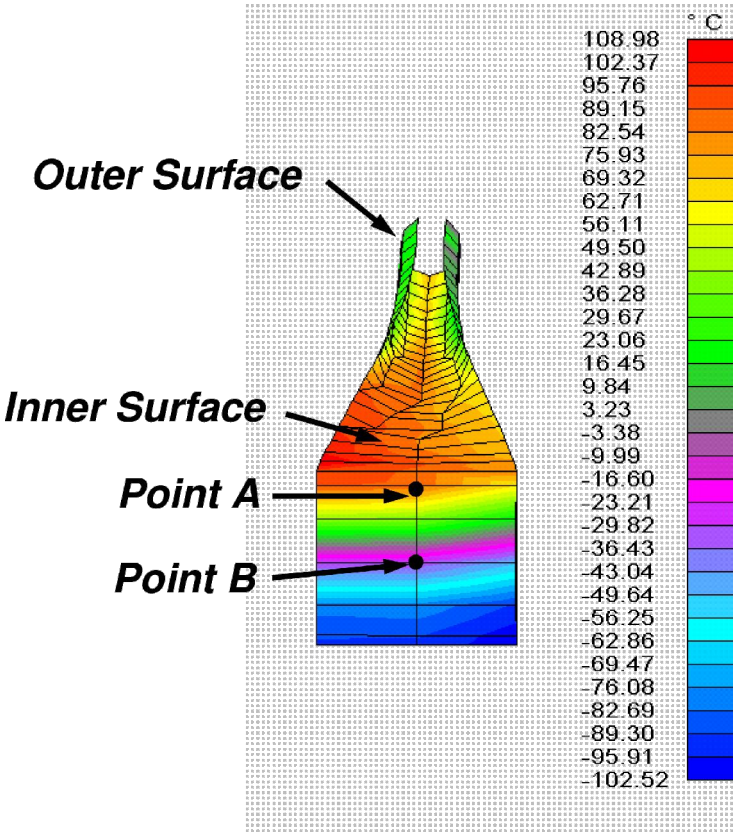

Figure 248: Temperature of deployment

- The key temperature results plotted in Figure are the temperatures at Points A and B, which are 90 degrees away from each other on the packaged-longeron roll.
- These minimum and maximum temperatures are plotted in Figure as a function of rotation rate RPM of the packaged longerons (relative to the sun). The results indicate that as the rotation rate increases, the maximum and minimum roll temperatures converge.

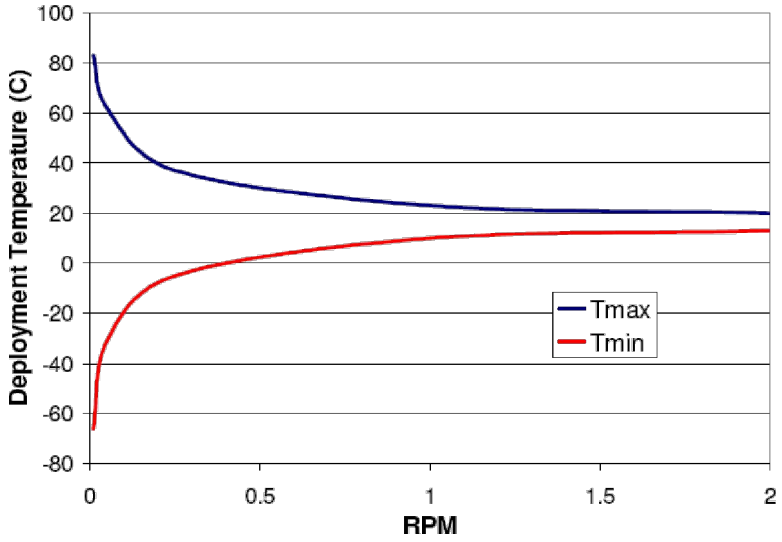

Figure 249: deployment temperature as a function of velocity deployment

- Figure above indicates that a longeron deployment rate of 0.1 revolutions-per-minute (RPM) could be achieved with a TEMBO EMC material that deploys at a temperature of 60°C. This is equivalent to a linear deployment rate of 7.2 m/hr based on assumed packaged geometry.
- This deployment rate enables complete deployment of the 50kW, 60m long array system in just over 8 hours. Therefore, the analysis results demonstrate the feasibility of achieving full deployment of the RAPDAR 50kW array within a single geosynchronous orbit which is a key requirement for the solar array system.
- Furthermore, a key conclusion of the thermal analyses is that the RAPDAR structure is deployment-rate limited due to the longeron heat-up time and viscoelastic properties inherent in the TEMBO® EMC longeron material.
- This is a significant advantage over traditional, elastically-strained deployable structures where energy containment during deployment is a major concern which impacts the overall system design.

5.9 LEMMB's Solar Array idea

In the previous sections of this chapter we have been analyzed the solar cells technologies at the present state of art.
Even though organic flexible solar cells seem to be a good promise for the future, the today's technology is not enough mature for space applications because, mainly, due to the low time duration when exposed to environmental conditions which cause rapid solar cells degradation.

On LEMMB module the aim is to have an efficient solar array packing system and an efficient and light weight solar panel.
After all the previous analysis, we conclude the best choice at this moment, fell on single-crystal silicon solar panels like those used on ISS (International Space Station 0.1 kW/kg).
This choice is reasonably due to the high efficiency η for this type of solar array.

LEMMB solar panels are expanded with the four Arms inflatable structures expansion.
This approach has the advantage of using a large surface available to the Sun rays once the four arms are completely expanded.
To increase the useful irradiated surface the rest of the LEMMB core surface could be covered with fixed solar arrays.

There are two main approach for the expandable solar array associated with the four expandable arms:

- The first is to use a structure similar to that used on ISS (International Space Station), approach preferred.
- The second is to use a texture directly on the four arms surface using some of the flexible solar arrays type previously mentioned.

5.9.1 First case: solar array developed as in ISS

A Partially deployed solar array wing on the ISS is showed below. The mechanism used to develop the solar array, is the *ISS Solar Array Beta Gimbal Assembly.*

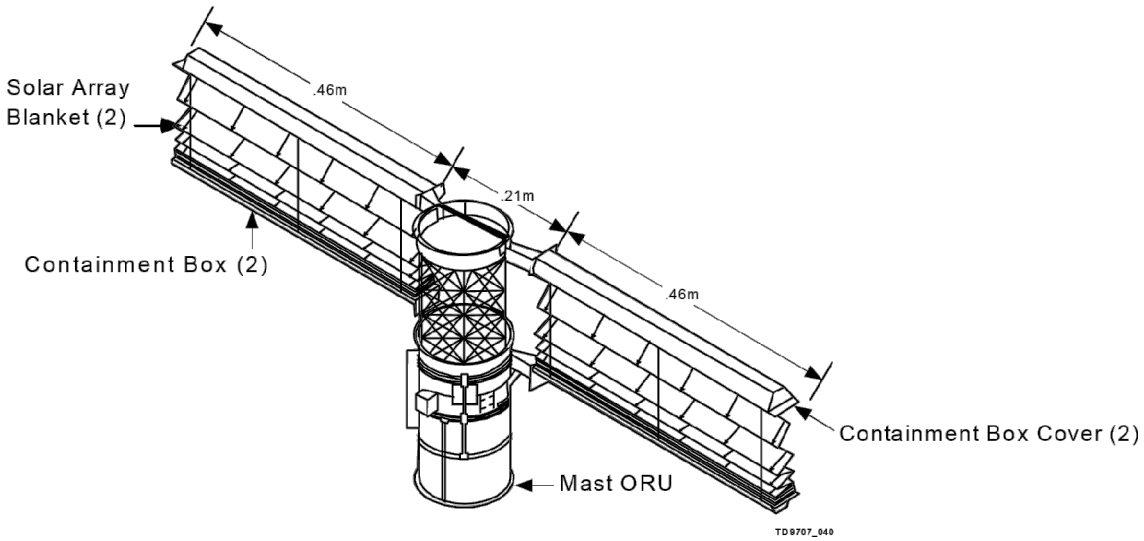

Figure 250: ISS Array Beta Gimbal Assembly

Figure 251: developed ISS solar array

As far as LEMMB is concerned, the four expandable arms are used as useful surface for solar array and as *Solar Array Beta Gimbal Assembly* (ISS mechanism).
Consequently the solar array expansion is a consequence of the four inflatable arms expansion, in fact each solar array top is fixed to the corresponding expandable arm top.
The concept are depicted in the following figures:

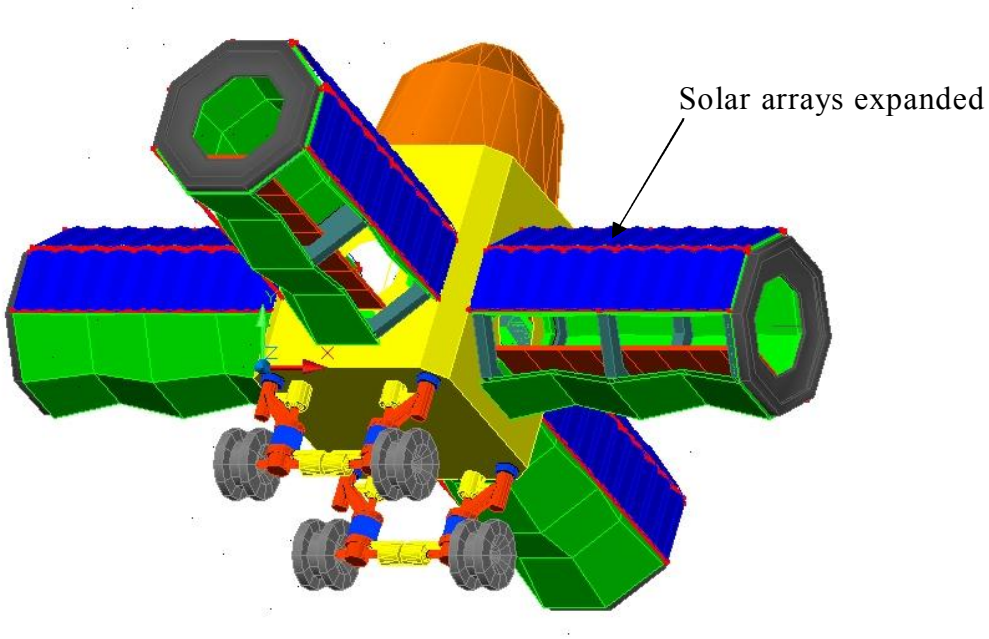

Figure 252: LEMMB solar array completely expanded above of the four arm surface

From the exposure sun of view it is convenient to put solar panels only on the surfaces potentially exposed to the Sun. As a consequence the lower part of each LEMMB's arm are not covered by the solar panels.

In order to avoid any contact and so any possible damage on the inflatable expandable surface, the ties are fixed to the clamp-band mechanism available on the top of the four arms. Figure below shows the details.

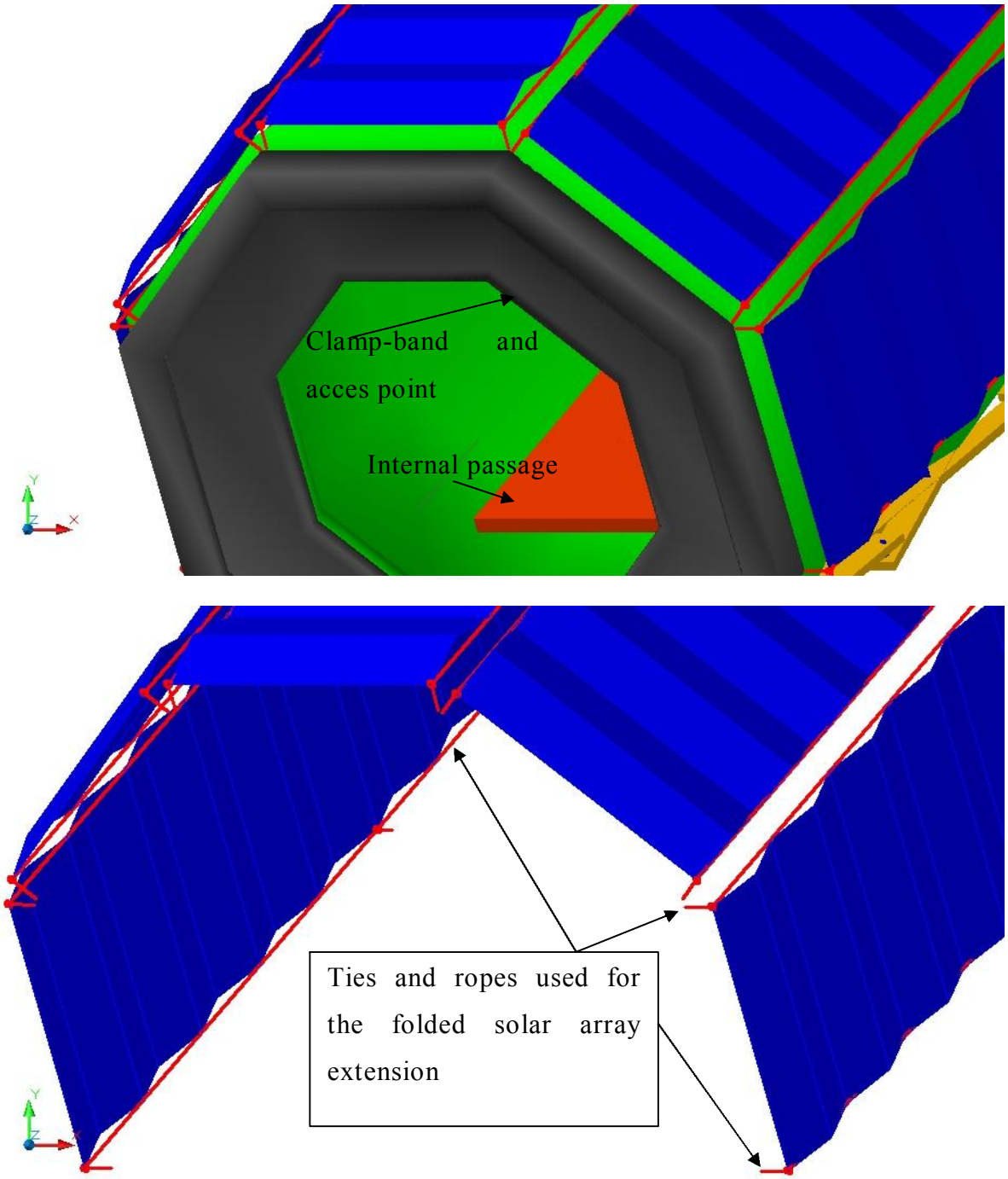

Figure 253: zoom particular of solar array

The internal astronauts' passages are developed automatically during arm expansion.

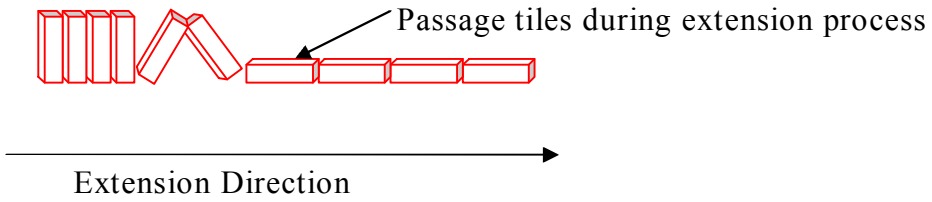

Figure 254: simplified extension mechanism for internal arms passages

When several LEMMB are connected to each other, in order to share the electrical power, the each one of LEMMB's arms must be provided by the electrical connections like on a train wagons.
Under the bridge within the arms structures there must be located electrical cables. This assures the communication data systems too.

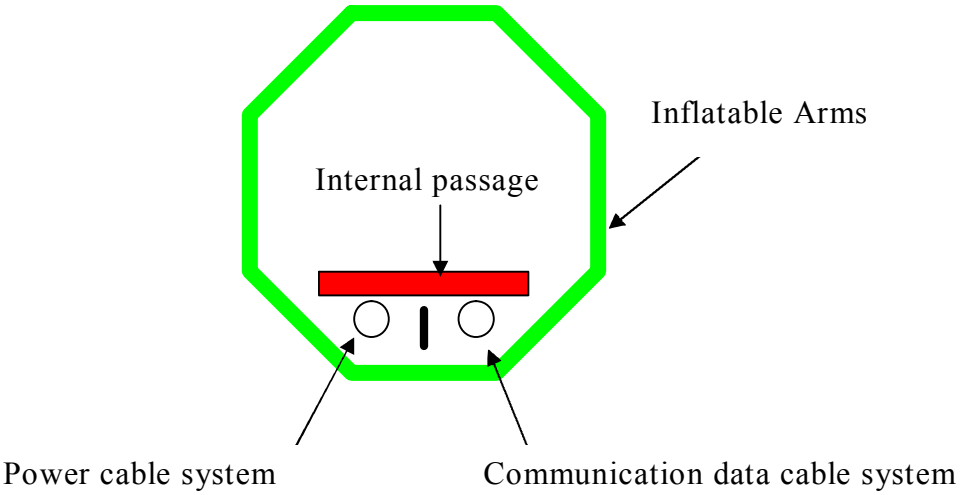

Figure 255: Inter-LEMMB electrical power and data communication systems connection.

5.9.1.1 How many electrical power can be generated by the solar arrays on LEMMB ?

Solar radiation has a spectrum peaked at the wavelength around **λ=0.5 μm**, plus it has a nearly black body profile with temperature **T=5770 K.**

In terms of the Stefan Boltzmann constant **σ**, the total luminosity is expressed by **L**:

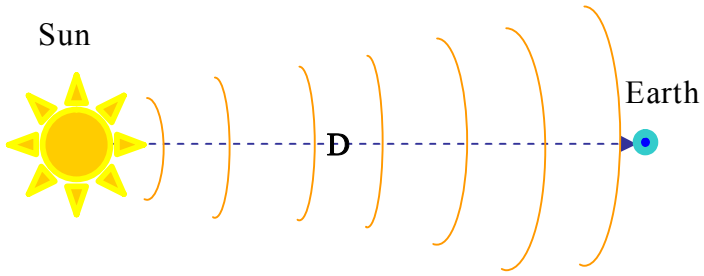

Figure 256: solar constant computing

$$L = 4\pi R_s^2 \sigma T_s^4 \cong 3.9 \cdot 10^{33} \left[\frac{erg}{s}\right] \cong 3.9 \cdot 10^{33} \left[\frac{10^{-7} J}{s}\right] = 3.9 \cdot 10^{26} [W]$$

eq 65

At a distance *D= 1AU (1 Astronomic Unit is about 150.000.000 Km)* the solar radiation corresponds to an energy flux **Φ** called **solar constant**:

$$\Phi_{Sun} = \frac{L}{4\pi D^2} = \left(\frac{R_s}{D}\right)^2 \sigma T_s^4 \cong \left\{1.366 \cdot 10^6 \left(\frac{AU}{D}\right)^2\right\} \quad \left[\frac{erg}{s \cdot cm^2}\right] \cong 1371 \pm 5 \left[\mathrm{W/m^2}\right]$$

$$\text{where:} \quad \left[\frac{W}{m^2}\right] = \left[\frac{J}{s \cdot m^2}\right] = \left[\frac{10^7 erg}{s \cdot 10^4 cm^2}\right]$$

eq 66

- **σ** = 5.67×10^{-8} W/(m^2 K^4) (Stefan-Boltzmann constant);

- **D** =1 AU mean Earth-Sun distance ≅1,496×10^{11}[m];
- **L** = solar luminosity [3.9×10^{26} W];
- **Rs** = solar radius=6.958×10^{8}[m];
- **T** = black body temperature of the sun [5770 K];
- Variations of Φ are the main cause of climate changes on Earth;

(the solar constant, is a crucial quantity) [**1371± 5 W/m^2**]

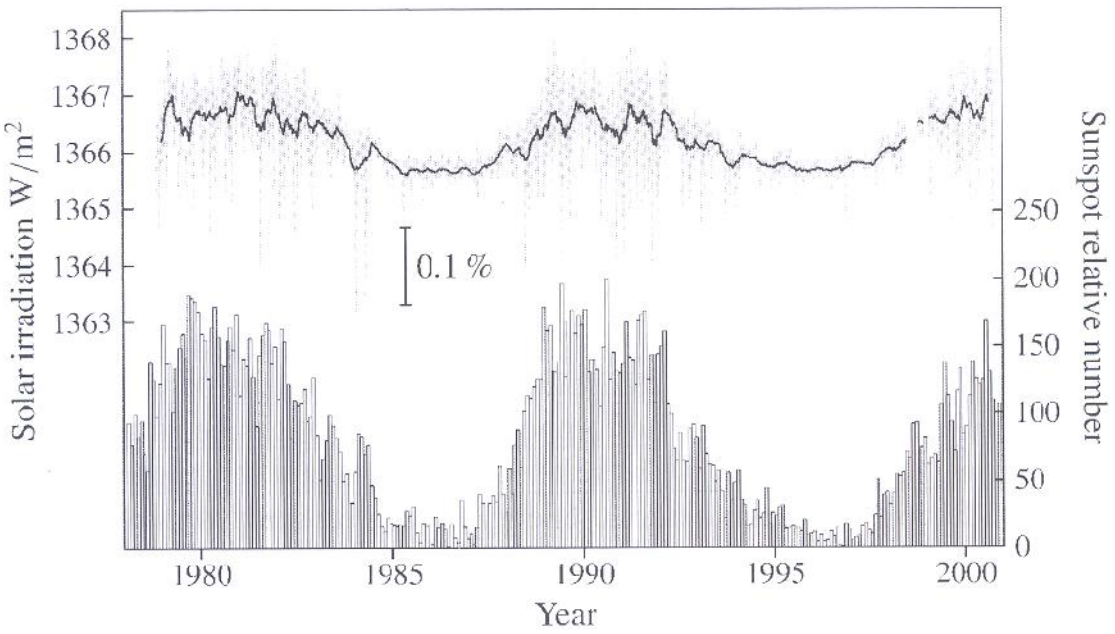

In the upper plot, temporal variations of the solar constant during the last two solar cycles, at high (grey curve) and low time resolution (black curve). This is a compilation from different space measurements (mainly with the spacecraft NIMBUS-7, SMM, ERBE and SOHO, since 1996), with the appropriate corrections to account for calibration and degradation of the instruments, operational noise, etc. The lower plot shows the monthly-averaged sunspot numbers R_W (Sec. 9.1). Data obtained from http://www.pmodwrc.ch/-solar_const/solar_const.html.

Figure 257; variation of the solar constant

Let us consider now the surface of LEMMB dedicated to the solar arrays.

Considering one Arm, then approximately 3/8 of the surface is always exposed to the sun rays at least.

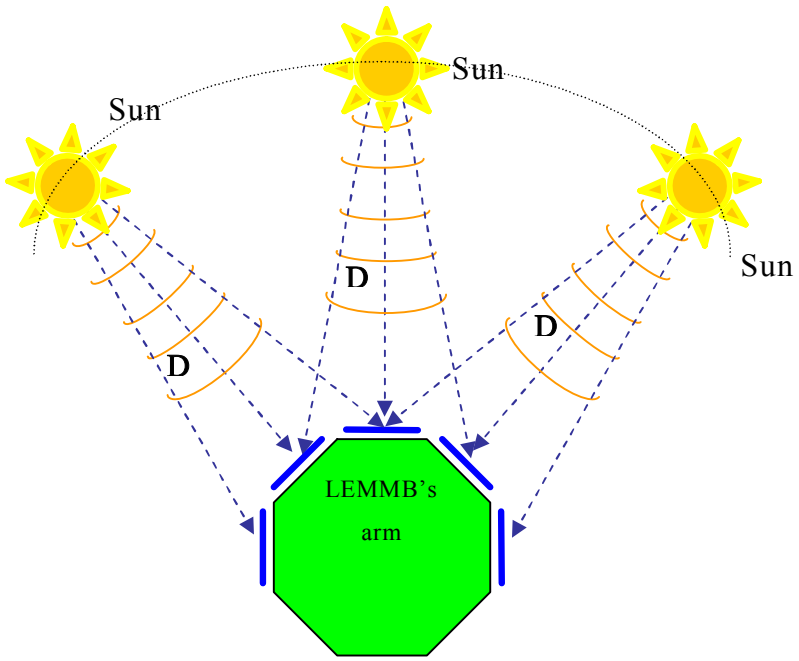

Figure 258: LEMMB's arm solar panel contemporary exposed to the sun rays

Since only one surface is approximately perpendicular to the sun rays then, the equivalent surface for the two other solar arrays should be about one half of the directly irradiated solar panel.

Finally, referring to the four Arms, the equivalent total surface is:

$$Total\_Surface \cong \left[\frac{1}{2}+\frac{1}{2}+1\right]\times\left[Single\_Solar\_Array\_Surface\right]\times\left[N^{\circ}Arms\right]=$$
$$2\times\left[Single\_Solar\_Array\_Surface\right]\times\left[N^{\circ}Arms\right]\cong 2\times 4\times 4=32 \quad m^2$$

eq 67

Let us now consider the LEMMB Core surface available for the solar array, then for the same reason, at least, about one face is always exposed to the Sun.

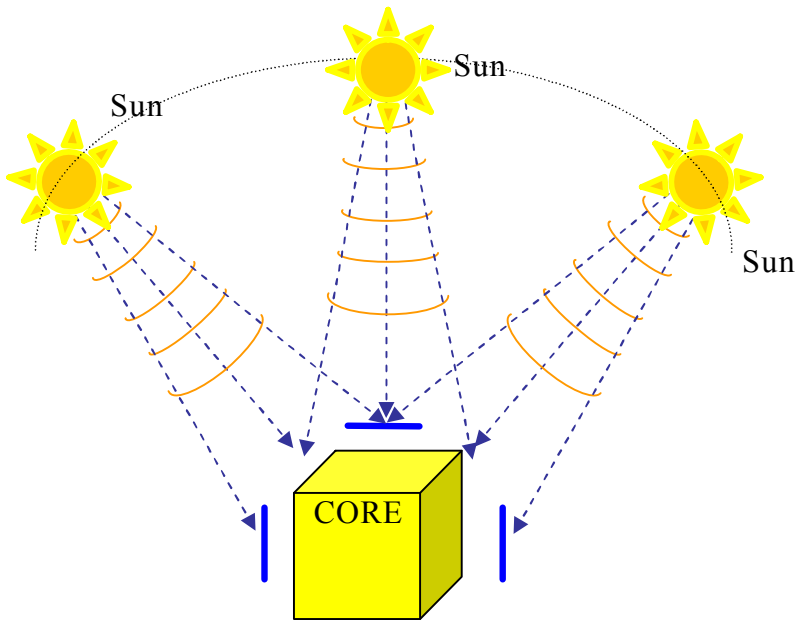

Figure 259: LEMMB's Core surface available for the sun rays

This surface is about the area of a single face: S_core=3×3=9 m^2
By adding this area to that already computed the result is about 40 m^2.

Let us consider, for example, a solar panel efficiency of about 15%, and decrease it of about 5% due to space and solar radiation degradation effect. Then the resulting efficiency is about 10%. This efficiency corresponds to an area of about 4 m^2.

Finally the total electrical power generated on LEMMB is defined by the solar constant (1370 W/m^2) multiplied to the total available surface of about 4 m^2.

$$Total\_available\_electrical\_power = [Solar\_const] \times [Total\_surface] \times [Efficiency] = \\ = 1370 \times 40 \times 0.1 \cong 5.5 \quad kW$$

Equation 1

5.9.1.2 Material used for solar array

The present **specific power** (**P/M, power per unit mass**) of single-crystal silicon solar panels on the **International Space Station** (**ISS**) is < *0.1 kW/kg* (breakdown is in the inset, but it doesn't include support structure that roughly halves P/M).
The silicon solar panels have high efficiency (around 15-22 %) but they are more expansive and heavier then thin film amorphous silicon solar cells.
Anyway since on LEMB, our main interest is in having a great efficiency then the best choice is the same solar array of ISS.

5.9.2 Second case: solar array as a special coating/fabric directly deposited on the Arm expandable surface

This situation is advanced from the material point of view, it requires mechanical flexible solar array which does not concern about the folds created while the expandable arms are compressed and foled for the storage.
Such solar array material must be capable of reacquiring the original shape once the Arm inflatable structures is expanded again after a long packing time period.

This system doesn't require any expansion mechanism for the solar array, in fact is intrinsic in the Arm's structures; as a consequence the reliability would be increased.

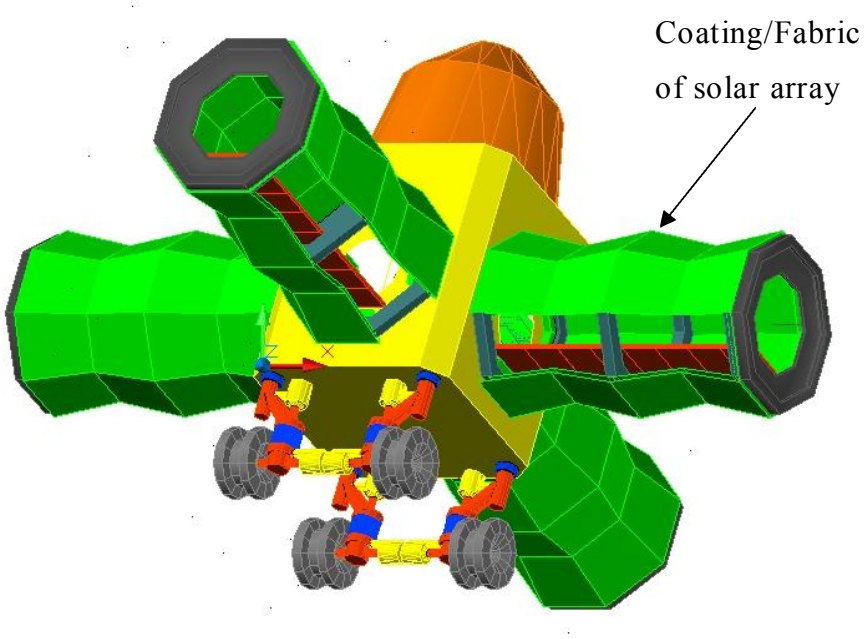

Figure 260: solar array deposited directly on the surface of LEMMB Arm inflatable structures

5.9.2.1 Material used for solar array coverage

Flexible solar panel seems to be the best choice for such type of solar array. As we have seen there are mainly two type of flexible solar panel:

- Organic flexible solar panel;
- Thin film Silicon based flexible solar panel;

Even though is not considered the time duration issue, the main problem remain the low efficiency.

For organic flexible solar panel the efficiency is about 3÷4% while for the thin film silicon solar panel the efficiency is about 10 %.

Whit such conversion efficiency, the power generated on each LEMMB, with organic flexible solar panel should be about 1÷2 kW max. Such power is very low and we must provide the lunar base with other external solar panel systems to reach the required electrical power.

5.10 Reference Table

1. A self-rechargeable and flexible polymer solar battery [G.Daniel; Solar Energy xxx (2007) xxx–xxx]
2. www.science.direct.com
3. http://solarcooking.org/saussure.htm
4. http://www.californiasolarcenter.org/history_solarthermal.html
5. http://www.californiasolarcenter.org/history_pv.html
6. http://www.sc.doe.gov/bes/reports/abstracts.html).
7. The Structural Factors Influence on Silicon Solar Cells PV Efficiency [2nd INTERNATIONAL WORKSHOPON TEACHING IN PHOTOVOLTAICS Małgorzata Pociask Institute of Physics, University of Rzeszów, Poland]
8. Solar PV on Earth and in Space: A New Perspective for Energy [by Marty Hoffert, Physics Dept., New York University]
9. Photovoltaics Information Brief No.1 *D. Garlovsky and W. Pickin*
10. http://www.aeema.asn.au/ArticleDocuments/41/peak.pdf
11. http://www.seav.vic.gov.au/sustainable_energy_challenge/current_energy_situation.asp
12. http://www.nemmco.com.au/
13. http://amptiac.alionscience.com/quarterly
14. EE 666 Advanced Semiconductor Devices 2005
15. N. H. Karam etc. Solar Energy Materials & Siolar cells 66 (2001) 453-466.
16. N. H. Karam etc. Trans. Electron Dev. 46 (10) 1999 pp.2116.
17. A. Marti, G. L. Araujo, Sol. Energy Mater. Sol. Cells 43 (1996) 203.
18. LBNL/Conell work: J. Wu et al. APL 80, 3967 (2002).
19. Space Power Systems 101 [Hartford Regional Convention NSTA October 2005 Dave McKissock NASA Glenn Research Center]
20. Solar Arrays [Shannon R. Wheatley]]
21. Issues and Consequences of Atomic Oxygen Undercutting of Protected Polymers in Low Earth Orbit [Glenn Research Center]
22. http://eo1.gsfc.nasa.gov/Technology/lfsa.html

23. INFLATABLE SOLAR ARRAY TECHNOLOGY [AIAA-99-1075]
24. POWER-SCALABLE INFLATION-DEPLOYED SOLAR ARRAYS [Frederick H. Redell * and David Lichodziejewski *L'Garde, Inc., Tustin, California 92780]*
25. APPLICATIONS OF INFLATABLE RIGIDIZABLE STRUCTURES 2006 [Stephen E. Scarborough and David P. Cadogan ILC Dover LP Frederica, DE 19946]
26. http://www.siliconsolar.com/Flexible-Solar-Panels-p-2-c-257.html
27. http://www.nedo.go.jp/english/archives/170210/170210.html
28. http://solarcellsinfo.com/blog/archives/category/info-on-solar-cell-panels-and-modules/flexible-solar-cells/

SAPIENZA
UNIVERSITÀ DI ROMA

6 Chapter 6
Radiations Protection for Lunar Expandable Mobile Modular Base (LEMMB)

6.1 Abstract

The space radiations effect is one of the main problems concerning astronaut's health and onboard electronic equipment's functionality like computers, sensors, and so on.
Radiation causes ionization in biological matter and charge deposition in semiconductors. It is one of the main threats to space activities and in Lunar and Mars planetary colonization.
On the Moon and Mars, the radiation environment is usually similar to that in interplanetary space, with no strong magnetic fields for shielding, and no dense atmosphere to block solar UV and X-rays.
There are many publications about passive and active methods studied in order to attenuate / deflect radiation flux.
Here in this chapter is presented a new method based on an active Electromagnetic system capable to deflect incoming energetic particles. The principle is based on a electromagnetic circularly polarized wave emitted by an antenna located close to the Moon Base we want protect from space radiation.

6.2 Basic concept of ionizing radiation

In the interaction of high-energy radiation (α- (alpha), β- (beta) γ- (gamma) radiation, X-rays, neutrons etc.), the radiation energy is completely or partially absorbed by the atoms involved.
Charge carriers of both signs (positive and negative ions) are thus generated. This process is known as ionization and the radiation causing it is termed ionizing radiation. Ionizing radiation occurs during the decay of radioactive substances (radionuclides) as well as in nuclear fission and may also be generated in accelerators and X-ray facilities. Space radiation can be a ionizing radiation as well.

6.2.1 α-,β-, γ radiation during radioactive decay

The atomic nuclei of radionuclides decay spontaneously without external impact. Ionizing radiation (α-,β-, γ-radiation) is emitted during this decay.
Each radionuclide decays with a characteristic **half-life**. This is the time in which half of the atoms decay. After two half-lives the number of atoms of the initial substance is reduced to ¼ and after 10 half-lives to approx. 1/1000 of those originally present. It is important to note that radioactivity decreases very greatly with time but never completely disappears.
There are radionuclides with half-lives of a fraction of a second and others with half-lives of many thousands of years. as an example the cobalt-60 (60Co) has a half-life of 5.27 years.

- **α-rays** are high-energy helium nuclei which are emitted typically during the decay of some heavy radionuclides.
  They are retarded in matter very easily. Their range in air is less than 10 cm and about 50/1000 millimeters in living tissue. These rays can be completely shielded by a sheet of paper. In the case of external irradiation, a-rays are not hazardous since they do not even penetrate the upper, radiation in sensitive layer of the skin. **α-emitters** are particularly dangerous if a radioactive substance is taken up into the body, e.g. by respiratory air, food or open wounds (incorporation).

- **β-rays** are fast electrons. Very many radionuclides are **β-emitters**. The range of β-radiation depends on its energy. Its range may be up to 10 m in air but it is frequently considerably less. β-radiation is completely shielded by 1 - 2 cm of Plexiglas. In the case of external irradiation, the skin (or more precisely the cell layer directly beneath the 70 µm layer of tissue which is insensitive to radiation) is particularly endangered.

- **Positrons** are positively charged fast antiparticles of electrons which may result upon the decay of some radionuclides. From the point of view of

radiation protection they behave similarly to β-radiation.

- When a positron and an electron collide their entire mass is converted into energy, and therefore in the case of positron emitters **γ-radiation** also always occurs as the annihilation radiation of the two particles.

6.2.2 X-Rays and γ-Rays

Like visible light, **X-rays** are also electromagnetic waves. The wavelength of X-rays is considerably smaller than that of light.
X-rays result from the slowing down of fast charged particles.
X-rays are the same type of radiation as γ-radiation (i.e. electromagnetic wave). They merely have a different name due to their different origin.
X-rays are generated in an X-ray tube, where electrons are accelerated by high electric voltage and then slowed down at the anode consisting of a heavy metal. X-rays thus result, and mainly escape from the X-ray tube through a window provided for this purpose.
The higher voltage at the tube, the current in the tube and the atomic number of the anode material, the greater is the intensity of the X-rays.
X-rays of different energies (i.e. of different wavelengths), are generated in the X-ray tube. The highest resulting energy depends on the voltage at the tube and rises with increasing tube voltage. Radiation of every energy below the maximum energy in the X-ray spectrum is present. X-ray tubes emitting practically single-energy X-rays (monoenergetic radiation) are used in special applications, e.g. in the investigation of crystal structure.

Devices in which X-rays are generated expressly for application in medicine, science and technology are known as X-ray units. Devices which serve a different purpose but which unavoidably emit X-rays during operation are known as parasitic sources.

Examples of parasitic sources are: special tubes for generating microwaves (travelling-wave tubes, magnetrons, klystrons), cathode ray tubes (oscillographs, television sets), further electron tubes (transmitting valves, thyratrons etc.), electron

microscopes, electron beam devices for metal working and experiments with high-energy ions.

6.2.3 Radiation on Reactors and Accelerators

Heavy atomic nuclei are split in nuclear reactors. This nuclear fission results in radioactive fission products, **γ-radiation** and **neutrons**. The reactor core - the zone in which nuclear fission takes place – is well shielded. Only low-intensity γ-radiation and neutrons are measurable outside this shielding. At the reactor it is ensured that radioactive substances cannot escape from the reactor core in unacceptable quantities.

Neutrons are electrically uncharged particles which are as heavy as a hydrogen atom. Apart from in nuclear fission, they also originate at accelerators and wherever **α-radiation** collides with light atomic nuclei. Neutrons are very penetrating. They are effectively slowed down by substances of light atomic weight (water, concrete). Neutrons can be captured by substances with stable atomic nuclei thus resulting in radioactive substances. Material which has been irradiated with a large number of neutrons may therefore be radioactive.

Accelerators are devices in which electrically charged particles (e.g. electrons, hydrogen atomic nuclei or α-particles) are accelerated to high energies. Other charged particles, γ-radiation, neutrons and also radioactive substances originate when these particles collide with matter. Accelerators are accommodated in well-shielded rooms where entry is forbidden while the device is in operation.

Outside the shielding, at most low-intensity neutrons or γ-radiation occur. There may be radioactive substances in the accelerator room itself - especially just after the device has been switched off.

6.3 The interplanetary Radiation Environment

Radiation causes ionization in biological matter and charge deposition in semiconductors. It is one of the main threats to space activities.

Three main sources of radiation are:

6.3.1 Galactic cosmic rays (GCR)

Electrons, protons and heavy nuclei coming from remote regions of our and distant galaxies energies are typically in the range: 10 MeV – 1 GeV.

GCR are deflected by the solar magnetic field (larger fluxes near solar minimum!)
GCR particles originate from distant parts of the galaxy, primarily from exploding stars. GCR is isotropic since the particle origins are distributed approximately uniformly over space.
The composition tends toward higher atomic- mass ions, maxing out at fully ionized iron. The GCR spectrum begins an energy cutoff at approximately 1,000 MeV, where lower-intensity-particle energies up to 10,000 MeV are observed. The overall radiations fluencies will also normally be quite low, posing no immediate hazard to astronauts.
However, accumulated GCR dosage will significantly increase the probability of cancer at some time in the unprotected astronaut's lifetime.
In figure below are shown the relation between total dose of radiation and the shielding matter, aluminum and lunar regolith.

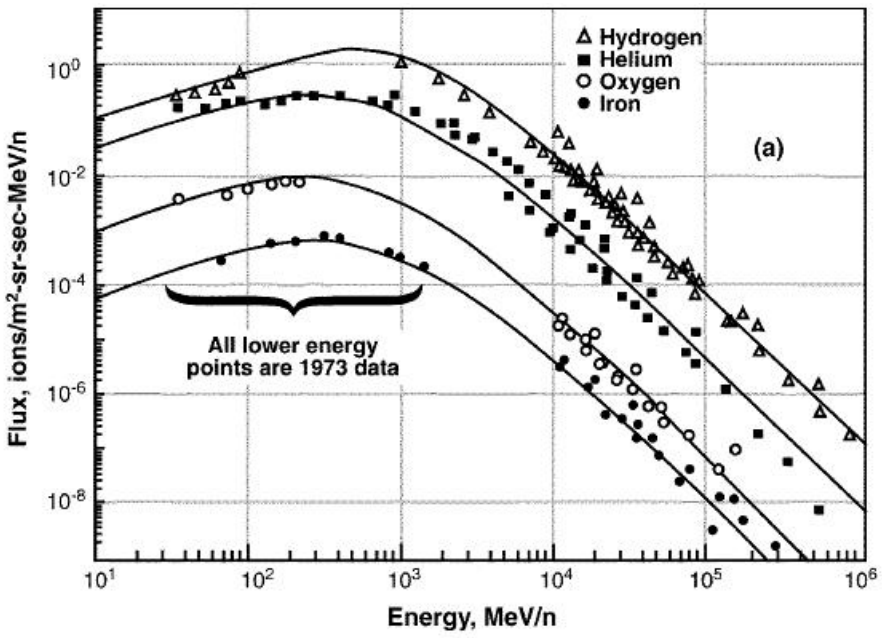

Figure 261: GCR spectra, solar minimum Parnell Watts & Armstrong MSFC 1998

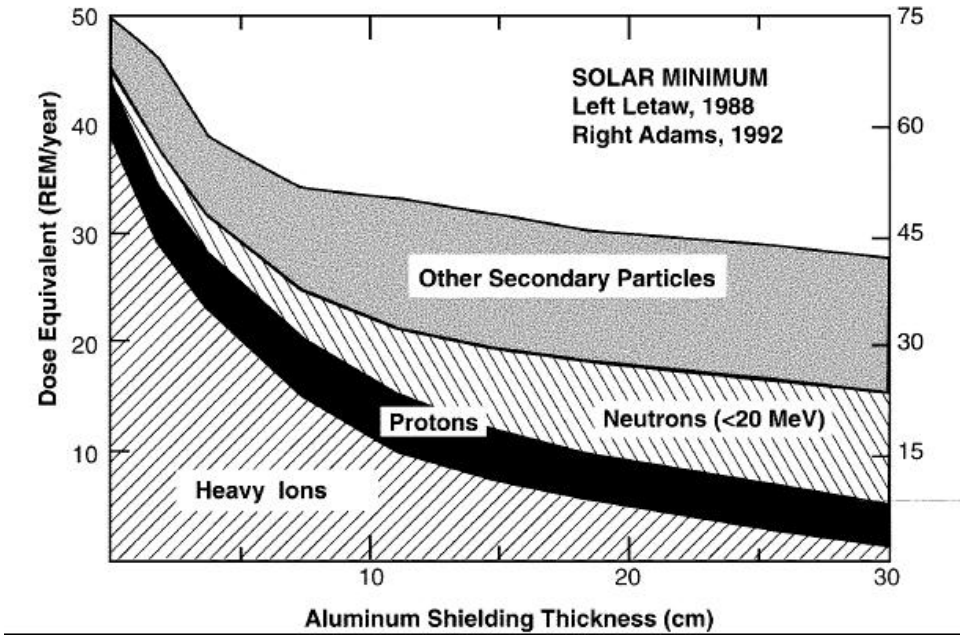

Figure 262: GCR dose vs shield thickness; Left scale: average solar minimum; Right scale: 1977 solar minimum [Parnell Watts & Armstrong MSFC 1998]

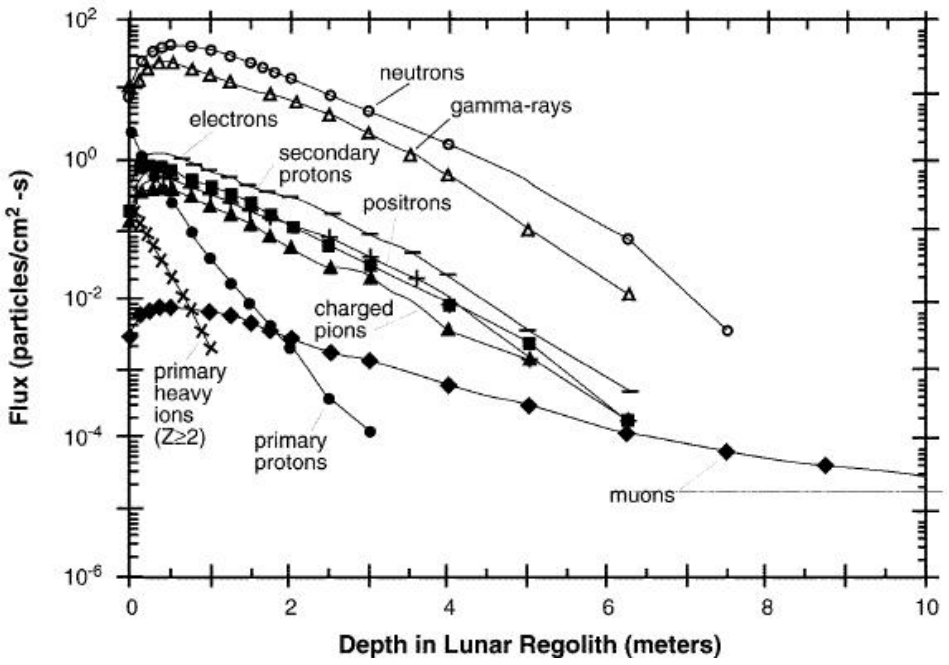

Figure 263: GCR flux vs depth in lunar regolith [Parnell Watts & Armstrong MSFC 1998]

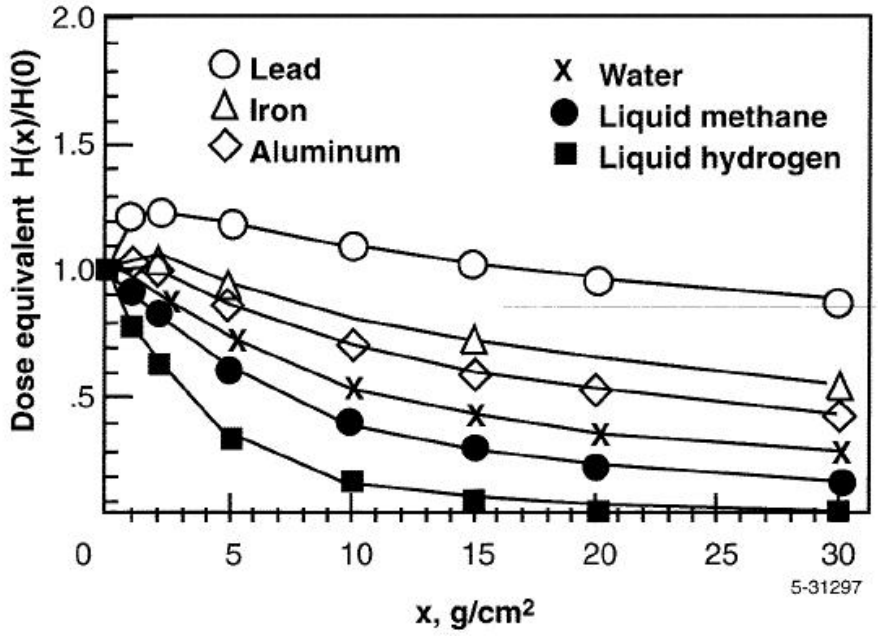

Figure 264: Relative dose vs. depth for GCR [Parnell, Watts & Armstrong MSFC 1998]

6.3.2 Solar Energetic Particle (SEP)

Electrons, protons and heavy nuclei emitted by the Sun in active phases (flares, coronal mass ejections). Energies are about 10 MeV (or larger). The events are time-localized and do not last long. However there are a few events per solar cycle producing high fluences (10^9-10^{10} protons/cm^2).

SEP originate from the Sun and are coincident with solar activity, such as solar flares. Most SPE (Solar Particle Event) radiation is approximately isotropic at a given point in space because of the influence of the solar system magnetic field lines on the charged particle trajectories. The composition of SEP radiation tends toward the low-atomic-mass ions, such as ionized hydrogen and helium, as well as free electrons. The SPE energy spectra typically cut off at around 100 MeV, even though particle energies up to 300 MeV are not uncommon. The radiation fluence (flux integrated over time of the event) will normally be quite low, posing little hazard to astronauts. However, during a solar storm, the radiation intensity will increase dramatically to levels that, under extreme conditions, may be lethal to unprotected astronauts.

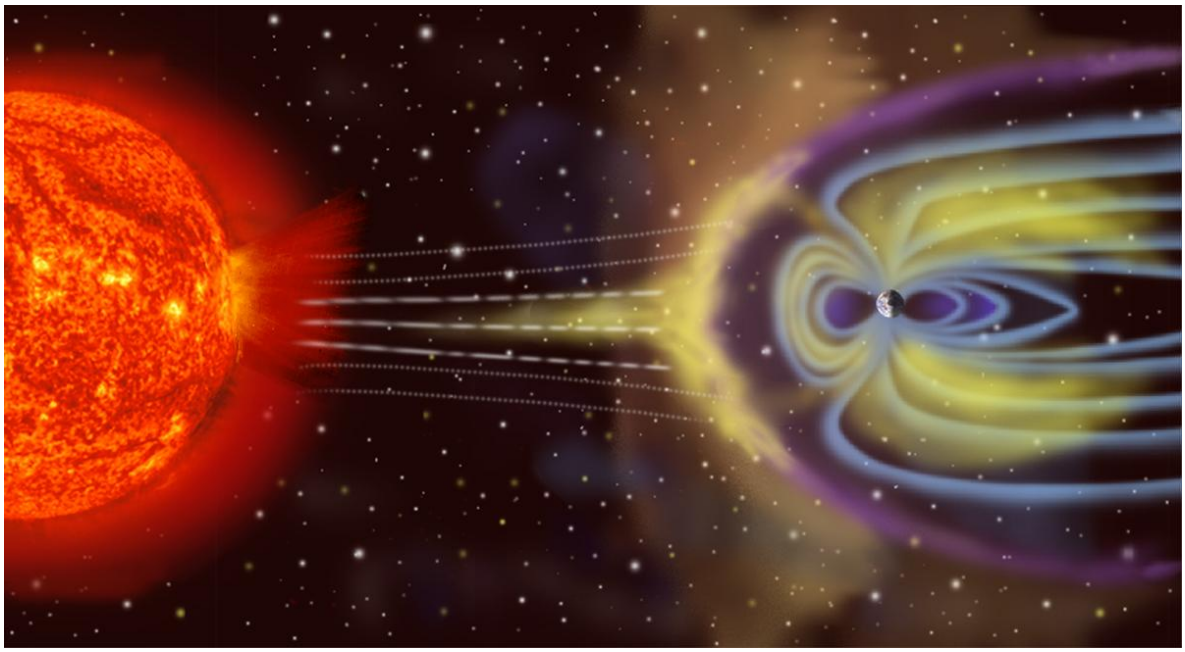

figure 265: A CME strikes the Earth's magnetosphere. Both prompt (SEPs) and delayed (magnetospheric storms) radiation increases are possible

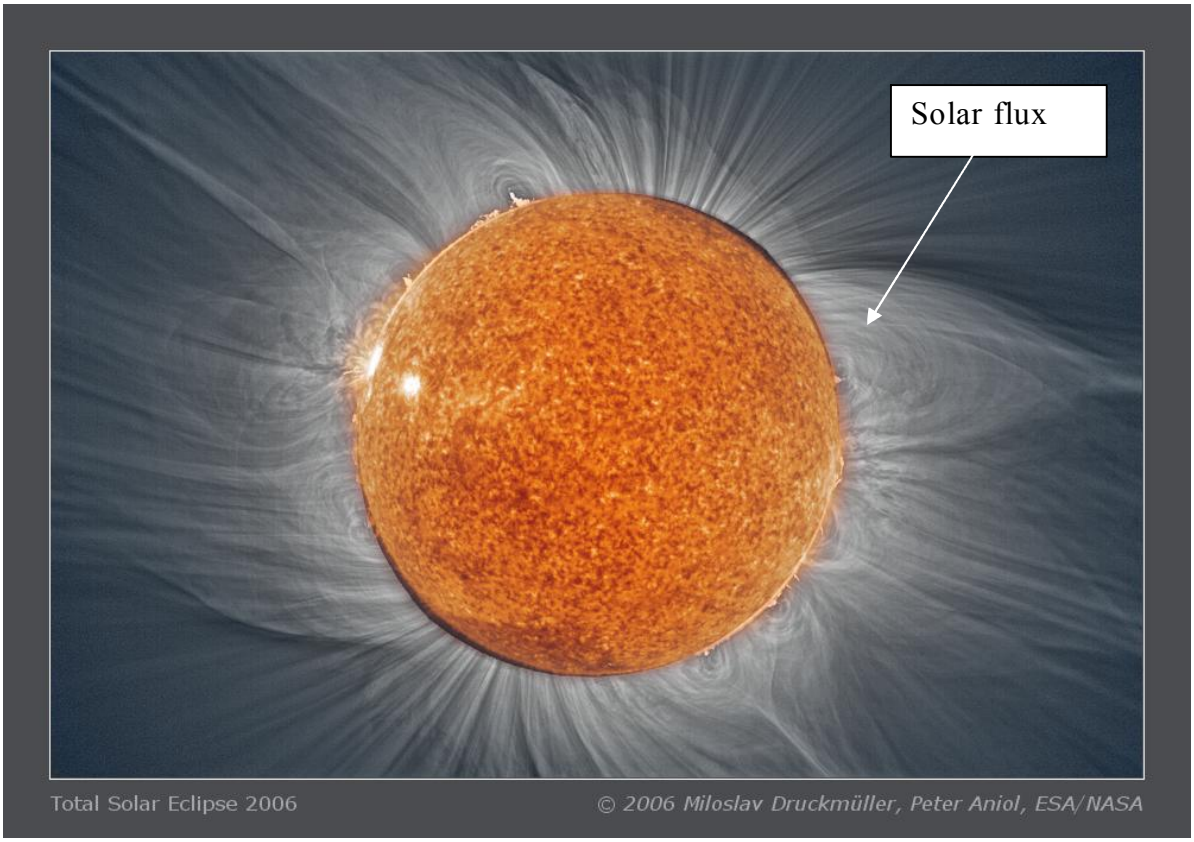

figure 266: total solar eclipse 2006

- **Galactic Cosmic Rays (GCRs)**
  - Median energy ~1800 MeV/nuc
  - Continuous flux, varies with the solar cycle

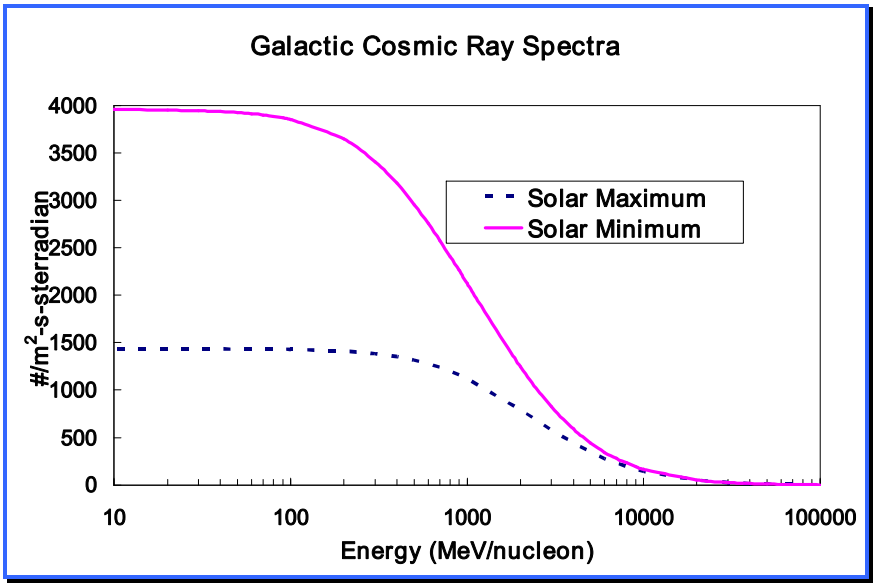

Figure 267: Galactic Cosmic Rays Energy

- **Solar Energetic Particles (SEPs)**
  - Sporadic, lasting hours to days ~100 MeV/nuc
  - Soft spectra with highly variable composition

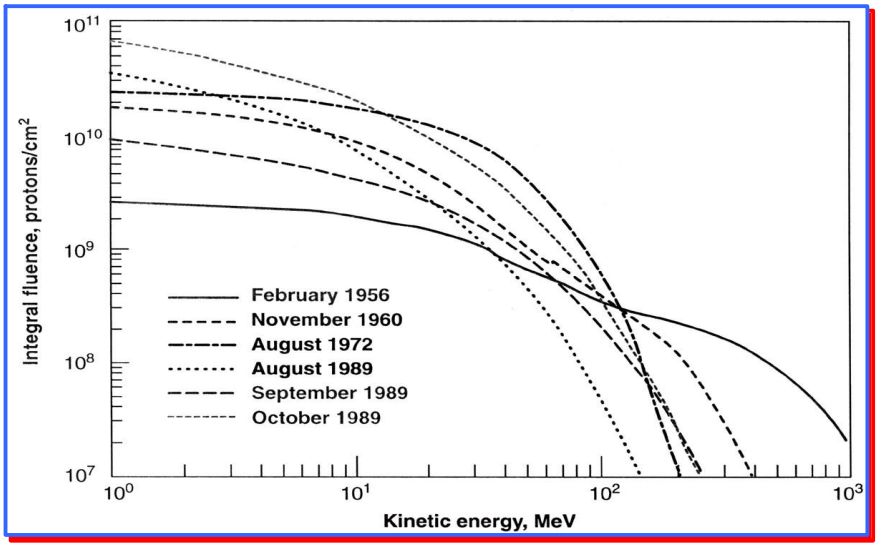

Figure 268: Solar Energetic Particle Energy

6.3.3 Bremsstrahlung effect and X Rays

Charged particles with extreme energy, especially relativistic electrons, can inadvertently generate another type of harmful radiation because of the electrodynamics of charged-particle motion. High-energy X rays are generated by an abrupt change in velocity, such as that associated with high-energy electrons colliding with a metal conductor or passive radiation shield. This bremsstrahlung radiation can potentially generate a lethal dose of X rays, leading to more biological damage than the original charged-particle radiation.

Other PHASE I REPORTS can be accessed at the University-Affiliated Spaceport Technology Development Contract (USTDC) Web site:
http://ustdc.com/niac_cp_04_01.cfm

6.3.4 Trapped Radiation Environment: Van Allen belt

Energetic protons and electrons of solar / cosmic ray origin. Electrons penetrate in the corotating magnetosphere through the polar cusps or precipitate from the tail and are trapped via magnetic bottle effect. Energy ranges from 1 keV to several MeV. Protons are mainly generated by the interaction of cosmic rays with the atmosphere. The inner belt (at 1.5-2 Earth radii) is dominated by protons. The outer belt, peaked at about 5 Earth radii, is made up by electrons. See the following link:

http://www.oma.be/BIRA-IASB/Scientific/Topics/SpacePhysics/RadiationEnvironment2.html

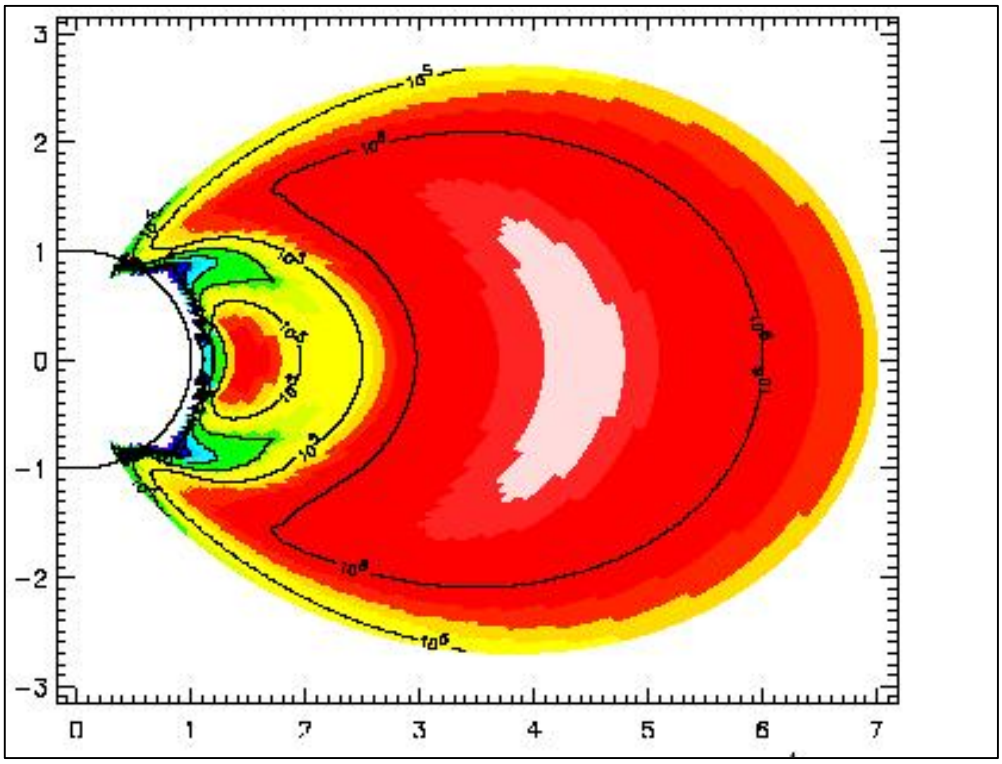

Figure 269: Earth trapped radiation environment

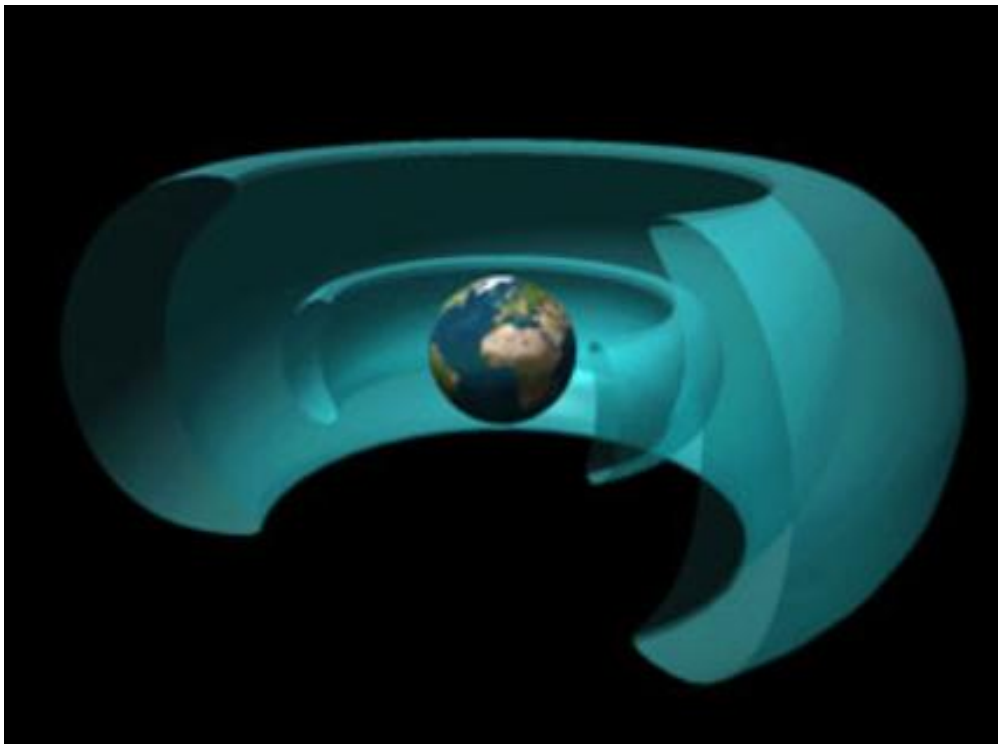

Figure 270: Van Allen Belts

- Most popular models are AE8MIN, AE8MAX, AP8MIN, AP8MAX
- http://nssdc.gsfc.nasa.gov/space/models/trap.html
- GEO (Geostationary Earth Orbit): http://leadbelly.lanl.gov/lanl_ep_data
- In LEO (Leo Earth Orbit), nearly all the dose & damage is concentrated into South Atlantic Anomaly

The belts of trapped radiation near the Earth were first detected by James Van Allen in 1958. Therefore these belts are also known as Van Allen Belts.

The Earth's radiation belts are one component of the larger and more complex system called the magnetosphere. The radiation belts of the Earth are made up of energetic, electrically charged particles or electrons, protons and heavier atomic ions. These particles essentially get trapped in the magnetic field of the Earth. The kinetic energy of these particles is greater than or equal to 30 keV.

The radiation belts, like the plamasphere, are toroidally shaped. These toroids encircle the planet. The inner radiation belt extends from about 400 km above the Earth to 12,000 km. The outer radiation belt extends from about 12,000 km to 60,000 km above the Earth. At times, the two belts overlap each other.

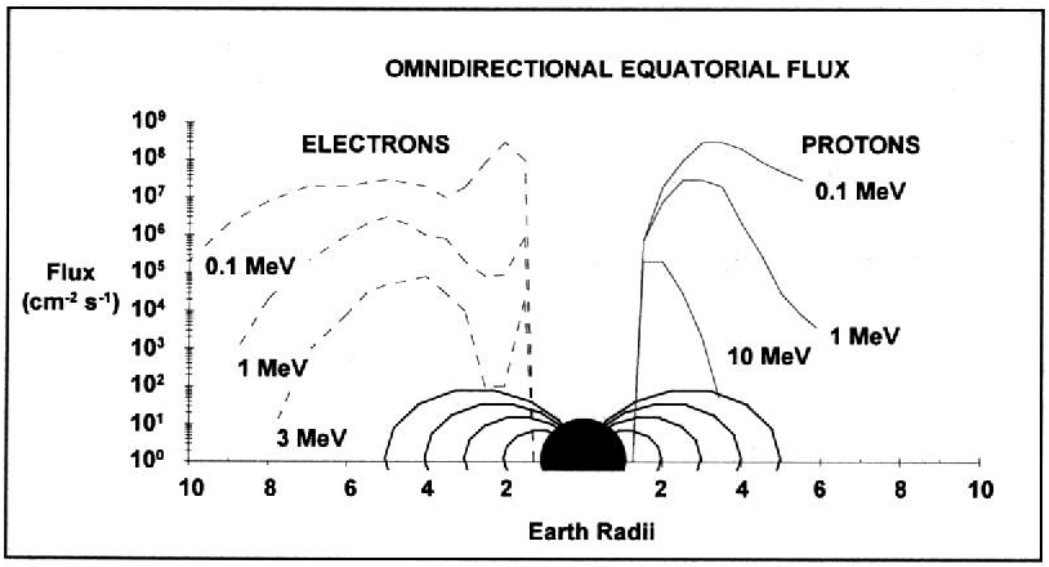

Figure 271: Electron and Proton Flux

Dr. Van Allen has found that the principal sources of particles for the outer radiation belt are the solar wind and the ionosphere. The main sources for the inner radiation belts are solar energetic particles and reactions with galactic cosmic rays. The eventual fate of particles in the radiation belts is to become part of the atmosphere, to collide with satellites or to escape into space.

It is extremely important that we have a good understanding of the radiation belts because the energetic particles in these toroids affect in situ measurements and may have an effect on the survival of electronic and optical equipment, human and animal life forms. "The particle population of the Earth's radiation belts makes it dangerous for humans without massive shielding to do more than quickly pass through them," reports Dr. James Van Allen.

Figure below display the Total dose of radiation measured in a typical Molniya Orbit.

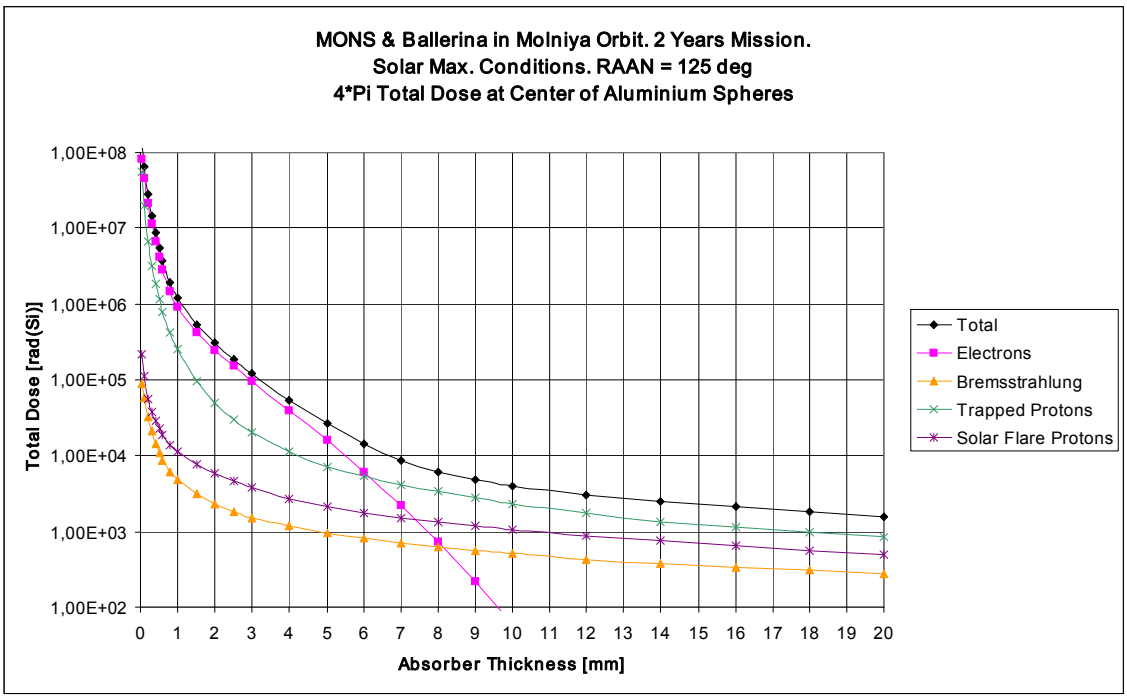

Figure 272: The Earth radiation belts;
Radiation Environment in Molniya Orbit - Total Dose as a function of absorber thickness

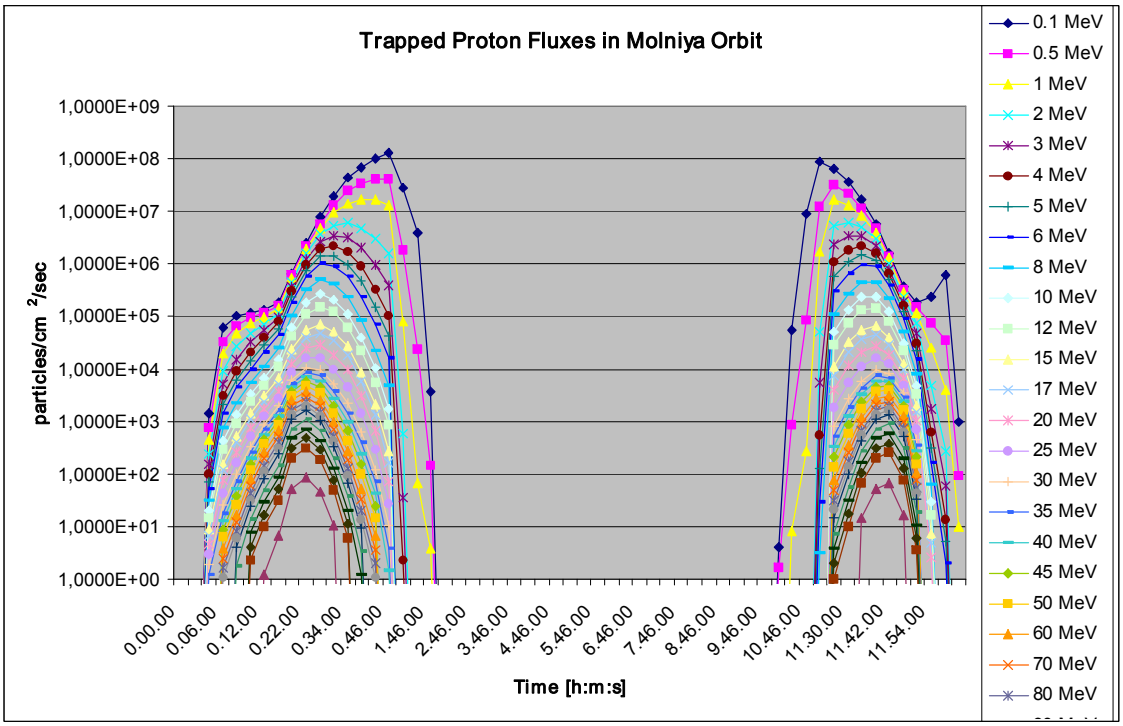

Figure 273; Radiation Environment in Molniya Orbit - Proton Flux over One Orbit

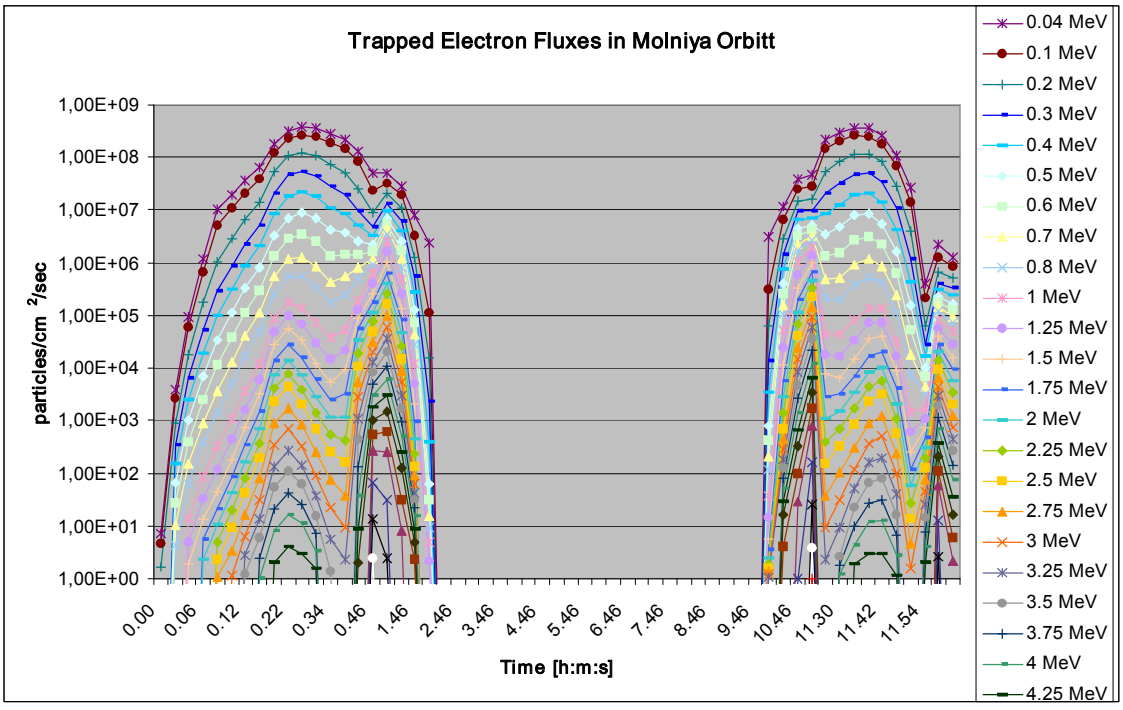

Figure 274: Radiation Environment in Molniya Orbit - Electron Flux over One Orbit

6.3.5 Average Radiation Environments

The radiation condition on Earth is a function of the orbit and environment:

- Sea level, houses: 270 microrad/day ave, mostly radon gas
  - steady
- Sea level, caves: 50 microrad/day ave, mostly gammas
  - steady
- LEO e.g. Hubble: 50 millirad/day ave, 1cm Al shielding
  - highly variable: SAA passages
- GEO e.g. comsat: 1 rad/day ave, 1cm Al shielding
  - highly variable: magnetic storm trapped electrons
- 700km Polar SunSync: 0.8 rad/day ave, 1cm Al shielding
  - highly variable: SAA passages; solar proton events
- Molniya orbit: 6 rad/day ave, 1cm Al shielding
  - hugely variable: SAA passages; solar proton events
- AXAF and XMM orbits: 2-10rad/day ave, 1cm Al shielding
  - hugely variable: SAA passages; solar proton events

6.4 Radiation by CME (Coronal Mass Ejection)

CME (Coronal Mass Ejection) begin when the Sun launches a billion tons of electrically conducting gas (plasma) into space at millions of miles per hour. A CME cloud is laced with magnetic fields, and CMEs directed our way smash into Earth's magnetic field. If the CME magnetic fields have the correct orientation, they dump energy into Earth's magnetic field, causing magnetic storms. These storms can cause widespread blackouts by overloading power line equipment with extra electric current.

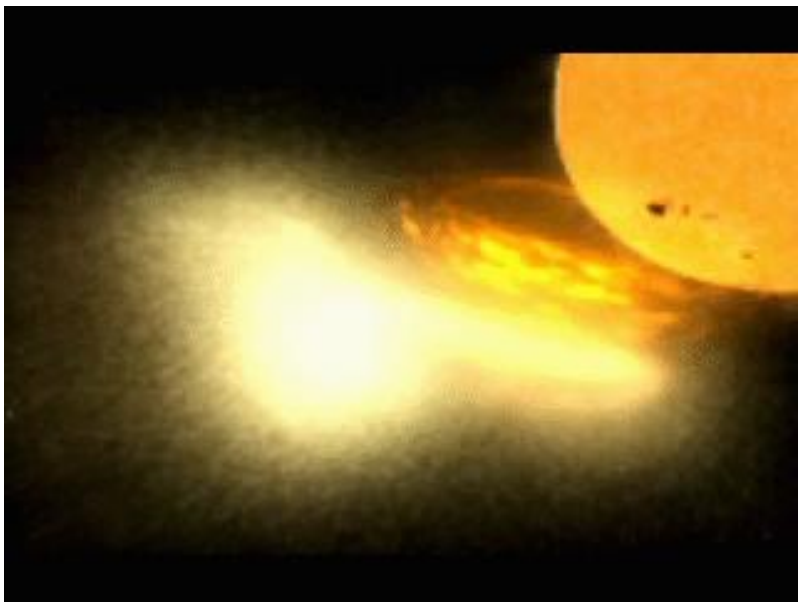

figura 1: CME throwing off solar energetic particles towards Earth

Some **CMEs** also bring intense radiation storms that can disable satellites or cause cancer in unprotected astronauts. As the **CME** blasts through space, it plows into a slower stream of plasma blown constantly from the Sun in all directions, called the solar wind. The **CME** causes a shock wave in the solar wind. If the shock is strong enough, it accelerates electrically charged particles that make up the solar wind to high speeds, forming the **radiation storm**.

"Some **CMEs** produce **radiation storms**, and some don't, or at least the level of radiation is significantly lower,"

Like a pro wrestler rotating before an attack, **CMEs** with powerful shocks capable of causing radiation storms "scream" in radio waves as they slam through the solar wind.

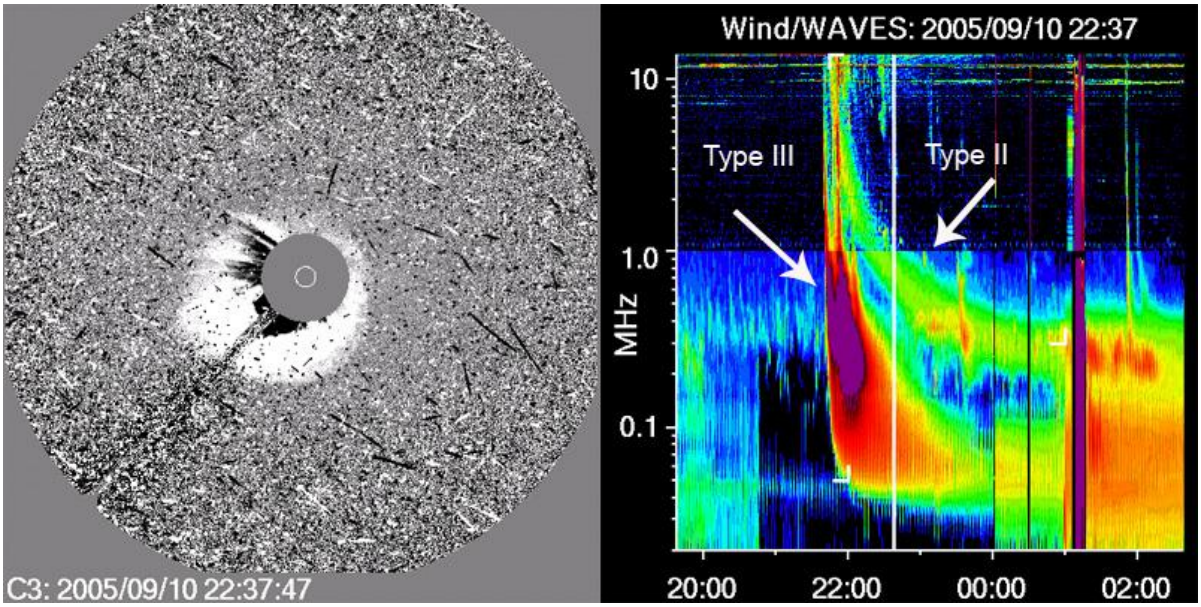

figura 2: Image above: Radio Loud CME:

(Left image) SOHO image of a CME blasting off the Sun.

(Right) A radio dynamic spectrum showing a type II and type III radio burst caused by electrons accelerated at the shock driven by the CME. Credit NASA/ESA.
+ High resolution images or to download video Credit NASA/ESA

CMEs generating a radio signal also produce radiation storms, but **CM**Es without a radio signal do not.

Strong **CME** shocks accelerate electrons (the particles that carry electricity) in the solar wind, which produce the radio signal. The same strong shock must also accelerate atomic nuclei (the central part of atoms) in the solar wind, which produce the radiation storm. "Since the radio signal moves at the speed of light while the particles follow behind, we can use a **CME's** radio noise to give warning that it is generating a radiation storm that will hit us soon,". This will give astronauts and satellite operators anywhere between a few tens of minutes to a couple hours to prepare, depending on how fast the particles are moving.

6.4.1 SMS/GOES Space Environment Monitor

The Synchronous Meteorological Satellites (SMS-1 and SMS-2) and the Geostationary Operational Environmental Satellites (GOES-1, GOES-2, etc.) all carry on board the Space Environment Monitor (SEM) instrument subsystem. The SEM has provided magnetometer, energetic particle, and soft X-ray data continuously since July 1974.

Below are reported some data and the key to read the data for detail see the link:

http://www.sec.noaa.gov/SolarCycle/index.html

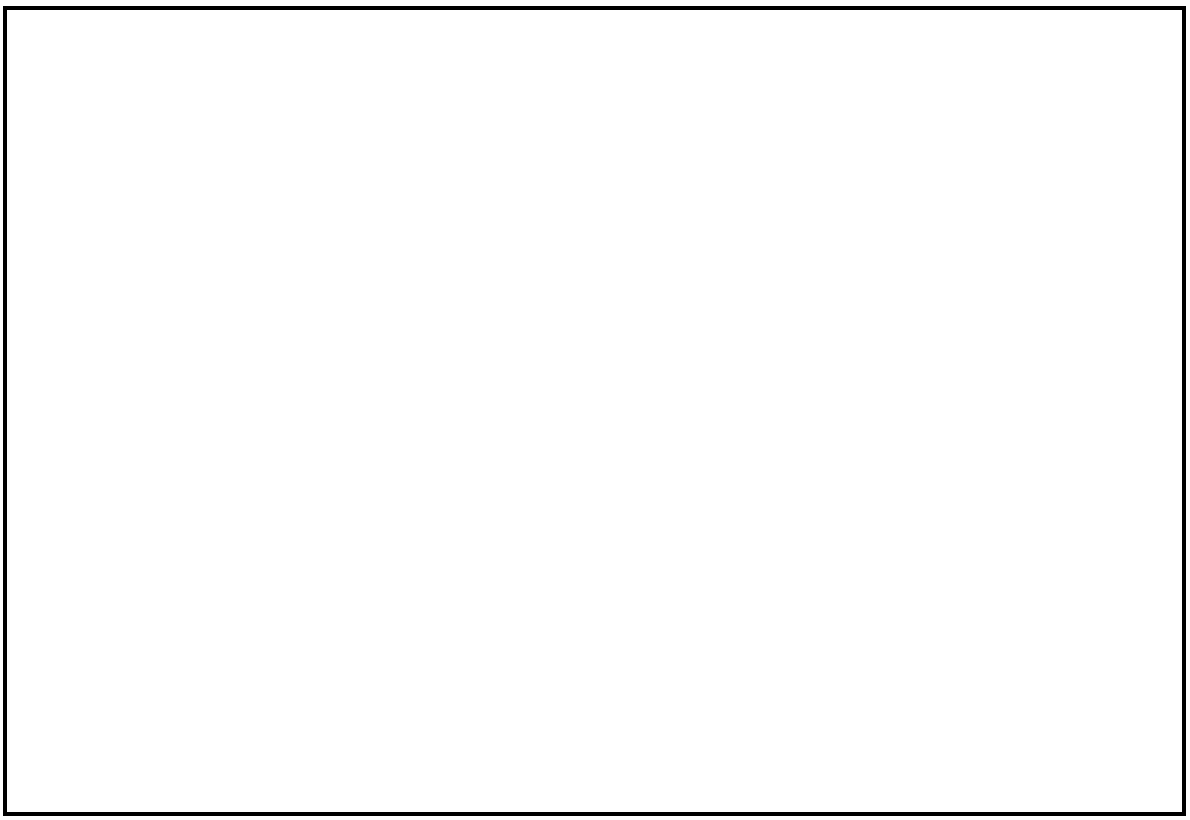

Figure 275: GOES satellite Data Key

6.4.2 Solar flare particle environment on 4-9 Nov. 1997

The large solar event on 4-9 November 1997 was observed by the GOES-9 spacecraft in seven proton integral flux channels ranging from *>1 MeV to >100 MeV*.
In the following, the measured proton spectra are given both as plots and as tables in two-day periods (4-5). The tabulated data starts at 00.00, is given in 5 minute intervals, and contain the following columns:

Column	*1:*	*>1*	*MeV*	*proton*	*flux*	*(1/cm2/s/sr)*
Column	*2:*	*>5*	*MeV*	*proton*	*flux*	*(1/cm2/s/sr)*
Column	*3:*	*>10*	*MeV*	*proton*	*flux*	*(1/cm2/s/sr)*
Column	*4:*	*>30*	*MeV*	*proton*	*flux*	*(1/cm2/s/sr)*
Column	*5:*	*>50*	*MeV*	*proton*	*flux*	*(1/cm2/s/sr)*
Column	*6:*	*>60*	*MeV*	*proton*	*flux*	*(1/cm2/s/sr)*
Column	*7:*	*>100*	*MeV*	*proton*	*flux*	*(1/cm2/s/sr)*

The plots contain also *>2 MeV* electron data, but these are partly missing on 6 November, presumably due to pile-up in the detector caused by the high fluxes.

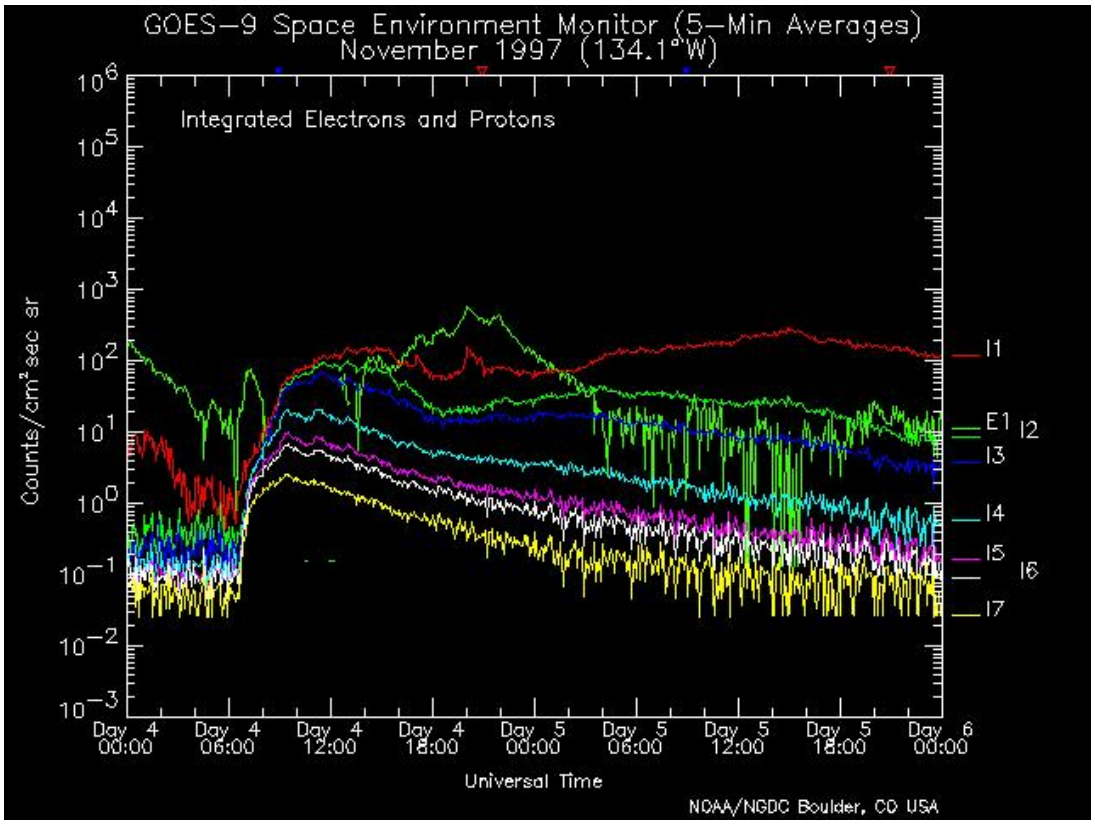

Figure 276: Solar Flare 4-5 November 1997

We have additionally translated these integral fluxes into differential proton fluxes as a function of time. A JPEG movie (~4 MB, ActiveMovie 2.0) of this data has been constructed by H. Evans (ESTEC), and can be downloaded here. Note the two separate surges on November 4 and 6, and especially on November 6 the onset of, first ~100 MeV protons, and afterwards, lower-energy ~10 MeV protons.

For more data, please access the GOES home page.

The high-energy particle emission from this solar event was also detected by several neutron monitors. Preliminary data from Moscow, Tixie Bay, and Apatity stations have been provided to us by the IZMIRAN Cosmic Ray Department in Moscow, and

6.4.3 Solar Cycle 24 Prediction

The official NOAA, NASA, and ISES Solar Cycle 24 prediction was released by the Solar Cycle 24 Prediction Panel. Press Briefings and presentations at the SEC Space Weather Workshop, are linked below.

http://www.sec.noaa.gov/SolarCycle/SC24/index.html)

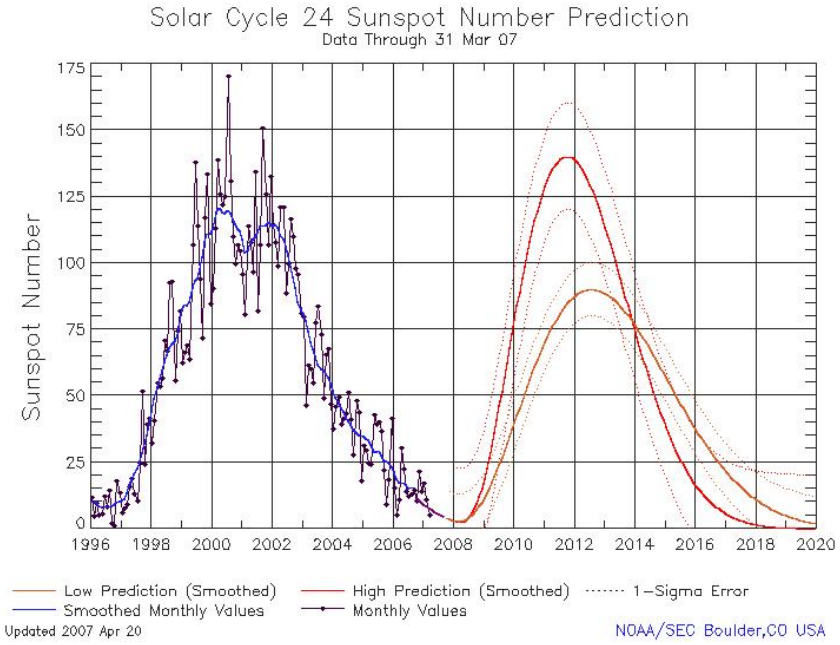

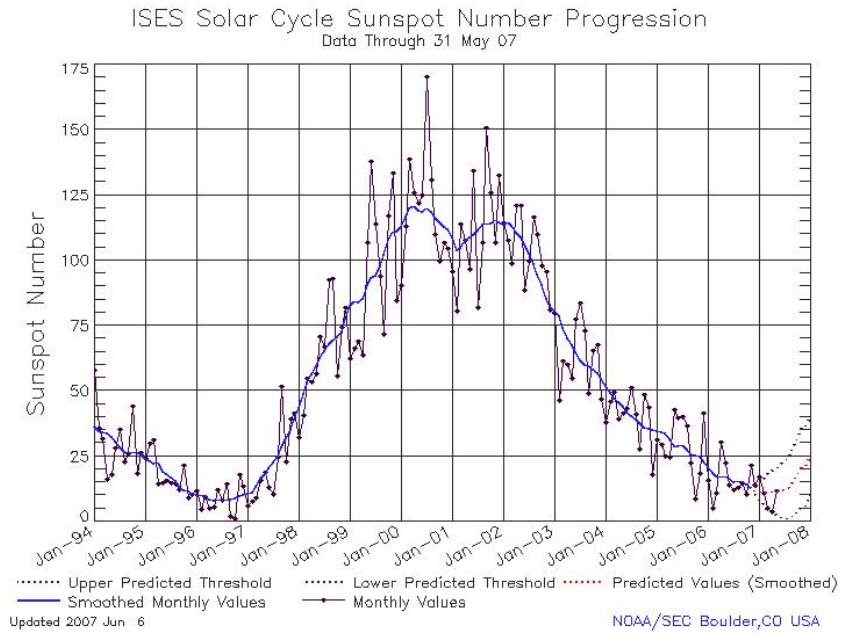

6.5 Solar wind particles

The solar wind streams off of the Sun in all directions at speeds of about 400 km/s (about 1 million miles per hour). The source of the solar wind is the Sun's hot corona. The temperature of the corona is so high that the Sun's gravity cannot hold on to it. Although we understand why this happens we do not understand the details about how and where the coronal gases (plasma) are accelerated to these high velocities. This question is related to the question of coronal heating.
http://solarscience.msfc.nasa.gov/SolarWind.shtml

6.5.1 Wind Variations

The solar wind is a stream of mostly charged particles that emanate from the Sun and blow throughout the Solar System.
The solar wind is not uniform. Although it is always directed away from the Sun, it changes speed and carries with it magnetic clouds, interacting regions where high speed wind catches up with slow speed wind, and composition variations.

*The solar wind speed is high **(800 km/s)** over coronal holes and low **(300 km/s)** over streamers. These high and low speed streams interact with each other and alternately pass by the Earth as the Sun rotates. These wind speed variations buffet the Earth's magnetic field and can produce storms in the Earth's magnetosphere.*

The Ulysses spacecraft has now completed one orbit through the solar system during which it passed over the Sun's south and north poles. Its measurements of the solar wind speed, magnetic field strength and direction, and composition have provided us with a new view of the solar wind.

On figure below the solar wind speed are shown.

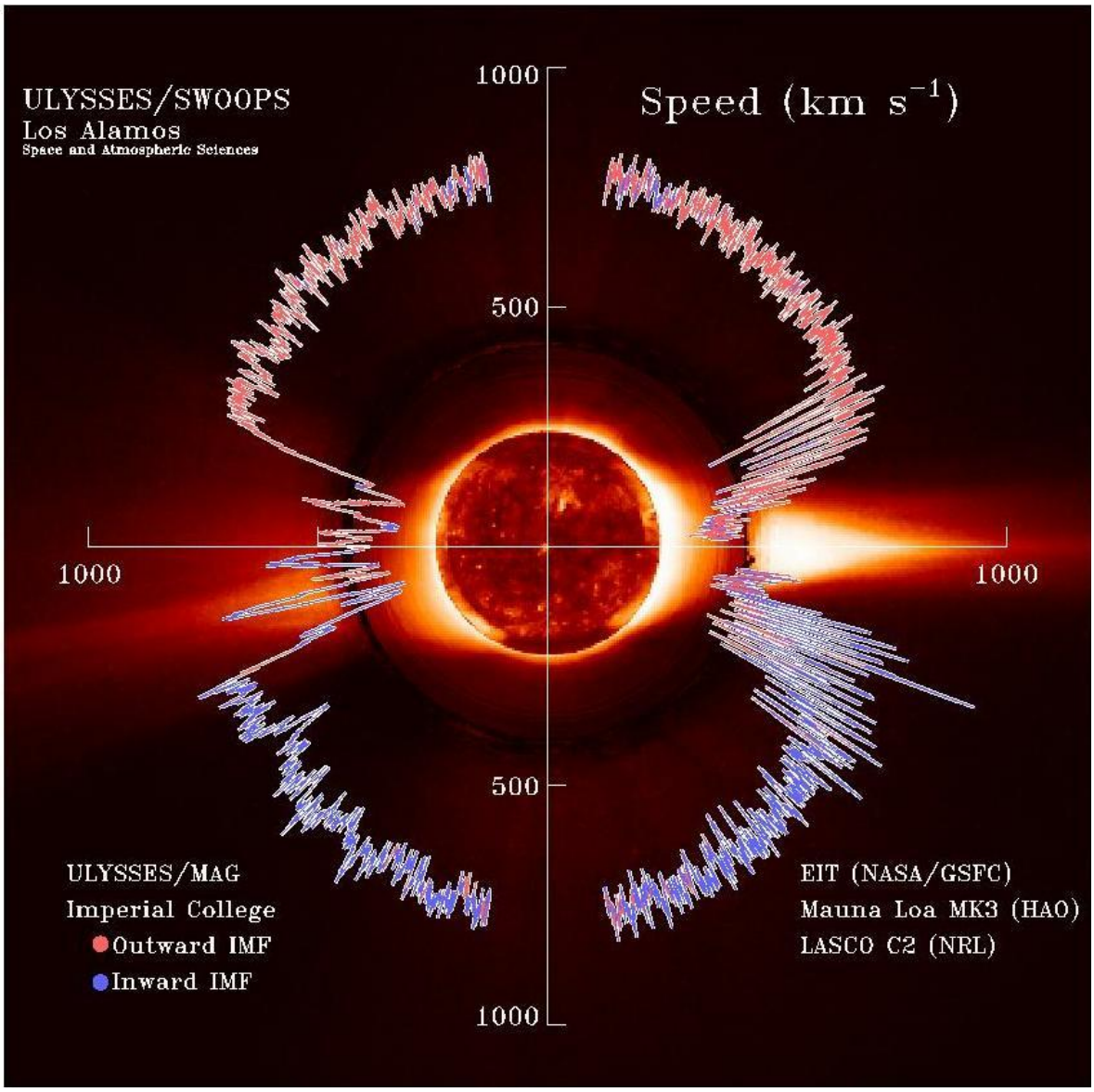

Figure 277: solar wind speed

The Advanced Composition Explorer (ACE) satellite was launched in August of 1997 and placed into an orbit about the L1 point between the Earth and the Sun. The L1 point is one of several points in space where the gravitational attraction of the Sun and Earth are equal and opposite. This particular point is located about 1.5 million km (1 million miles) from the Earth in the direction of the Sun. ACE has a number of

instruments that monitor the solar wind and the spacecraft team provides real-time information on solar wind conditions at the spacecraft.

On figure below the solar wind condition of seven days are shown.

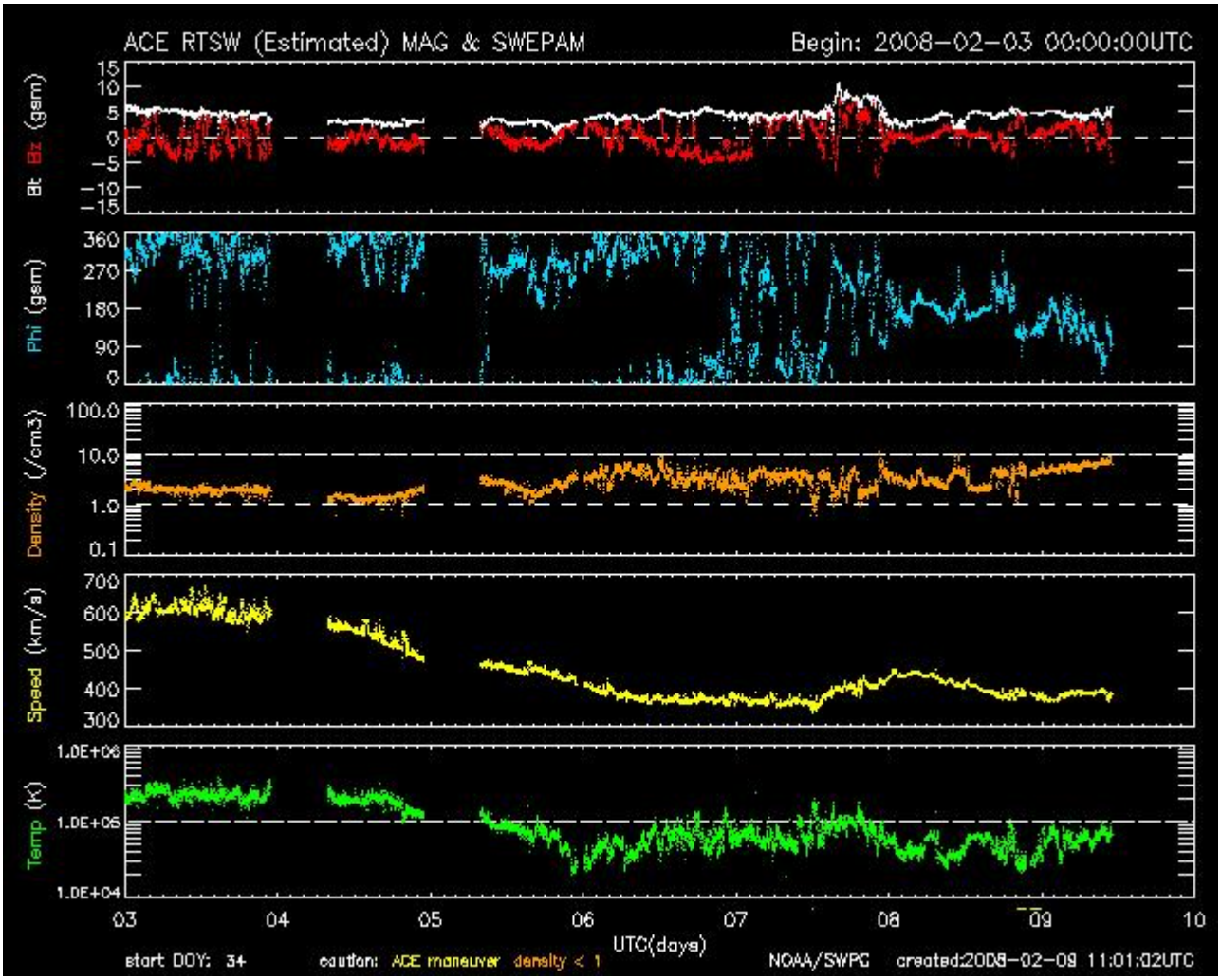

Figure 278: Solar wind conditions for the last seven days

Charge deposition

6.5.2 Activity, Dose, Dose Rate and Associated Units

The activity of a radioactive substance is defined by the number of decays taking place in this substance in a brief time divided by this time.
The activity does not provide any information about the type or energy of the radiation emitted.
The unit of activity is the **becquerel**. A radioactive source has an activity of **1 becquerel (Bq)** if one atom per second decays in the source.
An activity of 1 Bq corresponds to a very small amount of radioactive material.

The old unit of activity valid until the end of 1985 was the **curie**, the activity of 1 g of radium-226 (^{226}Ra).
A radioactive source has an activity of **1 curie (Ci)** if 37,000,000,000 = 37×10^9 atoms decay in the source every second.

During the interaction of radiation with matter, energy is absorbed by the irradiated material. The energy released by ionizing energy into matter is designated the **absorbed Dose D**.
The unit of the absorbed dose is the **gray (Gy).**
One gray corresponds to an absorbed energy of **1 joule/kilogram (J/kg)**. (1 Joule = 1 J = 1 Ws = 1 Watt × 1 second).
The old unit (until 1985) was the **rad (rd)**: **1 Gy = 100 rad**.

Legal units are used in radiation protection. They are based on the international system of units, Système International D'Unités (SI). Old units which have not been permitted in official and commercial use since 1 January 1986 are still occasionally used. These units are frequently still found on old radiation protection measuring devices. These devices may still be used even though the values are not given in legal units. The following values are required in radiation protection:

- the basic units from the SI system for length (m), mass (kg), time (s), current (A),
- the derived units for energy (1 J = 1 kg m^2s^{-2}), power (1 W = 1 J s^{-1}), electric charge (1 C = 1 As),
- and derived time units: minute (min), hour (h), day (d).

Formula sign	Significance	SI Unit	Old unit (until 31.12.1985)	Conversion formula	
A	activity	Becquerel (Bq) 1 Bq = 1 s^{-1}	Curie (Ci)	1 Ci = 3,70 · 10^{10} Bq	1 Bq = 2,70 · 10^{-11} Ci
H	dose equivalent	Sievert (Sv) $1\ Sv = 1\frac{J}{kg}$	rem	1 rem = 10^{-2} Sv	1 Sv = 100 rem
H	dose rate equivalent	Sv/h ; Sv/min ; Sv/h $1\frac{Sv}{s} = 1\frac{J}{kgs} = 1\frac{W}{kg}$	rem/h ; rem/min ; rem/s	100 rem/h = 1 Sv/h	$1rem/h = 2{,}78 \cdot 10^{-6}\ \frac{W}{kg}$
D	absorbed dose	Gray (Gy) $1\ Gy = 1\frac{J}{kg}$	Rad (rd) 1 Rd = 100 erg/g	1 rd = 10^{-2} Gy	1 Gy = 100 rd
D	absorbed dose rate	Gy/h ; Gy/min ; Gy/s $1\frac{Gy}{s} = 1\frac{J}{kgs} = 1\frac{W}{kg}$	rd/h ; rd/min ; rd/s	$1\frac{Gy}{h} = 100\frac{rd}{h}$	$1\frac{W}{kg} = 3{,}6 \cdot 10^{3}\ \frac{Gy}{h}$
J	ion dose	$\frac{C}{kg}\left(=\frac{As}{kg}\right)$	Röntgen (R)	$1\ R = 2{,}58 \cdot 10^{-4}\ \frac{C}{kg}$	$1\frac{C}{kg} = 3{,}88 \cdot 10^{3}\ R$
j	ion dose rate	$1\frac{A}{kg} = 1\frac{C}{kgs}$	R/h ; R/min ; R/s	$1\frac{R}{s} = 2{,}58 \cdot 10^{-4}\ \frac{A}{kg}$	$1\frac{A}{kg} = 1{,}4 \cdot 10^{7}\ \frac{R}{h}$

Table 30: Units in Radiation Protection Measurements

6.5.3 Radiations effects on Human body

Ionizing radiation is absorbed and spread to a different extent upon passing through matter, dependent on the type of radiation and the particle energy. For the human body this means that in the case of external radiation incidence, the individual organs receive different energy doses. Different types of radiation and radiation energies lead to different ionization densities and are therefore of differently strong biological effectiveness at the same absorbed energy. To take this different biological effectiveness into account, the **radiation weighting factors W_R** were introduced for use in health physics.

The value of the **radiation weighting factors** depends on the type of radiation and on the radiation energy. In general, densely ionizing radiation (e.g. alpha particles, protons, neutrons) is assigned high values and loosely ionizing radiation (e.g. beta particles, positrons, gamma and X-ray radiation) is assigned low values for the weighting factors. Multiplication of the *energy dose* D_T *of an organ T* by the *radiation weighting factor* W_R for the type of radiation and the radiation energy at the location of the organ then yields the **organ equivalent H_T** dose:

$$H_T = W_R \times D_T.$$

Type of radiation and energy		W_R
photons, all energies		1
beta radiation, all energies		1
neutrons	< 10 keV	5
	≥ 1 keV...100 keV	10
	< 100 keV…2 MeV	20
	< 2Mev…20 MeV	10
	> 20 MeV	5
protons		5
alpha particles, heavy nuclei, fission fragments		20

Table 31: Radiation Weighting Factors W_R

This quantity thus contains information about the effect of radiation on humans. The organ dose is therefore not a physical unit of measurement, but forms the basis for estimating the probability of leukemia and cancer as stochastic radiation injury. Since the **radiation weighting factor** is *dimensionless*, the **organ equivalent dose**, as well as the other dose equivalents still to be mentioned, is measured in the unit of **J/kg**.

In order to distinguish it from the **energy dose**, however, the special unit of **sievert (Sv)** and the derived units of **millisievert (mSv)** and **microsievert (µSv)** are used.

*The introduction of the dose equivalent makes it possible to describe and compare radiation exposure irrespective of the type of radiation. An organ equivalent dose of **1 Sv** due to gamma radiation has the same biological effectiveness as **1 Sv** of beta radiation or **1 Sv** of neutron radiation.*

The effective dose was introduced as a measuring quantity to assess the total radiation risk with respect to cancer and leukemia due to ionizing radiation. This takes account of the fact that there are organs and tissues which must be particularly considered due to their sensitivity to late radiation injuries . However, the sensitivity of these risk-relevant organs and tissues for triggering late injuries due to ionizing radiation is differently high. A partial body exposure leads to a lower radiological risk than a whole-body exposure. For the effective dose, the individual organ doses are multiplied by a weighting factor and added up. These **organ weighting factors** make allowance for the relative contribution of the organs and tissues affected to the risk of death due to late radiation injuries, i.e. due to leukemia and cancer, and to the risk of hereditary injuries. The sum of all weighting factors is equal to unity. In the case of a dose distributed equally over the entire body (whole body exposure), the value of the effective dose corresponds to the average organ dose for the entire body.

Example: Thyroid cancer contributes approximately 0.05 (= 5 %) to the total risk of death by cancer and of hereditary injuries caused by ionizing radiation. The **organ weighting factor** for the thyroid is thus 0.05. The thyroid was now irradiated e.g. with an organ dose (partial body dose) of 1 Sv. With the aid of the effective dose it is then possible to calculate the dose that would cause the same radiation risk for the whole body.

The effective dose for this thyroid exposure is thus 0.05 × 1 Sv = 0.05 Sv = 50 mSv. This means that a whole-body exposure of 50 mSv arithmetically leads to the same number of fatalities due to radiation injury as a thyroid exposure of 1 Sv due to thyroid cancer alone.

The most important limit values for the body doses of the population and radiation-exposed persons are stipulated in the Radiation Protection Ordinance (Articles 46, 55) and listed in Table below. As a rule, individual doses are not directly measurable, since they are defined as averages over organs and tissues in persons. For externally incident radiation, measuring quantities were therefore additionally introduced, which can be measured by health physics instruments or dosimeters and can provide an estimate for the individual doses, if possible, under all realistic exposure conditions.

These measurement quantities are defined by the ***energy dose*** *at one point, multiplied by a* ***quality factor Q****, as equivalent dose. The quality factor Q allows for the different biological effectiveness with respect to the different types of radiation. To put it more precisely, the quality factor is a function of the already mentioned linear energy transfer. The above-mentioned* ***radiation weighting factors*** *thus constitute formal approximation values of the* ***quality factor****. The unit of the equivalent dose is the* ***sievert****.*

		Persons occupationally exposed to radiation	
	Population	Category B	Category A
effective dose	1 mSv	6 mSv	20 mSv
lens of the eye	15 mSv	45 mSv	150 mSv
partial body exposure: skin, hands etc.	50 mSv	150 mSv	500 mSv
occupational lifetime dose		400 mSv	

Table 32: Limit Values of Individual Doses

Older measuring instruments in part still indicate the old unit of ***rem.***

Conversion: 1 Sv = 100 rem or 1 mSv =100 mrem.

Rem (Roentgen Equivalent Man) was used for biological matter. It is the radiation dose which produces the same amount of biological damage as *1 rad* of *200 keV X-rays*.

$$REM = RBE \times RAD.$$

The factor ***RBE*** (Relative Biological Effectiveness) measures the effectiveness of a given radiation relative to *200 keV X-rays*

On table below are reported the Relative Biological Effectiveness of various radiation source.

Radiation	RBE (Relative Biological Effectiveness)
5 MeV gamma rays	0.5
1 MeV gamma rays	0.7
200 keV gamma rays	1.0
Electrons	1.0
Protons	2.0
Neutrons	2--10
Alpha particles	10--20

table 33: RBE of various radiation source

On table below are reported the Probable radiation dose effect for a sample population

Dose (rem)	Probable Effect
0--50	No obvious effect except, possibility, minor blood changes.
50--100	Radiation sickness in 5—10% of exposed personnel. No serious disability
100--150	Radiation sickness in about 25 % of exposed personnel
150--200	Radiation sickness in about 50 % of exposed personnel
200-350	Radiation sickness in nearly all personnel. About 20% deaths
350--550	Radiation sickness. About 50% death
1000	Probably no survivors

table 34: Probable radiation dose effect for a sample population

On table below are shown the Gemini mission orbital parameter and average radiation doses.

Mission Launch Data	Apogee (NM)	Perigee (NM)	Inclination Revs	Inclination Deg	Average Dose Millrad
V Aug 21, 1965	189	87	120	32.5	176
VIII Mar 16, 1966	161	86	7	29	10
IX Jun 3, 1966	168	86	45	29	19
X Jul 18, 1966	412	161	8	29	726

table 35: Gemini mission radiation dose

On table below are shown the Recommended Radiation Dose Limit for Astronauts.

	Dose Limit—Rads (Tissue)		
Mission Duration	Skin (0.1 mm)	Eyes (3 mm)	Bone Marrow (5 cm)
30 days	75	37	25
90 days	105	52	35
180 days	210	104	70
1 year	225	112	75
Career total	1200	600	400

table 36: Recommended Radiation Dose Limit for Astronauts

Depending on the task to be performed by health physics staff and on the measurement method selected, a distinction is made between **area dose** and **personal dose.**

The **area dose H*** or **H'** is defined as **dose equivalent in soft tissue**, measured in a particular location.

- The **area dose rate** is the ratio of **area dose** and **time** in which it is irradiated. Its unit is the sievert by second. For the dose rate, however, the derived units of sievert by hour (Sv/h), millisievert by hour (mSv/h) or microsievert by hour (µSv/h) are more commonly used. If the (measured) area dose rate at one

location is multiplied by the time for which a person stays in this place, this area dose rate provides an estimate of the effective dose the person would receive there.

- The **personal dose equivalent H_P** is an individual measure of the exposure of an individual person to external radiation. The personal dose is generally determined by a so-called personal dosemeter (e.g. film badge, pen dosemeter, finger ring dosemeter) worn by the person on the body. The personal dose is defined as equivalent dose in soft tissue, measured at a location of the body surface representative of the radiation exposure.

Since the human body influences the radiation field – the radiation is spread in the body and absorbed– the values measured for the area and personal dose are generally not identical. Both dose values can therefore only be estimates of a person's effective dose. The radiation externally incident on a person can be characterized as strongly penetrating radiation or weakly penetrating radiation, depending on the individual dose limits relevant for the radiation involved.

- In the case of **weakly penetrating radiation**, the dose deposited in the terminative layer of the skin (depth approximately 0.07 mm) dominates.
- Whereas in the case of strongly penetrating radiation the dose in the deeper-lying tissue layers and organs is predominant.
- Weakly penetrating radiation is considered to be e.g. beta radiation with energies below 2 MeV and photon radiation with energies below 15 keV.
- Neutron radiation is always strongly penetrating. For the determination of the local skin dose, the eye lens dose and the effective dose, the equivalent dose values at a depth of 0.07 mm, 3 mm and 10 mm in the human body are suitable estimates.
- Table below shows the measurement quantities and their allocation to the body doses determined by limit values. The figures in brackets indicate the depth in millimeters for dose determination. Since for weakly penetrating radiation the dose at 0.07 mm depth may vary strongly with the direction of radiation incidence, a distinction is made for the area doses between ambient dose equivalent **H*** and directional dose equivalent **H'**.
- **H'**(0.07) is thus the maximum dose equivalent at 0.07 mm depth, irrespective

of the direction of incidence.

external radiation	limiting individual dose	measurement quantity for	
		area dose	personal dose
weakly penetrating radiation	effective dose	H* (10)	H_P (10)
strongly penetrating radiation	skin dose	H' (0.07)	H_P (0.07)
	eye lens dose	H' (3)	H_P (3)

Table 37: Measurement Quantities in Health Physics

6.5.3.1 Basic Processes of Biological Radiation Effects

Radiation from radioactive substances - as also cosmic radiation reaching the Earth from space – is characterized by the property of generating charge carriers (ions) upon colliding with matter.

Therefore, this ionizing radiation also generates charged particles (ions) in living tissue by stripping planetary electrons, or causes excitations in the atomic range, which may then lead to a molecule breaking apart or to the formation of very reactive molecular fragments (radicals). Neither the radiation type nor the origin of the radiation is of significance in the formation of this physical primary effect.

Thus in its basic effect there is no difference between natural and artificial or internal and external radiation exposure.

Apart from biological factors (such as radiation sensitivity), which are characteristic of a certain organ or tissue, the quantity of radiation taken up (radiation dose) and the ionization density already mentioned in the previous chapter are of significance for the biological effect of radiation.

Only an extremely small fraction of all primary physical events actually has an impact in the biological sphere. The living cell is largely in a position to repair the damage resulting from primary physical effects or in the case of irreparable damage to destroy the damaged cells.

These repair mechanisms are the more effective the lower the degree of damage is. If low-dose-rate radiation strikes living tissue then the probability is great that a new damage event only occurs in a cell when the previous damage has already been repaired. Furthermore, defence mechanisms may have been set in motion in a cell which has already been previously "hit" enabling renewed damage to be more effectively repaired. The same dose distributed over a prolonged period is therefore less effective than if it acts in a short period (time factor).
For similar reasons, a partial-body dose is less effective than a whole-body dose. It is frequently termed the organ dose.
With the biological effects, a differentiation is made between acute radiation damage observable immediately or a short time after radiation exposure, and late damage including genetic damage (changes of the genetic material in viable reproductive cells) and somatic injury (for example leukemia, cancer, cataracts).
If the severity of the damage is dose-dependent then it is termed deterministic or non-stochastic, if the probability of the occurrence of injury depends on the dose then it is termed stochastic.

6.5.3.2 Acute Radiation Injury

Above a certain threshold value (approx. 250 mSv for humans), characteristic syndromes occur in the case of whole-body exposure and high-dose rate which become increasingly severe with increasing dose (radiation sickness).
Radiation sickness is a typical deterministic injury. Its course does not only depend on the dose but also on the exposure conditions, whether for example it involves whole-body or partial-body exposure, external or internal exposure, the type of radiation causing the exposure or what environmental impacts have had an additional effect during and after radiation exposure.

Acute radiation injury also includes damage to the embryo (if the developing embryo is irradiated) which is stochastic damage since here the frequency of cases increases with rising dose. The rise in severity of acute radiation injury with increasing dose is shown in Table below.

Dose range	Probable effect
800 .. 1200 mSv	Nausea and vomiting for one day in 5 - 10 % of cases; fatigue but no serious symptoms.
1300 .. 1700 mSv	Nausea and vomiting for one day, followed by further mild symptoms of radiation sickness in approx. 25 % of cases; however, no fatalities are to be expected.
1800 .. 2200 mSv	Nausea and vomiting in about 50 % of those affected on the first day, followed by radiation sickness symptoms; no fatalities are to be expected.
2700 .. 3300 mSv	Nausea and vomiting in the case of almost all persons affected on the first day, followed by more serious symptoms of radiation sickness; approx. 20 % fatalities to be expected within 2 - 6 weeks after irradiation; survivors recover after about 3 months.
4000 .. 5000 mSv	Nausea and vomiting on the first day in the case of all those affected, followed by serious symptoms of radiation sickness; about 50 % fatalities can be expected within one month; survivors recover after about 6 months.
5500 .. 7500 mSv	Nausea and vomiting in the case of all those affected within 4 hours after irradiation, serious symptoms of radiation; most 100 % mortality; survivors recover after about 6 months.
10,000 mSv	Nausea and vomiting within 1 - 2 hours; probably no survivors of radiation sickness.

Table 38: Typical radiation effects after an individual has been exposed to brief whole body irradiation with g-radiation

6.5.3.3 Late Radiation Injury

Except for cataracts whose occurrence depends on a certain minimum dose, all late damage represents stochastic effects for which the probability of occurrence of damage is dose-dependent.

The occurrence of late injury is independent of whether acute damage has previously occurred or not.

A differentiation is made between somatic impacts - in the case of damage to the body cells of the affected person - and genetic impacts where the genetic material of the gametes is altered (mutated).

A latent period of years or decades elapses between the occurrence and the course of somatic damage, genetic effects only become apparent in subsequent generations.
Typical late somatic damage takes the form of cancer and leukemia. However, the body´s defence system provides a very effective barrier to the occurrence of this damage. Only a few cancer cells actually succeed in causing cancer.

Genetic change to a gamete is not synonymous with genetic damage in subsequent generations, although it can lead to such damage if mutated gametes succeed in reproducing. Genetic damage in the gametes can also be reversed by repair to or elimination of damaged cells.
As in the case of late radiation injury, a dose-rate dependence can be perceived. The risk of cancer and the genetic risk are less at a low dose rate.

Space radiation preferentially destroys specific forms of amino acids.

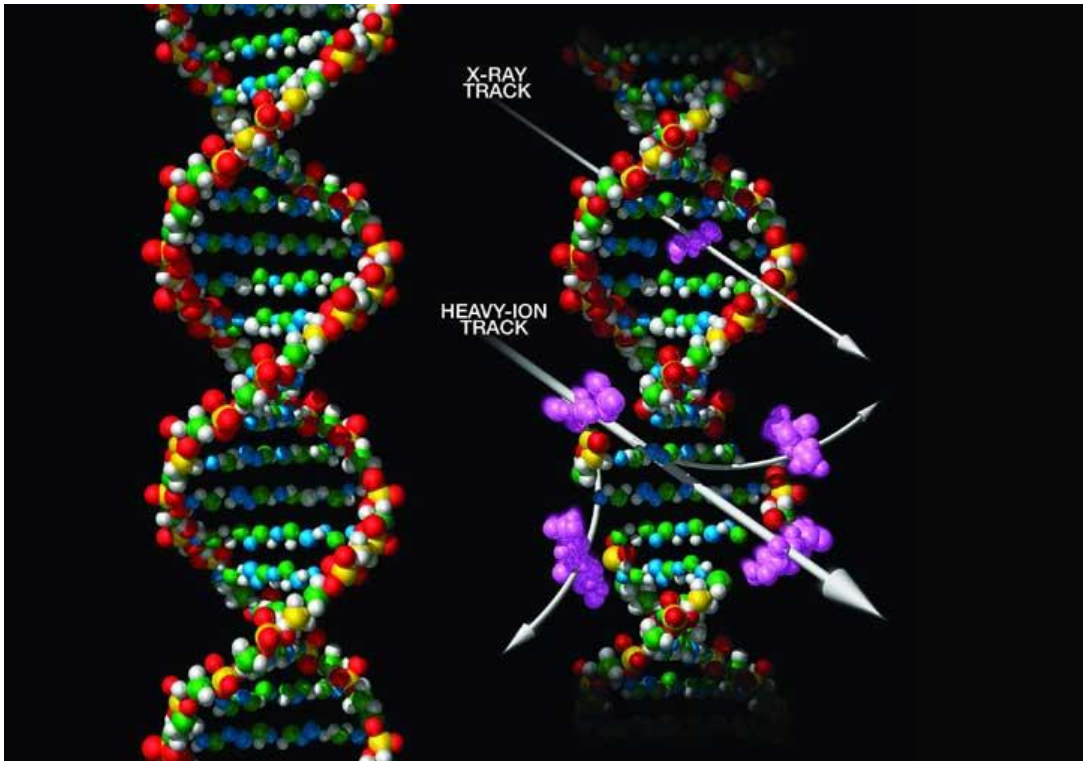

figure 279

6.5.4 Effect of radiations on Semiconductor

Charged particles can damage an impacted material by a combination of ionization and atomic displacements. These effects can lead in turn to chemical reactions and changes in the local morphology. Electrons slow by generating a continuous ionized path in materials. Protons are heavily ionizing and produce higher ionization near the end of the particle path. The size of damage depends upon total flux, intensity of radiation, and the angle of impingement. The interaction of these particles with organic materials can lead to outgassing, shrinkage, cracking, pitting, embitterment and discoloration.

Energetic particle radiation also influences the absorptivity of materials.

As seen with UV radiation, the solar absorptance of thermal control coatings show an increase over time. For example, when simulating the Galileo mission, the solar absorptance of ZincOrthoTitanate (ZOT), a thermal control coating, increased from 0.13 to 0.42. Charged particle radiation also can lead to "darkening" of optical materials.

Satellite electrical charging (the buildup of static electricity on the satellite surface) is one of the most common anomalies caused by radiation.

Charging occurs when a satellite moves through charged particles (called "wake charging"). Charging can also occur through direct particle bombardment or through a photoelectric effect, with some materials subjected to electromagnetic solar radiation. When the breakdown voltage of a material is exceeded, an electrostatic charge will ultimately result in a discharge or arc; which can severely damage materials, cause spurious circuit switching, or result in false sensor readings.

Materials especially prone to damage include electronic materials, thermal coatings, and solar cell materials.

The high-energy protons from either cosmic radiation or the inner Van Allen Belt can completely penetrate a satellite. As they pass through, they can ionize particles deep inside the system. A single proton can deposit enough charge to cause a circuit switch, spurious command, or memory change. These incidents are labeled "**single event upsets**". With a push towards lower voltage commercial-off-the-shelf

microelectronics, it is actually easier to cause electrical upsets than with older satellites.

Additionally, the lessening of the perceived nuclear threat has reduced the level of nuclear hardening of satellites. While intended to protect systems from the radiation of a nuclear explosion, this type of hardening also helped to protect satellites from the radiation naturally present in the space environment.

Many satellites use electro-optical sensors to maintain their orientation in space. These sensors reference the direction of certain stars to achieve precise pointing accuracy. When a high energy proton impacts a sensor material, a flash of light is produced and misinterpreted as a star.

The computer will then try to find the star in its star catalogue. At this point the satellite could become disoriented, creating the possibility that communications antennas, sensors, solar panels all could fail to orient themselves properly, thus impacting the mission. In extreme cases, the satellite could even be lost if the batteries were to drain from a lack of solar power. For this reason, nearly all satellites have a Sun sensor. While not providing the navigational accuracy of a star sensor; a Sun sensor can help the satellite recover its orientation following an upset.

The charge deposition in the semiconductors of the spacecraft electronics produces:

- *Single Event Upsets (SEU*): bit-flips in digital microcircuits, leading to loss of storage data, software damage and hang-ups of running codes. SEU are generally not mission-critical.

- *Single Event Latchups (SEL)*: permanent damage to microcircuits, which are short-circuited to ground. Rare, but may be mission-critical.

- *Single Event Burnout (SEB)* is a condition that can cause device destruction due to a high current state in a power transistor. SEB causes the device to fail permanently.
- *Degradation of solar cells*

NASA Thesaurus defines **SEU** as "radiation-induced errors in microelectronic circuits caused when charged particles (usually from the radiation belts or from cosmic rays) lose energy by ionizing the medium through which they pass, leaving behind a wake of electron-hole pairs."

- ***Solar flare and CME*** particle events pose the most extreme SEU producing environment, especially for spacecraft in interplanetary space.
- ***Combined Release and Radiation Effects Satellite (CRRES)*** data seem to indicate that most single-event upsets come from high energy protons via nuclear interactions and not through direct deposition from either protons or cosmic rays.
- For LEO satellites, ***trapped protons***, especially in the South Atlantic Anomaly, are the greatest SEE (Single Event Effects) threat.

The **SEUs** are predominantly caused by two different space radiation sources:

- high energy protons
- the heavy ion component of cosmic rays of solar and galactic origins.

The affects are:

- Heavy ions cause direct ionization within a device.
- Protons can make a large contribution to the overall upset rate (particularly for LEO).
- Protons typically do not cause an upset through direct ionization, but rather through complex nuclear reactions (spallation). Spallation is a nuclear reaction in which two or more fragments or particles are ejected from the target nucleus.

SEU effects have become worse as devices have evolved because of lower "critical charge" due to small device dimensions, and large numbers of transistors per chip and overall complexity.

The critical charge is the minimum charge deposited in a semiconductor unit capable of producing a flip in the logical state (**bit flip**).

Different semiconductor technologies show different susceptibility to SEU.

The present trends (device size and power reduction, line resolution increase, increased memory and speed) heighten the **SEU** susceptibility.

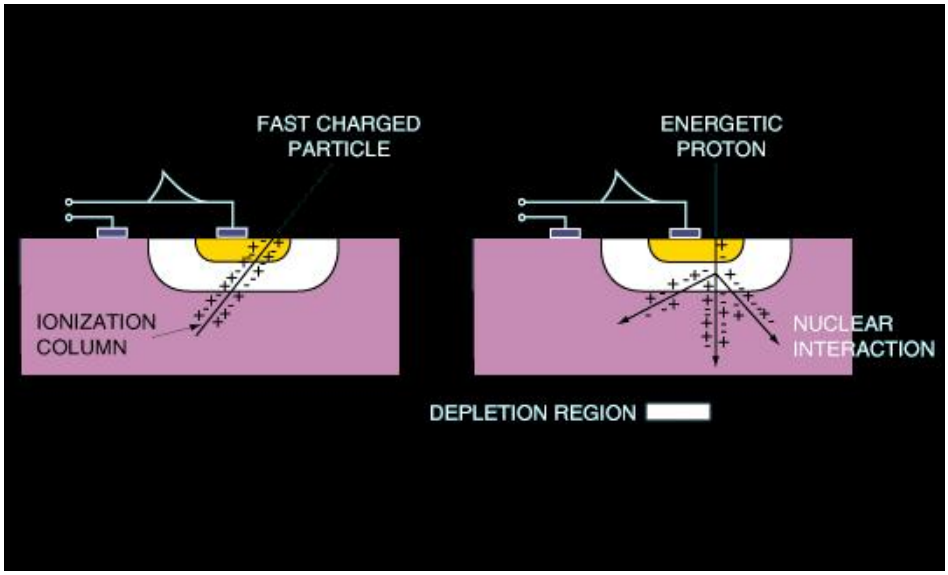

figure 280 Schematic showing how galactic cosmic rays deposit energy in an electronic device. The depletion region is a volume of a semiconductor where all of the mobile carriers have been swept out by an electric field. The depletion region is depleted of carriers.

6.5.5 Effect of Radiations on Water Chemistry

Radiation effect the water composition as on example below.

$$2(H + H \rightarrow H_2) \qquad \text{eq 68}$$

$$2H_2O_2 \rightarrow O_2 + 2H_2O \qquad \text{eq 69}$$

$$8H_2O + \text{radiation} \rightarrow 2H_2 + O_2 + 6H_2O \qquad \text{eq 70}$$

or

$$2H_2O + \text{radiation} \rightarrow 2H_2 + O_2 \qquad \text{eq 71}$$

The net result of these reactions is simply the decomposition of water. If **H** and **O** are allowed to escape from solution as gases, the reaction continues as written. If,

however, the water is contained in a closed system under pressure (as in a reactor coolant system), **H** and **O** are confined, and an equilibrium state is reached because radiation also causes the reverse of Reaction to take place. Primarily neutron and gamma radiation induce both the decomposition of water and the recombination of **H** and **O** to form water.

As an example if we are going to consider a water containment on the Moon surface we could have the following situation:

- Water containment on the Moon
  - Water, as an asymmetrical molecule, is susceptible to radiation
  - Radiation splits water into hydrogen and oxygen gases
    - Equilibrium between decomposition and recombination of water established by neutron and gamma radiation[10]
    - Useful under certain circumstances
      - Hydrogen and Oxygen are vital for life on the Moon
  - The problem: Prevent water from dissociating or becoming irradiated while using a radiation shielding that isn't hazardous to humans
    - Heavier atoms block radiation better
      - Lead, a typical "heavy" shield, is toxic.
    - Hydrogen (esp. liquid hydrogen) is the best shield
      - It's also very impractical to take to the Moon
    - **Polyethylene** is a great substitute
      - It has a lot of hydrogen—more than most polymers
  - The solution: Make bricks out of a combination of polyethylene and Moon **regolith** to shielding buildings, water containment facilities, etc.
    - Don't have to take as much weight to the Moon
    - **Regolith** makes an excellent filler material for radiation shields
      - Readily available on the Moon
      - Has few shielding properties of its own

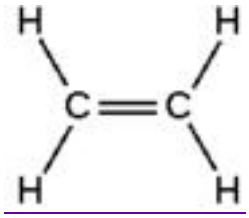

Figure 281: polyethylene structure

6.6 Radiations protection system

There are several method proposed in order to protect an useful volume from space radiations. These are mainly divided in two groups:

Passive Shielding

- *Passive shield (Conventional method)*
- *Lunar Lava tube passive shielding system (on the Moon)*

Active Shielding

- *Electrostatic shield – electric field only (time-independent)*
- *Magnetic shield – magnetic field only (time-independent)*
- *Both Electric and Magnetic fields (time-dependent,) for the first time, developed in this thesis*

6.6.1 Passive Shielding (Conventional method)

Passive shielding simply stops charged particles by multiple collisions with the shield material.
The force involved is primarily the Coulomb force.

Multiple collisions generate radiation by-products in the form of additional charged particles, each with less energy than the previous collision, until all kinetic energy is dissipated.
The magnitude of biological damage is proportional to the kinetic energy of the particle, as well as the cross-section. Even though biological damage will increase with increase in kinetic energy, as well as cross-sectional area, some researchers assert that at some point of increasing kinetic energy biological damage will begin to decrease because the interaction time of the particle with the biological media will decrease, resulting in fewer 2 collision by-products.

The shielding ability is density function of the shielding material; the appropriate material to be used for shielding depends on the type of radiation.

6.6.1.1 α-radiation

Special shielding is not required for α-radiation. In contact with the skin, the upper layer insensitive to radiation is already sufficient to protect the underlying tissue from radiation. α-emitters represent a hazard either if γ-radiation is emitted simultaneously with the α-radiation or else by incorporation.
α-emitters are particularly dangerous then since the body tissue is no longer protected against the effects of α-particles.

6.6.1.2 β-radiation

Due to its finite range, β-radiation can be shielded by moderately thick layers of materials with low atomic numbers (e.g. wood, glass, PMMA (Plexiglas, Perspex)). PMMA with layer thicknesses of 1 to 2 cm completely absorbs even very high-energy β-radiation. In addition to its shielding property, PMMA also has excellent chemical resistance, it can be easily worked, is shatterproof and also transparent like glass, so that a good view is ensured when working behind a PMMA shield.
With very strong β-sources and shielding material of a high atomic number (e.g. lead) it may be necessary to pay attention to the bremsstrahlung.
In most cases, the material of the container in which the β-emitter is stored is already sufficient shielding.

6.6.1.3 γ-radiation and X-rays

γ-radiation and X-rays are very penetrating (X-ray examinations are based upon this fact), nevertheless they are attenuated in matter. Materials with a high atomic number or of great thickness considerably attenuate γ-radiation and X-rays. Common shielding materials are lead, iron, baryte concrete and concrete containing scrap iron. On the other hand, air, water or aluminum only attenuate γ-radiation and X-rays to a slight extent. Shielding made of these materials must be correspondingly thicker.

Table below gives the layer thickness of various materials required to reduce the dose rate to 1/10 of its original value. The data are valid for high-energy γ-radiation.

Thus, a layer thickness of only 30 cm of water or 0.3 cm of lead is required to attenuate the dose rate of radiation with an energy of 0.1 MeV to 1/10 of its original value.

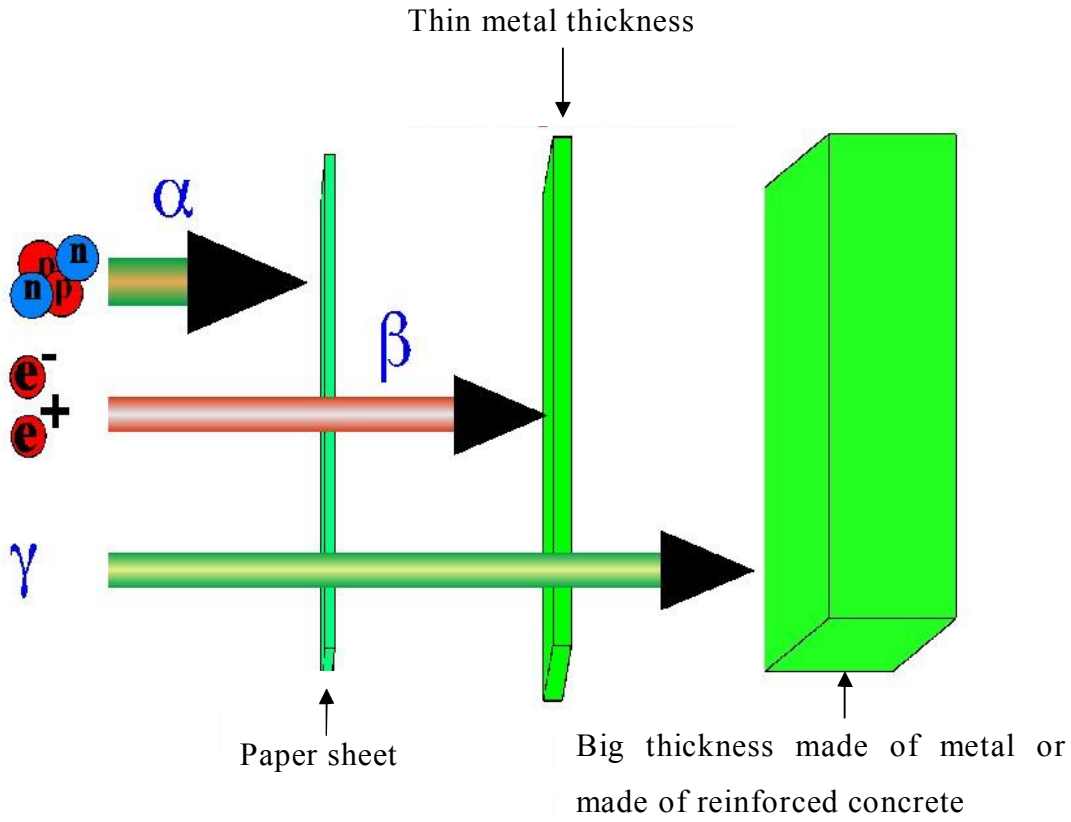

Figure 282: particles crossing ability

Material	Tenth-value thickness [cm]
Water	66
Normal concrete	31
Baryte concrete	21
Iron	9
Lead	4.7

Table 39: Layer thickness required to attenuate the dose rate to 1/10 (tenth-value layer thickness) for a broad high-energy γ-beam (1.25 MeV).

6.6.1.4 Neutrons

In the same way as γ-radiation, neutrons are also quite penetrating. For shielding purposes, the neutrons are first slowed down (moderated) by materials with a low atomic number (water, polyethylene, concrete) and then shielded by neutron absorbers (boron, cadmium) but these last material are toxic.

6.6.1.5 High-Energy Cosmic Rays –The effect of leakage through the radiation shield.

Any type of radiation shielding has an upper limit to the energy of particles against which it can shield. Above this energy, there will be leakage through the shield. Spacecraft structures have traditionally been made of aluminum, and many studies and measurements have been done to show cosmic ray shielding by different thicknesses of aluminum. Results are shown in figure below.

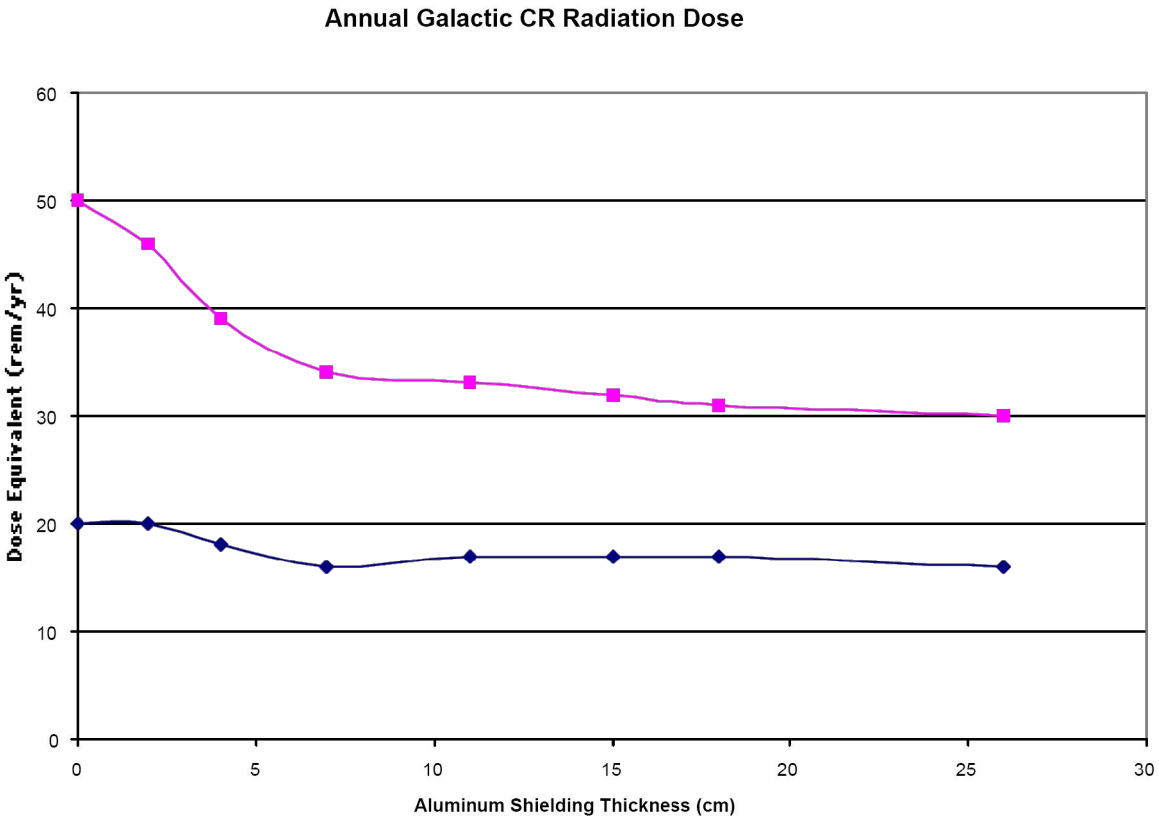

figure 283: Radiation doses received from galactic cosmic radiation with difference thicknesses of passive aluminium shielding. (Top curve: solar minimum; Bottom curve: solar maximum)

Passive shielding can be quite effective for particles with energies < 1 GeV/nucleon. However, for higher energy particles, nuclear interactions with the shielding material produce secondary particles which can actually be more numerous and detrimental to astronaut health than the incident radiation.

Figure above shows that the first ~10 cm. of aluminum partially reduces the radiation, but doubling the thickness produces almost no more net reduction. If the thickness is increased sufficiently, of course, all radiation can be absorbed, but the resulting mass will be impractically large.

Passive shielding only makes the problem worse for high-energy cosmic rays, which interact in the shielding to create secondary particles with a higher "**quality factor**" (i.e.more physiologically damaging) than the primary radiation. Using hydrogen as a passive shield reduces but does not eliminate secondary shower generation.

6.6.2 Lunar Lava Tubes passive shielding system

Humans on the Moon would be protected from solar and cosmic radiation by building habitats inside lunar lava tubes. Radiation shielding will need to be at least three meters thick to protect residents from cosmic radiation and solar flares. That is why an intact lunar lava tube is an ideal place to build the first lunar base. They are naturally occurring self-supporting radiation shields that have roofs which are tens of meters thick. Lunar lava tubes are much larger than those on Earth and are large enough to accommodate a large base. They are hundreds of meters wide. They can be thousands of meters long. A base in a lava tube could be easily expanded. An intact lunar lava tube will provide ideal protection from meteors, radiation, extreme temperature fluctuations and the abrasive lunar dust. It is also possible that the lava tubes will contain life support volatiles since they are a stable -20 degrees Celsius (Mendel) any water vapor which entered the tube would freeze and still be there. Intact lava tubes could be found near riles on the border between mare and highland. Partially collapsed lava tubes can be seen in photos of the Moon. They have been considered for use as a location for a lunar base by Coombs and Hawke. These lava tubes have questionable structural integrity because they are partially collapsed. It would be much better to find an intact lava tube. They will be larger since they are whole. They are probably deeper. Also in the future an entire tube could be sealed air tight so there could be Earth-like sub-selene cities.

figure 284: Earth example of lavatube

The only problem with using an intact lava tube is finding them. Two possible ways of finding lava tubes are radar or active seismic sounding. There are problems with both. Radar may not work. Seismic sounding only covers a small area a time. Radar on Earth only penetrates about 10 meters because the Earth is very wet. The Moon is extremely dry but other things, such as metals which, may not allow radar to penetrate the 1 kilometer needed for a complete survey for lava tubes. Even if radar does penetrate, large satellites may be required.

Seismic sounding will only cover a few square kilometers at a time. This would mean we would have to have a good idea where to look. Areas with partially collapsed lava tubes and areas with similar geology are a way to narrow the search. The area could also be narrowed by doing a very accurate gravity survey of the Moon. Areas which have too little mass could be areas with lava tubes. One complication with doing an active seismic survey of the Moon is that the dry lunar rock and regolith do not attenuate seismic waves. The Moon rings like a bell when it is impacted. There is no

water to absorb the sound vibrations. When the Apollo 12 Lunar Module was crashed into the Moon, the Moon reverberated for over two hours. This means we can not simply use terrestrial analysis techniques on lunar seismic data. Some one will have to develop new techniques.

Both radar and active seismic survey were done as part of the Apollo program. These experiments only obtained small amounts of data. Also the equipments used were primitive by today's standards. All of the Apollo experiments were designed with limited understanding of the lunar environment. The radar experiments where hindered by the limited data storage technology. This should not be a problem with modern computer equipment. The seismic experiment data had larger error bars then the magnitude of the data. More data and better designed experiments should solve this problem. The experience of Apollo and the technology developed since then along with experiments in the future will give us everything we need to find intact lunar lava tubes.

Once lunar lava tubes are found to use them all we would need to do is to drill an elevator shaft. Then floor of the lava tube will need to be cleared of debris and leveled. A dust-lock could be used to allow a cleaning area for equipment and space suits before entering the base. The ends of the base area could be sealed by stretching the same material used for the inflatable habitats over the opening sealing the section of the tube air tight, it would be a buffer between the lunar vacuum and the high internal pressure of the base. This would reduce the rate of air leakage from the habitat. Once prepared, the tube will be ready to receive inflatable structures.

6.6.3 Active shielding

Active shielding is based on deflecting charged particles by means of the Lorentz force:

$$\vec{F}_L = q\vec{E} + q\vec{v} \times \vec{B} = m_p \vec{a}_p \qquad \text{eq 72}$$

Where q is the charge of a single radiation particle, v is the particle velocity, E is the Electric field of the shield and B is the magnetic field component of the shield.

6.6.3.1 Magnetic shielding systems

Traditional methods for protecting spacecraft and occupants from these forms of radiation involve some configuration of a massive material shield to absorb the energy of incoming particles. For the high energy galactic cosmic rays (GCRs) that astronauts will be exposed to, these so-called passive shields are too massive to be practical and will likely produce showers of secondary radiation that could be more harmful than the GCRs themselves. Active shields which rely on magnetic (or electric) fields to deflect energetic particles offer a potential solution to the problem. Designing a magnetic shield strong enough to deflect GCR particles but weak enough to not harm astronauts is a challenge.

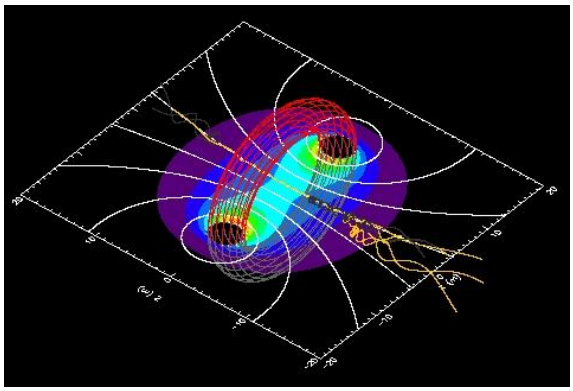

figure 285

6.6.3.2 Null Field Torus

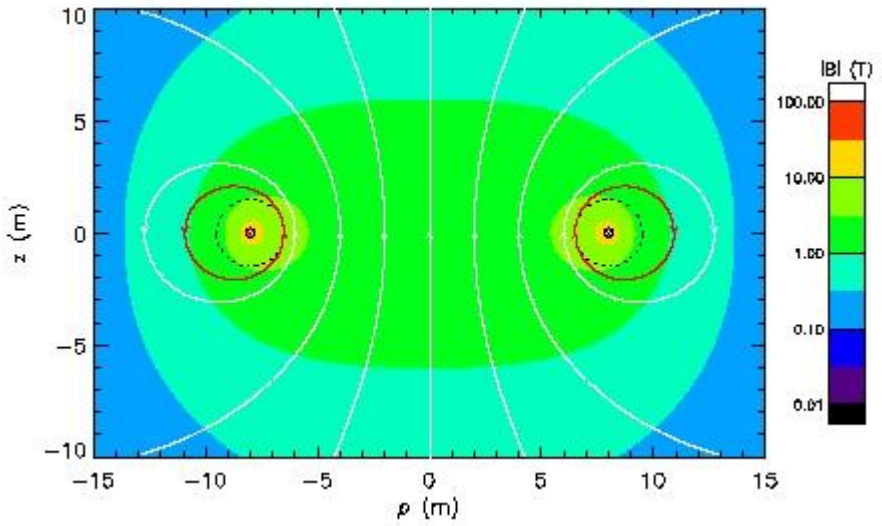

figure 286

Magnetic field due to a circular current loop of radius 8 m. Dashed line represents cross section of torus with minor radius or 1.5 m. Red line is magnetic field line that begins at inner edge of torus (6.5 m). Magnetic field is, by definition, tangential to the surface enclosed by the red magnetic field line.

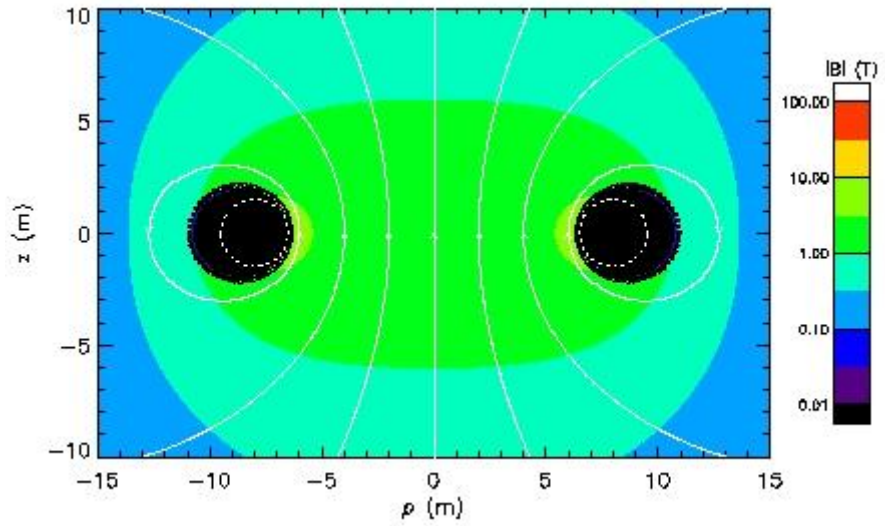

figure 287:

Amperes Law allows us to specify exactly the current density needed on the surface of the red magnetic field line in Figure above such that the magnetic field inside the region is everywhere exactly zero.

6.6.3.3 Basic Principles of Magnetic Shielding

Magnetic shielding has been the subject of several previous studies [Landis, 1991; Townsend, 2000]. Researchers are studying this complex engineering problem on the basis of recent advances in technology and computational models. The following key points have to be taken into consideration for the theoretical studies and engineering design of a shielding system to protect astronauts from the cosmic rays:

- Charged particles can be either absorbed in a relatively uncontrolled way by various materials or actively reflected by stationary electric and/or magnetic fields.
- During the process of absorption, the composition and spectrum of the radiation changes. If absorption is not complete, the transformed radiation enters the habitable zone with effects potentially much worse than the original incident radiation. Secondary particles which were not present in the incoming radiation (e.g. neutrons) can be produced in the shielding material and enter the habitable zone.

Reflection does not change the composition of the radiation; no new particles are created. Magnetic and electrostatic reflections have somewhat different effects on the incoming particle spectrum. In both cases, reflection has more of an effect on lower energy particles, so it effectively hardens the spectrum of radiation entering the habitable zone.

A magnetic field does no work on charged particles, so it does not change the energy of the incoming particles; it just diverts them. Thus, at all energies, the radiation penetrating the habitable zone is never greater than the incident radiation. Electrostatic deceleration actually lowers the energy of incoming particles, so the overall effect on the spectrum is more complex, as incoming particles at high relativistic energies are characterized not only by different masses, but also ionization states and velocity vectors at the impact.

No system can be purely reflective, since the mass of the reflecting system will interact with incoming particles. This is equivalent to partial shielding, which, as was stated above, can in some circumstances have deleterious effects.

6.6.3.4 Preliminary study of magnetic shield for space radiation

The initial study of the reduction in radiation exposure inside a magnetically shielded habitable volume assumed the conceptual design geometry as shown in Figure below. The coils are assembled in a double-toroidal-solenoid configuration to repel particles coming from all directions and to create a sufficiently large inner habitat with vanishing magnetic field. (Note that although the indicated field magnetic strength in the figure is 5T, we actually did the initial calculations at higher fields, ~9T.)

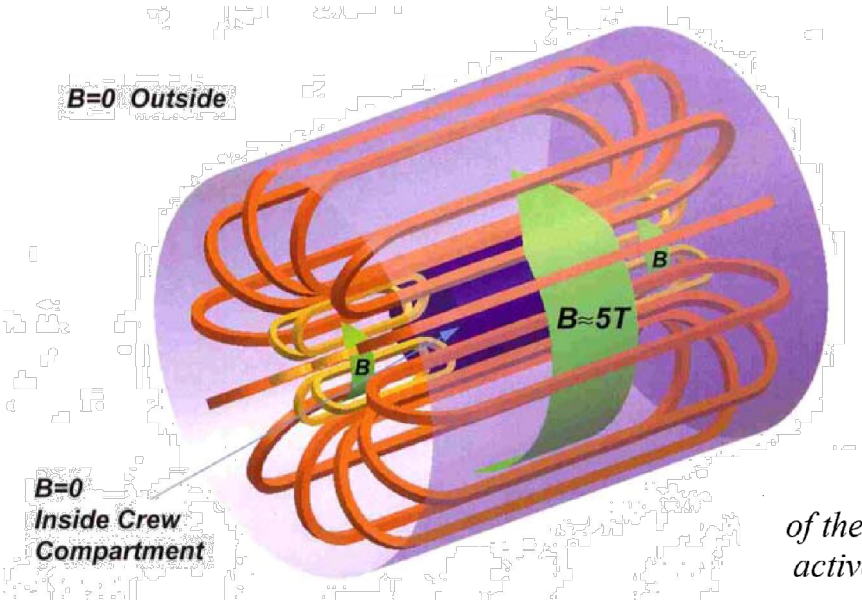

- *Proposed assembly of the magnetic coils forming active shield around habitat*

figure 288

The magnetic shield works by deflecting the incident charged particle radiation in a magnetic field. For a field **B** , a particle of charge **q** moving with velocity **v** will be subject to the Lorentz force

$$\vec{F}_L = \frac{q\vec{v}\times\vec{B}}{c} = \frac{qvB\sin\vartheta}{c} \qquad \text{eq 73}$$

where **θ** is the angle between the particle's velocity and the magnetic field. The Lorentz force always acts perpendicularly to the particle's direction of motion, causing the particle to travel along a curve. In the special case of a relativistic

particle with Lorentz factor γ moving perpendicularly to a magnetic field, the trajectory will be circular with radius $\rho = m\gamma v / \kappa B$ where $\kappa = 0.3 GeV/T - m$.

The idea for magnetic shielding of a spacecraft relies on a toroidal magnetic field surrounding the habitable volume, Figure above Oval coils arranged circularly around the habitat create the field, which is oriented circularly around the axis of the habitat.

Charged particles incident from outside the shield will then always have some component of their velocity perpendicular to the magnetic field and will thus be subject to the Lorentz force.

As a start, researchers chose a magnetic field of 9 T (which is 90,000 G; $1T=10^4$ Gaus), which has been achieved in large magnets for accelerators (the Large Hadron Collider at CERN). Studies indicate that the most damaging dosage in space comes from cosmic rays having energies below about 2-4 GeV/nucleon. Using the equation above, we find a field thickness of 1.5 to 3 meters is required for complete protection. NASA requirements for the dimensions of a habitat for an interplanetary flight are a diameter of 7 m and a height of 7 m (116 m^3) for a cylindrical habitat. For our baseline study, using a field thickness of 1.5 m gives outer dimensions of 10 m diameter and 10 m height.

This approach recall in mind what happen around the Earth by the Magnetic field !

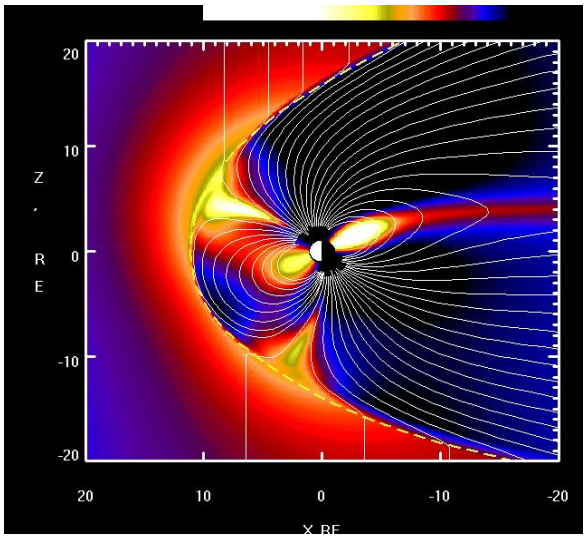

figure 289: Earth magnetic field region shielding form energetic solar wind particle

6.6.3.5 EXAMPLE of Magnetic shield for electronic circuits against charged particles coming from solar wind

In order to have a rough idea of the electric current involved in magnetic shielding, we can consider a scheme like Earth magnetic filed.

We know that an energetic particle remain trapped, by means of a circular motion, around the magnetic filed line around the Earth. This is the basic principle of the radiation belt around the Earth.

Thus the Earth magnetic field protect the Earth form the impact of the most part of the energetic particles.

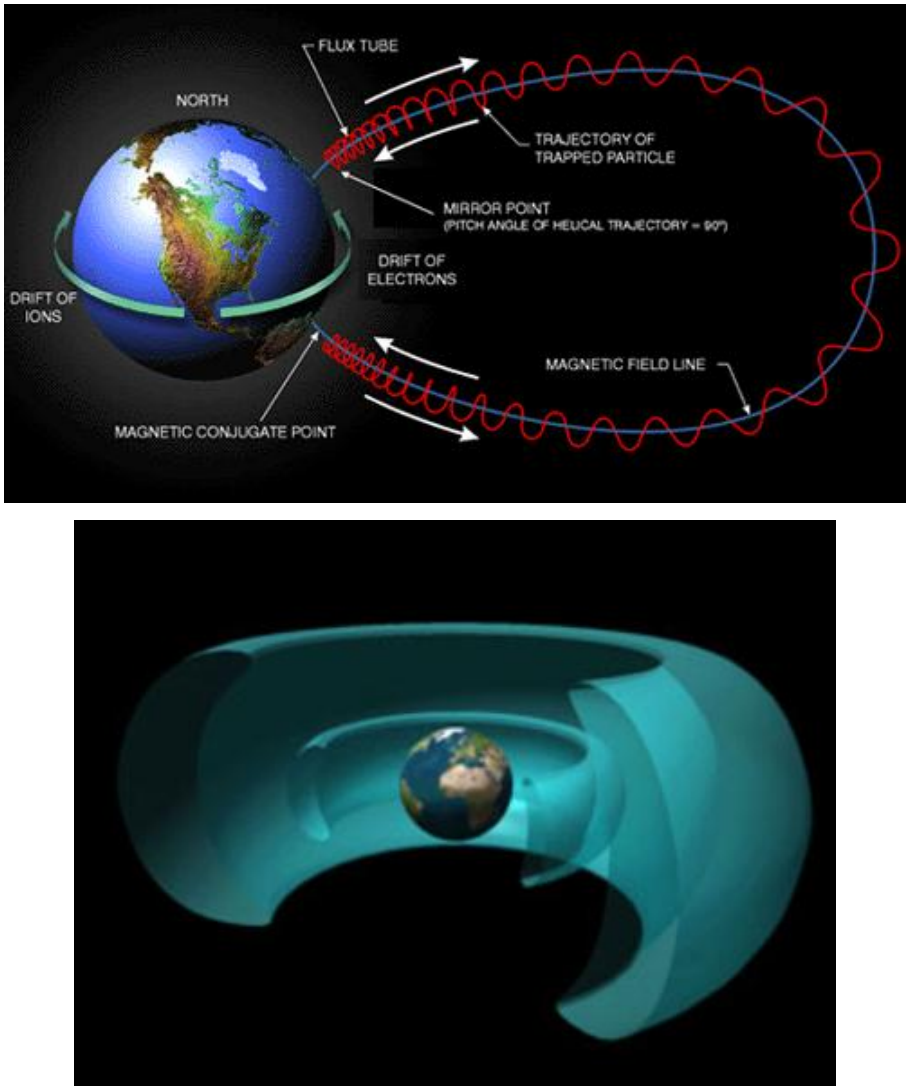

Figure 290: Van Allen Belts

- The Earth's radiation belts are one component of the larger and more complex system called the magnetosphere. The radiation belts of the Earth are made up of energetic, electrically charged particles or electrons, protons and heavier atomic ions. These particles essentially get trapped in the magnetic field of the Earth. The kinetic energy of these particles is greater than or equal to 30 keV.
- The radiation belts, like the plamasphere, are toroidally shaped. These toroids encircle the planet. The inner radiation belt extends from about 400 km above the Earth to 12,000 km. The outer radiation belt extends from about 12,000 km to 60,000 km above the Earth. At times, the two belts overlap each other.

Now let us to consider a little experiment in which we are interested to produce a magnetic field strong enough to trap an energetic particle incident. The purpose is to protect an hypothetic electronic circuit located as in figure below.
Suppose the scheme like on figure below:

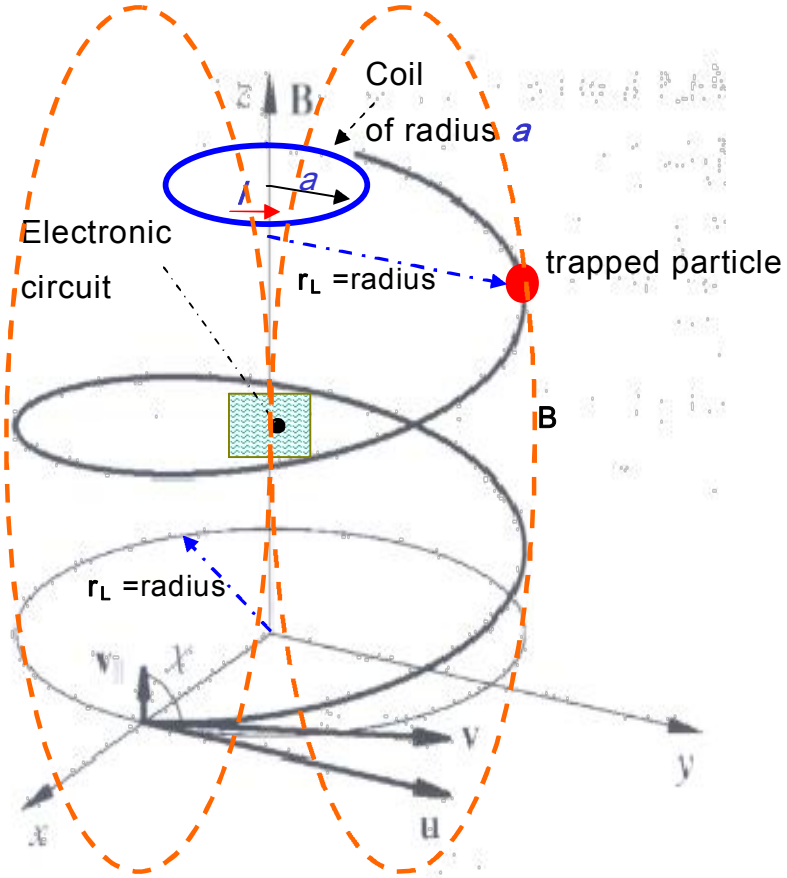

figure 291: trapped energetic particle around the magnetic field line of force induced by coil the current supplier

Consider naw the following data:

- Energy particle incident: proton with **E**=50 MeV;
- Protection Larmor radius dimension $\mathbf{r_L}$= 0.5 m (is the minimum distance we want to have between electronic circuit and energetic particle;

We are interested in finding a the current ***I*** to supply a coil of radius "**a**" to produce the needed magnetic field **B.**

(hp: B is supposed uniform along longitudinal direction ***z***)

$$r_L = \frac{u}{\frac{qB}{mc}} \quad \Rightarrow \quad B = \frac{u}{\frac{qr_L}{mc}} \text{ in the S.I. we don't have } c \Rightarrow B = \frac{u}{\frac{qr_L}{m}} = \frac{um}{qr_L}$$

$$B = \frac{um}{qr_L} = \frac{\left[\frac{m}{s}\right][kg]\left[\frac{m}{s}\right]}{[C][m]\left[\frac{m}{s}\right]} = \frac{[J]}{[C]\left[\frac{m^2}{s}\right]} = \frac{[V]}{\left[\frac{m^2}{s}\right]} = \frac{[V][s]}{[m^2]} = \frac{[Wb]}{[m^2]} = [T]$$

$$E = KT = \frac{1}{2}mv^2 = \frac{1}{2}m\left|v_{\parallel}\hat{i} + u_{\perp}\hat{j}\right|^2 \quad \text{supposing} \quad v_{\parallel} = 0 \Rightarrow E = KT = \frac{1}{2}mu^2$$

$$\Rightarrow \quad u = \sqrt{\frac{2KT}{m}} \ [\text{m/s}] \ \Rightarrow \ B = \frac{u}{\frac{qr_L}{m}} = \frac{\sqrt{\frac{2KT}{m}}}{\frac{qr_L}{m}} = \frac{\sqrt{2KTm}}{qr_L} \ [T]$$

eq 74

Then the current **I** can be found as follows:

$$I = \frac{B(z)2(a^2 + z^2)^{3/2}}{\mu_0 a^2} \quad \text{if :} \quad \left\{ \begin{array}{l} a = 0.3\ m \\ z = 0.1\ m \\ r_L = 0.5\ m \\ m_{protone} = 1.67 \cdot 10^{-27}\ kg \\ \mu_0 = 12.56 \cdot 10^{-7}\ H/m \\ q_{elementare} = 1.6022 \cdot 10^{-19}[C] \\ E_{protone}^{Vanallen} = KT \approx 50 MeV = \\ \quad = 50 \cdot 10^6 \cdot 1.6022 \cdot 10^{-19}[J] \cong 8 \cdot 10^{-12}[J] \end{array} \right\}$$

$$B(z) = \frac{\sqrt{2KTm}}{qr_L} = \frac{\sqrt{2 \cdot 8 \cdot 10^{-12}[J] \cdot 1.67 \cdot 10^{-27}[kg]}}{1.6022 \cdot 10^{-19}[C] \cdot 0.5[m]} \approx 2[T]$$

$$I = \frac{B(z) \cdot 2 \cdot \left(0.3^2[m^2] + 0.1\ [m^2]\right)^{3/2}}{12.56 \cdot 10^{-7}[H/m] \cdot 0.3^2[m^2]} \approx 1.14[MA] \qquad \text{eq 75}$$

This current is very high and consequently very expensive to produce in space so, already at the first side, this system seems to be not so feasible.

One possible application could be the system shown below, where the magnetic filed work as on the Earth :

Solutions for Radiation Shielding from Charged Particles. [Bryan Minor, Ph.D. ScienceOps 2004].

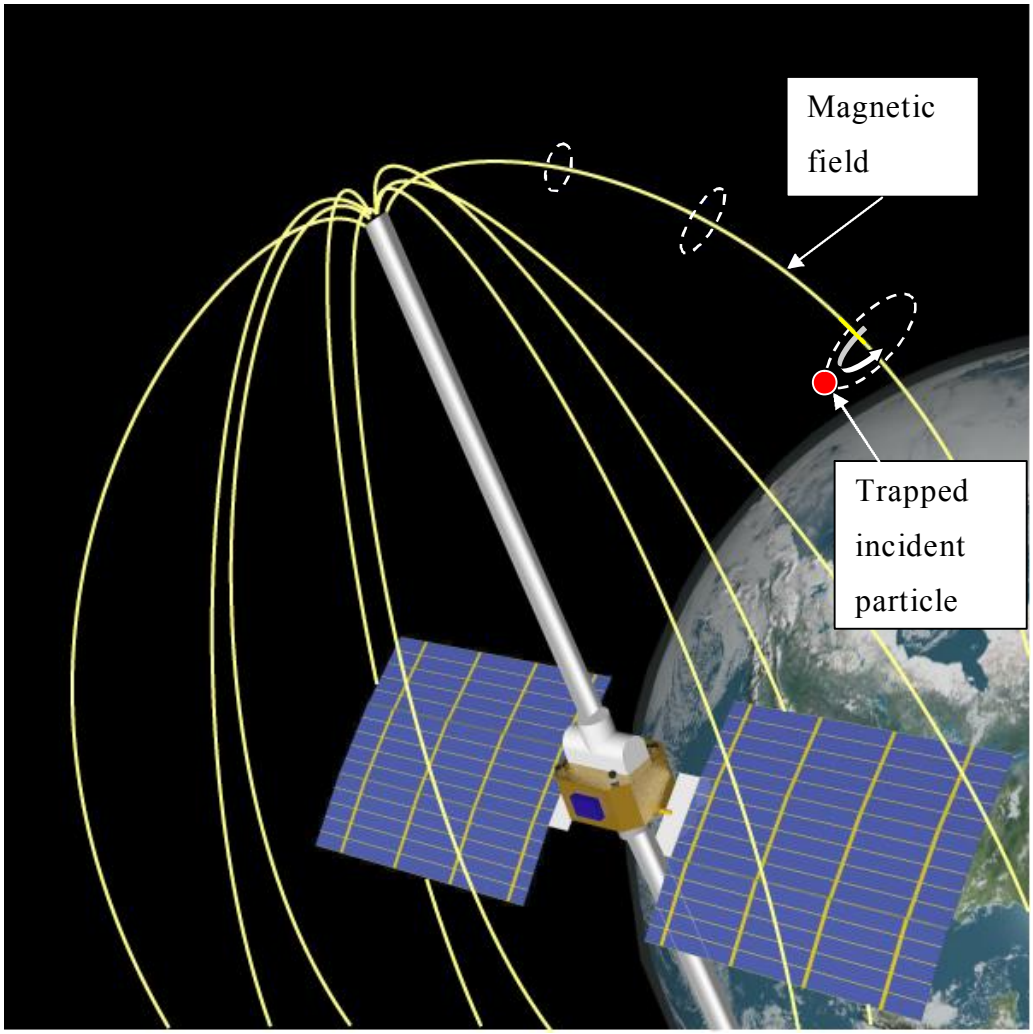

figure 292

6.6.3.6 Analysis of Electrostatic Radiation Shield for Lunar Base

The concept presented in this proposal is based on two recent but unrelated studies at the Kennedy Space Center (KSC) Applied Physics Laboratory and Electrostatics and Surface Physics Laboratory (ESPL): a multipole electrostatic radiation shield and an electrodynamic dust shield. Both advanced concepts are combined in this proposal for a lunar base radiation shield study.

The proposed radiation shield is composed of a cluster of charged conducting spheres, some positively charged and some negatively charged such that the total

charge of the system may be equal to zero. The potential field of the cluster of spheres is configured so that in the far field, relative to the center of the cluster, the potential will be weakly negative over a range of distance toward the shield's center. In the near field, the potential is strongly positive. Incoming negatively charged radiation particles of a given energy spectra are scattered by the farfield negative potential created by the shield. Incoming positively charged radiation particles of a given energy spectra are then scattered by the positive potential near the center of the shield. This shielding strategy results in a volume near the center of the electrostatic sphere network, where radiation of a given energy spectra is eliminated or significantly reduced. The electrodynamic dust shield, previously investigated by the ESPL for removing dust from solar panels on the surface of Mars, will be studied as the basis of a solution to the problem of lunar dust collecting on the radiation shield conducting spheres.

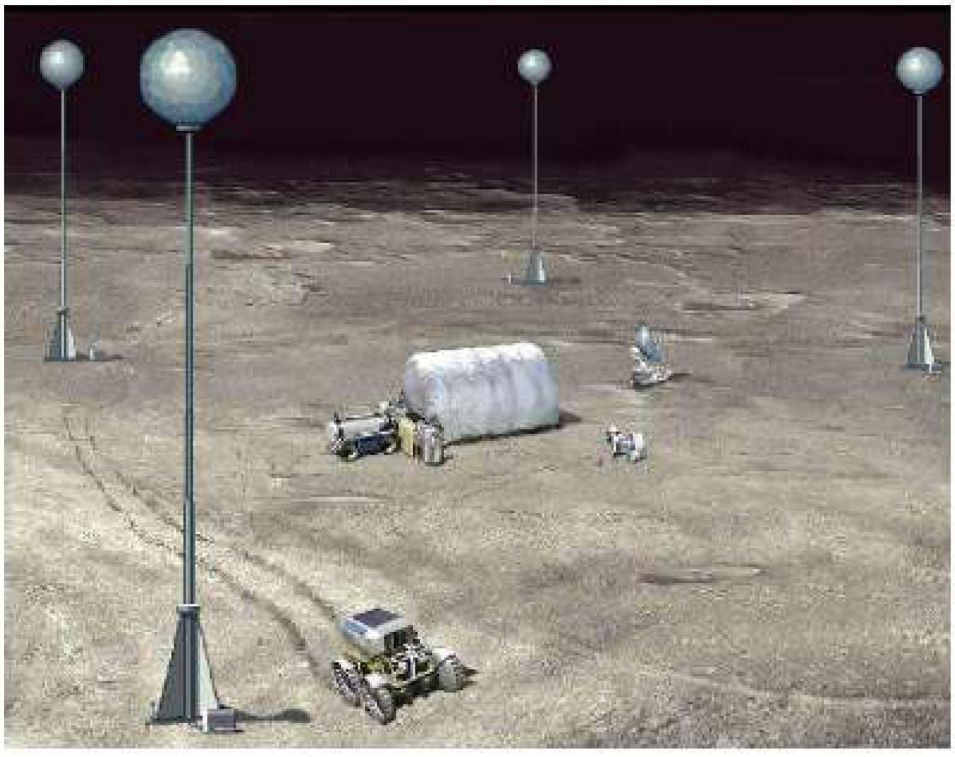

figure 293

6.6.4 Both Electric and Magnetic time dependent Active Protection System (in this thesis developed)

6.6.4.1 Synthesis

One new approach to the radioactive charged particles protection problem could be studied by using an antenna irradiating an *Electromagnetic wave circularly polarized*.

The useful effect on the charged particles should be a trajectory deflection of each single energetic particle from its original trajectory.

In this way, by deflecting the energetic charged particles, it could be possible to protect a certain target from the energetic particles impact.

Figure below displays the idea.

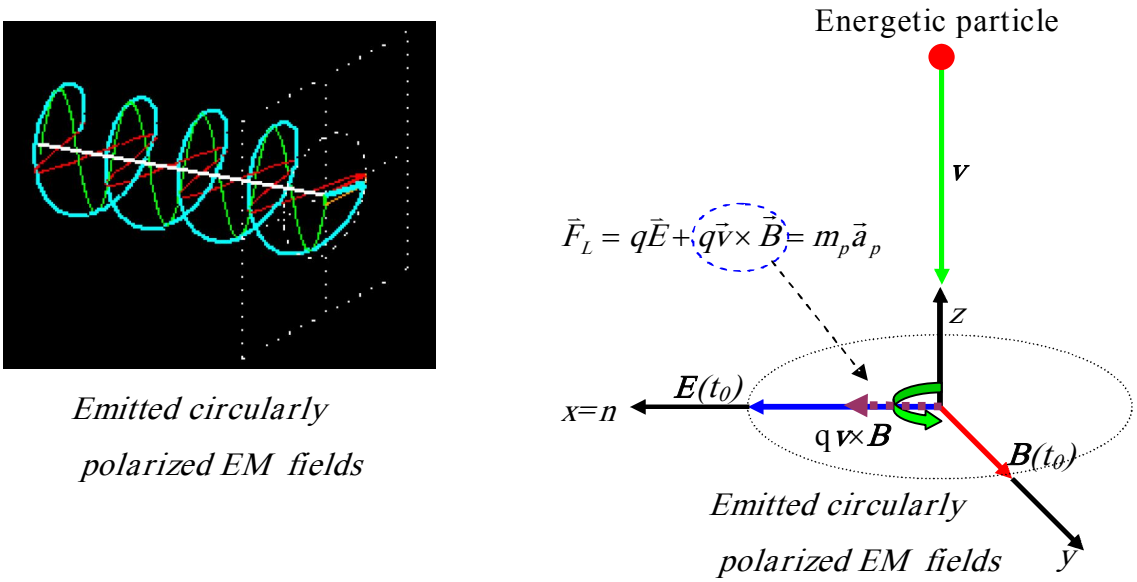

Figure 294: circular polarization and particle trajectory along EM wave propagation direction

6.6.4.2 Analysis

The basic equation is the Lorentz Force equation already seen.

$$\vec{F}_L = q\vec{E} + q\vec{v} \times \vec{B} = m_p \vec{a}_p \qquad \text{eq 76}$$

The fields ***E*** and ***H*** are time dependent as in Maxwell equation ***E=E(t)*** and ***H=H(t)***. In order to compute the power required to deflect the charged particles, we can start with the mathematical definition of *Power Density P(W/m^2)* for an Electromagnetic wave, from now on called EM wave.

$$P = \frac{WtGt}{4\pi r^2} = \frac{1}{2}\frac{|E|^2}{\eta_0} \qquad \left(W/m^2\right) \qquad \text{eq 77}$$

$$\left|\vec{E}\right| = \sqrt{2\eta_0 \frac{WtGt}{4\pi r^2}} = \sqrt{2\eta_0 \frac{WtGt}{4\pi (L-z)^2}} \cong \frac{1}{(L-z)}\sqrt{60\, WtGt}$$

$$\left|\vec{H}\right| = \frac{\left|\vec{E}\right|}{\eta_0} \qquad B = \mu_0 \mathrm{H} \qquad \text{eq 78}$$

Where:

- ***Wt*** is the power (W) at the antenna input;
- ***Gt*** is the antenna gain;
- ***E*** is the module of the electric field vector (V/m);
- ***B*** is the module of the magnetic induction vector (T);
- ***H*** is the module of magnetic field vector (A/m);
- $\eta_0 = (\mu_0/\varepsilon_0)^{0.5}$ is about 377 (Ω) and represent the electromagnetic impendence in the vacuum space;
- ***r=L-z*** is the time dependent distance, from the antenna, along ***z*** reference axes. It represent the point where the EM wave meet the energetic particles, we want to deflect, along its travel from the Sun to the Moon;
- ***L***=Earth-Sun distance ≅150 x10^{+6} (km)=1 AU (Astronomic Unit)
- μ_0 is the magnetic permeability ≅1.25663706143592x10^{-6} (N A^{-2});

The antenna gain **Gt** is a function of the antenna type.

As an example using a Large Cassegrain Antenna we have:

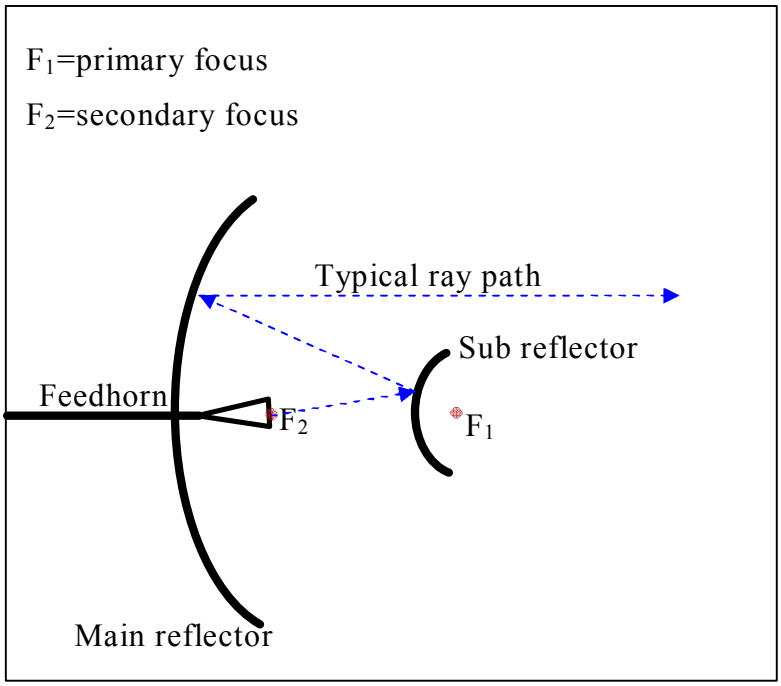

Figure 295: Large Cassegrain Antenna

$$Gt = \frac{4\pi A_{eff}}{\lambda^2} = \frac{4\pi\eta A_{Geom}}{\lambda^2} = \eta\frac{4\pi}{\lambda^2}A_{Geom} = \eta\frac{4\pi f^2}{c^2}A_{Geom} = \eta\frac{4\pi f^2}{c^2}\pi r_{ant}^2$$

where the efficiency is:

$\eta = \eta_I \times \eta_{SS} \times \eta_{MS} \times \eta_B$

η_I = Illumination efficiency

η_{SS} = Spillover Subreflector efficiency

η_{MS} = Spillover Mainreflector efficiency

η_b = Blockage efficiency

f = frequency

r_{ant} = antenna ray

eq 79

As a general rule we can assume an overall efficiency of about **η=70 %.**

Using a frequency of about 100 Mhz in order to have a linear gain with **Gt=10^5**, the diameter of the antenna should be around 1km.

In fact we are interested in using a low frequency in order to increase the particle deflection (see equation later). As a consequence the increasing of antenna gain could be done by changing the antenna dimension.

A so large antenna seems to be not feasible, but we can realize an array of antennas around the lunar base or in another way we can build the main reflector directly on a lunar surface.

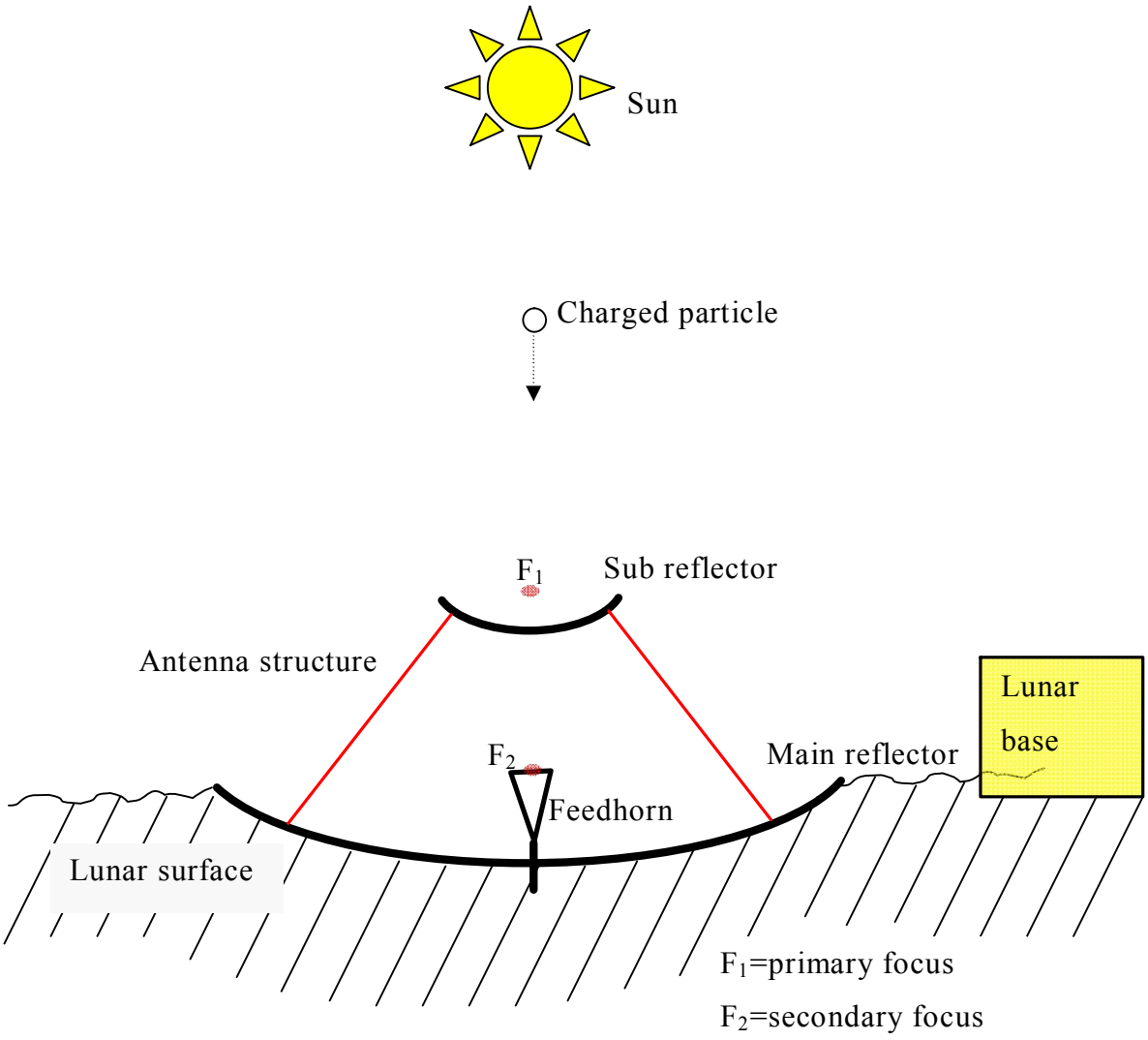

Figure 296: Large Cassegrain antenna built on the lunar surface

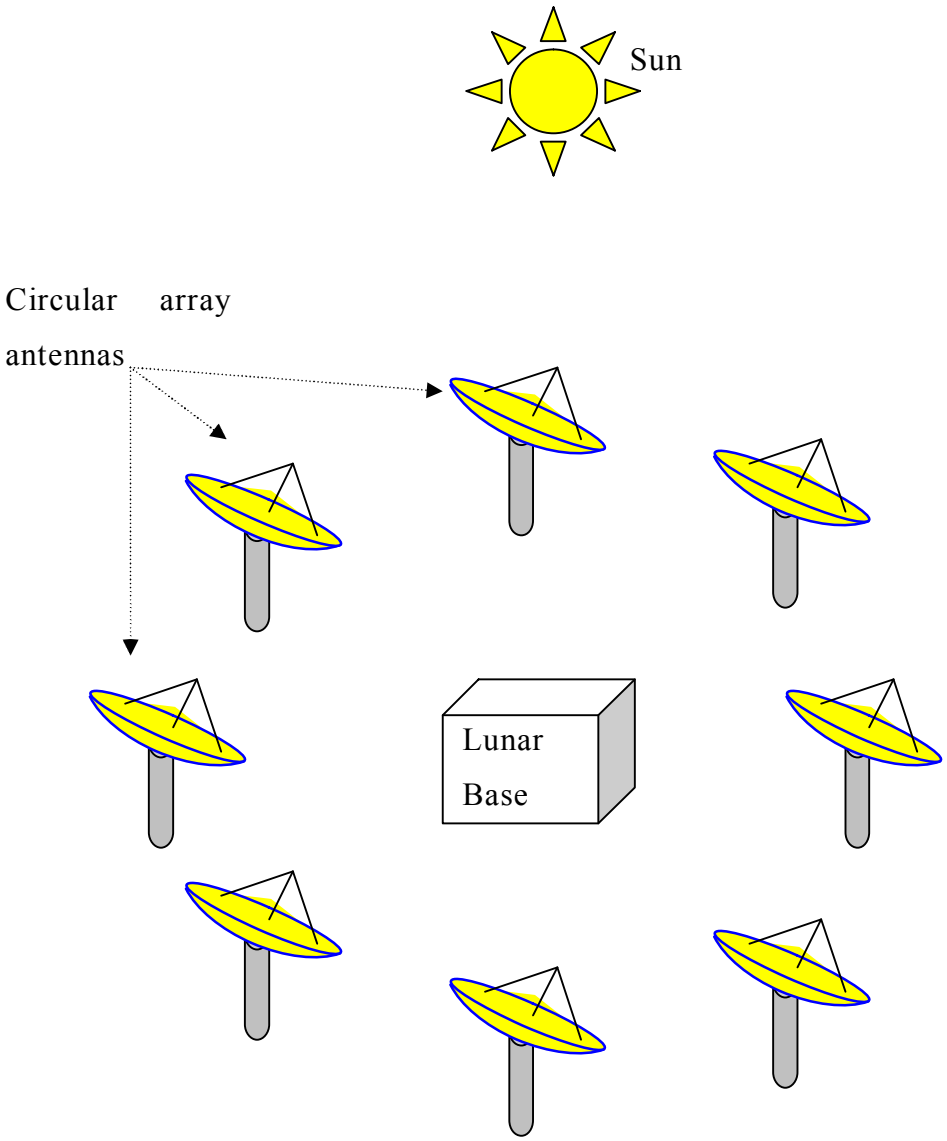

Figure 297: circular array antenna for energetic particle deflection

The Lorentz force applied on a single charged particle q^+ moving at a certain velocity $\underline{v}$ is:

$$\vec{F}_L = q\vec{E} + q\vec{v} \times \vec{B} = m_p \vec{a}_p \qquad \textbf{eq 80}$$

Where

- m_p is the charged particle mass
  - $m_p \cong 1.6726231 \text{x} 10^{-27} \pm 1.0 \text{x} 10^{-33}$ (kg) for a proton;
  - $m_p \cong 938.27231(28)$ MeV/c^2 for a proton;
  - $m_p \cong 1{,}6749 \text{ x } 10^{-27}$ (kg) for a neutron;
  - $m_p \cong 0{,}00091 \text{x} 10^{-27}$ (kg) for an electron;
- q^+ is the charge per unit mass of the proton ≅ 95788309 ± 29 (C/kg);
  - $q^+ \cong 1.60217653(14) \times 10^{-19}$ (C);
- F_L is the module of the Lorentz force applied on the particle (N);
- a_p is the charged particle acceleration (m/s^2);
- v is the particle velocity (m/s);

  supposing as an example a single proton charged particle of $E=1\ KeV$, $E=5\ KeV$, (like can happen in Solar Wind where the particle energy can range between 0.5 to 5 KeV) then the corresponding velocity is:

$$\text{v} = \sqrt{\frac{2\text{E}}{\text{m}_\text{p}}} \cong \sqrt{\frac{2 \cdot 1 \cdot 10^3 \cdot 1{,}602 \cdot 10^{-19}}{1{,}6726 \cdot 10^{-27}}} \cong 440 \quad \textit{(km/s)} \quad \textit{for proton energy} = 1 KeV$$

$$v = \sqrt{\frac{2E}{m_p}} \cong \sqrt{\frac{2 \cdot 5 \cdot 10^3 \cdot 1{,}602 \cdot 10^{-19}}{1{,}6726 \cdot 10^{-27}}} \cong 1000 \quad \textit{(km/s)} \quad \text{for proton energy} = 10\text{KeV}$$

  The solar wind is a stream of charged particles (i.e., a plasma) which are ejected from the upper atmosphere of the Sun. It consists mostly of high-energy electrons and protons (typically about 1 keV) that are able to escape the sun's gravity in part because of the high temperature of the corona and the high kinetic energy particles gain through a process that is not well-understood at this time.

- E is the electric field vector generated by the antenna (V/m);

- ***B*** is the related magnetic field vector perpendicular to the electric field vector (T).
- *1 eV*= 1.602 176 53(14)×10^{-19} (J);

The electronvolt (symbol eV, or, rarely and incorrectly, ev) is a unit of energy. It is the amount of kinetic energy gained by a single unbound electron when it passes through an electrostatic potential difference of one volt, in vacuum. In other words, it is equal to one volt (1 volt = 1 joule per coulomb) times the (unsigned) charge of a single electron.

Electronvolts and temperature: in certain fields, such as plasma physics, it is convenient to use the Electronvolt as a unit of temperature. The conversion to Kelvins (symbol: uppercase K) is defined by using K_B, the Boltzmann constant:

$$\frac{1eV}{K_{Boltzmann}} \cong \frac{1.60217653\times10^{-19}[J]}{1.3806505\times10^{-23}[J/K]} \cong 11604.505[K] \qquad \text{eq 81}$$

Let us going to consider again the EM field, then we can observe that only the electric field produce work accelerating the charge and varying its own electric potential. The magnetic field only change the direction of the velocity but not the module of velocity and so it does not produce any work, in fact the Lorentz force caused by the magnetic induction field is:

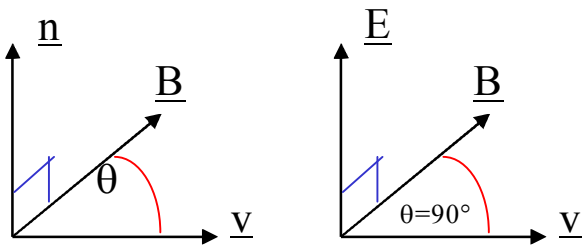

Figure 298

$$\left|\vec{F}_{L\_magnetic}\right| = \left|q\vec{v}\times\vec{B}\right| = qvBsen\vartheta\,\hat{n} \qquad \text{eq 82}$$

*The work **W** computed along the particle displacement **L** with velocity **v** is:*

$$W = \vec{F}_{L\_magnetic}\cdot\vec{L} = \left(\frac{q}{c}vBsen\vartheta\right)\hat{n}\cdot L\hat{v} = \left[\left(\frac{q}{c}vBsen\vartheta\right)L\right]\hat{n}\cdot\hat{v} = 0 \qquad \text{eq 83}$$

In our case the particle velocity is initially in the opposite direction with respect to the EM field emitted by the antenna, and then the relative magnetic Lorentz force component is directed in the same direction of the electric field.
This effect is shown on figure below:

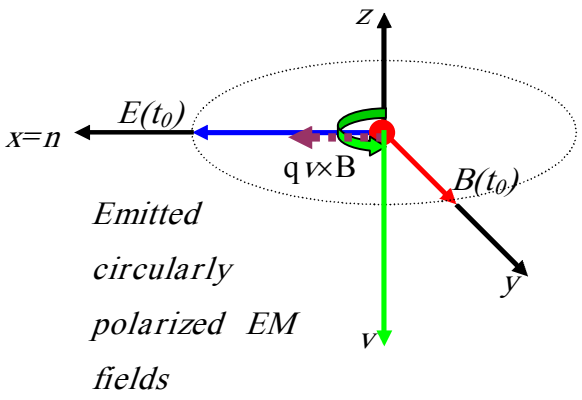

Figure 299

Suppose now a ***100 MeV particle energy*** then, the impact of the magnetic force with respect to the electric force is:

$$\frac{\vec{F}_{L\_magnetic}}{\vec{F}_{L\_electric}} = \frac{q\vec{v}\times\vec{B}}{qE} = \frac{qvBsen\frac{\pi}{2}\hat{n}}{qE} = \frac{qvB}{qE} = \frac{vB}{E} = \frac{v\mu_0 H}{E} = \frac{v\mu_0}{E}\frac{E}{\eta} = \frac{v\mu_0}{\eta} = \frac{v}{c} \approx \qquad \text{eq 84}$$

$$\approx \frac{69\cdot10^{6}\cdot1.25\cdot10^{-6}}{377}\hat{n} \approx 0.28.\hat{n}$$

The great the particle velocity (i.e. the particle kinetic energy $E=0.5\gamma mv^2$, the more result the magnetic contribution to the Lorentz force.

In this example the magnetic force $F_{L\_magnetic}$ is not negligible with respect to the electric force.
As a consequence we have to take it into account in our computations.

6.6.4.3 Lorentz Transformations

As we have seen, a particle of 100 MeV as a velocity close to **c**.
A particle of 1GeV has a velocity greater then c ! we know this is not possible !
Now from Lorentz transformations we know that when the velocity is close to c then the coordinate, the length, the time, the mass, the quantity of motion, and the energy of the particle change and we can no longer use the classical Galilean mechanical equation of motion.

Supposing two reference system traveling in the same direction with a relative velocity v;
The transformations are start with the definition of the *Lorentz Factor* γ:

$$\gamma = \frac{1}{\sqrt{1-\frac{v^2}{c^2}}} \qquad \text{eq 85}$$

If z is the particle velocity direction in the inertial system fixed with respect to antenna, while z' is the inertial system moving with a relative velocity v with respect to the other system, then :

$$\left\{\begin{array}{l} z' = \gamma(z - vt) \\ y' = y \\ x' = x \\ t' = \gamma\left(t - \frac{vz}{c^2}\right) \end{array}\right\} \Leftrightarrow \left\{\begin{array}{l} z = \gamma(z' + vt') \\ y = y' \\ x = x' \\ t = \gamma\left(t' + \frac{vz'}{c^2}\right) \end{array}\right\} \qquad \text{eq 86}$$

Length contraction

$$l = \frac{l_0}{\gamma} = l_0 \sqrt{1 - \frac{v^2}{c^2}} \qquad \text{eq 87}$$

Where l_0 is the length measured on the reference fixed system.
If $\boldsymbol{u}$ is the absolute velocity of the mass $\boldsymbol{m_0}$ (i.e. the mass assumed at the particle rest) then also the quantity of motion change;

$$\vec{p} = (m\gamma)\vec{u} = \frac{m_0}{\sqrt{1-\frac{u^2}{c^2}}}\vec{u} \qquad \text{eq 88}$$

If $\boldsymbol{u}$ is the absolute velocity of the mass $\boldsymbol{m_0}$ (i.e. the particle mass assumed at rest) then the relativistic mass $\boldsymbol{m}$ is:

$$m = \frac{m_0}{\sqrt{1-\frac{u^2}{c^2}}} = \gamma\, m_0 \qquad \text{eq 89}$$

The relativistic **force** $\boldsymbol{F}$ is

$$\vec{F} = \frac{d\vec{p}}{dt} = \frac{d}{dt}\left(\frac{m}{\sqrt{1-\frac{u^2}{c^2}}}\vec{u}\right) \qquad \text{eq 90}$$

The relativistic **kinetic energy** $\boldsymbol{E_k}$ is:

$$E_K = \gamma mc^2 - mc^2 = E_{\text{Tot}} - E_{\text{Rest}} \qquad \text{eq 91}$$

where

$$E_{\text{Tot}} = E_K + E_{\text{Rest}} = \gamma mc^2$$
$$E_{\text{Re}\,st} = mc^2 \qquad \text{eq 92}$$

- $\boldsymbol{E_{Tot}}$ is the total relativistic energy that remain constant within a system
- $\boldsymbol{E_{Rest}}$ is the intrinsic mass energy when the mass is at rest
- $\boldsymbol{E_K}$ is the relativistic Kinetic energy

The measure unit used for atomic particle is the MeV/c^2 which represent the particle rest energy divided for c^2.

As an example for the ***proton*** we have:

$E_{Rest}=m_p \cdot c^2/1eV=938\ (MeV)$ so $m_p=938\ MeV/c^2$

Particle	Mass at rest (kg)	Equivalent Mass at rest (MeV/c^2)
Photon		0
Electron	9.1E-31	0.511
Proton	1.67262E-27	938.28
Neutron	1.6749E-27	939.537
Muon		105.7

Table 40: Mass at rest for atomic particles

6.6.5 Motion of the charged particle affected by the EM wave circular polarized

We can start showing a possible scenario where the charged particle is traveling throughout the space, starting from the Sun corona and arriving to the Moon surface where is located the Moon Base we want to protect.

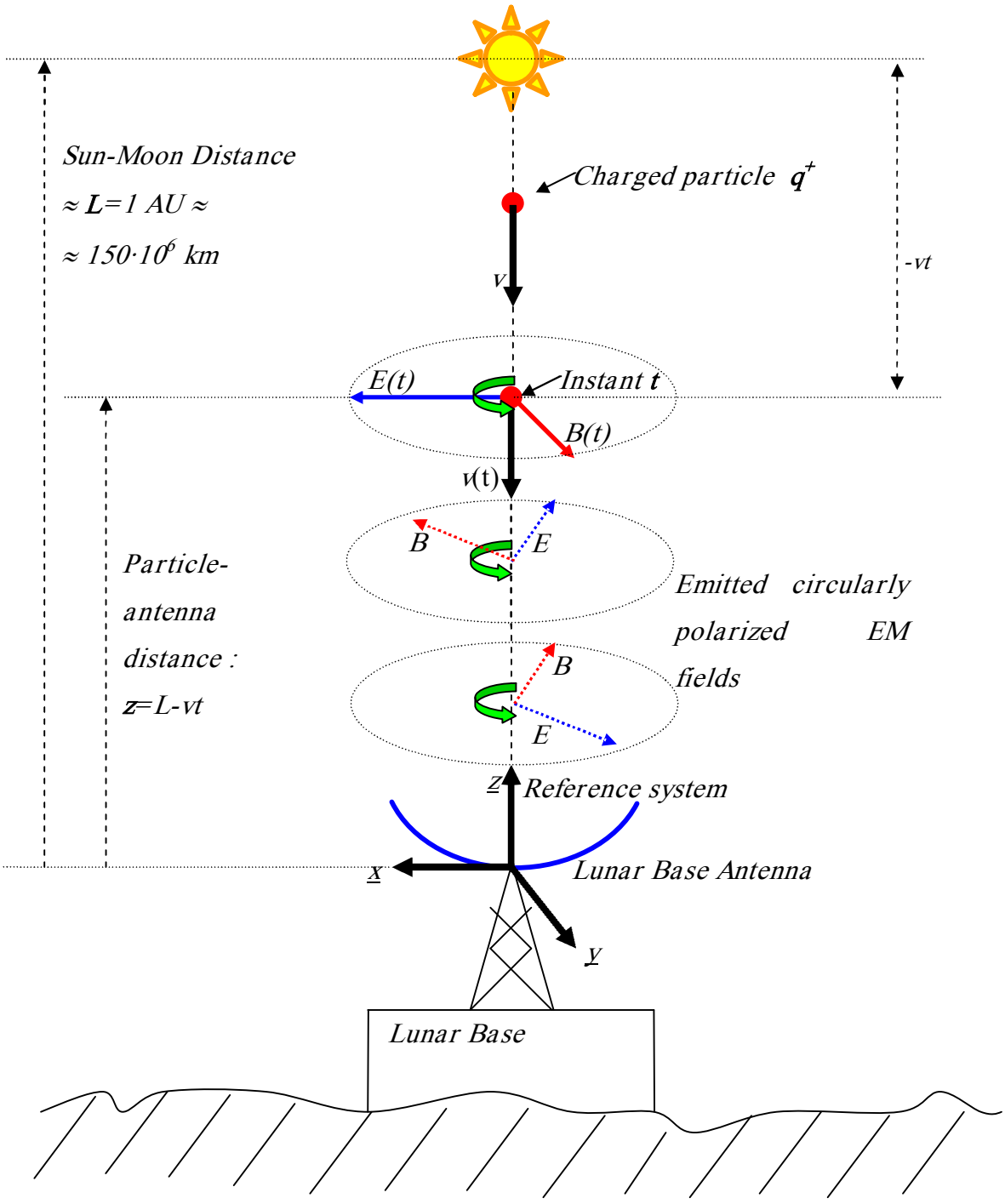

Figure 300

6.6.6 Polarization of the EM wave

Let us consider an EM wave propagating along **z** direction. Its phasor consists of two components:

$$\vec{E}(z) = E_x(z)\hat{x} + E_y(z)\hat{y} \qquad \text{eq 93}$$

Where:

$$E_x(z) = E_{x0}e^{-j\beta z}$$
$$E_y(z) = E_{y0}e^{-j\beta z} \qquad \text{eq 94}$$

Where E_{x0} and E_{y0}, are the complex amplitude of the E_x and E_y.
The polarization of the EM wave is a function of the E_{y0} ***phase*** with respect to the E_{x0} ***phase.***
Let us calling this phase difference as: $\Delta phase = e^{j\varphi}$ so we can write:

$$E_{x0} = a_x$$
$$E_{y0} = a_y e^{j\varphi} \qquad \text{eq 95}$$

As a consequence the previous equation can be rewritten as:

$$\vec{E}(z) = E_x(z) + E_y(z) = a_x e^{-j\beta z} + a_y e^{j\varphi} e^{-j\beta z} \qquad \text{eq 96}$$

To find the equation in the time domain we have to compute the real part i.e.

$$\vec{E}(z,t) = \mathrm{Re}\left[\vec{E}(z)e^{j\omega t}\right] = \mathrm{Re}\left[\left(a_x e^{-j\beta z} + a_y e^{j\varphi} e^{-j\beta z}\right)e^{j\omega t}\right] = \mathrm{Re}\left[\left(a_x e^{j\omega t - j\beta z} + a_y e^{j\omega t - j\beta z + j\varphi}\right)\right] =$$
$$= \mathrm{Re}\left[a_x\cos(\omega t - \beta z) + ja_x\sin(\omega t - \beta z) + a_y\cos(\omega t - \beta z + \varphi) + ja_y\sin(\omega t - \beta z + \varphi)\right] =$$
$$= a_x\cos(\omega t - \beta z)\hat{x} + a_y\cos(\omega t - \beta z + \varphi)\hat{y} =$$
$$= E_x(z,t)\hat{x} + E_y(z,t)\hat{y}$$

eq 97

then:

- if **φ=0°** the polarization is linear;
- if **φ=180°** the polarization is linear in opposition of phase;
- if **φ=90°** and **$a_x=a_y=a$** the polarization is circular;
- if **0°<φ<90°** the polarization is elliptical;

6.6.7 Circular polarized EM wave

Consider now the equation for a circularly polarized Electromagnetic Field:

$$\begin{cases} \vec{E}(z) = E\cos(\omega t - \beta z)\hat{x} + E\cos\left(\omega t - \beta z + \frac{\pi}{2}\right)\hat{y} \\ \vec{H}(z) = -H\sin(\omega t - \beta z)\hat{x} + H\sin\left(\omega t - \beta z + \frac{\pi}{2}\right)\hat{y} \end{cases}$$

eq 98

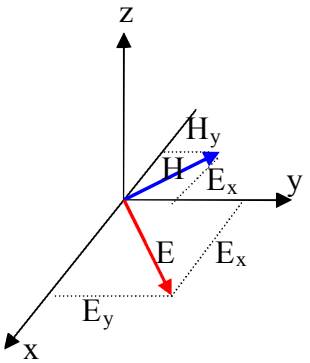

$$\begin{cases} \vec{E} = E\cos(\omega t - \beta z)\hat{x} + E\sin(\omega t - \beta z)\hat{y} \\ \vec{H}(z) = -H\sin(\omega t - \beta z)\hat{x} + H\cos(\omega t - \beta z)\hat{y} \end{cases}$$

eq 99

- Electric and Magnetic fields rotate at frequency f=ω/2π.
- Circular polarization because *E* and *B* vectors describe circles over time.

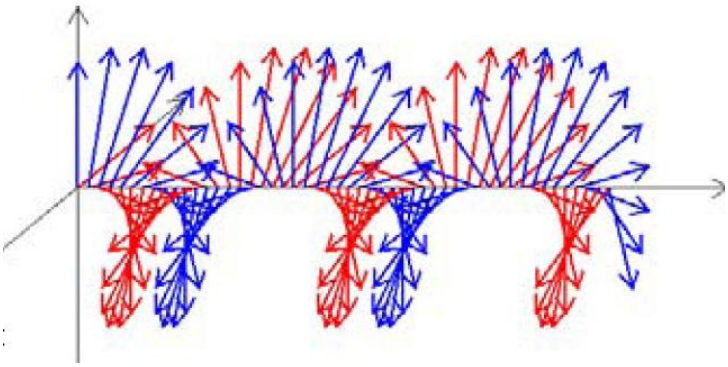

Figure 301: EM wave circularly polarized

Recalling the relation between the power and the EM wave equations then:

$$\begin{cases} \vec{E} = \dfrac{\sqrt{60\,WtGt}}{L - v_z t}\cos\left[\omega t - \beta\left(L - v_z t\right)\right]\hat{x} + \dfrac{\sqrt{60\,WtGt}}{L - v_z t}\sin\left[\omega t - \beta\left(L - v_z t\right)\right]\hat{y} \\ \vec{H} = -\dfrac{1}{377}\dfrac{\sqrt{60\,WtGt}}{L - v_z t}\sin\left[\omega t - \beta\left(L - v_z t\right)\right]\hat{x} + \dfrac{1}{377}\dfrac{\sqrt{60\,WtGt}}{L - v_z t}\cos\left[\omega t - \beta\left(L - v_z t\right)\right]\hat{y} \end{cases}$$

eq 100

Where:

$$|E| = \frac{\sqrt{60\,WtGt}}{L - z(t)} = \frac{\sqrt{60\,WtGt}}{L - v_z t} \qquad |\mathrm{H}| = \frac{|E|}{377}$$

$$\eta_0 = 377 \ \ [\Omega]$$

$$\omega = 2\pi f$$

$$\beta = \omega\sqrt{\mu_0 \varepsilon_0} = \frac{\omega}{c} \qquad \text{and} \qquad c = \frac{1}{\sqrt{\mu_0 \varepsilon_0}}$$

$L - z(t) = L - v_z t$ is the distance between the particle and the antenna; **eq 101**

$z(t) = v_z t$ is the distance crossed by the particle from the Sun to the antenna;

The time elapsed is :

$$0 < t < \frac{L}{v_z} \ \Rightarrow \ \text{when } \mathrm{t} = \frac{L}{v_z} \ \Rightarrow \ \text{then } \mathrm{z} = 0$$

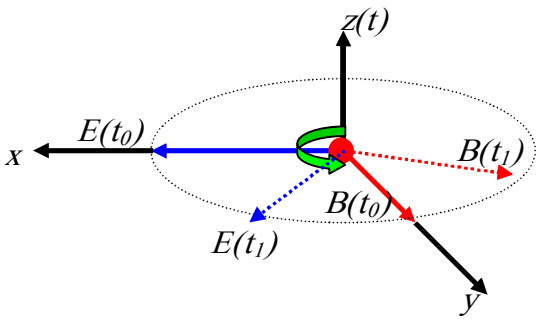

Emitted circularly polarized EM fields

Figure 302

From the Lorentz force equation we have:

$$\vec{F}_L = q\vec{E} + q\vec{v}\times\vec{B} = q\vec{E} + q\vec{v}\times\mu_0\vec{H} = m_p\vec{a}_p \qquad \text{eq 102}$$

$$\vec{v} = -v\hat{z} \qquad \text{eq 103}$$

$$\vec{F}_L = q\vec{E} - qv_z\hat{z}\times\vec{B} = q\vec{E} + q\vec{v}\times\mu_0\vec{H} = m_p\vec{a}_p \qquad \text{eq 104}$$

Then substituting the previous equations we have:

$$\vec{F}_L = q\vec{E} - qv_z\hat{z}\times\mu_0\vec{H} = q\left\{\frac{\sqrt{60WtGt}}{L-v_zt}\cos\left[\omega t-\beta(L-v_zt)\right]\hat{x}+\frac{\sqrt{60WtGt}}{L-v_zt}\sin\left[\omega t-\beta(L-v_zt)\right]\hat{y}\right\}+$$
$$-qv_z\hat{z}\times\mu_0\left\{-\frac{1}{377}\frac{\sqrt{60WtGt}}{L-v_zt}\sin\left[\omega t-\beta(L-v_zt)\right]\hat{x}+\frac{1}{377}\frac{\sqrt{60WtGt}}{L-v_zt}\cos\left[\omega t-\beta(L-v_zt)\right]\hat{y}\right\} = m_p\vec{a}_p$$

eq 105

Since the term βL is only a constant phase shift then from now on we will neglect this term:

$$\vec{F}_L = q\left\{\frac{\sqrt{60WtGt}}{L-v_zt}\cos\left[\omega t+\beta v_zt\right]\hat{x}+\frac{\sqrt{60WtGt}}{L-v_zt}\sin\left[\omega t+\beta v_zt\right]\hat{y}\right\}+$$
$$-qv_z\hat{z}\times\mu_0\left\{-\frac{1}{377}\frac{\sqrt{60WtGt}}{L-v_zt}\sin\left[\omega t+\beta v_zt\right]\hat{x}+\frac{1}{377}\frac{\sqrt{60WtGt}}{L-v_zt}\cos\left[\omega t+\beta v_zt\right]\hat{y}\right\} = m_p\vec{a}_p$$

eq 106

$$\vec{F}_L = q\frac{\sqrt{60WtGt}}{L-v_zt}\left\{\cos\left[\omega t+\beta v_zt\right]\hat{x}+\sin\left[\omega t+\beta v_zt\right]\hat{y}\right\}+$$
$$-qv_z\mu_0\frac{1}{377}\frac{\sqrt{60WtGt}}{L-v_zt}\left\{-\sin\left[\omega t+\beta v_zt\right](\hat{z}\times\hat{x})+\cos\left[\omega t+\beta v_zt\right](\hat{z}\times\hat{y})\right\} = m_p\vec{a}_p$$

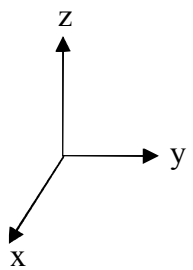

eq 107

$$\vec{F}_L = q\frac{\sqrt{60\,WtGt}}{L - v_z t}\{\cos[\omega t + \beta v_z t]\hat{x} + \sin[\omega t + \beta v_z t]\hat{y}\} +$$
$$- q v_z \mu_0 \frac{1}{377}\frac{\sqrt{60\,WtGt}}{L - v_z t}\{-\sin[\omega t + \beta v_z t]\hat{y} - \cos[\omega t + \beta v_z t]\hat{x}\} = m_p \vec{a}_p$$

eq 108

$$\vec{F}_L = q\frac{\sqrt{60\,WtGt}}{L - v_z t}\left\{\begin{array}{l}\cos[\omega t + \beta v_z t]\hat{x} + \sin[\omega t + \beta v_z t]\hat{y} + v_z \mu_0 \frac{1}{377}\sin[\omega t + \beta v_z t]\hat{y} + \\ + v_z \mu_0 \frac{1}{377}\cos[\omega t + \beta v_z t]\hat{x}\end{array}\right\} = m_p \vec{a}_p$$

eq 109

$$\vec{F}_L = q\frac{\sqrt{60\,WtGt}}{L - v_z t}\left\{\cos[\omega t + \beta v_z t]\cdot\left(1 + v_z \mu_0 \frac{1}{377}\right)\hat{x} + \sin[\omega t + \beta v_z t]\cdot\left(1 + v_z \mu_0 \frac{1}{377}\right)\hat{y}\right\} = m_p \vec{a}_p$$

eq 110

$$\vec{F}_L = q\frac{\sqrt{60\,WtGt}}{L - v_z t}\left(1 + v_z \mu_0 \frac{1}{377}\right)\{\cos[\omega t + \beta v_z t]\hat{x} + \sin[\omega t + \beta v_z t]\hat{y}\} = m_p \vec{a}_p$$

eq 111

but

$$\mu_0 \frac{1}{377} = \mu_0 \frac{1}{\eta_0}\mu_0 \frac{1}{\sqrt{\frac{\mu_0}{\varepsilon_0}}} = \sqrt{\mu_0 \varepsilon_0} = \frac{1}{c}$$

Consequently

$$\vec{F}_L = q\frac{\sqrt{60\,WtGt}}{L - v_z t}\left(1 + \frac{v_z}{c}\right)\{\cos[\omega t + \beta v_z t]\hat{x} + \sin[\omega t + \beta v_z t]\hat{y}\} = m_p \vec{a}_p \qquad \textbf{eq 112}$$

This term is due to the magnetic field in the Lorentz force equation.
The lower is the particle velocity v_z, the more negligible is the magnetic force effect on the particle.

But

$$\beta = \frac{\omega}{c}$$

Consequently:

$$\vec{F}_L = q\frac{\sqrt{60WtGt}}{L - v_z t}\left(1+\frac{v_z}{c}\right)\left\{\cos\left[\omega t+\frac{\omega}{c}v_z t\right]\hat{x}+\sin\left[\omega t+\frac{\omega}{c}v_z t\right]\hat{y}\right\} = m_p\vec{a}_p \qquad \textbf{eq 113}$$

$$\vec{F}_L = q\frac{\sqrt{60WtGt}}{L - v_z t}\left(1+\frac{v_z}{c}\right)\left\{\cos\left[\omega\left(1+\frac{v_z}{c}\right)t\right]\hat{x}+\sin\left[\omega\left(1+\frac{v_z}{c}\right)t\right]\hat{y}\right\} = m_p\vec{a}_p = m_p\left[\ddot{x}(t)\hat{x}+\ddot{y}(t)\hat{y}\right]$$

eq 114

Calling:

$$A = \frac{q\sqrt{60WtGt}}{m_p}\left(1+\frac{v_z}{c}\right)$$
$$\omega' = \omega\left(1+\frac{v_z}{c}\right)$$
$$\vec{a}_p = \left[\ddot{x}(t)\hat{x}+\ddot{y}(t)\hat{y}\right]$$

Then:

$$\vec{F}_L = \frac{A}{L - v_z t}m_p\left\{\cos[\omega' t]\hat{x}+\sin[\omega' t]\hat{y}\right\} = m_p\vec{a}_p = m_p\left[\ddot{x}(t)\hat{x}+\ddot{y}(t)\hat{y}\right] \qquad \textbf{eq 115}$$

Then finally the particle motion is expressed by the equation:

$$\vec{a}_p = \left[\ddot{x}(t)\hat{x}+\ddot{y}(t)\hat{y}\right] = \frac{\vec{F}_L}{m_p} = \frac{A}{(L - v_z t)}\left\{\cos[\omega' t]\hat{x}+\sin[\omega' t]\hat{y}\right\} \qquad \textbf{eq 116}$$

then separating the motion along the ***x*** and ***y*** axis we finally have:

$$\ddot{x}(t) = \frac{A}{L - v_z t}\cos[\omega' t]$$
$$\ddot{y}(t) = \frac{A}{L - v_z t}\sin[\omega' t]$$

eq 117

In order to find the trajectory of the particle affected by the circularly polarized EM wave, we need to compute a double integration of the equations above.

6.6.8 First integration method

If we try to integrate the function twice time we obtain sin-integral and cos-integral function which is difficult to integrate.

With the first method, in order to simplify the integration we can divide our distance ***L*** in equal part $z_n \div z_{n+1}$ within of which we can suppose the quantity $v_z \cdot t$ like a constant if compared to the quantity ***sin(ω't)*** or ***cos(ω't).***

In other words, within the elementary interval $z_n \div z_{n+1}$, the term $v_z \cdot t$ can be considered slowly variable when compared to the functions ***sin(ω't)*** and ***cos(ω't)*** which instead are fast variable due to the frequency term ***ω't***.

Under this hypothesis, in the integral, we can take out the constant term and we can rewrite the particle motion equation as shown:

$$\begin{cases} \dot{x}(t) = \int_{t_n}^{t} \ddot{x}(t)dt = \int_{t_n}^{t} \frac{A}{L - v_z t}\cos[\omega' t]dt \cong \frac{A}{L - v_z t}\int_{t_n}^{t}\cos[\omega' t]dt = \frac{A}{z_n}\int_{t_n}^{t}\cos[\omega' t]dt \\ \dot{y}(t) = \int \ddot{y}(t)dt = \int_{t_n}^{t} \frac{A}{L - v_z t}\sin[\omega' t]dt \cong \frac{A}{L - v_z t}\int_{t_n}^{t}\sin[\omega' t]dt = \frac{A}{z_n}\int_{t_n}^{t}\sin[\omega' t]dt \end{cases}$$

where eq 118

$$L - v_z t = z_n$$

$$\begin{cases} \dot{x}(t) = \frac{A}{z_n}\int_{t_n}^{t}\cos[\omega' t]dt = \frac{A}{\omega' z_n}[\sin(\omega' t)]_{t_n}^{t} = \frac{A}{\omega' z_n}[\sin(\omega' t) - \sin(\omega' t_n)] + \dot{x}(t_n) \\ \dot{y}(t) = \frac{A}{z_n}\int_{t_n}^{t}\sin[\omega' t]dt = -\frac{A}{\omega' z_n}[\cos(\omega' t)]_{t_n}^{t} = -\frac{A}{\omega' z_n}[\cos(\omega' t) - \cos(\omega' t_n)] + \dot{y}(t_n) \end{cases}$$

eq 119

Where

$$t_n \le t \le t_{n+1}$$

for $n = 0$ *then* $t_0 = 0$ $\dot{x}(t_0) = \dot{y}(t_0) = 0$

The particle motion can be find out by integrating again the equations:

$$\begin{cases} x(t)=\int_{t_n}^{t}\left\{\frac{A}{\omega' z_n}\left[\sin(\omega' t)-\sin(\omega' t_n)\right]+\dot{x}(t_n)\right\}dt=\left\{\frac{A}{\omega' z_n}\left[-\frac{1}{\omega'}\cos(\omega' t)-t\sin(\omega' t_n)\right]+t\,\dot{x}(t_n)\right\}_{t_n}^{t}= \\ \quad=\left\{\frac{A}{\omega' z_n}\left[-\frac{1}{\omega'}\cos(\omega' t)+\frac{1}{\omega'}\cos(\omega' t_n)-(t-t_n)\sin(\omega' t_n)\right]+(t-t_n)\dot{x}(t_n)\right\}+x(t_n) \\ y(t)=\int_{t_n}^{t}\left\{-\frac{A}{\omega' z_n}\left[\cos(\omega' t)-\cos(\omega' t_n)\right]+\dot{y}(t_n)\right\}dt=\left\{-\frac{A}{\omega' z_n}\left[+\frac{1}{\omega'}\sin(\omega' t)-t\cos(\omega' t_n)\right]+t\,\dot{y}(t_n)\right\}_{t_n}^{t}= \\ \quad=\left\{-\frac{A}{\omega' z_n}\left[+\frac{1}{\omega'}\sin(\omega' t)-\frac{1}{\omega'}\sin(\omega' t_n)-(t-t_n)\cos(\omega' t_n)\right]+(t-t_n)\dot{y}(t_n)\right\}+y(t_n) \end{cases}$$

eq 120

The iterative formula is valid when t_n is close to t_{n+1} so we can suppose $t \to t_{n+1}$:

$$\begin{cases} x(t_{n+1})=\left\{\frac{A}{\omega' z_n}\left[-\frac{1}{\omega'}\cos(\omega' t_{n+1})+\frac{1}{\omega'}\cos(\omega' t_n)-(t_{n+1}-t_n)\sin(\omega' t_n)\right]+(t_{n+1}-t_n)\dot{x}(t_n)\right\}+x(t_n) \\ y(t_{n+1})=\left\{-\frac{A}{\omega' z_n}\left[+\frac{1}{\omega'}\sin(\omega' t_{n+1})-\frac{1}{\omega'}\sin(\omega' t_n)-(t_{n+1}-t_n)\cos(\omega' t_n)\right]+(t_{n+1}-t_n)\dot{y}(t_n)\right\}+y(t_n) \end{cases}$$

eq 121

$$\begin{cases} x(t_{n+1})=-\frac{A}{(\omega')^2 z_n}\left[\cos(\omega' t_{n+1})-\cos(\omega' t_n)\right]-(t_{n+1}-t_n)\left[\frac{A}{\omega' z_n}\sin(\omega' t_n)-\dot{x}(t_n)\right]+x(t_n) \\ y(t_{n+1})=-\frac{A}{(\omega')^2 z_n}\left[\sin(\omega' t_{n+1})-\sin(\omega' t_n)\right]+(t_{n+1}-t_n)\left[\frac{A}{\omega' z_n}\cos(\omega' t_n)+\dot{y}(t_n)\right]+y(t_n) \end{cases}$$

eq 122

for $n=0$ *then* $t_0=0$ $x(t_0)=y(t_0)=0$

Now consider the following time instants where ***sin(ω't)*** and ***cos(ω't)*** are periodical:

$\omega' t_0 = 0$
$\omega' t_1 = 2\pi$
$\omega' t_2 = 2 \times 2\pi$
.
.
$\omega' t_n = n \times 2\pi$

This method is a cute system to take into account the envelope points of the actual integrated function. In fact since we are interested to the final distance of deflection and not to the oscillatory particle trajectory motion, then this system represent a good method to find out the trajectory deflection values.

Then substituting in the equation above we have:

$$\begin{cases} x(t_{n+1}) = -\dfrac{A}{(\omega')^2 Z_n}\left[\cos((n+1)\cdot 2\pi) - \cos((n)\cdot 2\pi)\right] - (t_{n+1} - t_n)\left[\dfrac{A}{\omega' Z_n}\sin((n)\cdot 2\pi) - \dot{x}(t_n)\right] + x(t_n) \\ y(t_{n+1}) = -\dfrac{A}{(\omega')^2 Z_n}\left[\sin((n+1)\cdot 2\pi) - \sin((n)\cdot 2\pi)\right] + (t_{n+1} - t_n)\left[\dfrac{A}{\omega' Z_n}\cos((n)\cdot 2\pi) + \dot{y}(t_n)\right] + y(t_n) \end{cases}$$

eq 123

$$\begin{cases} x(t_{n+1}) = -\dfrac{A}{(\omega')^2 Z_n}[1-1] - (t_{n+1} - t_n)\left[0 - \dot{x}(t_n)\right] + x(t_n) = (t_{n+1} - t_n)\dot{x}(t_n) + x(t_n) \\ y(t_{n+1}) = -\dfrac{A}{(\omega')^2 Z_n}[0-0] + (t_{n+1} - t_n)\left[\dfrac{A}{\omega' Z_n}1 + \dot{y}(t_n)\right] + y(t_n) = (t_{n+1} - t_n)\left[\dfrac{A}{\omega' Z_n}1 + \dot{y}(t_n)\right] + y(t_n) \end{cases}$$

eq 124

$$\begin{cases} x(t_{n+1}) - x(t_n) = (t_{n+1} - t_n)\dot{x}(t_n) \\ y(t_{n+1}) - y(t_n) = (t_{n+1} - t_n)\left[\dfrac{A}{\omega' Z_n} + \dot{y}(t_n)\right] \end{cases}$$

eq 125

If t_{n+1} is close to t_n then we can rewrite *dx, dy, dt,* in place of $x(t_{n+1}) - x(t_n)$ and $y(t_{n+1}) - y(t_n)$ and $t_{n+1} - t_n$

$$\begin{cases} dx = x(t_{n+1}) - x(t_n) = (t_{n+1} - t_n)\dot{x}(t_n) = \dot{x}(t)dt \\ dy = y(t_{n+1}) - y(t_n) = (t_{n+1} - t_n)\left[\dfrac{A}{\omega' Z_n} + \dot{y}(t_n)\right] = \left[\dfrac{A}{\omega' Z_n} + \dot{y}(t)\right]dt \end{cases}$$

eq 126

$$\begin{cases} dx = x(t_{n+1}) - x(t_n) = \dot{x}(t)dt \\ dy = y(t_{n+1}) - y(t_n) = \left[\dfrac{A}{\omega' z(t)} + \dot{y}(t)\right]dt \end{cases}$$

eq 127

Integrating we have

$$\begin{cases} x(t) = \int_o^{t^*} \dot{x}(t)dt = x(t^*) - x(t_0) = x(t^*) \\ y(t) = \int_0^{t^*}\left[\dfrac{A}{\omega' z(t)} + \dot{y}(t)\right]dt = \int_0^{t^*}\left[\dfrac{A}{\omega' z(t)}\right]dt + \int_0^{t^*}\left[\dot{y}(t)\right]dt = \int_0^{t^*}\left[\dfrac{A}{\omega'(L - v_z t)}\right]dt + y(t^*) \end{cases}$$

eq 128

$$\begin{cases} x(t) = x(t^*) \\ y(t) = \int_0^{t^*}\left[\dfrac{A}{\omega'(L - v_z t)}\right]dt + y(t^*) = -\dfrac{A}{\omega' v_z}\left[\ln(L - v_z t)\right]_0^{t^*} = -\dfrac{A}{\omega' v_z}\left[\ln(L - v_z t^*) - \ln(L - v_z 0)\right] = \end{cases}$$

eq 129

$$\begin{cases} x(t) = x(t^*) \\ y(t) = -\dfrac{A}{\omega' v_z}\left[\ln(L - v_z t^*) - \ln(L)\right] = -\dfrac{A}{\omega' v_z}\ln\dfrac{L - v_z t^*}{L} \end{cases}$$

eq 130

$$\begin{cases} x(t) = x(t^*) \\ y(t) = -\dfrac{A}{\omega' v_z}\ln\dfrac{L - v_z t^*}{L} = -\dfrac{q\sqrt{60\,WtGt}\cdot\left(1 + \frac{v_z}{c}\right)}{m_p}\dfrac{1}{\omega\left(1 + \frac{v_z}{c}\right)v_z}\ln\dfrac{L - v_z t^*}{L} \end{cases}$$

eq 131

$$\begin{cases} x(t) = x(t^*) \\ y(t) = -\dfrac{A}{\omega' v_z}\ln\dfrac{L - v_z t^*}{L} = -\dfrac{q\sqrt{60\,WtGt}}{m_p \omega v_z}\ln\dfrac{L - v_z t^*}{L} \end{cases}$$

eq 132

It is possible to note that:

- There is no deflection along x axes but only along y axes;
- The deflection is proportional to the charge q and to the square of the product **Wt×Gt**, this means that the greater is the power at the antenna input and the greater is the antenna gain, the higher is the deflection action oh the charged particle.
- The deflection is inversely proportional to the charged particle mass;
- The deflection is inversely proportional to the charged particle velocity i.e. its energy;
- The deflection is inversely proportional to the frequency of the electromagnetic wave emitted by the antenna, the lower is the frequency and the greater is the deflection, but this implies greater antennas the dimension of which is inversely proportional to the frequency band.
- Close to the antenna the deflection is great and ideally tends to an infinite distance.
- The function of deflection is qualitatively shown in figure below:

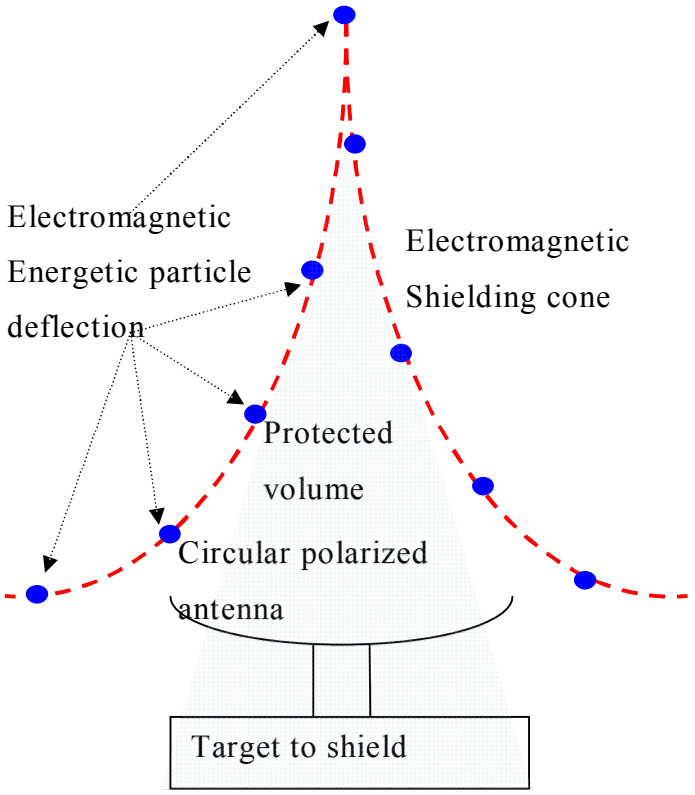

Figure 303: Qualitative picture of the charged particle shielding system

6.6.8.1 Plotted function for the first integration method

Now let us suppose to choose, as the energetic particle, a charged nucleon composed by one proton

Figure 304

Then taking in account three different particle velocities we have:

- $M_p \cong 1.67 \times 10^{-27}$ *(kg)*
- $q^+ \cong 1.60 \times 10^{-19}$ *(C)*
- $L \cong 150 \times 10^9$ *(m)*
- $v_z \cong 2000;\ 500;\ 100$ *(km/s)*
- t varies from zero to the final crossing value L/v_z
- $f \cong 100 \times 10^6$ *(Hz)*
- $Wt \cong 2 \times 10^3$ *(W)*
- $Gt \cong 10^5$

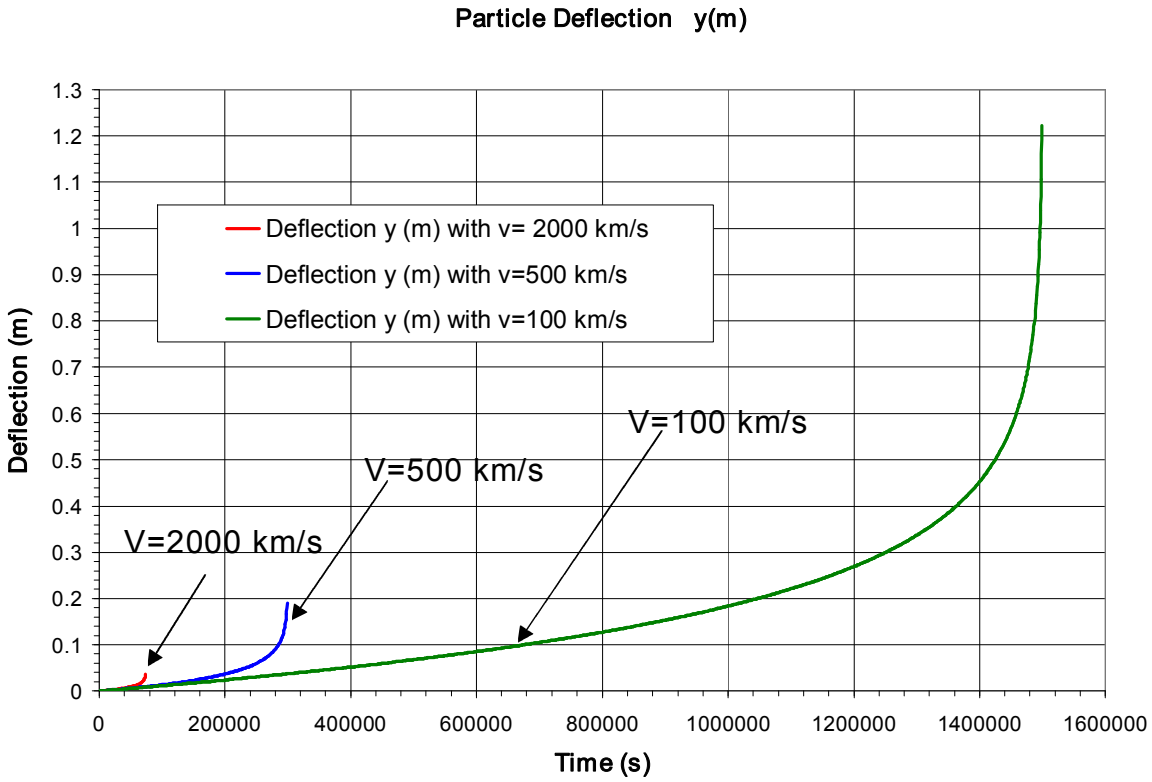

Figure 305

6.6.9 Series Expansion integration method

Consider again the function

$$\ddot{x}(t) = \frac{A}{L - v_z t}\cos\left[\omega\left(1 + \frac{v_z}{c}\right)t\right]$$
$$\ddot{y}(t) = \frac{A}{L - v_z t}\sin\left[\omega\left(1 + \frac{v_z}{c}\right)t\right]$$

Where:

$$A = \frac{q\sqrt{60\,WtGt}}{m_p}\left(1 + \frac{v_z}{c}\right)$$
$$\vec{a}_p = \left[\ddot{x}(t)\hat{x} + \ddot{y}(t)\hat{y}\right]$$

eq 133

Posing:

$$z = L - v_z t \quad \Rightarrow \quad t = \left(\frac{L - z}{v_z}\right) \quad \Rightarrow \quad dt = \frac{-1}{v_z}dz \quad \Rightarrow$$

$$\begin{cases} \dot{x}(t) = \int \ddot{x}(t)\,dt = \int \frac{A}{L - v_z t}\cos\left[\omega\left(1 + \frac{v_z}{c}\right)t\right]dt = -\frac{A}{v_z}\int \frac{1}{z}\cos\left[\omega\left(1 + \frac{v_z}{c}\right)\left(\frac{L - z}{v_z}\right)\right]dz \\ \dot{y}(t) = \int \ddot{y}(t)dt = \int \frac{A}{L - v_z t}\sin\left[\omega\left(1 + \frac{v_z}{c}\right)t\right]dt = -\frac{A}{v_z}\int \frac{1}{z}\sin\left[\omega\left(1 + \frac{v_z}{c}\right)\left(\frac{L - z}{v_z}\right)\right]dz \end{cases}$$

eq 134

$$\begin{cases} \dot{x}(t) = -\dfrac{A}{v_z}\int \dfrac{1}{z}\cos\left[\omega\left(1+\dfrac{v_z}{c}\right)\left(\dfrac{L-z}{v_z}\right)\right]dz = -\dfrac{A}{v_z}\int \dfrac{1}{z}\cos\left[\omega\left(1+\dfrac{v_z}{c}\right)\dfrac{L}{v_z} - \omega\left(1+\dfrac{v_z}{c}\right)\dfrac{z}{v_z}\right]dz \\ \dot{y}(t) = -\dfrac{A}{v_z}\int \dfrac{1}{z}\sin\left[\omega\left(1+\dfrac{v_z}{c}\right)\left(\dfrac{L-z}{v_z}\right)\right]dz = -\dfrac{A}{v_z}\int \dfrac{1}{z}\sin\left[\omega\left(1+\dfrac{v_z}{c}\right)\dfrac{L}{v_z} - \omega\left(1+\dfrac{v_z}{c}\right)\dfrac{z}{v_z}\right]dz \end{cases}$$

eq 135

Posing:

$$k = \omega\left(1+\frac{v_z}{c}\right)\frac{1}{v_z} \qquad \text{then:}$$

eq 136

$$\begin{cases} \dot{x}(t) = -\dfrac{A}{v_z}\int \dfrac{1}{z}\cos[kL - kz]dz \\ \dot{y}(t) = -\dfrac{A}{v_z}\int \dfrac{1}{z}\sin[kL - kz]dz \end{cases}$$

Recalling that:

$$\begin{aligned} sen(\alpha+\beta) &= sen\alpha\cos\beta + sen\beta\cos\alpha \\ \cos(\alpha+\beta) &= \cos\alpha\cos\beta - sen\alpha sen\beta \\ sen(\alpha-\beta) &= sen\alpha\cos\beta - sen\beta\cos\alpha \\ \cos(\alpha-\beta) &= \cos\alpha\cos\beta + sen\alpha sen\beta \end{aligned}$$

eq 137

Then:

$$\begin{cases} \dot{x}(t) = -\dfrac{A}{v_z}\int \dfrac{1}{z}\cos[kL - kz]dz = -\dfrac{A}{v_z}\int \dfrac{1}{z}[\cos(kL)\cos(kz) + \sin(kL)sen(kz)]dz \\ \dot{y}(t) = -\dfrac{A}{v_z}\int \dfrac{1}{z}\sin[kL - kz]dz = -\dfrac{A}{v_z}\int \dfrac{1}{z}[sen(kL)\cos(kz) - sen(kz)\cos(kL)]dz \end{cases}$$

eq 138

$$\begin{cases} \dot{x}(t) = -\dfrac{A}{v_z}\int \dfrac{1}{z}[\cos(kL)\cos(kz)]dz - \dfrac{A}{v_z}\int \dfrac{1}{z}[sen(kL)sen(kz)]dz \\ \dot{y}(t) = -\dfrac{A}{v_z}\int \dfrac{1}{z}[sen(kL)\cos(kz)]dz + \dfrac{A}{v_z}\int \dfrac{1}{z}[sen(kz)\cos(kL)]dz \end{cases}$$

eq 139

$$\begin{cases} \dot{x}(t) = -\frac{A}{v_z}\cos(kL)\int \frac{1}{z}[\cos(kz)]dz - \frac{A}{v_z}sen(kL)\int \frac{1}{z}[sen(kz)]dz \\ \dot{y}(t) = -\frac{A}{v_z}sen(kL)\int \frac{1}{z}[\cos(kz)]dz + \frac{A}{v_z}\cos(kL)\int \frac{1}{q}[sen(kz)]dz \end{cases}$$ eq 140

Multiplying and dividing by ***k*** we have:

$$\begin{cases} \dot{x}(t) = -\frac{A}{v_z}\cos(kL)\int \frac{k}{k}\frac{1}{z}[\cos(kz)]dz - \frac{A}{v_z}sen(kL)\int \frac{k}{k}\frac{1}{z}[sen(kz)]dz \\ \dot{y}(t) = -\frac{A}{v_z}sen(kL)\int \frac{k}{k}\frac{1}{z}[\cos(kz)]dz + \frac{A}{v_z}\cos(kL)\int \frac{k}{k}\frac{1}{z}[sen(kz)]dz \end{cases}$$ eq 141

Naw calling ***kz=u*** we have:

$$u = kz \quad \Rightarrow \quad z = \frac{u}{k} \quad \Rightarrow \quad dz = \frac{1}{k}du$$ eq 142

$$\begin{cases} \dot{x}(t) = -\frac{A}{v_z}\cos(kL)\int \frac{k}{u}[\cos(u)]\frac{1}{k}du - \frac{A}{v_z}sen(kL)\int \frac{k}{u}[sen(u)]\frac{1}{k}du \\ \dot{y}(t) = -\frac{A}{v_z}sen(kL)\int \frac{k}{u}[\cos(u)]\frac{1}{k}du + \frac{A}{v_z}\cos(kL)\int \frac{k}{u}[sen(u)]\frac{1}{k}du \end{cases}$$

Simplifying ***k*** we have:

$$\begin{cases} \dot{x}(t) = -\frac{A}{v_z}\cos(kL)\int \frac{1}{u}[\cos(u)]du - \frac{A}{v_z}sen(kL)\int \frac{1}{u}[sen(u)]du \\ \dot{y}(t) = -\frac{A}{v_z}sen(kL)\int \frac{1}{u}[\cos(u)]du + \frac{A}{v_z}\cos(kL)\int \frac{1}{u}[sen(u)]du \end{cases}$$ eq 143

As a consequence we obtain ***sin integral (Si)*** and ***cos integral (Ci)*** functions:

$$\begin{cases} \dot{x}(t) = -\frac{A}{v_z}\cos(kL)\int \frac{\cos(u)}{u}du - \frac{A}{v_z}sen(kL)\int \frac{sen(u)}{u}du \\ \dot{y}(t) = -\frac{A}{v_z}sen(kL)\int \frac{\cos(u)}{u}du + \frac{A}{v_z}\cos(kL)\int \frac{sen(u)}{u}du \end{cases}$$ eq 144

In order to try to solve this integral we can develop the function by series expansion but in this case the solution will be valid close to the point where we are expanding the function.

Since the integrals above can not solved in a closed form we are going to develop the terms ***sen(u)*** and ***cos(u)*** by *Taylor series*

Lets first define the point (u, u_0, u_f) around which we will use the Taylor series:

$$u = kz = \omega\left(1+\frac{v}{c}\right)\frac{1}{v}\left(L - vt\right) \qquad \text{i.e. the variable} \qquad \text{eq 145}$$

$$u_i = u(vt=0) = kz = \omega\left(1+\frac{v}{c}\right)\frac{1}{v}\left(L-0\right) = \omega\left(1+\frac{v}{c}\right)\frac{1}{v}L \qquad \text{i.e. the initial point} \qquad \text{eq 146}$$

$$u_f = u(vt=L) = \omega\left(1+\frac{v}{c}\right)\frac{1}{v}\left(L-L\right) = 0 \qquad \text{i.e. the final point} \qquad \text{eq 147}$$

The Taylor series with respect to a certain value u_0 is:

$$f(u) = f(u_0) + f^{(I)}(u_0)\frac{(u-u_0)^1}{1!} + f^{(II)}(u_0)\frac{(u-u_0)^2}{2!} + f^{(III)}(u_0)\frac{(u-u_0)^3}{3!} + \ldots\ldots + R(u)$$

eq 148: Taylor series

as a consequence the function ***sen(u)*** and ***cos(u)*** became:

$$sen(u) = sen(u_0)(u-u_0)^0 + \cos(u_0)\frac{(u-u_0)^1}{1!} - sen(u_0)\frac{(u-u_0)^2}{2!} - \cos(u_0)\frac{(u-u_0)^3}{3!} + sen(u_0)\frac{(u-u_0)^4}{4!} +$$
$$+ \cos(u_0)\frac{(u-u_0)^5}{5!} - sen(u_0)\frac{(u-u_0)^6}{6!} - \cos(u_0)\frac{(u-u_0)^7}{7!} + sen(u_0)\frac{(u-u_0)^8}{8!} + \cos(u_0)\frac{(u-u_0)^9}{9!} +$$
$$..... + \sin(u_0)^n \frac{(u-u_0)^{2n+1}}{(2n+1)!}$$

$$\cos(u) = \cos(u_0)(u-u_0)^0 - sen(u_0)\frac{(u-u_0)^1}{1!} - \cos(u_0)\frac{(u-u_0)^2}{2!} + sen(u_0)\frac{(u-u_0)^3}{3!} + \cos(u_0)\frac{(u-u_0)^4}{4!} +$$
$$- sen(u_0)\frac{(u-u_0)^5}{5!} - \cos(u_0)\frac{(u-u_0)^6}{6!} + sen(u_0)\frac{(u-u_0)^7}{7!} + \cos(u_0)\frac{(u-u_0)^8}{8!} - sen(u_0)\frac{(u-u_0)^9}{3!} +$$
$$... + \cos(u_0)^n \frac{(u-u_0)^{2n}}{(2n)!}$$

eq 149

now supposing $u_0=u_{initial}$ then we have:

$$\begin{cases} \dot{x}(t) = -\frac{A}{v}\cos(kL)\int \frac{1}{u}\left[\cos(u_0)(u-u_0)^0 - sen(u_0)\frac{(u-u_0)^1}{1!} - \cos(u_0)\frac{(u-u_0)^2}{2!} + sen(u_0)\frac{(u-u_0)^3}{3!} + \right.\\ \left. + ...\right] du + \\ \quad -\frac{A}{v}sen(kL)\int \frac{1}{u}\left[sen(u_0)(u-u_0)^0 + \cos(u_0)\frac{(u-u_0)^1}{1!} - sen(u_0)\frac{(u-u_0)^2}{2!} - \cos(u_0)\frac{(u-u_0)^3}{3!} + \right.\\ \left. + ...\right] du = \\ \dot{y}(t) = -\frac{A}{v}sen(kL)\int \frac{1}{u}\left[\cos(u_0)(u-u_0)^0 - sen(u_0)\frac{(u-u_0)^1}{1!} - \cos(u_0)\frac{(u-u_0)^2}{2!} + sen(u_0)\frac{(u-u_0)^3}{3!} + \right.\\ \left. + ...\right] du + \\ \quad +\frac{A}{v}\cos(kL)\int \frac{1}{u}\left[sen(u_0)(u-u_0)^0 + \cos(u_0)\frac{(u-u_0)^1}{1!} - sen(u_0)\frac{(u-u_0)^2}{2!} - \cos(u_0)\frac{(u-u_0)^3}{3!} + \right.\\ \left. + ...\right] du = \end{cases}$$

Substituting $u_0=u_i$ we have:

$$u = kz = \omega\left(1+\frac{v}{c}\right)\frac{1}{v_z}\left(L - v_z t\right)$$

$$u_0 = u_i = u(vt = 0) = \omega\left(1 + \frac{v}{c}\right)\frac{1}{v}\ (L - 0) = \omega\left(1 + \frac{v}{c}\right)\frac{1}{v}L$$

$$(u - u_0) = kz = \omega\left(1 + \frac{v_z}{c}\right)\frac{1}{v}\ (L - v_z t) - \omega\left(1 + \frac{v}{c}\right)\frac{1}{v_z}\ (L) = \omega\left(1 + \frac{v_z}{c}\right)\frac{1}{v_z}(-v_z t) = -\omega\left(1 + \frac{v_z}{c}\right)t$$

$$du = -\omega\left(1 + \frac{v}{c}\right)dt$$

Consequently the equation of motion became:

$$
\begin{cases}
\dot{x}(t) = -\dfrac{A}{v}\cos(kL)\displaystyle\int \dfrac{1}{\omega\left(1+\dfrac{v}{c}\right)\dfrac{1}{v_z}\ (L-v_z t)}
\left[\begin{array}{l}
\cos(u_0)\left(-\omega\left(1+\dfrac{v_z}{c}\right)t\right)^0 - sen(u_0)\dfrac{\left(-\omega\left(1+\dfrac{v_z}{c}\right)t\right)^1}{1!} \\
-\cos(u_0)\dfrac{\left(-\omega\left(1+\dfrac{v_z}{c}\right)t\right)^2}{2!} + sen(u_0)\dfrac{\left(-\omega\left(1+\dfrac{v_z}{c}\right)t\right)^3}{3!} + \\
+ \ldots\ldots\ldots
\end{array}\right]
\left[-\omega\left(1+\dfrac{v}{c}\right)dt\right] + \\
\quad -\dfrac{A}{v}sen(kL)\displaystyle\int \dfrac{1}{\omega\left(1+\dfrac{v}{c}\right)\dfrac{1}{v_z}\ (L-v_z t)}
\left[\begin{array}{l}
sen(u_0)\left(-\omega\left(1+\dfrac{v_z}{c}\right)t\right)^0 + \cos(u_0)\dfrac{\left(-\omega\left(1+\dfrac{v_z}{c}\right)t\right)^1}{1!} \\
-sen(u_0)\dfrac{\left(-\omega\left(1+\dfrac{v_z}{c}\right)t\right)^2}{2!} - \cos(u_0)\dfrac{\left(-\omega\left(1+\dfrac{v_z}{c}\right)t\right)^3}{3!} + \\
+ \ldots\ldots\ldots
\end{array}\right]
\left[-\omega\left(1+\dfrac{v}{c}\right)dt\right] = \\
\dot{y}(t) = -\dfrac{A}{v}sen(kL)\displaystyle\int \dfrac{1}{\omega\left(1+\dfrac{v}{c}\right)\dfrac{1}{v_z}\ (L-v_z t)}
\left[\begin{array}{l}
\cos(u_0)\left(-\omega\left(1+\dfrac{v_z}{c}\right)t\right)^0 - sen(u_0)\dfrac{\left(-\omega\left(1+\dfrac{v_z}{c}\right)t\right)^1}{1!} \\
-\cos(u_0)\dfrac{\left(-\omega\left(1+\dfrac{v_z}{c}\right)t\right)^2}{2!} + sen(u_0)\dfrac{\left(-\omega\left(1+\dfrac{v_z}{c}\right)t\right)^3}{3!} + \\
+ \ldots\ldots\ldots
\end{array}\right]
\left[-\omega\left(1+\dfrac{v}{c}\right)dt\right] + \\
\quad +\dfrac{A}{v}\cos(kL)\displaystyle\int \dfrac{1}{\omega\left(1+\dfrac{v}{c}\right)\dfrac{1}{v_z}\ (L-v_z t)}
\left[\begin{array}{l}
sen(u_0)\left(-\omega\left(1+\dfrac{v_z}{c}\right)t\right)^0 + \cos(u_0)\dfrac{\left(-\omega\left(1+\dfrac{v_z}{c}\right)t\right)^1}{1!} \\
-sen(u_0)\dfrac{\left(-\omega\left(1+\dfrac{v_z}{c}\right)t\right)^2}{2!} - \cos(u_0)\dfrac{\left(-\omega\left(1+\dfrac{v_z}{c}\right)t\right)^3}{3!} + \\
+ \ldots\ldots\ldots
\end{array}\right]
\left[-\omega\left(1+\dfrac{v}{c}\right)dt\right] =
\end{cases}
$$

$$
\begin{cases}
\dot{x}(t) = -\dfrac{A}{V}\cos(kL)\left[\begin{array}{l}
\displaystyle\int \frac{\cos(u_0)}{\omega\left(1+\frac{V}{c}\right)\frac{1}{V_z}\left(L-v_z t\right)}\left[-\omega\left(1+\frac{V}{c}\right)dt\right] - \int \frac{sen(u_0)\left(-\omega\left(1+\frac{V_z}{c}\right)t\right)}{\omega\left(1+\frac{V}{c}\right)\frac{1}{V_z}\left(L-v_z t\right)}\left[-\omega\left(1+\frac{V}{c}\right)dt\right] \\
\displaystyle -\int \frac{\cos(u_0)\frac{\left(-\omega\left(1+\frac{V_z}{c}\right)t\right)^2}{2!}}{\omega\left(1+\frac{V}{c}\right)\frac{1}{V_z}\left(L-v_z t\right)}\left[-\omega\left(1+\frac{V}{c}\right)dt\right] + \int \frac{sen(u_0)\frac{\left(-\omega\left(1+\frac{V_z}{c}\right)t\right)^3}{3!}}{\omega\left(1+\frac{V}{c}\right)\frac{1}{V_z}\left(L-v_z t\right)}\left[-\omega\left(1+\frac{V}{c}\right)dt\right] + + \\
+ \ldots\ldots\ldots
\end{array}\right] \\
-\dfrac{A}{V}sen(kL)\left[\begin{array}{l}
\displaystyle\int \frac{sen(u_0)}{\omega\left(1+\frac{V}{c}\right)\frac{1}{V_z}\left(L-v_z t\right)}\left[-\omega\left(1+\frac{V}{c}\right)dt\right] + \int \frac{\cos(u_0)\left(-\omega\left(1+\frac{V_z}{c}\right)t\right)}{\omega\left(1+\frac{V}{c}\right)\frac{1}{V_z}\left(L-v_z t\right)}\left[-\omega\left(1+\frac{V}{c}\right)dt\right] \\
\displaystyle -\int \frac{sen(u_0)\frac{\left(-\omega\left(1+\frac{V_z}{c}\right)t\right)^2}{2!}}{\omega\left(1+\frac{V}{c}\right)\frac{1}{V_z}\left(L-v_z t\right)}\left[-\omega\left(1+\frac{V}{c}\right)dt\right] - \int \frac{\cos(u_0)\frac{\left(-\omega\left(1+\frac{V_z}{c}\right)t\right)^3}{3!}}{\omega\left(1+\frac{V}{c}\right)\frac{1}{V_z}\left(L-v_z t\right)}\left[-\omega\left(1+\frac{V}{c}\right)dt\right] + \\
+ \ldots\ldots\ldots
\end{array}\right]
\end{cases}
$$

$$\dot{y}(t) = -\frac{A}{V} sen(kL) \left[\int \frac{\cos(u_0)}{\omega\left(1+\frac{V}{c}\right)\frac{1}{V_z}\left(L - v_z t\right)} \left[-\omega\left(1+\frac{V}{c}\right) dt \right] - \int \frac{sen(u_0)\left(-\omega\left(1+\frac{V_z}{c}\right)t\right)}{\omega\left(1+\frac{V}{c}\right)\frac{1}{V_z}\left(L - v_z t\right)} \left[-\omega\left(1+\frac{V}{c}\right) dt \right] \right.$$

$$- \int \frac{\cos(u_0)\frac{\left(-\omega\left(1+\frac{V_z}{c}\right)t\right)^2}{2!}}{\omega\left(1+\frac{V}{c}\right)\frac{1}{V_z}\left(L - v_z t\right)} \left[-\omega\left(1+\frac{V}{c}\right) dt \right] + \int \frac{sen(u_0)\frac{\left(-\omega\left(1+\frac{V_z}{c}\right)t\right)^3}{3!}}{\omega\left(1+\frac{V}{c}\right)\frac{1}{V_z}\left(L - v_z t\right)} \left[-\omega\left(1+\frac{V}{c}\right) dt \right] + \left. + \right.$$

$$\left. + \ldots\ldots\ldots \right]$$

$$+ \frac{A}{V} \cos(kL) \left[\int \frac{sen(u_0)}{\omega\left(1+\frac{V}{c}\right)\frac{1}{V_z}\left(L - v_z t\right)} \left[-\omega\left(1+\frac{V}{c}\right) dt \right] + \int \frac{\cos(u_0)\left(-\omega\left(1+\frac{V_z}{c}\right)t\right)}{\omega\left(1+\frac{V}{c}\right)\frac{1}{V_z}\left(L - v_z t\right)} \left[-\omega\left(1+\frac{V}{c}\right) dt \right] \right.$$

$$- \int \frac{sen(u_0)\frac{\left(-\omega\left(1+\frac{V_z}{c}\right)t\right)^2}{2!}}{\omega\left(1+\frac{V}{c}\right)\frac{1}{V_z}\left(L - v_z t\right)} \left[-\omega\left(1+\frac{V}{c}\right) dt \right] - \int \frac{\cos(u_0)\frac{\left(-\omega\left(1+\frac{V_z}{c}\right)t\right)^3}{3!}}{\omega\left(1+\frac{V}{c}\right)\frac{1}{V_z}\left(L - v_z t\right)} \left[-\omega\left(1+\frac{V}{c}\right) dt \right] + \left. \right.$$

$$\left. + \ldots\ldots\ldots \right]$$

$$\dot{x}(t) = -\frac{A}{v}\cos(kL)\left[\begin{array}{l} -\int \frac{v_z \cos(u_0)}{(L - v_z t)}\,dt + \int \frac{v_z sen(u_0)\left(-\omega\left(1+\frac{V_z}{c}\right)\right)t}{(L - v_z t)}dt + \\ + \int \frac{v_z \cos(u_0)\left(-\omega\left(1+\frac{V_z}{c}\right)\right)^2 t^2}{(L - v_z t)2!}\,dt - \int \frac{v_z sen(u_0)\left(-\omega\left(1+\frac{V_z}{c}\right)\right)^3 t^3}{(L - v_z t)3!}dt + \\ + ... \end{array}\right] +$$

$$-\frac{A}{v}sen(kL)\left[\begin{array}{l} -\int \frac{v_z sen(u_0)}{(L - v_z t)}\,dt - \int \frac{v_z \cos(u_0)\left(-\omega\left(1+\frac{V_z}{c}\right)t\right)}{(L - v_z t)}\,dt + \\ + \int \frac{v_z sen(u_0)\left(-\omega\left(1+\frac{V_z}{c}\right)\right)^2 t^2}{(L - v_z t)2!}dt + \int \frac{v_z \cos(u_0)\left(-\omega\left(1+\frac{V_z}{c}\right)\right)^3 t^3}{(L - v_z t)3!}\,dt + \\ + ... \end{array}\right]$$

$$\dot{y}(t) = -\frac{A}{v} sen(kL) \left[\begin{array}{l} -\int \frac{v_z \cos(u_0)}{(L - v_z t)} dt + \int \frac{v_z sen(u_0) \left(-\omega \left(1 + \frac{V_z}{c} \right) \right) t}{(L - v_z t)} dt \\ + \int \frac{v_z \cos(u_0) \left(-\omega \left(1 + \frac{V_z}{c} \right) \right)^2 t^2}{(L - v_z t) 2!} dt - \int \frac{v_z sen(u_0) \left(-\omega \left(1 + \frac{V_z}{c} \right) \right)^3 t^3}{(L - v_z t) 3!} dt + \\ + ... \end{array} \right] +$$

$$+ \frac{A}{v} \cos(kL) \left[\begin{array}{l} -\int \frac{v_z sen(u_0)}{(L - v_z t)} dt - \int \frac{v_z \cos(u_0) \left(-\omega \left(1 + \frac{V_z}{c} \right) \right) t}{(L - v_z t)} dt \\ + \int \frac{v_z sen(u_0) \left(-\omega \left(1 + \frac{V_z}{c} \right) \right)^2 t^2}{(L - v_z t) 2!} dt + \int \frac{\cos(u_0) \left(-\omega \left(1 + \frac{V_z}{c} \right) \right)^3 t^3}{\frac{1}{v_z} (L - v_z t) 3!} dt + \\ + ... \end{array} \right]$$

$$\dot{x}(t) = -\frac{A}{v} \cos(kL) \left[\begin{array}{l} -v_z \cos(u_0) \int \frac{1}{(L - v_z t)} dt + v_z sen(u_0) \left(-\omega \left(1 + \frac{V_z}{c} \right) \right) \int \frac{t}{(L - v_z t)} dt + \\ + v_z \cos(u_0) \left(-\omega \left(1 + \frac{V_z}{c} \right) \right)^2 \int \frac{t^2}{(L - v_z t) 2!} dt + \\ - v_z sen(u_0) \left(-\omega \left(1 + \frac{V_z}{c} \right) \right)^3 \int \frac{t^3}{(L - v_z t) 3!} dt + \\ + ... \end{array} \right] +$$

$$- \frac{A}{v} sen(kL) \left[\begin{array}{l} -v_z sen(u_0) \int \frac{1}{(L - v_z t)} dt - v_z \cos(u_0) \left(-\omega \left(1 + \frac{V_z}{c} \right) \right) \int \frac{t}{(L - v_z t)} dt + \\ + v_z sen(u_0) \left(-\omega \left(1 + \frac{V_z}{c} \right) \right)^2 \int \frac{t^2}{(L - v_z t) 2!} dt + \\ + v_z \cos(u_0) \left(-\omega \left(1 + \frac{V_z}{c} \right) \right)^3 \int \frac{t^3}{(L - v_z t) 3!} dt + \\ + ... \end{array} \right]$$

$$\dot{y}(t) = -\frac{A}{V} sen(kL) \left[\begin{array}{l} - v_z \cos(u_0) \int \frac{1}{(L - v_z t)} dt + v_z sen(u_0) \left(- \omega \left(1 + \frac{V_z}{c} \right) \right) \int \frac{t}{(L - v_z t)} dt \\ + v_z \cos(u_0) \left(- \omega \left(1 + \frac{V_z}{c} \right) \right)^2 \int \frac{t^2}{(L - v_z t) 2!} dt + \\ - v_z sen(u_0) \left(- \omega \left(1 + \frac{V_z}{c} \right) \right)^3 \int \frac{t^3}{(L - v_z t) 3!} dt + \\ + ... \end{array} \right] +$$

$$+ \frac{A}{V} \cos(kL) \left[\begin{array}{l} - v_z sen(u_0) \int \frac{1}{(L - v_z t)} dt - v_z \cos(u_0) \left(- \omega \left(1 + \frac{V_z}{c} \right) \right) \int \frac{t}{(L - v_z t)} dt \\ + v_z sen(u_0) \left(- \omega \left(1 + \frac{V_z}{c} \right) \right)^2 \int \frac{t^2}{(L - v_z t) 2!} dt + \\ + v_z \cos(u_0) \left(- \omega \left(1 + \frac{V_z}{c} \right) \right)^3 \int \frac{t^3}{(L - v_z t) 3!} dt + \\ + ... \end{array} \right]$$

The computation became very difficult and the equation can't be solved in a closed form.

6.6.10 Numerical integration

Recalling the Riemann Defined Integral definition, then the double integration for a certain function should be computed into two phases

1. First phase we compute the first numerical integration of the function:

$$f'(t) = \int_a^b f''(t) dt \cong \lim_{\max \Delta t_i \to 0} \sum_{i=0}^{n-1} f''(\xi_i) \cdot \Delta t_i$$

where

$\Delta t_i = (t_{i+1} - t_i)$

$\xi_i \in [t_i, t_{i+1}]$

eq 150

2. Second phase we perform the second numerical integrating of the function in the same way.

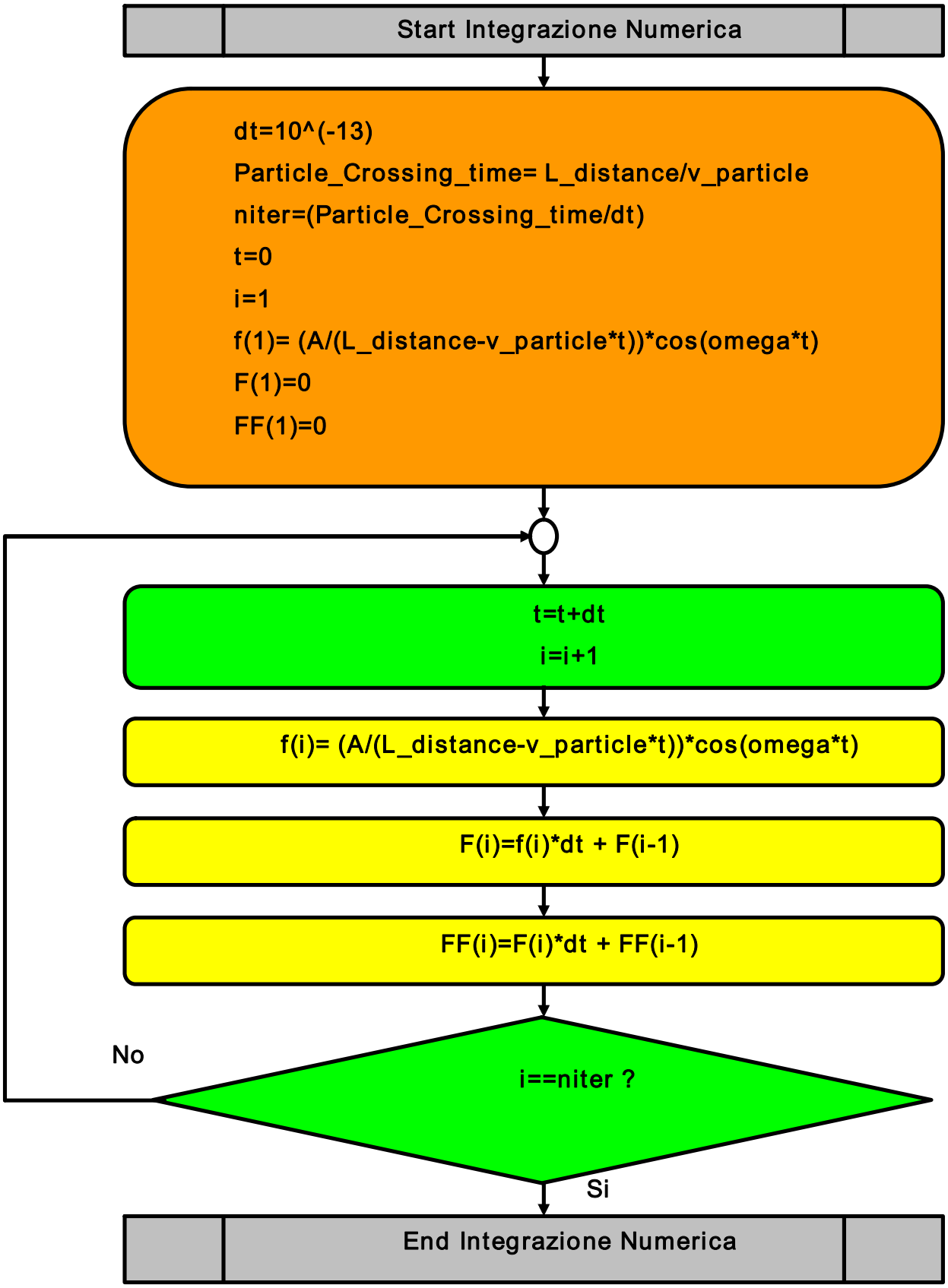

Figure 306: numerical integration flow chart

The simplest Matlab routine to perform a double numerical integration is shown below

```
%%%%%%%%%%%%  Numerical Integration of    COS(2x))  %%%%%%%%%%%%
%% this method is used to compute a double numerical integration of a certain function %%
%%% main data  %%%
dt=0.1;
omega=2;
niter=60;

%%% First Loop Cycle %%%
t=0;
f(1)=cos(omega*t)
F(1)=0;
FF(1)=0;
ascisse(1)=t;
t=t+dt;

%%% Computing Loop Cycle %%%
for i=2:1:niter;
      f(i)=sin(omega*t);
      F(i)=f(i)*dt+F(i-1);
      FF(i)=F(i)*dt+FF(i-1);
      ascisse(i)=t;
      t=t+dt;
end;
for i=1:1:niter;
I(i)=F(i);
II(i)=FF(i);
end;

%%% Plot routine %%%
c1=f(1:1:niter);    %%%  original vector of f(t)  %%%
c2=I(1:1:niter);   %%%  first integration vector of f(t)  %%%
c3=II(1:1:niter);   %%%  second integration vector of f(t)  %%%
plot(ascisse,c3);  %%%  plot of second integration vector of f(t)  %%%
```

Figure 307: Matlab script to figure out the double integration

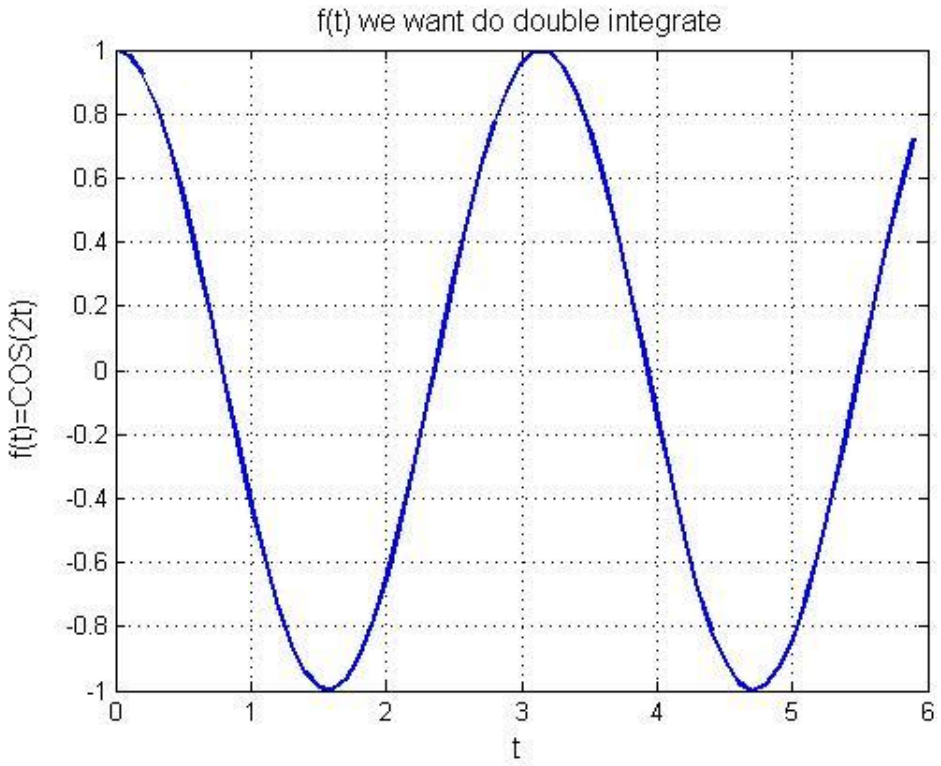

Figure 308: f(t)=cos(2t)

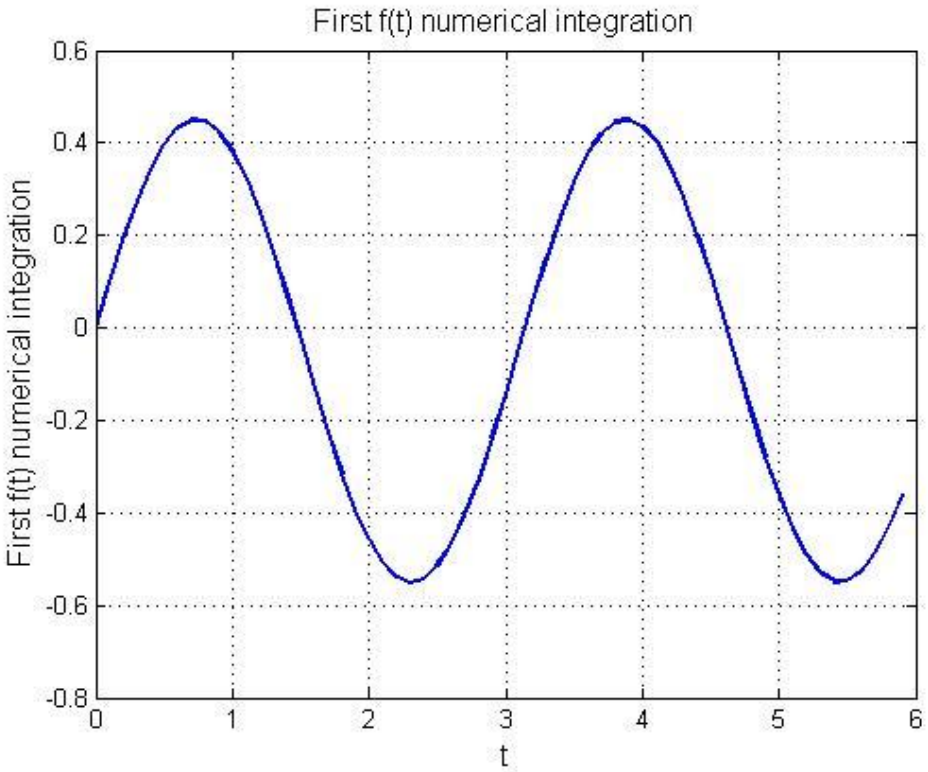

Figure 309: First integration F(t) of f(t)=cos(2t)

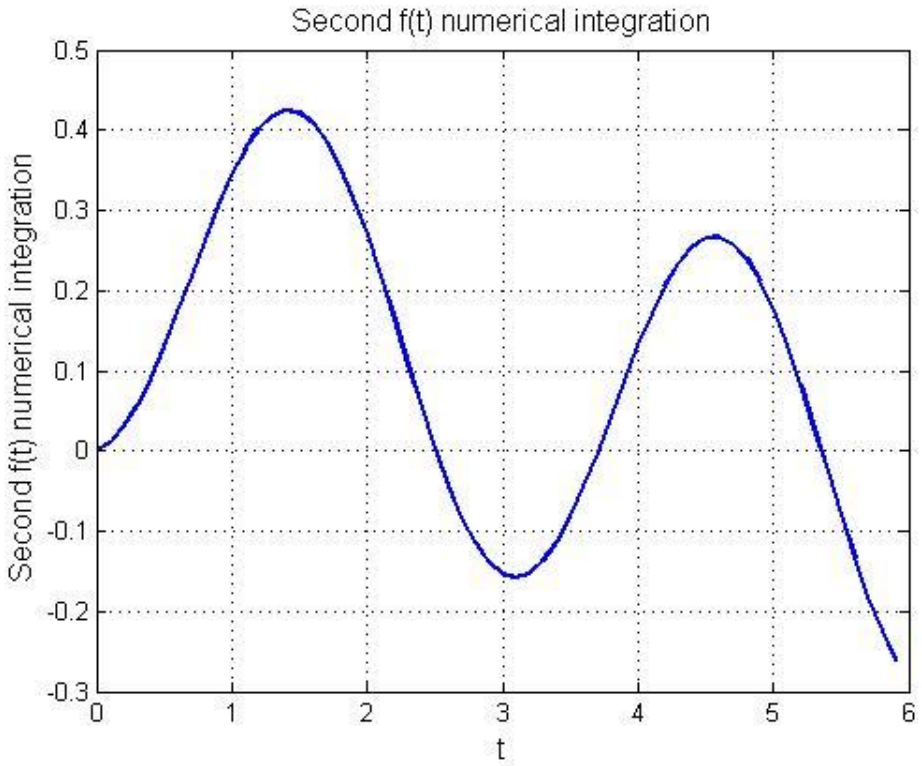

Figure 310: Second integration FF(t) of f(t)=cos(2t)

In fact:

$$f(t)=\cos(2t) \qquad \textbf{eq 151}$$

$$F(t)=\int \cos(2t)dt=\frac{1}{2}\sin(2t)+c_1 \qquad \textbf{eq 152}$$

$$FF(t)=\int\left(\frac{1}{2}\sin(2t)+c_1\right)dt=-\frac{1}{4}\cos(2t)+c_1 t+c_2 \qquad \textbf{eq 153}$$

6.6.10.1 Errors in numerical integration

In order to minimize the errors caused by the finite and discrete integration time interval Δt, we must to consider the better compromise between the total computing time machine required to perform the numerical integration and the minimum integration time interval Δt required to satisfy the integration accuracy.

In our sampling process the sampling frequency is ten time or even more the frequency of the original signal.

Because frequency is the inverse of the time, this mean that the integration time interval Δt should be approximately one tent of the inverse of the original signal frequency.
In other words:

$$dt_{\text{int }egration} \le \frac{1}{10}\frac{1}{f_{signal}} \qquad \text{eq 154}$$

As an example if the frequency of our transmitted EM wave is of the order of $f=10^6$ MHz then the integration time interval Δt should be approximately:

$$dt_{\text{int }egration} \le \frac{1}{10}\frac{1}{10^6} \qquad \text{eq 155}$$

As a consequence $\mathbf{dt=10^{-7}}$ (s) or much better $\mathbf{dt=10^{-8}}$ (s) could be considered.
Now as a function of the integration step number, the total time required to perform the numerical integration could range form some milliseconds to some month.

To show this let us to consider our case of study.

The functions we are interested to integrate are:

$$\ddot{x}(t) = \frac{A}{L - v_z t}\cos[\omega' t]$$
$$\ddot{y}(t) = \frac{A}{L - v_z t}\sin[\omega' t]$$

Where:

$$A = \frac{q\sqrt{60\,WtGt}}{m_p}\left(1+\frac{v_z}{c}\right)$$

$$\omega' = \omega\left(1+\frac{v_z}{c}\right)$$

$$\vec{a}_p = \left[\ddot{x}(t)\hat{x} + \ddot{y}(t)\hat{y}\right]$$

Now suppose to choose as the energetic particle a proton nucleon:

p+

Figure 311

Other data are:

- $M_p \cong 1.67\times10^{-27}$ *(kg)*
- $q^+ \cong 1.60\times10^{-19}$ *(C)*
- $L \cong 150\times10^{9}$ *(m)*
- $v_z \cong$ *500, (km/s)*
- $f \cong 100\times10^{6}$ *(Hz)*
- $Wt \cong 2\times10^{3}$ *(W)*
- $Gt \cong 10^{5}$

Supposing to adopt **dt=10^{-8}** (s) then the number of integration step can be computed in a very simple way.

Let us to consider the following data:

- $L \cong 150\times10^{9}$ *(m) (Sun – Moon Distance)*
- $v_z \cong$ *500, (km/s) (particle velocity considered constant)*

Then total particle crossing time form the Sun to the Moon is:

$$t_{crossing} = \frac{L}{v_z} = \frac{150\cdot10^9}{500\cdot10^3} \cong 300000 \quad (s) \qquad \textbf{eq 156}$$

Let us consider now the sampling time **dt=10^{-8}** (s) then the number of required iterations become:

$$N_{iter} = \frac{t_{crossing}}{dt} = \frac{3 \cdot 10^{5}}{10^{-8}} = 3 \cdot 10^{13} \quad (iterations) \qquad \text{eq 157}$$

At this point there are two new kinds of problems:

- The first is due to the number of bits needed to represent such quantity. In order to count $3 \cdot 10^{13}$, we need of 45 bits (2E+45= 3.51844E+13). Usually our computers work with 32 bits so we have to force our computation to 64 bit minimum. This operation slows down the computation velocity.
  Format of 64 bits, correspond to a double precision in programs written in C as is our final program.

Format	Used Bit	Bit of Mantissa	Bit of exponent	Bit of sign
float	32	23	8	1
double	64	52	11	1
Long double	80	64	15	1

Table 41: number of bit required to represent the precision in C program language

- The second problem is due to the total computation time required to solve the numerical integration. Taking into account the elementary computing time required to perform one single iteration (about 0.1 μs), then the total computation time is shown as a function of the particle velocity and the integral resolution time ***dt***.

Elementary Step computation time (s)	particle velocity (m/s)	Iterations Number Initial	Integrations time step dt (s)	Iterations Number Final	Integration time (s)	Integration time (days)
1.00E-07	5.00E+05	3.00E+05	1.00E-03	3.00E+08	3.00E+01	0.0
			1.00E-04	3.00E+09	3.00E+02	0.0
			1.00E-05	3.00E+10	3.00E+03	0.0
			1.00E-06	3.00E+11	3.00E+04	0.3
			1.00E-07	3.00E+12	3.00E+05	3.3
			1.00E-08	3.00E+13	3.00E+06	33.5
			1.00E-09	3.00E+14	3.00E+07	334.8

Table 42: Overall computation time as a function of "dt" and "particle velocity"

Observing table above we can see the total computation time of about one month, required to compute the numerical integration with dt=10E-8 (s).

Fore the numerical integration operation we have not used Matlab. In fact it works with matrix and vectors and, in order to address the internal memory (even for an elementary integration step), a higher computing time are required when compared to a program compiled in C where we do not need to use vectors.

6.6.10.2 Numerical Integration plotting problems

In order to plot the results of the Numerical Integration, we have to take into account the maximum number of rows we can represent with Matlab, Excell, and so on.
For example Excel can maximum use 25.000 rows. Matlab does not have a fixed limit but the more is the file dimensions the higher is the time and computer RAM required to load the file we want to plot.
In our example the file we want to plot has about $3 \cdot 10^{13}$ rows. As a consequence we can not use any program to plot such type of file.

In order to plot the file we can sample the integration output.
The integration output sampling can happen in two main ways:

- Constant step; as an example one point ever 1000000 (i.e. 1:1000000)
- Not constant step; as an example we could use an exponential function in

order to increase the resolution step by step.

The second method has the main advantage of a better representation when the iterations are close to end.
In the following figure the Numerical Integration results are shown.

6.6.10.3 Numerical integration Results

Using an integration step **dt=10E-8 (s)** the following result has been obtained. In order to facilitate the plot phase, the table of about 300000 of rows has been sampled in non linear form, close to the antenna the plotted point's density is greater than far from the antenna. As a consequence the oscillatory particle motion is not well visible here. The final deflection result is not far from that obtained by first integration method. Using a more accurate integration step, the final deflection could be more accurate and probably much closer to the first integration method result.

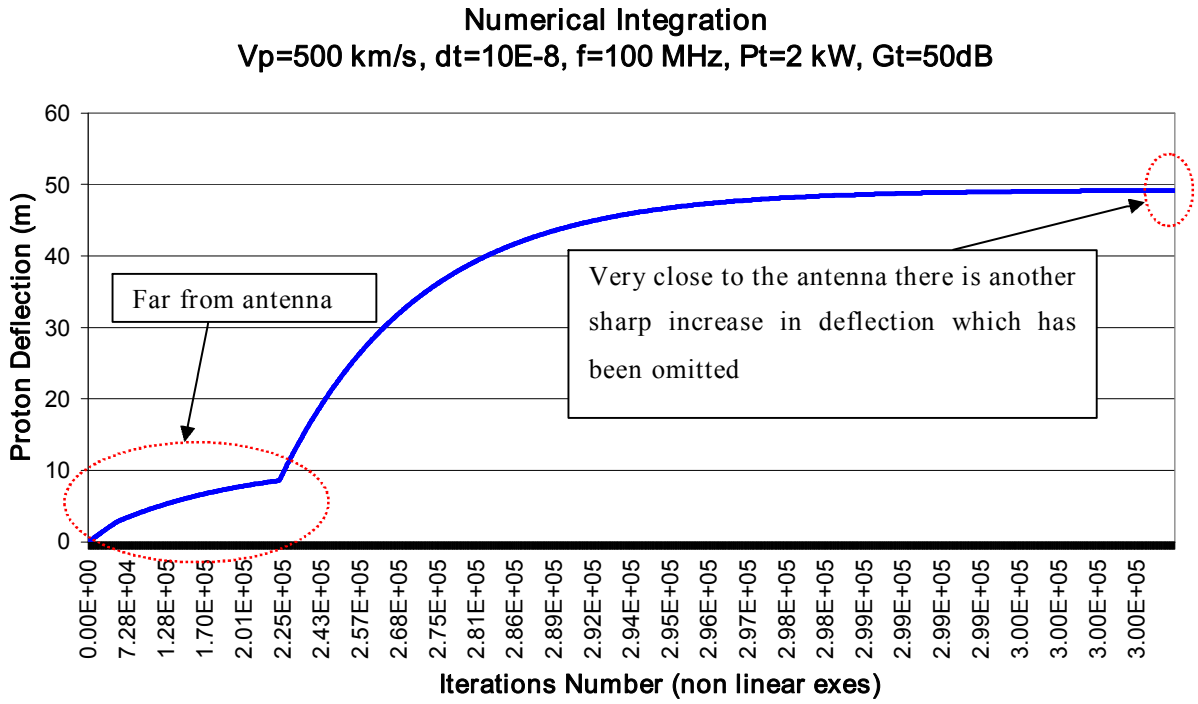

Figure 312: charged particle deflection using numerical integration

6.7 Conclusions

From theory point of view it seems possible to deflect charged particles by means of and Electromagnetic field circularly polarized.
From plot above we have been observed that in order to change the high energetic particle motion direction, we need of much antenna power.
The next step is to do an experiment to prove the theory.
Because it's difficult to have a proton source, an idea is to use an electron source like for example a cathode tube CRT.
This is the purpose of the next chapter.

6.8 Reference Table

- http://www.estec.esa.nl/wmwww/wma/ecss/ecsspres/index.htm
  in particular, Chapter 9 “Energetic Particle Environments” in ESA-ECSS-E-10-04, System Engineering:Space Environment
- http://www.spenvis.oma.be/spenvis/intro.html

SPENVIS is SPace ENVironment Information System set up and run orbit models, get doses & fluences

- http://nssdc.gsfc.nasa.gov/space/model/models_home.html

NSSDC models AE8min, AP8max, etc

- http://crsp3.nrl.navy.mil/creme96/

Cosmic Ray Effects on Micro Electronics

- http://www.kathryncramer.com/lunar_development/2004/11/lunar_lava_tube.html
- http://www.tpub.com/content/doe/h1015v2/css/h1015v2_22.htm
- http://www.pubs.asce.org/WWWsrchkwx.cgi?Construction+materials
- http://www.lunar-reclamation.org/papers/lavatube_pix.htm
- http://www.lunar-reclamation.org/lavatubes/index.htm
- http://www.nasa.gov/centers/goddard/news/topstory/2007/screaming_cmes.html
- http://engineering.dartmouth.edu/~Simon_G_Shepherd/research/Shielding/index.html

Spacecraft Shielding Documents Early Shielding: '60s and '70s

- Levy_61.pdf - Radiation Shielding of Space Vehicles by Means of Superconductings Coils.
  Levy_62.pdf and Willinski_62.pdf - Author's Reply to Willinski's Comment on "Radiation Shielding of Space Vehicles by Means of Superconductings Coils".
  Levy_64.pdf - Plasma Radiation Shielding.
  Levy_65.pdf - Comment on "Mass and Magnetic Dipole Shielding against Electrons of the Artificial Radiations Belt".
  Keffer_65.pdf - Experimental Investigation of Packaging and Deployment Characteristics of an Inflatable Toroidal-Space-Station Configuration.
  Levine_66.pdf - Forbidden Regions Produced by Two Parallel Dipoles.

Levy_67.pdf - The Status and Prospects for Plasma Radiation Shielding.

Levine_67.pdf - The Quasi-Hollow Conductor Magnet as a Space Shield Against Electrons.

Levine_68.pdf - Analog Studies of Magnetic Shields.

Levy_68.pdf - Plasma Radiation Shield: Concept and Applications to Space Vehicles.

vonBraun_69.pdf - Will Mighty Magnets Protect Voyagers to Planets?

Levine_71.pdf - An Active Radiation Shield for Cylindrically Shaped Vehicles.

Deployed Shield Papers

- Cocks_91.pdf - A Deployable High Temperature Superconducting Coil (DHTSC): A Novel Concept for Producing Magnetic Shields Against both Solar Flare and Galatic Radiation During Manned Interplanetary Missions.

  Watkins Thesis - Magnetic Shielding of Spacecraft Employing High Temperature Superconductors.

  Cocks_93.pdf - Magnetic Shielding of Interplanetary Spacecraft against Solar Flar Radiation.

  Hilinski_94.pdf - Deployed High-Temperature Superconducting Coil Magnetic Shield.

  Cocks_97.pdf - Applications for Deployed High Temperature Superconducting Coils in Spacecraft Engineering: A review and Analysis.

  Lanzerotti_04.pdf - Active Radiation Shielding in Space?

  Buckey_05.pdf - Next Stop, Mars.

  Singer_05.pdf - Comment on "Next Stop, Mars".

  Buckey_05a.pdf - More on Mars.

  2005 NIAC

  Parker_05.pdf - Shielding Space Explorers from Cosmic Rays.

  Parker_06.pdf - Shielding Space Travelers.

  Parker.pdf - Shielding Astronauts from Cosmic Rays.

  Shepherd_07.pdf - Comment on "Applications for Deployed High Temperature Superconducting Coils in Spacecraft Engineering: A Review and Analysis" by J. C. Cocks et al.

Shepherd_07a.pdf - Stormer Theory Applied to Magnetic Spacecraft Shielding.

Magnetic Shielding Papers

- Townsend_83.pdf - HZE Particle Shielding Using Confined Magnetic Fields.
  Spillantini_00.pdf - Radiation shielding of spacecraft's in manned interplanetary flights.
  Stephens_02.pdf - MONTE CARLO TRANSPORT MODEL COMPARISON WITH 1A GeV ACCELERATED IRON EXPERIMENT: HEAVY-ION SHIELDING EVALUATION OF NASA SPACE FLIGHT-CREW FOODSTUFF.
  Townsend_03.pdf - Carrington Flare of 1859 as a Prototypical Worst-Case Solar Energetic Particle Event.
  Rossi_04.pdf - A Superconducting Magnetic Lens for Solar Rays Protection in Manned Interplanetary Missions.
  Townsend_05.pdf - Critical Analysis of Active Shielding Methods for Space Radiation Protection.

Overview Papers

- Simonsen_91.pdfRadiation Protection for Human Missions to the Moon and Mars.
  NASA Conference Pub. 3360 - Shielding Strategies for Human Space Exploration.
  Sussingham_99.pdf - Forty Years of Developement of Active Systems for Radiation Protection of Spacecraft.
  Townsend_00.pdf - Overview of active methods for shielding spacecraft from energetic space radiation.
  NASA: Can People Go to Mars? 2005

Exposure Papers

- International Commission on Non-Ionizing Radiation Protection: Guidelines on Limits of Exposure to Static Magnetic Fields
  Shinn_94.pdf - GALACTIC COSMIC RAY RADIATION LEVELS IN SPACECRAFT ON INTERPLANETARY MISSIONS.

Setlow_99.pdf - The U.S. National Research Councilâ€™s views of the radiation hazards in space.

Schenck_00.pdf - Safety of Strong, Static Magnetic Fields.

Coutgnet_05.pdf - Radiation Exposure and Mission Strategies for Interplanetary Manned Missions (REMSIM).

deVocht_06.pdf - Critical Analysis of Active Shielding Methods for Space Radiation Protection.

Environmental Health Criteria Document 232: Static Fields

GCR Papers

- Wilson_94.pdf - GALACTIC COSMIC RAY TRANSPORT METHODS: PAST, PRESENT, AND FUTURE.

  Mewaldt_96.pdf - Cosmic Rays.

Related Papers

- Hertweck_58.pdf - (German) Particle Trajectories in the presence of a straight wire.

  Winglee_00.pdf - Mini-Magnetospheric Plasma Propulsion: Tapping the Energy of the Solar Wind for Spacecraft Propulsion.

  Lemaire_03.pdf - The Effect of a Southward Interplanetary Magnetic Field on Stormer's Allowed Regions.

  Winglee_04.pdf - Advances in Magnetized Plasma Propulsion and Radiation Shielding.

  Kress_04.pdf - Dynamic modeling of geomagnetic cutoff for the 23â€“24 November 2001 solar energetic particle event.

  Smart_06.pdf - A review of geomagnetic cutoff rigidities for Earth-orbiting spacecraft.

  O'Neill Senior Thesis - Computer Simulations of Radiation Shielding Materials for Use in the Space Radiation Environment.

Presentations

- Michigan Shielding Conference PDF

NASA Space Radiation Shielding Program PDF

2006 Plasma Seminar, Darin Knaus PDF PPT

2007 Plasma Seminar, Simon Shepherd PDF ODP

- NIAC Reports
- M2P2
- Winglee Phase I - 1 page
  Winglee Phase I - final report
  Winglee Phase II - 1 page
  Winglee Phase II - final report
- PMWAC
- Slough Phase I - 1 page
  Slough Phase I - final report
- Plasma Magnet
- Slough Phase I - 1 page
  Slough Phase I - final report
  Slough Phase I - report
  Slough Phase II - 1 page
  Slough Phase II - report

Plasma Magnetic Shield

- Slough Phase I - 1 page

MIT Solonoid

- Hoffman Phase I - 1 page
  Hoffman Phase I - final report

Electrostatic Shield

- Buhler Phase I - 1 page
  Buhler Phase I - final report

SAPIENZA
UNIVERSITÀ DI ROMA

7 Chapter 7
Electrons Deflection Experiment

7.1 Abstract

It is not so easy and at low costs to find a source of protons radiation for the experiment, so how can we prove the protection system shown in the previous chapter ?

An alternative source of charged particles we could use is a CRT (Cathode Ray Tube) like TV CRT, this source of particles is easier to find then the protons source.

The idea is to locate an antenna at the opposite side with respect to a CRT normally supplied.

When the antenna start the emission of the circularly polarized EM wave, the brightening point in the middle of the CRT Screen should disappear or goes out of focus because of the electron beam deflection. Obviously in order to satisfy all the conditions, the right EM wave power and frequency are required.

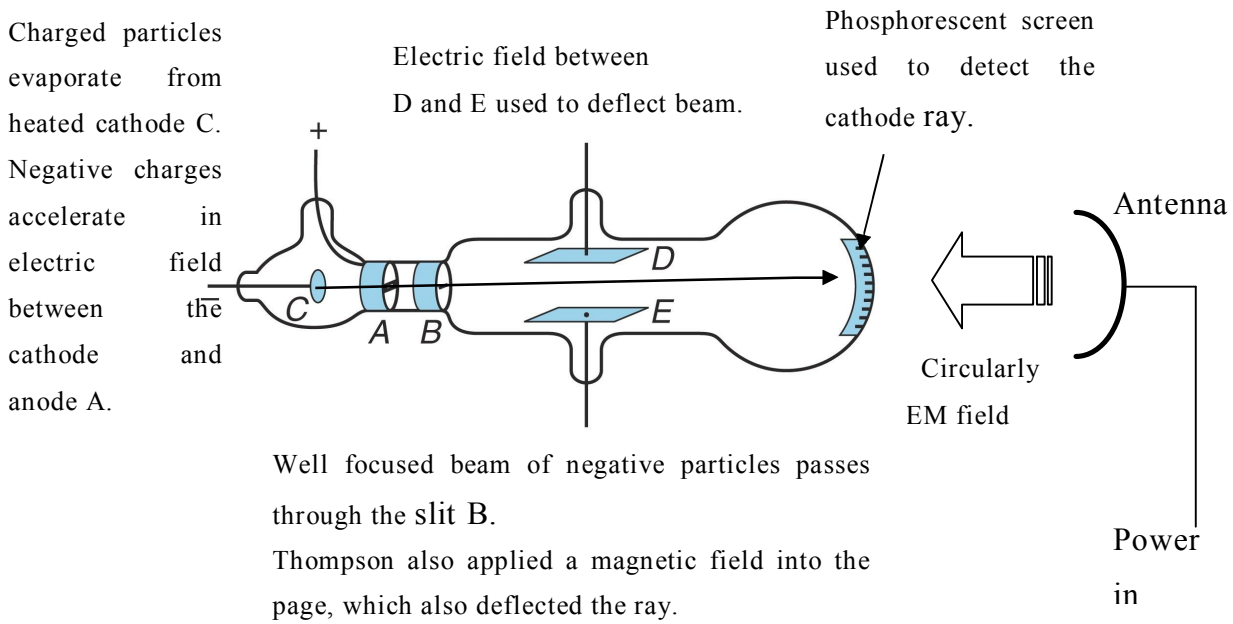

Figure 313: schematic of the CRT and Antenna

In order to measure ***q/m*** it is essential to know the velocity of the electrons.

$$F = qE \quad \Rightarrow \quad a = \frac{q}{m}E \qquad \text{eq 158}$$

7.2 The electron accelerator in your living room 1938

268 RADIO NEWS FOR NOVEMBER, 1933

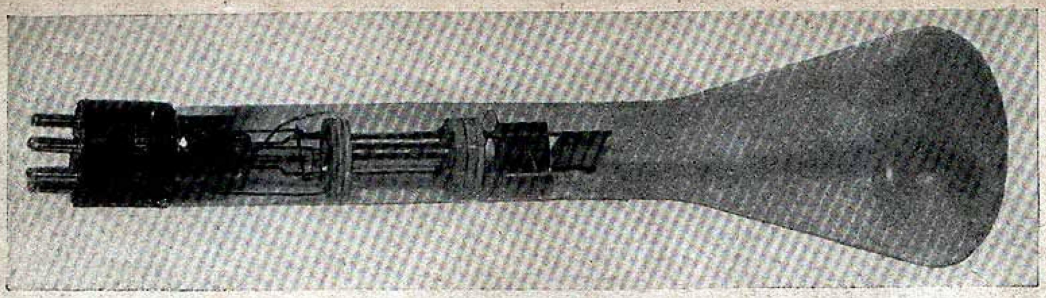

The How and Why of

CATHODE RAY TUBES

For Television and Other Uses

This series of articles will fill a long-felt need for practical construction data on cathode ray equipment. Complete details for making a cathode ray oscilloscope and television equipment will be given and the manifold applications of this equipment discussed

By John M. Hollywood
and Marshall P. Wilder

CATHODE ray tubes are essentially devices indicating by means of the movement of a spot of light on a screen, the value of a voltage or current applied to the proper terminals. Unlike the usual meter, the only moving part is a beam of electrons, which has such little inertia that there is practically no time lag between application of a voltage and the movement of the spot of light. The power consumed in moving the beam is practically negligible. The cathode ray tube may also be used as an ammeter by causing the unknown current to flow through coils, and applying the resulting magnetic field to the cathode ray tube; the power required to move the spot of light will then be of about the same value as that required by the ordinary ammeter, but unlike the ordinary instrument, a change in the flow of current will be indicated instantaneously by the movement of the spot. These characteristic features have made cathode ray tubes exceedingly useful for many purposes, and now that relatively inexpensive tubes which give very good performance are commercially available, the next few years will probably see an increasing use of this instrument by all persons interested in electrical measurements.

The electrode structure of the first cathode ray tubes was similar to that illustrated in Figure 1. In these tubes, the electrons were attracted from the cathode to the anode, which was pierced by a small hole. Some of the electrons, now moving with high velocity, would pass through this hole and impinge upon the glass wall (screen) of the tube, where a fluorescent light was produced. It was found that the electrons moved in straight lines unless deflected by a magnetic or electric field.

Until recently, in almost all cathode ray tubes the electron beam was focused to a spot on the screen by introducing a small amount of an inert gas into the tube. Heavy positive ions would be formed and collect along the beam, neutralizing the space charge of the electrons and condensing the beam into a thin line. This method had many objections. To focus the spot, the gas pressure had to be regulated by varying the cathode temperature; and as the tube became older some of the gas would become absorbed so that the cathode temperature had to be raised to dangerous limits, shortening its life. Positive ion bombardment of the cathode also cut short its life.

When deflecting plates were inserted in the tube, to which a voltage could be connected so that the electron beam would be sent in proportion to the voltage, the ionized gas would cause leakage currents to flow between the plates so that the instrument could not be

Cathode Tubes in Television

THE radio public has been hearing and reading much about the wonders of the cathode ray tube, and particularly of its recent application to television experiments which have been going on behind the locked doors of some of the world's leading laboratories. But there has been almost a total lack of authentic and practical information on the cathode ray tubes themselves; and a complete lack of any kind of constructional data on television, laboratory or other apparatus employing these tubes. RADIO NEWS therefore takes pleasure in presenting this series of articles. This first concerns itself primarily with the theory and design of the tube. Subsequent articles will provide detailed data to enable the builder to construct cathode ray equipment at home, including television receivers capable of reproducing images with a degree of fidelity and definition never before possible with home-made apparatus.

—*The Editors.*

THE EARLIEST TYPE OF CATHODE RAY TUBE

This type of tube provided a beam focused on the screen by the introduction of gas in the tube, making the cathode adjustment critical and behavior erratic

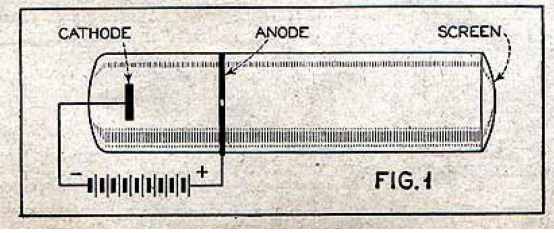

FIG. 1

Cathode Ray Tube (CRT) has the basic ingredients of a scientific accelerator:

- Particle source
- Acceleration scheme
- Focusing scheme
- Beam steering
- Beam observation

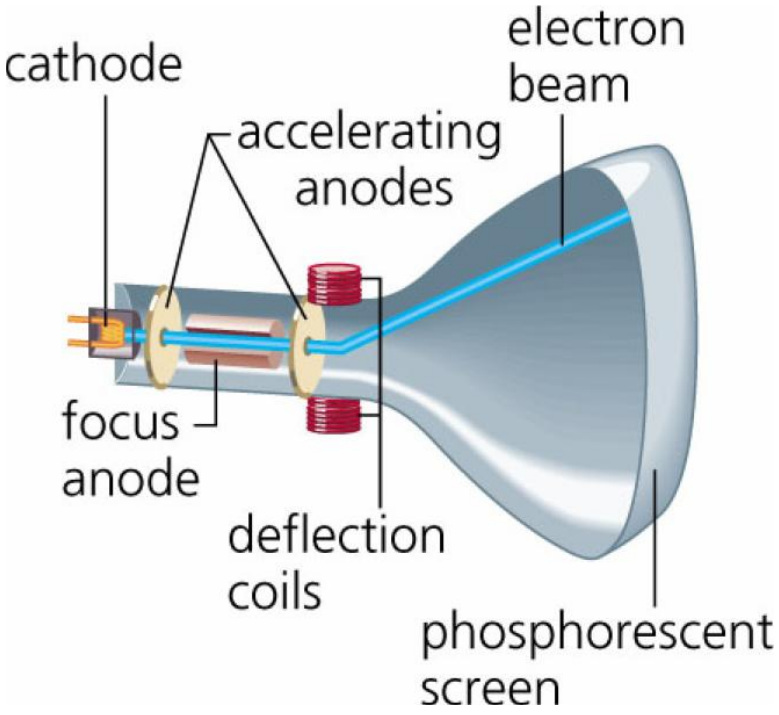

Figure 314: CRT

Particle motion can be found by Lorentz force equation:

$$\frac{d\vec{p}}{dt} = m_p\vec{a} = \vec{F} = q\left(\vec{E} + \vec{v}\times\vec{B}\right)$$

where : **eq 159**

$\vec{p}$ = Particle Momentum $\vec{v}$ = Particle Velocity q = Particle Charge

$\vec{E}$ = Electric Field $\vec{B}$ = Magnetic field

7.2.1 Particle Acceleration

Starting from:

$$\frac{d\vec{p}}{dt} = m_p\vec{a} = \vec{F} = q\left(\vec{E} + \vec{v}\times\vec{B}\right) \qquad \text{eq 160}$$

Since in the CRT the longitudinal particle acceleration is produced only by mean of the Electric field applied, then we can rewrite the previous equation:

$$\frac{d\vec{p}}{dt} = m_p\vec{a} = \vec{F} = q\vec{E} \qquad \text{eq 161}$$

Suppose no relativistic effect then, the Kinetic energy of the particle is:

$$E_{kin} = \frac{1}{2}m_p v^2 \qquad \text{eq 162}$$

Changes in the Kinetic energy is given by

$$\frac{dE_{kin}}{dt} = 2\frac{1}{2}m_p|\vec{v}|\frac{d|\vec{v}|}{dt} = vm_p|\vec{a}| = \vec{v}\cdot\vec{F} = q\vec{v}\cdot\vec{E} \qquad \text{eq 163}$$

The acceleration from electric field component parallel to the particle velocity is given by:

$$\Delta E_{kin} = q\vec{v}\cdot\vec{E}\Delta t = qL_{acc}E_{\|} \quad \Rightarrow \quad \Delta E_{kin} = qU_{acc}$$

where eq 164

$\vec{v}\Delta t = L_{acc}$ is the distance crossed by the electron with velocity $\vec{v}$ in the time Δt

$U_{acc} = L_{acc}E_{\|}$

7.2.2 Velocity of electrons within a CRT

In order to find the Electrons velocity we need in the equation of the particle motion found in chapter six, we can use a typical small TV set; then we should have:

- Accelerating Voltage $E_{\|} \cong 15.000$ V as a consequence the electron Energy Gain is:
  - Energy gain/electron ≅ 15.000 eV=15 keV (1eV=1.6×10^{-19} Joule)
- Typical Number Particle ≅ 1000.000
- Beam size ≅ mm
- $L_{acc} \cong$ 0.1 m

$$\Delta E_{kin} = q\vec{v}\cdot\vec{E}\Delta t = qL_{acc}E_{\|} \quad \Rightarrow \quad \Delta E_{kin} = qU_{acc}$$

with

$$U_{acc} = L_{acc}E_{\|} = 0.15\times15.000$$

$$\Delta E_{kin} = qU_{acc} = 1.6\times10^{-19}\times0.15\times15.000 \cong 3.6\times10^{-16} \ (\text{Joule})$$

But:

$$\Delta E_{kin} = \frac{1}{2}m_p(\Delta v)^2 \quad \Rightarrow \quad \Delta v = \sqrt{\frac{2\Delta E_{kin}}{m_p}} \cong \sqrt{\frac{2\times1.6\times10^{-19}\times0.15\times15.000}{0.00091\times10^{-27}}} \cong 28\times10^{6} \text{ m/s}$$

eq 165

Where

- m_p=0,00091x10^{-27} (kg) is the electron mass:
- $q^- \cong 1.60217653\times10^{-19}$ (C) is the electron charge.

In the equation above, we haven't been taken into account the relativistic effect. Consequently in equation of the particle motion we can substitute

- v_p=28.000.000 m/s
- m_p=0.00091×10^{-27} kg

An electron which travels at about 30.000 km/s has a corresponding kinetic energy of about 2.5 keV:

$$v = \sqrt{\frac{2E}{m_e}} \cong \sqrt{\frac{2\cdot2.5\cdot10^{3}\cdot1{,}602\cdot10^{-19}}{0.00091\cdot10^{-27}}} \cong 30000 \ (\text{km/s}) \qquad \text{for electron energy} = 2.5 \ \text{keV}$$

eq 166

7.2.3 CRT and Transverse Particle Deflection effect

Starting again from:

$$\frac{d\vec{p}}{dt} = m_p\vec{a} = \vec{F} = q\left(\vec{E} + \vec{v}\times\vec{B}\right) \qquad \text{eq 167}$$

The transverse magnetic field are used for Electrons beam deflection

$$F_x = qv_zB_y$$
$$F_y = qv_zB_x \qquad \text{eq 168}$$

The Deflection depends on the particle energy and by the transverse field

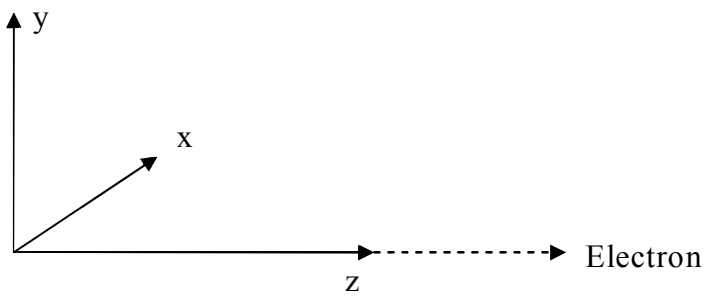

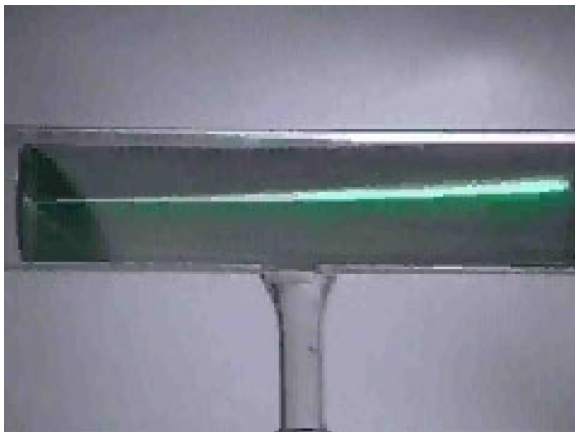

Figure 315: CRT particle deflection

The transverse magnetic field, if applied, produces some forces which have to be taken into account when we apply the circularly polarized EM field to the antenna input.

In fact the circularly polarized EM field tends to deflect the electron beam from the axial velocity direction while, the CRT magnetic field tend to maintain the axial velocity direction.

7.3 Electron Motion under the effect of the Circular Polarized EM field

In our experiment we where interested in creating the required conditions in order to deflect the electrons beam from its longitudinal motion.
Let us to consider the scenario where no CRT transverse deflection Magnetic field is applied and where the electrons are traveling from the Cathode to the anode along axial direction.
The antenna used to deflect the electron beam was located in front of the CRT as in figure below.

For our experiment we have been used typical high frequency components easily available for microwave applications: frequency around 450 MHz, a power amplifier of 500 W and an antenna with gain around 12 dB.
The distance between antenna and CRT were not under the meters since we liked to stay in the so called far field antenna.
In order to cancel any interference from other sources, the experiment has been conducted within sheltered anechoic room.

The configuration experiment scheme was like on figure below.

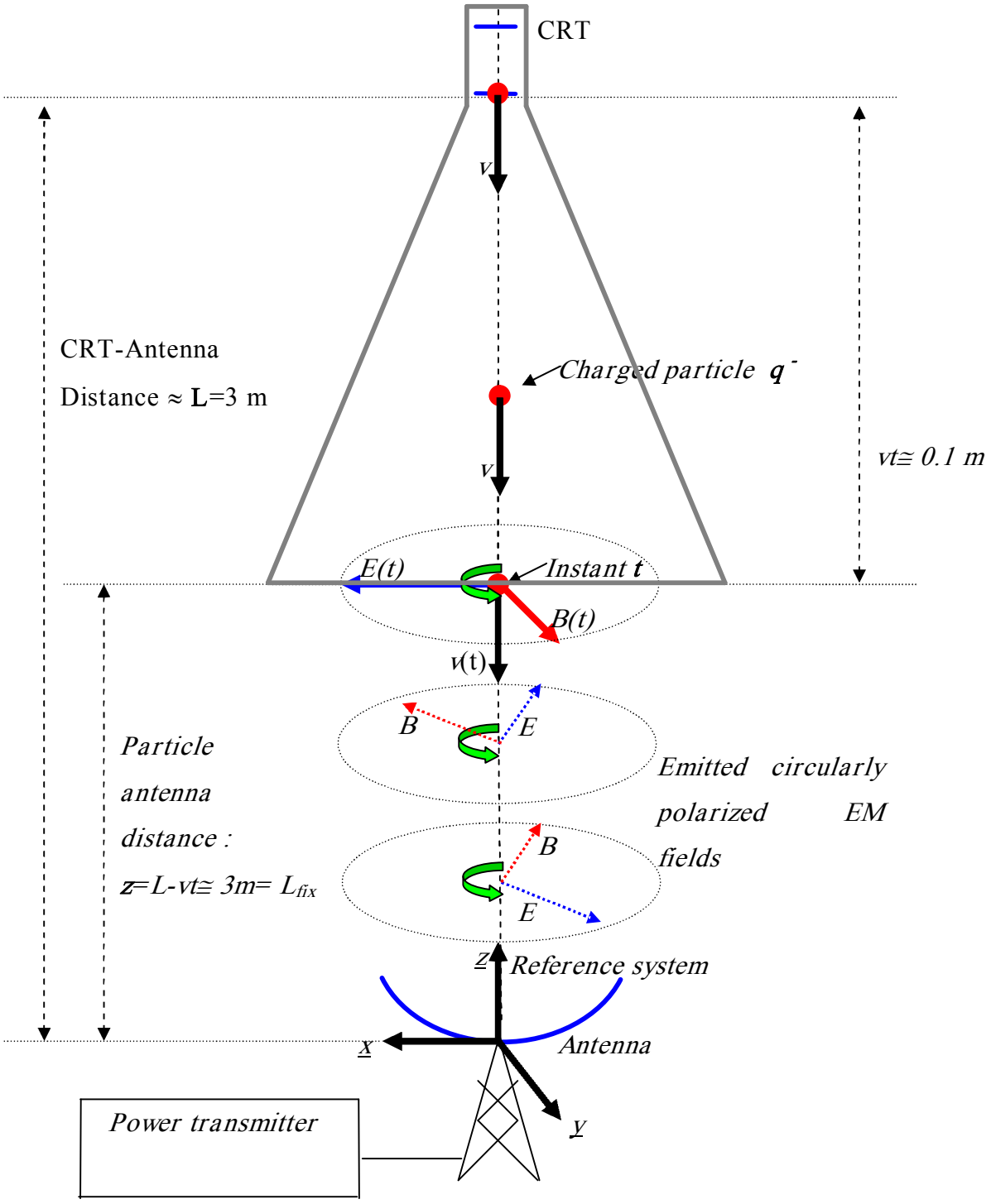

Figure 316

We were interested in study the electrons beam motion directly on the CRT screen.

7.3.1 Hypothesis no CRT transverse control deflection field is applied

7.3.1.1 First integration method

We are going to consider the case where no CRT transverse field deflection is applied. In this scenario the electrons motion equations are those we have been found before in the chapter six:

$$\ddot{x}(t) = \frac{A}{L - v_z t}\cos[\omega' t]$$
$$\ddot{y}(t) = \frac{A}{L - v_z t}\sin[\omega' t] \qquad \text{eq 169}$$

i.e.

$$\begin{cases} x(t) = x(t^*) \\ y(t) = -\dfrac{A}{\omega' v_z}\ln\dfrac{L - v_z t^*}{L} = -\dfrac{q\sqrt{60\,WtGt}}{m_p \omega v_z}\ln\dfrac{L - v_z t^*}{L} \end{cases} \qquad \textbf{eq 170}$$

Where:

$$A = \frac{q\sqrt{60\,WtGt}}{m_p}\left(1 + \frac{v_z}{c}\right)$$
$$\omega' = \omega\left(1 + \frac{v_z}{c}\right)$$
$$\vec{a}_p = \left[\ddot{x}(t)\hat{x} + \ddot{y}(t)\hat{y}\right]$$

Taking in account a particle velocity as we found before we have:

- $M_p \cong 0.00091 \times 10^{-27}$ *(kg)*
- $q^- \cong 1.60 \times 10^{-19}$ *(C)*
- $L \cong 3$ *(m)*
- $v_z \cong$ *19000 (km/s)*
- t varies from zero to the final crossing value L/v_z
- $f \cong 450 \times 10^6$ *(Hz)*
- $Wt \cong 150$ *(W)*
- $Gt \cong 12$ *dB*

Plotting the corresponding motion equation we can find the following figure:

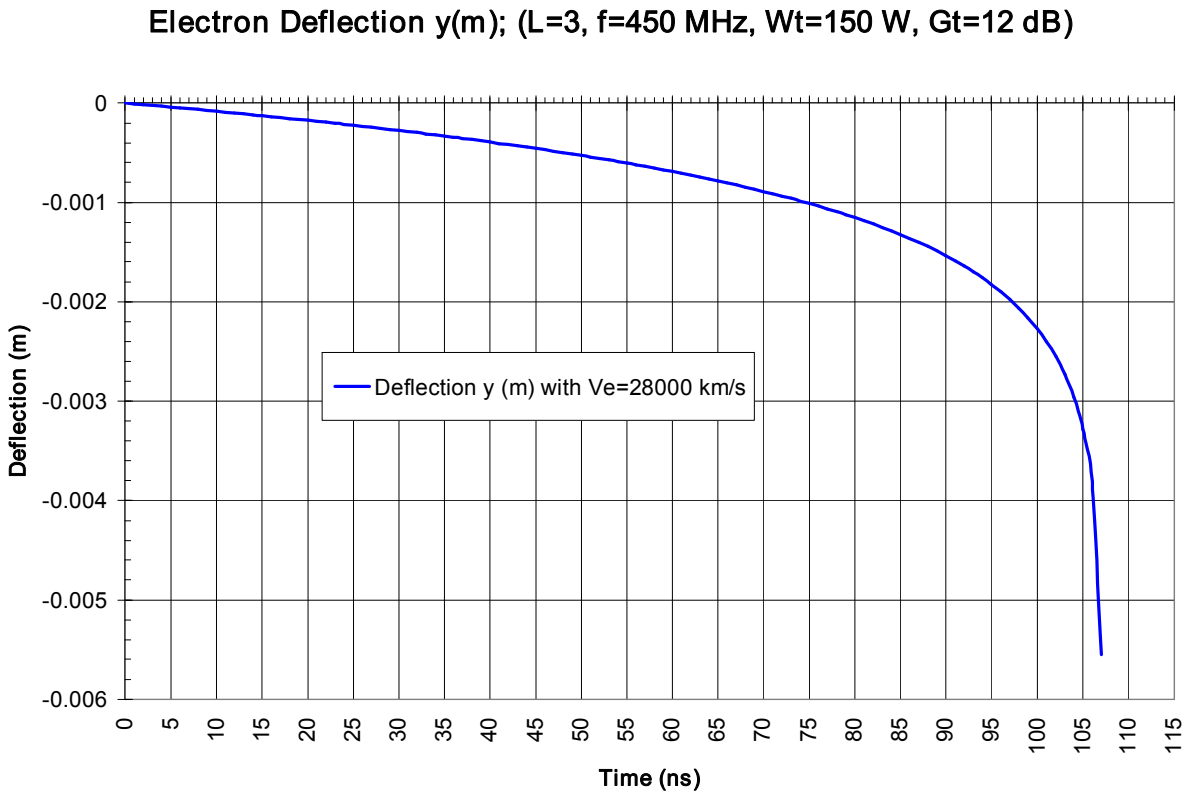

Figure 317: electrons deflection Y(m) with first integration method

At velocity of 28.000.000 m/s, after about 100 ns, the electron potentially, could have crossed almost the distance of about 3 m.

After about 100 ns, the total Y(m) deflection should be about 1÷2 mm.

7.3.1.2 Numerical Integration

Now we can compare the electron deflection values obtained by this integration method with the others values obtained considering Second integration method (Numerical Integration).

We can use the Matlab software to perform the double numerical integration.

The results are close to those obtained with the previous method; the total displacement along Y axes is about 1 mm as before.

According to the equations above the total displacement along X axes is null.

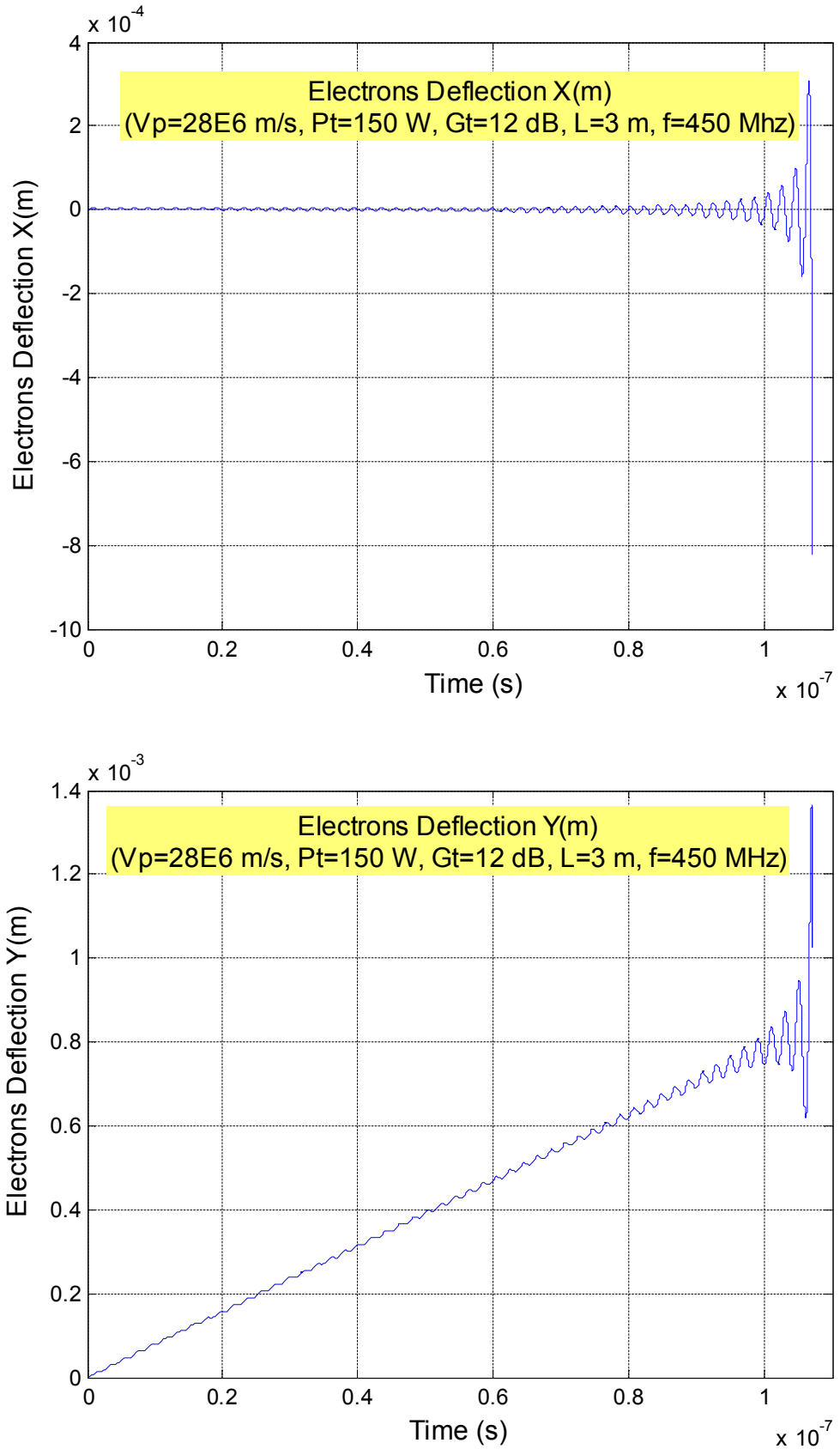

Figure 318: electrons deflection by numerical integration for L=3 *m* and Vp=28000 *km/s*

Note that the deflection along X(t), has an average value of zero, in fact we know that in such direction we do not have any useful deflection with respect to the longitudinal direction. The magnitude of the periodical oscillation increases close to antenna but the average direction of motion remain the same: "longitudinal".
In case of Y(t), instead, we have a useful deflection for the velocity of the electrons beam. The closer to antenna is the electrons; the greater is the deflection effect.

We could ask now what happen to the particle velocity.
Once again using the numerical integration we can observe picture below.
In this picture the electron velocity is sometime positive and sometimes negative; when it is negative it means that the electron is being decelerated by the Lorentz forces which act in the opposite direction with respect to the particle motion. This means that we are wasting some part of the wave energy to decrease and not to increase the particle deflection.

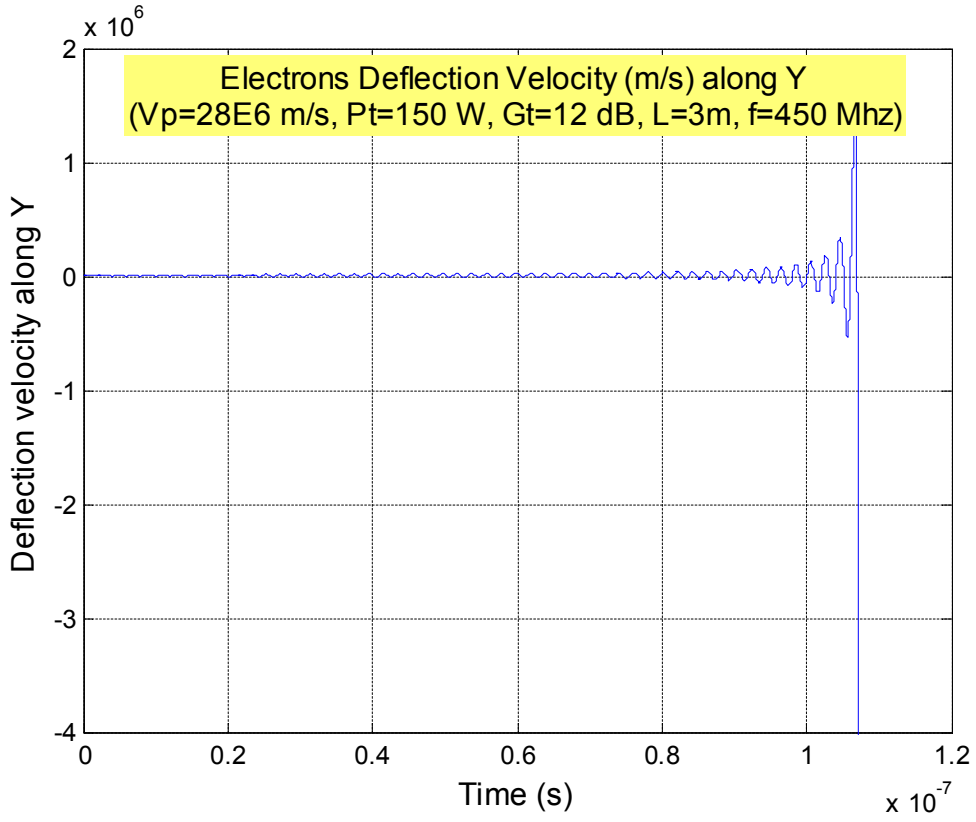

Figure 319: Particle velocity along Y

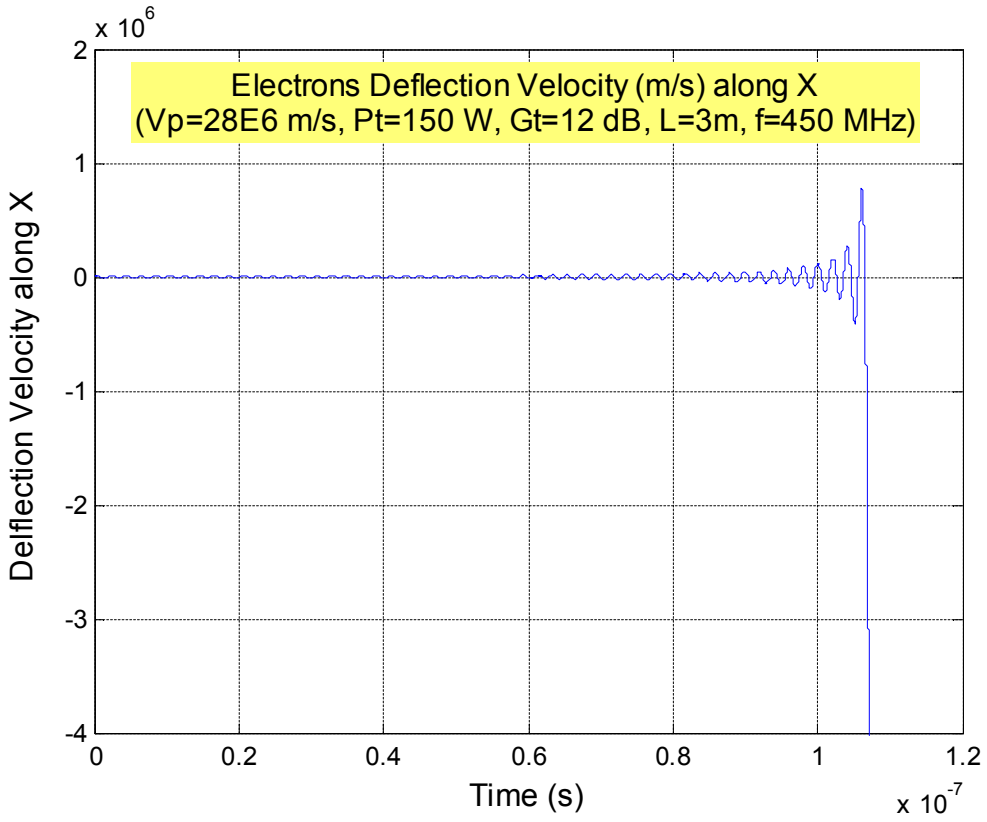

Figure 320: Particle velocity along X

7.3.2 Haw does the Lorentz Forces Act on the charged particle?

Observing the figures above i.e. the particle deflection along Y and the particle velocity variation we can suppose the following electron deflection motion:

- At time $t=t_0=0$ the electric field is horizontal, at this time the particle is affected by the electric field and it start to move horizontally as the electric field impose.
- After t=0, the particle try to follow the rotating force vector applied by the electric field.
- Because of the particle mass, the particle is not able to instantly follow the rotating electric field vector, the higher is the wave frequency the lower is the ability to follow the electric field.

- As a consequence the particle remains confined in a divergent deflection motion along Y axes, bouncing back and forth as a function of the rotating electric field vector versus.

A qualitative picture of the particle motion is shown in figure below:

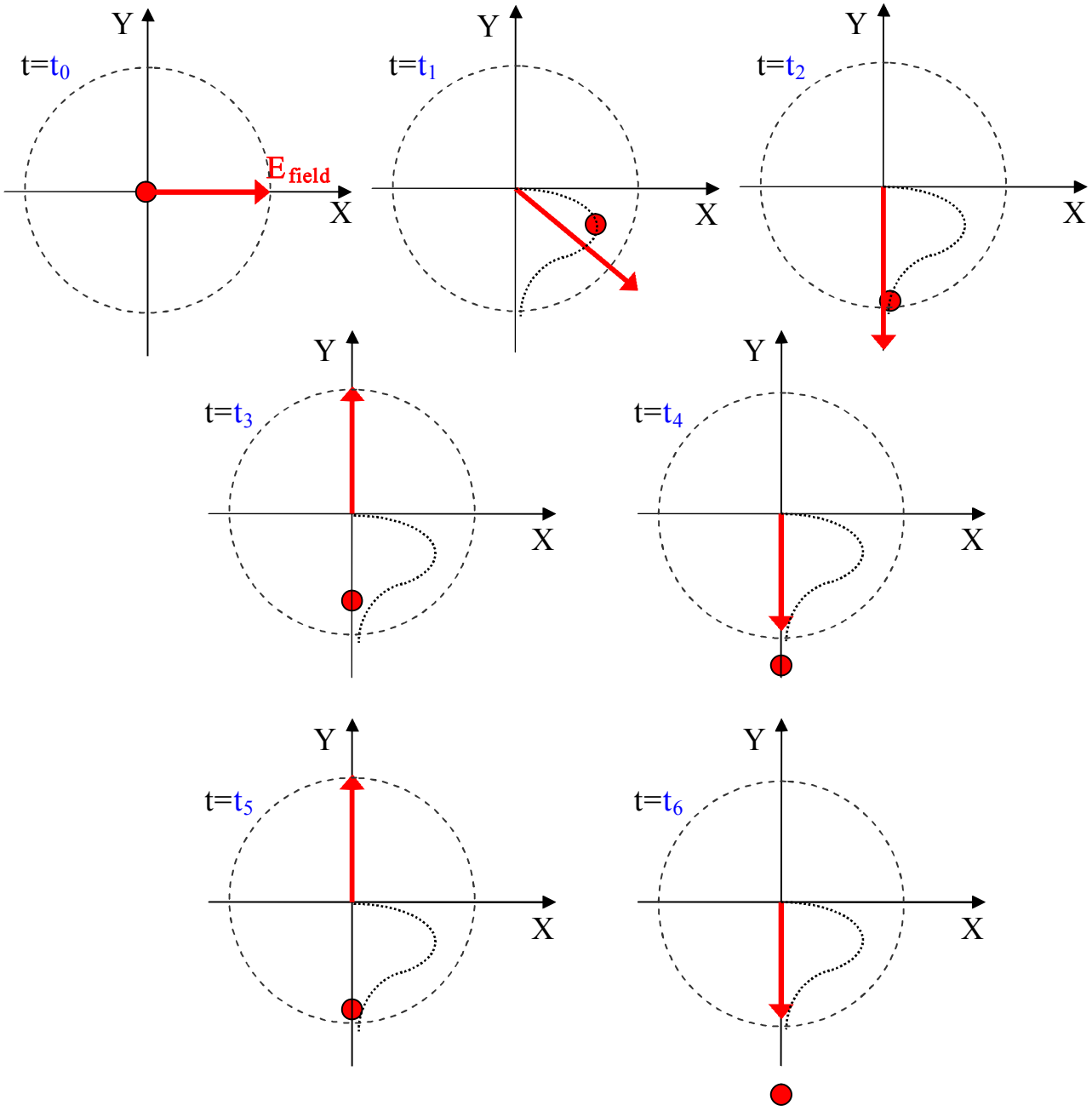

Figure 321: qualitative particle motion pictures

7.4 Particle Deflection using linear polarized antenna

In order to avoid the EM wave energy waste phenomenon, another type of EM wave polarization could be used.

Scenario (a).
Let us suppose an EM wave linearly polarized then, if the particle motion is affected by this EM field the total resulting deflection is null.
This is because the EM field is oscillating back and forth and it does not produce any final deflection with respect to the initial particle velocity direction (see Figure (a) below), the average deflection is zero.

Scenario (b).
Suppose now a different scenario in which we are able to take only one part of the EM wave. Suppose for example to take only the positive part of the EM wave, then there will not be any forces against the particle motion. Each time the EM impulse will produce a positive acceleration in the same direction and versus.
The total resulting effect will be a good charged particle deflection.
This second scenario implies the capability to transmit only the semi-positive part of the EM wave. This could be not easy because the propagation effect is due to oscillating current on the antenna. It is difficult to propagate a continue component from one antenna. Using two antennas propagating the same signal, the particle should be affected by the resulting EM field emitted by the two antennas. Changing the phase of the sinusoidal signal transmitted by one of them in some instant we could obtain the net effect of having only the positive part we need.

Figure below shows, at quality level, the basic idea of Linear Polarization method.
Some theoretical simulations have been performed assuming the same starting data used in EM wave circularly polarized scenario.
The final results are reported here after.

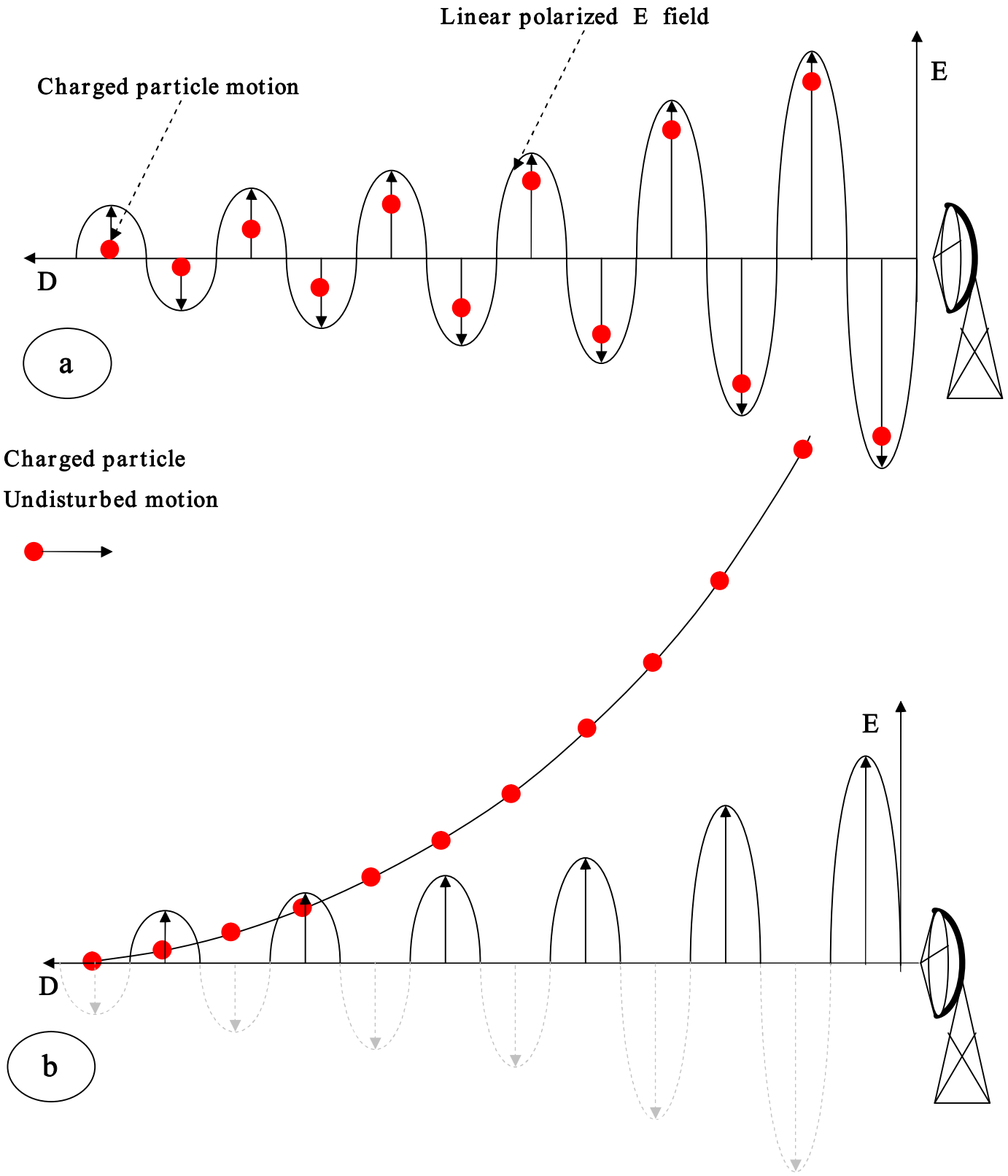

Figure 322: a) particle motion affected by linear polarized E field b) particle motion affected by linear polarized E field transmitted only when the field is positive.

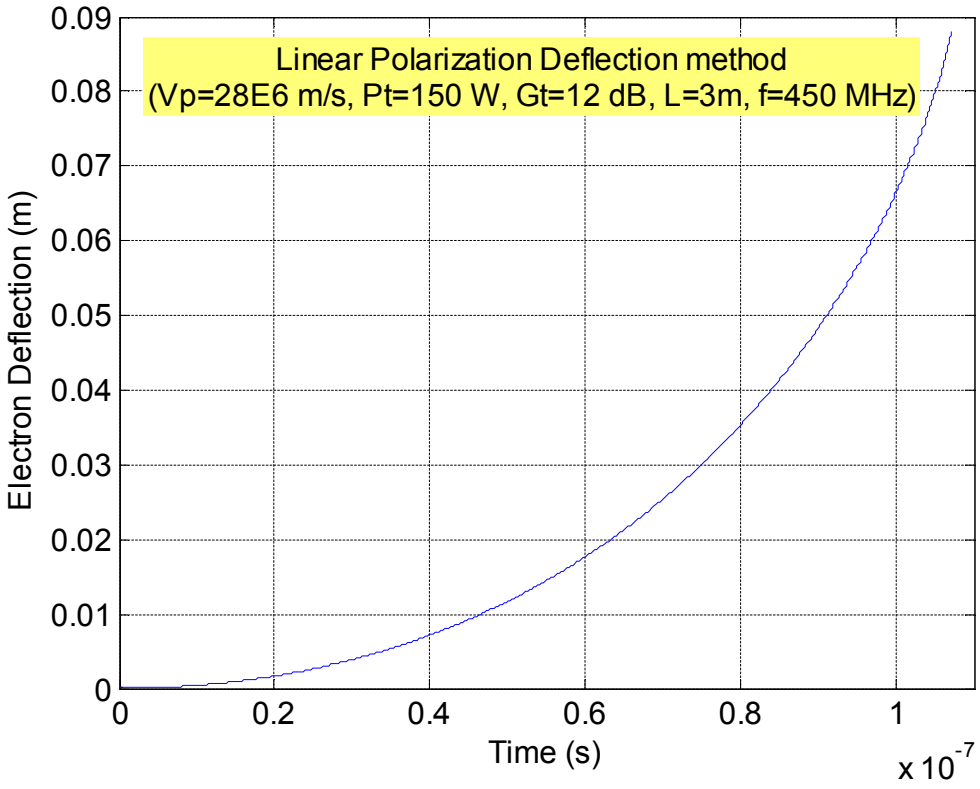

Figure 323: Electron Deflection using Linear Polarization EM field

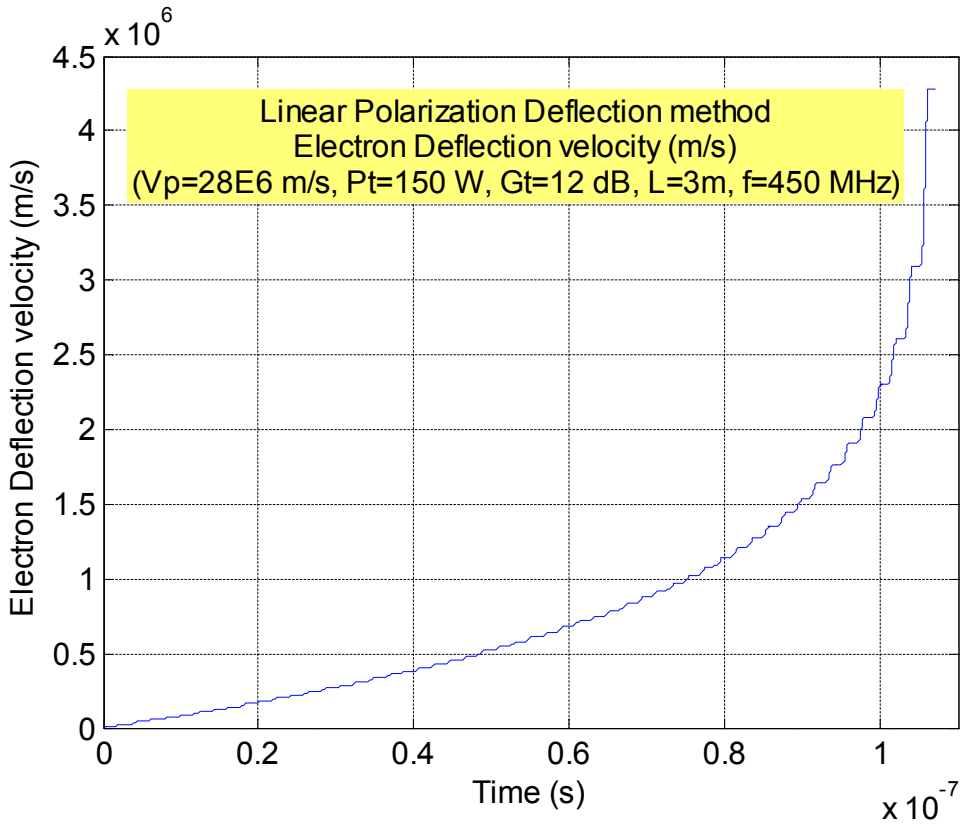

Figure 324: Electron Deflection Velocity using Linear Polarization EM field

On figures above we can note two main behaviors:

- In the Electron Velocity plot, the velocity changes step by step. At each positive impulse of the EM field linearly polarized, the Electron Velocity Deflection increases while between two consecutive impulse remain unchanged.
- In the Electron Trajectory Deflection plot, even when there is no EM impulse, the deflection continues. This behavior is due to the inertia of the particle which has its own mass and so continues its unperturbed motion until the next impulse. The trajectory behavior corresponds to the integration of the velocity curve as shown in the qualitative picture reported below.

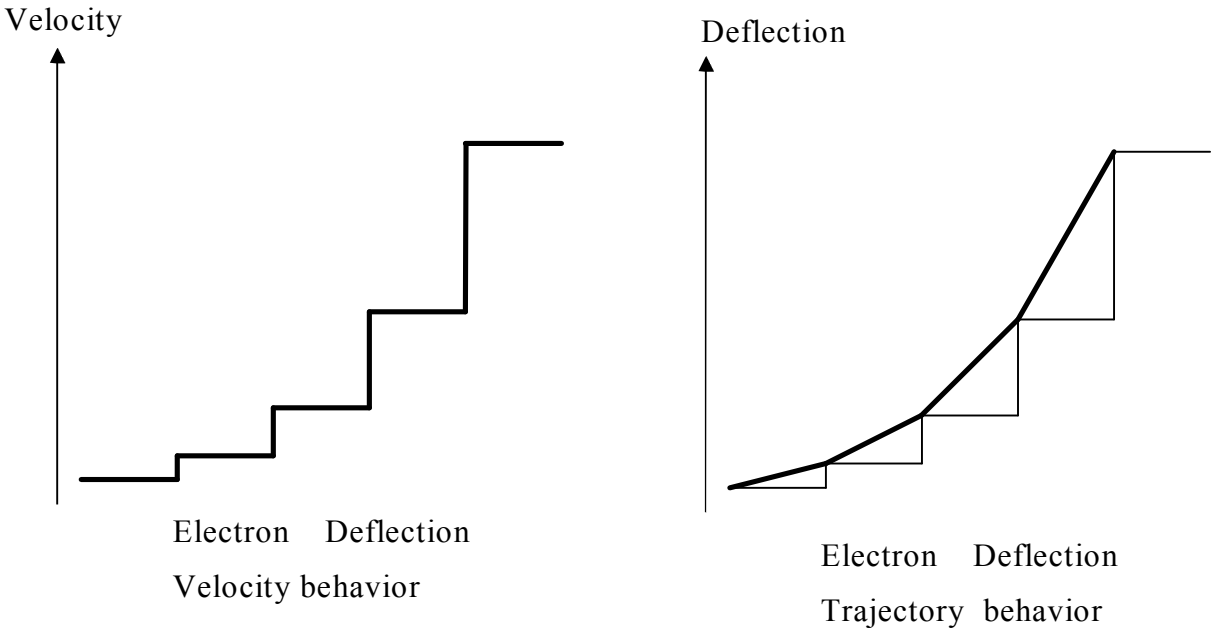

Figure 325: Electron Velocity and Electron Deflection using Linear Polarized EM field

7.4.1 Circular and Linear polarization deflection method comparison

Comparing the simulations results obtained with the two different methods, we can observe that the efficiency of the Linear Polarization method is greater than Circular Polarization method, the difference in deflection is about one order of magnitude.

7.5 TiLab Electrons deflection experiment with EM field circularly polarized

In order to compute the Experiment, the Telecom Italia LAB Structures, Instruments and Shielded room has been used. Here all the used instruments are certified every year.

The used instrumentation is listed below:

- **"W" Series ultra-broadband RF power amplifier 500 W 1000M7**
  - Power Out, cw, linear (less than 1 dB compression 50 ohm)=300 W minimum
  - Frequency response: 100÷1000 MHz.
  - Power Gain 57 dB minimum; the gain is almost linear along the entire band
- **FM1000 Broadband Radio Frequency (RF) measurement system**
  Used in electromagnetic compatibility (RFI/EMC)
- **Tektronix Oscilloscope 475**
- **Anechoic Room (CSA Telecom Italia LAB Torino)**
- **Rhode&Schwarz Signal generator 100 KHz÷2 GHz**
- **Hewlett Packard Power Meter 437B**
- **KATHEREIN Helix Antenna Right Handed Circular Polarization**
  - **Frequency Range 400÷470 MHz**
  - **Gain 12 dBi**
  - **Half-Power beam width 33°**
  - **Max power 560 W**
  - **VSWR<1.2**

Some pictures of the Instruments are displayed below:

7.5.1 Instrumentations in CSA (TILAB Torino)

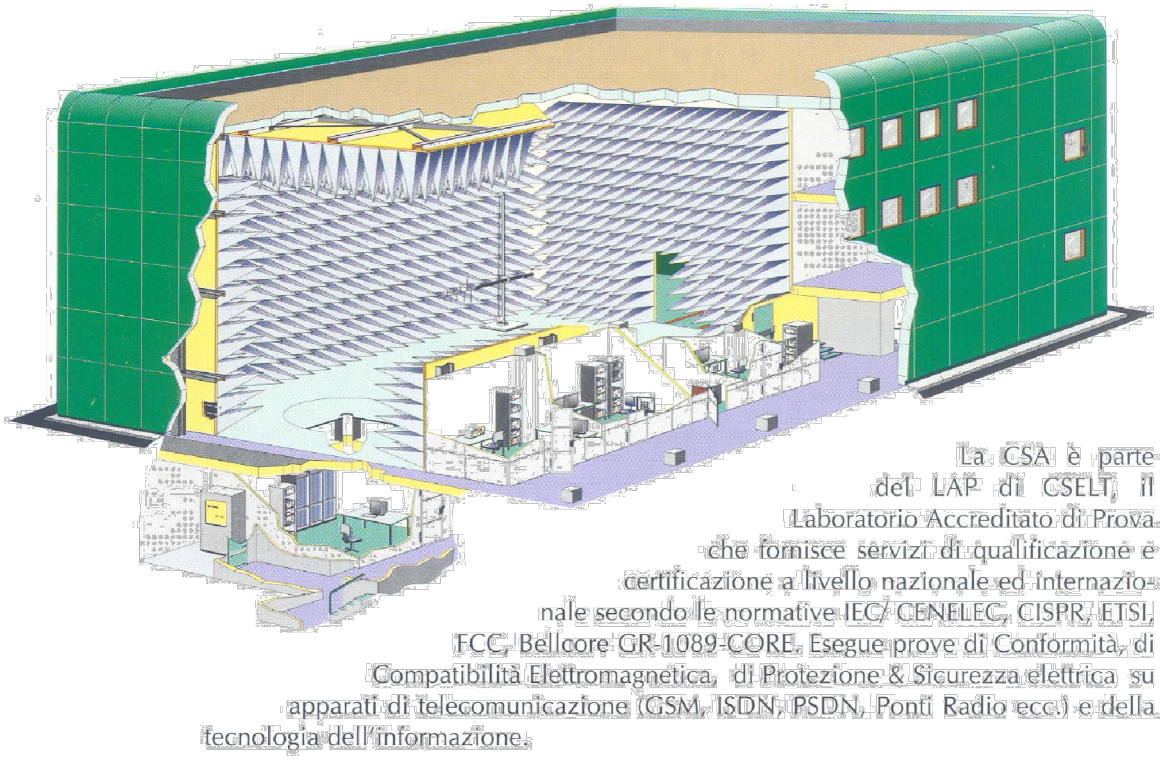

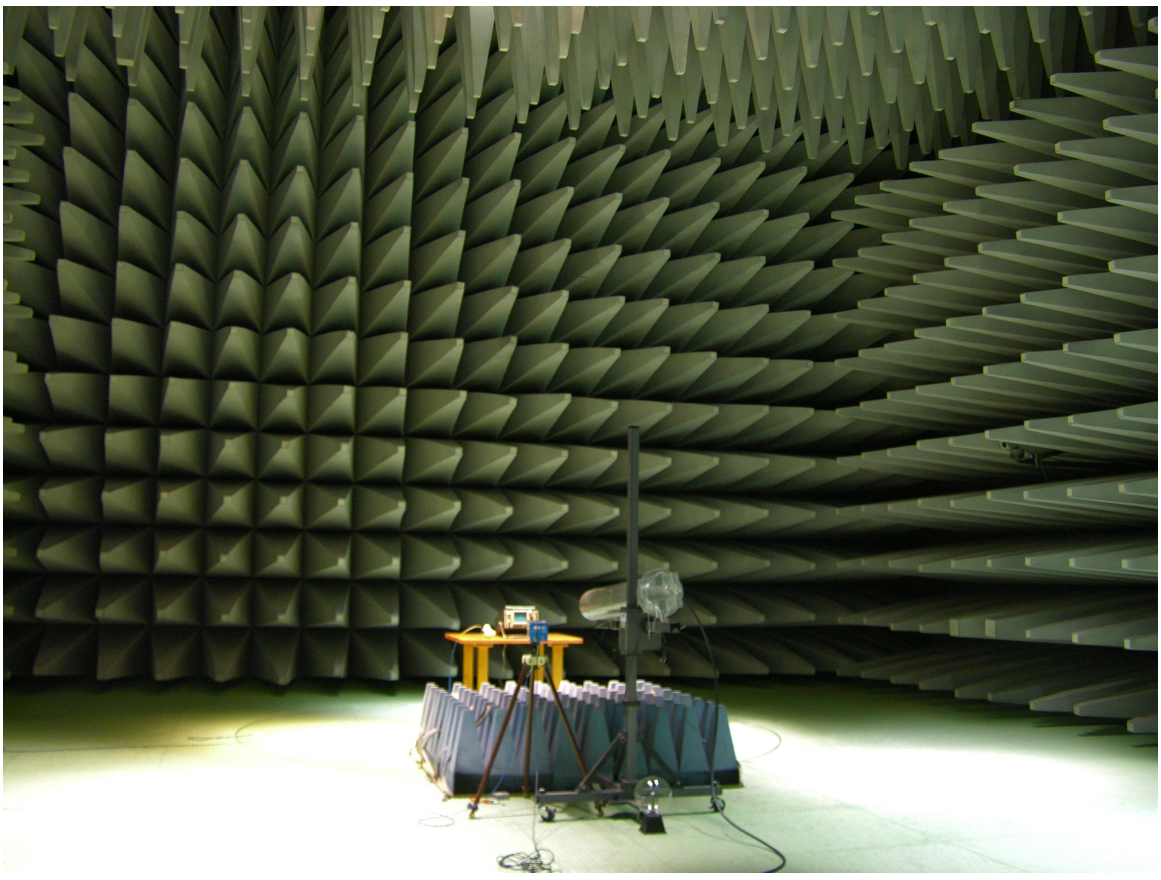

Figure 326: Shielded Anechoic Room (CSA)

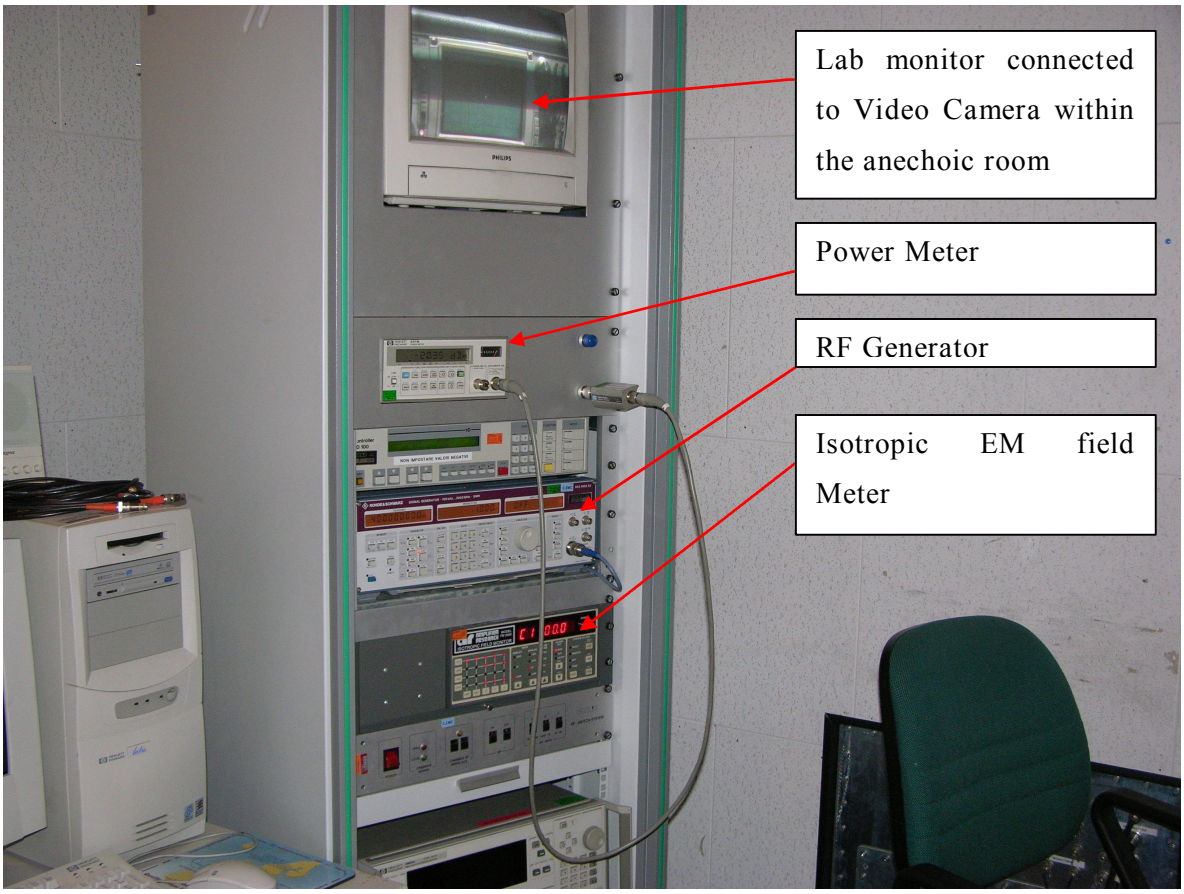

Figure 327: Several instruments used for generating and measuring EM field

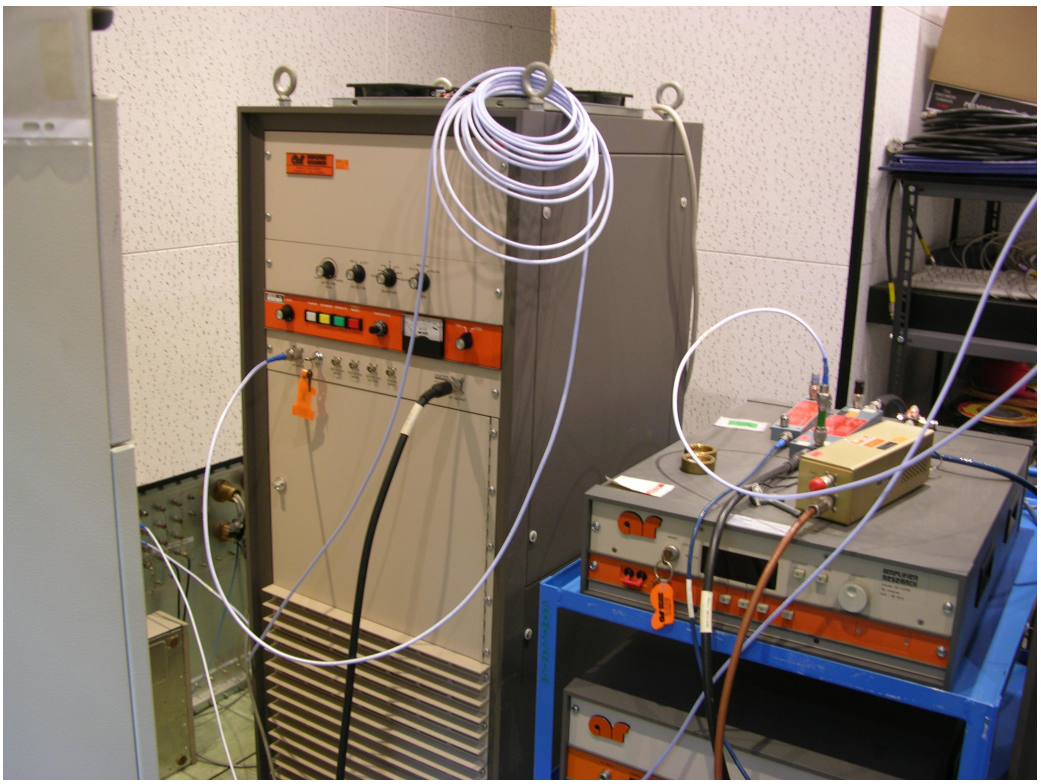

Figure 328: RF Power Amplifier

Helix Antenna
Right Handed Circular Polarization
Half-power Beam Width

400 – 470
RHCP
33°

KATHREIN
Antennen · Electronic

RHCPol Helix 400–470 33° 12dBi

Type No.	K 73 51 21
Frequency range	400 – 470 MHz
Polarization	Right handed circular
Gain	12 dBi (ref. to the circularly polarized isotropic antenna)
Half-power beam width	33°
Impedance	50 Ω
VSWR	< 1.2
Max. power	560 W (at 50 °C ambient temperature)

Scope of supply: Antenna with weather protective casing for straight connectors, mounting kit included.

Material: Antenna: Copper band helix in protective fiberglass tube, colour: Grey.
Reflector screen: Weather-resistant aluminum.
Attachment construction: Hot dip galvanized steel.
All screws and nuts: Stainless steel.

Attachment: To tubular masts of 60 – 125 mm diameter using supplied U-bolts.

Special features: The reflector screen is made of two parts and can be removed for transport.

Grounding: All metal parts of the antenna including the mounting kit and the inner con ductor are DC grounded.

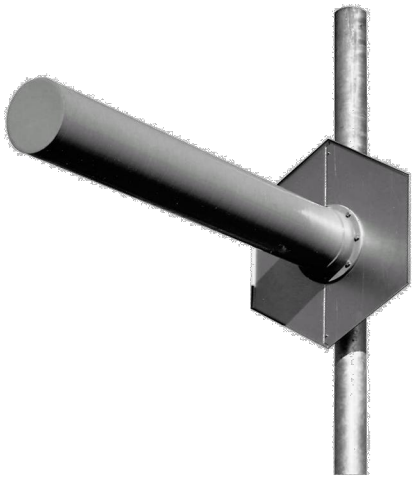

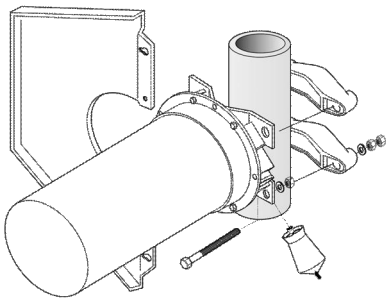

Mounting Instructions

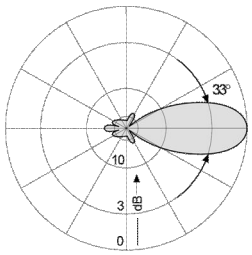

Relative field strength in mid-band

Mechanical specifications	
Input	N female
Weight	12 kg
Wind load	Frontal: 450 N (at 150 km/h) Lateral: 175 N (at 150 km/h)
Max. wind velocity	200 km/h
Packing size	1684 x 388 x 277 mm
Reflector diameter	718 mm
Length / tube dia.	1540 / 204 mm

Internet: http://www.kathrein.de
KATHREIN-Werke KG · Anton-Kathrein-Straße 1 – 3 · PO Box 10 04 44 · D-83004 Rosenheim · Germany · Telephone +49 8031 1 84-0 · Fax +49 8031 1 84-9 73

Figure 329: Circular polarized Antenna

Tektronix Oscilloscope

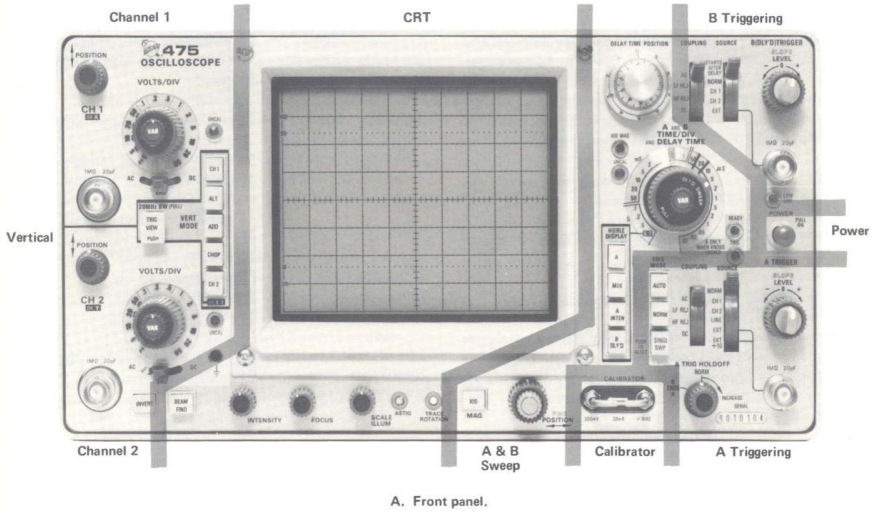

Figure 330: Tektronix oscilloscope

The accelerating voltage is about 15000 V.

The CRT controlling circuit scheme is displayed in figure below.

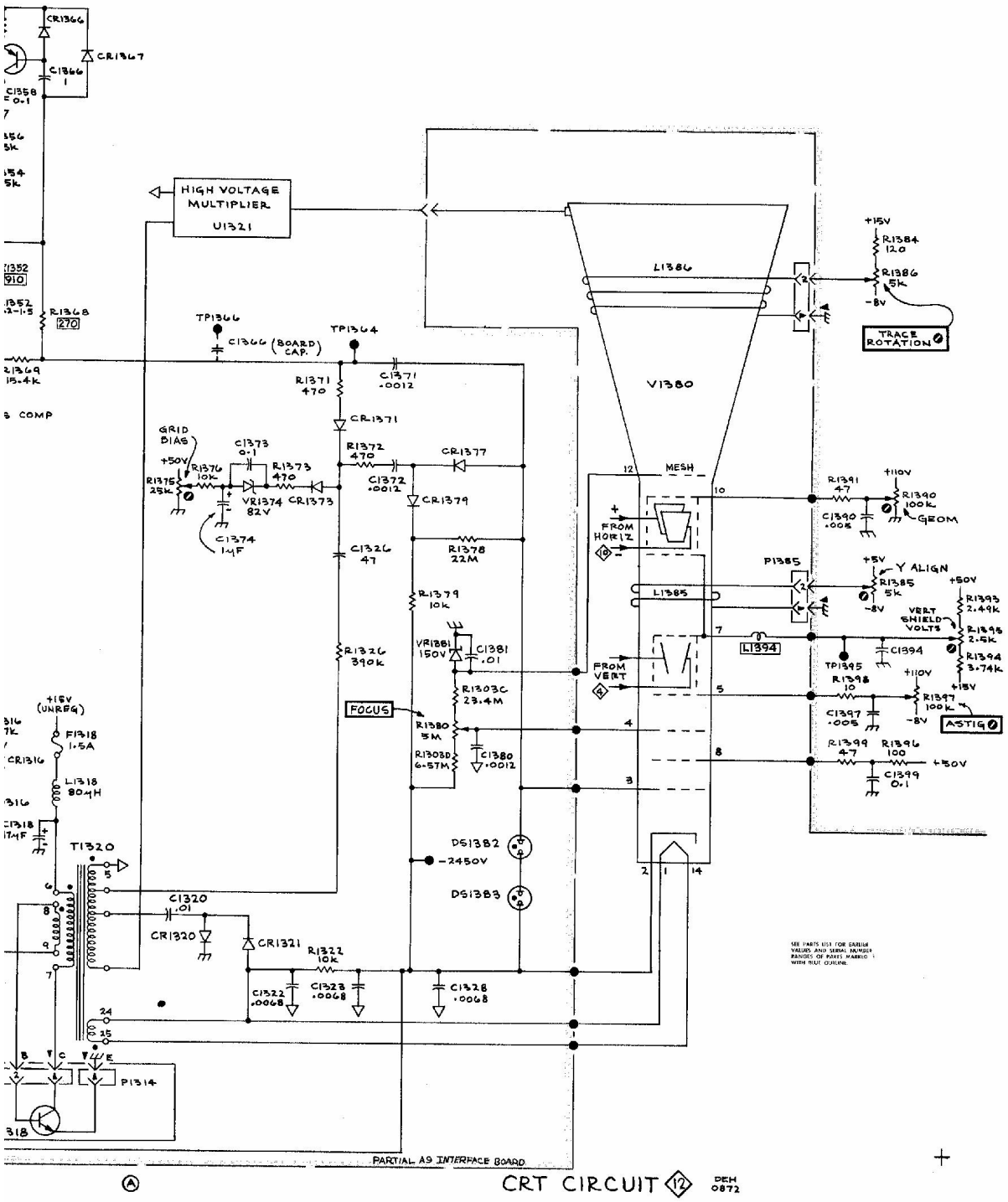

Figure 331: CRT Circuit

7.5.2 Trial Description

Trial consists in deflecting the electrons beam emitted within the CRT (Cathode Ray Tube) of the Tektronix Oscilloscope.

The electrons deflection action has been made by using a Circularly Polarized Electromagnetic field emitted by the Kathrein Circular polarized antenna.
The antenna has been connected to the RF Power Amplifier.
The input of the RF Amplifier has been connected to the output of the RF Generator.

In order to cut multipath and reflection effects, the trial has been confined within the anechoic room.
This room is shielded too and this has permitted us to do the trial under all safety work conditions.
All the commands and observations have been made safely in another shielded room.
The electrons deflection has been observed by using a shielded video camera located close to the Oscilloscope and connected via optical fiber to the display monitor located within our shielded room.
Close to the Oscilloscope has been put an Isotropic RF sensor connected via optical fiber to the RF Isotropic Meter located within our shielded room. This instrument was the purpose to measure the EM filed, radiated by the antenna, close to the Oscilloscope.
Before starting the trial we have tuned all the instruments and power; we have seen that the maximum input power to the RF amplifier was -3 dBm.
Above this power level we would have been incurred in Amplifier power input saturation and consequently in the non linear distortion phenomenon.
The trial has been made by using two power reference values at the input of the amplifier:

Phase a) **Pin=-10 dBm at a frequency of 450 MHz**

Phase b) **Pin=-3 dBm at a frequency of 450 MHz**

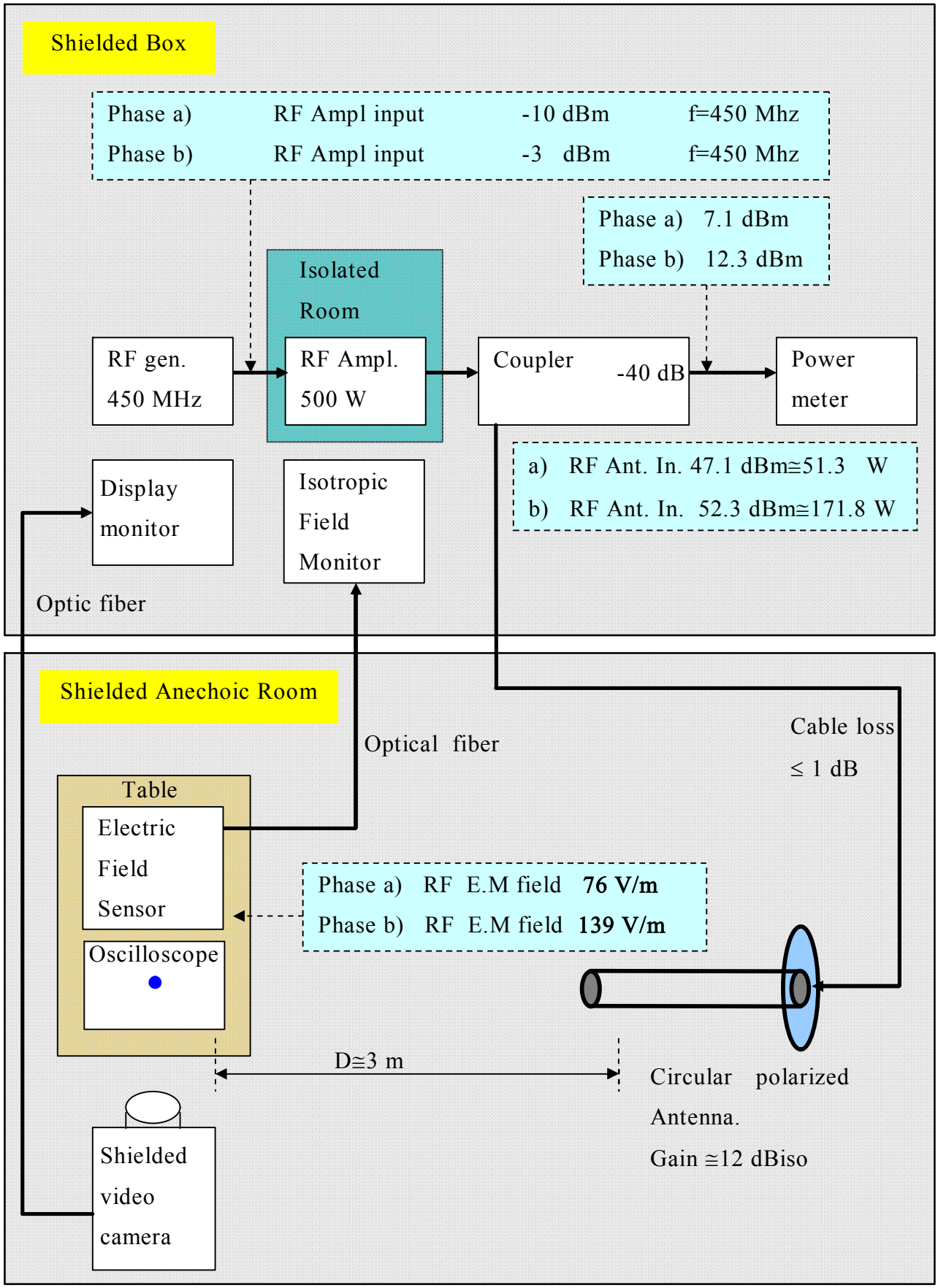

Figure 332: laboratory measurement system

The **Theoretical** Electric Field close to the oscilloscope was:

$$Theoretical \quad \left|\vec{E}\right| = \sqrt{2\eta_0 \frac{WtGt}{4\pi r^2}} = \sqrt{2\eta_0 \frac{WtGt}{4\pi (L-z)^2}} \cong \frac{1}{(L-z)}\sqrt{60\, WtGt}$$

$$\Downarrow$$

$$Theoretical \quad \left|\vec{E}\right|_{phase-a} \cong \frac{1}{3}\sqrt{60 \cdot 51.29 \cdot 15.85} = 73.61 \quad V/m$$

$$Theoretical \quad \left|\vec{E}\right|_{phase-b} \cong \frac{1}{3}\sqrt{60 \cdot 171.79 \cdot 15.85} = 134.7 \quad V/m \qquad \text{eq 171}$$

where :

$$\left|\vec{H}\right| = \frac{\left|\vec{E}\right|}{\eta_0} \qquad B = \mu_0 \, \mathrm{H} \qquad \mathrm{L - z} \cong 3\mathrm{m}$$

Since the **measured** Electric Field was about:

$$Measured \quad \left|\vec{E}\right|_{phase-a} \cong \frac{1}{3}\sqrt{60 \cdot 51.29 \cdot 15.85} = 76 \quad V/m$$

$$Measured \quad \left|\vec{E}\right|_{phase-b} \cong \frac{1}{3}\sqrt{60 \cdot 51.29 \cdot 15.85} = 139 \quad V/m$$

Then the error is very small and it is about:

$$\left|Error(dB)\right| = \left|20\,Log\left[\frac{Measured \quad \left|\vec{E}\right|_{phase-a}}{Theoretical \quad \left|\vec{E}\right|_{phase-a}}\right]\right| \approx 0.3 \quad (dB)$$

$$\left|Error(dB)\right| = \left|20\,Log\left[\frac{Measured \quad \left|\vec{E}\right|_{phase-b}}{Theoretical \quad \left|\vec{E}\right|_{phase-a}}\right]\right| \approx 0.3 \quad (dB) \qquad \text{eq 172}$$

The error is a function of:

- Cable loss neglected;
- No frequency linearity of the RF Amplifier Gain;
- No frequency linearity of the Antenna Gain;

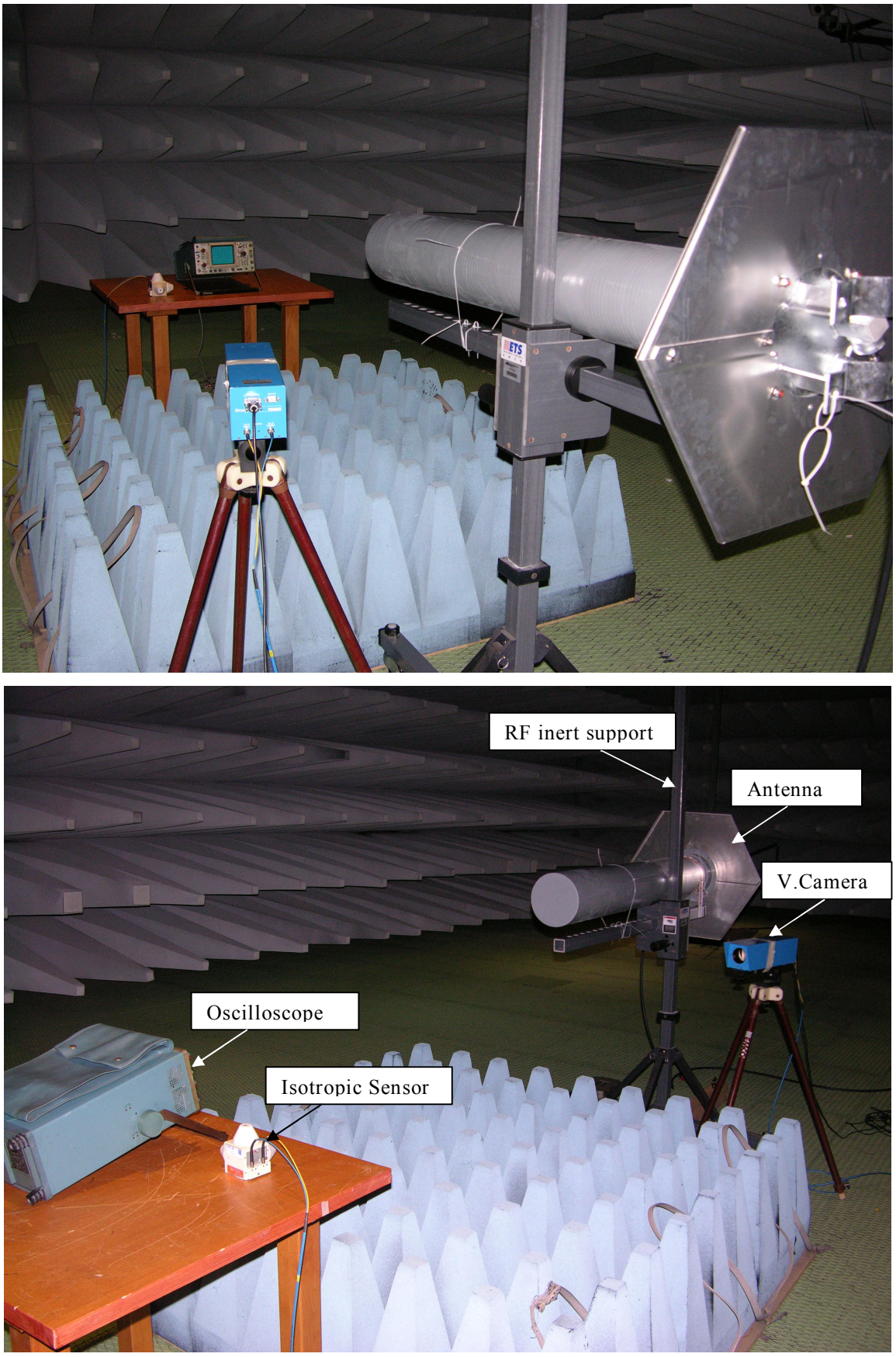

Figure 333: Trial Description

7.5.3 Trial Results

The results of the trial are shown below:

1. When no antenna power is emitted, then the Oscilloscope Screen shows a lighter point located approximately at the center of the display.

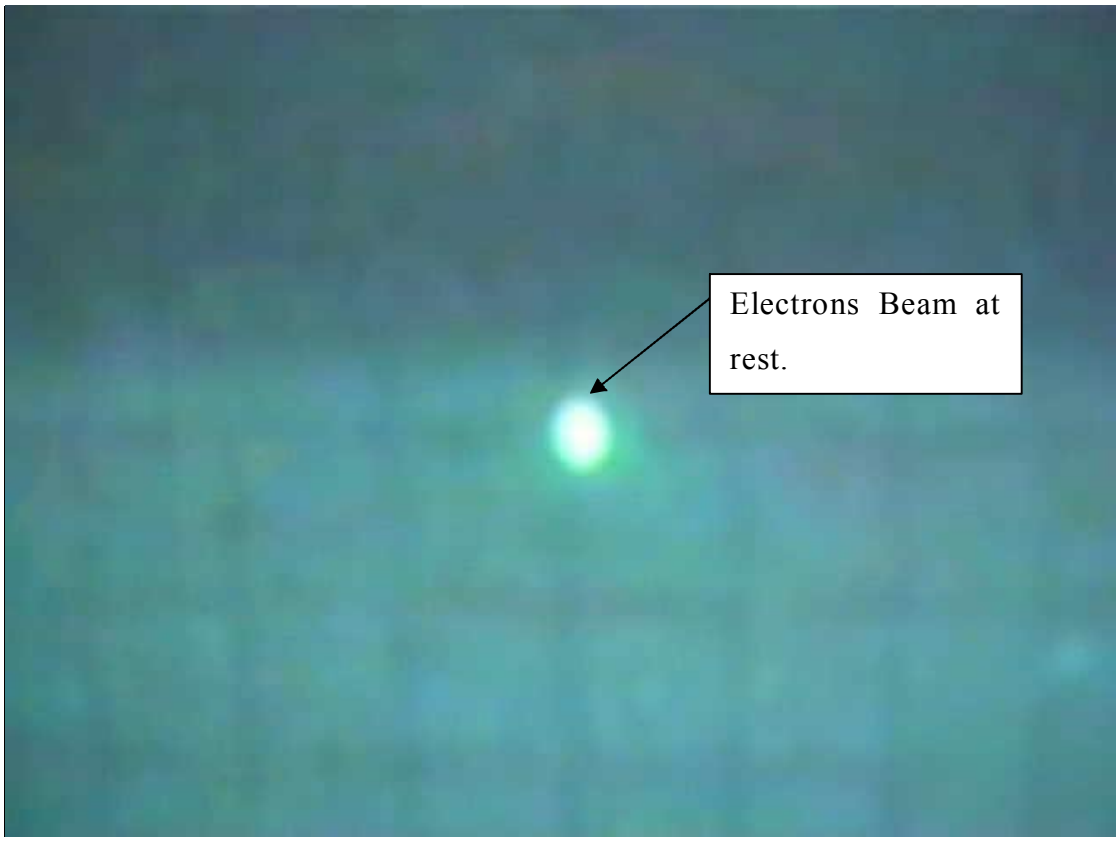

Figure 334: No power is applied

2. When a power of -10 dBm is applied to the input of RF Amplifier, the Electric Field close to the Oscilloscope rise to about 76 V/m. Under these conditions we can observe a deflection of the electron beam. The point in the center of the display become out of focus.

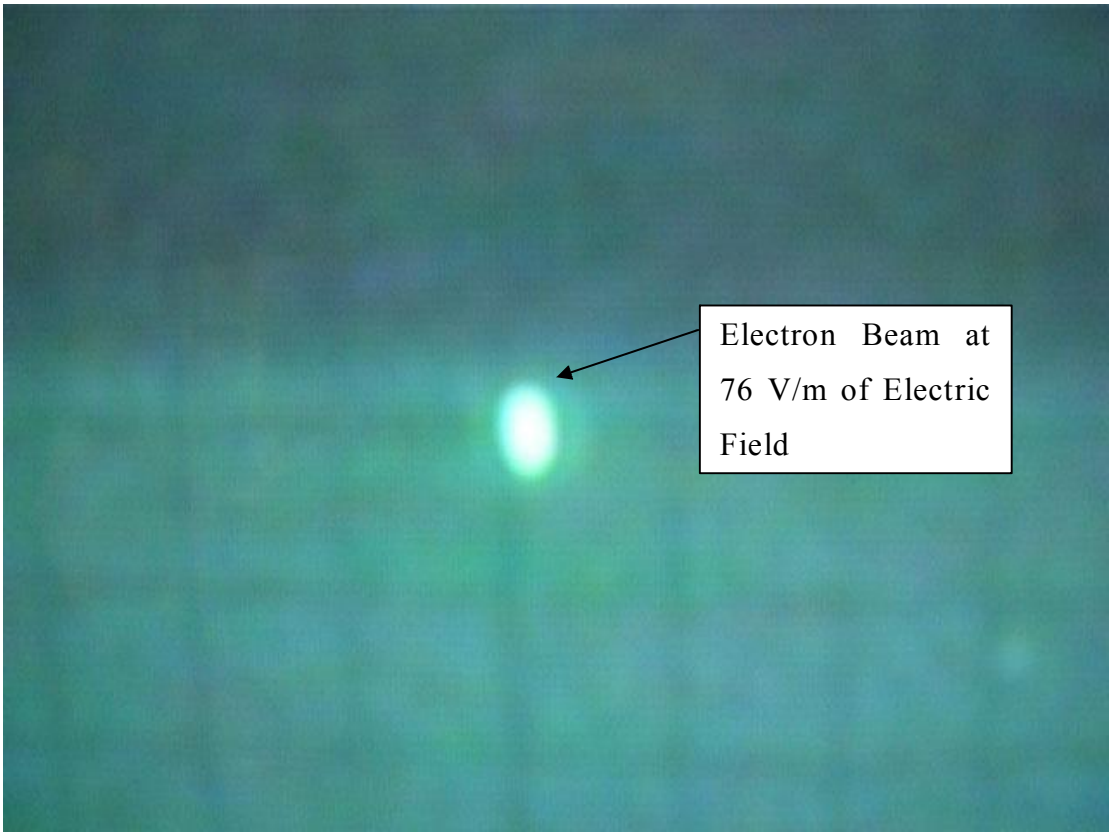

Figure 335: Electric filed of 76V/m is applied on the Oscilloscope

3. When a power of -3 dBm is applied to the input of RF Amplifier, the Electric Field close to the Oscilloscope rise to about 139 V/m. Under these conditions we can observe a deflection of the electron beam greater then the previous value.

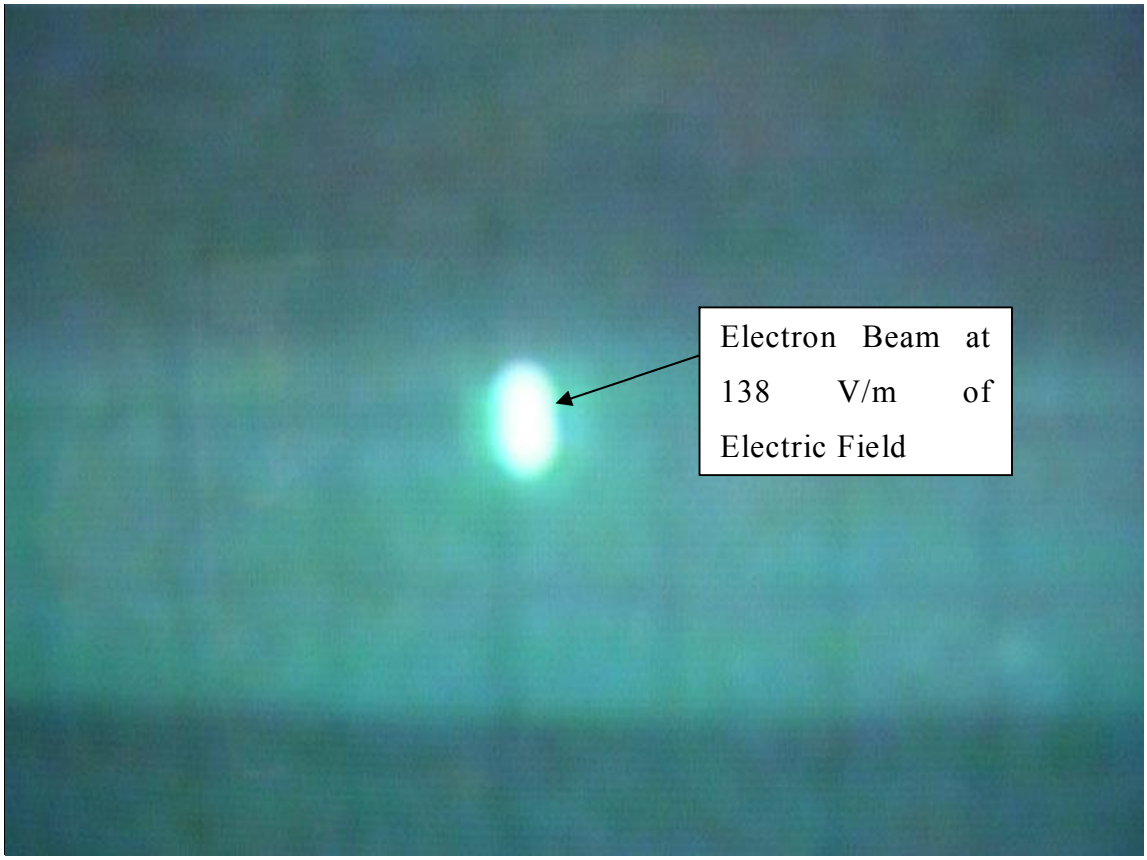

Figure 336: Electric filed of 138 V/m is applied on the Oscilloscope

Some errors could are possible:

The electronic circuits of the oscilloscope could not be shielded enough from Electromagnetic Compatibility (EMC) point of view so the general trial result could also have been bad affected by this Electromagnetic field.

7.6 Conclusions

Trial Results seem to confirm the theoretical mathematical model.
Trial Results seem to confirm the theoretical mathematical model for deflection of the charged particle.
By using an Electromagnetic field circularly polarized we can deflect a charged particle from its original trajectory.
Because of the potential EMC problems of the Oscilloscope, some doubts remain about the electron beam displacement values obtained. In particular the out of focus of the shining point in the center of the screen should be circular in shape. We explain the non circular shape as caused by the internal CRT horizontal deflection field which were dominating over the external electromagnetic field coming from the antenna. This aspect is worthy of study.

In particular the Simulations made by using linearly polarized EM field confirm that this method is more efficient with respect to the circularly polarized EM field, since in this last case some power is wasted in decelerating the charged particle motion. The main problem concerns the propagation of such kind of EM wave.

In a future application in the Space or as an example on the Moon or Mars planet an array of antennas could be designed in order to increase the overall gain of the antenna system, in fact the more is the antenna gain, the higher is the charged particle deflection. In other words the higher is the antenna gain, the more efficient is the protection shielding effect against charged particle coming for example by Solar Wind.

7.7 Reference Table

TILAB documents about the instrumentation reported below:

- "W" Series ultra-broadband RF power amplifier 500 W 1000M7
- FM1000 Broadband Radio Frequency (RF) measurement system
- Tektronix Oscilloscope 475
- Anechoic Room (CSA Telecom Italia LAB Torino)
- Rhode&Schwarz Signal generator 100 KHz÷2 GHz
- Hewlett Packard Power Meter 437B
- KATHEREIN Helix Antenna Right Handed Circular Polarization

SAPIENZA
UNIVERSITÀ DI ROMA

8 Appendix
MATLAB and C code used for numerical integration programs

8.1 MATLAB code

8.1.1 MATLAB code for Circular Polarization

Inizializzazione variabili:

```
num_particles=1;
num_protons=0;
num_neutrons=0;
num_electrons=1;
q_protons=1.6*(10^-19);
q_electrons=1.6*(10^-19);
m_proton=1.67*(10^-27);
m_neutron=1.67*(10^-27);
m_electron=0.00091*(10^-27);
v_particle=28*(10^6);
L_distance=3;
Particle_Crossing_time=L_distance/v_particle;
EM_frequency=450*(10^6);
P_tx=150;
GdB_ant=12;
c=3*(10^8);
A=(((q_protons*num_protons+q_electrons*num_elect
rons)*((60*P_tx*(10^(GdB_ant/10)))^0.5))/(m_proton
*num_protons+m_neutron*num_neutrons+m_electron
*num_electrons))*(1+v_particle/c);
omega=2*pi*EM_frequency*(1+v_particle/c);
dt=10^-13;
niter=(Particle_Crossing_time/dt);
```

Primo ciclo di integrazione

```
t=0;
f1(1)=(A/(L_distance-v_particle*t))*cos(omega*t);
F1(1)=0;
FF1(1)=0;
f2(1)=(A/(L_distance-v_particle*t))*sin(omega*t);
F2(1)=0;
FF2(1)=0;
ascisse(1)=t;
t=t+dt;
```

Secondo ciclo di integrazione

```
for i=2:1:niter;
    f1(i)=(A/(L_distance-v_particle*t))*cos(omega*t);
    F1(i)=f1(i)*dt+F1(i-1);
    FF1(i)=F1(i)*dt+FF1(i-1);
    f2(i)=(A/(L_distance-v_particle*t))*sin(omega*t);
    F2(i)=f2(i)*dt+F2(i-1);
    FF2(i)=F2(i)*dt+FF2(i-1);
    ascisse(i)=t;
    t=t+dt;
end;
```

Stampa risultati

```
plot(ascisse,f1);
plot(ascisse,F1);
plot(ascisse,FF1);

plot(ascisse,f2);
plot(ascisse,F2);
plot(ascisse,FF2);
```

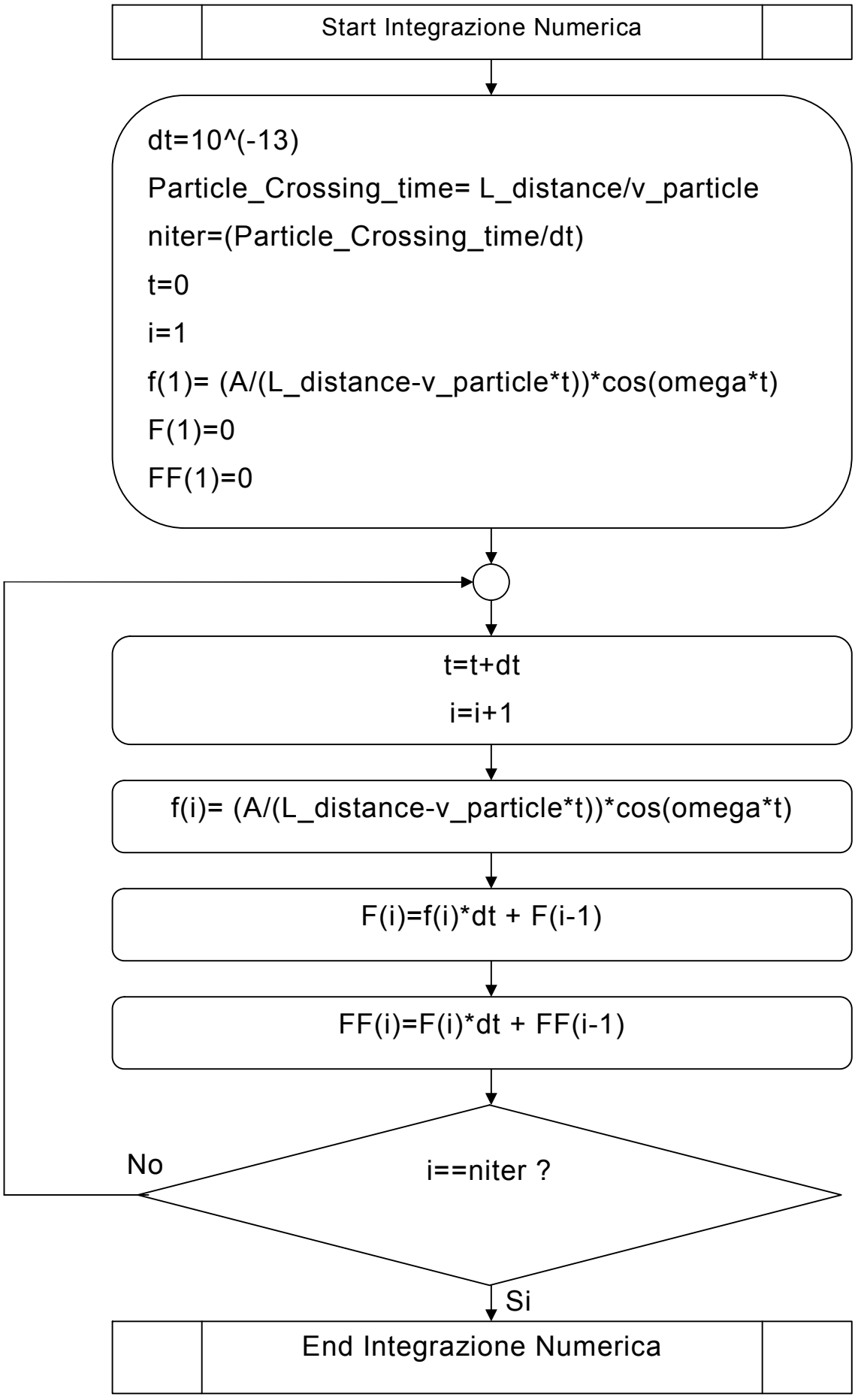
Start Integrazione Numerica
dt=10^(-13)
Particle_Crossing_time= L_distance/v_particle
niter=(Particle_Crossing_time/dt)
t=0
i=1
f(1)= (A/(L_distance-v_particle*t))*cos(omega*t)
F(1)=0
FF(1)=0
t=t+dt
i=i+1
f(i)= (A/(L_distance-v_particle*t))*cos(omega*t)
F(i)=f(i)*dt + F(i-1)
FF(i)=F(i)*dt + FF(i-1)
No
i==niter ?
Si
End Integrazione Numerica

```
%%This code has been used to find the particle trajectory on the Experiment in chapter 7 %%
%% Double Numerical Integration CIRCULAR POLARIZATION %%
%  This method is used to compute a double numerical integration of a certain function %%
%% Input Data %%

num_particles=1;
num_protons=0;
num_neutrons=0;
num_electrons=1;
q_protons=1.6*(10^-19);          %% is the charge in Coulomb of a protons %%
q_electrons=1.6*(10^-19);        %% is the charge in Coulomb of an electrons %%
m_proton=1.67*(10^-27);          %% is the mass in kg of a protons %%
m_neutron=1.67*(10^-27);         %% is the mass in kg of a neutron %%
m_electron=0.00091*(10^-27);     %% is the mass in kg of an electron %%
v_particle=28*(10^6);            %% is the particle velocity in m/s %%
L_distance=3;                    %% is the distance in m between the source and target. This distance is crossed by the particle %%
Particle_Crossing_time=L_distance/v_particle; %% is the L_distance crossing time pf the particle %%
EM_frequency=450*(10^6);         %% is the circularized Electromagnetic frequency wave in Hz %%
P_tx=150;                        %% is the circularized Electromagnetic power at the antenna input in W %%
GdB_ant=12;                      %% is the antenna gain in dB %%
c=3*(10^8);                      %% is light velocity in an eampty space %%

A=(((q_protons*num_protons+q_electrons*num_electrons)*((60*P_tx*(10^(GdB_ant/10)))^0.5))/(m_proton*num_protons+m_neutron*num_neutrons+m_electron*num_electrons))*(1+v_particle/c);
%% is the constant A which is multiplied by the rest of the function %%%
omega=2*pi*EM_frequency*(1+v_particle/c);
```

```
%% is the pulsation of the function we want to integrate %%%
%  the function we want integrate f(t)=(A/(L_distance-v_particle*t))*sin(omega*t);

%%  the following routines is used to compute a double  numerical integration of a certain function f(t)  %%

dt=10^-13;                  % is the integration step expressed in radiant   %%
niter=int32(Particle_Crossing_time/dt);
%%    is the integrations number, expressed in radiants, equal to the crossing time divided by the resolution dt %%

%%% First Loop Cycle %%%
t=0;
f1(1)=(A/(L_distance-v_particle*t))*cos(omega*t);
F1(1)=0;
FF1(1)=0;
f2(1)=(A/(L_distance-v_particle*t))*sin(omega*t);
F2(1)=0;
FF2(1)=0;
ascisse(1)=t;
t=t+dt;

%%% Subsequent Loop Cycle %%%
for i=2:1:niter;
      f1(i)=(A/(L_distance-v_particle*t))*cos(omega*t);
      F1(i)=f1(i)*dt+F1(i-1);
      FF1(i)=F1(i)*dt+FF1(i-1);
      f2(i)=(A/(L_distance-v_particle*t))*sin(omega*t);
      F2(i)=f2(i)*dt+F2(i-1);
      FF2(i)=F2(i)*dt+FF2(i-1);
      ascisse(i)=t;
      t=t+dt;
      Num_iterazioni_=niter   %stampa a video il numero di iterazioni da compiere%
```

```
      Sei_alla_iterazione_num_=i  % stama a video la iterazione corrente %%
end;

for i=1:1:niter;
I1(i)=F1(i);
II1(i)=FF1(i);
I2(i)=F2(i);
II2(i)=FF2(i);

end;

%%  plotting results %%
a1=I1(1:1:niter);
a2=I2(1:1:niter)
c1=II1(1:1:niter);
c2=II2(1:1:niter);
plot(ascisse,c2);
```

8.1.2 MATLAB code for Linear Polarization

```
%%This code has been used to find the particle trajectory on the Experiment in chapter 7 %%
%% Double Numerical Integration LINEAR POLARIZATION %%
%  This method is used to compute a double numerical integration of a certain function %%
%% Input Data %%

num_particles=1;
num_protons=0;
num_neutrons=0;
num_electrons=1;
q_protons=1.6*(10^-19);          %% is the charge in Coulomb of a protons %%
q_electrons=1.6*(10^-19);        %% is the charge in Coulomb of an electrons %%
m_proton=1.67*(10^-27);          %% is the mass in kg of a protons %%
m_neutron=1.67*(10^-27);         %% is the mass in kg of a neutron %%
m_electron=0.00091*(10^-27);     %% is the mass in kg of an electron %%
v_particle=28*(10^6);            %% is the particle velocity in m/s %%
L_distance=3;                    %% is the distance in m between the source and target. This distance is crossed by the particle %%
Particle_Crossing_time=L_distance/v_particle; %% is the L_distance crossing time pf the particle %%
EM_frequency=450*(10^6);         %% is the circularized Electromagnetic frequency wave in Hz %%
P_tx=150;                        %% is the circularized Electromagnetic power at the antenna input in W %%
GdB_ant=12;                      %% is the antenna gain in dB %%
c=3*(10^8);                      %% is light velocity in an eampty space %%
```

```
A=(((q_protons*num_protons+q_electrons*num_electrons)*((60*P_tx*(10^(GdB_an
t/10)))^0.5))/(m_proton*num_protons+m_neutron*num_neutrons+m_electron*num_e
lectrons))*(1+v_particle/c);
%% is the constant A which is multiplied by the rest of the function  %%%
omega=2*pi*EM_frequency*(1+v_particle/c);
%% is the pulsation of the function we want to integrate %%%
%  the function we want integrate is
f1(t)=(A/(L_distance-v_particle*t))*cos(omega*t);

dt=10^-13; %%is the integration step expressed in radiant %%
niter=int32(Particle_Crossing_time/dt);    %%   is the integrations number, expressed
in radiant's, equal to the crossing time divided by the resolution dt %%

%%% First Loop Cycle %%%
t=0;
x=(A/(L_distance-v_particle*t));
y=cos(omega*t);
f1(1)=x*y;
F1(1)=0;
FF1(1)=0;
ascisse(1)=t;
t=t+dt;

%%% Subsequent Loop Cycle %%%
for i=2:1:niter;
    x=(A/(L_distance-v_particle*t));
    y=cos(omega*t);
    f1(i)=x*y;
        if f1(i)>0;
        F1(i)=f1(i)*dt+F1(i-1);
        FF1(i)=F1(i)*dt+FF1(i-1);
        else
```

```
            F1(i)=F1(i-1);
            FF1(i)=F1(i)*dt+FF1(i-1);
        end;
        ascisse(i)=t;
        t=t+dt;
        Num_iterazioni_=niter    %stampa a video il numero di iterazioni da compiere
Sei_alla_iterazione_num_=i    % stampa a video la iterazione corrente %%
end;
%%  plotting results %%
plot(ascisse,FF1);
```

8.2 C code for Circular polarization

```
// this program is used to integrate the motion equations of chapter 6 in CIRCULAR
POLARIZATION
#include <stdio.h>
#include <math.h>
#define TRUE   1
#define FALSE -1
main(int argc, char *argv[]) {
   double pi = M_PI;
   double num_particles=1;
   double num_protons=1;
   double num_neutrons=0;
   double num_electrons=0;
   double q_protons=1.6*(1E-19);       //          %%    is the charge in Coulomb of a
protons      %%
   double q_electrons=1.6*(1E-19);     //          %%    is the charge in Coulomb of an
electrons   %%
   double m_proton=1.67*(1E-27);       //          %%    is the mass in kg of a protons
%%
   double m_neutron=1.67*(1E-27);      //          %%    is the mass in kg of a neutron
%%
```

```
   double m_electron=9.31*(1E-31);    //        %%   is the mass in kg of an electron
%%
   double v_particle=500*(1E3);       //         %%   is the partcle velocity in m/s
%%
   double L_distance=150*(1E9);       //        %%   is the distance in m between the
SUN and MOON.
//                                    This distance is crossed by the particle  %%
   double Particle_Crossing_time=L_distance/v_particle; // %%   is the L_distance
crossing time pf the particle %%
   double EM_frequency=100*(1E6);     //  %%   is the circularized Electromagnetic
frequency wave in Hz  %%
   double P_tx=1000;                  //        %%   is the circularized Electromagnetic
power at the antenna input in W  %%
   double GdB_ant=50;                 //        %%   is the antenna gain in dB  %%
   double c=3*(1E8);                  //        %%   is light velocity in an eampty space
%%
   double                A=(((q_protons*num_protons+q_electrons*num_electrons)*(
pow(60.0*P_tx*pow(10,(GdB_ant/10)),0.5)
))/(m_proton*num_protons+m_neutron*num_neutrons+m_electron*num_electrons))
*(1+v_particle/c);
   // %% is the constant A which is multiplied by the rest of the function  %%%
   double omega=2*pi*EM_frequency*(1+v_particle/c);

// %% is the pulsation of the function we want to integrate %%%
//        %              the          function        we        want        integrate
f1(t)=(A/(L_distance-v_particle*t))*cos(omega*t)  and
//    f2(t)=(A/(L_distance-v_particle*t))*sin(omega*t);
   // %  the following routineis is used to compute a double  numericalintegration of
a certain function f(t)  %
// %
      long double dt=1E-8;                //  %%   is the integration step
//    float inputdt;
//    if (argc == 2) {
```

```
//      sscanf(argv[1],"%e",&inputdt);
//      dt = (double) inputdt;
//   }
//                                                %
   long long int   niter = (Particle_Crossing_time/dt);   // %%   is the integrations number, expressed in radiants, equal to
   // the crossing time divided by the resolution integration step  dt
//%%% First Loop Cycle %%%
   long double t=0;
   double f1;
   double F1;
   double FF1;
   double f2;
   double F2;
   double FF2;
   double A1;
   long long int   passoDecimazioneOutput=1000000LL;
   long long int contatoreDecimazioneOutput;
   double i;
   double k1;
   double omegat;
   double dw;
   double dcrossed_space;
   double crossed_space;

   F1  = 0;
   FF1 = 0;
   F2  = 0;
   FF2 = 0;

// %%% Subsequent Loop Cycle %%%

   int    righe;
```

```
    int    sweep = TRUE;
    int    n_p_plot = 300;
    double margin_n_p_plot_for_rounding = 0.15;  // trunc. effect
    long double base_sweep = exp (log(niter) / (n_p_plot) / (1 +
margin_n_p_plot_for_rounding));
    long double sweep_count = niter;
    long double temp;

    if (sweep == TRUE) {
          righe = (int) n_p_plot; // Dato di input n_p_plot
          passoDecimazioneOutput = sweep_count - sweep_count / base_sweep;
          sweep_count = sweep_count - passoDecimazioneOutput;
          if (sweep_count < 1) sweep_count = 1;
          if (passoDecimazioneOutput < 1) passoDecimazioneOutput = 1;
    } else {
      righe = (int) (niter / passoDecimazioneOutput);
      righe = righe + 1;
    }
    printf("# Generated By: integral.c\n");
    printf("# Step: dt=%e\n", (double) dt);
    if (sweep == TRUE) {
     printf("# Base sweep: %e\n", (double) base_sweep);
     printf("#          Variabile          passoDecimazioneOutput:          %e\n",
(double)passoDecimazioneOutput);
    }
    printf("# name: b\n");
    printf("# type: matrix\n");
    printf("# rows: %d\n", righe);
    printf("# columns: 3\n");
    printf("%e %e %e\n", FF1, FF2, (double)t);
    contatoreDecimazioneOutput = passoDecimazioneOutput;

    omegat         = omega * t;
```

```
dw              = omega * dt;
crossed_space   = v_particle * t;
dcrossed_space  = v_particle * dt;
A1              = A * dt;
// Incrementa Contatori
t=t+dt;
omegat = omegat + dw;  // omega * t
crossed_space = crossed_space + dcrossed_space;
while (t < Particle_Crossing_time) {
   // Calcolo Funzione
   k1  = A1/(L_distance-crossed_space);
   F1  = (k1*cos(omegat))+F1;
   FF1 = (F1*dt)+FF1;
   F2  = (k1*sin(omegat))+F2;
   FF2 = (F2*dt)+FF2;
   // Generazione Output
   contatoreDecimazioneOutput--;
   if (contatoreDecimazioneOutput <= 0) {
     if (k1 !=  HUGE_VAL) printf("%e %e %e\n", FF1, FF2, (double)t);  // In caso
di overflow non generare

     if (sweep == TRUE) {
       // In caso di sweep determina il nuovo passo di decimazione
       passoDecimazioneOutput = sweep_count - floor (sweep_count /
base_sweep);
       sweep_count = sweep_count - passoDecimazioneOutput;
       if (sweep_count < 1) sweep_count = 1;
       if (passoDecimazioneOutput < 1) passoDecimazioneOutput = 1;
     }
     contatoreDecimazioneOutput = passoDecimazioneOutput;
   }
   // Incremento per integrazione iterativa
   t=t+dt;
```

```
        omegat = omegat + dw;  // omega * t
        crossed_space = crossed_space + dcrossed_space;
    }

    if (contatoreDecimazioneOutput != passoDecimazioneOutput)
      if (k1 !=  HUGE_VAL) printf("%e %e %e\n", FF1, FF2, (double)t);

}
```